

## General formulation for the strength of thin-walled cold-formed steel columns under buckling modes interaction

Eduardo de M. Batista<sup>1</sup>, Gustavo Y. Matsubara<sup>2</sup>

### Abstract

The typical cold-formed steel (CFS) members are classified as thin-walled structures, highly susceptible to structural stability phenomena: local (L), distortional (D) and global (G) buckling modes. In addition to the single buckling modes, L, D and G, interactions between the buckling modes may take place depending on the members' geometry and the contribution of the ductility of the material. These interactions may lead to strength erosion that should be considered in structural design, which is mostly performed on the basis of the Direct Strength Method (DSM). In this context, the present research presents a unified approach to predict the post-buckling behavior and the compressive strength of CFS columns, including L, D and LD buckling modes. The proposed approach is based on available experimental data and finite element extensive results of CFS columns, integrating Winter-type equations to a general design proposition for lipped channel, hat, zed and rack columns. Moreover, an introduction to the next stage of the ongoing research is referred, involving the global mode participation and its interaction with local and distortional buckling modes.

### 1. Introduction

The present research aims at developing a unified method to predict the post-buckling behavior and strength and of cold-formed steel (CFS) columns, targeting in new set of design equations that provide sufficiently accurate strength estimates and maintain the easiness of design expressions. The propositions and results presented in the following take into consideration well established and accepted solutions, based on the direct strength method (DSM) principles and rules, as those addressed to single global (G) and local-global (LG) buckling interaction, as well as the single distortional D buckling formulation, presented respectively by Eqs. 1, 2 and 3 ( $f_n = P_n/A$  is the column strength,  $\lambda$ 's,  $f_{cr}$ 's and  $f_y$  are the typical slenderness factors, parametric critical buckling loads  $f_{cr} = P_{cr}/A$  and yield stress of the material, respectively). These are the solutions included up to now in the standards and codes AISI (2016), AS/NZS (2018) and ABNT (2010). European design rules for CFS members EN-3 (2006) are not based on the same principles and because of this are not included in the present considerations. In addition to the phenomena predicted by the Eqs. 1, 2 and 3, CFS are susceptible to instabilities involving buckling interaction LD, DG and LDG.

<sup>1</sup> [eduardo.batista@luc.edu.br](mailto:eduardo.batista@luc.edu.br), [gustavo.matsubara@luc.edu.br](mailto:gustavo.matsubara@luc.edu.br), [eduardo.batista@luc.edu.br](mailto:eduardo.batista@luc.edu.br), [gustavo.matsubara@luc.edu.br](mailto:gustavo.matsubara@luc.edu.br)

<sup>2</sup> [gustavo.matsubara@luc.edu.br](mailto:gustavo.matsubara@luc.edu.br), [eduardo.batista@luc.edu.br](mailto:eduardo.batista@luc.edu.br), [gustavo.matsubara@luc.edu.br](mailto:gustavo.matsubara@luc.edu.br), [eduardo.batista@luc.edu.br](mailto:eduardo.batista@luc.edu.br)

$$f_{nG} = \begin{cases} (0.658\lambda_G^2) f_y & \text{if } \lambda_G \leq 1.50 \\ \left(\frac{0.877}{\lambda_G^2}\right) f_y & \text{if } \lambda_G > 1.50 \end{cases} \quad \text{with } \lambda_G = \sqrt{\frac{f_y}{f_{crG}}} \quad (1)$$

$$f_{nLG} = \begin{cases} f_{nG} & \text{if } \lambda_{LG} \leq 0.776 \\ \left[1 - \left(\frac{0.15}{\lambda_{LG}^{0.80}}\right)\right] \frac{f_{nG}}{\lambda_{LG}^{0.80}} & \text{if } \lambda_{LG} > 0.776 \end{cases} \quad \text{with } \lambda_{LG} = \sqrt{\frac{f_{nG}}{f_{crL}}} \quad (2)$$

$$f_{nD} = \begin{cases} f_y & \text{if } \lambda_D \leq 0.561 \\ \left[1 - \left(\frac{0.25}{\lambda_D^{1.20}}\right)\right] \frac{f_y}{\lambda_D^{1.20}} & \text{if } \lambda_D > 0.561 \end{cases} \quad \text{with } \lambda_D = \sqrt{\frac{f_y}{f_{crD}}} \quad (3)$$

Studies on LD interaction phenomenon were performed by Dinis *et al.* (2007), Silvestre *et al.* (2012), Young *et al.* (2013), Dinis *et al.* (2014), Dinis and Camotim (2015), Martins *et al.* (2015b), Martins *et al.* (2015b), Martins *et al.* (2017a), Martins *et al.* (2017b), Matsubara *et al.* (2019) and Batista *et al.* (2019) and Campos (2020). These studies contributed to the improvement of the comprehension of the LD coupled buckling, based on experimental and numerical results.

Batista *et al.* (2019) developed alternative solution for CFS lipped channel columns under LD interaction, based on the DSM formulation and taking into account the classical Winter-type equation Eq. 4 for the column strength, with the coefficients  $A$  and  $B$  shown in Eqs. 5 and 6, defined on the basis of numerical results developed by Matsubara *et al.* (2019). The proposed approach was validated with the help of available experimental tests data and numerical (FEM) sets of columns results, produced by recognized research activities. In this proposed approach  $R_{\lambda DL} = \lambda_D/\lambda_L$  and  $\lambda_{maxLD} = \max(\lambda_L, \lambda_D)$  are respectively the LD slenderness ratio and the maximum (L or D) slenderness factor of the column. As cited above, the proposed formulation for LD interaction of CFS columns was originally formulated and calibrated for lipped channel CFS. It is worthy of citation that the solution expressed by Eqs. 4, 5 and 6 is the strength surface that bridges a new DSM solution integrating L, D and LD buckling modes, since no effect of the global modes (flexural or flexural-torsional) develops along the loading equilibrium path of the column: this condition was achieved by taking columns with (approximately)  $\lambda_G/\lambda_{maxLD}$  lower than 0.40.

$$f_{nLD} = \left[1 - \frac{A}{\lambda_{maxLD}^B}\right] \frac{f_y}{\lambda_{maxLD}^B} \quad \text{with } \lambda_{maxLD} = \max\{\lambda_L; \lambda_D\} \quad \text{and} \quad \frac{f_{nLD}}{f_y} \leq 1.00 \quad (4)$$

$$A = \begin{cases} 0.15 & \text{if } R_{\lambda DL} < 0.80 \\ 0.40R_{\lambda DL} - 0.17 & \text{if } 0.80 \leq R_{\lambda DL} \leq 1.05 \\ 0.25 & \text{if } R_{\lambda DL} > 1.05 \end{cases} \quad (5)$$

$$B = \begin{cases} 0.80 & \text{if } R_{\lambda DL} < 0.45 \\ -2.26 R_{\lambda DL}^2 + 4.06 R_{\lambda DL} - 0.57 & \text{if } 0.45 \leq R_{\lambda DL} \leq 1.05 \\ 1.20 & \text{if } R_{\lambda DL} > 1.05 \end{cases} \quad (6)$$

DG interaction was recently investigated by Martins *et al.* (2018), concluding that this type of interaction can be considered with the traditional DSM's global buckling strength solution for steel columns Eq. 1. A more recent research conducted by Lazzari and Batista (2020) confirmed this assumption with the help of numerical and experimental results.

Lastly, the triple LDG interaction has been mainly studied for lipped channels columns. Numerical studies (*e.g.* Cava *et al.* (2016), Dinis *et al.*, 2012 and 2017) concluded that this interaction is safely handled by the current LG approach, Eq. 2. The same assumption was confirmed by experimental campaigns, Santos *et al.* (2012, 2014) and Young *et al.* (2017), compressive tests of lipped channel columns specifically designed to study the LDG interaction.

Taking into account these results, as well as a large number of additional results and experience accumulated during the last decades regarding the buckling interaction effects for the design of CFS columns, a complete set of design equations including all the possible L, D and G modes interaction would be possible. For this, it was decided to take the following principles: (i) DSM-based procedure; (ii) respect the well-established and already traditional design solutions and equations (*e.g.*, for LG and D buckling, Eqs. 1 to 3); (iii) keep simple and easy-to-apply procedure, avoiding "black box" procedures, with hidden structural meaning and far from the comprehension by engineers; (iv) the slenderness factor  $\lambda_i = (f/f_{cri})^{0.5}$  is the basis of the strength equations, according to the design methods and practical experience usually found in codes and standards, with "i" as the reference buckling mode, L, D or G;  $f$  can be the steel yield stress ( $f_y$ ) or a different limiting stress (*e.g.*  $f_{nG}$  for global slenderness factor);  $f_{cri}=P_{cri}/A$  is the parametric critical buckling axial load referred to L, D or G (flexural or flexural-torsional) mode. In this condition, two different approaches are presented in the following, including their calibration results with the help of available numerical and experimental results in the literature.

## 2. LD interaction approach for usual CFS

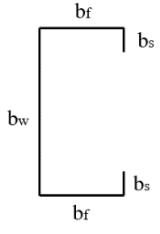
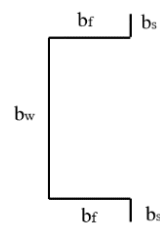
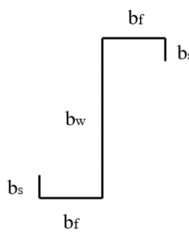
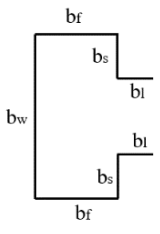
In order to extend the solution proposed by Batista *et al.* (2019) - CFS lipped channel columns - to other usual CFS, it was added a correction factor  $S_n$  for each type of section, as presented by Eq. 7. The coefficients A and B are the same previously proposed by the authors, Eqs. 5 and 6.

$$f_{nLD} = \left[ 1 - \frac{A}{\lambda_{maxLD}^B} \right] \frac{S_n f_y}{\lambda_{maxLD}^B} \text{ with } \lambda_{maxLD} = \max\{\lambda_L; \lambda_D\} \text{ and } \frac{f_{nLD}}{f_y} \leq 1.00 \quad (7)$$

The calibration process of the correction factor  $S_n$  was carried out with the help of the numerical results presented by Dinis and Camotim (2015), Martins *et al.* (2015b), Campos (2020). The calibrated results of the correction factor  $S_n$  are summarized in Table 1.

Table 2 shows that the proposed  $f_{nLD}$  approach (Eqs.7, 5 and 6) displays quite accurate results of the comparison with finite element method (FEM) computed strength  $f_u= P_u/A$ . The results of the Load and Resistance Factor Design (LRFD) resistance factor obtained for sets of Lipped Channel, Hat, Zed and Rack numerical results are in accordance with the North American Specification (AISC, 2016),  $\phi \geq 0.85$ .

Table 1: Calibrated  $S_n$  values for different CFS types.

CFS Types	$S_n$
<p>Lipped Channel</p> 	$S_n = 1.00$
<p>Hat</p> 	$R_{\lambda_{DL}} < 0.45 \quad S_n = 1.00$ $0.45 \leq R_{\lambda_{DL}} \leq 1.05$ $S_n = -0.98 R_{\lambda_{DL}}^2 + 1.47 R_{\lambda_{DL}} + 0.54$ $R_{\lambda_{DL}} > 1.05 \quad S_n = 1.00$
<p>Zed</p> 	$R_{\lambda_{DL}} < 0.45 \quad S_n = 1.00$ $0.45 \leq R_{\lambda_{DL}} \leq 1.00$ $S_n = -1.34 R_{\lambda_{DL}}^2 + 1.95 R_{\lambda_{DL}} + 0.39$ $R_{\lambda_{DL}} > 1.00 \quad S_n = 1.00$
<p>Rack</p> 	$R_{\lambda_{DL}} < 0.45 \quad S_n = 1.00$ $0.45 \leq R_{\lambda_{DL}} \leq 0.95$ $S_n = -1.12 R_{\lambda_{DL}}^2 + 1.57 R_{\lambda_{DL}} + 0.52$ $R_{\lambda_{DL}} > 0.95 \quad S_n = 1.00$

In addition, Figure 1 shows the comparison between the experimental strength of lipped channel columns  $f_{uexp} = P_{exp}/A$  and  $f_{nLD}$  approach (Eqs.7, 5 and 6). In order to avoid interference of the global mode, columns with  $\lambda_G/\lambda_{maxLD} \leq 0.40$  were selected. The experimental LFRD resistance factor obtained is in line with the North American Specification,  $\phi > 0.87$ . For  $R_{\lambda_{DL}} \leq 0.45$ ,  $f_{nLD}$  approach converges to local Winter-type equation,  $f_{nL}$ , with  $A = 0.15$  and  $B = 0.80$ .

Table 2: Comparison between FEM strength results  $f_u$  and  $f_{nLD}$  approach (Eqs. 7, 5 and 6).

CFS Type	Number of tests	$f_u / f_{nLD}$				
		Range	Mean	St. Dev.	Coef.Var.	$\phi$
Lipped Channel <sup>1</sup>	593	0.77 - 1.26	1.02	0.08	0.08	0.88
Hat <sup>2</sup>	531	0.86 - 1.23	1.01	0.06	0.06	0.90
Zed <sup>2</sup>	554	0.85 - 1.27	1.02	0.07	0.07	0.90
Rack <sup>3</sup>	595	0.83 - 1.28	1.01	0.09	0.09	0.88

<sup>1</sup> Numerical results, Silvestre *et al.* (2012), Dinis and Camotim (2015), Martins *et al.* (2015b), Matsubara *et al.* (2019) and new original results of the present authors.

<sup>2</sup> Numerical results, Dinis and Camotim (2015), Martins *et al.* (2015b).

<sup>3</sup> Numerical results, Dinis and Camotim (2015), Martins *et al.* (2015b) and Campos (2020).

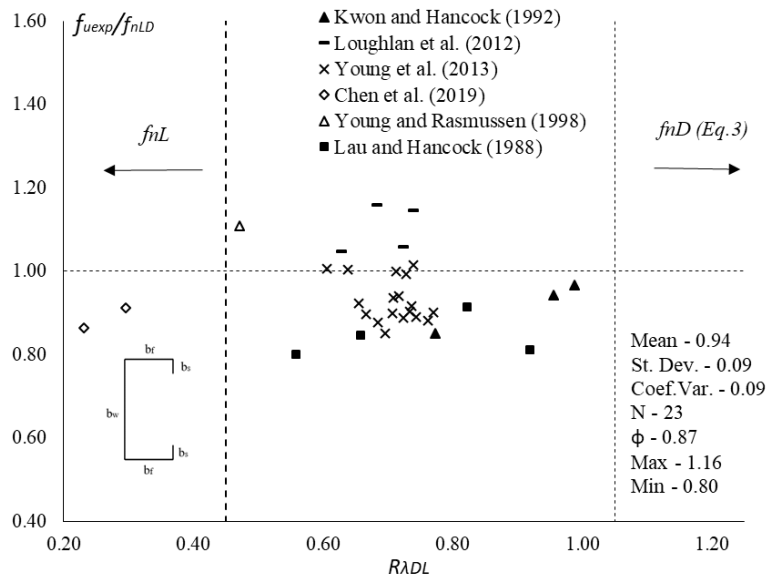


Figure 1: Comparison between experimental results and  $f_{nLD}$  approach (Eqs. 7, 5 and 6) for lipped channel columns.

### 3. Assessment of the global buckling mode

The assessment of global mode influence in the  $f_{nLD}$  approach (Eqs. 7, 5 and 6) is illustrated in Figs. 2 and 3. Numerical and experimental column strength results are respectively  $f_u$  and  $f_{uexp}$ . For both sets of experimental and numerical results in Figs. 2 and 3, respectively, the higher the slenderness ratio  $\lambda_G/\lambda_{maxLD}$  the lower the results of the comparison between the sets of columns structural strength with the proposed design equations ( $f_{uexp}/f_{nLD}$  and  $f_u/f_{nLD}$ ), diverging from the target expected results, with the mean value of  $f_u/f_{nLD}$  and  $f_{uexp}/f_{nLD}$  around unity. Furthermore, one may note that  $f_{nLD}$  (Eq.7) approach confirms accurate results in the range of  $\lambda_G/\lambda_{maxLD} < 0.40$ . These results indicate the growing presence of the global buckling mode participation in the column behavior the higher is the slenderness ratio  $\lambda_G/\lambda_{maxLD}$ .

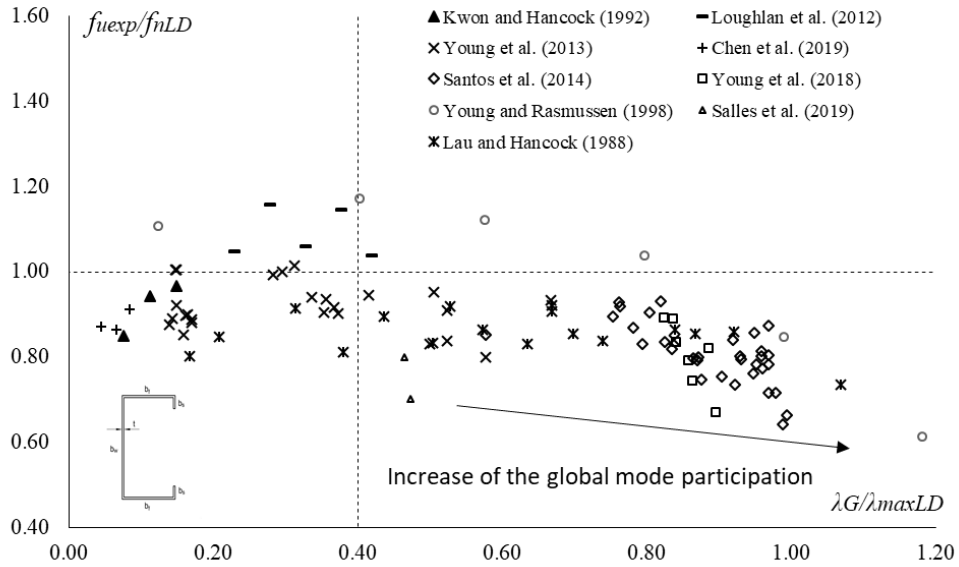


Figure 2: Increase of the global buckling mode participation – lipped channel experimental results.

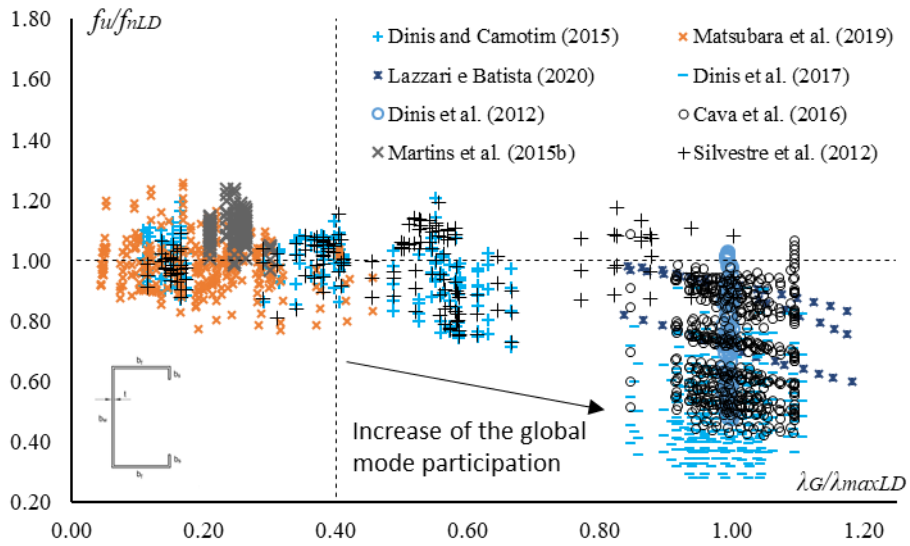


Figure 3: Increase of the global buckling mode participation – lipped channel numerical results.

Finally, a more general approach to estimate the failure load of CFS columns, including L, D and G modes relevant participation, is under development with promising results. This can be achieved with additional parameter in the tested sets of equations (Eqs. 7, 5 and 6) that introduces the global mode contribution, according with the slenderness ratio  $\lambda_G/\lambda_{maxLD}$ .

#### 4. Final remarks

The results presented in this paper are aligned with previous results of Matsubara *et al.* (2019) and Batista *et al.* (2020). The column strength  $f_{nLD}$  (Eq. 7, 5 and 6) approach proved to be easy to apply and accurate for the design purposes of CFS columns. The proposed solution was extended for the most usual CFS section types (lipped channel, hat, zed and rack).

The present research is on track to find a unified solution to deal with the buckling modes interaction LD, LG, DG, LDG, keeping the widely accepted DSM-based principles and typical equations (namely the Winter equation). A parametric study is underway to improve the proposed solution, incorporating the interaction of the global mode with local and distortional buckling modes.

#### Acknowledgments

The second author acknowledges the financial support of CNPq, National Council for Scientific and Technological Research, through scholarship for his Doctoral degree research.

#### References

- American Iron and Steel Institute 2016, North American Specification for the Design of Cold-Formed Steel Structural Members (AISI S100-16), Washington, DC.
- Australian/New Zealand Standard 2018, AS/NZS 4600:2018 – Cold-Formed Steel Structures, Sydney-Wellington.
- Batista, E.M, Matsubara, G. Y., Franco, J.M.S. (2019). “Local-distortional buckling interaction of cold-formed steel columns design approach.” *International Colloquium on Stability and Ductility of Steel Structures*, Prague, Czech Republic. 164-172.
- Brazilian Association of Standards (ABNT) 2010, Brazilian standard on design of cold-formed steel structures (NBR 14762:2010), Rio de Janeiro, Brazil (Portuguese).
- Campos, R.G.A. (2020). “Análise da interação entre os modos de flambagem local e distorcional em perfis de aço formados a frio com seção rack sob compressão axial.” Master’s Dissertation, University of Rio de Janeiro, 2020, p. 108.
- Cava, D., Camotim, D., Dinis, P.B., Madeo, A. (2016). “Numerical Investigation and Direct Strength Design of Cold-formed Steel Lipped Channel Columns Experiencing Local-distortional-global Interaction.” *Thin-Walled Structures*, 105 (8) 231-247.
- Dinis, P.B., Batista, E.M., Camotim, D., Santos, E.S. (2012). “Local– distortional–global interaction in lipped channel columns: Experimental results, numerical simulations and design considerations.” *Thin-Walled Structures* 61 2–13.
- Dinis, P.B., Camotim, D. (2015). “Cold-formed steel columns undergoing local-distortional coupling: Behaviour and direct strength prediction against interactive failure.” *Thin-Walled Structures* 101 181-204.
- Dinis, P.B., Camotim, D., Silvestre, N. (2007). “FEM-based analysis of the local-plate/distortional mode interaction in cold-formed steel lipped channel columns.” *Computers & Structures*, 85 (19-20) 1461-1474.
- Dinis, P.B., Young, B., Camotim, D. (2014). “Local–distortional interaction in cold-formed steel rack-section columns.” *Thin-Walled Structures*, 81 185-194.
- Chen, J., Chen, M., Young, B. (2019). “Compression Tests of Cold-Formed Steel C- and Z-Sections with Different Stiffeners.” *Journal of Structural Engineering*, 145 (5) 1-10.
- EUROCODE 3 2006, Design of steel Structures – Part 1-3: General rules – Supplementary rules for cold-formed members and sheeting, European Standard.
- Kwon, Y.B., Hancock, G.J. (1992). “Tests of Cold-Formed channels with Local and Distortional Buckling.” *Journal of Structural Engineering*, 118, 1786-1803.
- Lau, S.C.W., Hancock, G.J. (1988). “Distortional Buckling Tests of Cold-formed Channel Sections.” *Proceedings of the 9<sup>th</sup> International Specialty Conference on Cold-Formed Steel Structures*, St. Louis, MO 45-73.
- Lazzari, J.A., Batista, E.M. (2020). “Distortional-Global Buckling Interaction Relevance in Cold-Formed Steel Lipped Channel Columns.” *Latin American Journal of Solids and Structures* 17 (9) 1–30.

- Loughlan, J., Yidris, N., Jones, K. (2012). "The failure of thin-walled lipped channel compression members due to coupled local-distortional interactions and material yielding." *Thin-Walled Structures* 61 14–21.
- Matsubara, G.Y., Batista, E.M., Salles, G.C. (2019). "Lipped channel cold-formed steel columns under local-distortional buckling mode interaction." *Thin-Walled Structures* 137 (4) 251–270.
- Martins, A.D., Camotim, D., P.B. (2015a). "Local-Distortional Interaction in Cold-formed Steel Columns: Mechanics, Testing, Numerical Simulation and Design." *Structures* 4, 38-57.
- Martins, A.D., Camotim, D., Dinis, P.B. (2018). "On the distortional-global interaction in cold-formed steel columns: Relevance, post-buckling behaviour, strength and DSM design." *Journal of Constructional Steel Research*, 145 (6) 449–470.
- Martins, A.D., Camotim, D., Dinis, P.B. (2017a). "On the direct strength design of cold-formed steel columns failing in local-distortional interactive modes." *Thin-Walled Structures* 120 (11) 432–445.
- Martins, A.D., Camotim, D., Dinis, P.B. (2017b). "Behaviour and DSM design of stiffened lipped channel columns undergoing local-distortional interaction." *Journal of Constructional Steel Research*, 128, 99-118.
- Martins, A.D., Dinis, P.B., Camotim, D., Providencia, P. (2015b). "On the relevance of local distortional interaction effects in the behaviour and design of cold-formed steel columns." *Computers & Structures* 160 (1) 57–89.
- Salles, G. C.; Batista, E.M.; Matsubara, G. Y. (2019). "Evidências experimentais da interação entre modos de flambagem local e distorcional em perfis de aço formado a frio sob compressão axial." *Oitavo Congresso Latino Americano de Construção Metálica*, São Paulo, Brazil. 359-373.
- Santos, E.S., Batista, E.M., Camotim, D. (2012). "Experimental investigation concerning lipped channel columns undergoing local–distortional–global mode interaction." *Thin-Walled Structures* 54 19–34.
- Santos, E.S., Batista, E.M., Camotim, D. (2014). "Cold-formed steel columns under L-D-G interaction: Experimental investigation." *Steel Construction* 7 (3) 193–198.
- Silvestre, N., Camotim, D., Dinis, P.B. (2012). "Post-buckling behaviour and direct strength design of lipped channel columns experiencing local/distortional interaction." *Journal of Constructional Steel Research*, 73 (6) 12–30.
- Young, B., Dinis, P.B., Camotim, D. (2017). "CFS lipped channel columns affected by L-D-G interaction. Part I: Experimental investigation." *Computers & Structures* 207 (9) 219–232.
- Young, B., Rasmussen, K.J.R. (1998). "Design of lipped channel columns", *Journal of Structural Engineering*, 124 (2), 140–148.
- Young, B., Silvestre, N., Camotim, D. (2013). ". Cold-Formed Steel Lipped Channel Columns Influenced by Local-Distortional Interaction: Strength and DSM Design." *Journal of Structural Engineering* 139, 1059-1074.

## Fixed-ended stainless steel equal-leg angle section columns – behaviour and design

Behnam Behzadi-Sofiani<sup>1</sup>, Leroy Gardner<sup>2</sup>, M. Ahmer Wadee<sup>3</sup>

### Abstract

The stability and design of fixed-ended stainless steel equal-leg angle section members subjected to axial compression are studied herein. Existing experimental data on stainless steel equal-leg angle section columns collected from the literature are used for the validation of numerical (shell finite element) models, developed within the commercial package ABAQUS. Validation is performed by means of comparisons between the test and numerical results, considering ultimate loads, failure modes and the load-deformation responses, all of which are shown to be generally in good agreement. A numerical parametric study is then presented considering angle section columns in the three main families of stainless steel (austenitic, ferritic and duplex) with a wide range of slenderness values. The behaviour and normalised load-carrying capacity of the studied members is shown to be dependent on not only the column slenderness, but also the ratio of the elastic torsional-flexural buckling load to the elastic minor-axis flexural buckling load. Finally, a design approach recently proposed for carbon steel angle section columns is extended for application to stainless steel and verified against the experimental and numerical results. The proposed approach offers substantially improved accuracy and consistency in strength predictions compared to the existing codified design rules.

### 1. Introduction

Angle section compression members feature in a range of structures, including towers and trusses, and in the bracing of buildings and bridges. Although angles have been studied since the 1920s (Stang & Strickenberg 1922), their complex mechanical behaviour continues to pose challenges, and current structural design provisions in international standards are known to have limitations (Behzadi-Sofiani et al. 2021, Dinis and Camotim 2015, Rasmussen 2005). New resistance functions for carbon steel angle section columns in the American (Dinis and Camotim 2015) and European (Behzadi-Sofiani et al. 2021) design frameworks have been recently developed, leading to substantial improvements in the accuracy and consistency of capacity predictions.

Building on this previous work, the aim of the present paper is to develop a new approach to the design of stainless steel equal-leg angle section columns suitable for incorporation into EN 1993-1-4 (2006) and to assess the accuracy of the proposals.

<sup>1</sup> Behnam Behzadi-Sofiani, MSc, PhD, Senior Lecturer, School of Mechanical Engineering, LUT, 11-010, ul. Żytkiewicza 3, 91-348 Łódź, Poland

<sup>2</sup> Leroy Gardner, MSc, PhD, Senior Lecturer, School of Mechanical Engineering, LUT, 11-010, ul. Żytkiewicza 3, 91-348 Łódź, Poland

<sup>3</sup> M. Ahmer Wadee, MSc, PhD, Senior Lecturer, School of Mechanical Engineering, LUT, 11-010, ul. Żytkiewicza 3, 91-348 Łódź, Poland

## 2. Review of previous research

Tests on fixed-ended stainless steel angle section columns have been reported by Menezes et al. (2019), Liang et al. (2019), Sun et al. (2019), Zhang et al. (2019), Sarquis et al. (2020) and Sirqueira et al. (2020). Design rules for stainless steel angle section columns are included in a number of international standards, including EN 1993-1-4 (2006), SEI/ASCE-8 (2002) and AS/NZS4673 (2001). Liang et al. (2019) and Zhang et al. (2019) investigated the accuracy of EN 1993-1-4 (2006), SEI/ASCE-8 (2002) and AS/NZS4673 (2001) in determining the ultimate capacity for hot-rolled and cold-formed stainless steel equal-leg angle section columns; highly conservative with scattered predictions were revealed. Zhang et al. (2019) also studied the accuracy of the direct strength method (DSM) based design rules developed by Dinis and Camotim (2015); the strength predictions were found to be accurate and consistent, though, owing to the fact that the provisions were established for carbon steel rather than stainless steel angles, with a large portion of the results on the unsafe side. Menezes et al. (2019), Sun et al. (2019), Sarquis et al. (2020) and Sirqueira et al. (2020) evaluated the accuracy of EN 1993-1-4 (2006) in predicting the strength of stainless steel angle section columns, revealing undue conservatism. Menezes et al. (2019) and Sarquis et al. (2020) developed new design proposals based on EN 1993-1-4 (2006). Sun et al. (2019), alongside Sirqueira et al. (2020), showed that the continuous strength method (CSM) capacity predictions were more accurate and consistent than EN 1993-1-4 (2006). In the present study, numerical models are validated and used to perform a parametric study and new structural design rules are developed. The new design proposals are shown to offer substantially more accurate and consistent resistance predictions than the existing rules given in Eurocode 3.

## 3. Numerical modelling

The commercial software ABAQUS was used herein to create finite element (FE) models to simulate the mechanical behaviour of stainless steel equal-leg angle section members under axial compression. Validation of the FE models against existing experimental data on stainless steel equal-leg angle section columns is first presented. A parametric study is then conducted to investigate the behaviour of equal-leg angle section columns of different stainless steel grades and geometries.

### 3.1. General modelling assumptions

The general modelling assumptions are described in the current section. A 4-noded shell element with reduced integration, 6 degrees of freedom (3 translational and 3 rotational) at each node, designated S4R in the ABAQUS (2016) element library, was employed to model the angle section members. Both hot-rolled and cold-formed angles were modelled following the general approach employed by Behzadi-Sofiani et al. (2020). To model the axial load applied to the members, a longitudinal displacement was imposed at one end through a reference point that was free to move longitudinally. The geometrically and materially nonlinear analyses were executed using the Riks arc-length method (Riks 1979).

For validation of the FE models, a series of experiments on stainless steel angle section columns were simulated (see Section 3.2). The measured geometric properties and stress-strain curves were employed in the analyses. For the cases in which the full stress-strain curves were not reported, and throughout the parametric study, the two-stage Ramberg-Osgood material model (Arrayago et al. 2015), with measured or defined values for the key mechanical properties, was utilised. A Poisson's ratio of 0.3 in the elastic range was assumed in all cases. The material properties were input into ABAQUS in the form of true stress and true plastic strain, converted from the measured engineering stress and strain values. For the hot-rolled stainless steel angles, a bilinear residual stress distribution with a peak value of 70 MPa, constant with thickness and leg width, was employed (Behzadi-Sofiani et al. 2021). For the cold-formed stainless steel angles, the dominant bending residual stresses were assumed to be inherently captured in the stress-strain curves (Jandera et al. 2008) and were therefore not explicitly defined.

For the validation study, if reported, the measured amplitude and direction of initial imperfections were used. However, where measured data were not available, and throughout the parametric study, a sinusoidal half wave function over the member length  $L$  with an amplitude of  $L/1000$  at midspan was adopted about both principal axes for the initial bow imperfections. The direction of the minor-axis bow imperfection was chosen to give the lowest resistance, which was consistently towards the tips of the cross-section legs. A similar shape was also adopted for the initial twist with an amplitude of  $\vartheta = \tan^{-1}(L/1000b)$ , where  $b$  is the leg width, at midspan. Boundary conditions were applied to the end supports through kinematic coupling constraints to link all degrees of freedom of the member end-nodes to two reference points. Fixed-ended boundary conditions were created by restraining the necessary degrees of freedom at the reference points. By employing kinematic coupling constraints, warping was also prevented at both ends.

### 3.2. Validation

The FE models were validated against a total of 122 experiments on stainless steel angle section columns from the literature (Menezes et al. 2019, Liang et al. 2019, Sun et al. 2019, Zhang et al. 2019, Sarquis et al. 2020, Sirqueira et al. 2020, Zhang et al. 2020a, Zhang et al. 2020b, Dobric et al. 2020, Zhang et al. 2021); a summary of the comparisons between the FE model ultimate loads and those obtained experimentally is presented in Table 1. Overall, there is good agreement between the test and FE ultimate loads for both fixed-ended (F) and cylindrically-pinned (CP) boundary conditions (B/C) and both considered manufacturing processes (hot-rolling and cold-forming) with a mean  $N_{u,FE}/N_{u,Test}$  ratio (where  $N_{u,FE}$  and  $N_{u,Test}$  are the FE and test ultimate loads, respectively) of 1.00 and a coefficient of variation (CoV) of 0.08.

Table 1: Summary of comparisons of FE model ultimate loads  $N_{u,FE}$  with those obtained experimentally  $N_{u,Test}$ .

Source	Manufacturing process	B/C	No. of tests	$N_{u,FE}/N_{u,Test}$			
				Mean	CoV	Min	Max
Menezes et al. (2019)		F	13	1.04	0.06	0.96	1.16
Liang et al. (2019)		F	16	1.01	0.04	0.91	1.09
Sun et al. (2019)		F	10	1.00	0.07	0.92	1.12
Sarquis et al. (2020)	Hot-rolling	F	10	0.98	0.07	0.90	1.09
Sirqueira et al. (2020)		F	18	0.96	0.05	0.87	1.07
Zhang et al. (2020a)		CP	12	0.98	0.06	0.91	1.09
Zhang et al. (2021)		CP	12	0.98	0.04	0.93	1.03
Zhang et al. (2019)		F	16	1.00	7.00	0.92	1.12
Zhang et al. (2020b)	Cold-forming	CP	4	0.99	0.05	0.90	1.50
Dobric et al. (2020)		F	3	1.12	0.02	1.10	1.15
Dobric et al. (2020)		CP	8	1.02	0.22	0.71	1.29
Total			122	1.00	0.08	0.71	1.29

### 3.3. Parametric study

Following validation of the numerical models, a parametric study was conducted considering different material properties and a wide range of cross-section geometries and member lengths. The two-stage Ramberg-Osgood material model was used in combination with the standardised material properties proposed by Afshan et al. (2019). For the cold-formed members, an enhanced strength, calculated using the predictive model presented in (Rossi et al. 2013), was applied to the corner region of the angles. A total of 1146 FE results was generated across a range of geometric properties. The parametric study results for the fixed-ended hot-rolled stainless steel equal-leg angle section columns are presented in Fig. 1, where the buckling reduction factor  $\chi = N_u / A f_y$  (where  $N_u$  is the ultimate load obtained from the FE models,  $A$  is the cross-section area and  $f_y$  is the material yield strength) is plotted against the corresponding normalised slenderness. For reference, the Eurocode 3 (EC3) local (for single outstand

flanges from EN 1993-1-4 (2006)) and flexural (from EN 1993-1-4 (2006)) buckling curves are also shown, corresponding to the torsional and minor-axis flexural buckling modes, respectively, for angle section columns. The results are analysed and discussed in the following section.

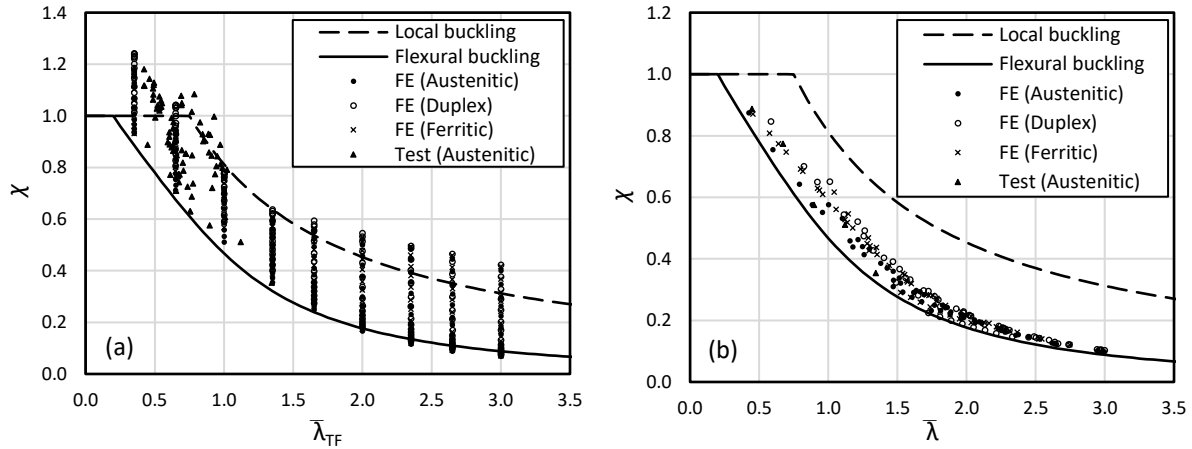


Figure 1: Comparison of test and FE results for fixed-ended hot-rolled austenitic, ferritic and duplex stainless steel equal-leg angle section columns where (a) torsional-flexural buckling and (b) minor-axis flexural buckling are critical against EC3 buckling curves.

#### 4. Analysis and discussion of results

The assembled experimental and numerical data are analysed and discussed in the current section. It can be seen from Fig. 1a that, where torsional-flexural buckling is critical, stainless steel angle section columns with the same slenderness can have very different buckling reduction factors. This contrasts with the existing EC3 design approach, where angle section columns with the same member slenderness have the same member buckling reduction factor because, regardless of the critical buckling mode, the flexural buckling curve is always applied. Similar trends in results have been seen for steel equal-leg angle section columns in Behzadi-Sofiani et al. (2021). The vertical spread of data in Fig. 1a is caused by the changing post-buckling stability with the  $N_{cr,TF}/N_{cr,F,v}$  ratio, where  $N_{cr,TF}$  and  $N_{cr,F,v}$  are the torsional-flexural and minor-axis flexural elastic buckling loads, respectively. When torsional-flexural buckling is critical (Fig. 1a), for the same slenderness  $\bar{\lambda}_{TF}$ , the  $N_{cr,TF}/N_{cr,F,v}$  ratio can vary between zero (indicating torsional-dominant buckling with plate-like behaviour and corresponding to the high data points on the graph) and 1.0 (denoting the transition point from torsional-flexural buckling to minor-axis flexural buckling and corresponding to the low data points on the graph). For  $N_{cr,TF}/N_{cr,F,v}$  ratios greater than 1.0, minor-axis flexural buckling becomes critical, for which the results are presented in Fig. 1b. In Fig. 1a, the top data points correspond to the stainless steel angle section columns with the lowest  $N_{cr,TF}/N_{cr,F,v}$  ratio (0.01) and lie in the region of the local buckling curve, set out in EN 1993-1-4 (2006), which reflects the beneficial stable post-buckling behaviour of plates; as this ratio increases, the reduction factor decreases and converges to the flexural buckling curve, which reflects the approximately neutral post-buckling stability of columns failing in this mode. For  $N_{cr,TF}/N_{cr,F,v}$  ratios greater than 1.0, the corresponding reduction factors generally follow the column flexural buckling curve, as shown in Fig. 1b.

#### 5. Design of stainless steel equal-leg angle section columns (Eurocode 3 – EN 1993-1-4)

Stainless steel members are designed according to the rules set out in EN 1993-1-4 (2006). Comparisons of the test and FE ultimate capacities  $N_u$  with the resistances predicted by EC3  $N_{b,EC3}$  are made for hot-rolled stainless steel angles in Fig. 2. The current EC3 provisions are extremely conservative in predicting the strength of stainless steel equal-leg angle section columns where torsional-flexural buckling is critical. This can be explained, as described by Dinis et al. (2012) and Behzadi-Sofiani et al. (2021), by the double-

counting of the same buckling mode in the local and member buckling checks and the failure to recognise the stable post-buckling behaviour in the member-level buckling curves for torsional-flexural buckling. New design proposals are presented in the subsequent section to address and resolve this issue.

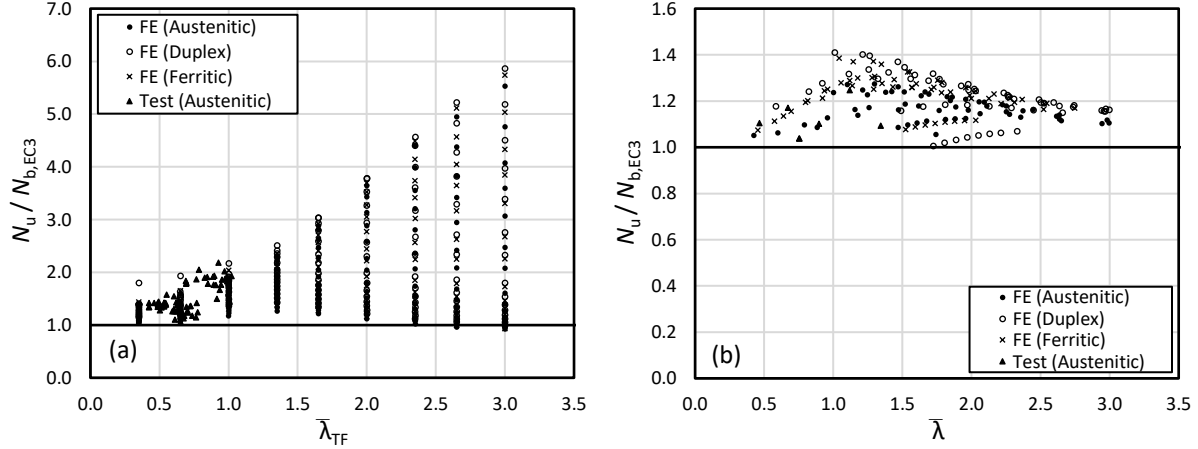


Figure 2: Comparisons between test/FE and EC3 ultimate capacities for fixed-ended hot-rolled austenitic, duplex and ferritic stainless steel equal-leg angle section columns where (a) torsional-flexural and (b) minor-axis flexural buckling are critical.

## 6. New design proposals

Mirroring recent proposals (Behzadi-Sofiani et al. 2021) for the design of fixed-ended steel equal-leg angle section columns, new proposals for the design of fixed-ended stainless steel equal-leg angle section columns are presented and assessed in the current section.

### 6.1. Torsional-flexural buckling

The proposed design buckling resistance  $N_{b,Rd}$  of stainless steel equal-leg angle section columns where  $N_{cr,TF}/N_{cr,F,v} \leq 1.0$  is given thus:

$$N_{b,Rd} = \frac{\chi_{TF} A f_y}{\gamma_{M1}} \quad (1)$$

noting that the gross area  $A$  is used for all classes of cross-section to eliminate the effective double-counting of the torsional-dominant buckling mode in the cross-section (i.e. local) and member level stability checks, as occurs in the current EC3 design provisions. In Eq. 1  $f_y$  is the material yield strength and  $\chi_{TF}$  is the reduction factor for torsional-flexural buckling, given by:

$$\chi_{TF} = \chi_F + \Delta_F (\chi_T - \chi_F) \quad (2)$$

in which the torsional buckling reduction factor  $\chi_T$  is given by:

$$\chi_T = \frac{\bar{\lambda}_{TF}^{-0.188}}{\bar{\lambda}_{TF}^2} \quad \text{but } \chi_T \leq 1.0 \quad (3)$$

and  $\Delta_F$  is given thus:

$$\Delta_F = \left(1 - \frac{N_{cr,TF}}{N_{cr,F,v}}\right)^p \quad (4)$$

where

$$p = \begin{cases} 2.0 \bar{\lambda}_{TF} & \text{for } \bar{\lambda}_{TF} \leq 2.0 \\ 2.93 \bar{\lambda}_{TF}^{0.45} & \text{for } \bar{\lambda}_{TF} > 2.0 \end{cases} \quad (5)$$

with the torsional-flexural slenderness  $\bar{\lambda}_{TF}$  and  $\phi$  being thus:

$$\bar{\lambda}_{TF} = \sqrt{\frac{A f_y}{N_{cr,TF}}} \quad (6)$$

$$\phi = 0.5[1 + \alpha\beta(\bar{\lambda}_{TF} - \bar{\lambda}_0)^\beta + \bar{\lambda}_{TF}^2] \quad (7)$$

For both hot-rolled and cold-formed angles, the proposed values for  $\beta$  and limiting slenderness  $\bar{\lambda}_0$  are 1.45 and 0.2, respectively. For the imperfection factor  $\alpha$ , values of 0.6 and 0.49 are recommended for hot-rolled and cold-formed stainless steel angles, respectively. Note though for  $\bar{\lambda}_{TF}$  and  $\bar{\lambda}$  values greater than about 1.0, that despite the lower value for the imperfection factor  $\alpha$ , with the newly introduced parameter  $\beta$ , the proposed buckling curves lie below the existing EN 1993-1-4 buckling curve in the region  $N_{cr,TF}/N_{cr,F,v}=1.0$ , reflecting the influence of mode interaction between torsional-flexural and minor-axis flexural buckling.

### 6.2. Minor-axis flexural buckling

The design buckling resistance  $N_{b,Rd}$  for equal-leg angle section columns where  $N_{cr,TF}/N_{cr,F,v}>1.0$  is obtained thus:

$$N_{b,Rd} = \frac{\chi_F A f_y}{\gamma_{M1}} \quad (8)$$

where

$$\chi_F = \frac{1}{\phi + \sqrt{\phi^2 - \lambda^2}} \quad \text{but} \quad \chi_F \leq 1.0 \quad (9)$$

in which the normalised slenderness  $\bar{\lambda}$ ,  $\phi$  and the generalized initial imperfection factor  $\eta$  are given by:

$$\bar{\lambda} = \sqrt{\frac{A f_y}{N_{cr,F,v}}} \quad (10)$$

$$\phi = 0.5 [1 + \eta + \bar{\lambda}^2] \quad (11)$$

$$\eta = \alpha \beta (\bar{\lambda} - \bar{\lambda}_0)^\beta \quad (12)$$

with  $\beta$  being a factor allowing for the influence of interactive buckling:

$$\beta = 1.9 - 0.45 \frac{N_{cr,TF}}{N_{cr,F,v}} \quad \text{but} \quad 1.0 \leq \beta \leq 1.45 \quad (13)$$

Note that, unlike in the case of torsional-flexural buckling, the gross area  $A$  is replaced by the effective area  $A_{eff}$  (EN1993-1-5 2006) in Eqs. 8 and 10 for Class 4 cross-sections when minor-axis flexural buckling is critical;  $A_{eff}$  is determined from EN 1993-1-4 (2006). The imperfection factor and limiting slenderness remain as specified above:  $\alpha=0.60$  and  $\alpha=0.49$  for hot-rolled and cold-formed stainless steel angles, respectively, and  $\bar{\lambda}_0=0.2$  for both hot-rolled and cold-formed stainless steel angles.

### 6.3. Assessment of design proposals

A summary of the comparisons of the test and FE capacities against the resistance predictions according to the new proposals  $N_{b,prop}$  is presented in Fig. 3 and Table 2.

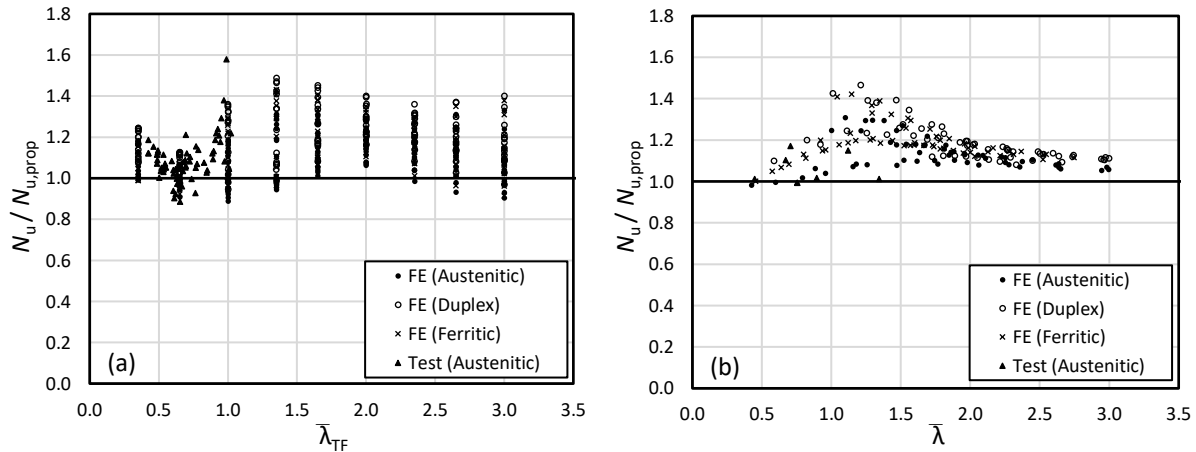


Figure 3: Comparisons of test and FE results against the new proposals for the design of fixed-ended hot-rolled austenitic, duplex and ferritic stainless steel equal-leg angle section columns for the cases of: (a) torsional-flexural buckling and (b) minor-axis flexural buckling being critical.

By comparing Figs. 2a and 3a, it can be seen that the resistance predictions are significantly improved for stainless steel angles exhibiting torsional-flexural buckling using the new proposals relative to the current Eurocode 3 provisions. Comparing Figs. 2b and 3b, the proposed resistance predictions can also be seen to be more accurate than those given by the current Eurocode 3 provisions for stainless steel angles failing by minor-axis flexural buckling.

Table 2: Summary of comparisons between test/FE capacities and resistance predictions obtained from proposed design method for fixed-ended stainless steel equal-leg angle section columns.

Source	Manufacturing process	Stainless steel family	Evaluation parameter	$N_u/N_{b,prop}$		
				Torsional-flexural	Flexural	Total
FE	Hot-rolling	Austenitic	Mean	1.09	1.13	1.10
			CoV	0.10	0.07	0.09
		Duplex	Mean	1.21	1.19	1.20
			CoV	0.10	0.08	0.10
		Ferritic	Mean	1.15	1.19	1.16
			CoV	0.11	0.07	0.10
	Cold-forming	Austenitic	Mean	1.12	1.14	1.13
			CoV	0.10	0.07	0.09
		Duplex	Mean	1.21	1.15	1.19
			CoV	0.10	0.08	0.10
		Ferritic	Mean	1.16	1.16	1.16
			CoV	0.10	0.08	0.10
Test	Hot-rolling	Austenitic	Mean	1.09	1.04	1.09
			CoV	0.10	0.06	0.10
	Cold-forming	Austenitic	Mean	1.14	-	1.23
			CoV	0.11	-	0.11

## 7. Conclusions

A comprehensive study into the behaviour and stability design of fixed-ended stainless steel equal-leg angle section members subjected to axial compression has been presented. Finite element models were developed and validated against existing experimental data from the literature. Good agreement was shown between the test and numerical results. A parametric study was subsequently conducted on both hot-rolled and cold-formed angle section columns in austenitic, duplex and ferritic stainless steel with fixed-ended support conditions covering a wide spectrum of cross-section and member geometries. A total of 1146 numerical results was generated. The numerical data were combined with existing test results from the literature and used to assess the current design provisions in EN 1993-1-4 (2006) for stainless steel equal-leg angle section columns. The current Eurocode 3 design provisions are shown to be conservative in cases where the torsional-flexural buckling mode is critical due to effective double-counting of the same buckling mode in the cross-section and member checks alongside the failure to recognise the stable post-buckling characteristic of the torsional-flexural mode in the member buckling curves. New design provisions are developed for both torsional-flexural and minor-axis flexural buckling that capture the influence of the transition in post-buckling behaviour from stable to neutral with increasing  $N_{cr,TF}/N_{cr,F,v}$  ratios and the effects of interactive buckling between the torsional-flexural and minor-axis flexural buckling modes in the region where  $N_{cr,TF}/N_{cr,F,v} \approx 1.0$ . The new design rules provide dramatic improvements in both the accuracy and consistency of strength predictions for all grades of stainless steel equal-leg angle section columns with fixed-ended support conditions.

## References

- ABAQUS (2016). "Version 6.16 Analysis User's Guide." Dassault Systemes Simulia Corporation. Providence, USA.
- Afshan, S., Zhao, O., Gardner, L. (2019). "Standardised material properties for numerical parametric studies of stainless steel structures and buckling curves for tubular columns." *Journal of Constructional Steel Research*, 152, 2-11.
- Arrayago, I., Real, E., Gardner, L. (2015). "Description of stress-strain curves for stainless steel alloys." *Materials and Design*, 87, 540-552.
- AS/NZS4673 (2001). "Cold-formed stainless steel structures." Sydney.
- Behzadi-Sofiani, B., Gardner, L., Wadee, M.A., Dinis, P.B., Camotim, D. (2021). "Behaviour and design of fixed-ended steel equal-leg angle section columns." *Journal of Constructional Steel Research*, 182, 106649.
- da S. Sirqueira, A., da S. Vellasco, P., de Lima, L., Sarquis, F. (2020). "Experimental assessment of stainless steel hot-rolled equal legs angles in compression." *Journal of Constructional Steel Research*, 169, 106069.
- de Menezes, A.A., da S. Vellasco, P.C., de Lima, L.R., da Silva, A.T. (2019). "Experimental and numerical investigation of austenitic stainless steel hot-rolled angles under compression." *Journal of Constructional Steel Research*, 152, 42-56.
- Dinis, P.B., Camotim, D. (2015). "A novel DSM-based approach for the rational design of fixed-ended and pin-ended short-to-intermediate thin-walled angle columns." *Thin-Walled Structures*, 87, 158-182.
- Dinis, P.B., Camotim, D., Silvestre, N. (2012). "On the mechanics of thin-walled angle column instability." *Thin-Walled Structures*, 52, 80-89.
- Dobric, J., Filipovic, A., Markovic, Z., Baddoo, N. (2020). "Structural response to axial testing of cold-formed stainless steel angle columns." *Thin-Walled Structures*, 156, 106986.
- EN 1993-1-4 (2006). "Eurocode 3: Design of steel structures - Part 1-4: General rules - Supplementary rules for stainless steels." European Committee for Standardisation (CEN). Brussels, Belgium.
- Jandera, M., Gardner, L., Machacek, J. (2008). "Residual stresses in cold-rolled stainless steel hollow sections." *Journal of Constructional Steel Research*, 64, 1255-1263.
- Liang, Y., Jeyapragasam, V.V.K., Zhang, L., Zhao, O. (2019). "Flexural-torsional buckling behaviour of fixed-ended hot-rolled austenitic stainless steel equal-leg angle section columns." *Journal of Constructional Steel Research*, 154, 43-54.
- Rasmussen, K.J.R. (2005). "Design of angle columns with locally unstable legs." *Journal of Structural Engineering*, 131, 1553-1560.
- Riks, E. (1979). "An incremental approach to the solution of snapping and buckling problems." *International Journal of Solids and Structures*, 15, 529-551.
- Rossi, B., Afshan, S., Gardner, L. (2013). "Strength enhancements in cold-formed structural sections - Part II: Predictive models." *Journal of Constructional Steel Research*, 83, 189-196.
- Sarquis, F., de Lima, L., da S. Vellasco, P., Rodrigues, M. (2020). "Experimental and numerical investigation of hot-rolled stainless steel equal leg angles under compression." *Thin-Walled Structures*, 151, 106742.
- SEI/ASCE8-02 (2002). "Specification for the design of cold-formed stainless steel structural members." American Society of Civil Engineers (ASCE). Reston.
- Stang, A.H., Strickenberg, L.R. (1922). "Results of some compression tests of structural steel angles." US Government Printing Office.
- Sun, Y., Liu, Z., Liang, Y., Zhao, O. (2019). "Experimental and numerical investigations of hot-rolled austenitic stainless steel equal-leg angle sections." *Thin-Walled Structures*, 144, 106225.
- Zhang, L., Liang, Y., Zhao, O. (2020a). "Experimental and numerical investigations of pin-ended hot-rolled stainless steel angle section columns failing by flexural buckling." *Thin-Walled Structures*, 156, 106977.
- Zhang, L., Tan, K.H., Zhao, O. (2019). "Experimental and numerical studies of fixed-ended cold-formed stainless steel equal-leg angle section columns." *Engineering Structures*, 184, 134-144.
- Zhang, L., Tan, K.H., Zhao, O. (2020b). "Local stability of press-braked stainless steel angle channel sections: Testing, numerical modelling and design analysis." *Engineering Structures*, 203, 109869.
- Zhang, L., Liang, Y., Zhao, O. (2021). "Laboratory testing and numerical modelling of pin-ended hot-rolled stainless steel angle section columns failing by flexural-torsional buckling." *Thin-Walled Structures*, 161, 107395.

## Linking the von Karman equations to the design of steel plates

Jurgen Becque<sup>1</sup>

### Abstract

In this paper the von Karman system of partial differential equations describing the nonlinear post-buckling response of plates is simplified into a single equation, while taking caution to preserve the main mechanisms through which plates develop post-buckling reserve capacity. The resulting equation is solved for the case of a perfect plate using a single Fourier term, and for the case of an imperfect plate using two Fourier terms. Good agreement with finite element simulations, used as a benchmark, is obtained. The theory is further used to derive a closed form expression for the plate capacity as a function of the slenderness, which agrees very well with the well-known Winter equation.

### 1. Introduction

The von Karman (or Föppl-von Karman) equations comprise a system of two coupled nonlinear partial differential equations (Föppl 1907, von Karman 1910). They describe the post-buckling behaviour of thin elastic plates:

$$D \left[ \frac{\partial^4 w}{\partial x^4} + 2 \frac{\partial^4 w}{\partial x^2 \partial y^2} + \frac{\partial^4 w}{\partial y^4} \right] = p_z + D \left[ \frac{\partial^2 \phi}{\partial y^2} \frac{\partial^2 (w + w_0)}{\partial x^2} - 2 \frac{\partial^2 \phi}{\partial y \partial x} \frac{\partial^2 (w + w_0)}{\partial x \partial y} + \frac{\partial^2 \phi}{\partial x^2} \frac{\partial^2 (w + w_0)}{\partial y^2} \right] \quad (1)$$

$$\frac{\partial^4 \phi}{\partial x^4} + 2 \frac{\partial^4 \phi}{\partial x^2 \partial y^2} + \frac{\partial^4 \phi}{\partial y^4} = D \left[ \left( \frac{\partial^2 w}{\partial x \partial y} \right)^2 - \frac{\partial^2 w}{\partial x^2} \frac{\partial^2 w}{\partial y^2} + 2 \frac{\partial^2 w_0}{\partial x \partial y} \frac{\partial^2 w}{\partial x \partial y} - \frac{\partial^2 w_0}{\partial x^2} \frac{\partial^2 w}{\partial y^2} - \frac{\partial^2 w_0}{\partial y^2} \frac{\partial^2 w}{\partial x^2} \right] \quad (2)$$

In these equations  $w$  is the vertical plate deflection,  $w_0$  is the initial geometric imperfection,  $\phi$  is the Airy stress function,  $E$  is the elastic modulus,  $t$  is the (constant) plate thickness,  $p_z$  is the lateral pressure on the plate and  $D$  is the flexural plate stiffness, given by:

$$D = \frac{Et^3}{12(1-\nu^2)} \quad (3)$$

A sufficiently general solution to the von Karman equations does not exist. Instead, numerical solutions have been developed, typically based on finite element, finite strip or finite difference approaches. Sadly, this lack of an analytical closed form solution also renders the von Karman equations next to irrelevant in the context of the practical design of metal plates. However, a simplified version of Eqs. (1-

<sup>1</sup> Jurgen Becque, PhD, is a senior research scientist at the University of Waterloo, Ontario, Canada.

2) has previously been developed by the author (Becque 2019), which condenses the system of coupled equations into a single equation and eliminates the Airy stress function  $\phi$ :

$$\gamma \left[ \frac{\partial^2 w}{\partial x^2} + 2 \frac{\partial^2 w}{\partial x^2 \partial y^2} + \frac{\partial^2 w}{\partial y^2} \right] = \left[ \int_0^L \left( \frac{\partial w}{\partial x} \right)^2 dx - 2 U_0 \right] \left( \frac{\partial^2 w}{\partial x^2} \right) \quad (4)$$

with:

$$\gamma = \frac{2 E t^3}{E t^3} = \frac{t^3}{t^3 (1 - \nu^2)} \quad (5)$$

In Eq. (4)  $L$  is the length of the plate and  $U_0$  is the end shortening (Fig. 1). Eq. (4) is valid for a plate under uniaxial compression and the full derivation is presented in (Becque 2019). However, it is important to mention that the following assumptions underlie the equation:

1. The cross-sectional profile of the longitudinal membrane stresses remains unchanged along the length of the plate.
2. The membrane shear stresses are zero.
3. The transverse membrane stresses are zero.
4. The loaded edges of the plate remain straight, while the longitudinal edges are free to move inwards horizontally (Fig. 1).

Assumption (1) is inspired by von Karman's effective width concept, while assumption (2) is the extension of Vlasov's assumption into the post-buckling range. Assumption (4) approximates the typical situation of a (long) plate in a plate assembly (i.e. a cross-section) under compression, where the transverse 'nodal lines' remain straight as a result of symmetry and the longitudinal edges of the plate are only weakly restrained against in-plane movement by bending of the adjacent plates about their in-plane axis. The latter also justifies assumption (3), as significant membrane action is not thought to develop in the transverse direction of the plate for this reason. Assumptions (1-3) were verified against the results of an FE simulation of a square elastic plate (Fig. 2) (Abaqus 2017). The stress state is depicted at the moment when the maximum longitudinal membrane stress  $\sigma_x$  reached 350 MPa, which represents an advanced post-buckled state. The leftmost diagram shows that the  $\sigma_x$  contours form approximately vertical lines, thus confirming assumption (1). The membrane shear stress ( $\tau_{xy}$ ) plot (middle) shows some localized shear stress concentrations near the corners of the plate, which reached up to 34 MPa. However, in the remainder of the plate  $\tau_{xy}$  remained limited to 5 MPa in absolute value (indicated by the pale green colours). Since this constitutes less than 2% of the maximum longitudinal membrane stress, the  $\tau_{xy}$  stresses can indeed be neglected. The plot of the transverse membrane stresses  $\sigma_y$  (right) shows some stress concentrations near the transverse edges. However, in the central area of the plate stresses do not exceed 19 MPa (= 5.5% of 350 MPa), justifying assumption (3).

For a plate with an initial imperfection  $w_0$ , Eq. (4) transforms into:

$$\gamma \left[ \frac{\partial^2 w}{\partial x^2} + 2 \frac{\partial^2 w}{\partial x^2 \partial y^2} + \frac{\partial^2 w}{\partial y^2} \right] = \left[ \int_0^L \left[ \left( \frac{\partial w}{\partial x} \right)^2 + 2 \left( \frac{\partial w}{\partial x} \right) \left( \frac{\partial w_0}{\partial x} \right) \right] dx - 2 U_0 \right] \left( \frac{\partial^2 (w + w_0)}{\partial x^2} \right) \quad (6)$$

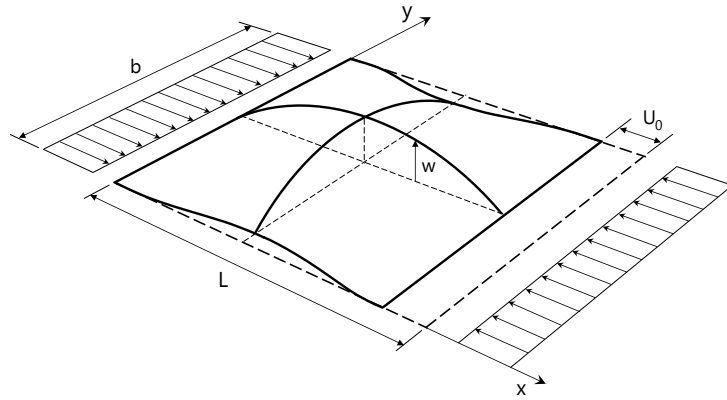


Figure 1: Boundary conditions of rectangular plate under uniaxial in-plane compression

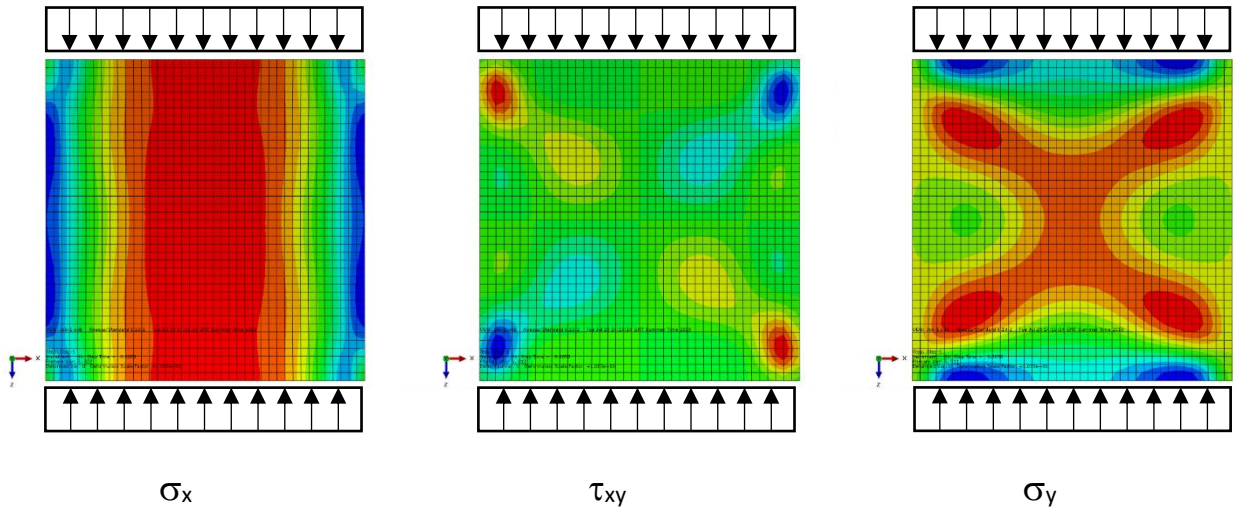


Figure 2: Stress contours of  $\sigma_x$ ,  $\tau_{xy}$  and  $\sigma_y$  obtained from FE analysis

## 2. Approximate solution for a geometrically perfect plate

Eq. (4) has previously been solved in approximate form (Becque 2019) for a square plate without imperfections, by substituting the following proposed solution:

$$w = w_{11} \cos\left(\frac{\pi x}{L}\right) \cos\left(\frac{\pi y}{b}\right) \quad (7)$$

Eq. (7) is the solution to the classical St. Venant plate equation. In the context of Eq. (4), Eq. (7) can be seen as the first term of a Fourier series, which, by virtue of being the solution to the St. Venant equation, is dominant in the initial post-buckling range over the remaining terms. The substitution eventually leads to the following load-shortening relationship:

$$P = P_0 \left[ \frac{P_0}{3} + \frac{P_0}{3} \gamma \left( \frac{\pi}{\lambda} \right)^2 \right] \quad (8)$$

where  $P$  is the applied load on the plate. The above equation is plotted in Fig. 3, where it is compared to FE results for the case of a  $200 \times 200 \text{ mm}^2$  plate with  $t = 1 \text{ mm}$ ,  $E = 200 \text{ GPa}$  and  $\nu = 0.3$  (Abaqus 2017). The FE model is fully elastic and contains a minute imperfection of  $0.004 \text{ mm}$  in order to induce buckling at the theoretical bifurcation point. It is seen that Eq. (8) accurately predicts the initial post-buckling stiffness (at  $1/3$  of the original pre-buckled stiffness) and provides a good representation of the post-buckling range up to a strain of about 5-6 times the buckling strain.

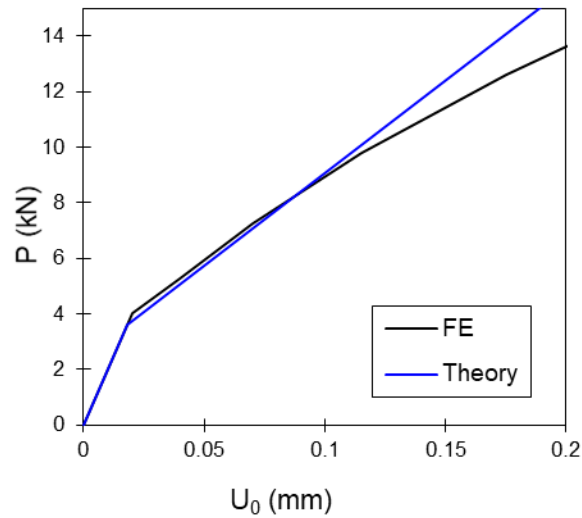


Figure 3: Comparison of predicted and experimental load-shortening behaviour

According to von Karman's effective width concept failure occurs when the maximum longitudinal membrane stress (occurring along the longitudinal plate edges) reaches the yield stress  $f_y$ . It was previously demonstrated (Becque 2019) that, in the context of Eq. (4), this is equivalent to:

$$\sigma_{x, \max} = \frac{P_0}{b} = f_y \quad (9)$$

Using Eq. (9), Eq. (8) can be re-arranged into a Winter-type equation:

$$\frac{P_u}{P_y} = \frac{1}{3} \left( 1 + \frac{2}{\lambda^2} \right) \quad (10)$$

where  $P_u$  is the ultimate load of the plate,  $P_y$  is the yield load and  $\lambda$  is the slenderness defined as:

$$\lambda = \sqrt{\frac{w_y}{\sigma_{cr}}} \quad (11)$$

In Eq. (11)  $\sigma_{cr}$  is the elastic buckling stress of the plate. Eq. (10) is compared to the Winter equation in Fig. 4. For reference, the Winter equation reads as:

$$\frac{w_u}{w_y} = \frac{1}{\lambda} \left( 1 - \frac{0.22}{\lambda} \right) \leq 1.0 \quad (12)$$

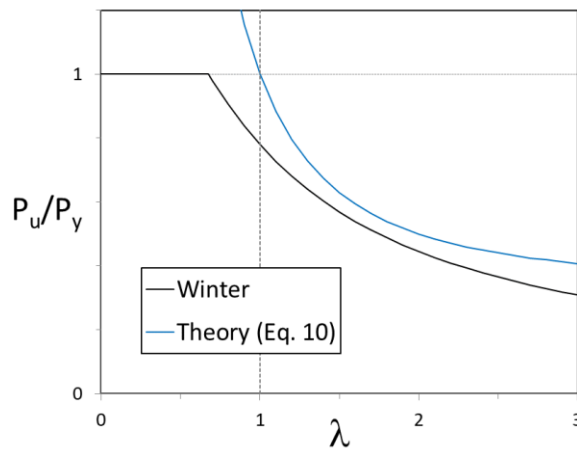


Figure 4: Comparison of Winter curve with analytical prediction

It is seen that both equations exhibit a similar trend. However, Eq. (10) results in significantly higher predictions of the plate capacity. For lower slenderness values  $\lambda$  this discrepancy is mainly due to the fact that imperfections have not yet been accounted for, while for higher slenderness values it is the result of the approximate character of the solution proposed in Eq. (7). Indeed, it is seen in Fig. 3 that the actual plate behaviour is not linear in the post-buckling range, but loses stiffness at larger plate deformations. This effect is more important for more slender plates, which display a more extensive post-buckling range before yielding sets in. Both issues are rectified in the following paragraph.

### 3. Solution for a geometrically imperfect plate

The solution provided in Section 2 is further extended and refined by first including an imperfection of the following shape:

$$w_0 = w_0 \cos\left(\frac{\pi x}{a}\right) \cos\left(\frac{\pi y}{b}\right) \quad (13)$$

Second, an additional Fourier term is added to Eq. (7):

$$w = A_{11} \cos\left(\frac{\pi x}{L}\right) \cos\left(\frac{\pi y}{L}\right) + A_{13} \cos\left(\frac{\pi x}{L}\right) \cos\left(\frac{3\pi y}{L}\right) \quad (14)$$

Substituting Eqs. (13-14) into Eq. (6) leads to the following system of equations in the coefficients  $A_{11}$  and  $A_{13}$ :

$$\left(\frac{A_{11}}{A_{13}}\right) \left[ \gamma A_{11} - 2(A_{11} + A_0) A_0 \left(\frac{A_{11}}{\pi}\right)^2 \right] = -3A_{11}^3 - A_0 A_{11}^2 + 3A_{11}^2 A_{13} + A_0 A_{11} A_{13} - A_{11} A_{13}^2 - A_0^2 A_{11} + 2A_0^2 A_{13} - A_0^2 A_{13}^2 \quad (15)$$

$$A_{13} \left(\frac{A_{11}}{A_{13}}\right) \left[ 100\gamma - 2A_0 \left(\frac{A_{11}}{\pi}\right)^2 \right] = A_{11}^3 + 3A_0 A_{11}^2 - A_{11}^2 A_{13} - 12A_0 A_{11} A_{13} + 2A_0^2 A_{11} - A_0^2 A_{13} - 3A_{13}^3 \quad (16)$$

This system of equations can be solved numerically (e.g. using Solver in Excel (Microsoft 2007)) for a range of chosen  $U_0$  values. The resulting  $A_{11}$  and  $A_{13}$  values then determine the load  $P$  through the equation:

$$P = \int_0^L \sigma_x dy = A_{11} \left[ A_0 - \frac{\pi^2}{L^2} (A_{11}^2 + 2A_0 A_{11} + A_{13}^2) \right] \quad (17)$$

An example of a thus obtained load-shortening plot is shown in Fig. 5. The  $200 \times 200 \text{ mm}^2$  plate geometry previously considered in Section 2 was used with  $A_0 = L/200 = 1 \text{ mm}$ . This curve is compared to the corresponding curve obtained from FE analysis of a square elastic plate with the same geometry and imperfection. Very good agreement was obtained up to a strain of about 20 times the buckling strain.

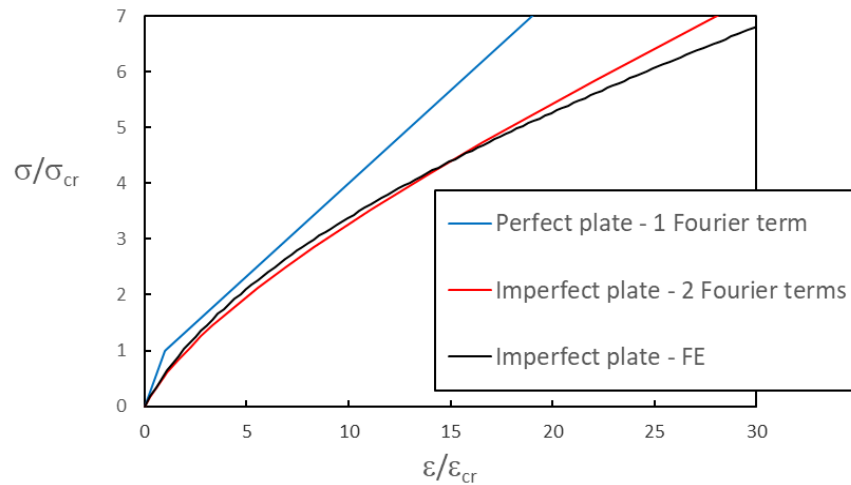


Figure 5: Comparison of predicted load-shortening behavior with FE results

Eqs. (15-17) can be used to derive an approximate closed form equation for the plate capacity analogous to Eq. (10). To achieve this, the terms in  $(A_{13})^3$  and  $(A_{13})^2$  are first neglected. This is justified by the

observation that the first term in Eq. (14) dominates the plate behavior. Only at higher loads much further into the post-buckling range does the second term grow somewhat in importance. A single equation then results from eliminating  $A_{13}$  from Eqs. (15-16). The failure criterion (Eq. 9) determines the plate shortening  $U_0$ , while  $A_{11}$  can be related to the load  $P$  through Eq. (17) (in which  $(A_{13})^2$  is again ignored in comparison with  $(A_{11})^2$ ). This procedure results in the following relationship between the slenderness  $\lambda$  and the plate capacity  $P_u$ :

$$\frac{1}{\lambda^2} = 0.01 \frac{U_0}{y} - 0.005 \alpha - 0.025 \frac{3 \frac{U_0}{y} - 1}{\sqrt{1 + \frac{1}{\alpha} \left(1 - \frac{U_0}{y}\right) - 1}} + \frac{\left[ c_3 \left( \frac{U_0}{y} \right)^3 + c_2 \left( \frac{U_0}{y} \right)^2 + c_1 \left( \frac{U_0}{y} \right) + c_0 \right] + d_2 \left( \frac{U_0}{y} \right)^2 + d_1 \left( \frac{U_0}{y} \right) + d_0}{\left( \sqrt{1 + \frac{1}{\alpha} \left(1 - \frac{U_0}{y}\right) - 1} \right)^2 + \sqrt{1 + \frac{1}{\alpha} \left(1 - \frac{U_0}{y}\right) - 1}} \quad (18)$$

In the above equation the imperfection factor  $\alpha$  is given by:

$$\alpha = \frac{\pi^2}{y} \left( \frac{U_0}{y} \right)^2 \quad (19)$$

while the coefficients  $c_0$ - $c_3$  and  $d_0$ - $d_2$  are listed in Table 1.

Table 1. Coefficients in Eq. (18)

$c_3$	$0.50 \alpha$	$d_2$	$0.053$
$c_2$	$0.51 \alpha - 0.05 \alpha$	$d_1$	$0.02 \alpha - 0.01$
$c_1$	$0.01 \alpha - 0.330 - 0.02 \alpha$	$d_0$	$0.0001 \alpha^2 - 0.013 \alpha - 0.01$
$c_0$	$0.01 \alpha^2 - 0.01 \alpha - 0.022 + 0.0001 \alpha$		

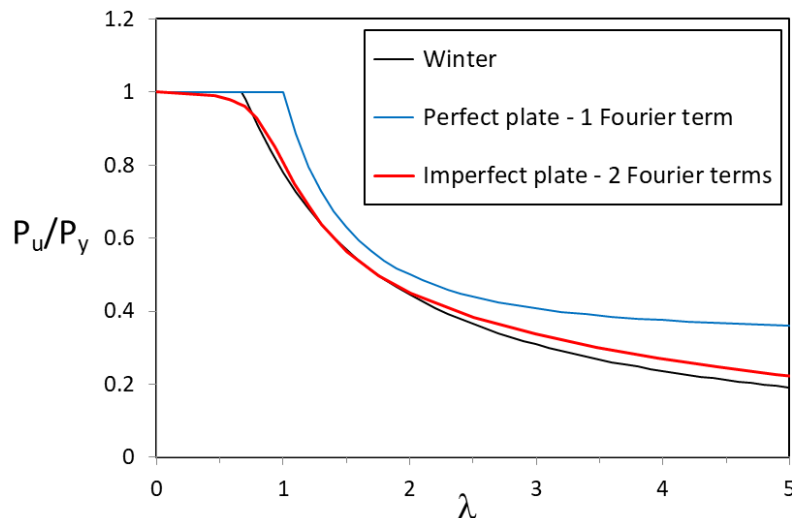


Figure 6: Comparison of theoretical strength prediction with Winter curve

The predictions of Eq. (18) are compared to the Winter equation in Figure 6. An imperfection  $A_0$  of  $L/200$  (where  $L$  is the plate width) was included in the model, as recommended by EN1993-1-5 (CEN 2006).

This 'equivalent' imperfection takes into account geometric imperfections, as well as residual stresses. The agreement is quite astounding, given the initial simplifications underlying the model, and is maintained over the whole slenderness range up to  $\lambda = 5$ . Figure 5 suggest that the solution with two Fourier terms diverges from reality beyond strains equal to approximately 20 times the buckling strain and, therefore, Eq. (18) should not be used for slenderness values in excess of  $\sqrt{20} \approx 4.5$ . Unlike the Winter curve, Eq. (18) captures the gradual transition into full yielding. However, Eq. (18) is obviously more cumbersome in its application and specifies the slenderness as a function of the ultimate load, rather than vice versa. Beyond a slenderness of about 2, Eq. (18) predicts slightly higher capacities than the Winter curve. While the Winter curve is known to be on the conservative side in this region, only a comparison with experimental data can indicate which model is more accurate. This is planned as further research.

#### 4. Conclusions

In this paper the Föppl-von Karman equations have been simplified into a single equation, while being mindful of preserving the modeling of the main mechanics which govern the post-buckling behaviour of plates. These mechanical features first of all include the two-dimension character of plate behaviour, recognizing that plates deflect while displaying transverse as well as longitudinal bending, supplemented with twisting (as already fully accounted for by the classical St. Venant equation). In addition, however, the longitudinal membrane action, resulting from longitudinal fibres being 'tensioned up' while deflecting between nodal lines which are forced to remain straight, was identified as the single most important mechanical phenomenon to be accounted for. This superimposed tension causes additional compression along the plate edges, where fibres deflect less.

An approximate solution to the simplified equation was pursued. Using a single Fourier term in the solution provided an excellent approximation of the actual plate behavior up to a longitudinal strain of about 5-6 times the buckling strain. This range could be considerably extended to about 20 times the buckling strain by including a second Fourier term, while an initial imperfection was also accounted for. The model allowed for the derivation of a closed form analytical expression for the plate capacity as a function of the plate slenderness, analogous to the well-known and extensively used Winter equation. For the latter case, where 2 Fourier terms and an initial imperfection of  $L/200$  were included, the analytical solution displayed remarkable agreement with the Winter equation. The theoretically derived solutions also confirm that the capacity of a geometrically perfect plate is only a function of its plate slenderness (thus acknowledging Winter's genius), while the capacity of an imperfect plate is a sole function of the plate slenderness and an imperfection factor  $\alpha$ , given by Eq. (19).

#### References

- Abaqus (2017). Abaqus CAE 2017, Dassault Systèmes, France.
- Becque, J. (2019). "Solutions to simplified von Karman plate equations." *Proceedings of the International Colloquia on Stability and Ductility of Steel Structures*, Prague, Czech Republic. 173-180.
- CEN (2006). *Eurocode 3: Design of Steel Structures, Part 1.5: Plated Structural Elements*. European Committee for Standardization, Brussels.
- Föppl, A. (1907). *Vorlesungen Über Technische Mechanik*, Druck und Verlag von B.G. Teubner.
- Microsoft (2017). Microsoft Excel, Redmond, Washington, USA.
- Von Karman, T. (1910). Festigkeitsprobleme im Maschinenbau. In: Klein, F., Müller, C., *Encyklopädie der Mathematischen Wissenschaften*, Druck und Verlag von B.G. Teubner, 311-385.

## **Semi-analytical solutions for the compressed thin plate with large displacements**

Mihai Nedelcu<sup>1</sup>

### **Abstract**

The thin plane plates are largely used in practice as single elements or as components of the thin-walled members. When subjected to compression, they exhibit a large post-critical strength reserve. Various analytical solutions of the uniformly compressed simply supported plate with large deflections were reported almost a century ago, mainly solving the fundamental equations of the flat thin plates or using classic energy methods. Owing to several disadvantages, these solutions were not introduced in the design codes of thin-walled structures, instead the semi-empirical Winter formula is nowadays largely used. This study presents a new semi-analytical solution based on classic energy methods. The main innovation is brought by the considered displacement field which is far more accurate than the ones used by the previous formulations. The advantages over the Winter formula are the improved accuracy and the consideration of the initial geometric imperfections. The advantages over the numerical simulations are the very small number of degrees of freedom and consequently the speed of the geometric nonlinear analysis in the elastic domain. The proposed solutions are validated against numerical solutions and experimental data.

### **1. Introduction**

To find the ultimate strength capacity of thin flat plates, numerous analytical and experimental studies were conducted, starting more than a century ago. One promising approach is to propose a displacement field compatible with the boundary conditions, then the strain energy of the buckled plate is determined, and finally the deflection degrees of freedom (DOFs) are determined based on some energy equilibrium criterion. Such an analytical solution of the uniformly compressed simply supported plate is presented in Timoshenko & Gere 1961 and apparently attributed to Lahde & Wagner 1936. This solution provides a good representation of the stress distribution (see Fig. 1). However, the predicted ultimate loads were not in agreement with the experiments and the initial geometric imperfections were not considered. This study follows the same technique, but the proposed displacement field is much improved, and the initial geometric imperfections are considered. The displacement field is expressed by a combination of linear functions and trigonometric series which satisfy the boundary conditions. The Principle of Virtual Displacements leads to a system of cubic equations with rather complex, yet analytical expressions for the system coefficients. The solution of this non-linear problem is found by using the classic Newton-Raphson method for each load increment. Validation is done by comparisons with the numerical results obtained from shell FE simulations developed in Abaqus. It must

---

<sup>1</sup> Associate Professor, Technical University of Cluj-Napoca, Romania, <mihai.nedelcu@mecon.utcluj.ro>

be underlined that for a certain slenderness range, the post-1<sup>st</sup> yield strength reserve is significant, a fact that is largely ignored nowadays in the study of thin flat plates. The proposed method covers only the elastic analysis; therefore, after the yield stress is reached in one point of the plate, the strength reserve is evaluated using the Abaqus simulations and empirical formulas for the ultimate strength capacity are proposed. The validation of the proposed formulation is done by comparisons with experimental data available in literature. A detailed study on this subject was recently published by the author (Nedelcu 2020) and the method was implemented in EFFWidth (2019) - a publicly available software application written in Matlab.

This paper also presents comparisons with the solutions given by the Winter formula which is currently used by most of the design methods for the Cold Formed Steel members (e.g. Eurocode 3, EN 1993-1-3:2006). Fig. 1 presents the post-buckling longitudinal normal stresses for uniform axial compression.

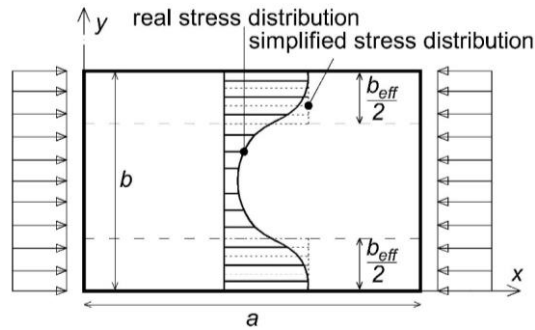


Figure 1: Stress distribution for the simply supported plate in uniform axial compression

This complex stress distribution can be simplified by replacing it with constant longitudinal normal stress on an effective width  $b_{eff}$  formed by two longitudinal strips. Von Kármán et al. (1932) proposed that the critical load of this equivalent system is equal with the ultimate capacity of the plate, as follows:

$$\sigma_{cr,b_{eff}} = \frac{k_{\sigma}\pi^2 E}{12(1-\mu^2)} \left( \frac{h}{b_{eff}} \right)^2 = \sigma_{max} \quad (1)$$

where  $h$  is the plate thickness,  $E$  and  $\mu$  are the Young modulus and the Poisson's ratio respectively, and  $k_{\sigma}$  is a coefficient which depends on the boundary conditions ( $k_{\sigma} = 4$  for the simply supported plate). By considering  $\sigma_{max}$  equal with the material yield stress  $f_y$ , the effective width is found:  $b_{eff}/b = \sqrt{\sigma_{cr}/f_y} = 1/\lambda_p$ ,

where  $b$  is the plate width,  $\sigma_{cr}$  is the critical stress of the entire plate without imperfections, and  $\lambda_p$  is the normalized slenderness. Winter adjusted the formula obtained by von Kármán et al. to match the experimental data obtained on a large series of tests (Winter 1947) and the Winter equation is given as:  $b_{eff}/b = 1/\lambda_p (1 - 0.22/\lambda_p)$ .

## 2. The proposed semi-analytical solution

Fig. 2 presents the analysed simply supported plate.

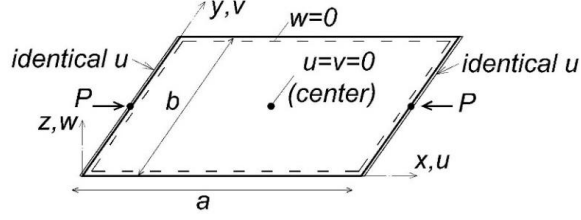


Figure 2: Simply supported plate

The loaded edges are restrained to have identical longitudinal displacements  $u$ . This phenomenon is in accordance with the usual experiments when the load  $P$  is transmitted by a rigid block. If multiple waves occur along the longitudinal axis, identical  $u$  displacements occur along the lines parallel to  $y$ -axis having null vertical displacements  $w$ .

This plate was modelled in Abaqus using shell finite elements, and then the Geometric Nonlinear Analysis with Imperfections (GNIA) was performed for several configurations varying the plate slenderness via material properties and plate geometry. The displacement field was next extracted, and then it was expanded in combinations of linear functions, single and double trigonometric series. So far, the best candidate of the assumed displacement field was found as follows:

$$\begin{aligned}
 u &= -u_L \left( x - \frac{a}{2} \right) + \sum_{i=1}^n \sum_{j=1}^n \left( u_i + u_{ij} \sin \frac{(2j-1)\pi y}{b} \right) \sin \frac{2i\pi x}{a} \\
 v &= v_L \left( y - \frac{b}{2} \right) + \sum_{i=1}^n \sum_{j=1}^n \left\{ \left[ v_{ij} \sin \frac{2j\pi y}{b} - v_{Li} \left( y - \frac{b}{2} \right) \right] \cos \frac{2i\pi x}{a} + v_i \sin \frac{2i\pi y}{b} \right\} \\
 w &= \sum_{i=1}^n \sum_{j=1}^n w_{ij} \sin \frac{(2i-1)\pi x}{a} \sin \frac{(2j-1)\pi y}{b} \\
 w_0 &= \sum_{i=1}^n \sum_{j=1}^n w_{0,ij} \sin \frac{(2i-1)\pi x}{a} \sin \frac{(2j-1)\pi y}{b}
 \end{aligned} \tag{2}$$

where  $n$  determines the number of terms considered for both single and double trigonometric series, and  $w_0$  is the initial geometric imperfection. Next, one constructs the DOFs vector  $\{d\} = \{u_L, u_i, u_{ij}, v_L, v_{ij}, v_{Li}, w_i, w_{ij}\}^T$  for  $i, j = 1..n$ , and the shape vectors  $\{\varphi_u\}$ ,  $\{\varphi_v\}$  and  $\{\varphi_w\}$  which contain the functions of  $x$  and  $y$  as given next:

$$\begin{aligned}
 \{\varphi_u\} &= \left\{ -\left( x - \frac{a}{2} \right) \quad \sin \frac{2i\pi x}{a} \quad \sin \frac{(2j-1)\pi y}{b} \sin \frac{2i\pi x}{a} \quad 0 \dots 0 \right\} \\
 \{\varphi_v\} &= \left\{ 0 \dots 0 \quad y - \frac{b}{2} \quad \sin \frac{2j\pi y}{b} \cos \frac{2i\pi x}{a} \quad \left( y - \frac{b}{2} \right) \cos \frac{2i\pi x}{a} \quad \sin \frac{2i\pi y}{b} \quad 0 \dots 0 \right\} \\
 \{\varphi_w\} &= \left\{ 0 \dots 0 \quad \sin \frac{(2i-1)\pi x}{a} \sin \frac{(2j-1)\pi y}{b} \right\}
 \end{aligned} \tag{3}$$

Eq. 2 is rewritten as follows:

$$u = \{\varphi_u\}\{d\} \quad v = \{\varphi_v\}\{d\} \quad w = \{\varphi_w\}\{d\} \quad w_0 = \{\varphi_w\}\{d_0\} \tag{4}$$

where  $\{d_0\}$  has the same size as  $\{d\}$  and contains the known amplitudes of the initial geometric imperfections. Using the kinematic and constitutive relations

$$\begin{aligned}
\varepsilon_x &= \frac{\partial u}{\partial x} + \frac{1}{2} \left( \frac{\partial w}{\partial x} \right)^2 + \frac{\partial w_0}{\partial x} \frac{\partial w}{\partial x} \\
\varepsilon_y &= \frac{\partial v}{\partial y} + \frac{1}{2} \left( \frac{\partial w}{\partial y} \right)^2 + \frac{\partial w_0}{\partial y} \frac{\partial w}{\partial y} \\
\gamma_{xy} &= \frac{\partial v}{\partial x} + \frac{\partial u}{\partial y} + \frac{\partial w}{\partial x} \frac{\partial w}{\partial y} + \frac{\partial w_0}{\partial x} \frac{\partial w}{\partial y} + \frac{\partial w_0}{\partial y} \frac{\partial w}{\partial x}
\end{aligned}
\quad
\begin{bmatrix} \sigma_x \\ \sigma_y \\ \tau_{xy} \end{bmatrix} = \frac{E}{1-\mu^2} \begin{bmatrix} 1 & \mu & 0 \\ \mu & 1 & 0 \\ 0 & 0 & \frac{1-\mu}{2} \end{bmatrix} \begin{bmatrix} \varepsilon_x \\ \varepsilon_y \\ \gamma_{xy} \end{bmatrix} \quad (5)$$

the strain energy having Membrane and Bending components, is next computed as follows:

$$\begin{aligned}
W &= W^M + W^B = \frac{h}{2} \int_0^a \int_0^b (\sigma_x \varepsilon_x + \sigma_y \varepsilon_y + \tau_{xy} \gamma_{xy}) dx dy + \\
&+ \frac{1}{2} D \int_0^a \int_0^b \left[ \left( \frac{\partial^2 w}{\partial x^2} \right)^2 + \left( \frac{\partial^2 w}{\partial y^2} \right)^2 + 2\mu \frac{\partial^2 w}{\partial x^2} \frac{\partial^2 w}{\partial y^2} + 2(1-\mu) \left( \frac{\partial^2 w}{\partial x \partial y} \right)^2 \right] dx dy
\end{aligned} \quad (6)$$

where  $D = Eh^3/12/(1-\mu^2)$  is the plate bending stiffness. The external work  $\Pi_{ext}$  is created only by the load  $P$  acting on its corresponding displacement  $u_L$ . Using the Principle of Virtual Displacements, the variation of the strain energy is equal with the variation of external work  $\delta W = \delta \Pi_{ext}$ . This expression leads to the well-known matrix formulation:

$$[K_L + K_{NL}(\{d\})]\{d\} = \{P\} \quad (7)$$

where  $[K_L]$  is the linear stiffness matrix,  $[K_{NL}]$  is the geometric nonlinear stiffness matrix,  $\{d\}$  is the DOFs vector, and  $\{P\}$  is the load vector which apart from the first component equal with the compression resultant load  $P$ , it has only null components. The order of the square stiffness matrices as well as the size of  $\{d\}$  and  $\{P\}$  is equal with  $n_{DOF} = 3n^2 + 3n + 2$ . The expressions of  $[K_L]$  and  $[K_{NL}]$  depending on the shape vectors  $\{\varphi_u\}$ ,  $\{\varphi_v\}$  and  $\{\varphi_w\}$  are given in (Nedelcu 2020). Eq. 7 represents a system of non-linear third-order algebraic equations in which the components of  $\{d\}$  are the unknowns of the problem. To solve this system of equations an incremental-iterative process is required, and the Newton-Raphson method was used. Thus, GNIA provides the plate behaviour in the elastic domain. For each loading step the von Mises stresses are calculated on the entire mid-thickness surface. The analysis stops when the maximum of the von Mises stresses reaches the yield stress  $f_y$ . The yielding outside the mid-thickness can not be represented by the proposed formulation, but fortunately for simply supported thin plates this phenomenon does not have a significant effect on the global structural response.

The semi-analytical solution has symbolic stiffness matrices and 2-3 orders of magnitude less DOFs than the numerical solutions. For these two reasons the proposed formulation is much faster than the numerical FE formulations – 2-3 seconds on an average computer, compared with 5-10 minutes for Abaqus, depending on the mesh density and FE type.

### 3. Parametric study

For this study the number of terms from Eq. 2 was chosen  $n = 4$ , leading to 62 DOFs. A simply supported square plate with dimensions  $a = b = 100$  mm is subjected to uniform compression. The material properties are  $E = 210$  GPa,  $\mu = 0.3$ ,  $f_y = 350$  MPa; 16 values were considered for the plate thickness  $h$  in the range (3.2 - 0.4) mm, leading to the range (1.276 - 10.206) for the slenderness parameter  $\lambda = b/h\sqrt{f_y/E}$ . The minimum value of  $\lambda$  corresponds to the case when the Winter formula provides no reduction of the plate width ( $b_{eff} = b$ ). The maximum value of  $\lambda$  corresponds to the application limit of the proposed solution - for higher slenderness, the assumed displacement field is no longer accurate and more DOFs are needed. In practice, for single plates and Cold-Formed Steel members, the plate slenderness is usually under this value. The initial geometric imperfection has a single halfwave on each direction, giving  $w_{0,1} \neq 0$  and all the other coefficients of  $w_0$  are null. In this study 5 values for the

maximum imperfection were considered, namely  $w_{0,11} = (0.10, 0.25, 0.50, 0.75, 1.00)\%b$ . While most of the experiments are reporting imperfection amplitudes in the range of  $(0.1 - 0.25)\%b$ , the Eurocode EN 1993-1-5 (2006) recommends an equivalent imperfection amplitude of  $0.50\%b$ . In total, this parametric study consists of 80 analyses (16 thickness values and 5 imperfection amplitude values), all performed using the public application EffWidth written by the author. The 1<sup>st</sup> yield load  $P_y$  is computed, and the corresponding effective width is extracted based on the simple relation  $b_{eff,y} = P_y / (h \cdot f_y)$ . For validation and ultimate strength capacity evaluation, numerical analyses using S4 shell elements were performed in Abaqus. The number of DOFs in Abaqus is 15606 (2601 nodes) in comparison with the 62 DOFs of the proposed formulation. Fig. 3 presents the state of stress in the middle plane at 1<sup>st</sup> yield for the case  $h = w_{0,11} = 1\text{mm}$ : the von Mises stresses, the normal and shear, all based on the proposed formulation. The stress distributions were found using shell finite element analysis (SFEA) for all cases and the differences with respect the von Mises and normal stresses versus the EffWidth stresses are under 5%. However, the shear stresses are not as well represented and the Abaqus values can be 3-4 times larger than the ones given by EffWidth. Owing to their small values, the shear stresses do not significantly affect the von Mises stresses and the global structural behaviour.

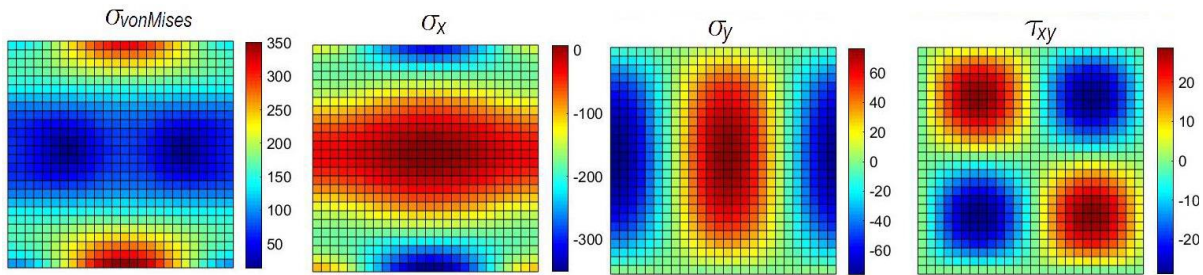


Figure 3: State of stress in the middle plane at 1<sup>st</sup> yield for  $h = w_{0,11} = 1\text{mm}$

Fig. 4-8 present different results of this parametric study, with one figure for each imperfection amplitude  $w_{0,11}$ . First, the effective width is calculated using the Winter formula (x). The same characteristic is calculated at the 1<sup>st</sup> yield by means of SFEA (♦) and the proposed formulation (▲). A procedure for calculating the effective width at ultimate load is later presented and the ratio between the predicted values and the SFEA ones are also shown in Fig. 4-8 (O).

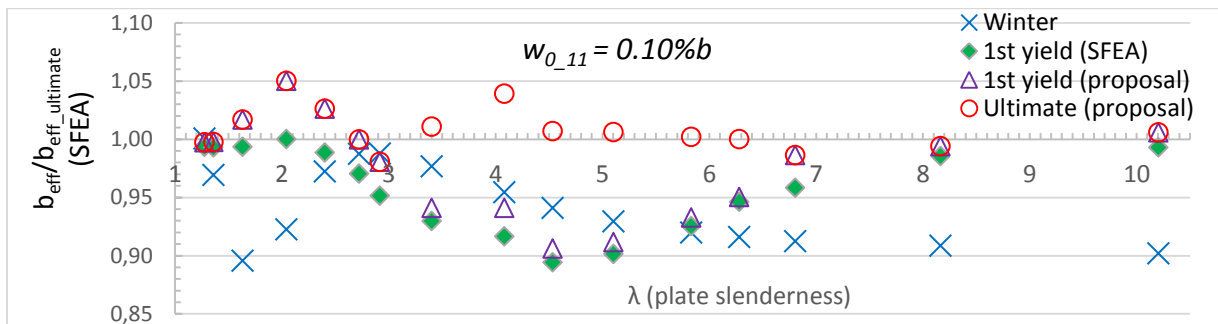


Figure 4: 1<sup>st</sup> yield and ultimate strength estimates for  $w_{0,11} = 0.10\%b$

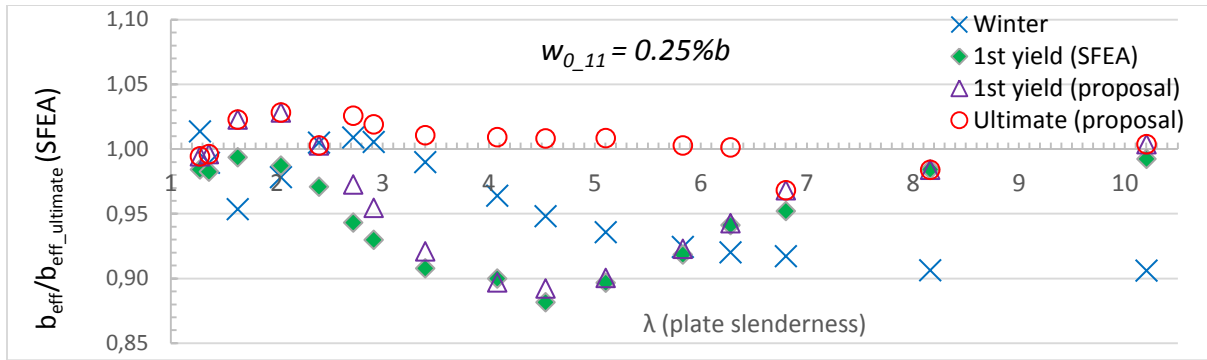


Figure 5: 1<sup>st</sup> yield and ultimate strength estimates for  $w_{0,11} = 0.25\%b$

*Winter formula.* The Winter predictions are not depending on the imperfection amplitudes and the corresponding SFEA values clearly show their dependence of  $w_{0,11}$ . One can see that for  $w_{0,11} < 0.5\%b$ , the Winter formula provides relatively good estimates, between 0.9-1.054 of the ultimate strength capacities given by SFEA. This was expected, as the Winter formula was calibrated experimentally for imperfection amplitudes commonly met in practice. The unsafe predictions of the ultimate strength are under 5.4%, while the safe predictions go up to 10%, usually for very slender plates. If one goes to higher imperfection amplitudes, the Winter formula is no longer accurate, giving differences up to 15% on the unsafe side, while maintaining a maximum of 10% on the safe side.

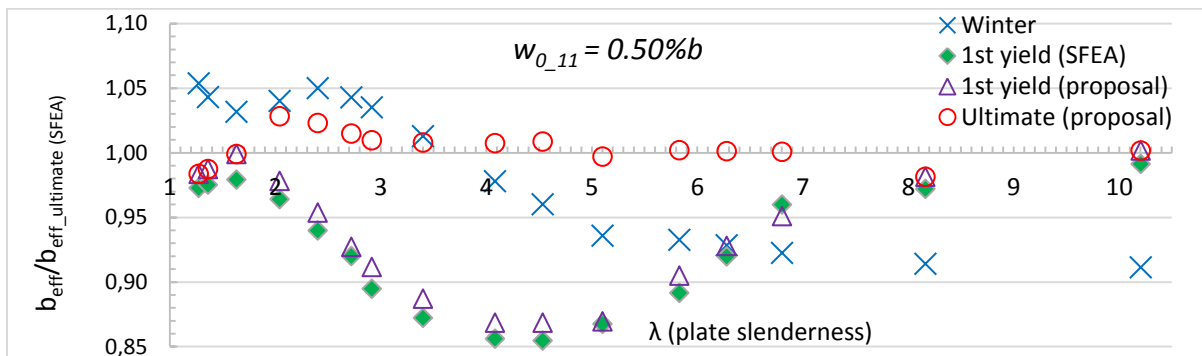


Figure 6: 1<sup>st</sup> yield and ultimate strength estimates for  $w_{0,11} = 0.50\%b$

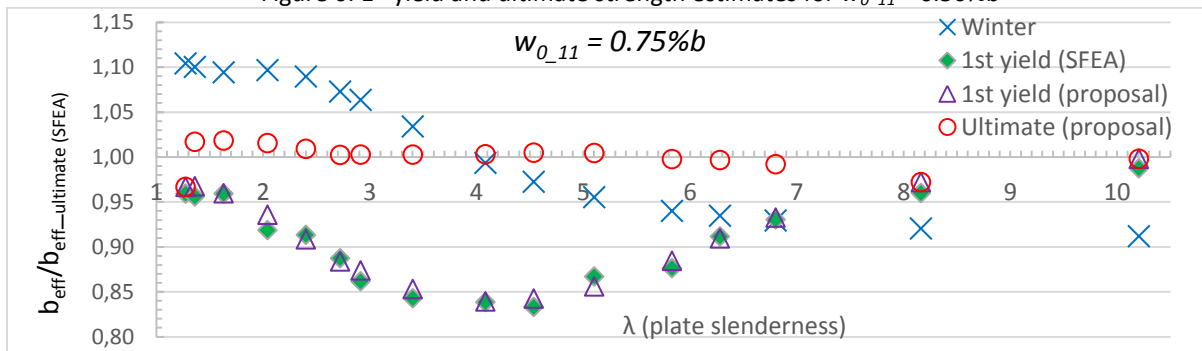


Figure 7: 1<sup>st</sup> yield and ultimate strength estimates for  $w_{0,11} = 0.75\%b$

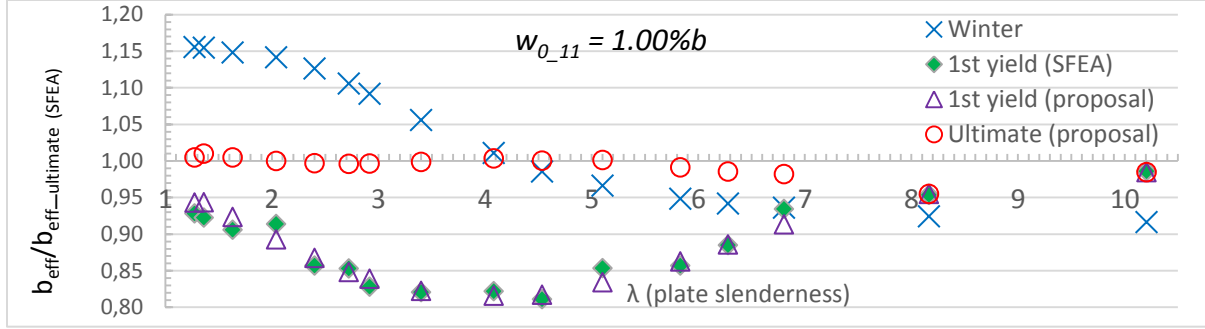


Figure 8: 1<sup>st</sup> yield and ultimate strength estimates for  $w_{0.11} = 1.00\%b$

*Proposed formulation – 1<sup>st</sup> yield strength capacity.* Comparing the effective widths based on the 1<sup>st</sup> yield load provided by the proposed formulation and SFEA, one can see the satisfactory agreement. The maximum difference is 5% for  $\lambda = 2.041$  and  $w_{0.11} = 0.10\%b$ . An interesting phenomenon must be here highlighted. By checking either of the 1<sup>st</sup> yield ratios (SFEA or proposal) one can see a significant post-1<sup>st</sup> yield strength reserve for slenderness  $\lambda < 7-8$  (it depends on the imperfection amplitude). Even for common imperfections ( $w_{0.11} = 0.25\%b$ ) this reserve can be up to 11%, and it is larger than 5% in the range of  $\lambda = (3, 6.5)$ . For higher imperfection amplitudes, this favourable reserve can be almost 20% of the ultimate capacity. To the author's knowledge this phenomenon was not presented and quantified until present time, the general belief being that the ultimate and the 1<sup>st</sup> yield loads are practically identical.

*Proposed formulation – ultimate strength capacity.* As presented in the previous paragraph there is a certain strength reserve after the 1<sup>st</sup> yield which depends on the slenderness and imperfection amplitude. The ultimate load or the corresponding effective width can be represented as  $P_u = P_y(1+r_{pl})$ , where  $P_u$  is the ultimate load,  $P_y$  is the 1<sup>st</sup> yield load and  $r_{pl}$  represents the strength reserve after the 1<sup>st</sup> yield, as a percentage of  $P_y$ . Based on SFEA values regarding the 1<sup>st</sup> yield and the ultimate load, a trendline formula of 4<sup>th</sup> order was developed for  $r_{pl}$ , given as follows:

$$r_{pl} = (-7.246w_{0.11} + 0.212)\lambda^4 + (150w_{0.11} - 3.79)\lambda^3 + (-1165w_{0.11} + 0.212)\lambda^2 + (3687w_{0.11} - 49.47)\lambda - 2443w_{0.11} + 33.65 \quad (8)$$

The above equation was developed for the plate slenderness  $\lambda < 8$ , considering that over this value the post-1<sup>st</sup> yield strength reserve is not significant. The application effect of Eq. 8 to the 1<sup>st</sup> yield effective width calculated with the proposed formulation is presented in Figs. 4-8. The goal of this procedure is to emphasize that even for large imperfections, very good results can be obtained from the GNIA based on the proposed formulation if the post-1<sup>st</sup> yield strength reserve is considered. If the strength reserve is not considered, GNIA still predicts safe estimates (with few exceptions - all the unsafe estimates being under 5% of the ultimate load predicted by SFEA) but with significant underestimations of the plate ultimate capacity depending on the imperfection amplitudes.

#### 4. Experimental validation

The considered tests were reported by Dwight and Moxham (1969) and they were made by Harrison, Chin and Moxham on square welded box-columns after the stress-relieved technique was applied. The initial imperfection shapes or magnitudes are not given, therefore two plausible values were considered in this study ( $0.1\%b$  and  $0.25\%b$ ). The material properties are  $E = 204$  GPa and  $\mu = 0.3$ . Table 2 presents in the first 6 columns the experimental data ordered in the ascending order with respect  $\lambda$ . The next four columns present the ratios between the effective width determined with the proposed formulation and

the one reported from tests. For the plates with very low slenderness ( $\lambda < 3$ ), the post 1<sup>st</sup> yield strength reserve calculated with Eq. 8 is under 5% and it is disregarded. The 1<sup>st</sup> yield strength estimates for these cases are in very good agreement with the experimental data.

Table 1. Test and numerical results for square welded box-columns with stress-relieved

Test	$h$ [mm]	$f_y$ [MPa]	$b/h$	$\lambda$	$b_{eff\_test}/h$	$b_{eff\_}/b_{eff\_test}$				Winter
						$w_{0,11} = 0.1\%b$		$w_{0,11} = 0.25\%b$		
						1 <sup>st</sup> yield	ultimate	1 <sup>st</sup> yield	ultimate	
Harrison RB2	11.1	227	31.2	1.04	30.4	1.02	1.02	1.01	1.01	1.03
Harrison RC1	9.5	233	40.1	1.36	39.9	1.00	1.00	0.97	0.97	0.98
Harrison RD2	7.9	236	49.9	1.70	47.6	1.01	1.01	0.93	0.93	0.89
Harrison RD1	7.9	236	50	1.70	46	1.05	1.05	0.96	0.96	0.92
Moxham RT1	12.7	312	48	1.88	43.7	1.01	1.01	0.93	0.93	0.87
Moxham RT2	12.7	312	48	1.88	43.5	1.01	1.01	0.93	0.93	0.88
Harrison RE1	6.4	255	59.4	2.10	47.5	1.01	1.01	0.93	0.93	0.92
Harrison RE2	6.4	255	60	2.12	46.9	1.04	1.04	0.94	0.94	0.93
Chin RG1	5.6	375	65	2.79	36.9	1.03	1.03	0.98	<u>1.04</u>	1.03
Chin RG2	5.6	375	66	2.83	38.3	0.99	0.99	0.94	<u>1.00</u>	1.00
Chin RF3	4.8	385	80.4	3.49	38.4	0.96	<u>1.04</u>	0.93	<u>1.03</u>	1.02
Chin RF4	4.8	385	80.8	3.51	40.2	0.92	<u>1.00</u>	0.89	<u>0.98</u>	0.97

For the last two tests, one can see the effect of considering the strength reserve with respect the ultimate capacity (the underlined values from Table 2), especially for the last case when the 1<sup>st</sup> yield capacity is below 8% of the experimental one, but the ultimate capacity is in perfect agreement with the experimental value.

For an assumed imperfection amplitude of  $0.25\%b$ , the post 1<sup>st</sup> yield strength reserve is larger than 5% for the last four tests ( $\lambda > 2.5$ ), and again by considering this effect the estimates of the ultimate capacity are improved in comparison with the experimental data. From the last column one can see that the Winter predictions are inferior to the ones given by the proposed formulation, the maximum error is 13% on the safe side and 3% on the unsafe side. Fig. 9 presents the results of the last five columns of Table 2.

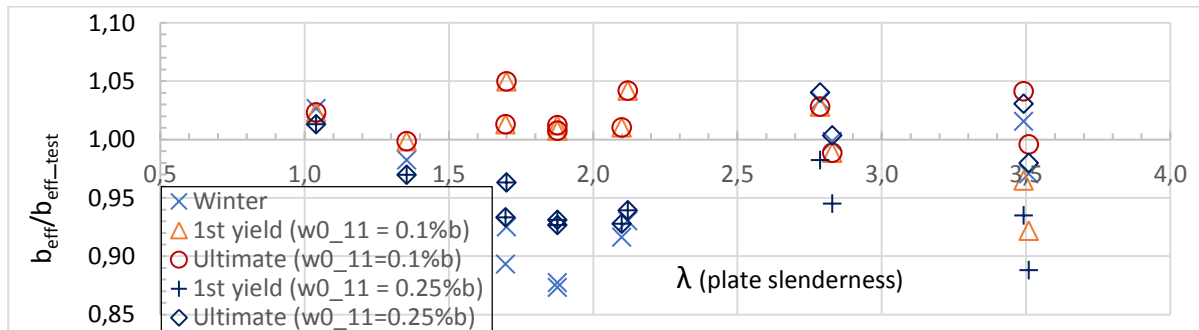


Figure 9: Winter and proposed formulation results against experimental results

Other experimental validations of the proposed solution are provided in Nedelcu (2020).

## 5. Conclusions

This paper presented a semi-analytical solution for the uniform compressed simply supported imperfect flat plate. The solution starts with a complex displacement field with multiple DOFs, described by a

combination of linear functions, single and double trigonometric series, and it is based on the Principle of Virtual Displacements. The solution yields a system of cubic equations that can be solved by an incremental-iterative process. The main advantage versus the numerical methods (as FEM) lies in the analytical expressions of the equation system coefficients, an advantage that makes the method fast and versatile. Also, the number of DOFs is at least 2 orders of magnitude fewer than the one used by FEM.

## References

- ABAQUS Standard (Version 6.3), 2002, Hibbit Karlsson and Sorensen Inc.
- Dwight, J.B., Moxham, K.E. (1969). "Welded steel plates in compression", *The Structural Engineer*, 2.
- EffWidth ver. 01.2019 - <http://users.utcluj.ro/~mnedelcu/EffWidth.htm>
- Eurocode 3, EN 1993-1-3:2006. Design of steel structures - Part 1-3: General rules - Supplementary rules for CFS members and sheeting.
- Eurocode 3, EN 1993-1-5:2006. Design of steel Structures - Part 1.5: Plated structural elements.
- von Kármán, T., Sechler, E.E., Donnell, L.H. (1932). "Strength of thin plates in compression", *ASCE Transactions*, 54.
- Lahde, R., Wagner, H. (1936). „Versuche zur Ermittlung der mittragenden Breite von verbeulten Blechen“, *Luftfahrt-Forsch*, 13: 214-223.
- Matlab 2005. Version 7.1.0246 Documentation, The Mathwork Inc.
- Nedelcu, M. (2020) "Semi-Analytical Solutions for the Uniformly Compressed Simply Supported Plate with Large Deflections", *International Journal of Structural Stability and Dynamics*, 20 (9).
- Timoshenko, S.P., Gere, J.M. (1961). "Theory of elastic stability. 2nd Ed.", New York, McGraw-Hill.
- Winter, G. (1947). "Strength of thin steel compression flanges", *ASCE Transactions*, Paper No. 2305, *Trans.*, 112, 1.

## **Analytical solutions for the GNI analysis for lateral-torsional buckling of thin-walled beams with doubly-symmetric and mono-symmetric cross-sections**

Muhammad Z. Haffar<sup>1</sup>, Sandor Adany<sup>2</sup>

### **Abstract**

In this paper a novel analytical solution is presented for the geometrically nonlinear analysis of beams subjected to lateral-torsional buckling, by assuming an initial geometric imperfection in the form of the buckled shape from a linear buckling analysis. The novelty of the solution is that it takes into consideration of the changing geometry as the load is increasing. Numerical results by the new analytical formula are compared to those from other methods. The results suggest that new formulae are able to correctly capture the most important elements of the behavior.

### **1. Introduction**

When a beam is subjected to bending, lateral-torsional buckling (LTB) is a potential failure mode. LTB has extensively been studied in the past decades. It can be observed, however, that the vast majority of the research was devoted to beams with doubly-symmetrical cross-sections subjected to major-axis bending. In the practice mono-symmetric and asymmetric cross-sections are used, too, they are especially typical in cold-formed steel construction. It is, therefore, important to understand the LTB behavior of beams with general cross-sections.

There is a trend nowadays to build more and more complete (finite element) models, to apply realistic loads, to (even if approximately but) directly consider imperfections, and to perform nonlinear analysis in order to get the load bearing capacity of the structure. If the material is assumed to be elastic, the analysis is popularly termed as GNI analysis, which is in the focus of the reported research.

Analytical solution for the linear buckling (LB) problem (which means the critical load calculation and buckled shape determination) of simple beams is available for general cross-sections, see Glauz (2017). Some analytical solution for the geometrically nonlinear problem with initial imperfection (GNI) is available, too, see Agüero et al. (2015), which is the generalization of Young's classic solution for an imperfect compressed column (Young, 1807). Recently it was shown by the authors, however, that there is discrepancy between the results predicted by the classic analytical GNI solution and those calculated by shell finite element GNI analyses, see Haffar et al. (2019). The discrepancies can be quite important. Also, the discrepancies are not limited to the difference of certain numerical values, but some basic features of the behavior are affected. For example, while the classic analytical solutions predict symmetric bifurcation for LTB, independently of the cross-section, shell finite element GNI analysis suggests asymmetric bifurcation in some cases. Moreover, while the classic analytical solutions predicts that the maximal moment equals the critical moment, numerical results do not always confirm this prediction.

---

<sup>1</sup> [muhammad.haffar@lupat.com](mailto:muhammad.haffar@lupat.com), [muhammad.haffar@lupat.com](mailto:muhammad.haffar@lupat.com)

<sup>2</sup> [sandor.adany@lupat.com](mailto:sandor.adany@lupat.com), [sandor.adany@lupat.com](mailto:sandor.adany@lupat.com)

In order to understand the reasons of the experienced differences, some fundamental problems are revisited in the reported research, namely: the analytical solution for the lateral-torsional behavior of beams with initial geometrical imperfections. In order to have closed-form solutions, the simplest supports and loading conditions are assumed: fork supports and uniform bending (resulted from two opposing end moments), see Fig. 1.

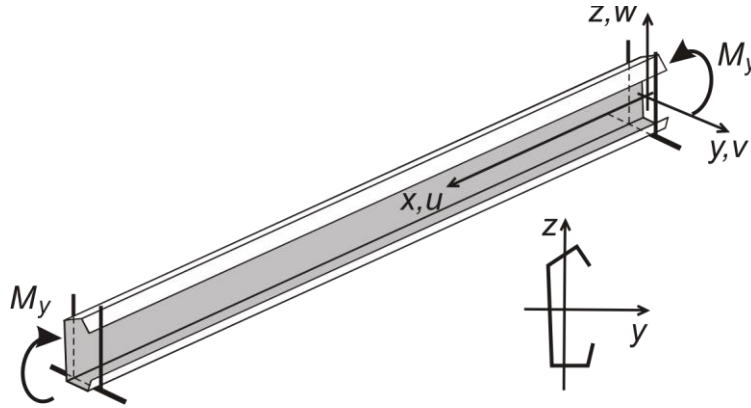


Figure 1: Simply supported thin-walled beam in uniform bending

## 2. Classic analytical solution for doubly-symmetrical cross-sections

In classic LB and GNI analytical solutions for LTB the main assumptions are as follows: (i) the primary and secondary displacements are independent, (ii) the second-order effects (e.g., expressed by the geometric stiffness matrix) are defined on the original undeformed beam (in other words: by assuming the primary stress distribution), (iii) small displacements are assumed and the nonlinearity of the strain-displacement relationship is considered by the Green-Lagrange strains, (iv) for simple supported beams the secondary displacements are half-sine waves, i.e.,

$$W = W_m \sin\left(\frac{\pi x}{L}\right), \quad V = V_m \sin\left(\frac{\pi x}{L}\right), \quad \phi = \phi_m \sin\left(\frac{\pi x}{L}\right) \quad (1)$$

where  $W_m$ ,  $V_m$  and  $\phi_m$  are the amplitudes for the vertical and lateral translations and for the twisting rotation, respectively,  $x$  is the longitudinal coordinate axis, and  $L$  is the beam length. A major axis  $M_y$  bending moment is considered, which causes uniform bending along the beam in the vertical  $x$ - $z$  plane. By using e.g. the energy method, the total potential can be expressed by the displacement parameters ( $W_m$ ,  $V_m$ ,  $\phi_m$ ), then the theorem of stationarity of potential energy leads to a system of linear equations, which, in other words, is a generalized eigen-value problem. In the case of doubly-symmetric cross-section and principal-axis bending, this can be written as:

$$\begin{bmatrix} F_y & 0 & 0 \\ 0 & F_z & 0 \\ 0 & 0 & F_x \end{bmatrix} \cdot \begin{bmatrix} W_m \\ V_m \\ \phi_m \end{bmatrix} + \begin{bmatrix} 0 & 0 & 0 \\ 0 & 0 & M_y \\ 0 & M_y & 0 \end{bmatrix} \cdot \begin{bmatrix} W_m \\ V_m \\ \phi_m \end{bmatrix} = \begin{bmatrix} 0 \\ 0 \\ 0 \end{bmatrix} \quad (2)$$

where the  $F_x$ ,  $F_y$  and  $F_z$  symbols are defined as follows:

$$F_y = \frac{\pi^2 EI_y}{L^2}, \quad F_z = \frac{\pi^2 EI_z}{L^2}, \quad F_x = GI_t + \frac{\pi^2 EI_w}{L^2} \quad (3)$$

where  $I_y$  and  $I_z$  are the second moment of areas calculated for the  $y$ -axis and  $z$ -axis, respectively,  $I_w$  is the warping constant,  $I_t$  is the torsion constant,  $E$  and  $G$  are the modulus of elasticity and the shear modulus, respectively. The first matrix is the  $\mathbf{K}_e$  elastic stiffness matrix, while the second one is the  $\mathbf{K}_g$

geometric stiffness matrix of the problem. The first equation can be eliminated, i.e., the secondary displacements in the plane of the bending do not lead to instability. The eigen-values are the  $M_{cr}$  critical moment values. By back-substituting the critical moment, we get the buckled shape with lateral translation and twisting rotation.

If an initial geometric imperfection is assumed in the form of this buckling shape, the above derivation can similarly be completed, however, the right-hand side of Eq. (2) will not be zero any more but will depend on the amplitude of the initial imperfect geometry.

$$\begin{bmatrix} F_y & 0 & 0 \\ 0 & F_z & 0 \\ 0 & 0 & F_x \end{bmatrix} \cdot \begin{bmatrix} W_m \\ V_m \\ \phi_m \end{bmatrix} + \begin{bmatrix} 0 & 0 & 0 \\ 0 & 0 & M_y \\ 0 & M_y & 0 \end{bmatrix} \cdot \begin{bmatrix} W_m \\ V_m \\ \phi_m \end{bmatrix} = \begin{bmatrix} 0 \\ -F_z V_{m,ini} \\ -M_{cr} V_{m,ini} \end{bmatrix} \quad (4)$$

Again, the first equation has no role, while from the other two equations the actual value of the displacement amplitudes can be calculated. This leads to the well-known formula for the displacement amplification (also known as Young's formula):

$$V_m = V_{m,ini} \frac{1}{1 - M_y/M_{cr}}, \quad \phi_m = \phi_{m,ini} \frac{1}{1 - M_y/M_{cr}} \quad (5)$$

Similar derivations can be done for mono-symmetric or non-symmetric cases. For the critical load and buckled shape determination for general cross-sections, see Glauz (2017). Some classic analytical solution for the geometrically nonlinear problem with initial imperfection (GNI) is available in Agüero et al. (2015).

### 3. Advanced analytical solution

When the finite element method is applied to a similar problem, there are some major differences: (i) the load is applied in increments and/or iteration is used, which means that the actual stiffness of the member is updated during the analysis as the member deforms, (ii) the primary and secondary displacements are not separated, (iii) there is no predefined sinusoidal shape for the displacements, and (iv) depending on the selected finite element there might be further differences, too. The aim here is to directly consider at least the first two of the above factors in the analytical solution for the GNI analysis.

The energy method was employed. For the primary displacements a quadratic function is used (in accordance with the first-order solution), while for the secondary displacements half-sine-waves are assumed. The displacement functions are as follows:

$$W = W_m \frac{4}{L^2} (L - x)x, \quad V = V_m \sin\left(\frac{\pi x}{L}\right), \quad \phi = \phi_m \sin\left(\frac{\pi x}{L}\right) \quad (6)$$

with the initial geometry as:

$$V_{ini} = V_{m,ini} \sin\left(\frac{\pi x}{L}\right), \quad \phi_{ini} = \phi_{m,ini} \sin\left(\frac{\pi x}{L}\right) \quad (7)$$

We assume that the load is applied in increments. After a certain number of increments, the load is  $M_{y1}$ , and the corresponding displacement amplitudes are:  $W_{m1}$ ,  $V_{m1}$  and  $\phi_{m1}$ . Then the goal is to find the displacement increments,  $\Delta \mathbf{d}$ , as the load is further increased by  $\Delta M_y$ . The derivations are not shown here, but finally we got the following system of equations.

$$\mathbf{K}_e \Delta \mathbf{d} + M_{y2} \mathbf{K}_g \Delta \mathbf{d} = \Delta \mathbf{f} \quad (8)$$

with

$$M_{y2} = M_{y1} + \Delta M_y \quad (9)$$

where

$$\Delta \mathbf{d} = \begin{bmatrix} \Delta W_m \\ \Delta V_m \\ \Delta \Phi_m \end{bmatrix} \quad \mathbf{K}_e = \begin{bmatrix} F_y \frac{64}{\pi^2 L} & 0 & 0 \\ 0 & F_z \frac{\pi^2}{2L} & 0 \\ 0 & 0 & F_x \frac{\pi^2}{2L} \end{bmatrix} \quad \mathbf{K}_g = \begin{bmatrix} 0 & 0 & -\Phi_{m1} \frac{2}{L} \\ 0 & 0 & \frac{\pi^2}{2L} \\ -\Phi_{m1} \frac{2}{L} & \frac{\pi^2}{2L} & \frac{\pi^2}{L} \beta_z + \Phi_{m1} \frac{4\pi}{3L} \beta_y \end{bmatrix} \quad (10)$$

$$\Delta \mathbf{f} = \begin{bmatrix} -M_{y2} \frac{8}{L} + M_{y2} \Phi_{m1}^2 \frac{2}{L} - W_{m1} F_y \frac{64}{\pi^2 L} \\ -M_{y2} \Phi_{m1} \frac{\pi^2}{2L} - (V_{m1} - V_{m,i}) F_z \frac{\pi^2}{2L} \\ -M_{y2} V_{m1} \frac{\pi^2}{2L} - M_{y2} \Phi_{m1} \frac{\pi^2}{L} z_j - M_{y2} \Phi_{m1}^2 \frac{4\pi}{3L} y_j + M_{y2} W_{m1} \Phi_{m1} \frac{2}{L} - (\Phi_{m1} - \Phi_{m,i}) F_x \frac{\pi^2}{2L} \end{bmatrix} \quad (11)$$

where  $y_j$  and  $z_j$  are non-symmetry factors defined as follows:

$$y_j = y_s - 0.5 \int_A (y^2 + y^2) y dA \quad z_j = z_s - 0.5 \int_A (y^2 + y^2) z dA \quad (12)$$

where  $y_s, z_s$  are the coordinates of shear center relative to the centroid.

The above equation system can be solved analytically. By introducing

$$\hat{M}_{cr}^2 = M_{cr}^2 - 2M_{cr} F_z z_j \quad (13)$$

the displacement increments can be written as follows.

$$\Delta W_m = \frac{-M_{y2} \frac{\pi^2}{8F_y} \left[ \frac{\hat{M}_{cr}^2}{M_{y2}^2} - 1 \right] - V_{m,i} \Phi_{m1} \frac{\pi^2 F_z}{32F_y} + \Phi_{m,i} \Phi_{m1} \frac{\hat{M}_{cr}^2 \pi^2}{M_{y2} 32F_y} - \Phi_{m1} \frac{\pi F_z y_j}{3F_y} - \frac{F_z z_j \pi^2}{4F_y}}{\frac{\hat{M}_{cr}^2}{M_{y2}^2} - 1 + \Phi_{m1} \frac{8F_z y_j}{3\pi M_{y2}} + \frac{2F_z z_j}{M_{y2}} - \Phi_{m1}^2 \frac{F_z}{8F_y}} - W_{m1} \quad (14)$$

$$\Delta V_m = \frac{V_{m,i} + \Phi_{m1} \frac{M_{y2}}{2F_y} - \Phi_{m,i} \frac{F_x}{M_{y2}}}{\frac{\hat{M}_{cr}^2}{M_{y2}^2} - 1 + \Phi_{m1} \frac{8F_z y_j}{3\pi M_{y2}} + \frac{2F_z z_j}{M_{y2}} - \Phi_{m1}^2 \frac{F_z}{8F_y}} - (V_{m1} - V_{m,i}) \quad (15)$$

$$\Delta \Phi_m = \frac{-V_{m,i} \frac{F_z}{M_{y2}} - \Phi_{m1} \frac{F_z}{2F_y} + \Phi_{m,i} \frac{\hat{M}_{cr}^2}{M_{y2}^2}}{\frac{\hat{M}_{cr}^2}{M_{y2}^2} - 1 + \Phi_{m1} \frac{8F_z y_j}{3\pi M_{y2}} + \frac{2F_z z_j}{M_{y2}} - \Phi_{m1}^2 \frac{F_z}{8F_y}} - \Phi_{m1} \quad (16)$$

## 4. Numerical studies

### 4.1. Doubly-symmetric I-sections

The expressions for the displacement increments can be simplified if the cross-section is doubly symmetric, i.e. if  $y_j = z_j = 0$ . Moreover, it can also be considered that the initial shape is the buckling shape, therefore, the initial twist and initial lateral translation are dependent on each other. Still, it is clear that the second-order lateral translation and twisting rotation are different from those predicted by the Young's formula. Moreover, the formulae for  $V$  and  $\Phi$  are different. However, an important characteristic of these formulae is that if the sign of the initial geometry is reversed then (i) the vertical  $W$  displacement is unchanged, (ii) the sign of the lateral increment is reversed, and (iii) the sign of the twisting rotation

increment is reversed. This also means that a symmetric bifurcation is predicted (as the initial displacement converges to zero).

As the bending moment increases, the denominator of the formulae can decrease to zero, which identifies singularity. From the formulae it can be seen that the singularity belongs to a bending moment smaller than  $M_{cr}$ . The distance of the singularity to  $M_{cr}$  is largely dependent on the twisting rotation (squared), and since the whole theory is based on the assumption that the rotations are small, the bending moment where singularity happens is only marginally smaller than  $M_{cr}$ .

A final theoretical observation is that the primary ( $W$ ) and secondary ( $V$  and  $\Theta$ ) displacements are not independent. However, the secondary ones are not affected by the primary one, only the primary one is affected by the secondary ones.

To illustrate the results, two members are considered. Both are simply supported and subjected to uniform major-axis bending, and both have doubly-symmetric I-shaped sections. The depth of each section is 200 mm, the flange and web thicknesses are 20 mm. One cross-section has a flange width of 50 mm (referred to as *narrow I-section*), the other has a flange width of 200 mm (referred to as *wide I-section*). The member length is 2 m, and standard steel material is considered. The initial value of the lateral translation was set to 2 mm, which is 1/1000 of the length.

The GNI analyses are performed by the newly developed updated analytical formulae, by using a large number of load incremental steps. Moreover, the GNI analyses have been performed by shell finite element method, using the commercial Ansys software (Ansys, 2020), by using the so-called shell181 finite elements. The results are summarized in Figs. 2 and 3. Only the results with the positive initial lateral translations are shown, however, the plots with negative initial lateral translations would look exactly the same. For reference, the results from the Young-formula are plotted, too.

The plots demonstrate that the second-order lateral translation and twisting rotation are smaller than what the Young-formula predicts. The deviation increases as the moment increases. It can also be observed that: the wider the flanges are, the larger the deviation from the Young-prediction is. Though the vertical, primary displacement is slightly different from the first-order solution (which is a straight line in the load-displacement plot), the deviation from the first-order solution is rather small.

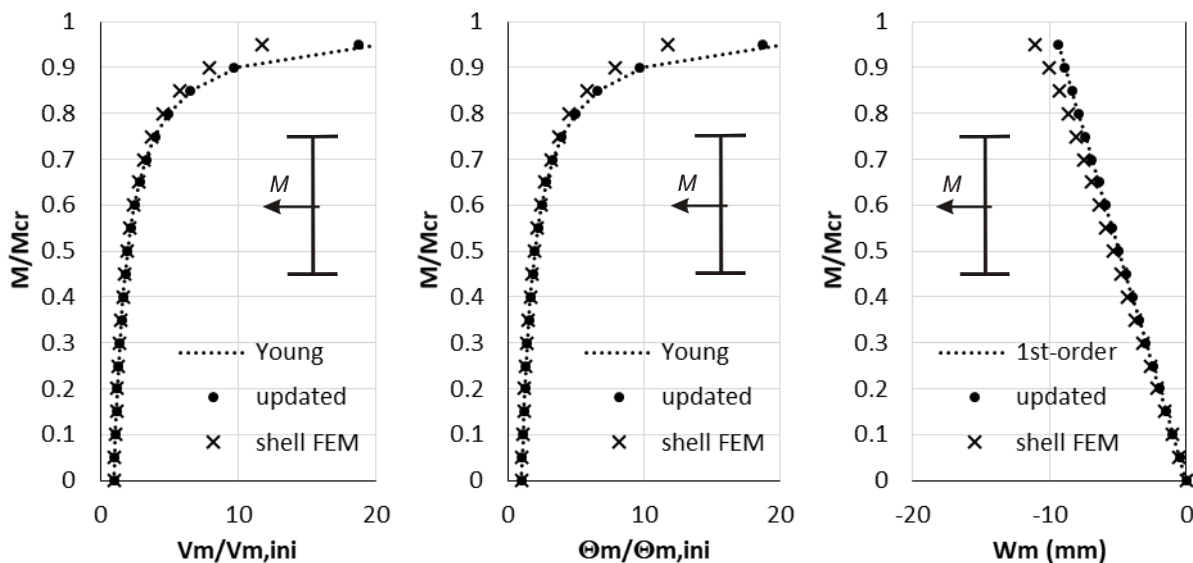


Figure 2: Load-displacement plots, narrow I-section

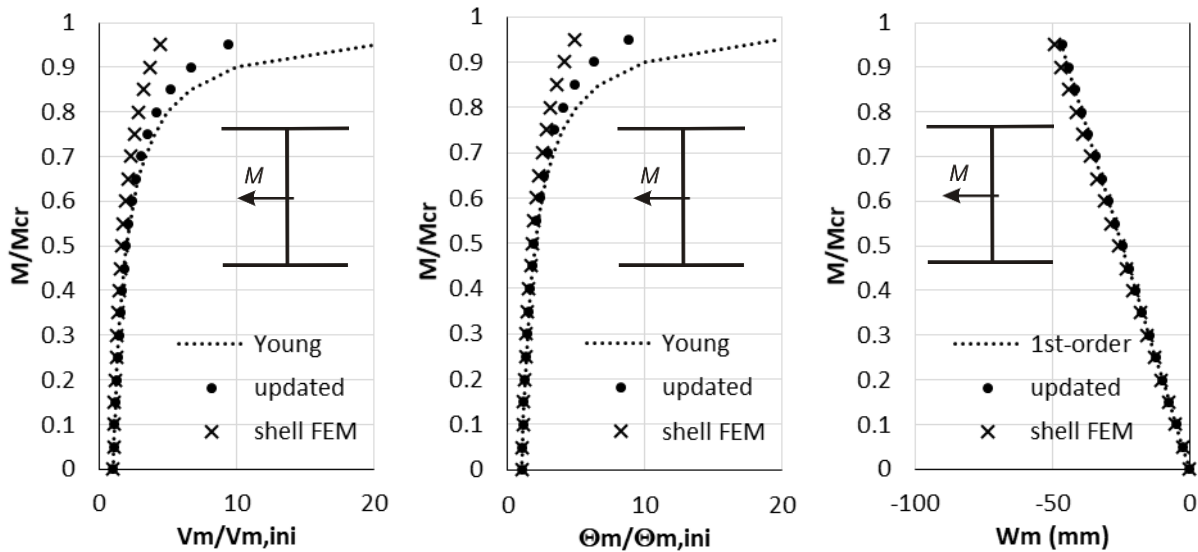


Figure 3: Load-displacement plots, wide I-section

A general observation is (which is relevant to all the other examples, too), that the actual values from the analytical solution and from the shell FEM are not identical, even though the tendencies are rather similar. It is important to understand that exact agreement cannot be expected due to the differences between the two models. One difference is that in the shell FE model the longitudinal distribution of the displacements can slightly be different from those assumed in the analytical model. However, almost certainly other factors have much larger effect, namely those deformations in the shell model which are neglected in the analytical model: in-plane shear deformations, small localized plate bending deformations, and also out-of-plane shear deformations (since the shell181 finite element of Ansys is based on the Reissner-Mindlin plate theory). The differences between the analytical and shell FEM results are not limited to the secondary displacements, but considerable differences are experienced in the critical moments as well as in the primary displacements (see the right plots in Figs. 2 and 3).

#### 4.2. Mono-symmetric cross-sections, bending in the symmetry plane

Now we consider a mono-symmetric cross-section. The axis of symmetry is the  $z$ -axis, i.e.  $y_j = 0$ , hence the bending is acting in the symmetry plane. The expressions in Eqs. (14)-(16) for the displacement increments can slightly be simplified. By analyzing the formulae for the lateral translation and for the twisting rotations, it can be seen that, again, they are different from the Young-formula and from each other. It can be understood that if the sign of the initial geometry has no real effect, a symmetric bifurcation is predicted (as the initial displacement converges to zero).

To illustrate the results, two cases are considered, with identical mono-symmetric T-shaped sections. The width and depth of the cross-section are 200 mm, the flange and web thicknesses are 20 mm. The member length is 2 m, and standard steel material is considered. The initial value of the lateral translation was set to 2 mm, which is 1/1000 of the length. The only difference between the two analyzed cases is that in the first case the flange is in tension, while in the second case the flange is in compression.

The results are summarized in Fig. 4. Only the lateral translation results are plotted, but considering both positive and negative initial values. The plots demonstrate that the behavior is symmetric. Moreover, the second-order lateral translation is smaller than what the Young-formula predict, similarly what we have seen in the case of the doubly-symmetric I-section. In this case there is a further factor: the sign of the bending moment. The results are clearly dependent on whether the flange is in tension or compression.

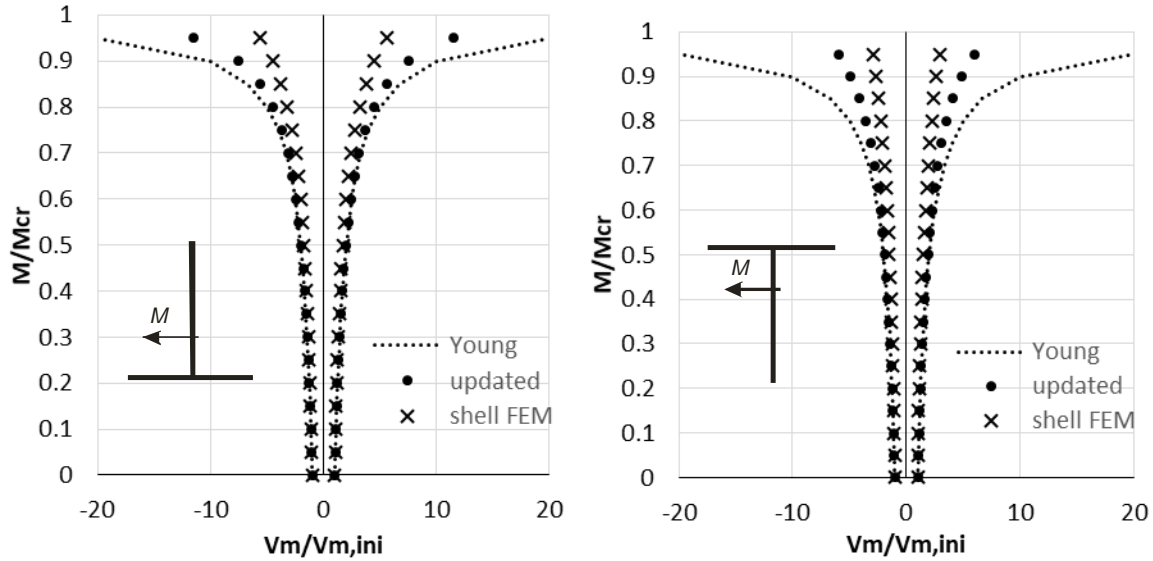


Figure 4: Load-displacement plots, T-sections

#### 4.3. Mono-symmetric cross-sections, bending perpendicular to the symmetry plane

Now we consider mono-symmetric cross-sections where the axis of symmetry is the  $y$ -axis, i.e.  $z_j = 0$ . The bending is still in the vertical plane, that is in a plane perpendicular to the symmetry plane. The expressions for the displacement increments in Eqs. (14)-(16) can be simplified. The most important observation is that the absolute values of the denominators of the formulae are dependent on the sign of the initial displacement. This means that the magnitudes of both the primary (vertical) and secondary displacements are influenced by whether the initial displacement is considered with positive or negative sign. This also means asymmetric bifurcation. Since asymmetric bifurcation is more sensitive to imperfections compared to symmetric ones, this is an important difference which potentially influences the design resistance, too.

As the bending moment increases, the denominator of the formulae can decrease to zero, which identifies singularity. This singularity point is affected by the sign of the initial displacement: depending on the sign, the singularity belongs to a bending moment smaller or larger than  $M_{cr}$ . The distance of the singularity to  $M_{cr}$  is mostly dependent on the twisting rotation. Even though the whole analytical solution is based on the assumption that the rotations are small, the bending moment where singularity happens is non-negligibly different from  $M_{cr}$ , as the following numerical examples prove.

To illustrate the results, two U-shaped channel-sections are considered. The depth of the cross-sections is 200 mm, the plate thicknesses is 20 mm, the member length is 2 m, and standard steel material is considered. The difference between the considered two cross-sections is the flange width, the two values are 50 mm and 100 mm. The initial value of the lateral translation was set to 2 mm, which is 1/1000 of the length, both with positive and negative sign.

The results are summarized in Fig. 5. Only the lateral translation results are plotted, but considering both positive and negative initial values. The asymmetric nature of the behavior can clearly be seen. In this actual case if the initial lateral translation is positive, the amplification is significantly smaller than the one predicted by the Young-formula. At the same time, the bending moment can exceed the critical moment. However, if the initial lateral translation is negative, singularity is reached well below the critical moment, and the amplification is similar to that predicted by the Young-formula. (In fact, the amplification can even be larger.) It can also be observed that the asymmetry of the behavior is smaller for the narrower cross-section. Even though the analytical and shell FEM results are not identical, the tendencies of the results are the same from both methods.

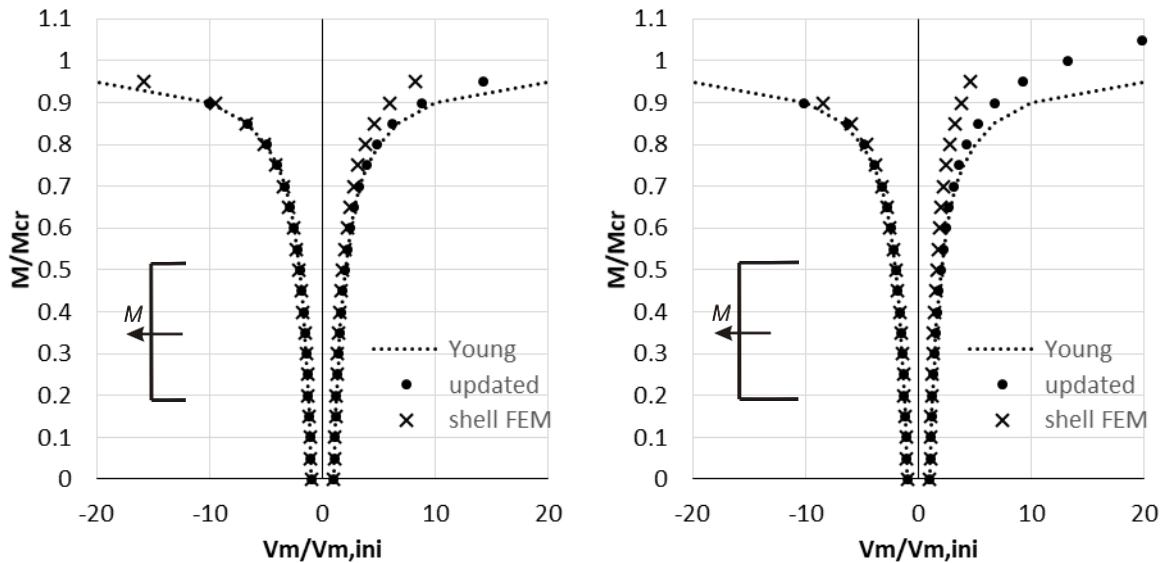


Figure 5: Load-displacement plots, U-section

## 5. Conclusions

In this paper new, updated analytical solutions were shown for the GNI analysis of beams with lateral-torsional buckling. Numerical examples show that the derived new formulae are able to capture the behavior predicted by shell finite element analysis. The new analytical solutions well explain the differences between the results of classic analytical solutions and shell finite element analyses. The new analytical formulae predict symmetric bifurcation for doubly-symmetric cross-section and mono-symmetric cross-sections loaded in the symmetry plane. However, the bifurcation is asymmetric as soon as the cross-section is not doubly symmetric and the load is perpendicular to the plane of symmetry. This feature of the analytical solution is in perfect agreement with the observations from shell FE results. Finally, unlike the classic analytical solution, the new analytical formulae suggest that maximum load is different from the critical load, which is again justified by shell finite element results.

## Acknowledgment

The presented work was conducted with the financial support of the K119440 project of the National Research, Development and Innovation Office of Hungary.

## References

- Agüero, A, Pallares, F.J., Pallares, L. (2015), Equivalent geometric imperfection definition in steel structures sensitive to lateral torsional buckling due to bending moment, *Engineering Structures*, Vol 96, pp. 41-55.
- Ansys (2020), Ansys Inc., Release 2020 R1.
- Glauz, R.S. (2017), Elastic lateral-torsional buckling of general cold-formed steel beams under uniform moment, *Thin-Walled Structures*, Vol 119, pp. 586-592.
- Haffar M.Z., Taher M.H., Ádány S. (2019), On the GNI analysis of simple thin-walled beams with using linear buckling mode as geometric imperfection, Proceedings of the International Colloquium on Stability and Ductility of Steel Structures (SDSS 2019), Prague, Czech Republic 11-13 September 2019, pp. 468-475.
- Young, T. (1807), A course of lectures on natural philosophy and the mechanical arts, Royal Institution of Great Britain, London (1807)

## New transverse extension modes for the constrained finite strip analysis of thin-walled members

Trung Hoang<sup>1</sup>, Sandor Adany<sup>2</sup>

### Abstract

In this paper a new way to define transverse extension modes is introduced in the context of modal analysis of thin-walled members. The new primary transverse extension modes are inspired by the strain distributions of global and distortional modes. The new modes are employed here in the constrained finite strip method. The new modes require some change in the interpolation functions of the semi-analytical finite strip method, which change is briefly discussed. The practical advantage of the proposed new transverse extension modes is that the artificial stiffness increase, which is characteristics to constrained analyses, can be compensated by the consideration of the relevant new transverse extension mode(s), as illustrated by numerous proof-of-concept examples in the paper.

### 1. Introduction

A widely used practical approach to understand and analyse the complex behaviour of a structural member is to decompose the complex phenomenon into simpler ones, and then to interpret the complex phenomenon as a superposition of simpler phenomena. In accordance with this approach, the deformations of thin-walled members (e.g., cold-formed steel members) are frequently categorized into characteristic classes as follows: global (G), distortional (D), local-plate (L), shear (S) and transverse extension (T) behaviour. There are two major approaches for the modal decomposition. One approach is the enhancement of classic beam models, followed most prominently by the generalized beam theory (GBT), see e.g. Bebiano et al (2015). The other approach is the constraining of shell models; the idea first appeared in the constrained finite strip method (cFSM), see e.g. Adany and Schafer (2008), but later applied in a number of other methods, too.

The modal decomposition of the behaviour of a thin-walled member has been found especially useful to understand and analyse the stability behaviour which is governing in many practical situations due to the thin-walled nature, i.e., high slenderness of the structure. In buckling problems these are the G, D and L which are the most important ones, but shear and transverse extension deformations might have an important role, too.

Since in the G and D modes the transverse strains are forced to be zero, while the longitudinal normal strains are forced to be non-zero, the longitudinal normal stiffness of the plate elements are increased

---

<sup>1</sup> Trung Hoang, Ph.D., Faculty of Mechanical Engineering, Lodz University of Technology, ul. Zeromska 14, 91-401 Lodz, Poland, e-mail: trung.hoang@p.lodz.pl

<sup>2</sup> Sandor Adany, Ph.D., Faculty of Mechanical Engineering, Lodz University of Technology, ul. Zeromska 14, 91-401 Lodz, Poland, e-mail: sandor.adany@p.lodz.pl

whenever a static analysis is performed in the G and/or D deformation spaces. The phenomenon was reported in various cFSM papers and fully explained in Adany (2012) by analytical considerations. Obviously, the increased stiffness is initiated by the restrained transverse contraction/stretching. By allowing transverse extension deformations, therefore, the artificial extra stiffness can be released. It was also shown that the extra stiffness can (typically) be avoided by defining zero Poisson's ratio.

In the here reported research new, practically meaningful transverse extension modes are presented. The practical advantage of the introduced new T modes is that artificial stiffness increase can be released from the global and/or distortional solutions by adding the corresponding T modes. For example, flexural buckling of a thin-walled member with truly rigid cross-sections requires one single mode to consider, namely one of the global bending modes. If we want to have flexural buckling while allowing small transverse extensions (which are typically allowed in a classic buckling solution), we need to add one extra mode, namely the corresponding "transverse extension bending" mode.

The new T modes have been proposed similarly to the S modes. First, primary and secondary T modes are distinguished, the primary modes being characterized by linear transverse normal strain distributions for any flat part of the member. Then, the primary modes have been further subdivided into "transverse extension bending", "transverse extension torsion", "transverse extension distortional", and "other transverse extension" modes. The transverse distribution of the transverse normal strains are identical to those of the longitudinal strains in global and distortional modes.

There is a practical difficulty: the existing constrained finite strip and finite element implementations assume linear transverse shape functions for the in-plane translations, which means that linear variation of the transverse strains is not possible within one element. The most straightforward solution is to change the shape functions, which will briefly be presented in the paper.

## 2. The new transverse extension modes

In GBT and cFEM the G and D modes are characterized by specific warping distributions over the cross-section. The specialty is that the distribution is linear along any flat plate. This is true not only for the warping (i.e. longitudinal) translations, but also for their derivatives (with respect to the longitudinal coordinate), that is for the longitudinal normal strains. This means that if a simple open or closed cross-section has  $n$  main nodes (called also natural nodes), the number of independent G+D distributions is  $n$ , i.e., the number of G and D modes altogether equals  $n$ . (In the case of complex cross-sections the number of G+D modes can be smaller than  $n$ .) By further assuming that the transverse normal strains and the in-plane shear strains are zero, in a typical open cross-section 4 modes can be found where the warping distribution is piece-wise linear and the cross-section is displaced as a rigid body. These are usually called global (G) modes. The remaining modes are the distortional (D) ones, still with piece-wise linear warping. The strain distributions are illustrated in Fig. 1 for a lipped channel cross-section.

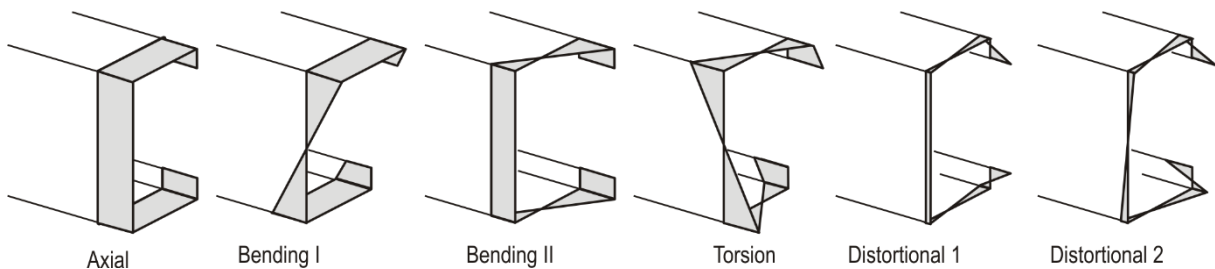


Figure 1: Load-displacement plots, 3-DOF approach

The in-plane shear deformations are discussed in detail in Adany (2013), where the distinction of “primary” and “secondary” shear modes was introduced. Primary shear modes (SP) are characterized by linear distribution of the in-plane shear strain in the transverse direction in any flat part of the cross-section, while secondary shear modes (SS) are those with nonlinear shear strain distribution even within one flat plate element. Since G and D and SP modes all share the piece-wise linear nature of the relevant strain distribution, it is possible and meaningful to categorize the primary shear modes into “shear bending”, “shear torsion”, “shear distortional”, and “other shear” modes. All are characterized by linear distribution of the (in-plane) shear strains in the transverse direction for any flat part of the cross-section, and, furthermore, the distributions are similar to the longitudinal normal strain distributions of the global bending, global torsion and distortional modes, respectively. This makes it possible to easily imitate shear-deformable beam theories, or, to solve problems of hollow sections with twisting. It is to note that “shear axial” mode does not exist, since if the warping is uniform, there is no associated in-plane shear. It is also to note that “other shear” modes exist only in branched cross-sections. The details can be found in Adany (2013).

The idea here is to apply the approach of shear modes to the transverse extension modes (T). In the case of T modes the characterizing strain is the transverse normal strain. We want to have, therefore, “primary transverse extension” modes (TP) with piece-wise linear transverse strain distributions, identical to the ones illustrated in Fig. 1. Furthermore, we introduce “transverse bending” (TB), “transverse torsion” (TT), “transverse distortional” (TD), and “other transverse” (TO) modes, with the relevant strain distributions.

The above description of the transverse extension modes is independent of the numerical method, and can potentially be applied in any modal decomposition method. Here its application in the constrained finite strip method (cFSM) is presented and briefly discussed.

### 3. Modified FSM

In the semi-analytical finite strip method (FSM) the members are discretized into longitudinal strips as shown in Fig. 2. Note, Fig. 2 illustrates the nodal displacements for the simplest longitudinal shape function as given in Eqs. (1)-(3), with  $m=1$ .

Within a strip, local displacement fields  $u$ ,  $v$ , and  $w$  are expressed by the linear combination of basis functions and the nodal displacements, which latter ones now should be interpreted as characteristic displacement values at nodal lines. In the classic FSM the displacements are interpolated as follows (Cheung, 1968):

$$u(x, y) = \left[ \left(1 - \frac{x}{b}\right) \quad \left(\frac{x}{b}\right) \right] \begin{bmatrix} u_1 \\ u_2 \end{bmatrix} \sin \frac{m\pi y}{a} \quad (1)$$

$$v(x, y) = \left[ \left(1 - \frac{x}{b}\right) \quad \left(\frac{x}{b}\right) \right] \begin{bmatrix} v_1 \\ v_2 \end{bmatrix} \cos \frac{m\pi y}{a} \quad (2)$$

$$w(x, y) = \left[ \left(1 - \frac{3x^2}{b^2} + \frac{2x^3}{b^3}\right) \quad \left(-x + \frac{2x^2}{b} - \frac{x^3}{b^2}\right) \quad \left(\frac{3x^2}{b^2} - \frac{2x^3}{b^3}\right) \quad \left(\frac{x^2}{b} - \frac{x^3}{b^2}\right) \right] \begin{bmatrix} w_1 \\ \theta_1 \\ w_2 \\ \theta_2 \end{bmatrix} \sin \frac{m\pi y}{a} \quad (3)$$

where  $a$  is the member length, and  $b$  is the strip width. The above longitudinal shape functions correspond to locally and globally pinned end restraints, and in typical buckling solutions  $m=1$  is used. It is to note for other end restraints (e.g. clamped-clamped) other functions are necessary.

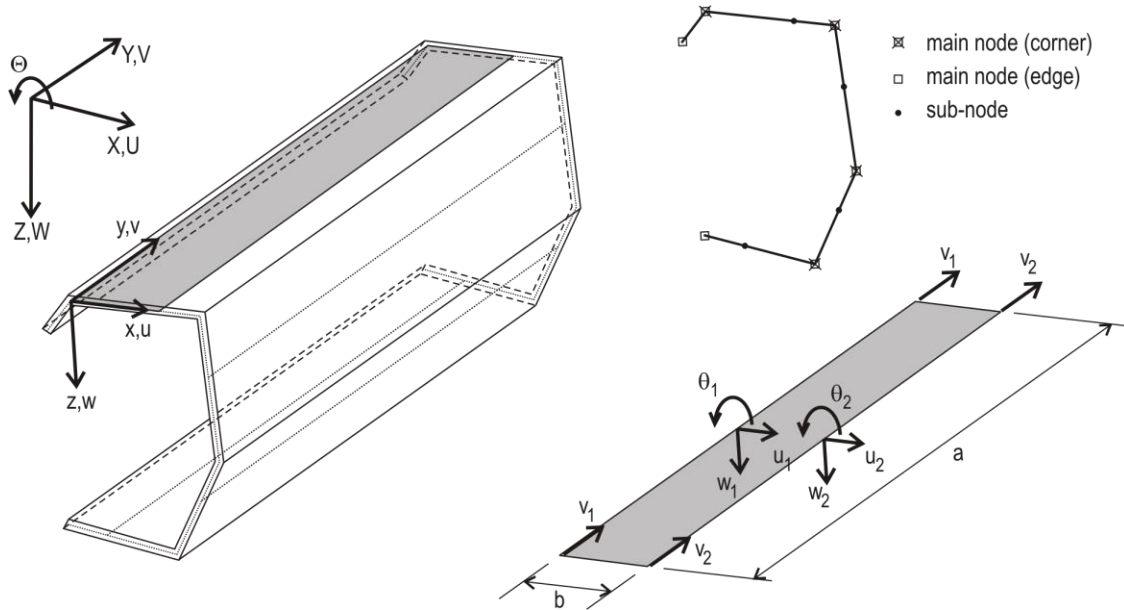


Figure 2: Load-displacement plots, 3-DOF approach

It is to observe that the  $v$  longitudinal translations are interpolated by linear functions in the transverse direction. Consequently, for the global modes as well as for the primary shear modes one single element is enough to use for one flat plate between two main nodes. However, it can also be seen that for the  $u$  transverse translations the interpolation functions are linear in the transverse direction (i.e., in  $x$ ). A consequence of this is that within one element the transverse normal strain  $\epsilon_x = du/dx$  is constant. If one single strip is used in one flat plate, the  $\epsilon_x$  distribution cannot be linear in  $x$ . But even if multiple strips were used within one flat plate, a linearly varying  $\epsilon_x$  could not have been achieved, only approximated.

A straightforward solution is to change the transverse interpolation functions for the  $u$  displacements: instead of linear, we need quadratic function, so that its first derivative could be linear. To do so, we need three nodes (or nodal lines), and the  $u$  displacements can be expressed as:

$$u(x, y) = \left[ \left( 1 - \frac{3x}{b} + \frac{2x^2}{b^2} \right) \quad \left( -\frac{x}{b} + \frac{2x^2}{b^2} \right) \quad \left( \frac{4x}{b} - \frac{4x^2}{b^2} \right) \right] \begin{bmatrix} u_1 \\ u_2 \\ u_3 \end{bmatrix} \sin \frac{m\pi y}{a} \quad (4)$$

This change of the interpolation has several consequences for the FSM. The number of degrees of freedom of a single strip is changing from 8 to 9, hence the size of the local stiffness matrix changes from  $8 \times 8$  to  $9 \times 9$ , etc. Also, certain terms of the stiffness matrix change and new terms appear. The new stiffness matrices can be derived by following the usual steps, the details are not shown here.

The change of the interpolation function has an important effect on the constraining, too. However, since in G, D, L and S modes the transverse extension is zero, these modes are not affected. The T modes are obviously affected. Most notably, the number of primary transverse extension modes increases, in fact roughly doubles. Also the number of secondary T modes increases significantly. The exact number of TP and TS modes is dependent on the topology of the cross-section, and not detailed here.

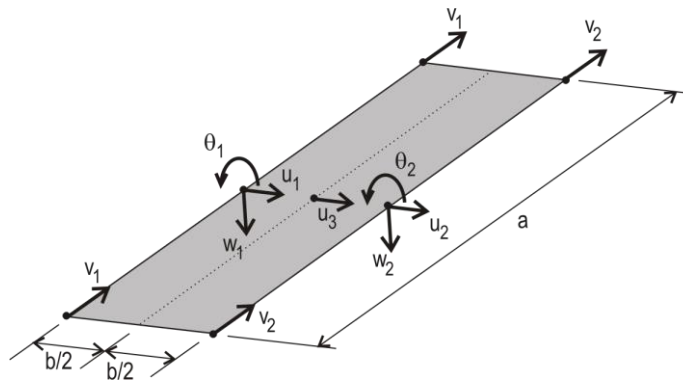


Figure 3: Strip with new DOF

#### 4. Examples

In this Section proof-of-concept examples are presented. A lipped channel member is selected, with typical geometric dimensions: 200 mm web depth, 80 mm flange width and 15 mm lip length. (The lips are perpendicular to the flanges.) The thickness is 1.5 mm. The material is steel with 210 GPa of Young's modulus and  $\nu=0.3$  Poisson's ratio. The load is uniform compression.

The cross-section is open, with 6 main nodes. Consequently, there are 6 characteristic piece-wise linear warping distributions (as in Fig. 1), four of them global (G), two of them distortional (D). In Figs. 4-6 the two pure bending buckling modes and the one pure torsion buckling mode are studied. 4 curves are plotted in each figure. The first one is the solution with one single mode, e.g., in Fig. 4 the pure minor-axis buckling mode by using the GBmin deformation mode only. The second curve is calculated by the same one mode, but with an orthotropic material by setting the Poisson's ratio to zero. The third curve is calculated with the normal isotropic material, but with adding the relevant transverse extension mode, too. E.g., in the case of minor-axis buckling the minor-axis bending transverse extension mode (i.e. TBmin) is added with a strain distribution similar to that of GBmin. Finally, the fourth curve is the ordinary signature curve of the cross-section, calculated by regular FSM without any constraints. It can be observed that the introduced T mode reduces the critical load values, practically the same way as the zero Poisson's ratio. For the actual material the reduction is 9%, which comes from the  $1/(1-\nu^2)$  expression. The critical load values nicely coincide with the classic analytical solutions.

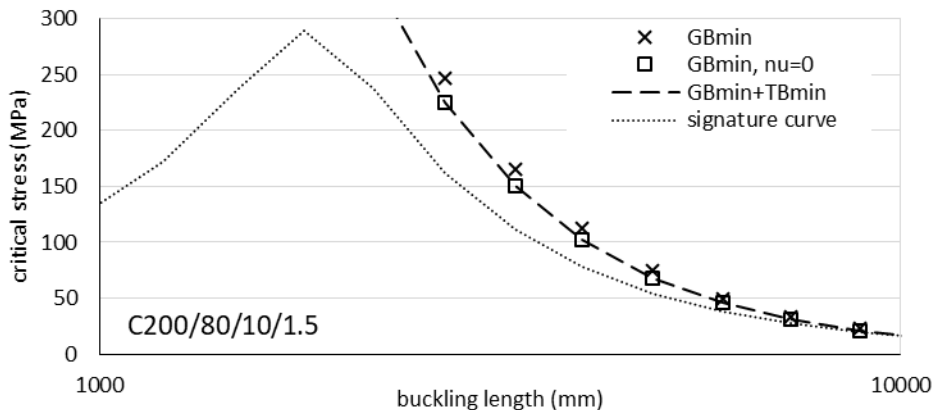


Figure 4: Comparison of various options: minor-axis global mode

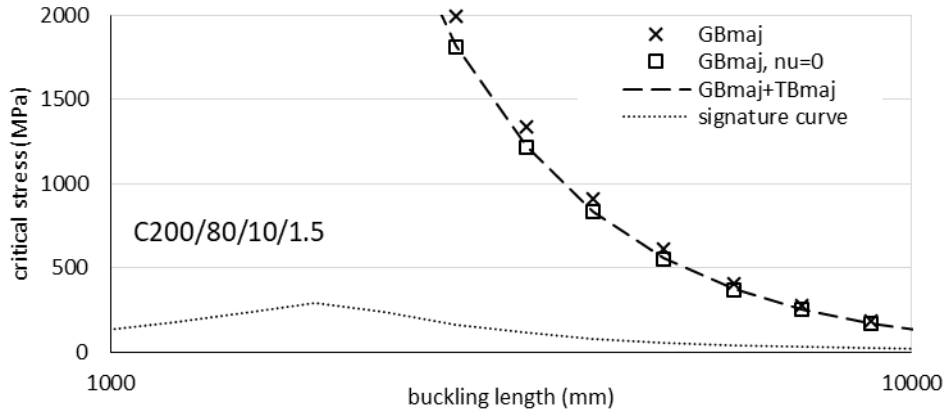


Figure 5: Comparison of various options: major-axis global mode

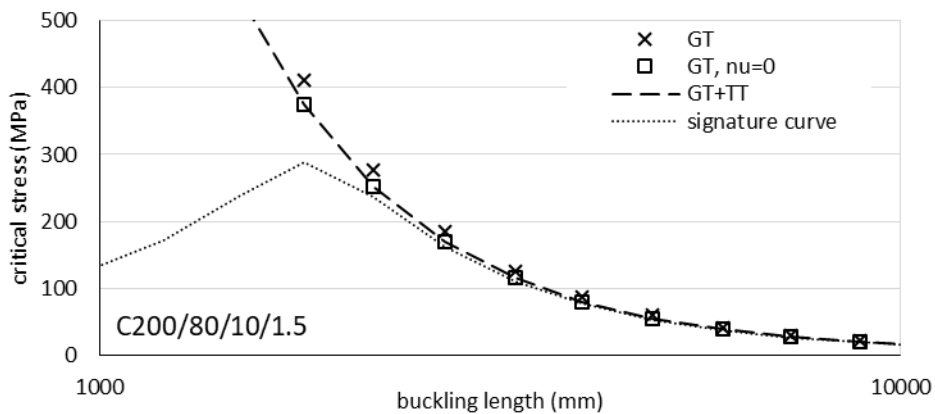


Figure 6: Comparison of various options: global (pure) torsional mode

Since the first real buckling mode of the actual channel member (if long enough) is flexural-torsional buckling, the pure buckling modes (especially the pure flexural modes) are well above the signature curve. In Fig. 7 the flexural-torsional buckling solutions are presented. Essentially the same 4 options are used. However, since flexural-torsional buckling is consisted of major-axis bending mode (GBmaj) and global torsional mode (GT), pure flexural-torsional buckling requires two deformation modes: GBmaj and GT. Consequently, when transverse extension modes are added (in the third curve), the corresponding two transverse extension modes are to be added: TBmaj and TT. The numerical values prove again that the consideration of the appropriate new transverse extension modes introduces the necessary additional flexibility to have critical values practically identical to those from classic analytical solutions. For the actual member the critical values are very close to the signature curve, too, at least for large member lengths.

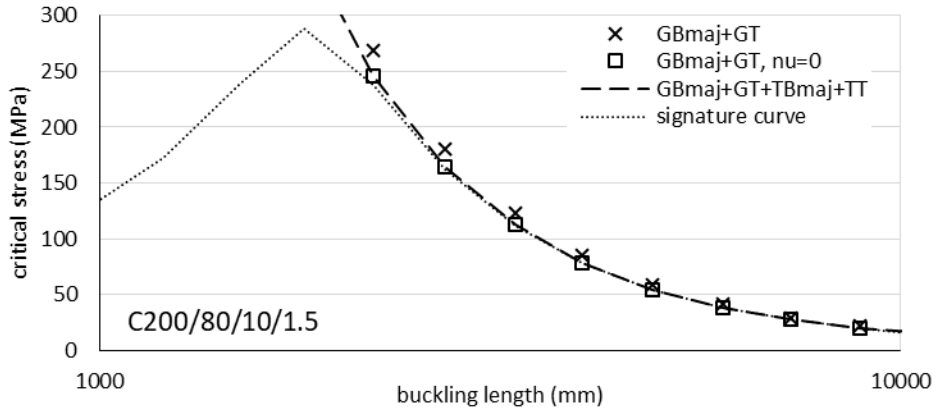


Figure 7: Comparison of various options: flexural-torsional mode

In Figs. 8 and 9 the pure distortional buckling results are presented: symmetric and point-symmetric modes, respectively. The figures follow the logic of the previous figures, solutions are given in 4 options. The difference between the 1<sup>st</sup> and 2<sup>nd</sup> option is again 9 %, just in the case of global buckling. However, consideration of the relevant T mode (third curve) does not lead to the critical values identical to those from the 2<sup>nd</sup> option. Consideration of the relevant T mode does mean some extra flexibility, hence the critical load values are smaller than those in the 1<sup>st</sup> option, but the difference between the 3<sup>rd</sup> and 1<sup>st</sup> options is length-dependent: for larger lengths the difference is negligible, and the difference is getting larger as the length decreases. In the actual example this difference at the distortional minimum is approx. 4%. We believe that the total elimination of the Poisson's ratio is not a proper solution for distortional buckling, since distortional modes involve transverse bending of the plate elements, where the Poisson effect is reasonable to consider, hence simply setting the Poisson's ratio to zero introduces too much flexibility to the member. On the contrary, the consideration of the relevant transverse extension mode seems to introduce the proper amount of additional flexibility.

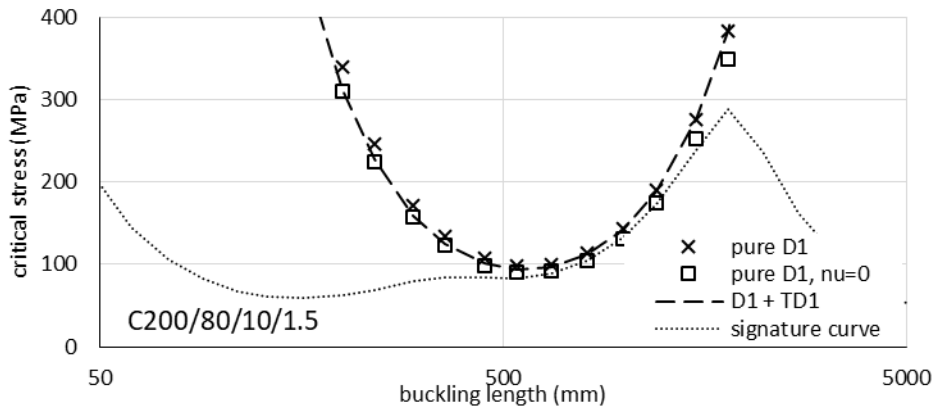


Figure 8: Comparison of various options: symmetric distortional mode

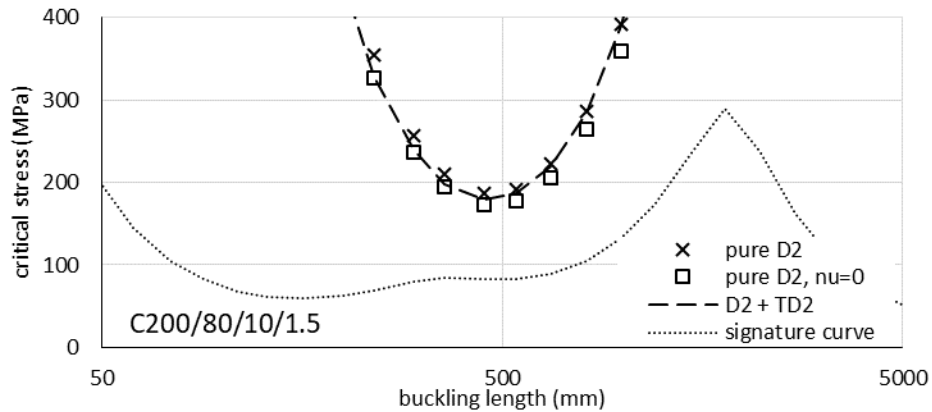


Figure 9: Comparison of various options: point-symmetric distortional mode

#### 4. Conclusions

In this paper new transverse extension modes are introduced, applicable in the modal analysis of thin-walled members. The new modes are inspired by the strain distributions of global and distortional modes, of which the strain distributions have earlier been applied to define meaningful primary shear modes. In this paper the new modes were applied in the context of constrained finite strip analysis. The new modes require the modification of the interpolation of the transverse translational displacements, which slightly modifies the classic semi-analytical finite strip method, e.g., by modifying the size and the terms of the stiffness matrices. The practical advantage of the proposed new transverse extension modes is that the artificial stiffness increase, which is characteristic of constrained analyses, can be compensated by the consideration of the relevant new transverse extension mode(s). For example, to have a flexural buckling solution practically identical to the one predicted by the Euler formula, one global bending deformation mode plus the relevant (one single) transverse extension mode should be considered in a constrained finite strip analysis. The applicability of the new transverse extension modes were illustrated by numerous proof-of-concept examples.

#### Acknowledgment

The presented work was conducted with the financial support of the K119440 project of the National Research, Development and Innovation Office of Hungary.

#### References

- Bebiano, R., Gonçalves, R., Camotim, D. (2015) A cross-section analysis procedure to rationalise and automate the performance of GBT-based structural analyses, *Thin-Walled Structures*, Vol 92, pp. 29-47.
- Ádány, S., Schafer, B.W. (2008) A full modal decomposition of thin-walled, single-branched open cross-section members via the constrained finite strip method, *Journal of Constructional Steel Research*, 64 (1), pp. 12-29.
- Ádány, S. (2012) Global Buckling of Thin-Walled Columns: Analytical Solutions based on Shell Model, *Thin-Walled Structures*, Vol 55, pp 64-75.
- Ádány S. (2013) Decomposition of in-plane shear in thin-walled members, *Thin-Walled Structures*, Vol 73, pp 27-38.
- Cheung Y.K. (1968) Finite strip method in the analysis of elastic plates with two opposite ends simply supported, *Proc Inst Civ Eng*, 40, 1-7.

## Some aspects of buckling behavior of channel section members under eccentric compression

Dubina D.<sup>1</sup>, Czechowski L.<sup>2</sup>, Koteřko M.<sup>3</sup>, Ungureanu V.<sup>4</sup>

### Abstract

The paper presents the results of a numerical parametric study into the influence of relatively large load eccentricities with respect to minor and major axis upon buckling strength and buckling modes of thin-walled cold-formed steel lipped channel section columns subjected to eccentric compression. The study was performed using Finite Element Method (code Ansys) and Finite Strip Method (code CUFSM). Selected theoretical results were compared with experimental test results. Some conclusions concerning sensitivity of buckling strength and redundancy of load-carrying capacity in the post-buckling (either elastic-plastic or plastic) range to the magnitude of eccentricity, depending on the eccentricity position (minor/major axis) and column dimensions are derived.

### 1. Introduction - State of art review

Thin-walled cold-formed steel (TWCFs) sections commonly have mono-symmetric or point symmetric shapes, and normally have stiffening lips on flanges and/or intermediate stiffeners in wide flanges and webs. Both simple and complex shapes can be formed for structural and non-structural applications. Cold-formed steel design is dominated by some main problems (EN1993-1-1:2005, EN 1993-1-3:2006), i.e. stability behavior, which is dominant for design criteria of cold-formed steel sections, and connecting technology (Rhodes 1997, EN 1993-1-3:2006), which is specific and strongly influences the structural behavior and design detailing. In the last years, the seismic performance of cold-formed steel structures started to be examined. The problem of buckling loads and the load carrying capacity of TWCFs members subjected to simple loading systems (pure bending or uniform compression) has been with satisfactory accuracy solved within the theory of thin-walled structures, as well as in design code specifications. EN 1993-1-3 (2006) gives accurate predictions of the buckling load and ultimate strength of TWCFs members under concentric axial compression but is less accurate in the examination of eccentrically compressed columns. Thus, the problem concerning members subjected to combined loadings (compression and bending, eccentric compression) is still an open question.

---

<sup>1</sup> Professor, Department of Steel Structures and Structural Mechanics, Politehnica University of Timisoara / Laboratory of Steel Structures, CCTFA, Romanian Academy - Timisoara Branch, <dan.dubina@upt.ro>

<sup>2</sup> Senior Lecturer, Department of Strength of Materials, Łódź University of Technology, <leszek.czechowski@p.lodz.pl>

<sup>3</sup> Professor, Department of Strength of Materials, Łódź University of Technology, <maria.kotelko@p.lodz.pl>

<sup>4</sup> Professor, Department of Steel Structures and Structural Mechanics, Politehnica University of Timisoara / Laboratory of Steel Structures, CCTFA, Romanian Academy - Timisoara Branch, <viorel.ungureanu@upt.ro>

There are relatively few reported results of both theoretical and experimental research into structural behavior of thin-walled columns under eccentric compression. The very first investigation results concerning channel section members under eccentric compression were reported by Rhodes and Harvey (1977). In 2000, Rhodes et al. have presented results of research into buckling strength of stainless steel TWCF lipped channel sections under concentric and eccentric compression (with respect to minor axis). Results of experiments were compared with AISI and EUROCODE recommendations. The comparison showed good agreement for concentric loading and less accurate for eccentric one.

Miller and Pekoz (1994) investigated the effect of load eccentricity in TWCF long lipped channel sections with perforated and non-perforated webs. Sections were subject to eccentric load both with respect to minor and major axis. The experimental results were compared with AISI buckling strength predictions for combined load (compression and bending). Mulligan and Pekoz (1984) proposed relations of effective width of lipped channel section members under eccentric load with respect to minor axis. They compared ultimate load predictions obtained on this basis with experimental results and code recommendations.

More recently, Wysmulski et al. (2017) investigated channel section columns made of multiply laminate, loaded with very small eccentricities, which were rather small deviations from axial direction. They stated that the eccentricity of the applied load influences significantly buckling load, even for small eccentricities.

Zhao et al. (2016a) performed experimental investigations into 29 extruded columns with box-type and L-type sections made of aluminum alloy, to study the stability behavior of these columns when subjected to eccentric loads. Using FE models, an extensive parametric study was performed to investigate the effects of section dimensions, slenderness ratio, and eccentricity on the stability bearing capacity of the eccentrically loaded columns. The test and parametric study results were compared to the design capacity predictions in the existing design codes. It was found that the predicted stability bearing capacities in the two design codes was generally conservative for the eccentrically loaded columns.

Zhao et al. (2016b) presented an experimental program employed on four CHS sizes made of austenitic stainless steel subjected to combined load (compression and bending), particularly for a wide range of loading eccentricities, followed by a numerical modelling program and including parametric studies. Improved design rules were also sought through extension of the deformation-based continuous strength method (CSM) to the case of stainless steel CHS under combined loading.

Liang et al. (2019) investigated the local cross-section behavior of stainless steel channel sections under the combined axial compression and minor axis bending moment. They performed experiments together with FE simulations. They carried out a parametric study for a wider range of cross-section aspect ratios and slenderness, loading combinations and bending orientations. They also compared the obtained results with standard predictions and proposed modifications of those predictions.

Zhang et al. (2021) studied buckling behavior of press-braked stainless steel channel section beam-columns under combined compression and minor-axis bending. They carried out experiments and FE simulations. The FE simulations were performed for different cross-section dimensions, member effective lengths and loading combinations. Both experimental and numerical results were compared with standard design rules. They stated not entirely satisfactory consistency of standards predictions and obtained results.

Liang et al. (2020) presented experimental and numerical FE investigation results into the behavior of laser-welded stainless steel channel sections under combined compression and bending moment about the major axis. They proposed an improved design approach through extension of the deformation-based continuous strength method (CSM) to the case of laser-welded stainless steel channel sections under combined compression and major axis bending.

The above literature review shows that the problem concerning members subjected to combined loadings (compression and bending, eccentric compression) is still an open question. Particularly, design rules (European, American and others) have to be improved and new proposals of standard predictions have to be elaborated.

There are two aspects, which make the theoretical investigations of the analyzed problem (both analytical and numerical) complex. Short members buckle in local-global interactive mode and buckling is of plastic-elastic type. Secondly, due to the interaction of axial load and bending (caused by the eccentricity) the problem is structurally non-linear. These aspects are discussed in the paper.

## 2. Subjects of investigation

The objective of the present work is a study on the buckling behavior of TWCFs lipped channel section columns subjected to eccentric compression about the minor ( $e_y$ ) and major ( $e_z$ ) axis. The subject of the study is shown in Fig.1. The typology of analyzed columns is shown in Table 1. Dimensions of columns to be under investigation were determined in order to classify the members in class 4 (EN 1993-1-1:2005). It means that local buckling will occur before the attainment of yield stress in one or more parts of the cross-section.

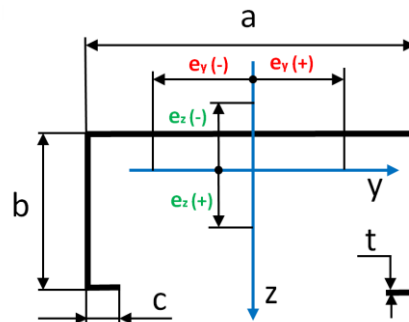


Fig. 1.: Lipped channel section – indication of eccentricities

Table 1: Typology of columns

No.	$a$ (mm)	$b$ (mm)	$c$ (mm)	$t$ (mm)	$l$ (mm)
1	150	60	20	2	450
2	150	60	20	1	450
3	150	47	16	2	450
4	150	47	16	1.5	450
5	150	47	16	1	450
6	250	100	25	3	600
7	250	100	25	2.5	600
8	250	100	25	2	600
9	250	100	25	1.5	600

Internal radii  $r = 1.5$  mm (for  $t = 1$  mm) and  $r = 2.5$  mm (for  $t = 2, 2.5$  mm)

Consequently, for Class 4 cross-sections effective widths may be used to make the necessary allowances for reductions in resistance due to the effects of local buckling. Since these sections are prematurely prone to local or distortional buckling and they do not have a real post-elastic capacity, a failure of such members is initialized by the local-global interactive buckling of plastic-elastic type, not an elastic-elastic one.

### 3. Methodology of the buckling analysis

Buckling loads of members under investigation were determined using Finite Element (FE) and Finite Strip (FS) methods. FE calculations were carried out using the commercial FE ABAQUS codes v. 6.14 (Dassault Systemes 2014) and **Ansys 18.2 software (Ansys 2018)**. To create adequate discrete models of considered structures, 4-node 181-shell element was assumed. The size of finite element amounted to 2 mm. The nonlinear analysis was conducted for large strains and deflections on the basis of Green-Lagrangian equations. The number of sub-steps for the single calculation was assumed to be from 400 up to 50,000. The maximum number of iterations for each sub-step was set up to 5000. The full material characteristic of one-directional tensile test expressed as truth stress-logarithmic strain was implemented to software. Nonlinear estimations and convergence analysis were conducted by using the Newton-Raphson algorithm. FS calculations were performed using CUFSM code (Li and Schafer 2010). Buckling loads were calculated for pin-jointed columns in the elastic range (linear eigenvalue problem).

### 4. Results of the analysis

#### 4.1 Eccentric compression with respect to minor axis

The analysis carried out using CUFSM code (Li and Schafer 2010) based on Finite Strip Method as well as FE analysis (code ANSYS) showed, that for nearly all positive eccentricities a typical distortional buckling takes place. For the smallest negative eccentricities ( $e = -5$  mm) a local-distortional buckling mode was observed. For larger negative eccentricities, the local buckling of the web takes place (Fig. 2).

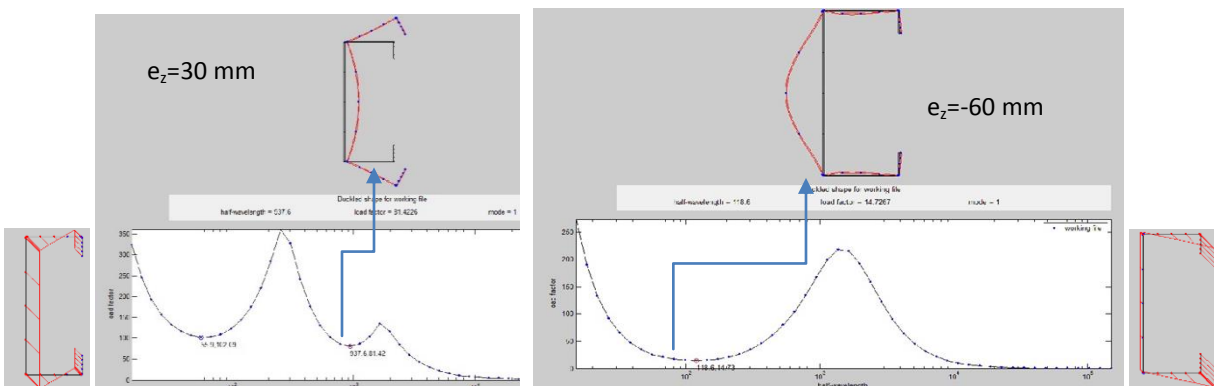


Fig. 2: Buckling modes for eccentric loads (minor axis) - results of CUFSM analysis; model No 1 (Table 1)

Fig. 3 shows diagrams of normalized buckling loads in terms of normalized eccentricity with respect to position of the centroid (3b) and eccentricity (3a). Fig. 3a shows loads normalized with respect to buckling load in concentric compression (purely axial), while Fig 3b – with respect to fully plastic compressive load for gross section A. Buckling loads diminish significantly with the increasing absolute value of the eccentricity, however a distinctive maximum is observed for about  $0.6 y_c$  (position of the centroid of gross cross-section – Fig. 3a). It is caused by the “migration” of the centroid of the effective cross-section (effective centroid). This phenomenon was also reported by other researchers (Miller, Pekoz 1994). Fig. 4 presents buckling loads (red points) and ultimate loads in terms of the eccentricity. Ultimate loads are obtained both from FE non-linear analysis (Abaqus) and experiment (Dubina et al

2020). Also, ultimate loads display a distinctive maximum. It can be noticed, that buckling loads for positive eccentricities obtained using FS analysis and FE eigenvalue linear analysis exceed ultimate loads, determined both by non-linear FE simulation and experiment (despite buckling stresses do not exceed yield stress). The same was reported by Kotefko et al. (2018). These results indicate, that even in the elastic range linear eigenvalue analysis is not adequate, because of structural non-linearity of the problem. The analysis should take into account load-deflection history using an incremental, iterative procedure (Miller, Pekoz 1994).

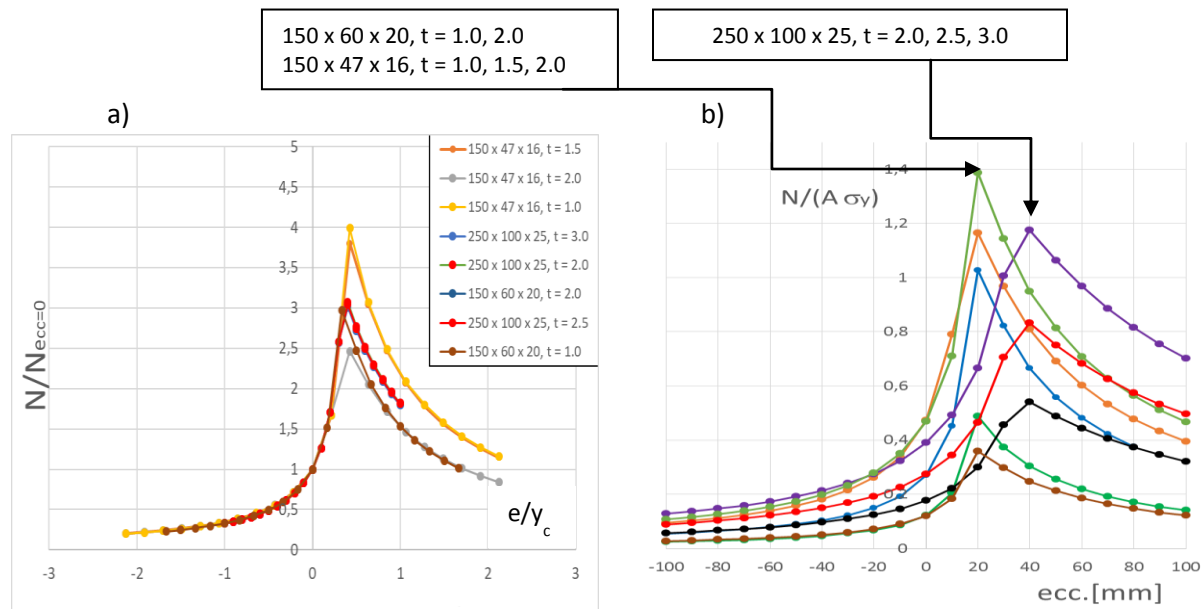


Fig. 3: Buckling modes (eccentricity with respect to minor axis) – results of CUFSM analysis ( $\sigma_y = 355$  MPa)

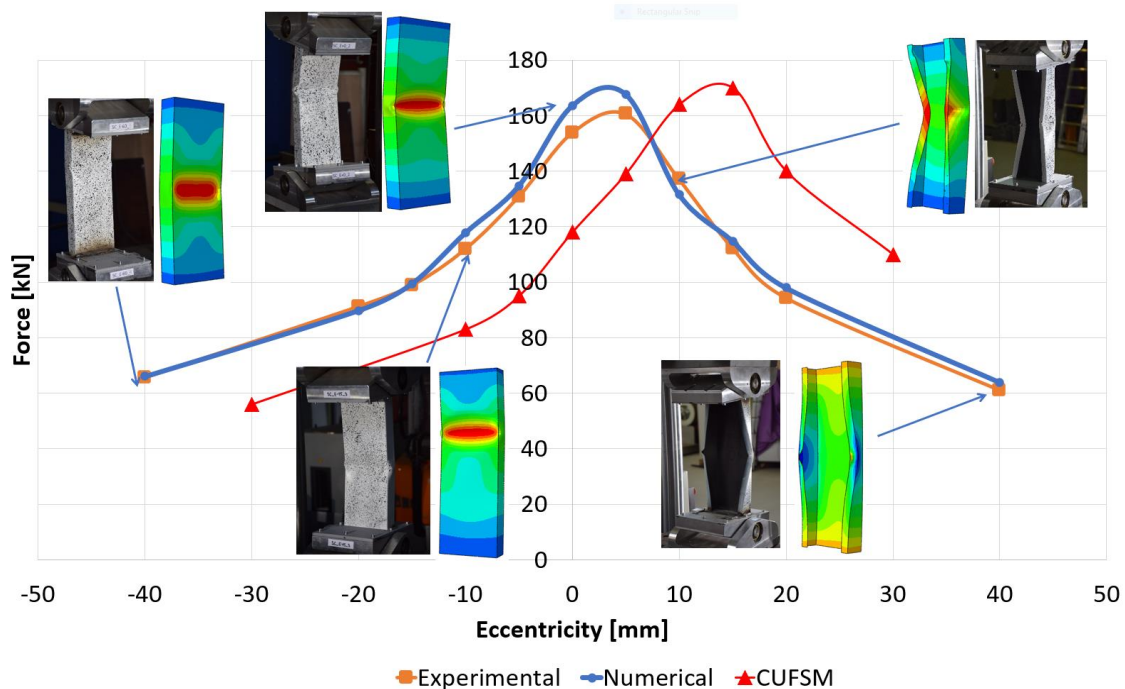


Fig. 4: Buckling and ultimate loads for columns no. 1 (Table 1) - ( $\sigma_y = 355$  MPa); red dots – buckling loads (CUFSM)

#### 4.2 Eccentric compression with respect to major axis

In the case of eccentricities with respect to major axis local buckling modes were observed only (Fig. 5). Both buckling loads (CUFSM and Ansys analysis) and ultimate loads (Ansys non-linear analysis) in terms of the eccentricity are shown in Fig. 6 for columns No. 1 and No. 2 (Table 1). In the contrary to the eccentricity with respect to the minor axis, a pure symmetry takes place for negative and positive eccentricities, which was predicted. Also, as predicted, maximum buckling load is obtained for concentric load. Ultimate loads significantly decrease with an increase of the eccentricity. However, in the contrary to eccentricities with respect to the minor axis, buckling loads are much less sensitive to the eccentricity of applied load. Also in that case, buckling loads obtained from the linear analysis (both FS and FE) exceed ultimate loads determined from FE non-linear analysis, however for columns indicated as model 1 (No. 1 in Table 1) buckling stress exceeds the yield stress.

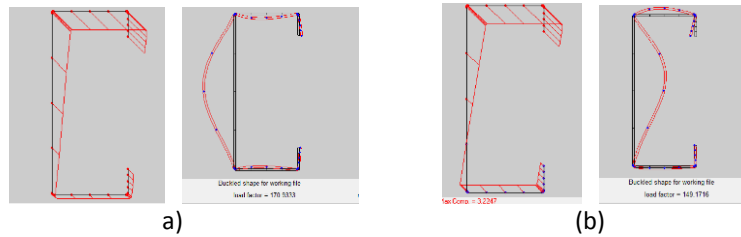


Fig. 5: Buckling modes (major axis): a)  $e_y = 35$  mm, b)  $e_y = 110$  mm (model No. 2 – Table 1)

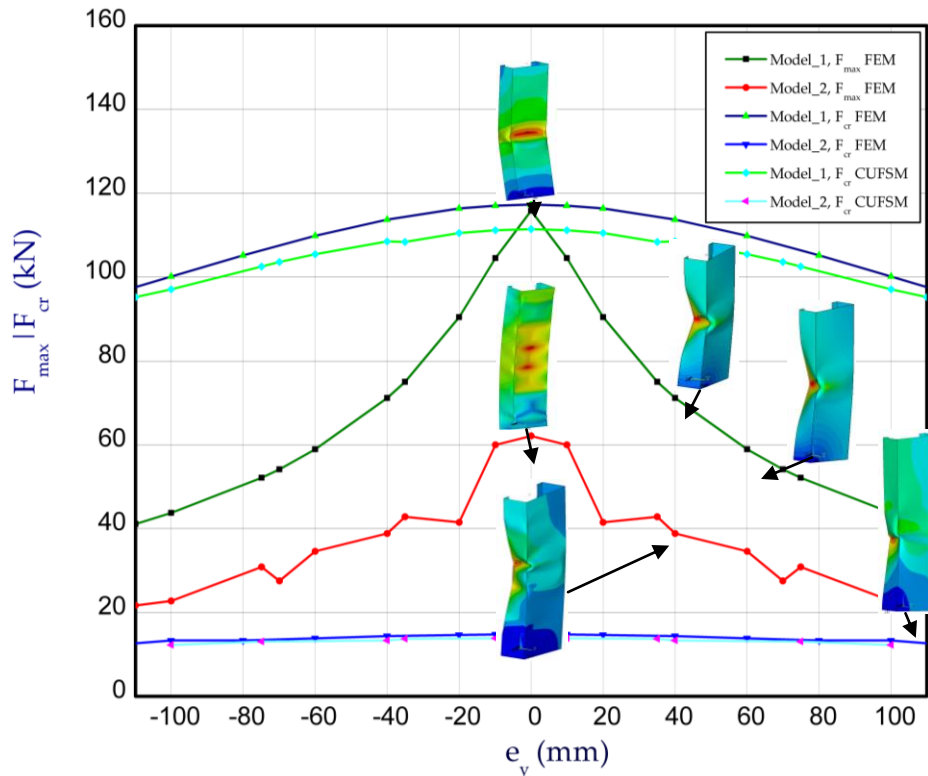


Fig. 6: Buckling and ultimate loads versus  $e_y$  for columns No. 1 and No. 2 (Table 1) –  $\sigma_\gamma = 200$  MPa

Fig. 7 presents buckling loads (obtained from the linear eigenvalue FS and FE analysis) versus the eccentricity  $e_y$  (major axis) for the whole typology of columns specified in Table 1. Dotted lines indicate results, which exceed yield stress. For the whole typology, the decrease in buckling load due to the eccentricity is not as significant, as for the case of the eccentricity with respect to minor axis.

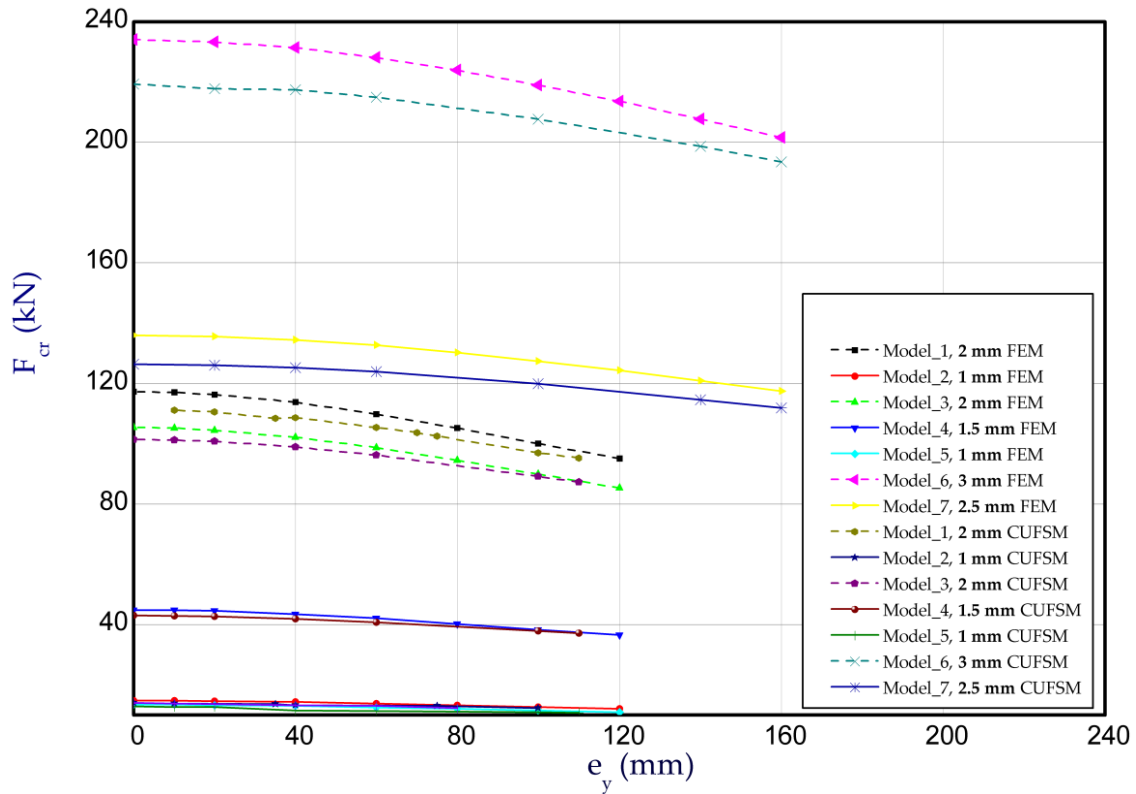


Fig. 7: Buckling loads versus  $e_y$

## 5. Final remarks

The paper presents the results of a numerical analysis of buckling strength of columns subject to eccentric compression, based on eigenvalue, linear solutions (FS and FE). The results show that these solutions are not entirely adequate, because of structural non-linearity of the problem. Those numerical solutions are particularly useful to recognize buckling modes. A more precise analytical method of buckling and ultimate strength prediction should take into account load-deformation history and load-stress history and should be performed using incremental iterative algorithms.

The redundancy of the load-carrying capacity in comparison with buckling loads is relatively large for both examined cases (eccentricity with respect to minor/major axis). "Migration" of the effective cross-section centroid, taking place for columns under eccentric compression with respect to minor axis, should be taken into account in the buckling strength estimations, also in standard predictions.

The presented work is a part of larger research program, within which further research will be continued into derivation of analytical incremental procedures, as mentioned above.

## Acknowledgments

Project number 2019/35/B/ST8/02823 - *Implementation of yield line theory to the load-capacity estimation of thin-walled members under combined load*, National Science Centre of the Polish Ministry of Science and Higher Education.

Project PN-III-CEI-EUREKA-2019/ E113493 - *CFSExpert - Structural design tool for cold-formed steel structures*, CCCDI – UEFISCDI, Romanian Ministry of Research and Innovation.

The Polish - Romanian Joint Research Project: Yield line theory for load-capacity estimation of thin-walled cold-formed steel members under combined loading, 2019-2021, under the agreement on scientific cooperation between the Polish Academy of Sciences and the Romanian Academy.

## References

- Dassault Systemes (2014), "Abaqus 6.14 Documentation," Providence, RI.
- Dubina, D., Ungureanu, V., Kotelko, M. (2020), "Post-elastic capacity of thin-walled, cold-formed steel members", *Proceedings of the Cold-Formed Steel Research Consortium Colloquium*, Baltimore, 20-22 October 2020.
- EN 1993-1-1 (2005), "Eurocode 3: Design of steel structures - Part 1-1: General rules and rules for buildings", CEN, Brussels, Belgium (including EN 1993-1-1:2005/AC, 2009).
- EN 1993-1-3 (2006), "Eurocode 3: Design of Steel Structures, Part 1.3: General Rules, Supplementary Rules for Cold-formed Thin Gauge Members and Sheetting", CEN, Brussels, Belgium, 2006.
- Kotelko, M., Karmazyn, A., Borkowski, Ł., Ungureanu, V., Dubina, D. (2018), "Buckling of TWCFs open-section members under eccentric compression", *Proceedings of the Stability of Structures XV-th Symposium*, Zakopane, Poland, September 17-21, 2018, 81-82.
- Li, Z., Schafer, B.W. (2010), "Buckling analysis of cold-formed steel members with general boundary conditions using CUFSM: conventional and constrained finite strip methods", *Proc. of the 20th Int. Spec. Conf. on Cold-Formed Steel Structures*, St. Louis, MO., USA.
- Liang, Y., Zhao, O., Long, Y., Gardner, L. (2019), "Stainless steel channel sections under combined compression and minor axis bending-Part 1: Experimental study and numerical modeling", *Journal of Constructional Steel Research*, 152, 154-161.
- Liang, Y., Zhao, O., Long, Y., Gardner, L. (2019) "Stainless steel channel sections under combined compression and minor axis bending-Part 2: Parametric studies and design", *Journal of Constructional Steel Research*, 152, 162-172.
- Liang, Y., Zhao, O., Long, Y., Gardner, L. (2020), "Experimental and numerical studies of laser-welded stainless steel channel sections under combined compression and major axis bending moment", *Thin-Walled Structures*, 157, 107035.
- Miller, T.H., Pekoz, T. (1994), "Load-eccentricity effects on cold-formed steel lipped-channel columns", *J. Struct. Eng.*, 120, 805-823.
- Mulligan, G. P., Peköz, T. (1984) "Locally Buckled Thin-Walled Columns". *Journal of Structural Engineering, ASCE*, 110 (11), 2635-2654.
- Rhodes, J., Harvey, J.M. (1977), "Interaction behaviour of plain channel columns under concentric or eccentric loading", *Proc. 2<sup>nd</sup> Int. Colloquium on the Stability of Steel Struct.*, ECCS, Liege (Belgium), 439-444.
- Rhodes J., MacDonald M., McNiff W., "Buckling of cold formed stainless steel columns under concentric and eccentric loading", *Proc. of the Fifteenth International Specialty Conference on Cold-Formed Steel Structures*, St. Louis, Missouri U.S.A., October 19-20, 2000.
- User's Guide ANSYS® 18.2, Ansys, Inc.
- Wysmulski, P., Teter, A., Dębski, H. (2017), "Effect of eccentricity of load on the buckling of thin-walled composite C-columns", *Proceedings of the 22nd Computer Methods in Mechanics - CMM-2017*, Lublin, Poland (13-16/09).
- Zhao, Y., Zhai, X., Sun, L. (2016a), "Test and design method for the buckling behaviors of 6082-T6 aluminum alloy columns with box-type and L-type sections under eccentric compression", *Thin-Walled Structures*, 100, 62-80.
- Zhao, O., Gardner, L., Young, B. (2016b), "Structural performance of stainless steel circular hollow sections under combined axial load and bending - Part 1: Experiments and numerical modelling", *Thin-Walled Structures*, 101, 231-239.
- Zhang, L., Li, S., Tan, K.H., Zhao, O. (2021), "Experimental and numerical investigations of press-braked stainless steel channel section beam-columns", *Thin-Walled Structures*, 161, 107344.

## Alternative complementary shear and transversal elongation modes in Generalized Beam Theory (GBT) for thin-walled circular cross-sections

M.J.Bianco\*, A.K.Habtemariam<sup>†</sup>, C.Könke<sup>‡</sup>, F.Tartaglione<sup>§</sup>, V.Zabel<sup>¶</sup>

### abstract

This paper presents alternative complementary shear and transversal elongation modes of Generalized Beam Theory (GBT) for thin-walled hollow circular cross-sections and compares them to the recent developments concerning membrane's shear and transversal elongation. The main features of the alternative complementary modes are: i) despite of Poisson's effect, each complementary mode is related to a clear membrane's behavior: transversal elongation and shear deformation; ii) The coupling between these complementary modes is minimized, as well as the coupling between these modes and the respective original GBT's mode; iii) the remained coupling effect is limited to plate's behavior. To illustrate the present alternative, complementary modes and its limitations, the detailed examples applied in a short and deep pipe are carried out and their final results are compared with a full shell element model.

### 1. INTRODUCTION

GBT, Generalized Beam Theory, is a structural mechanics theory that involves 2D features of shell theory condensed into 1D beam theory. Originally, its creator, Richard Schardt (Schardt 1989), developed it as an extension of Vlasov beam theory (Vlasov 1961): a set of amplification functions, which represent the magnitude of predefined shapes of cross-section's warping. Moreover, Schardt proved that high order cross-section's warping shapes are combined to transversal bending cross-section distortion. Furthermore, GBT can be not only extended to geometrically non-linear analysis (Schardt 1994a, Schardt 1994b, Davies 1994), but also to physically non-linear analysis (Abambres 2013, Abambres 2014a, Abambres 2014b).

Based on Fourier-Series and superposition of orthogonal modes, GBT can handle the analysis of hollow circular cross-sections (Schardt 1989, Silvestre 2007), especially concerning the effects of warping and ovalization. Furthermore, following the concept of separation of variables, GBT uses amplification functions to represent the magnitude of each orthogonal mode in the beam's longitudinal direction. As a result, this theory presents the numerical performance of beam element analysis together with the result's quality of shell element analysis.

Besides these attractive properties, original GBT has its limitations. Among them, one can highlight the neglect of shear and transversal elongation energies of membrane's behavior. Although Bebiano and Gonçalves (Bebiano 2014) Silvestre (Silvestre 2003, Silvestre 2012) and Miranda (Miranda & Ubertini 2013) developed well-defined solution for segmented cross-sections, thin-walled circular cross-sections are still under development, with a recent and remarkable approach proposed by Nedelcu et.al,

---

\*Researcher, Bauhaus-University Weimar <marcelo.jose.bianco@uni-weimar.de>

<sup>†</sup>Researcher, Bauhaus-University Weimar <abinet.habtemariam@uni-weimar.de>

<sup>‡</sup>Professor for Statics of Structures at the Institute of Structural Mechanics at Bauhaus-University Weimar <carsten.koenke@uni-weimar.de>

<sup>§</sup>Researcher, Bauhaus-University Weimar <fabiola.tartaglione@uni-weimar.de>

<sup>¶</sup>Researcher, Bauhaus-University Weimar <volkmar.zabel@uni-weimar.de>

(Muresan, Nedelcu, & Gonçalves 2019). In this work, Nedelcu creates two complementary modes for each original GBT mode, based on the possible displacements related to shear membrane strain. Such complementary modes lead to a substantial coupling among these and original GBT modes due to the membrane deformation energy.

As an alternative, the presented study proposes two other complementary modes: the first related to membrane shear strains; and the second to transversal elongation strains due to membrane's behavior. Consequently, the coupling among these alternatives and the original GBT's modes are limited to the plate's deformation energy.

## 2. Original GBT analysis of hollow circular cross-section

### 2.1. GBT's assumption for the displacement field

The displacement field in GBT has two major ideas: i) the superposition of orthogonal modal cross-section displacement/deformation functions for the longitudinal/axial  $u(\theta)$ , tangential  $v(\theta)$  and radial  $w(\theta)$  directions (as illustrated in figure 1.a); ii) an amplification function  $V(x)$  of these displacement functions along the beam length. Thus, the displacement field in original GBT analysis (without membrane's shear and transversal elongation deformation energies) in the middle-line of hollow circular cross-section is expressed by:

$$u(x, \theta) = \sum_{i=1}^n i u(\theta) i V'(x) \quad (1)$$

$$v(x, \theta) = \sum_{i=1}^n i v(\theta) i V(x) \quad (2)$$

$$w(x, \theta) = \sum_{i=1}^n i w(\theta) i V(x) \quad (3)$$

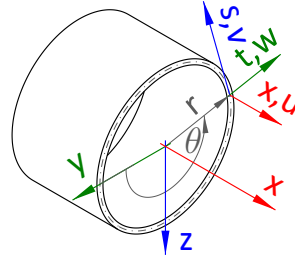


Figure 1: Coordinate systems adopted in GBT's analysis of thin-walled circular hollow section

Here, the upper-left index  $i$  indicates GBT's deformation mode. It is important to note that the first derivative,  $V'(x)$ , in eq. 1 is not arbitrary, but it is necessary to enable the assumption of membrane non-shear energy deformation, which is related to the longitudinal displacement in the cross-section,  $u(x, \theta)$ , with the transversal displacements:  $v(x, \theta)$  and  $w(x, \theta)$ . Thus, one has a clear understanding of the functionality of each cross-section functions: i)  $u(\theta)$  leads to warping; ii)  $v(\theta)$  and  $w(\theta)$  lead to cross-section distortion (ovalization).

### 2.2. Hollow circular cross-section's analysis

One of the major characteristics of GBT is the cross-section analysis, which is only related to geometry and mechanical properties of the cross-section. Such analysis leads to  $n$  natural numbers of orthogonal mode shapes of deformation, which i) the lower modes, i.e.  $i = 1, 2$  and  $3$ , represent the longitudinal elongation, the major and minor bending directions; ii) the higher modes  $i > 3$  involve cross-section distortions and ovalizations. Furthermore, in hollow circular cross-sections, two additional modes are introduced (Silvestre 2007): the pure axial extension mode  $i = a$  and the pure Saint-Venant torsion mode  $i = t$ .

For a non-circular cross-section, the analysis starts in assembling stiffness matrices related to longitudinal, transversal and shear strains. This assembly step has a non-trivial setup (Jönsson & Andreassen 2011, Jönsson & Andreassen 2012b, Jönsson & Andreassen 2012a, Bebiano 2015), which leads to a generic eigenvalue problem in lower modes and a quadratic eigenvalue problem for GBT's high deformation modes (Jönsson & Andreassen 2012b). Fortunately, in circular hollow sections, this laborious step is replaced by orthogonal deformation shapes based on Fourier series (Schardt 1989) (Silvestre 2007). In figure 2, some of these deformation shapes are presented, with their respective values given by:

- For pure axial extension mode,  $i = a$ :  $a u(\theta) = 0 \quad a v(\theta) = 0 \quad a w(\theta) = 1 \quad (4)$
- For pure torsion mode,  $i = t$ :  $t u(\theta) = 0 \quad t v(\theta) = 1 \quad t w(\theta) = 0 \quad (5)$
- For pure longitudinal extension mode,  $i = 1$ :  $1 u(\theta) = 1 \quad 1 v(\theta) = 0 \quad 1 w(\theta) = 0 \quad (6)$

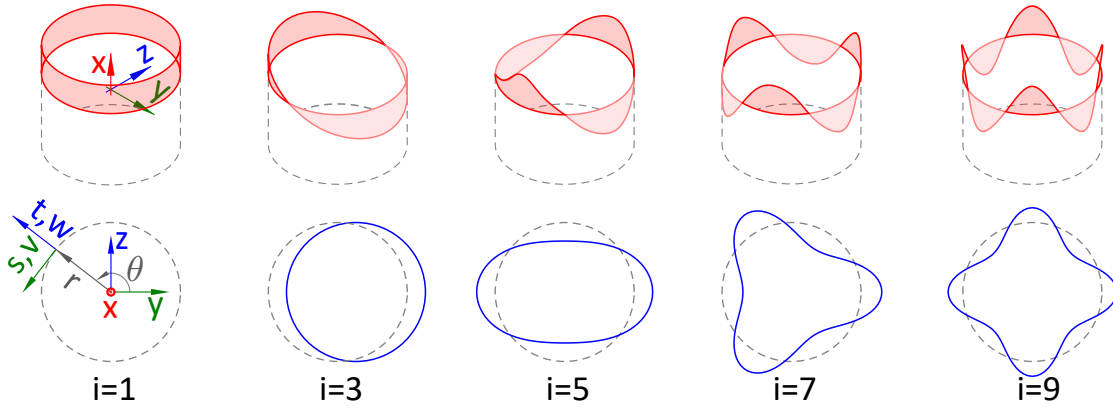


Figure 2: Longitudinal and transverse deformation shape modes of a circular hollow section according to GBT.

$$\begin{aligned}
 & \text{- For odd modes, } i = 3, 5, 7, \dots \text{ with } m = (i-1)/2 \quad \begin{cases} i u(\theta) = -r \cos(m\theta) \\ i v(\theta) = -m \sin(m\theta) \\ i w(\theta) = m^2 \cos(m\theta) \end{cases} \quad (7) \\
 & \text{- For even modes, } i = 2, 4, 6, \dots \text{ with } m = i/2 \quad \begin{cases} i u(\theta) = r \sin(m\theta) \\ i v(\theta) = -m \cos(m\theta) \\ i w(\theta) = -m^2 \sin(m\theta) \end{cases} \quad (8)
 \end{aligned}$$

where  $r$  is the middle-line radius.

From these functions of the orthogonal modes, one obtains the generalized cross-section properties based on each modal strain. For instance, the longitudinal strain given by:

$$\epsilon_x(x, \theta, t) = [u(\theta) - tw(\theta)] V''(x) \quad (9)$$

leads to the generalized warping inertia  ${}^i C$ , with the membrane  ${}^i C^M$  and the plate  ${}^i C^P$  contributions:

$${}^i C = {}^i C^M + {}^i C^P = \oint \left( tr^3 {}^i u(\theta)^2 + \frac{t^3 r {}^i w(\theta)^2}{12} \right) d\theta \quad (10)$$

where  $t$  is the thickness of the cross-section's wall.

The transversal elongation strain is given by:

$$\epsilon_\theta(x, \theta, t) = \frac{\dot{v}(x, \theta) + w(x, \theta)}{r} - t \frac{w(x, \theta) + \ddot{w}(x, \theta)}{r^2} \quad (11)$$

where the dot index represents the derivative  $d/d\theta$ . Since the first term in the above expression represents transversal elongation's membrane strain, the original GBT approach neglects this term. Therefore, one reaches the following restrain condition:

$$w(\theta) = -\dot{v}(\theta) \quad (12)$$

And the second term in eq. 11 leads to the generalized distortion stiffness:

$${}^i B = \frac{t^3}{12r^2} \oint ({}^i w(\theta) + \dot{w}(\theta))^2 d\theta \quad (13)$$

Concerning the shear strain, the first term in the expression:

$$\gamma_{x\theta}(x, \theta, t) = \frac{\dot{u}(x, \theta) + rv'(x, \theta)}{r} - t \frac{\dot{u}(x, \theta) - rv'(x, \theta) + 2rv'(\dot{v}(x, \theta))}{r^2} \quad (14)$$

is vanished in original GBT analysis. Therefore, one reaches the following restrain:

$$v(\theta) = -\frac{\dot{u}(\theta)}{r} \quad (15)$$

The second term in eq. 14 leads to the inertia concerning the cross-sectional shear,  ${}^iD$ , in eq. 16. Also, the coupling of this second term together with the second term in eq. 11 provides the Poisson effect stiffness,  ${}^iD_{\mu}$ , as presented in eq. 17

$${}^iD = \frac{r}{3}t^3 \oint \left( \frac{{}^i\dot{w}(\theta) - {}^i\dot{v}(\theta)}{r} \right)^2 d\theta \quad (16)$$

$${}^iD_{\mu} = r \oint \frac{{}^i\dot{w}(\theta) + {}^i\ddot{w}(\theta)}{r^2} w(\theta) d\theta \quad (17)$$

Evaluating the closed line integral in equations 10, 13, 16 and 17, one obtains the practical expressions:

$${}^iC = \begin{cases} 0 & \text{for } i = t \\ \frac{\pi r t^3}{6} & \text{for } i = a \\ 2\pi r t & \text{for } i = 1 \\ \pi t r^3 \left( 1 + \frac{t^2 m^2 (m^2 + 2)}{12 r^2} \right) & \text{for } i > 1 \end{cases} \quad (18)$$

$${}^iD = \begin{cases} \pi \frac{t^3}{3r} m^2 (m^2 - 1) & \text{for } i > 1 \\ 0 & \text{for all other cases} \end{cases} \quad (19)$$

$${}^iD_{\mu} = \begin{cases} \frac{\pi}{r} m^4 (1 - m^2) & \text{for } i > 1 \\ 0 & \text{for all other cases} \end{cases} \quad (20)$$

$${}^iB = \begin{cases} 0 & \text{for } i = t \text{ and } i = 1 \\ 2\pi t / r & \text{for } i = a \\ \pi t^3 \frac{m^4 (m^2 - 1)^2}{12 r^3} & \text{for } i > 1 \end{cases} \quad (21)$$

### 2.3. GBT's external force decomposition and orthogonal ordinary differential equation

From all infinite possible modes of GBT, only a few are required to evaluate a problem. Since GBT presents the external deformation energy also as modal superposition, the modal decomposition of the external loads filter the relevant modes. Similar to the internal strain energy, the separation of variables can represent the external general loads functions:

$$p_x(x, \theta) = f_x(x) q_x(\theta) \quad (22) \quad p_v(x, \theta) = f_v(x) q_v(\theta) \quad (23) \quad p_w(x, \theta) = f_w(x) q_w(\theta) \quad (24)$$

The inner product between the deformation modes (equations 7- 8) and the functions  $q_x(\theta)$ ,  $q_v(\theta)$  and  $q_w(\theta)$  provides the modal decomposition:

$${}^i q_x = -r \oint q_x(\theta) {}^i u(\theta) d\theta \quad (25) \quad {}^i q_v = r \oint q_v(\theta) {}^i v(\theta) d\theta \quad (26) \quad {}^i q_w = r \oint q_w(\theta) {}^i w(\theta) d\theta \quad (27)$$

Thus, from the Hamilton's principle, one can reach the GBT's ordinary differential equation:

$$\frac{E^i C}{1 - \mu^2} {}^i V''''(x) - \left( G^i D - \frac{E \mu t^3 {}^i D_{\mu}}{6(1 - \mu^2)} \right) {}^i V''(x) + \frac{E^i B}{1 - \mu^2} {}^i V(x) = f_x(x) {}^i q_x(x) + f_v(x) {}^i q_v(x) + f_w(x) {}^i q_w(x) \quad (28)$$

Here,  $E$  and  $\mu$  are Young's modulus and Poisson's ratio, respectively and the modal amplification function  ${}^i V(x)$  acts as a generalized beam problem.

## 3. Complementary Modes for hollow circular cross-section

### 3.1. Shear and Shear-Transversal Complementary Modes for Membrane Energies

The focus of the complementary modes proposed by Nedelcu et al. (Muresan, Nedelcu, & Gonçalves 2019) is the shear strains energy, which has two major sources: the longitudinal and the transversal elongation displacement. Thus, each complementary mode concerns a displacement direction  $u$  or  $v$ . Namely, as shear  $u$  and shear  $v$  modes, that have the following definitions:

$${}^k u(\theta) = {}^k u(\theta) \quad (29) \quad {}^k v(\theta) = {}^k v(\theta) \quad (30) \quad {}^k v(\theta) = {}^k w(\theta) = {}^k u(\theta) = {}^k v(\theta) = 0 \quad (31)$$

The lower-left indexes  ${}^k$ ,  ${}^u$  and  ${}^v$  indicate the modes of original GBT, complementary shear  $u$  and  $v$ , respectively. In these definitions, the complementary mode shear  $u$  has membrane's strain energy not only related to shear but also related to longitudinal elongation. Thus, this mode type presents a strong coupling with the original GBT's mode. Meanwhile, the complementary mode shear  $v$  has no coupling with the original GBT's mode due to the membrane's behavior. However, this mode presents a strong coupling with the complementary mode shear  $u$ . Table 1 summarises the generalized geometry properties of these complementary modes, as well as the coupling among them and the original GBT mode, with the simplification of non-Poisson's ratio.

Table 1: Summary of generalized inertia of each complementary mode (Nedelcu et al.) and their coupling terms with the simplification of non-Poisson's ratio

Inertia	compl. mode u	compl. mode v	coupl. mode k-u	coupl. mode k-v	coupl. mode u-v
C	$\pi tr^3$	0	$\pi tr^3$	0	0
D	$\pi trm^2$	$\pi m^2 t \left( r + \frac{t^2}{12r} \right)$	0	$\frac{\pi t^3 m^2}{12r} (1 - 2m^2)$	$-\pi m^2 rt$
B	0	$\frac{\pi m^4 t}{r} \left( 1 + \frac{t^2}{r^2} \right)$	0	$\frac{\pi t^3 m^4}{12r^3} (1 - m^2)$	0

### 3.2. Alternative Complementary Modes for decoupled Shear and Transversal Membrane Energies

In original GBT analysis, deformation modes involve all possible strain energy from plate behavior (longitudinal, transversal and shear strains) and only longitudinal strain energy due to membrane behavior. Inspired by this feature, the alternative complementary modes present strain energy deformation for the full plate's behaviour. Moreover, each of these alternative modes is related to a specific membrane strain: the first one to shear strains; the second one to transversal elongation strains. Consequently, the couplings in the linear analysis among the original and the complementary deformation modes are limited to: i) plate's behavior, involving terms of the order  $t^3$ ; ii) Poisson's ratio between the original and the complementary modes related to transversal strain elongation.

The above assumptions require no membrane longitudinal strain energy for either of the complementary modes. Thus, from eq. 9 one obtains the condition of non-longitudinal middle-line displacement:

$$\gamma u(\theta) = \theta u(\theta) = 0 \quad (32)$$

The lower-left indexes  $\gamma$  and  $\theta$  indicate the terms related to shear and transversal elongation, respectively.

For the transversal displacements  $\theta v(\theta)$ ,  $\theta w(\theta)$ ,  $\gamma v(\theta)$  and  $\gamma w(\theta)$ , each complementary mode leads to different definitions. In the case of the complementary mode of shear strain,  $\gamma$ , it requires the same constraint related to transversal elongation presented in eq. 12. Thereby, the transversal displacement definition of this complementary mode is the same of the original GBT modes:

$$\gamma v(\theta) = {}_k v(\theta) \quad (33) \quad \gamma w(\theta) = {}_k w(\theta) \quad (34)$$

The alternative mode of transversal elongation strain,  $\theta$ , requires no shear strain energy, which leads to the constraint of non-tangential displacement. Thus, this complementary mode has only  $w(\theta)$  components that are the same as the original GBT modes:

$$\theta v(\theta) = 0 \quad (35) \quad \theta w(\theta) = {}_k w(\theta) \quad (36)$$

Thus, the application of Hamilton's principle uses the strains expressions, equations 11 and 14, based on these displacements definitions. As a result, one achieves the generalized cross-section for the alternative complementary modes, summarized by Table. 2:

Table 2: Summary of generalized inertia of each alternative mode and their coupling terms.

Inertia	compl. mode $\gamma$	compl. mode $\theta$	coupl. modes k- $\gamma$	coupl. modes k- $\theta$	coupl. modes $\gamma - \theta$
C	$\pi t^3 r \frac{m^4}{12}$	$\pi t^3 r \frac{m^4}{12}$	$\pi t^3 r \frac{m^2(m^2+1)}{12}$	$\pi t^3 r \frac{m^2(m^2+1)}{12}$	$\pi t^3 r \frac{m^4}{12}$
D	$\pi trm^2 \left( 1 + \frac{(3-8m^2+4m^4)t^2}{12r^2} \right)$	$\pi t^3 \frac{m^6}{3r}$	$\pi t^3 \frac{m^2(m^2-1)^2}{3r}$	$\pi t^3 \frac{m^4(m^2-1)}{3r}$	$\pi t^3 \frac{m^4(m^2-1)}{3r}$
B	$\pi t^3 \frac{m^4(m^2-1)^2}{12r^3}$	$\pi t \frac{m^4}{r} \left( 1 + \frac{(m^4-1)t^2}{12r^2} \right)$	$\pi t^3 \frac{m^4(m^2-1)^2}{12r^3}$	$\pi t^3 \frac{m^6(m^2-1)}{12r^3}$	$\pi t^3 \frac{m^6(m^2-1)}{12r^3}$

Concerning the external load of the alternative complementary modes, there is no longitudinal terms,  $\gamma q_x(\theta) = \theta q_x(\theta) = 0$ , and the transversal terms are the same of respective GBT's original modes:

$$\gamma q_v(\theta) = {}_k q_v(\theta) \quad (37) \quad \theta q_v(\theta) = 0 \quad (38) \quad \gamma q_w(\theta) = \theta q_w(\theta) = {}_k q_w(\theta) \quad (39)$$

#### 4. NUMERICAL EXAMPLES

The numerical examples use the same thin-walled circular hollow steel cross-section with different boundary conditions. The first example has no boundary conditions in any node, i.e., the thin-walled circular hollow cross-section is allowed to deform freely under the load conditions. The second example has at the initial node constraints for all displacements and rotations, in all directions. Both structures represent a segment of 1m of a buried pipeline, as shown in figure 3, under a downward and upward linear projected surface load that represents the earth pressure. I.e., the total load applied on the structure is not a product of the surface load and the area of the surface, but it is the product of the surface load and the projected area on the global coordinate direction  $z$ . The material parameters are Young's modulus  $E = 205,000N/mm^2$ , Poisson's ratio  $\mu = 0.3$ , and shear modulus  $G = 78,846.2N/mm^2$ .

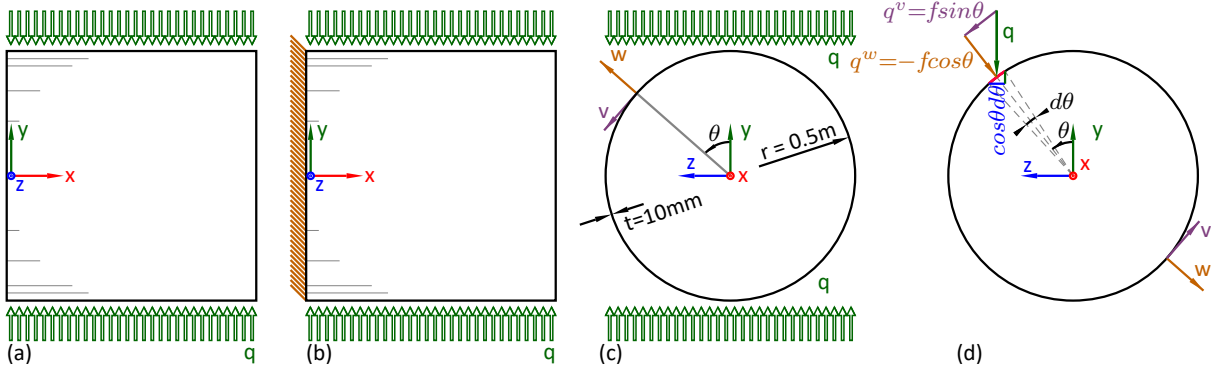


Figure 3: Buried pipeline segment under downward and upward pressure: a) and b) boundary conditions in Example 1 and 2, respectively; c) layout configuration; d) pressure load in polar coordinates.

##### 4.1. Setup of finite element and GBT Analysis

The projected pressure in figure 3.b leads to the following expressions:  $q_v = q \cos(\theta) \sin(\theta)$  and  $q_w = -q \cos^2(\theta)$ , which has in the GBT modal decomposition only participation in mode  $a$  and 5. Hence, one obtains:  ${}^a q_v = 0$ ,  ${}^a q_w = -50\pi$ ,  ${}^5 q_v = -12.5\pi$  and  ${}^5 q_w = -6.25\pi$  (in N/mm). After the filtering of GBT modes, one needs to solve a linear differential equation system. To achieve this system's solution, one uses the finite element based on the exact solution (Bianco 2018) of the GBT's differential equation, eq. 28. It is essential to observe that the coupling among the original and the complementary modes of GBT does not share the same solution of a single-mode. Therefore, the coupling system requires an element discretization of the structure, which uses five elements in these examples. From this finite element assembly, one obtains the modal amplification functions shown in figure 4 and table 3:

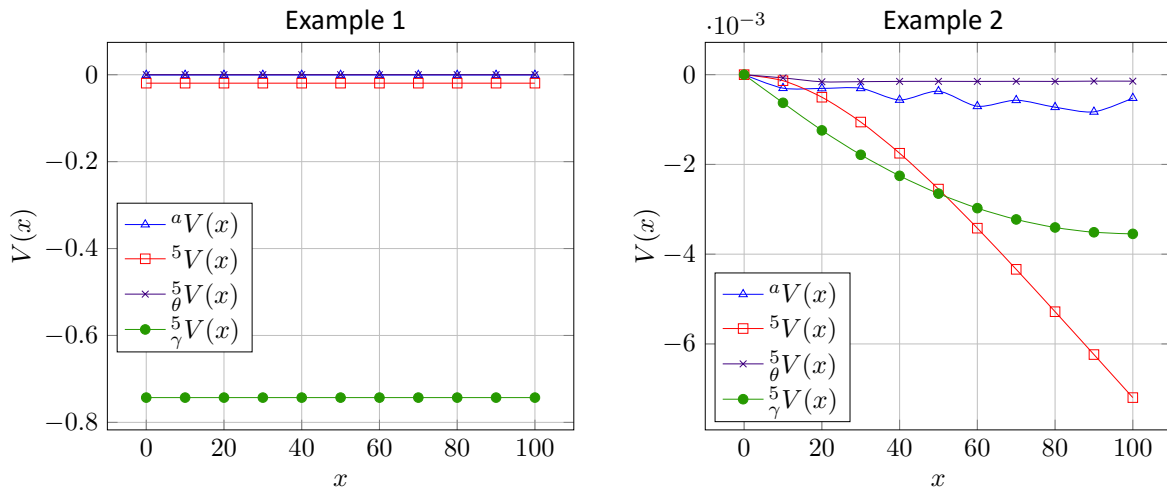


Figure 4: Model amplification functions  $V(x)$  for examples 1 and 2, respectively

Table 3: Displacement field: nodal results of the amplification functions at the center and tip points.

Example	Function	Middle Node				Tip Node			
		mode a	mode 5	mode $\gamma 5$	mode $\theta 5$	mode a	mode k	mode $\gamma 5$	mode $\theta 5$
1	$V(x)$	$-6.10E-4$	$-1.94E-2$	$-7,43E-1$	$1.52E-4$	$-6.10E-4$	$-1.94E-2$	$-7,43E-1$	$1.52E-4$
2	$V(x)$	$-3.70E-4$	$-2.55E-3$	$-2.65E-3$	$-1.49E-4$	$-6.1E-4$	$-7.20E-3$	$-3.55E-3$	$-1,45E-4$
	$V'(x)$	$-7.60E-6$	$-8.40E-5$	$-3.60E-5$	$6.06E-7$	$-2.85E-7$	$-9.59E-5$	$-2,17E-7$	$-1,21E-6$

In Example 1, all derivatives are null, due to the constant geometry, loading and boundary conditions.

From these displacement fields, one can achieve the membrane forces of shear,  $N_\gamma$ , and the transversal force,  $N_\theta$ , based on the following expressions:

$$N_\theta(x, \theta) = \frac{Et}{r} \left( {}^a V(x) + \sum_{i=2}^n {}^i_\theta w(\theta) {}^i_\theta V(x) \right) \quad (40) \quad N_\gamma(x, \theta) = Gt \left( {}^t V'(x) + \sum_{i=2}^n {}^i_\gamma v(\theta) {}^i_\gamma V'(x) \right) \quad (41)$$

The applications of eq. 40 at the tip point in example 1 and eq. 40 at the middle longitudinal point in example 2 lead to the diagrams Fig. 5.a and Fig. 5.b-c, respectively. Also, these figures present the results of the control models, which use a full shell element model developed in commercial software pack ANSYS®. These models use four nodes shell elements based on Reissner-Middle Theory (Shell-181), with a transversal discretization of 100 nodes for 25 elements segments in the longitudinal direction. Thus, each model has 15,600 degrees-of-freedom.

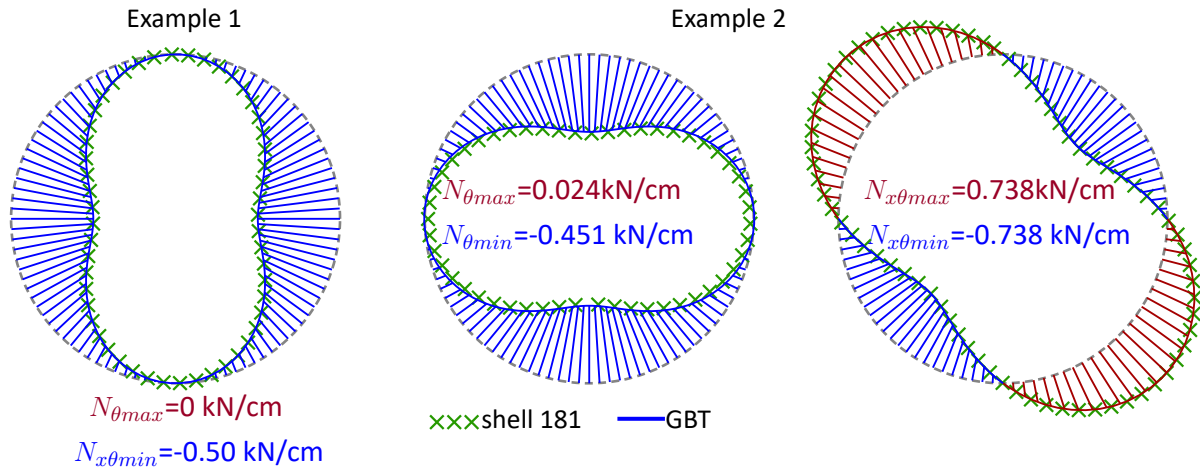


Figure 5: Comparison of results between GBT with the full shell model: a) and b) transversal membrane forces,  $N_\theta$ , at the tip node in Examples 1 and 2, respectively; c) shear membrane forces,  $N_{x\theta}$ , at the middle node in Example 2

Table. 4 presents the Mean Differences and Standard Deviation of the internal membrane forces in Fig. 5:

## 5. CONCLUSIONS

This study presents an alternative extension in GBT to include the shear and transversal elongation energies of membrane behavior. Based on two additional mode shapes, each one exclusively related to a particular membrane's energy. These alternative extensions in GBT have a minimal coupling effect, related to the plate's deformation energy. Such property is relevant for thin-walled structures since the plate's coupling terms are proportional to the thickness in the power of three. Thus, these alternative modes limited the coupling effect, due to the membrane's deformation energy, only in non-linear analysis. The numerical examples show an almost exact agreement between the full shell element model

Table 4: Mean differences and standard deviation between the alternative GBT modes and the full shell element model.

	Example 1	Example 2	
	$N_\theta$	$N_\theta$	$N_{x\theta}$
Mean Difference	0.032%	-0.739%	0.155%
Standard Deviation	0.029%	-3.123%	0.001%

and the proposed GBT model.

## 6. ACKNOWLEDGE

This work was carried out with the support of Horizon 2020 MSCA-RISE-2015 project No. 691213 entitled “Exchange Risk”.

## REFERENCES

- Abambres, M., C. D. S. N. (2013). Physically non-linear gbt analysis of thin-walled members. *129*, 148–165.
- Abambres, M., C. D. S. N. (2014a). Gbt-based elastic-plastic post-buckling analysis of stainless steel thin-walled members. *83*, 85–102.
- Abambres, M., C. D. S. N. R. K. (2014b). Gbt-based structural analysis of elastic-plastic thin-walled members. *136*, 1–23.
- Bebiano, R., G. R. C. D. (2014). On the shear deformation modes in the framework of generalized beam theory. *84*, 325–334.
- Bebiano, R., G. R. C. D. (2015). A cross-section analysis procedure to rationalise and automate the performance of gbt-based structural analyses. *92*, 29–47.
- Bianco, M. J., K. C. H. A. Z. V. (2018). Exact finite element formulation in generalized beam theory. *International Journal of Advanced Structural Engineering* *10*(3), 295–323.
- Davies, J.M., L. H. D. (1994). Second-order generalised beam theory. *Journal of Constructional Steel Research* *31*, 221–241.
- Jönsson, J. & M. Andreassen (2011). Distortional eigenmodes and homogeneous solutions for semi-discretized thin-walled beams. *Thin-Walled Structures* *49*, 691–707.
- Jönsson, J. & M. Andreassen (2012a). Distortional buckling modes of semi-discretized thin-walled columns. *Thin-Walled Structures* *51*, 53–63.
- Jönsson, J. & M. Andreassen (2012b). Distortional solutions for loaded semi-discretized thin-walled beams. *Thin-Walled Structures* *50*, 116–127.
- Miranda, S., G. A. M. R. & F. Ubertini (2013). A generalized beam theory with shear deformation. *Thin-Walled Structures* *67*, 88–100.
- Muresan, A.-A., M. Nedelcu, & R. Gonçalves (2019, 01). Gbt-based fe formulation to analyse the buckling behaviour of isotropic conical shells with circular cross-section. *Thin-Walled Structures* *134*, 84–101.
- Schardt, R. (1989). *Verllgemeinerte Technische Biegetheorie*. Springer-Vertrag.
- Schardt, R. (1994a). Generalized beam theory - an adequate method of coupled stability problems. *Thin-Walled Structures* *19*, 161–180.
- Schardt, R. (1994b). Lateral torsional and distortional buckling of channel-and hat-sections. *Journal of Constructional Steel Research* *31*, 243–265.
- Silvestre, N., C. D. (2003). Influence of shear deformation on the local and global buckling behaviour of composite thin-walled members. In J. Loughlan (Ed.), *Proceedings of the 4th International Conference on Thin-Walled Structures*, pp. 659–668. IOP Publishing Ltd.
- Silvestre, N., C. D. (2012). A shear deformable generalized beam theory for the analysis of thin-walled composite members. *Journal of Engineering Mechanics* *139*, Issue 8.
- Silvestre, N. (2007). Generalized beam theory to analyse the buckling behaviour of circular cylindrical shells and tubes. *45*.
- Vlasov, V. (1961). *Thin-Walled Elastic Beams*. Israel Program for Scientific Translations.

## Experimental investigation of compressed beams/columns using optical methods

Aleksandra Pawlak<sup>1</sup>, Piotr Paczos<sup>2</sup>

### Abstract

The subject of this work are cold formed, thin-walled non-standard channel columns with stiffened flanges and modified webs. The recent developments in cold forming allow the production of increasingly modified column cross-section shapes. Buckling forces and column buckling modes were determined and loaded with compressive force. Experimental tests were carried out using optical methods (ATOS system). The research includes the description and solution of the problem of column stability and the influence of the cross-sectional shape change on the obtained load values. Modified column cross-sections show higher resistance to loss of stability compared to classical channel cross-sections.

### 1. Introduction

The cold-formed thin-walled channel beams/columns with non-standard cross sections are the subject of researches (Fig. 1). The columns are thin-walled members made of cold-rolled steel sheets. Thin-walled, cold-formed structural members such as beams and columns are popular constructional elements due to their many advantages.

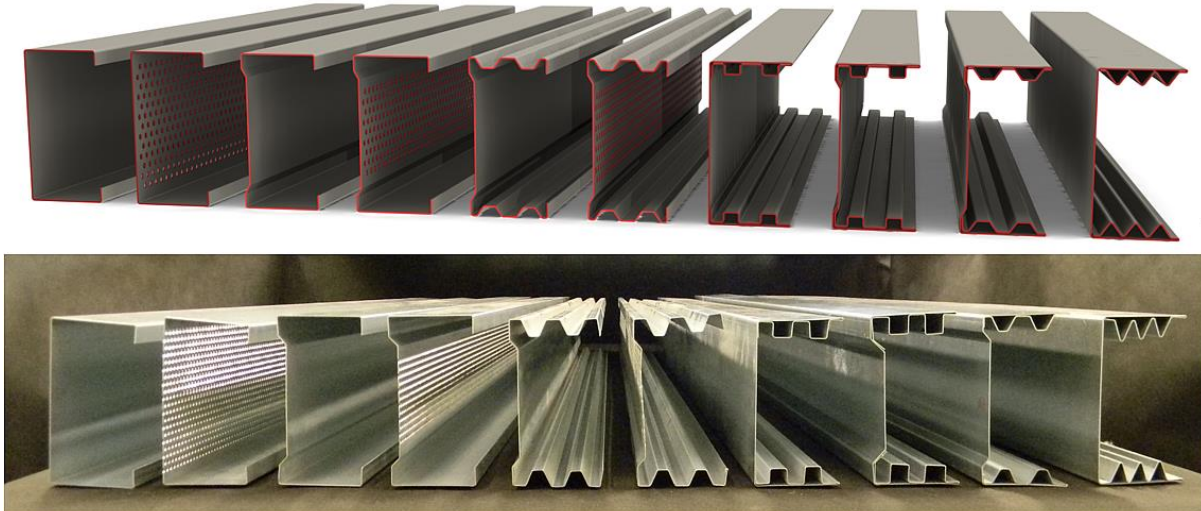


Figure 1: Cross section thin-walled channel beams/columns

<sup>1</sup> Postgraduate student, Poznan University of Technology, <aleksandra.ar.pawlak@doctorate.put.poznan.pl>

<sup>2</sup> Professor, Poznan University of Technology, <piotr.paczos@put.poznan.pl>

Ostwald and et al. (Ostwald 2013) as the advantages of thin-walled cold-formed beams they mention: good strength properties, relatively low weight, ability to carry heavy loads and a favorable relation between the weight of the structure and its load capacity. They are made of a single steel sheet, which can be protected against corrosion. Kasprzak et al. (Kasprzak 2019) point out that beams which are made in cold forming technology do not need to be re-protected as this process does not damage the anti-corrosion coating. In addition, cold forming allows to obtain beams with a large cross section but small wall thickness or beams with a complicated cross section. Obst et al. (Obst 2016) also mention some advantages of cold forming technology. The authors point out that to produce a beam requires a small energy, and the process is cheap. Sabbagh et al. (Sabbagh 2010) write that cold forming of members is a simple technology and therefore it is possible to offer a greater variety of profiles, and that this will allow for more efficient construction. In their opinion, a very important advantage is the appropriate strength to weight ratio.

The cross-section of channel beams/columns has evolved over the last years. New shapes of column cross-sections were explored in order to increase their strength, stability and bearing capacity. Baldissino et al. (Baldissino 2019) referred to the load-bearing capacity, because of the high strength-to-weight ratio, the assessed load-bearing capacity is much higher than the characteristic-experimental one. Scientists are investigating increasingly complex, unusual cross-sectional shapes of channel beam/columns. The shape of the cross-section has a significant impact on the strength, resistance to loss of stability or load bearing capacity of the structure. Huang et al. (Huang 2018) described beams with a classic lipped channel cross-section, but with a modified web. Szymczak et al. (Szymczak 2016) examined channels with modified flange. They loaded the members with bending moment and compressive force. Ren et al. (Ren 2019) describes numerical tests of cold-formed steel perforated rack uprights subjected to axial compression. Researchers are also studying other cross-section shapes, such as: Z-beams or closed rectangular cross-sections. De Miranda Batista (De Miranda Batista 2010) describes channels with stiffened edges of the flange, but also the Z-beams with such bends. The stability bearing capacity of axially compressive loaded fixed-ended channels with complex edge stiffeners were analyzed by Wang et al. (Wang 2012). C- and Z-beams are also used to construct roofs. Wang et al. (Wang 2018) examined channels with a high, modified web and a narrow flange that has bends at the edges. Such members are used in the construction of roof sheathing. Yerudkar et al. (Yerudkar 2017) compared cold-formed channels with stiffeners on the web or flange.

The studies include actual experimental investigation. The researches consists of description and solution of a problem of stability of columns and the influence of cross-section change on the obtained load values. By using modern, optical measuring methods, it is possible to investigate the influence of distortion of the cross-section on local buckling of short and medium length beams/columns. The non-standard flanges of considered channel columns reinforce them and increase their stability and a strength-to-weight ratio. By changing the parameters defining the shape of cross-section of beams/columns such as the size of boxes, the length of lip the strength, stability and load capacity can further improved. Many years of experience in analysing the strength and stability of thin-walled beams encouraged the author to use a new and modern approach (optical methods).

There are few papers in literature that present the application of optical measuring techniques to the structural analysis of thin-walled members. The examples are Styles et al. (Styles 2007), Hühne et al. (Hühne 2008) and Miehe et al. (Miehe 2009). In this paper, authors described experimental investigations of different structures: beams made of aluminium foam sandwich, perforated cylindrical shells and glass polymers. They all were based on the use of ARAMIS optical strain measuring system. Urbaniak et al. (Urbaniak 2016) examined thin-walled channel columns and considered three different

variants of arrangement of individual layers in an eight-layer laminate. Perret et al. (Perret 2010) examined aircraft composite fuselage loaded with compressive force. For the research, similarly to the previous authors used the ARAMIS system. Czapski et al. (Czapski 2015), thanks to the strain gauge method, determined the deformations at the points of the tested structure, whereas thanks to the optical system they obtained deflection maps. The mode of buckling of compressed columns is also influenced by column length. Jeleniewicz et al. (Jeleniewicz 2016) examined the classic lipped channel cross-section and took into account various columns of different lengths. They used a pulse laser scanner and a digital camera.

The presented subject is the development of researches that have been conducted in the Division of Strength of Materials and Structures of Poznan University of Technology. Experimental investigations loss of stability, distribution of stresses and displacements of cold-formed thin-walled beams were presented by Grenda and Paczos (Grenda 2019).

## 2. Experimental investigation

Eight thin-walled columns made in cold bending technology were examined. The bending process was performed on numerically controlled bending machines, which made it possible to obtain such complex cross-sectional shapes presented in Figure 2.



Figure 2: Cross-sections of the tested columns

The tested cross sections had mainly stiffeners on the flanges: B5, B7, B8, B9 and B10. The shape of the web also had a significant impact on the loss of stability due to compressive loading, so modified web shape columns were also examined: B3, B5, B8 and B9. The more classical cross-sections: B0, B1 were also examined to assess the effect of non-standard column cross-section shape on the load values. Columns with single and double plates on shelves were investigated. Overall dimensions of all tested cross-sections are: height  $H = 80\text{mm}$ , width  $b = 40\text{mm}$ , wall thickness  $t = 0,5\text{mm}$ .

Experimental tests were performed, for this purpose optical and strain gauge methods were used. In this article we will describe the optical tests performed with the ATOS system, which allows for non-contact 3D measurements. The measurements are made with a scanner using a structured blue light technology. The tested members were loaded with a compressive force applied in the center of gravity of the cross-section. Tests were performed on a ZWICK Z100 testing machine with a measuring range of 0.2 - 100kN. The columns were supported by spacers. The lower spacer blocked three translations, while the upper spacer blocked two translations. Translation along the column axis (x axis) was possible. Rotations against all axes on both spacers were possible. The tests were carried out until the column load capacity was exhausted. The test stand is shown in Figure 3.

For experimental tests, carried out using the strain gauge method, foil resistance strain gauges with a constant  $K=2.01$  were used. The strain gauges tested the strain at two points: web and flange. Deformations in the measuring points were recorded by computer. During the measurement the

following were recorded: measurement time, compressive force and deformation, shortening of columns. The tests were carried out in accordance with the requirements of the EUROKOD 3 standard.

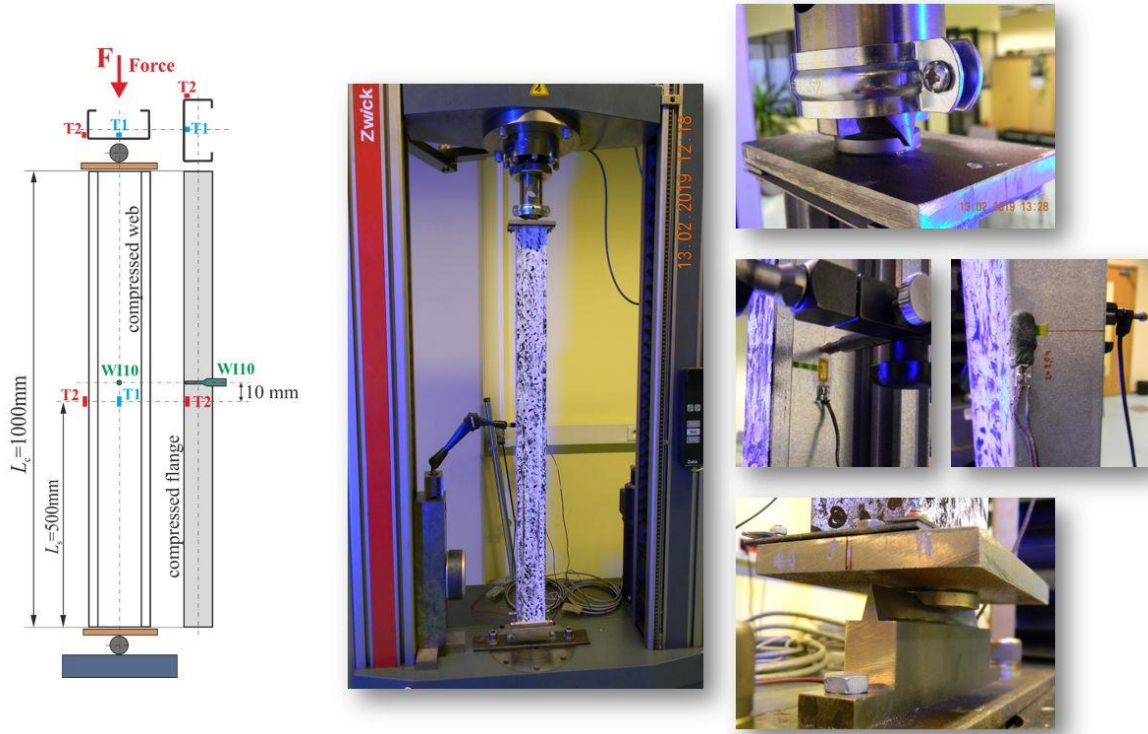


Figure 3: Test stand

The ATOS optical system generates test results in the form of 3D images, which were taken at 0.25 frames per second. The optical test results are obtained by processing this data in GOM Correlate. This program allows the measurement of deformation at specific points, which makes it possible to compare the optical test results with strain gauges.

### 3. Results of experimental studies

The test results were developed on the basis of optical and strain gauge tests. The buckling force and maximum force were determined. The critical force values, obtained from the strain gauge method, were determined using the linear regression method tangent to the compression plot. The optical method allows to estimate the value of the critical force from the moment when the first signs of buckling appear. Additionally, the beams were weighed and their stiffness was calculated. The results are shown in Table 1.

Table 1: Results of experimental studies

Beam/column	Weight (kg)	Buckling force $F_{cr}$ (kN)	Maximum force $F_{max}$ (kN)	Stiffness C (kN/mm)
B0	0,842	3,89	4,69	4,4
B1	0,612	1,35 – 3,48	3,89	5,2
B3	0,614	5,80 – 7,00	9,99	7,2
B5	0,721	10,42	13,53	8,4
B7	1,090	7,20 – 8,00	13,63	9,5
B8	1,115	9,50 – 11,00	17,60	8,4
B9	1,074	11,30 – 20,13	22,80	11,1
B10	1,068	3,75	12,75	8,7

Columns B0, B7, B8, B9 and B10 are subject to local buckling and columns B1, B3 and B5 are subject to distortional buckling. Figure 4 shows the webs of the tested columns and the modes of their buckling. The webs of the tested columns show characteristic half-waves for local buckling. Optical testing allows the analysis of buckling modes and the time during which the columns start to lose stability. It was observed that column B10 began to lose stability 6s after the load started. In the case of column B0 this time has increased. This member began to lose stability after 40s.

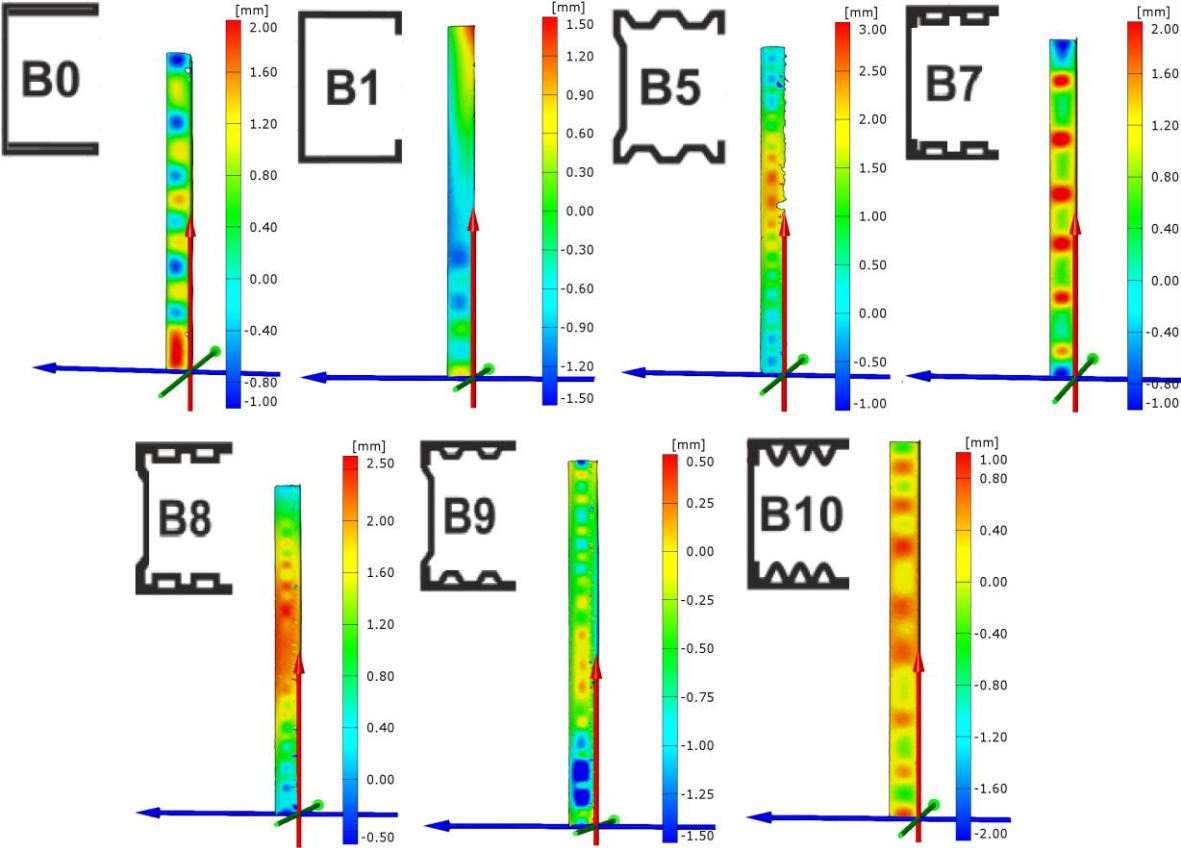


Figure 4: Modes of buckling - results of optical tests

The research was carried out until the load capacity of the columns was exhausted. The highest maximum force was obtained for column B9. The lowest value of bearing capacity was obtained for column B1. Figure 5 shows the modes of destruction of some of the columns tested.

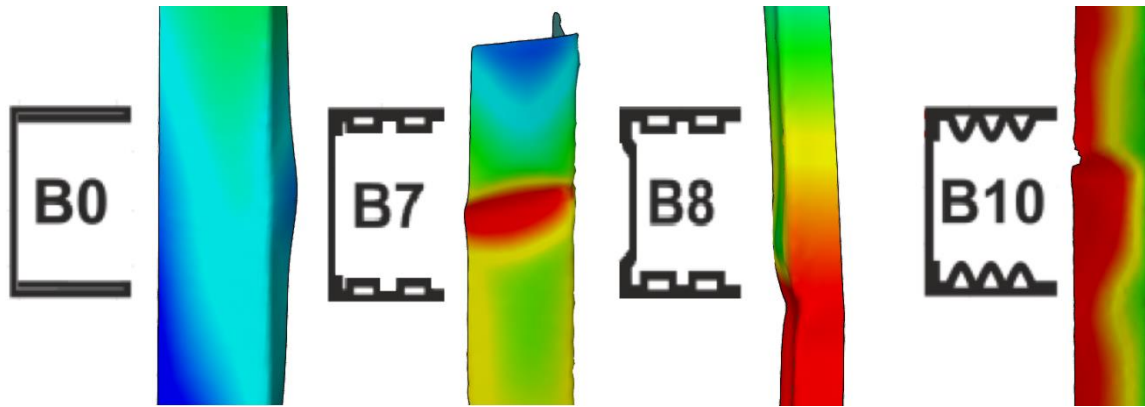


Figure 5: Forms of destruction

Figure 6 shows the results of strain gauge tests in the form of a graph. The results of optical tests and strain gauges made it possible to determine the buckling forces for the tested columns. The highest value of buckling force was obtained for column B9, the lowest for column B1.

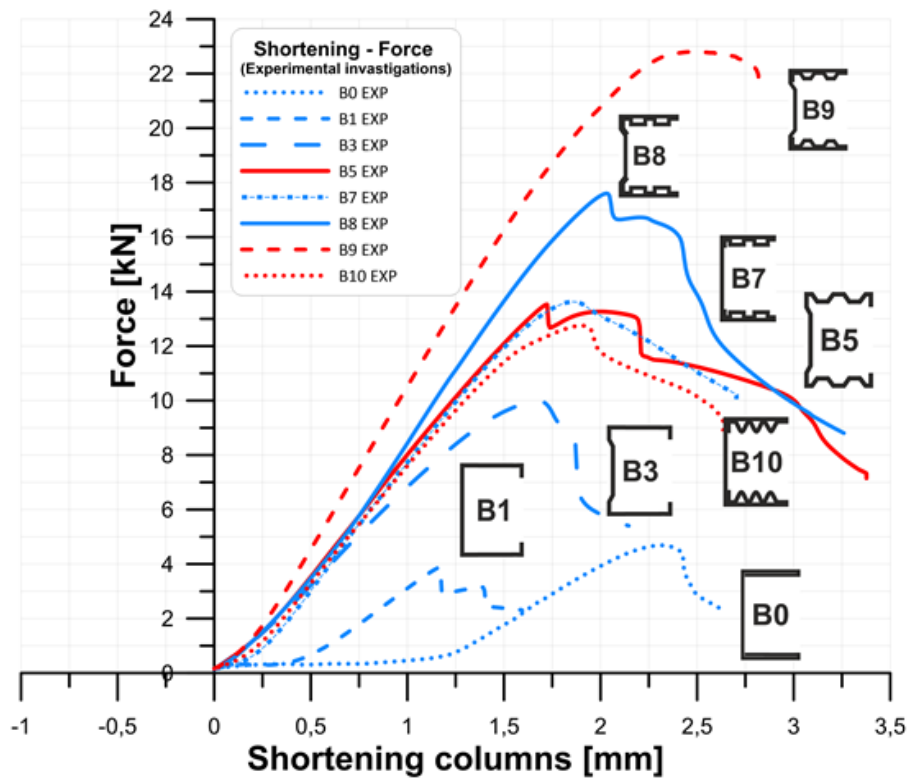


Figure 6: Results of strain gauge tests

#### 4. Conclusion

This article describes experimental research: optical and strain gauge tests of cold-formed, thin-walled channel columns with stiffeners on flanges and web. Eight different cross-sections were examined. The columns were loaded with axial compressive force. The researches consists of description and solution of a problem of stability of columns and the influence of cross-section change on the obtained load values.

Columns with double flange sheets have suffered a local loss of stability, while columns with single flange sheets have suffered a distortional loss of stability. The most resistant to loss of stability are the columns with stiffeners and double sheet on the flanges and modified web shape. The shape of the flange stiffeners is important when assessing the strength of the columns. The buckling force value for the B10 column is low compared to columns that have trapezoidal and box bends on the flanges. The differences in the buckling force values may result from the fact that the contact between the sheets on the flanges, in the case of column B10, is much smaller than in the case of the other columns. The highest values of buckling force and maximum force were obtained for column B9. It is a column with a double trapezoidal sheet on the flange and a modified web shape. The above considerations show a significant influence of the column cross-sectional shape on its resistance to loss of stability. The proper (optimal) shape of cross-section may help to reduce the weight/wall-thickness of columns, even by half, without big influence on its load capacity. Column B5 due to trapezoid corrugation of flanges has the highest ratio of the buckling load to the beam weight, buckling mode in this case is distortional one

As previously mentioned, the columns lost their stability locally or distortionally. In some cases, when the column was close to being exhausted, a general loss of stability was also noticed. Despite the different modes of loss of stability, the mechanisms of loss of stability were very similar for the examined columns. The mechanisms of destruction are shown in Figure 5.

The main advantage of optical testing is that it gives insight into the movements of the entire column. Comparing it with strain gauges, which only allow for measuring deformations at specific points in the structure, optical testing gives a broader view of what happens to the structure during loading. It is possible to analyse the deformation of the columns at any stage of loading. Optical testing has been analyzed in the GOM Correlate program. Measurement points were generated in the middle of the web and in the middle of the flange. The location of these points was dictated by the location of the strain gauges. This allowed to compare the results of optical tests with those of strain gauges.

### Acknowledgments

The project was funded by the National Science Centre allocated on the basis of the decision No. DEC-2017/25/B/ST8/00266 of 2017-11-23 – Contract No. UMO-2017/25/B/ST8/00266.

### References

- Ostwald, M., Rodak, M. (2013). "Multicriteria optimization of cold-formed thin-walled beams with generalized open shape under different loads." *Thin-Walled Structure*, 65 245-307.
- Kasprzak, J., Paczos, P. (2019). "The influence of imperfections on the Strength and Stability of Cold-Formed Sigma Channels with Corrugated Flanges." *Lecture Notes in Mechanical Engineering*, 36-49.
- Obst, M., Kurpisz, D., Paczos, P. (2016). "The experimental and analytical investigation of torsion phenomenon of thin-walled cold formed channel beams subjected to four-point bending." *Thin-Walled Structures*, 106 179-186.
- Sabbagh, A.B., Mirghaderi, M., Petkovski, K., Pilakoutas, K. (2010). "An integrated thin-walled steel skeleton structure (two full scale test)." *Journal of Constructional Steel Research*, 66 470-479.
- Baldassino, N., Bernuzzi, C., Simoncelli, M. (2019). "Evaluation of European approaches applied to design of TWCF steel members." *Thin-Walled Structure*, 143.
- Huang, X., Yang, J., Liu, Q., Bai, L., Wang, F., Wang, J. (2018). "A simplified flange-lip model for distortional buckling of cold-formed steel channel-section with stiffened web." *International Journal of Mechanical Sciences*, 136 451-459.
- Szymczak, C., Kujawa, M. (2016). "On local buckling of cold-formed channel members." *Thin-Walled Structure*, 106 93-101.
- Ren, C., Wang, B., Zhao, X., (2019). "Numerical predictions of distortional-global buckling interaction of perforated rack uprights in compression." *Thin-Walled Structure*, 136 292-301.

- De Miranda Batista, E. (2010). "Effective section method: A general direct method for the design of steel cold-formed members under local-global buckling interaction." *Thin-Walled Structure*, 48 345-356.
- Wang, C., Ma, P., Song, D., Yu, X. (2012). "Design of cold-formed thin-walled steel fixed-ended channels with complex edge stiffeners under axial compressive load by direct strength method." *Applied Mechanics and Materials*, 226-228 1232-1235.
- Wang, F., Zhang, H., Bai, L., Ren, C. (2018). "Numerical studies of the rotational stiffness of purlin-sheeting system." *International Journal of Steel Structure*, 18(3) 719-733 .
- Yerudkar, D.S., Vesmawala G.R. (2017). "Finite Element Simulation of Cold Formed Steel Stiffened Zed Section for Local, Dostortional And Lateral Torsional Buckling." *American Journal of Engineering Research*, 6 249-255.
- Styles, M., Compston, P., Kalyanasundaram S. (2007). "The effect of core thickness on the flexural behavior of aluminum foam sandwich structures." *Composite Structure*, 80 532-538.
- Huhne, C., Rolfes, R., Breitbach, E., TeBmer, J. (2008). "Robust design of composite cylindrical sheels under axial compression – Simulation and validation." *Thin-Walled Structure*, 46 947-962.
- Miehe, C., Göktepe, S., Méndez Diez, J. (2009). "Finite viscoplasticity of amorphous glassy polymers in the logarithmic strain space." *International Journal of Solids and Structures*, 46 181-202.
- Urbaniaik, M., Teter, A., Kubiak, T. (2016). "Influence of boundary conditions on the critical and failure load in the GFPR channel cross-section columns subjected to compression." *Solid State Phenomena*, 240 212-217.
- Perret, A., Mistou, S., Fazzini, M., Brault, R. (2010). "Global behavior of a composite stiffened panel in buckling. Part 2: Experimental investigation." *Composite Structure*, 94 367-385.
- Czapski, P., Kubiak, T. (2015). "Numerical and experimental investigation of the post-buckling behavior of square cross-section composite tubes." *Composite Structure*, 132 1160-1167.
- Jeleniewicz, K., Raczyński, S., Karsznia, K., Uchański, Ł., Gilewski, W. (2016). "Badania eksperymentalne krótkich cienkościennych profili stalowych z użyciem technik geodezyjnych." *Acta Sci. Pol. Architectura*, 15 (4) 17-30.
- Grenda, M., Paczos, P. (2019). "Experimental and numerical study of local stability of non-standard thin-walled channel beams." *Journal of Theoretical and applied mechanics*, 57 549-562.

## Investigating local buckling in highly slender elliptical hollow sections through analysis of 3D-printed analogues

Finian McCann<sup>1</sup>, Federico Rossi<sup>2</sup>

### Abstract

Tubular structural members with slender cross-sections are susceptible to failure through local buckling of their tube walls. Previous numerical studies of steel elliptical hollow sections in compression predicted the local buckling modes and the ultimate loads of particularly slender specimens, with the results used to calibrate design methods for slender elliptical sections. Although these numerical parametric studies were conducted across a wide slenderness range, it was only possible to validate the models against experimental results in the low slenderness range since commercially available steel EHS are intended to satisfy non-slender geometric limits prescribed by structural design codes. Such limitations to the experimental scope are circumvented in the present study through testing of highly slender specimens produced using additive manufacturing techniques. A total of eight specimens of various cross-sectional aspect ratios and tube wall thicknesses were fabricated at London South Bank University using additive manufacturing techniques, which were then tested in compression; the observed load-deflection behaviour, ultimate loads, longitudinal strains and failure modes are discussed. Through appropriate rescaling of relevant parameters, design predictions for the ultimate load of the 3D-printed analogues are obtained using a design method intended for use with steel elliptical hollow sections. It is shown that the design predictions are safe-sided when compared to the present experimental results, with the accuracy generally increasing with aspect ratio and slenderness.

### 1. Introduction

Steel elliptical hollow sections (EHS) have found increased use in recent years in construction, having been employed in landmark projects such as Heathrow Terminal 5, Madrid Barajas Airport and Cork Airport (see Fig. 1a) (Chan et al, 2010). Such sections are characterized by their maximum outer cross-sectional diameter  $2a$ , their minimum outer cross-sectional diameter  $2b$  and their tube wall thickness  $t$ , as shown in Fig. 1b. The combination of the mechanical efficiency offered by having a greater major axis flexural resistance and the aesthetic appeal of elliptical geometry has been a factor in the increased popularity of EHS in steel construction (Ruiz-Teran & Gardner, 2008). Reflecting this increased usage, the sections are included in European structural specifications (Comité Européen de Normalisation, 2006) and the recent revision to EN 1993-1-1 (Comité Européen de Normalisation, 2018).

Studies into the behaviour of steel EHS are extensive, encompassing cross-section classification (Gardner & Chan, 2007), compressive resistance (Chan and Gardner, 2008a), bending resistance (Chan & Gardner,

<sup>1</sup> Finian McCann, School of Mechanical Engineering, Loughborough University, Leicestershire, UK

<sup>2</sup> Federico Rossi, School of Mechanical Engineering, Loughborough University, Leicestershire, UK

2008b), resistance in shear (Gardner et al, 2008), elastic buckling (Silvestre, 2008) and flexural buckling (Chan & Gardner, 2009). Studies have also been conducted on stainless steel EHS (Theofanous et al, 2009) and on cold-formed steel EHS (Chen & Young, 2020).



Figure 1: a) Steel EHS at Cork Airport; b) cross-sectional geometry of EHS showing dimensions and axes.

Studies into the local buckling of EHS conducted by Silvestre & Gardner (2011) and Insausti & Gardner (2011) characterized elastic buckling modes and postbuckling behaviour. Leading from these previous studies, a numerical parametric study conducted by McCann et al (2016) confirmed that, with increasing aspect ratio  $a/b$ , the postbuckling behaviour of slender steel EHS in compression transitions from unstable imperfection-sensitive behaviour like that observed in cylindrical shells to stable imperfection-insensitive behaviour like that observed in flat plates. Although the numerical parametric study was conducted across a wide slenderness range, it was only possible to validate the models against experimental results from Chan & Gardner (2008a) in the relatively lower slenderness range since commercially available steel EHS are intended to satisfy non-slender geometric limits prescribed by structural design codes. In order to confirm that a design method proposed by McCann et al (2016) for slender EHS in compression is valid for use with cross-sections in the high slenderness range, it is appropriate that such highly slender specimens be tested. However, the required tube wall thickness would be too thin to fabricate or the outer dimensions too large to manipulate for testing.

In order to circumvent such issues, highly slender analogues fabricated from polymer using additive manufacturing techniques are investigated in the present study. In the context of structural engineering, additive manufacturing techniques have been primarily employed in the production of concrete-framed structures (Zhang et al, 2019), with other more limited applications in continuously-printed steel reinforcement (Paolini et al, 2019) and fibre-reinforced polymer formwork (Paolini et al, 2019); the world's first 3D-printed metal bridge was fabricated in the Netherlands in 2018 (de Zeen, 2018). Polymer structural components fabricated using additive manufacturing techniques offer advantages such as better environmental and corrosion resilience, greater precision and reliability, and, if recycled plastic is used, more sustainable structures. At present, the cost-effectiveness of using 3D-printed polymers in construction is hampered by production speeds and material strengths, but it is forecast that such limitations can be surmounted through advances in additive manufacturing and material science.

The objective of the present study is to examine the behaviour of highly slender steel elliptical hollow sections in compression through the use of polymer analogues fabricated using additive manufacturing techniques; the use of such techniques for educational purposes in structural mechanics has been

demonstrated successfully by Virgin (2018). An experimental campaign is described where EHS specimens of various cross-sectional aspect ratios and tube wall thicknesses are loaded in compression. Results for the ultimate load, the failure mode and the load–deflection behaviour are discussed. Comparison is made between the experimental ultimate loads and the design method for slender steel EHS proposed by McCann et al (2016), where it is found the design method provides safe-sided results with the accuracy increasing with aspect ratio and slenderness.

## 2. Experimental setup

In this section, the experimental campaign is described, including discussions on specimen geometry, the fabrication method, imperfections and the setup of the apparatus used in the experiments.

### 2.1 Geometry of EHS specimens

Eight additive-manufactured EHS specimens were fabricated at London South Bank University (LSBU) with cross-sectional aspect ratios  $a/b = 1.5, 2.0$  and  $3.0$ , and nominal tube wall thickness  $t$  between  $1.5$  mm and  $3.0$  mm. The specimens were labelled thus: EHS[specimen number]-[ $2a$ ]-[ $2b$ ]-[nominal  $t$ ], e.g. Specimen 1 is labelled EHS01-100-50-3.0 (see Table 1). The maximum and minimum outer diameters of the sections were chosen so that the mean perimeter  $P_m$  is approximately constant for all specimens; the values of  $P_m$  and the cross-sectional area  $A$  calculated using the measured properties of the specimens are shown in Table 1. The nominal length  $L = 280$  mm for all specimens, reflecting the maximum dimension producible by the printer used; this relatively short length also ensures that global buckling is precluded.

### 2.2 Additive manufacturing process

Geometric model files created using the nominal dimensions shown in Table 1 were used as input for an Ultimaker 3 Extended fused filament fabrication (FFF) printer based in the Digital Architecture Laboratory (DARLAB) at LSBU. The specimens were fabricated from filaments of polylactic acid (PLA) thermoplastic polymer with a nominal elastic modulus  $E = 2346.5$  N/mm<sup>2</sup>, a nominal yield strength of  $49.5$  N/mm<sup>2</sup> and a nominal fracture strain of  $5.2\%$  (Ultimaker, 2018); the finished specimens are shown in Fig. 2. Considering that the yield strain of S355 steel is  $0.17\%$  while that of PLA is  $12.5$  times higher at  $2.1\%$ , PLA sections exhibit a considerably greater elastic deformation capacity than steel sections and are hence more susceptible to failure initiating through buckling as opposed to inelastic effects.



Figure 2: Fabricated EHS stub specimens.

Given that extruded filaments of PLA were deposited about the circumference of the section, the fabrication process thus leads to a degree of anisotropy within the completed specimens, with the

circumferential material properties being greater than those in the longitudinal direction. It was found that the degree of anisotropy in the elastic modulus  $E$ , which governs local buckling, was minimal.

### 2.3 Precision of fabrication process

Prior to testing, the geometry of each specimen was measured in order to assess the level of deviation from the nominal dimensions. The outer diameters  $2a$  and  $2b$ , and the specimen length  $L$  were found to be within 0.3% of the nominal values. Average wall thicknesses  $t$  are shown in Table 1 along with the standard deviations from the nominal dimensions. As can be seen, the coefficient of variation (COV) of  $t$  is between 2.4% and 4.0% for all specimens other than Specimen EHS08-105-35-1.5 where COV = 8.6%. When applying the design method of McCann et al (2016) in Section 4, the magnitude of the wall thickness imperfection  $\Delta w$  is assumed to be  $0.05t$  for all specimens, which is comparable to the average imperfection magnitude of  $\Delta w = 0.051t$  reported by Chan & Gardner (2008a) for steel EHS.

Table 1: Cross-sectional properties of specimens.

Specimen	$a/b$	Wall thickness $t$				$P_m$	$A$
		Nominal (mm)	Average (mm)	St.Dev (mm)	COV (mm)		
EHS01-100-50-3.0	2.0	3.00	3.17	0.07	0.024	233	737
EHS02-90-60-2.0	1.5	2.00	2.07	0.05	0.027	232	478
EHS03-90-60-2.0	1.5	2.00	2.08	0.05	0.025	232	481
EHS04-90-60-2.0	1.5	2.00	2.04	0.05	0.025	232	473
EHS05-100-50-3.0	2.0	3.00	3.10	0.05	0.018	233	721
EHS06-100-50-1.5	2.0	1.50	1.45	0.06	0.040	238	344
EHS07-105-35-2.0	3.0	2.00	2.02	0.05	0.024	228	459
EHS08-105-35-1.5	3.0	1.50	1.39	0.13	0.086	230	344

### 2.4 Buckling of elliptical sections

The critical local buckling stress  $f_{cr}$  of an elliptical section is estimated by adapting the equivalent expression for a circular section:

$$f_{cr} = \frac{E}{\sqrt{3(1-\nu^2)}} \frac{2t}{D_{eq}} \quad (2)$$

where the Poisson's ratio  $\nu = 0.35$  for PLA and the equivalent diameter  $D_{eq} = 2(a^2/b)$ ; this value is twice the maximum radius of curvature in the elliptical section and reflects the point of initiation of buckling being at the extreme of the minimum radius. The slenderness parameter  $\bar{\lambda}_\ell$  is defined as:

$$\bar{\lambda}_\ell = \sqrt{\frac{f_y}{f_{cr}}} \quad (3)$$

According to the classification limits prescribed by EN 1993-1-1 (CEN, 2018), an EHS in compression is classified as susceptible to local buckling if  $D_{eq}/t\varepsilon^2 > 90$ , where the material modification factor  $\varepsilon = [(235/f_y)(E/210000)]^{0.5}$ . The values of  $D_{eq}$ ,  $D_{eq}/t\varepsilon^2$ ,  $f_{cr}$  and  $\bar{\lambda}_\ell$  calculated using the measured properties of the specimens are shown in Table 2. It should be noted that the maximum value of  $D_{eq}/t\varepsilon^2$  found for the

steel EHS used to validate the model of McCann et al (2016) was 189, thus demonstrating the relatively high slendernesses being investigated presently.

Table 2: Buckling parameters calculated using measured properties.

Specimen	$a/b$	$D_{eq}$ (mm)	$D_{eq} / t\epsilon^2$	$f_{cr}$ (N/mm <sup>2</sup> )	$\bar{\lambda}_l$
EHS01-100-50-3.0	2.0	200	1189	45.9	1.04
EHS02-90-60-2.0	1.5	135	1233	44.2	1.06
EHS03-90-60-2.0	1.5	135	1225	44.5	1.05
EHS04-90-60-2.0	1.5	135	1246	43.8	1.06
EHS05-100-50-3.0	2.0	200	1216	44.8	1.05
EHS06-100-50-1.5	2.0	200	2603	20.9	1.54
EHS07-105-35-2.0	3.0	315	2948	18.5	1.64
EHS08-105-35-1.5	3.0	315	4281	12.7	1.97

### 2.5 Experimental method

Compression tests were conducted on the specimens in the Strength of Materials laboratory at London South Bank University. The specimen was placed in a Zwick/Roell 250 kN universal testing machine as shown in Fig. 3a; care was taken to position the specimens so that the load was applied as concentrically as possible in order to achieve an even stress distribution throughout the cross-section. A linear variable transducer (LVDT) was placed in contact with the upper loading platen in order to record the vertical displacement. Strain gauges were affixed to Specimen 1 at the positions indicated in Fig. 3b in order to measure the longitudinal strain (strain gauges were not affixed to the other specimens). The specimens were loaded in displacement control at a rate of 0.5 mm/min until failure.

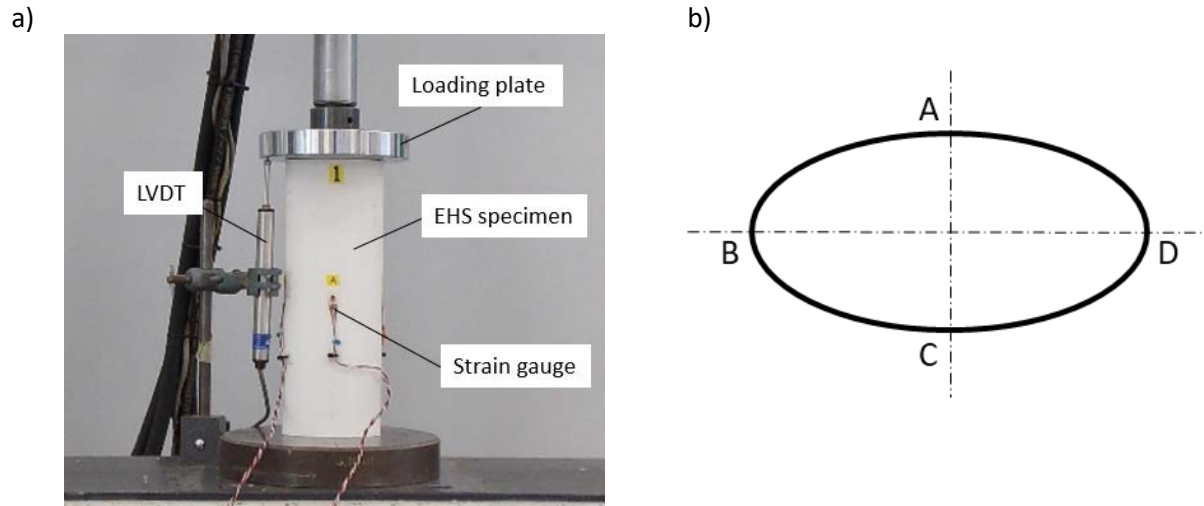


Figure 3: a) Specimen 1 in position for testing; b) locations of strain gauges at mid-height cross-section.

### 3. Experimental results

The load–displacement relationships recorded for each specimen are shown in Fig. 4, where it can be seen that each specimen underwent linear elastic deformation up to a sudden failure with a negligible amount of softening visible. The failure mode observed in each specimen involved sudden brittle ruptures initiating at the point of maximum radius of curvature, i.e., either point A or C in Fig. 3b. The

experimental ultimate load  $N_{u,exp}$  for each specimen is compared with the fully-effective compressive resistance  $Af_y$  in Table 3 (the design predications for cross-sectional resistance  $N_{c,Rd}$  discussed in Section 4 are also shown). It can be seen that the utilization of the full cross-sectional resistance diminishes with increasing slenderness, indicating that buckling had indeed occurred. Specimen EHS01-100-50-3.0 is shown post-failure in Fig. 5 – ruptures occurred at two cross-sections in each specimen tested.

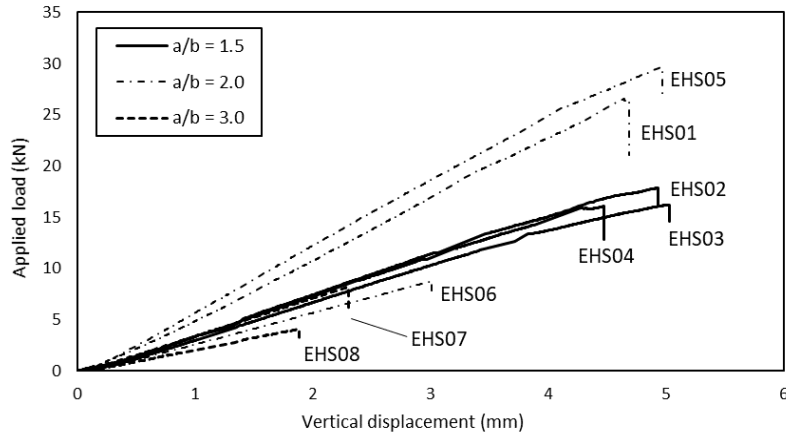


Figure 4: Load–displacement curves for all specimens.

Table 3: Experimental ultimate loads.

Specimen	$a/b$	$\bar{\lambda}_\ell$	$Af_y$ (kN)	$N_{u,exp}$ (kN)	$N_{c,Rd}$ (kN)	$N_{u,exp} / Af_y$	$N_{u,exp} / N_{c,Rd}$
EHS01-100-50-3.0	2.0	1.01	36.5	26.6	19.1	0.73	1.39
EHS02-90-60-2.0	1.5	1.03	23.7	17.9	12.0	0.76	1.50
EHS03-90-60-2.0	1.5	1.03	23.8	16.2	12.1	0.68	1.34
EHS04-90-60-2.0	1.5	1.04	23.4	16.1	11.7	0.69	1.37
EHS05-100-50-3.0	2.0	1.03	35.7	29.7	18.5	0.83	1.61
EHS06-100-50-1.5	2.0	1.50	17.0	8.76	5.14	0.51	1.71
EHS07-105-35-2.0	3.0	1.60	22.7	8.22	7.10	0.36	1.16
EHS08-105-35-1.5	3.0	1.92	15.8	4.10	3.97	0.26	1.03

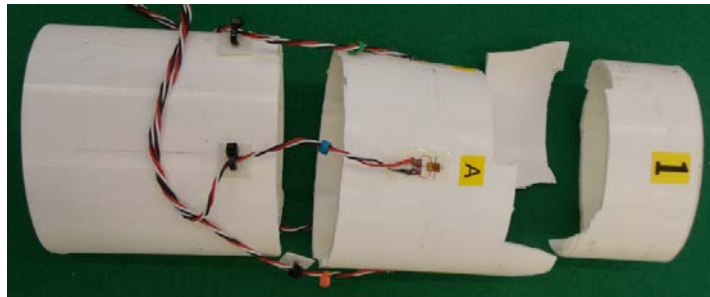


Figure 5: Specimen EHS01-100-50-3.0 post-failure.

The strains at mid-height are plotted against the average compressive stress in Fig. 6 for Specimen EHS01-100-50-3.0. It can be seen that the strain is higher at points A and C where the section is less stiff locally at the points of minimum curvature. The effective elastic modulus of the section calculated at point A is 2397 N/mm<sup>2</sup>, a close approximation of the nominal value of 2346 N/mm<sup>2</sup>.

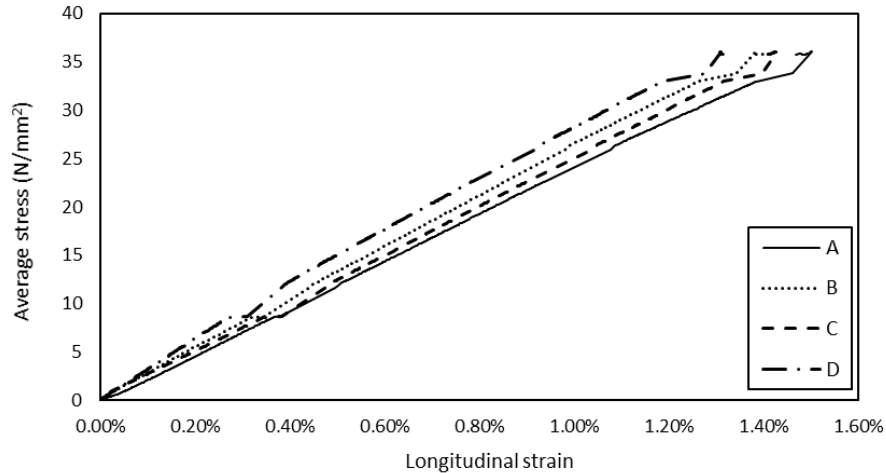


Figure 6: Longitudinal strains measured at the mid-height cross-section of Specimen EHS01-100-50-3.0.

#### 4. Comparison with previous design method

The design method proposed by McCann et al (2016) is used to calculate a strength reduction factor  $\rho$  such that the design resistance in compression of EN 1993-1-1 (CEN, 2018)  $N_{c,Rd} = \rho A f_y / \gamma_{M0}$ ; here, the material partial factor  $\gamma_{M0}$  is set equal to unity. The design method is not reproduced here in full; it suffices to say that it reflects the dependence of  $\rho$  on the local buckling slenderness, the aspect ratio  $a/b$  and the imperfection magnitude  $\Delta w$ . The calculated values of  $N_{c,Rd}$  are shown in Table 3. In Fig. 7, design curves are plotted for  $a/b = 1.5, 2.0$  and  $3.0$  with the imperfection magnitude  $\Delta w = 0.05t$ ; the values for  $N_{u,exp} / Af_y$  shown in Table 3 are also overlain. It can be seen that the design curves provide safe-sided predictions for all the experimental results with the accuracy generally increasing with aspect ratio and slenderness as also indicated by the values of  $N_{u,exp} / N_{c,Rd}$  shown in Table 3.

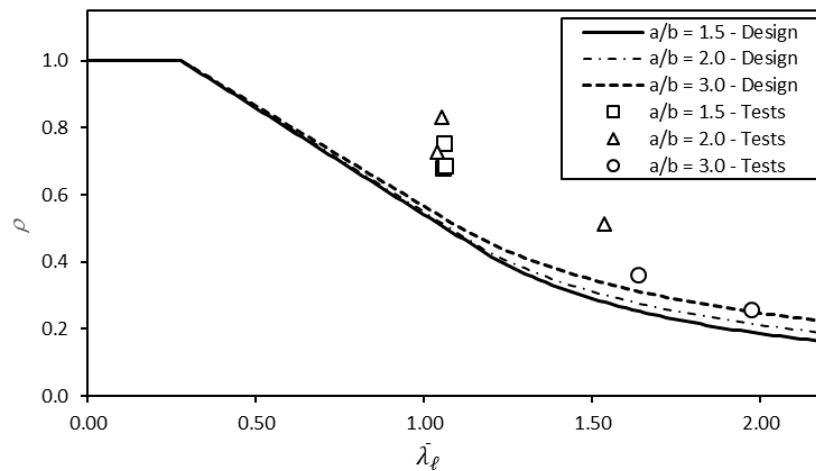


Figure 7: Comparison of experimental and design predictions for the local buckling reduction factor  $\rho$ .

#### 5. Conclusions

A sample of eight elliptical hollow section specimens manufactured from polylactic acid polymer using the fused filament fabrication technique were tested in compression in order to assess their susceptibility to local buckling. It was found that, although the failure mode was brittle and very sudden, the results for ultimate load, failure mode and longitudinal strains indicate that local buckling occurred at the point of minimum curvature within the cross-sections. The experimental results for ultimate load

were compared with the predictions of an existing design method for slender steel elliptical hollow sections in compression. It was found that, upon rescaling the slenderness parameter to account for the change in material, the design method provided safe-sided predictions for the cross-sectional resistance for all specimens, with the accuracy increasing with aspect ratio and slenderness. This provides additional validation of the applicability of the design method for use with highly-slender specimens in various materials.

### Acknowledgments

The authors wish to extend their thanks to Mr Paul Elsdon of the Strengths of Materials laboratory for conducting the experiments, and to Mr Ryan Lafferty for creating the specimen geometry models.

### References

- Comité Européen de Normalisation. (2006). *EN 10210-1:2006 Hot finished structural hollow sections of non-alloy and fine grain steels – Part 1: Technical delivery conditions*. British Standards Institution.
- Comité Européen de Normalisation. (2018). *prEN 1993-1-1:2018 Final Draft - Eurocode 3 - Design of steel structures, Part 1.1: General rules and rules for buildings*, CEN.
- Chan, T.M., Gardner, L. (2008). Compressive resistance of hot-rolled elliptical hollow sections. *Eng. Struct.*, 30(2), 522–532.
- Chan, T.M., Gardner, L. (2008). Bending strength of hot-rolled elliptical hollow sections, *J. Const. Steel Res.*, 64(9), 971–986.
- Chan, T.M., Gardner, L. (2009). Flexural buckling of elliptical hollow section columns, *J. Struct. Eng., ASCE*, 135(5), 546–557.
- Chan, T.M., Gardner, L., Law, K.H. (2010). Structural design of elliptical hollow sections: a review, *Proc. Inst. Civil Eng. – Struct. Build.* 163 (6), 391–402.
- Chen, M.T., Young, B. (2020). Beam-column tests of cold-formed steel elliptical hollow sections, *Eng. Struct.*, 210 10991.
- De Zeen (2018). “World’s first 3D-printed steel bridge unveiled at Dutch Design Week”, online article available at [www.dezeen.com/](http://www.dezeen.com/) published 22 October 2018.
- Gardner, L., Chan, T.M. (2007). Cross-section classification of elliptical hollow sections. *Steel & Comp. Struct.*, 7(3):185–200.
- Gardner, L., Chan, T.M., Wadee, M.A. (2008). Shear response of elliptical hollow sections, *Proc. Inst. Civil Eng. – Struct. & Build.*, 161(6):301–309.
- Insausti, A., Gardner, L. (2011). Analytical modelling of plastic collapse in compressed elliptical hollow sections. *J. Const. Steel Res.*, 67:678–89.
- McCann, F., Fang, C., Gardner, L., Silvestre, N. (2016). Local buckling and ultimate strength of slender elliptical hollow sections in compression, *Eng. Struct.*, 111, 104–118.
- Paolini, A., Kollmannsberger, S., Rank, E. (2019). Additive manufacturing in construction: a review on processes, applications, and digital planning methods, *Additive Manufacturing*, 30, 100894.
- Ruiz-Teran, A.M., Gardner, L. (2008). Elastic buckling of elliptical tubes, *Thin-Walled Struct.* 46 (11) (2008) 1304–1318.
- Silvestre, N. (2008). Buckling behaviour of elliptical cylindrical shells and tubes under compression, *Intl. J. Solids & Struct.*, 45(16):4427–4447.
- Silvestre, N., Gardner, L. (2011). Elastic local postbuckling of elliptical tubes, *J. Const. Steel Res.*, 67(3):281–292.
- Theofanous, M., Chan, T.M., Gardner, L. (2009). Structural response of stainless steel oval hollow section compression members, *Eng. Struct.*, 31(4):922–34.
- Ultimaker. (2018). UM180821 TDS PLA RB V11 Technical data sheet PLA. Ultimaker.
- Virgin, L. (2018). Enhancing the teaching of elastic buckling using additive manufacturing, *Eng. Struct.*, 174:338–345.
- Zhang, J., Wang, J., Dong, S., Yu, X., Han, B. (2019). A review of the current progress and application of 3D printed concrete. *Composites Part A: Appl. Sci. & Manuf.*, 125.

## **Coupled buckling of hybrid thin-walled channel sections under compression in the elastic range**

Zbigniew Kolakowski<sup>1</sup>, Andrzej Teter<sup>2</sup>

### **Abstract**

Nonlinear buckling problems of hybrid thin-walled C-columns in the elastic range are discussed. A multimodal approach using Koiter's approximation theory (SAM) was assumed to investigate an effect of different buckling modes on the ultimate load-carrying capacity. All columns were made of two layers of isotropic materials characterised by various mechanical properties and were simple supported at the ends. The results attained were verified with the finite element method (FEM). The boundary conditions applied in the FEM allowed us to confirm the eigen-solutions obtained within Koiter's theory with very high accuracy. Nonlinear problem was solved using the Riks algorithm, which allows for investigating unsteady paths. The results for the ultimate load-carrying capacity obtained within the FEM are higher than those attained with Koiter's approximation method, but the leap takes place on the identical equilibrium path as the one determined from Koiter's theory.

### **1. Formulation of the problem**

A problem of rapid, unexpected exceeding the load-carrying capacity has been discussed on the example of hybrid thin-walled C-columns (Fig. 1). The walls of the columns under investigation were made of two layers. The aluminum layer was outer one. The titanium layer was inner one. Nonlinear buckling problems were solved within Koiter's approximation theory. A multimodal approach was assumed to investigate an effect of different buckling modes on the ultimate load-carrying capacity (Kolakowski Z., Teter A. 2016). The conducted numerical simulations allowed for solving the linear eigenproblem and components of membrane sectional forces. Distributions of membrane sectional forces are in balance based on the linear solution it is possible to indicate the eigenvalue and its corresponding eigenvectors, which can affect rapid, unexpected exceeding the load-carrying capacity of the hybrid thin-walled structure under discussion. The results were verified with the FEM in a full range of loads.

While selecting the column lengths, the authors followed the principle that the determined maximal absolute values of longitudinal forces should attain their maxima in the solutions to the eigenproblem, which causes strong interactions between the selected eigenmodes. Summing up the results obtained for the assumed lengths and the determined maximal absolute values of membrane longitudinal forces

---

<sup>1</sup> Professor, Lodz University of Technology (TUL), Department of Strength of Materials (K12), PL – 90-924 Lodz, Stefanowskiego 1/15, Poland <zbigniew.kolakowski@p.lodz.pl>

<sup>2</sup> Professor, Lublin University of Technology (LUT), Faculty of Mechanical Engineering, Department of Applied Mechanics, PL – 20-618 Lublin, Nadbystrzycka 36, Poland <a.teter@pollub.pl>

with their corresponding buckling modes, one can see that there is a coupling between them based on the displacement of the corner for a given mode, it is possible to indicate that it is caused by a strong longitudinal sectional force. The reverse reasoning is correct as well (Zaczynska M., Kolakowski Z. 2020, Zaczynska M., Kazmierczyk F. 2020, Teter A., Kolakowski Z. 2020). An effect of distortional modes on post-buckling equilibrium paths and the load-carrying capacity of structures was also investigated in (Martins A.D. et al. 2017, 2018, 2019, Niu R. et al. 2014, Szymczak C., Kujawa M. 2017, 2019).

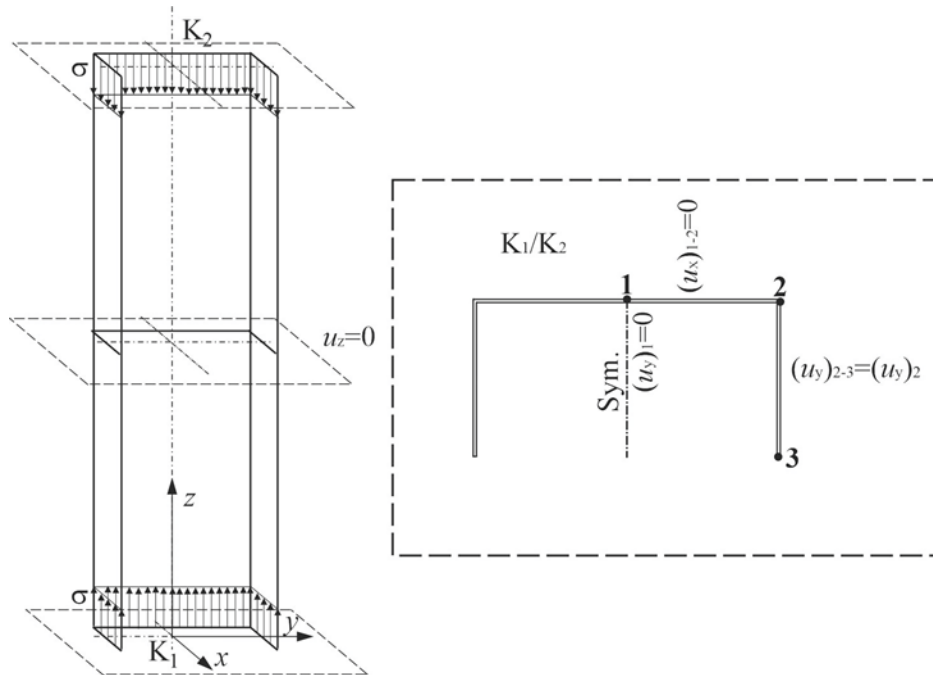


Figure. 1. Cross-sections of the hybrid columns under analysis and FEM's boundary conditions

In the analytical-numerical method (SAM), it is possible to consider a precisely defined and finite number of buckling modes considered in the interaction of these modes. This allows one to determine the key modes which decide about post-buckling equilibrium paths and the load-carrying capacity of the structure. In the FEM, it is practically not possible to choose which modes are to be considered. Including two anti-symmetrical modes in the multimodal approach causes a significant decrease in the load-carrying capacity, and the stronger it is, the higher values of longitudinal sectional forces are observed for the selected modes. The most crucial interactions of anti-symmetrical modes take place for the distortional global and local mode. In the FEM, it was not possible to confirm the results obtained when the anti-symmetrical modes were analysed. The ultimate load-carrying capacity determined within the FEM corresponds to the SAM only if symmetrical modes are considered.

## 2. Results and discussion

Detailed simulations were carried out for simple supported columns with a C-section of medium lengths. The web width of the C-sections was 80mm, the flange width was 40 mm and the thickness of the walls under analysis is 1mm. The columns were made of two isotropic materials i.e., of aluminium and titanium. The thickness of each layer is the same and equal to 0.5mm. The material constants for the aluminium layer are: Young's modulus – 71GPa, Poisson's ratio – 0.33, and for the titanium layer – 107GPa and 0.34, respectively.

Table 1 lists values of bifurcational stresses for two assumed total lengths (i.e., 210mm and 250mm) of the channel determined with two methods, namely: the SAM and the FEM. For the SAM, maximal absolute values of membrane sectional forces and several half-waves (in brackets) along the longitudinal direction that form along the length of the columns under analysis (denoted as the parameter  $m$ ) and letter notations of the conditions on the axis of symmetry of the cross-section (i.e., S or A), are given.

Table 1. Bifurcational stresses (i.e.,  $\sigma_i$  in MPa) and maximal absolute values of membrane forces (i.e.,  $|N_{xi}|_{\max}/|N_{yi}|_{\max}/|N_{xyi}|_{\max}$  in N/mm) for selected buckling modes

Mode number denoted as $i$ -index	Bifurcation parameters	L=210mm		L=250mm	
		SAM	FEM	SAM	FEM
1	$\sigma_1$ in MPa	49.7 (1S)	49.4	60.2 (1S)	59.8
	$ N_{xi} _{\max}/ N_{yi} _{\max}/ N_{xyi} _{\max}$ in N/mm	1.24/0.21/0.25	-	1.55/0.18/0.27	-
2	$\sigma_2$ in MPa	332 (1S)	330	442 (1S)	438
	$ N_{xi} _{\max}/ N_{yi} _{\max}/ N_{xyi} _{\max}$ in N/mm	19.4/1.84/4.05	-	27.6/1.85/4.92	-
3	$\sigma_3$ in MPa	3980 (1S)	3859	3254 (1S)	3186
	$ N_{xi} _{\max}/ N_{yi} _{\max}/ N_{xyi} _{\max}$ in N/mm	458/19.1/91.3	-	370/13.6/63.8	-
4	$\sigma_4$ in MPa	35.3 (2S)	34.9	36.0 (2S)	35.6
	$ N_{xi} _{\max}/ N_{yi} _{\max}/ N_{xyi} _{\max}$ in N/mm	0.68/0.50/0.27	-	0.77/0.38/0.25	-
5	$\sigma_5$ in MPa	115 (2S)	114	145 (2S)	145
	$ N_{xi} _{\max}/ N_{yi} _{\max}/ N_{xyi} _{\max}$ in N/mm	6.75/2.16/2.39	-	8.40/1.98/2.64	-
6	$\sigma_6$ in MPa	1303 (2S)	1302	1747 (2S)	1749
	$ N_{xi} _{\max}/ N_{yi} _{\max}/ N_{xyi} _{\max}$ in N/mm	4.60/9.17/2.05	-	7.02/8.83/2.44	-
7	$\sigma_7$ in MPa	96.5 (1A)	95.1	124 (1A)	122
	$ N_{xi} _{\max}/ N_{yi} _{\max}/ N_{xyi} _{\max}$ in N/mm	3.47/0.39/0.98	-	4.71/0.36/1.10	-
8	$\sigma_8$ in MPa	1650 (1A)	1638	1580 (1A)	1553
	$ N_{xi} _{\max}/ N_{yi} _{\max}/ N_{xyi} _{\max}$ in N/mm	139/5.94/24.0	-	214/4.54/30.6	-
9	$\sigma_9$ in MPa	3054 (1A)	2968	3414 (1A)	3377
	$ N_{xi} _{\max}/ N_{yi} _{\max}/ N_{xyi} _{\max}$ in N/mm	190/7.34/35.0	-	95.0/4.05/23.1	-
10	$\sigma_{10}$ in MPa	48.6 (2A)	48.1	54.1 (2A)	53.6
	$ N_{xi} _{\max}/ N_{yi} _{\max}/ N_{xyi} _{\max}$ in N/mm	1.52/0.71/0.80	-	1.75/0.59/0.81	-
11	$\sigma_{11}$ in MPa	596 (2A)	596	785 (2A)	791
	$ N_{xi} _{\max}/ N_{yi} _{\max}/ N_{xyi} _{\max}$ in N/mm	24.6/7.13/8.33	-	33.7/6.77/9.79	-
12	$\sigma_{12}$ in MPa	1569 (2A)	1533	2085 (2A)	2036
	$ N_{xi} _{\max}/ N_{yi} _{\max}/ N_{xyi} _{\max}$ in N/mm	31.8/11.8/15.4	-	48.3/11.5/19.5	-

The buckling modes from Table 1 for shorter length of the channel (i.e., 210 mm) are shown in Fig. 2 that:

- (a) modes 1-3 are symmetrical modes, corresponding to subsequent modes with one half-wave along the column length (i.e.,  $m=1$ ),
- (b) modes 4-6 are symmetrical modes, corresponding to subsequent modes with two half-waves along the column length (i.e.,  $m=2$ ),
- (c) modes 7-9 are anti-symmetrical modes, corresponding to subsequent modes with one half-wave along the column length (i.e.,  $m=1$ )
- (d) modes 10-12 are anti-symmetrical modes, corresponding to subsequent modes with two half-waves along the column length (i.e.,  $m=2$ )

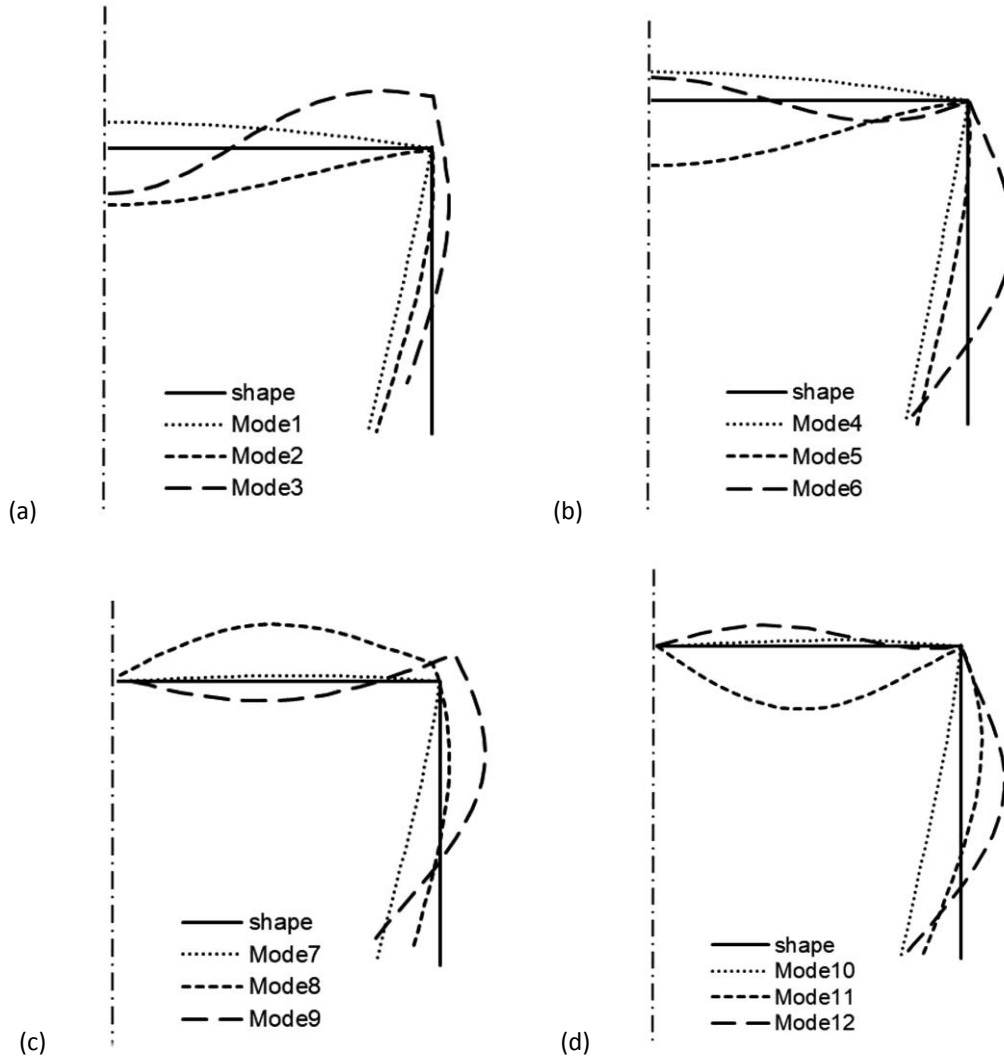


Figure 2. Buckling modes of the channel of the total length 210 mm (Table 1): symmetrical modes 1,2,3 - (a), modes 4,5,6 - (b) and anti-symmetrical 7,8,9 - (c), modes 10,11,12 - (d)

In Table 2, the dimensionless ultimate load-carrying capacities  $\sigma_s/\sigma_4$  obtained with the SAM and the FEM for both the lengths of channels under consideration are presented. In the SAM, 3-, 4- and 6-modal approaches were considered, selecting various combinations of modes (Table 1 – buckling modes 1-12). For the first two, only symmetrical modes were considered, whereas when also anti-symmetrical modes were accounted for, a 6-modal approach was applied. It is caused by a necessity to consider an even number of anti-symmetrical modes in the interaction. Indices of buckling modes (i.e.,  $i$ -index), which were considered in the SAM, and the dimensionless value of the ultimate load-carrying capacity referred to the minimal value of the buckling load, i.e.,  $\sigma_s/\sigma_{\min}=\sigma_s/\sigma_4$  for the given total length of the column, were also given. In the channel's case of the length 210mm, for an interaction of 3 modes, the ultimate load-carrying capacity was not obtained. The post-buckling equilibrium path is an ascending curve.

Similar differences in the evaluation of the load-carrying capacity when a coupled interaction of anti-symmetrical buckling modes in the SAM multimodal approach was included and an invisible effect of these modes on the load-carrying capacity in the FEM were found in Teter A., Kolakowski Z. 2020.

**Table 2.** Absolute ultimate load-carrying capacity of channels

Total length $L$ in mm	SAM			FEM
	$J$ -mode approach	Mode numbers ( $i$ -index in Table 1) used in SAM	$\sigma_s/\sigma_{\min}=\sigma_s/\sigma_4$	$\sigma_s/\sigma_{\min}=\sigma_s/\sigma_4$
210	3	4; 1; 2	-	1.49/1.20*
		4; 1; 3	-	
	4	4; 1; 2; 3	1.42	
	6	4; 1; 2; 3; 8; 9	1.42	
		4; 1; 2; 3; 8; 10	0.94	
	4; 1; 2; 3; 9; 10	0.95		
250	3	4; 1; 2	2.52	1.49/1.20*
		4; 1; 3	1.81	
	4	4; 1; 2; 3	1.39	
	6	4; 1; 2; 3; 8; 9	1.39	
		4; 1; 2; 3; 8; 10	0.90	
	4; 1; 2; 3; 9; 10	1.04		

\* The Riks algorithm loses convergence

In the FEM numerical simulations, the Riks algorithms were employed to solve the nonlinear problem of stability loss. This algorithm allowed us to catch the effect of a jump between two stable equilibrium paths. The post-buckling equilibrium path determined with the Riks method under low overloads is the same as the one obtained within the SAM (Fig. 3). At higher overloads, it overestimates the ultimate load-carrying capacity, then it jumps onto another equilibrium path, coming closer to the SAM path, when only symmetrical buckling modes are accounted for in the interaction. In the authors' opinion, a jump between equilibrium paths results from the fact that new buckling modes appear. It causes that the outcomes attained within both the methods become closer.

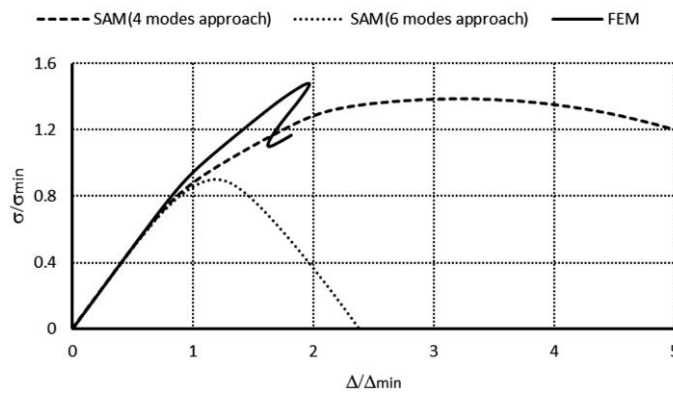


Figure 3. Comparison of dimensionless equilibrium paths for channels of the length 250mm

Fig. 4 shows a destruction form that corresponds to the ultimate load-carrying capacity  $\sigma_s/\sigma_4$  of channels of the lengths: 210mm and 250mm. The FEM destruction forms for both the column lengths are identical. Two buckling half-waves appear along the channel length. In the half-length, a visible deviation from the straight line can be seen, which corresponds to an effect of the distortional buckling mode.

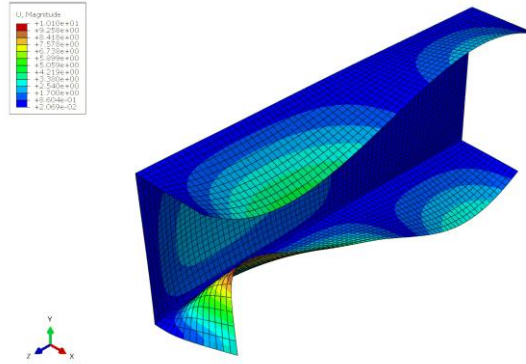


Figure 4. Destruction form for the channel of the lengths 210mm/250mm in the ultimate point

#### 4. Conclusions

The post-buckling equilibrium path determined with the Riks method (FEM) under low overloads is the same as the one obtained within the SAM. At higher overloads, it overestimates the ultimate load-carrying capacity, then it jumps onto another equilibrium path, coming closer to the SAM path, when only symmetrical buckling modes are accounted for in the interaction. A jump between equilibrium paths results from the fact that new buckling modes appear. It causes that the results attained within both the methods become closer.

#### Acknowledgments

The investigations were carried out thanks to the financial support of the National Science Centre of Poland (UMO-2017/25/B/ST8/01046).

#### References

- Kolakowski Z., Teter A. (2016). "Coupled static and dynamic buckling modelling of thin-walled structures in elastic range review of selected problems." *Acta Mechanica et Automatica*, 10(2) 141-149.
- Kolakowski Z., Kubiak T., Zaczynska M., Kazmierczyk F. (2020). "Global-distortional buckling mode influence on post-buckling behaviour of lip-channel beams." *International Journal of Mechanical Sciences* 184 105723.
- Zaczynska M., Kolakowski Z. (2020). "The influence of the internal forces of the buckling modes on the load-carrying capacity of composite medium-length beams under bending." *Materials* 13 455.
- Zaczynska M., Kazmierczyk F. (2020). "Multi-Mode Buckling Analysis of FGM Channel Section Beams." *Materials* 13 2567.
- Teter A., Kolakowski Z. (2020). "Catastrophic influence of global distortional modes on the post-buckling behaviour of opened columns." *Materials* 13(15) 3314.
- Martins A.D., Landesmann A., Camotim D., Dinis P.B. (2017). "Distortional failure of cold-formed steel beams under uniform bending: Behaviour, strength and DSM design." *Thin-Walled Structures* 118 196–213.
- Martins A.D., Camotim D., Gonçalves R., Dinis P.B. (2018). "On the mechanics of local–distortional interaction in thin-walled lipped channel columns." *Thin-Walled Structures* 125 187–202.
- Martins A.D., Gonçalves R., Camotim D. (2019). "On the local and distortional post-buckling behaviour of thin-walled regular polygonal tubular columns." *Thin-Walled Structures* 138 46–63.
- Niu R., Rasmussen K.J.R., Fan F. (2014). "Distortional–global interaction buckling of stainless steel C-beams: Part II– Numerical study and design." *J. Constr. Steel Res.* 96 40–53.
- Szymczak C., Kujawa M. (2017). "Buckling of thin-walled columns accounting for initial geometrical imperfections." *Int. J. Non-Linear Mech.* 95 1–9.
- Szymczak C., Kujawa M. (2019). "Buckling and initial post-local buckling behaviour of cold-formed channel member flange." *Thin Walled Struct.* 137 177–184.

## **Numerical simulation and verification of adaptive shading modules with buckling as the driver for functionality**

Yang Hu<sup>1</sup>, Mani Khezri<sup>2</sup>, Kim J.R. Rasmussen<sup>3</sup>

### **Abstract**

In the conventional design paradigm, buckling of slender structural members is seen as a route toward failure and measures are taken to avoid its onset. In recent years, a new approach challenging this paradigm is emerging where the mechanical instability of slender elements is utilised to achieve novel modes of functionality. By adopting such a framework, the flexural-torsional buckling of frame geometries can be exploited as a driver to change the shape of slender structural frames to fulfil specific shading functionalities. This study is concerned with the numerical simulation of recently developed simple frames in which out-of-plane buckling of component members is judiciously harnessed to construct adaptive shading modules. Advanced numerical simulations are conducted using Abaqus software to gain a better understanding of the factors that affect the behaviour and performance of the proposed solutions. Building on the gained insight, a comprehensive search strategy is devised for finding optimum solutions for the governing geometrical and actuation parameters. Within the constructed search space, non-linear post-buckling analyses are carried out to determine the resultant shading area and to quantify the influence of the governing parameters.

### **1. Introduction**

The rising public awareness of the environmental implications of generating energy using conventional fuels and the need to minimise energy consumption have stimulated great interest in building energy usage, especially the correlations between climate and daylight and visual comfort (Fiorito, Sauchelli et al. 2016). The ever-increasing demand for improving space heating in winter and comfort cooling in summer has resulted in a substantial increase in building energy consumption (Lam, Wan et al. 2008). Motivated by the requirements for reducing building energy consumption and CO<sub>2</sub> emissions, adaptive façade systems have emerged in the construction industry. As the interface that interacts with the external environment, the building façade plays a pivotal role in blocking and absorbing solar irradiance. Adaptive shading facades have gained extensive attention due to their prominent advantages, including lower energy consumption in the cold season, protection from external noise and wind loads, as well as their high-tech image. A high-performance building shading system can be applied to regulate solar

---

<sup>1</sup> PhD student, The University of Sydney, <yang.hu@sydney.edu.au>

<sup>2</sup> Lecturer, The University of Sydney, <mani.khezri@sydney.edu.au>

<sup>3</sup> Professor, The University of Sydney, <kim.rasmussen@sydney.edu.au>

radiations and heat gains, thereby controlling the indoor temperature to minimise heating and cooling loads and improve building thermal comfort to achieve low energy consumption. Dakheel and Aoul (2017) found that active shading systems could reduce 12% to 50% of the building cooling energy consumption. Nielsen et al. (2011) quantified the potential reduction in energy demand by implementing automated dynamic solar shading. They suggested that the shading façade showed a decrease in total annual energy demand between the worst and the best-performing facades, amounting to approximately 12% - 16% depending on the facing orientation.

Although conventional passive façade technologies, especially external shading devices, can effectively control heat gain and daylighting in buildings, they still have shortcomings. One of the most significant limitations of static passive façades is their inability to adapt to changeable external weather and temperature conditions (Aldawoud 2013). On the contrary, active shading systems provide a superior approach that allows the user to directly control the shading devices according to the exterior environment and occupants' requirements. Some typical adaptive shape morphing systems include smart glazing systems (Long and Ye 2014, Favoino, Giovannini et al. 2017), dynamic building-integrated photovoltaic (BIPV) modules (Liu, Duan et al. 2010) and shape morphing devices (Fiorito, Sauchelli et al. 2016). While smart glazing systems and BIPV modules have been investigated extensively, shape morphing façade systems still require a complete understanding. They have immense potential to exploit shape morphing mechanisms by controlling materials, and geometrical and actuation parameters.

As stated by Fiorito et al. (2016), the design of shape morphing solar shadings should consider two aspects: climate adaptivity, and daylight and visual comfort. Some innovative thermally activated solar shading devices have been developed and studied. Lienhard et al. (2011) proposed a Flectofin façade shading system using glass fibre reinforced polymer (GFRP). This façade shading system was inspired by the sophisticated valvular pollination mechanism of the Bird-Of-Paradise flower. A simple Flectofin model contains a thin shell element (a "wing") connected orthogonally to a rib or beam element (the "backbone"). A uniaxial bending of the backbone could introduce subsequent elastic deformation to the wing triggered by torsional buckling. Doumptioti et al. (2010) developed a novel facade system for the Piraeus Tower controlled through rule-based collective intelligence and empowered by integrated shape memory alloys (SMAs). The SMA strips can change their shape to decrease the transparency of the façade and increase the ventilation to the interior when there is sufficient solar heat gain on the façade.

In this paper, the authors aim to provide an insight into the shape morphing solution that can achieve large deformation by induced controlled buckling. The proposed shading façade system is a three-member frame that can generate large out-of-plane flexural-torsional buckling deformations when subjected to torques at the supports. Numerical simulations using the finite element method (FEM) are conducted to obtain the non-linear post-buckling behaviour of the proposed frame. The paper focuses on discovering the possible optimum solutions to achieve a large shading area/volume with a low actuation force. The optimisation analyses are conducted by coupling the Matlab optimisation toolbox with Abaqus finite element models. Different objective functions are considered to investigate the impacts of the geometric variables and actuation forces.

## **2. Buckling analysis of a three-member frame subjected to end torques**

### *2.1 Problem statement*

This paper investigates the buckling behaviour of thin-walled three-member frames with rectangular cross-section subjected to end-torsional moments at the supports. The three beam members are all placed within the XY-plane, and the undeformed frame is symmetric about the centreline placed along the Y-axis, as shown in Fig. 1(a). The inclined members, Member 1 and Member 3, are positioned with

an angle  $\alpha$  with respect to the X-axis, while Member 2 is parallel to the X-axis. The total length of the frame ( $L_T$ ) is equivalent to the summation of the lengths of two inclined members ( $2L_1$ ) and the central member ( $L_2$ ) (i.e.  $L_T = 2L_1 + L_2$ ). The frame is built using a steel strip with a cross-section of  $H \times t$  (width  $\times$  thickness), as shown in Fig. 1(b).

The boundary conditions at supports A and D are considered equivalent to typical built-in support conditions, and are defined based on the local coordinate systems. The only unconstrained degree of freedom at the built-in supports is the twist rotation, which allows members 1 and 3 to rotate about their longitudinal axes; i.e. apart from the twist rotation ( $\theta$ ), all translational and rotational DOFs at the supports are restrained. Torques (T) are applied at the supports to generate the twist rotations.

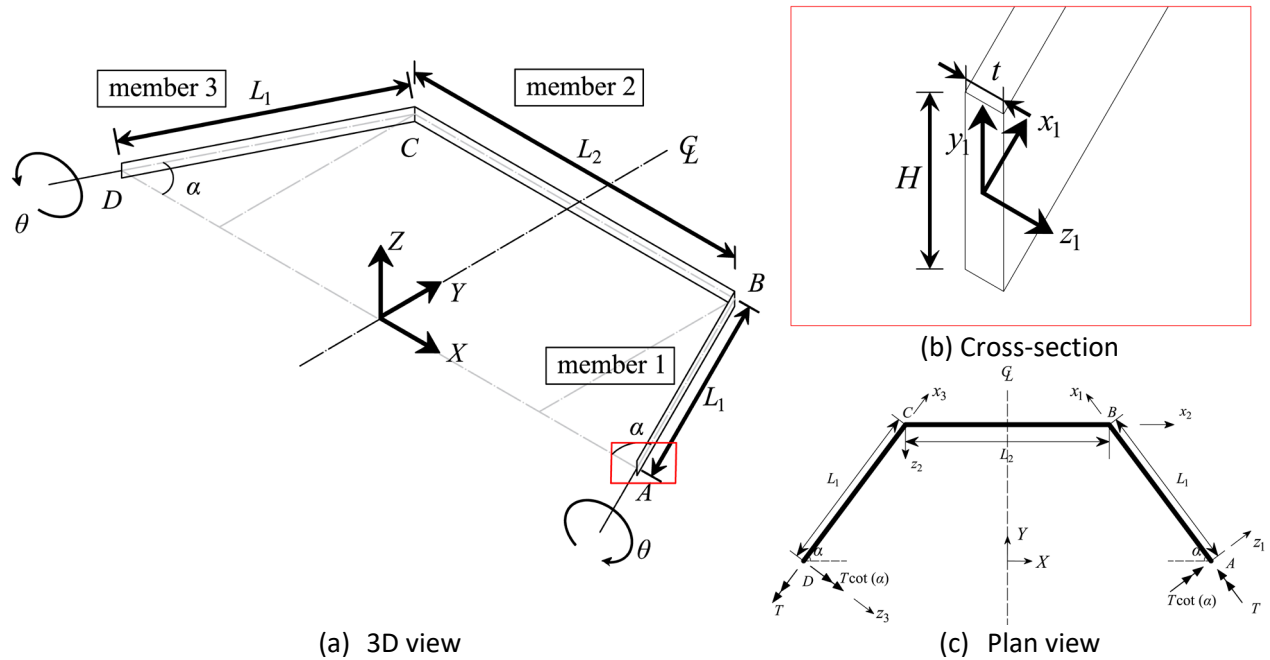


Fig. 1. Schematic diagram of a three-member frame subjected to end twist rotations

## 2.2 Numerical analyses

As determined from a static pre-buckling analysis, when applying torques (T) at supports, bending moments ( $T \cot(\alpha)$ ) are generated simultaneously to achieve equilibrium. Thus, when the inclinations ( $\alpha$ ) of members 1 and 2 are angles other than  $90^\circ$  (Fig. 1c), the applied torsion is accompanied by bending deformations out of the plane of the frame. As the applied torques rotate the supports, the stiffness of the inclined members against out-of-plane bending declines, and large out-of-plane deflections are induced through buckling and bending deformations. Therefore, the post-buckling behaviour of the three-element frame is inherently geometrically non-linear. ABAQUS is herein used to perform the non-linear post-buckling analysis using shell finite elements.

A non-linear analysis is performed using the general static method in Abaqus/standard considering both the geometric non-linearity and material inelasticity. Due to the abrupt change in response (i.e. bifurcation) at the point of buckling, the post-buckling problem needs to be transformed into a problem with a continuous response by introducing a geometric imperfection pattern. The plasticity property of the steel is specified using typical true stress-strain values for high-grade steels. Pre-defined twist rotations ( $\theta$ ) at the supports, with the same magnitude but opposite sign, are enforced in the non-linear

analysis. The applied torques are adjusted to increase twist rotations ( $\theta$ ) until reaching the target value and generate out-of-plane deflections, which can be utilised to produce a shading area (Fig. 2).

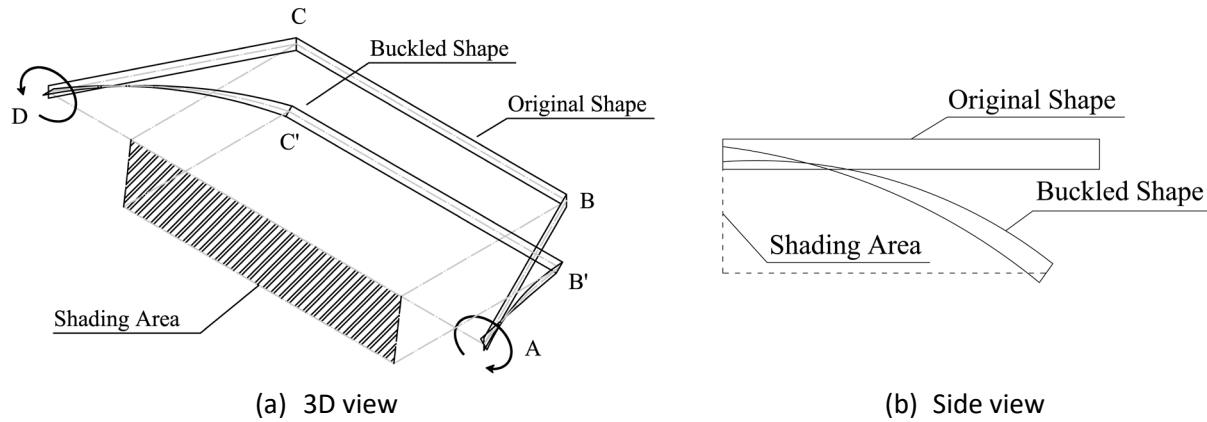


Fig. 2: Schematic diagram showing shading area generated by buckling of frame

### 2.3 Particle swarm optimisation (PSO)

The research presented in this paper aims to investigate the parameters influencing the function optimisation of shading area induced by post-buckling of the three-member frame. The Matlab optimisation toolbox thereby is called in the Abaqus non-linear buckling analyses to accomplish optimal design solutions. The main available optimisation tools in Matlab (Coleman, Branch et al. 1999) include Particle Swarm Optimisation (PSO), Genetic algorithm (GA) and Pattern Search (PS), which are coded algorithms that can be implemented to find optimal solutions. Herein, PSO is selected to attain the optimal combinations of frame configurations and enforced twisting angles ( $\theta$ ) to achieve the maximum shading area.

Particle Swarm Optimisation (Kennedy and Eberhart 1995, Shi and Eberhart 1998) has become a favourable optimisation algorithm for discovering optimum solutions for various problems in the design and engineering fields (Alam 2016). Particle swarm optimisation is a population-based search algorithm inspired initially by social behaviour displayed by a bird flock or fish school to fill their needs in the search space (Wang, Tan et al. 2018). At the beginning of the PSO, initial particles are generated with initial velocities, and the objective function is assessed at each particle location. Then, the optimal solutions are found by iteratively updating the particle locations, their velocities and the best locations of their neighbours until the algorithm reaches a convergence criterion. The default number of particles for each iteration is ten times the number of variables. The maximum number of iterations, function tolerance, variable boundaries and initial configurations are stated explicitly for the numerical example in Section 3.

### 3. Numerical example

This section presents an example to demonstrate the optimisation analysis of the developed FE non-linear post-buckling analysis for a frame with a high width-to-thickness ratio ( $H/t \gg 1$ ). In the problem considered, the frames have a total length  $L_T = 2L_1 + L_2 = 2000\text{mm}$  and a constant cross-section  $40\text{mm} \times 1\text{mm}$  in all three members. In the conducted numerical analyses, the S4R element in Abaqus is utilised, which is a general-purpose 4-node, quadrilateral, stress or displacement shell element with reduced integration.

Three variables are considered for the optimisation purpose, the length of the inclined members ( $L_1$ ), the inclined angle ( $\alpha$ ) and the twist rotation at the supports ( $\theta$ ). The lower and upper boundaries of  $L_1$  are 50mm and 800mm, respectively. The inclined angle  $\alpha$  can range from  $5^\circ$  to  $90^\circ$ , and the applied twisting angle  $\theta$  can range from  $20^\circ$  to  $180^\circ$ . Particle swarm optimisation (PSO) is coupled with Abaqus to search for the variables for optimising each objective function. The maximum number of iterations of this optimisation problem is set to be 80, and the function tolerance is defined as  $10^{-4}$ . Three objective functions  $E_i$  ( $i = 1, 2$  and  $3$ ) are considered to investigate the impacts of various parameters to the optimum solutions:

$$E_1 = \frac{U_3 \times L_1 \sin \alpha \times L_2}{\theta}, \quad (1)$$

$$E_2 = \frac{U_3 \times \sqrt{L_1 \sin \alpha} \times L_2}{\theta}, \quad (2)$$

$$E_3 = \frac{U_3 \times \sqrt{L_1 \sin \alpha} \times L_2}{\theta}, \quad (3)$$

where  $U_3$  is the out-of-plane deflection at the mid-length of the central beam (i.e. member 2). The cuboid shading volume formed by the frame and the out-of-plane deformation can be estimated as  $U_3 \times L_1 \sin \alpha \times L_2$ . The twist rotation ( $\theta$ ) is placed at the denominator of the objective functions to represent its inversely proportional relationships. The square roots in  $E_2$  and  $E_3$  are established to reduce the impact of the terms  $L_1 \sin \alpha$  or  $L_2$ .

The PSO running processes considering the three objective functions are shown in Fig. 3 to Fig. 5. As stated, the PSO processes examined a default population of 30 cases for each iteration. The optimisation processes for  $E_1$ ,  $E_2$  and  $E_3$  terminated in the 48<sup>th</sup>, 48<sup>th</sup> and 51<sup>st</sup> iteration, respectively, when the relative difference between the best objective function value and the last 20 iterations (i.e. default maximum stall iterations) was less than the pre-defined function tolerance  $10^{-4}$ .

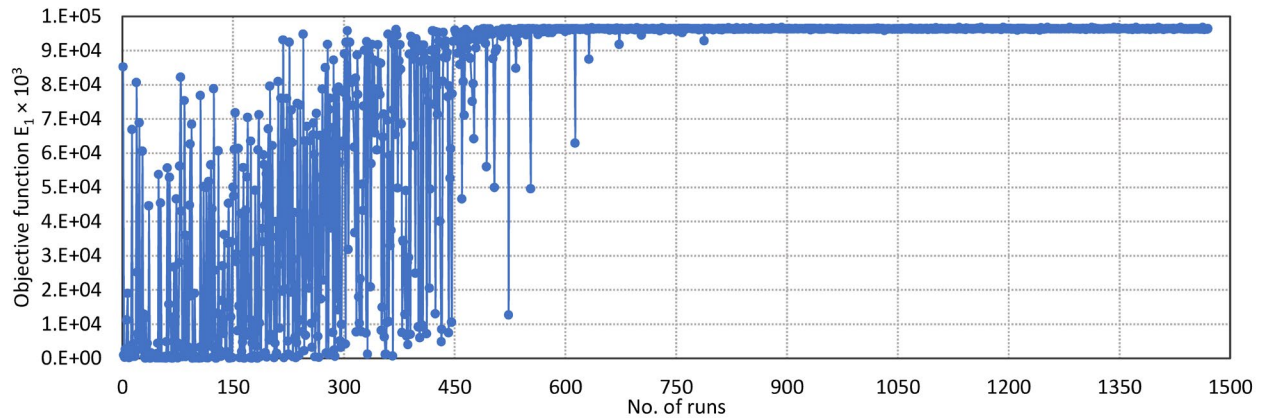


Fig. 3: Running process of PSO coupling with Abaqus for objective function  $E_1$

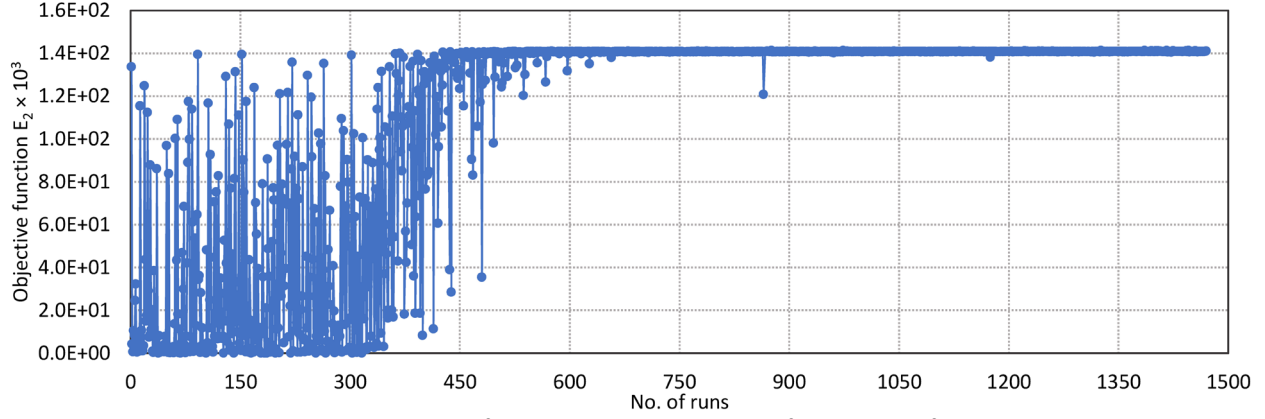


Fig. 4: Running process of PSO coupling with Abaqus for objective function  $E_2$

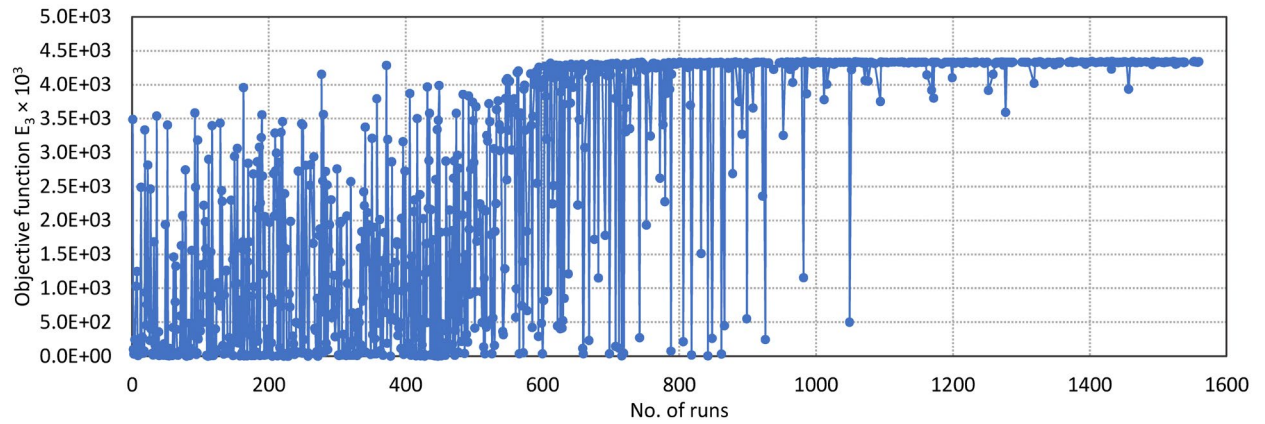


Fig. 5: Running process of PSO coupling with Abaqus for objective function  $E_3$

The optimum solutions of the three analyses are tabulated in Table 1. It can be seen that the optimal frame configurations and twisting angles  $\theta$  are similar for the three examined objective functions. As a result of the post-buckling performance, the out-of-plane deflections for the optimum solutions (i.e. 494.0mm) reach about 90% of the length of the inclined members. The resultant post-buckling shape using the optimum solution for  $E_1$  are extracted from Abaqus software and shown in Fig. 6. It demonstrates that the non-linear buckling behaviour of the three-member frames can be regulated and functionalised to attain large shape morphing and generate large shading areas.

Table 1: Optimised results of a frame with constant widths using three objective functions

	$L_1$ (mm)	$L_2$ (mm)	$\alpha$ ( $^\circ$ )	$\theta$ (rad)	$u_3$ (mm)	$E_i (\times 10^3)$	Iterations
$E_1$	539.2	921.6	72.4	2.416	493.4	96314.4	48
$E_2$	560.3	879.4	70.5	2.382	494.1	141.3	48
$E_3$	517.2	965.6	71.3	2.416	490.9	4343.2	51

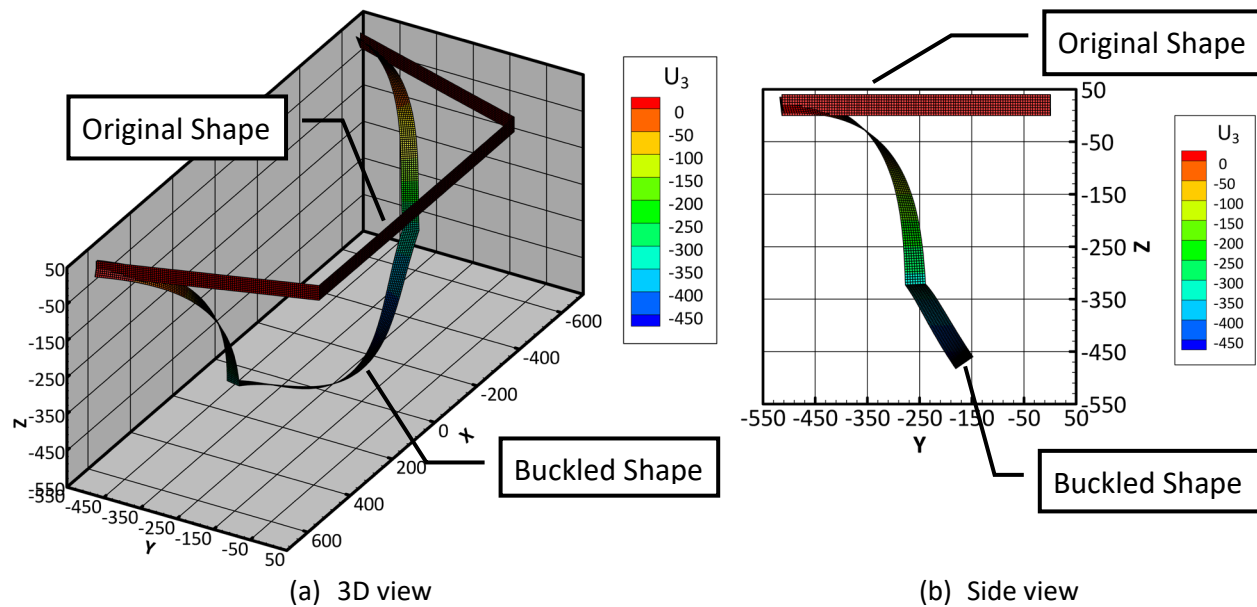


Fig. 6: The frame shape obtained from Abaqus post-buckling analysis using the optimum solution for  $E_1$

#### 4. Conclusions

This paper presents an optimisation framework for the non-linear post-buckling analysis of three-member frames subjected to torques to maximise the ratio of shading volume over twist rotations at the supports. Finite element models considering geometry and material non-linearity are defined using Abaqus software for frames with various configurations and enforced twist rotation at two supports. The Matlab optimisation tool PSO is coupled with Abaqus to search for the optimised solutions.

The study demonstrates the feasibility of achieving structural morphing via functionalised non-linear buckling and the excellent potential of employing such structural systems in the construction industry to reduce building energy consumption. The optimised solutions of the numerical example in Section 3 show significant out-of-plane deflections, which create large shading areas for all three considered objective functions. It provides an insight into delivering sustainable building solutions via their capability to undergo shape morphing to facilitate temperature control.

#### Acknowledgments

This project was undertaken as part of the Australian Research Council (ARC) Discovery Project DP170104016.

#### References

- Al Dakheel, J. and K. Tabet Aoul (2017). "Building Applications, opportunities and challenges of active shading systems: A state-of-the-art review." *Energies* **10**(10): 1672.
- Alam, M. N. (2016). "Particle swarm optimization: algorithm and its codes in MATLAB." DOI: 10.13140/RG.2.1.4985.3206.
- Aldawoud, A. (2013). "Conventional fixed shading devices in comparison to an electrochromic glazing system in hot, dry climate." *Energy and Buildings* **59**: 104-110.
- Coleman, T., et al. (1999). "Optimization toolbox." For Use with MATLAB. User's Guide for MATLAB 5, Version 2, Release II.
- Doumpioti, C., et al. (2010). Embedded intelligence: Material responsiveness in façade systems. Proceedings of the 30th Annual Conference of the Association for Computer Aided Design in Architecture (ACADIA), ISBN 978-1-4507-3471-4: 258-262. New York.

- Favoino, F., et al. (2017). Smart glazing in Intelligent Buildings: what can we simulate? All eyes on glass: conference proceedings of Glass Performance Days 2017, 28-30 June 2017, Tampere, Finland, Glass Performance Days, Glaston Finland Oy.
- Fiorito, F., et al. (2016). "Shape morphing solar shadings: A review." *Renewable Sustainable Energy Reviews* **55**: 863-884.
- Jayathissa, P., et al. (2017). "Optimising building net energy demand with dynamic BIPV shading." *Applied Energy* **202**: 726-735.
- Kennedy, J. and R. Eberhart (1995). Particle swarm optimization. Proceedings of ICNN'95-international conference on neural networks, IEEE.
- Lam, J. C., et al. (2008). "Building energy efficiency in different climates." *Building Conversion and Management* **49**(8): 2354-2366.
- Lienhard, J., et al. (2011). "Flectofin: a hingeless flapping mechanism inspired by nature." *Bioinspiration & biomimetics* **6**(4): 045001.
- Liu, B., et al. (2010). "Photovoltaic DC-building-module-based BIPV system—Concept and design considerations." *IEEE Transactions on Power Electronics* **26**(5): 1418-1429.
- Long, L. and H. Ye (2014). "Discussion of the performance improvement of thermochromic smart glazing applied in passive buildings." *Solar Energy* **107**: 236-244.
- Nielsen, M. V., et al. (2011). "Quantifying the potential of automated dynamic solar shading in office buildings through integrated simulations of energy and daylight." *Solar Energy* **85**(5): 757-768.
- Shi, Y. and R. Eberhart (1998). A modified particle swarm optimizer. 1998 IEEE international conference on evolutionary computation proceedings. IEEE world congress on computational intelligence (Cat. No. 98TH8360), IEEE.
- Vergauwen, A., et al. (2014). The design and physical modelling of deployable structures based on curved-line folding. 4th International Conference on Mobile, Adaptable and Rapidly Assembled Structures, MARAS.
- Wang, D., et al. (2018). "Particle swarm optimization algorithm: an overview." *Soft Computing* **22**(2): 387-408.

## Shading module with buckling as driver for shape morphing

Mani Khezri<sup>1</sup>, Kim J.R. Rasmussen<sup>2</sup>

### Abstract

The recent requirements in construction for lower energy consumption have accelerated the trend towards the use of high performance buildings. In these Nearly Zero Energy Buildings (NZEB), simple measures such as natural light control are practiced for maximising the light intake and minimising the heat gain, as required. These modern building envelopes interact with the external environment and are designed to respond to occupant demand, achieving the target energy efficiency and comfort needs. In these kinetic façades, shape morphing triggered by buckling is targeted for energy-saving structural applications. Among the structural forms that are suitable for such applications are thin plates, which are prone to buckling under small in-plane strains. This study presents a novel concept with application in shading control modules. In the proposed models, buckling of slender plates are configured to create a bistable mechanism with closed and open states. The proposed mechanism is simulated using finite element software to validate the feasibility of the core concept and to evaluate buckling as a reliable mechanism in kinetic façade control modules.

### 1. Introduction

Over the past decades, both governmental and public sectors are demanding increased performance, improved efficiency and reduced energy consumptions of buildings. These demands have been intensified because of environmental and global warming concerns, and engineers are exploring innovative solutions that satisfy the growing economic and sustainable design requirements. Façades, being the primary constituent of building envelopes, are crucial for enhancing energy efficiency and indoor comfort. Research is increasingly focused on exploiting simple design measures, including natural ventilation, thermal mass and shading, to control the indoor environment and minimise the need for active cooling and heating. In recent years, adaptive façades have been pursued as promising solutions for the aforementioned needs and are used by industry in the construction sector.

In existing adaptive façades, a control system transmits signals to façade components to change form according to the current climatic conditions. For example, Al-Bahr towers in UAE (Fig. 1) are equipped with dynamic solar screens that respond to the sun's movement and angle, thus reducing the interior heat gain by 50%. Although such technologically enabled kinetic façades may substantially improve the energy performance of a building, they rely on energy supply, involve high levels of complexity and expenditure, and often face maintenance and reliability issues. In recent years, to remedy these shortcomings and in contrast to centrally controlled façades, a new strategy is being explored for designing intelligent and resilient building envelopes, in which the responsive capacity is built into the structural components. In

---

<sup>1</sup> Lecturer, The University of Sydney, <mani.khezri@sydney.edu.au>

<sup>2</sup> Professor, The University of Sydney, <kim.rasmussen@sydney.edu.au>

this approach, the minimal applications of electric motors, complex moving mechanisms and hinges are pursued. New strategies such as structural instability and buckling are utilised to enhance/amplify the displacements, reduce parts and the required input energy.

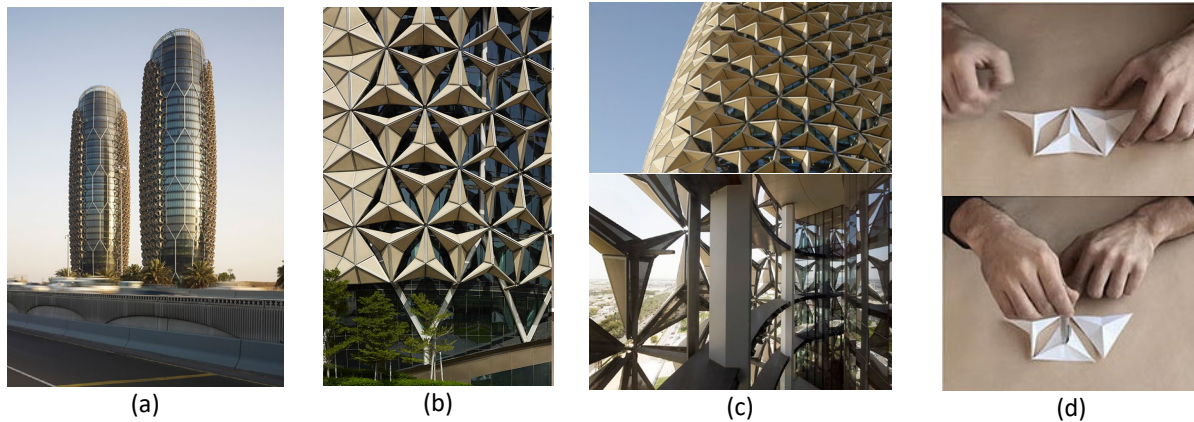


Fig. 1. (a) Al-Bahr towers (b)-(c) Façade of towers with opened and closed shading devices (d) concept development (AHR, 2014)

In conventional design, the buckling of slender structural members is seen as a route toward failure and is avoided. As indicated before, a new paradigm is emerging where the mechanical instability of slender structural elements is used to achieve novel modes of functionality (Formentini and Lenci, 2018). Buckling is characterised by the sudden release of energy and high rate of motion, both perfect attributes for smart and responsive façade solutions. The high rate of motion associated with buckling was utilised in designing the ribbed kinetic façade system of the Yeosu Expo 2012 Pavilion (Soma-Architects, 2012) to enable the building to react to light and physical building conditions. Buckling is induced by mechanical jacks applying compressive loads at the ends of the ribs. More generally, the attributes of buckling provide a new framework for designing structural components and materials at multiple scales with switchable functionalities, morphogenesis, etc.

Among the responses associated with structural instability, ‘snapping’ has seen significant research interest in recent years as a framework for developing responsive structural mechanisms. In this form of elastic instability, a structural member that is buckled and rests in a stable position jumps to another equilibrium configuration when the applied actions pass a critical value, see Fig. 2. This behaviour has been utilised to create adaptive morphing trailing edges for wind turbine blades (Lachenal et al., 2013). Also, a biomimetic design of a hingeless flapping device using snap buckling proposed by (Lienhard et al., 2011) was utilised to create shading façade lamellas.

The snap-through buckling can be harnessed to create bi-stable mechanisms. In applications where a binary response is preferred, e.g. close/open, on/off bi-stable mechanisms can be configured to output the desired response. They have been researched for the design of nonexplosive release mechanisms in deployment systems in space applications (Zirbel et al., 2016). They offer interesting features, including motion without friction or bearings, and also better reliability and precision. These features are of great interest in kinetic façade applications. Following this line of thought, in this study, a bi-stable shading module is proposed for application in building façade structure. The proposed module is an independent unit that can be incorporated as windows in building envelopes. Buckled plate elements attached to flexible membranes are configured to create a system with open and closed states. Although the input for the transition of the system from one state to the other is assumed to be mechanical input from electric

motors or human operation, smart materials such as shape memory alloy can be utilised to induce the required input.

In section 2, the concept development from the underlying mechanics to integration in a kinetic facade system is presented in detail. In section 3, a numerical simulation using finite element method software, Abaqus, is conducted to validate a proof-of-concept prototype. Section 4 concludes the paper and identifies new areas that can be explored for future research.

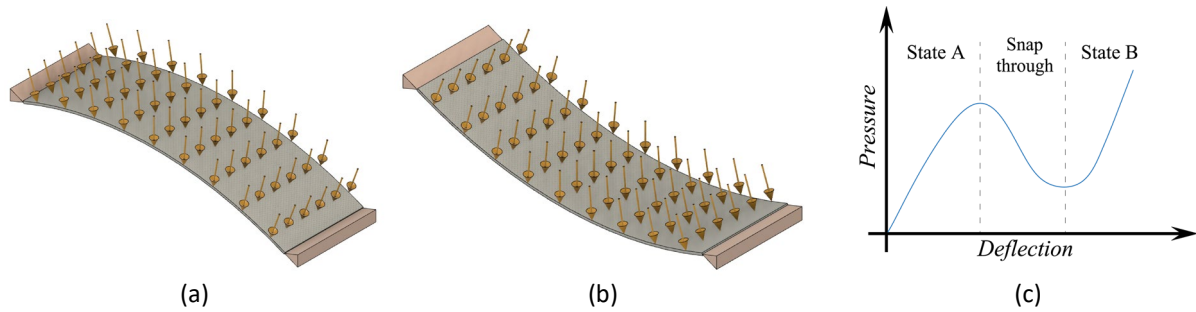


Fig. 2. The classic equilibrium paths for snap-through buckling, (a) initial stable state (A), (b) second stable state (B), (c) load-deflection curve

## 2. Concept development

Buckling of slender beam or plate elements have been incorporated as a functional driver in various systems. For example, snap-through buckling of beam was utilised as actuator (Han et al., 2004) for large-displacement optical switching. In this study, we intend to use the buckling of thin plates to create a shading module. Two plate elements are combined to create a system with precise open and closed configurations. Thin plates with large aspect (length to width) ratios have distinctive first and second mode shapes as shown in Fig. 3. The second mode occurs when the lateral deflection of the strip is constrained at its midlength. Temporary and retractable point-supports (Hu et al., 2019; Hu et al., 2020) can be used at the midlength to guide the strip into the second mode. It is evident that removing the point-supports will cause the panel to snap to its first mode. This sudden release of energy and transition from one stable state to another can be used to create a bistable shading mechanism.



Fig. 3. Buckling of slender strips (a) first mode shape (b) second mode shape

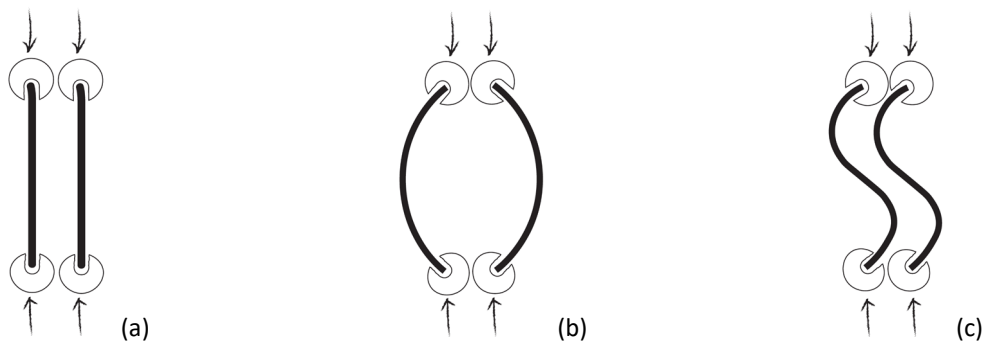


Fig. 4. Parallel plates with simply-supported boundary conditions (a) pre-buckling (b) plates buckled in first mode (c) plates buckled in second mode.

Consider two parallel plates as shown in Fig. 4(a). The plates are free along the longitudinal edges and simply-supported on the transverse edges at the ends. With these boundary conditions, the plates will buckle into the first mode, as shown in figure Fig. 4(b), when subjected to sufficiently large in-plane loads/displacements. It is noted that the plates in Fig. 4(b) can also buckle in the same direction, which can be avoided by the introduction of initial curvature. Deploying lateral supports at the midlength of the plates will cause the plates to buckle, as presented in Fig. 4(c). In this study, the latter buckled configuration is tuned to be the closed configuration, and the state shown in Fig. 4(b) is set to be the open state. To propose a proof-of-concept prototype, first, the behaviour of a single plate element is studied to determine the practical range of displacements and induced stresses.

A single plate with length  $a = 2400$  mm, width  $b = 200$  mm and thickness  $t = 3.5$  mm is simply-supported along the transverse edges and free along the longitudinal edges, see Fig. 5(a). The plate is discretised using S4R shell elements, and assumed to be made of grade G550 steel with Young's modulus  $E = 210$  GPa and Poisson's ratio  $\nu = 0.3$ . In lieu of introducing initial curvature of the plate element, a pair of concentrated loads ( $F_i = 35$  N), as shown in Fig. 5(b), is applied to invoke deflections compatible with the second mode and consequently guide the plate into this mode of buckling. The deflection of the plate at midlength is also constrained with a cohesive contact interaction between the plate and the support block at the centre. In the next step (Fig. 5 (c)), compressive in-plane displacements  $u$  are imposed under which the lateral displacements  $\delta$  will occur. The deformed shape in this stage creates the closed setting. The plate will snap to the first buckling mode by releasing the lateral support at mid-length, as presented in Fig. 5 (d), experiencing the deflection  $\Delta$  at midlength. The deformed shape in Fig. 5 (d) is used to generate the opening. The model will go back to the state shown in Fig. 5 (c), when subjected to sufficiently large torque/rotation ( $\theta$ ) at one (or both) supports, see Fig. 5 (e). In summary, the system will open when the constraint at midlength is removed, and revert to the closed configuration when the support is rotated past a critical rotation  $\theta$ .

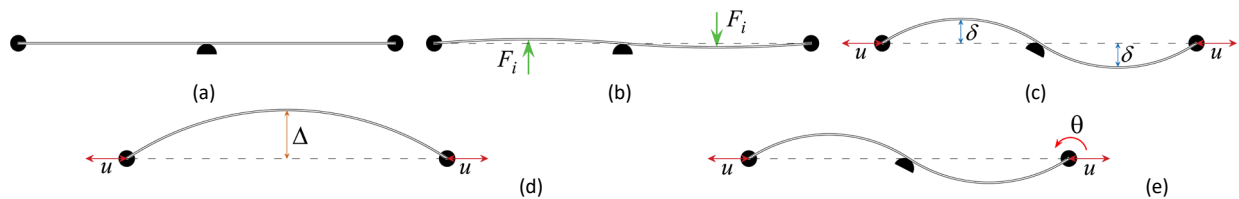


Fig. 5. Single plate model for numerical simulation (a) initial state (b) introduction of initial curvature (c) enforcement of in-plane compressive displacements  $u$  (d) release of midlength support (e)

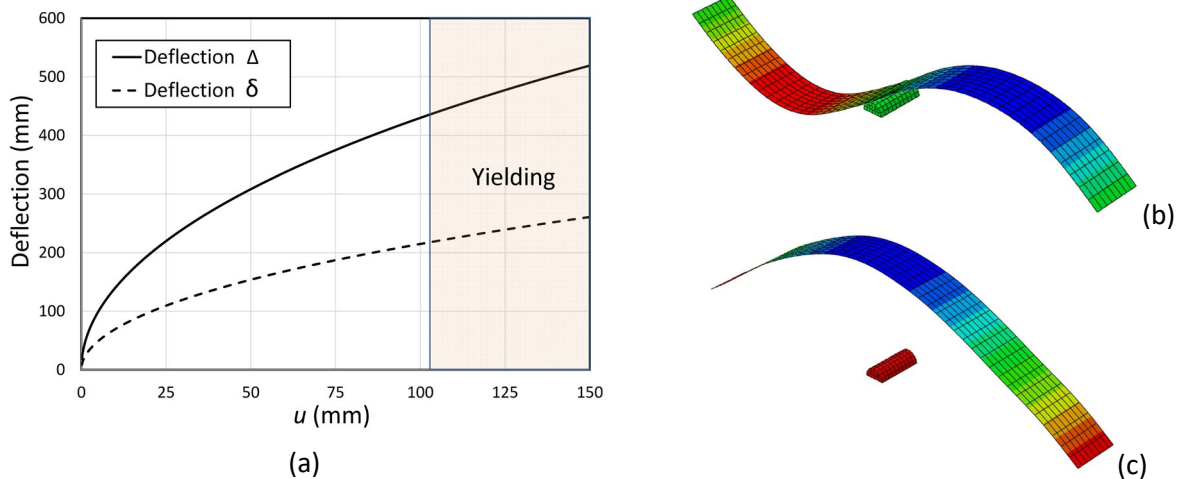


Fig. 6. (a) Maximum deflections ( $\delta$  and  $\Delta$ ) of simulated plates (in mode I and mode II) vs compressive in-plane displacement ( $u$ ) (b) closed configuration, mode II (c) open configuration, mode II

A series of finite element analyses are conducted to simulate the process explained in Fig. 5. Because of the dynamic nature of the problem, Abaqus explicit is utilised to incorporate the inertia effects and to accurately model the experienced snapping from one mode to the other. The objective is to achieve large openings ( $\Delta$ ) while the system remains in the elastic range. To this end, the in-plane displacement  $u$  is varied from 5 mm to 150 mm with 5 mm increments. The results obtained for deflections ( $\Delta$ ) and ( $\delta$ ), (Fig. 5(c)-(d)) are presented in Fig. 6(a). The FE models are also checked for possible yielding of the plate elements. It is observed that for models with compressive displacement ( $u$ ) larger than 105 mm, yielding is initiated in the parts of plates with maximum deflection when the plate is in the second mode, Fig. 6(b). To achieve a model which functions in the elastic range and transitions between open (Fig. 6(c)) and closed (Fig. 6(b)) states, the maximum compressive displacement is limited to 100 mm. Extracting from Fig. 6(a) for this case, an opening of  $\Delta \approx 400$  mm can be achieved. In the next section, a conceptual shading module with buckling of plate elements (using the process explained above) is visualised and incorporated in a double skin façade.

### 3. Module proposal and façade application

A shading module can be developed using plate elements as presented in Fig. 7. Two plate elements with the same dimensions (2400 mm  $\times$  200 mm) are placed inside hinged grips and then compressed inwards by 100 mm at the ends. Flexible membranes, which provide the shading, are attached to the plates and the hosting frame, as shown in Fig. 7.

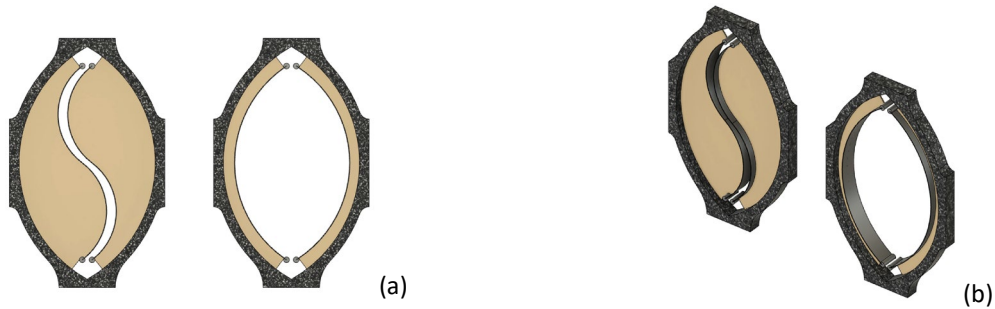


Fig. 7. Conceptualised shading module with buckling as driver (a) front view (b) 3D view

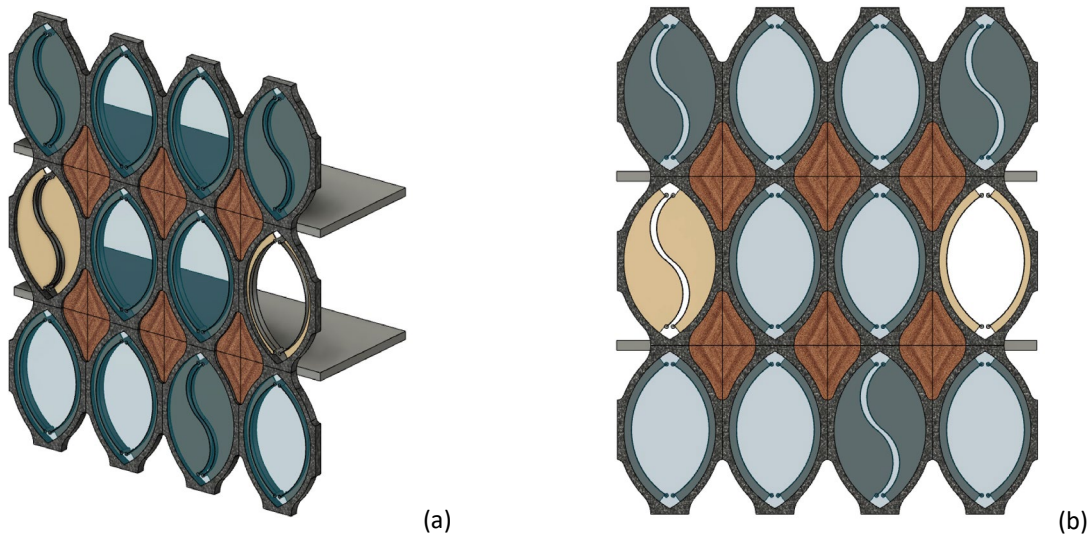


Fig. 8. Proposed concept shading module incorporated into a double skin façade (a) 3D view (b) front view

The shading membranes are stretched in closed setting and provide an opaque layer within the frame. In the closed setting, a deployable component with hooks bonds the two plates at the midlength and

constrains their translational movements. It is noted this constraint does not restrict the rotation of the plates. A simple design for this component is presented in the following section. To open the module, the retractable midlength support is disengaged, causing the plates to buckle in the first mode. In this instance, the plates are nudged to buckle in two opposite directions making an oval opening in the centre of the module. The module can be closed by rotating the hinges, as explained in Fig. 5(e). A schematic integration of the concept modules in a double skin façade is shown in Fig. 8.

### 3. Numerical simulation

In this section, a detailed proof-of-concept numerical simulation is conducted to prove the feasibility of the proposed mechanism. The components utilised in the module include (1) double hook tie bar, Fig. 9(a) (2) hinge blocks, Fig. 9(b) (3) plates, Fig. 9(c) (4) external frame, Fig. 9(d). These components are assembled as shown in Fig. 9(e). In the closed setting, the perforations in the plates will be engaged with the hooks to constrain the out-of-plane deflection of the plates at midlength. By rotating the tie bar along its longitudinal axis, the edges of the perforations will be released from the hooks, and the plates will snap to the first mode of buckling by oval extensions placed on the top and bottom of the tie bar.

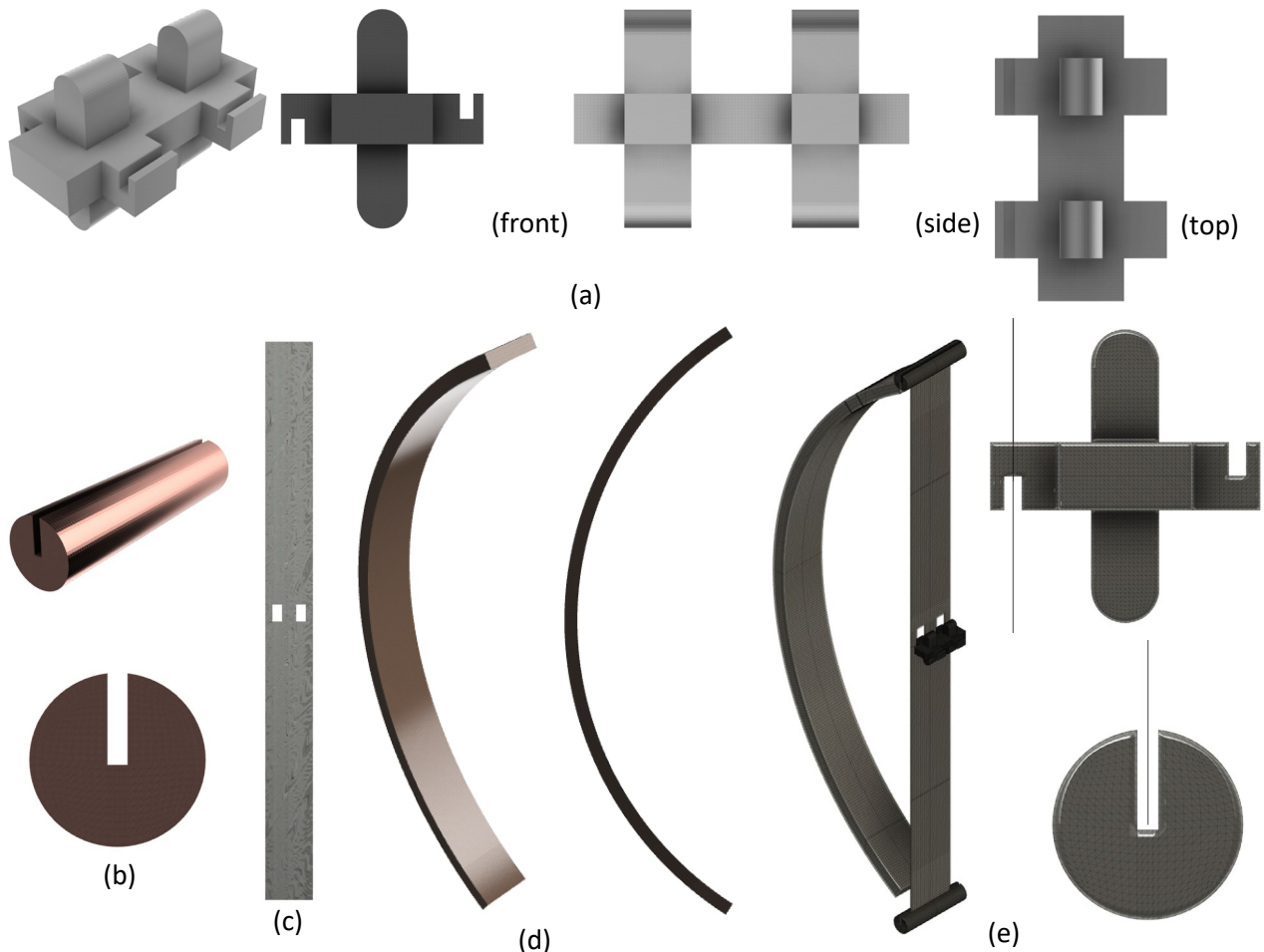


Fig. 9. Components of the proposed model (a) retractable point supports (b) hinge (c) plate with perforations (d) external frame (e) half of the assembly and positioning of the components

In the first step of the analysis, the curvature required to deform in the second mode is introduced by enforcing concentrated forces as explained for the plate element in Fig. 5 (b). In this stage, the tie bar between the plates is active (Fig. 10(a)) and limits the out-of-plane deflection of the plates. Fig. 10(b)

shows the set-up of the module including induced curvature with a maximum deflection value of 32.4 mm. In the next step, the four hinges that host transverse edges of the plates are moved by 100 mm vertically toward the centre. At the end of this loading, the plates buckle in the second mode and assume the configuration presented in Fig. 11(a), which is the closed state for shading. Again, the tie bar is engaged and keeps the module in a closed state. To open the module, the bar is rotated counter-clockwise about its longitudinal axis (perpendicular to the page), thus releasing the edges of the perforations from the hooks and removing the lateral constraints, see Fig. 10(c). Hence, the plates will snap to the first buckling mode shape which correspond to the open state, Fig. 11(b).

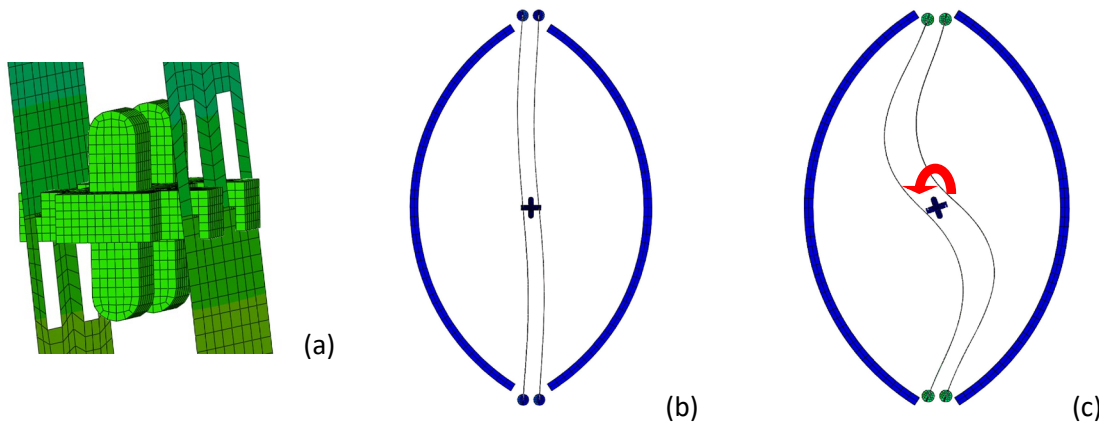


Fig. 10. (a) Active tie bar constraining the plates deflections (b) module with induced imperfection compatible with mode two (c) the tie bar is rotated, and the constraint on deflections is released.

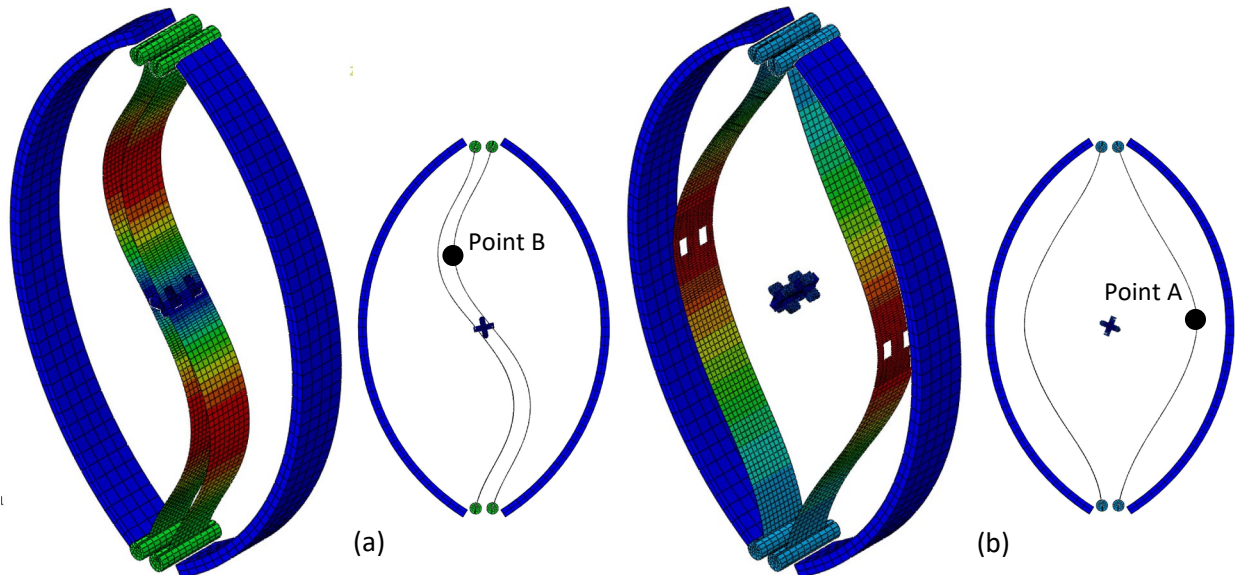


Fig. 11. The FE simulation of the module with displacements magnitude contour in (a) closed and (b) open settings. The response of the module is captured using Abaqus explicit software. The results for the deflection of points A and B (Fig. 11) are presented in Fig. 12. As can be seen, the deflection of point B is increased by introduction of the horizontal loads. In the loading step, the deflection of point B is increased to 225 mm. In these two steps (initial curvature and axial loading), point A remains stationary as its deflection is constrained. In the releasing step, when the tie bar is rotated, both points A and B experience a jump in their deflections. Because of inertia effects, the plates fluctuate before becoming stationary in the new stable position. Point A reaches a deflection of 450 mm, implying the module will have a 900 mm opening at the centre.

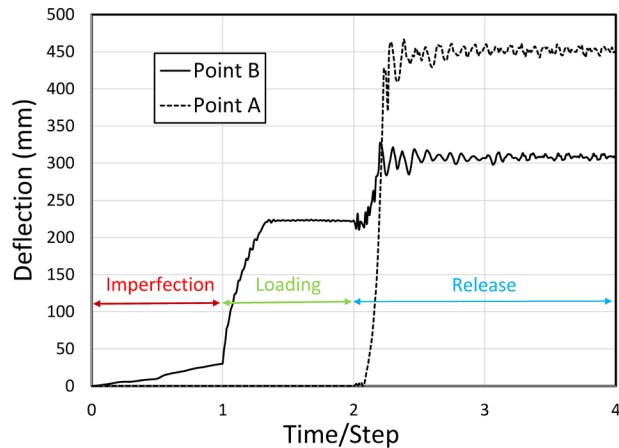


Fig. 12. Deflection of Points A and B

#### 4. Conclusions

In this paper, it is demonstrated that the instability and snap-through buckling of thin plates can be utilised as driver for opening and closing shading modules. The system can work with mechanical and electronic devices, or alternatively, smart materials such as shape memory alloys can be used for sensing and actuation. In the presented numerical simulations, the performance of the system is evaluated and it is shown that a shading module with binary (open/close) response can be achieved by configuring the snapping between the first and second modes of buckling.

#### Acknowledgments

This project was undertaken as part of the Australian Research Council (ARC) Discovery Project DP170104916.

#### References

- AHR (2014). "Architecture & Planning Group", Al-Bahr Towers.
- Formentini, M., Lenci, S. (2018). "An innovative building envelope (kinetic façade) with Shape Memory Alloys used as actuators and sensors." *Automation in Construction*, 85 220-231.
- Han, J.S., Ko, J.S., Korvink, J.G. (2004). "Structural optimization of a large-displacement electromagnetic Lorentz force microactuator for optical switching applications." *Journal of Micromechanics and Microengineering*, 14(11) 1585-1596.
- Hu, Y., Khezri, M., Rasmussen, K.J.R. (2019). "Analytical buckling solutions for Levy-type plates with edge and interior point-support(s)." *Thin-Walled Structures*, 145 106419.
- Hu, Y., Khezri, M., Rasmussen, K.J.R. (2020). "Optimal positioning of internal point-supports in Levy-type plates for buckling load maximisation." *Thin-Walled Structures*, 157 106940.
- Lachenal, X., Daynes, S., Weaver, P.M. (2013) "Review of morphing concepts and materials for wind turbine blade applications." *Wind Energy*, 16(2) 283-307.
- Lienhard, J. et al. (2011). "Flectofin: a hingeless flapping mechanism inspired by nature." *Bioinspiration & Biomimetics*, 6(4) 045001.
- Soma-Architects (2012). "Theme Pavilion Expo Yeosu", Yeosu - Korea.
- Zirbel, S.A., Tolman, K.A., Trease, B.P., Howell, L.L. (2016). "Bistable mechanisms for space applications." *PLoS one*, 11(12) e0168218.

## **Buckling activated ventilation control modules: A concept proposal and numerical simulations**

Mani Khezri<sup>1</sup>, Kim J.R. Rasmussen<sup>2</sup>, Yang Hu<sup>3</sup>

### **Abstract**

As the requirements in construction industry for lower energy consumption are becoming more stringent, shape morphing triggered by buckling is targeted for energy-saving structural applications. Among the structural forms that are suitable for such applications are thin plates, which are prone to buckling under small in-plane strains. Deployable point-supports can be utilised to enhance and guide the buckling behaviour of thin plates based structural systems and subsequently to achieve desired morphogenesis. In adapting such framework, this study presents novel concepts with application in ventilation control modules. In the proposed models, temporary point-restraints are initially deployed to load the plate into the post-buckling range of the primary plate element. The ventilation system is activated when the temporary point-supports are released, causing the primary plate to buckle into the desired opening form. The proposed models are simulated using finite element software to determine the feasibility of the proposed idea and determine the effectiveness of buckling as a reliable mechanism in kinetic façade control modules. The proposed prototype can be operated using electric and mechanical external motors or alternatively smart materials can be used for sensing and actuation as required.

### **1. Introduction**

Energy consumption in buildings has seen great attention because of growing concerns about carbon emissions and climate change. New stricter building regulations (ABCB, 2015) and roadmaps (LaFrance, 2013) are placing increasing demands on the use of highly energy-efficient technologies and equipment, as well as modern façade solutions. This demand has made building façades the subject of recent experiments and studies on increasingly innovative systems and technologies such as “double-skin” façades (DSFs) (Ghaffarianhoseini et al., 2016), in which a second layer is placed in front of a regular building façade. The expected attribute among variants of DSFs is controllable ventilation (airflow) between the skins of the façade. The air cavity between the layers acts as an insulator against the undesired impacts of the outer environment and loss of energy from the building. In addition, DSFs are a suitable framework for implementing a solar chimney that utilises solar thermal energy to induce airflow. In a conventional solar chimney, the difference between the inside and outside air temperatures causes ventilation flow because of buoyancy effect. In comparison with mechanical ventilation systems, the solar

---

<sup>1</sup> Lecturer, The University of Sydney, <mani.khezri@sydney.edu.au>

<sup>2</sup> Professor, The University of Sydney, <kim.rasmussen@sydney.edu.au>

<sup>3</sup> PhD Candidate, The University of Sydney, <yang.hu@sydney.edu.au>

chimney offers a sustainable solution as it requires virtually no energy to operate, and has low operation costs and zero carbon-dioxide emission (Fig. 1).

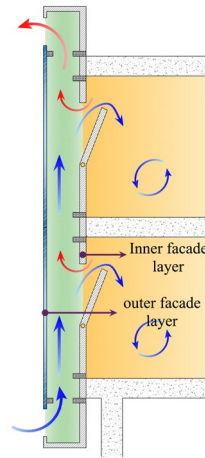


Fig. 1. Double skin façade with integrated solar chimney for passive ventilation

Like other cooling/heating solutions, the solar chimney should be equipped with a control module to respond to temperature changes and occupants' demands. In the closed configuration, the cavity acts as thermal insulation (in winter) and in the open setting allows for natural ventilation (in summer). In recent years, smart materials have been used to create moving surfaces that interact visually and physically with the external environment. In this type of evolving façade technology, also known as "kinetic façade", the designed systems respond to environmental conditions and perform desired functions that are not feasible for static structures (Formentini and Lenci, 2018).

Within this framework, this study is devoted to the presentation and numerical validation of a novel concept for use in kinetic façades. The proposed module is a binary system with closed and open configurations that can be used to control the airflow in a solar chimney. In this module, the buckling of thin panels is the main driver for functionality, and smart materials such as shape memory alloys can be used to trigger the instability. Previous contributions to this area of research include works by Coelho and Maes (2009), who proposed a shutter model motorised by shape-memory alloys to control ventilation and light, and Lignarolo et al. (2011), who developed shape-memory alloy actuated elements to enhance the aerodynamic behaviour of high-rise buildings by changing the roughness of the building skin. Formentini and Lenci (2018) proposed a panel actuated by SMA for building envelopes to be incorporated as ventilation openings. They used SMA wires as low-energy thermal sensors and force-inducing elements that cause buckling of the panel, see Fig. 2.



Fig. 2. The proposed ventilation panel by Formentini and Lenci, 2018 in (a) closed and (b) open positions. NiTi SMA wires connected to the plate to stress the plate into the buckled position

In this study, we also present a concept for ventilation modules that harnesses buckling to create openings for airflow in an integrated solar chimney in DSFs. To create a binary system with only open and closed configurations, deployable point-supports are utilised to enhance and guide the buckling behaviour of thin plates. The deployable point-restraints are engaged to load the plate into the post-buckling range of the primary element, see Fig. 3(a). The module opens the airflow passage when the temporary point-supports are released, causing the plate to buckle into the desired form, Fig. 3(b).

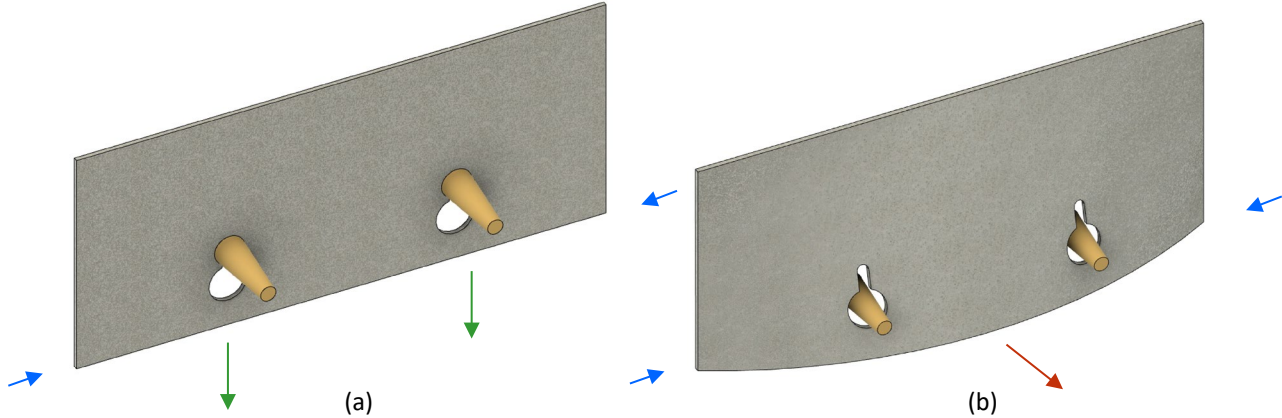


Fig. 3. Schematic presentation of the proposed module in (a) closed state and (b) open configuration

## 2. Buckling-activated ventilation control modules

Having the basic concept and the general mechanics of the proposed module presented, we seek to identify the key questions that are required to be answered for the realisation of the proposed idea. The placement of temporary point-supports is an important factor that influences the outcome and the module's response. It is evident that the introduction of point-supports enhances the buckling capacity of the panel. The maximum enhancement of the buckling capacity can be expected when the point-supports are positioned in optimal locations. This, in turn, means that when the point-supports are released, the plate is subjected to higher in-plane stresses and consequently undergoes larger lateral buckling displacements. Thus, the first problem to be investigated is the optimal placement of point-supports. This research question has been investigated in detail by the authors (Hu et al., 2019; Hu et al., 2020), and a brief summary of the methodology and the relevant solutions is presented in the next section.

### 2.1 Analytical tools and investigation

Consider a rectangular plate as shown in Fig. 4(a), with two parallel simply-supported edges of width  $b$ , and arbitrary support condition along the other edges with length  $a$ .

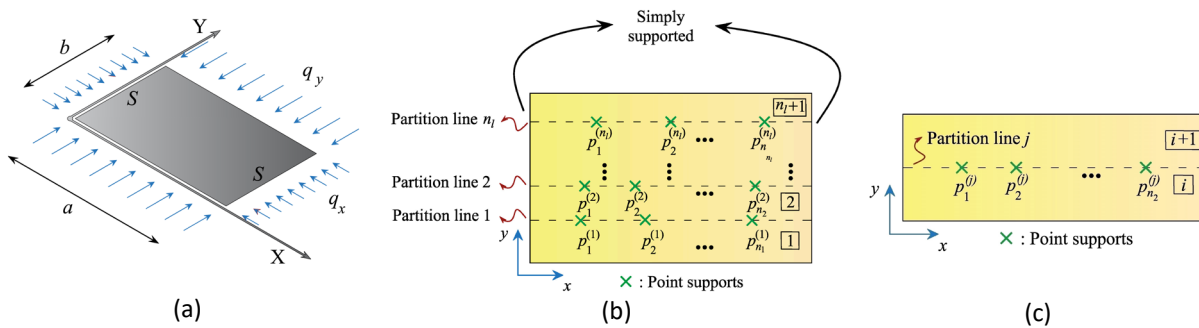


Fig. 4. (a) Schematic diagram of a Levy-type plate subjected to biaxial loads ( $q_x$  and  $q_y$ ) (b) Levy-type plate with multiple point-supports, (c) partition line  $j$  between adjacent sub-plates  $i$  and  $i+1$

The governing differential equation for the deflection ( $w$ ) of such plates can be expressed as (Timoshenko and Woinowsky-Krieger, 1959)

$$\frac{\partial^4 w}{\partial x^4} + 2 \frac{\partial^4 w}{\partial x^2 \partial y^2} + \frac{\partial^4 w}{\partial y^4} - \frac{1}{D} \left( q_x \frac{\partial^2 w}{\partial x^2} + q_y \frac{\partial^2 w}{\partial y^2} \right) = 0. \quad (1)$$

In Eq. (1),  $q_x$  and  $q_y$  are in-plane compressive stresses in the  $x$  and  $y$  directions, respectively, and  $D$  is the plate flexural rigidity. The introduction of point-supports is achieved by using the one dimensional (1-D) impulse function approach (IFA) (Bapat and Suryanarayan, 1989; Bapat et al., 1988). In the IFA, the core idea is to represent the shear force or bending moment distribution along the longitudinal lines passing through point-supports (Fig. 4(b)) using a single Fourier expansion of the impulse function. The externally exerted shear and moment contributions at point-supports (if the point is clamped) along the  $j$ -th partition line can be expressed as Fourier series expansions as follows,

$$\hat{V}_y^j(x) = \sum_{k=1}^{NP_j} (I_V)_k^j \times 2 \underbrace{\sum_{m=1}^{\infty} \sin\left(\frac{m\pi X_k^j}{a}\right) \sin\left(\frac{m\pi x}{a}\right)}_{\delta(x-X_k^j)}, \quad (2)$$

$$\hat{M}_y^j(x) = \sum_{k=1}^{NP_j} \chi_k^j \times (I_M)_k^j \times 2 \underbrace{\sum_{m=1}^{\infty} \sin\left(\frac{m\pi X_k^j}{a}\right) \sin\left(\frac{m\pi x}{a}\right)}_{\delta(x-X_k^j)}, \quad (3)$$

where  $NP_j$  is the number of point-supports located on the  $j$ -th partition line,  $(I_V)_k^j$  and  $(I_M)_k^j$ , respectively, are the amplitudes of the shear and moment reactions at the point-support  $p_k^{(j)}$  ( $k$ th point at the  $j$ th partition line), and  $\delta(x - X_k^j)$  is the impulse function. Using the Levy Fourier series expansion (Timoshenko and Woinowsky-Krieger, 1959), the generalised solution of Eq. (1) is given in the following form:

$$w(x, y) = \sum_{m=1}^{\infty} \underbrace{\left[ \begin{array}{l} A_m \cosh(r_m y) + B_m \sinh(r_m y) \\ + C_m \cos(s_m y) + D_m \sin(s_m y) \end{array} \right]}_{E_m(y)} \times \sin\left(\frac{m\pi x}{a}\right) = \sum_{m=1}^{\infty} E_m(y) \times \sin\left(\frac{m\pi x}{a}\right), \quad (4)$$

where  $A_m$ ,  $B_m$ ,  $C_m$ , and  $D_m$  are constants which are determined using prescribed BCs and  $m$  is the term number in the series expansion. The constants  $r_m$  and  $s_m$  are defined as:

$$r_m = \sqrt{\frac{m^2 \pi^2}{a^2} - \frac{q_y}{2D}} + \sqrt{\frac{q_x - q_y}{D} \frac{m^2 \pi^2}{a^2} + \frac{q_y^2}{4D^2}}, \quad (5)$$

$$s_m = \sqrt{-\frac{m^2 \pi^2}{a^2} + \frac{q_y}{2D}} + \sqrt{\frac{q_x - q_y}{D} \frac{m^2 \pi^2}{a^2} + \frac{q_y^2}{4D^2}}.$$

Having the general solution, one can obtain the equations for the slope (S), shear force (V) and moment (M), viz.

$$S_y(x, y) = \frac{\partial w}{\partial y} = \sum_{m=1}^{\infty} \left( r_m [A_m \sinh(r_m y) + B_m \cosh(r_m y)] \right) \times \sin\left(\frac{m\pi x}{a}\right), \quad (6)$$

$$V_y(x, y) = D \left( \frac{\partial^3 w}{\partial y^3}(x, y) + (2-\nu) \frac{\partial^3 w}{\partial x^2 \partial y}(x, y) \right) = D \sum_{m=1}^{\infty} \left( \alpha_m [A_m \cosh(r_m y) + B_m \sinh(r_m y)] + \beta_m [C_m \cos(s_m y) + D_m \sin(s_m y)] \right) \times \sin\left(\frac{m\pi x}{a}\right), \quad (7)$$

$$M_y(x, y) = -D \left( \frac{\partial^2 w}{\partial y^2}(x, y) + \nu \frac{\partial^2 w}{\partial x^2}(x, y) \right) = D \sum_{m=1}^{\infty} \left( \lambda_m [A_m \sinh(r_m y) + B_m \cosh(r_m y)] + \gamma_m [C_m \sin(s_m y) - D_m \cos(s_m y)] \right) \times \sin\left(\frac{m\pi x}{a}\right). \quad (8)$$

where

$$\begin{aligned} \alpha_m &= -vm^2 \pi^2 / a^2 + r_m^2, & \beta_m &= -vm^2 \pi^2 / a^2 - s_m^2, \\ \lambda_m &= r_m^3 - (2-\nu)m^2 \pi^2 r_m / a^2, & \gamma_m &= s_m^3 - (2-\nu)m^2 \pi^2 s_m / a^2. \end{aligned} \quad (9)$$

Utilising Eqs. (2) and (3) in combination with Eqs. (7) and (8), the total shear  $\bar{V}$  and moment  $\bar{M}$  along partition line  $j$  ( $y = Y^j$ ) are given as:

$$\begin{aligned} \bar{V}_y^j(x) &= V_y(x, Y^j) + \hat{V}_y^j(x) \\ &= \left( D \sum_{m=1}^{\infty} \left( \alpha_m [A_m \cosh(r_m Y^j) + B_m \sinh(r_m Y^j)] + \beta_m [C_m \cos(s_m Y^j) + D_m \sin(s_m Y^j)] \right) \right) + \sum_{k=1}^{NP_j} (I_V)_k^j \times 2 \sum_{m=1}^{\infty} \sin\left(\frac{m\pi X_k^j}{a}\right) \times \sin\left(\frac{m\pi x}{a}\right), \end{aligned} \quad (10)$$

$$\begin{aligned} \bar{M}_y^j(x) &= M_y(x, Y^j) + \hat{M}_y^j(x) \\ &= \left( D \sum_{m=1}^{\infty} \left( \lambda_m [A_m \sinh(r_m Y^j) + B_m \cosh(r_m Y^j)] + \gamma_m [C_m \sin(s_m Y^j) - D_m \cos(s_m Y^j)] \right) \right) + \sum_{k=1}^{NP_j} \chi_k^j \times (I_M)_k^j \times 2 \sum_{m=1}^{\infty} \sin\left(\frac{m\pi X_k^j}{a}\right) \times \sin\left(\frac{m\pi x}{a}\right). \end{aligned} \quad (11)$$

For all harmonic terms, by enforcing the BCs along the longitudinal edges as well as the continuity and restraints at each discrete point-support, a coefficient matrix can be derived. The determinant of the coefficient matrix yields the characteristic equation that defines the stability of the plate. By solving the characteristic equations buckling solutions are obtained. Hu et al. 2020 presented solutions for the optimal positioning of discrete point-supports in Levy-type plates for buckling load maximisation. A comprehensive set of plate problems with various aspect ratios, boundary conditions and different number of point-supports was considered. Among the considered cases, a few are suitable for development as ventilation modules. In this study, we consider the case of plate with SSSF support conditions and aspect ratio  $\Phi = 3$  with two internal point-supports. The results for the optimised point-supports locations,  $P_1$  and  $P_2$ , for the considered plate are shown in Fig. 5.

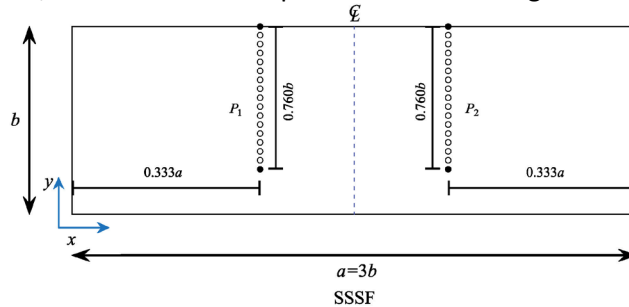


Fig. 5. Optimised point-supports locations of SSSF plates with two point-supports with aspect ratios  $\Phi = 3$

It is noted that placing the point-supports along the line segment shown increases the buckling load factor from 0.534 (for the primary plate without intermediate restraints) to 1.402. Based on the analytical

studies, a concept model is proposed as a ventilation control module that incorporates two retractable point-supports. It is noted that the positioning of the point-supports based on the analytical solutions is a starting guess. Accurate positioning of the retractable point-supports can be addressed in an optimisation framework. A series of numerical simulations are conducted to prove the feasibility of the concept. The force-inducing mechanism is not discussed but various options including smart materials such as SMA wires (Formentini and Lenci, 2018) could be used.

### 2.2 Proposed prototype and function process

A prototype is presented with sufficient details for proof of concept numerical simulations. Cones with deep, circular grooves, as shown in Fig. 6(a) are utilised to introduce retractable constraints. The panel is perforated as shown in Fig. 6(b) to accommodate the retractable points-supports. The cones are assembled into the module as shown in Fig. 6(c). The cones effectively restrain the out-of-plane deflection of the panel when the grooves are positioned within the narrow segment of the key-hole shaped perforations. This configuration with some approximation simulates a plate with two internal point-supports. The plate is compressed along the transverse edges while the cones are engaged with the edges of perforations. Because of the discrete restraints, the plate can be loaded beyond the buckling load of the primary panel. The passage for the airflow opens when the cones (point-supports) are lowered into the bigger circles of the perforations. As the cones slide into the circles, they are no longer in contact with the narrow part of the perforations. Consequently, the discrete constraints on the out-of-plane deflection of the panel are removed and the plate suddenly buckles. The process of the proposed prototype has been numerically simulated using Abaqus finite element software. The detail of the analyses are presented in the following.

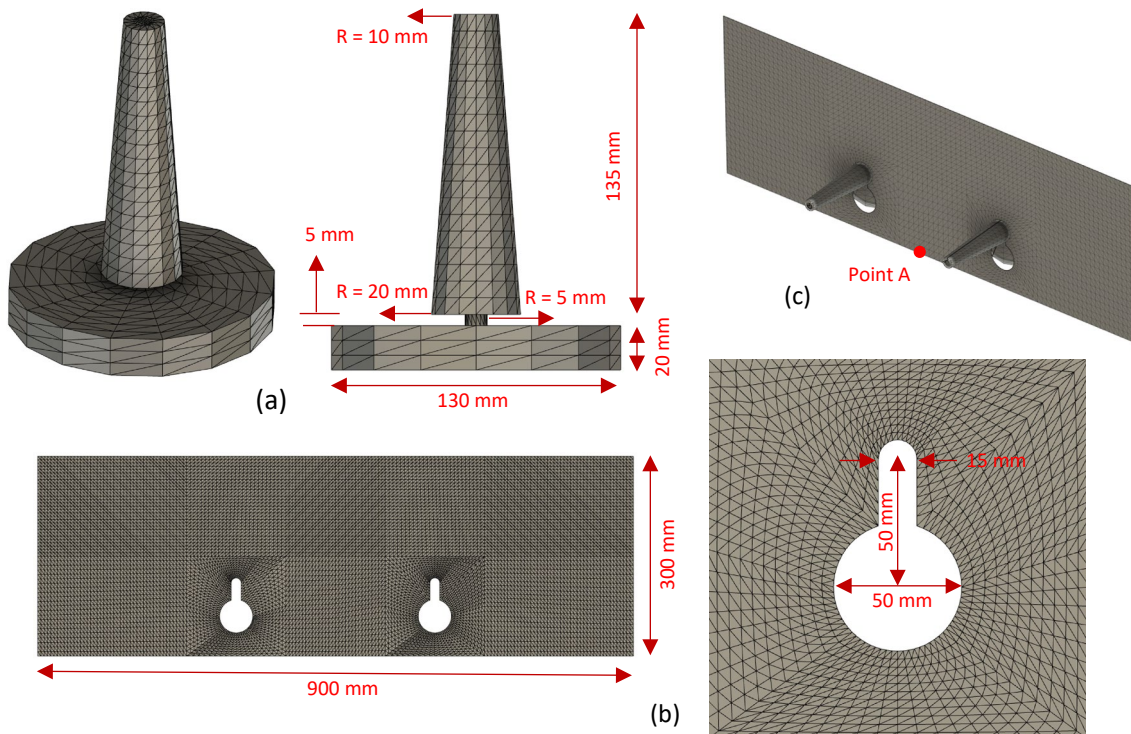


Fig. 6. Developed prototype (a) cone used to simulate point-supports (b) panel with key-hole shaped perforations (c) the initial assembling of the parts

### 3. Numerical Simulation

It is assumed that all components are made of steel with Young's modulus  $E = 210$  GPa and Poisson's ratio  $\nu = 0.3$ . Due to the dynamic nature of the problem, i.e. sudden release of the panel upon removal of the point-supports, the dynamic explicit method is used to simulate the process. The plate is discretised using

S4R shell elements with an average global size (length and width) of 5 mm, and C3D8R 8-node linear brick elements are utilised for meshing the solid cones. The plate is simply-supported along the two transverse edges loaded in uniform compression and one of the longitudinal edges. The point-supports are positioned close to the free edge to control the out-of-plane deflection. First, a buckling analysis is conducted to determine the three first modes of the primary plate and their associated buckling load factors. The solutions for the buckling analysis are presented in Fig. 7, and as can be seen, the first mode provides a suitable pattern for the opening of the ventilation module. Thus, this mode shape is introduced as imperfection in the analysis. This is achieved by enforcing a concentrated force equal to 15 N at point A at the centre of the free edge, (Fig. 6 (c)). The results obtained for the deflection of point A are presented in Fig. 8. Imposing the point load induces a deflection of 3.24 mm at point A.

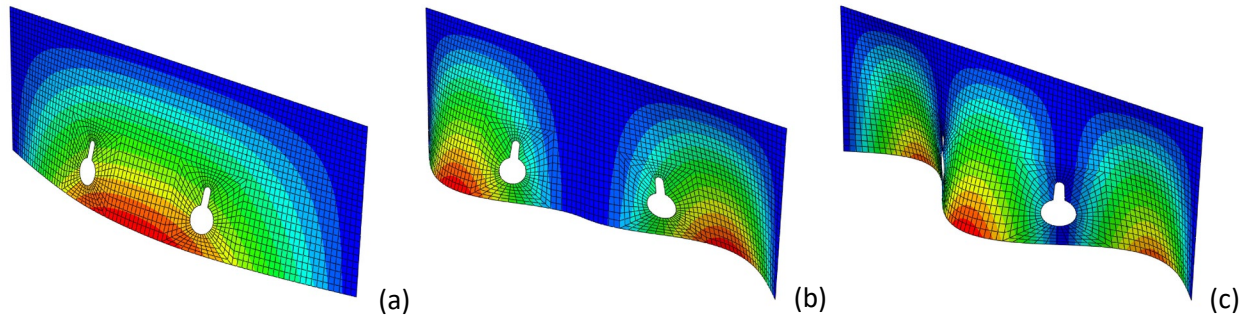


Fig. 7. The buckling mode shapes of the primary plate (a) First mode, buckling load 8.87 N/mm (b) Second mode, buckling load 22.51 N/mm (c) Third mode, buckling load 24.34N/mm

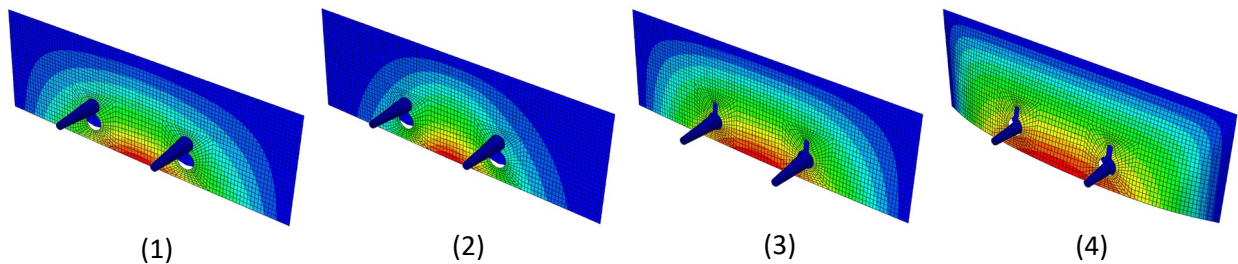
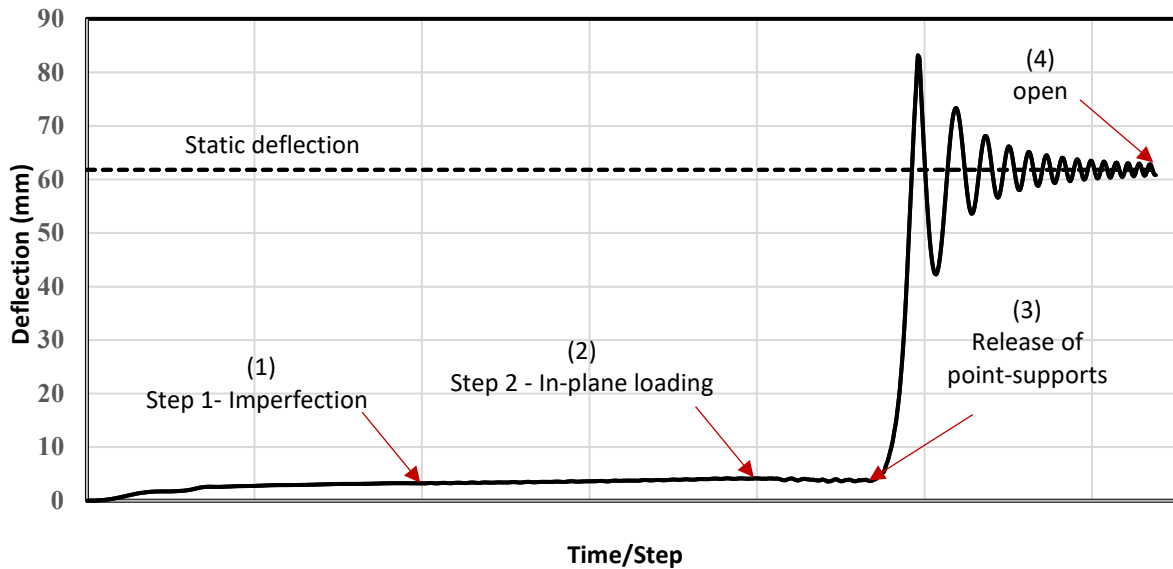


Fig. 8. Deflection of point A during operation of the panel (opening) (1) introduction of imperfection (2) in-plane loading (3) release of point-supports (4) buckling of panel (open configuration)

After introducing an imperfection as step 1, the panel is subjected to compressive stress along the transverse edges. The loads are gradually increased until reaching the intensity of 27 N/mm, Fig. 8(2). It can be seen that the deflection of Point A under in-plane loading increases modestly to 4.17 mm. At the end of this step the plate is fully loaded and removal of point-supports will cause sudden deflection along the free edge. The point-supports are lowered and disengaged in the next step, Fig. 8(3), and therefore the buckling of the primary plate under the imposed in-plane loading occurs. Because of inertia effects the panel fluctuate around the static configuration (deflection of 61.8 mm) until damping dissipates the dynamic energy of the mechanism, Fig. 8(4).

#### 4. Conclusions

In this paper, it is shown how buckling of thin panels can be used as a mechanism for opening and closing ventilation modules in kinetic facades. The system can work with mechanical and electronic devices, or alternatively, smart materials such as shape memory alloy can be used for sensing and actuation. The feasibility of the idea is proved by numerical simulation of a prototype. To this end, FE software Abaqus is used to model an accurately designed system. The results obtained show that a binary system that snaps from closed to open configuration can be achieved, driven by buckling. Due to the dynamic nature of the sudden release of the incorporated retractive intermediate restraints, fluctuation is visible in the numerical simulation, which may be greatly reduced using simple dampers if required.

#### Acknowledgments

This project was undertaken as part of the Australian Research Council (ARC) Discovery Project DP170104916.

#### References

- ABCB, A.B.C.B., (2015). "National Construction Code". ABCB.
- Bapat, A.V., Suryanarayan, S. (1989). "Free vibrations of periodically point-supported rectangular plates." *Journal of Sound and Vibration*, 132(3) 491-509.
- Bapat, A.V., Venkatramani, N., Suryanarayan, S. (1988). "A new approach for the representation of a point support in the analysis of plates." *Journal of Sound and Vibration*, 120(1) 107-125.
- Coelho, M., Maes, P. (2009). "Shutters: a permeable surface for environmental control and communication", *Proceedings of the 3rd International Conference on Tangible and Embedded Interaction*, pp. 13-18.
- Formentini, M., Lenci, S. (2018). "An innovative building envelope (kinetic façade) with Shape Memory Alloys used as actuators and sensors." *Automation in Construction*, 85 220-231.
- Ghaffarianhoseini, A. et al. (2016). "Exploring the advantages and challenges of double-skin façades (DSFs)". *Renewable and Sustainable Energy Reviews*, 60 1052-1065.
- Hu, Y., Khezri, M., Rasmussen, K.J.R. (2019). "Analytical buckling solutions for Levy-type plates with edge and interior point-support(s)." *Thin-Walled Structures*, 145 106419.
- Hu, Y., Khezri, M., Rasmussen, K.J.R. (2020). "Optimal positioning of internal point-supports in Levy-type plates for buckling load maximisation." *Thin-Walled Structures*, 157 106940.
- LaFrance, M. (2013). "Technology Roadmap: Energy efficient building envelopes". Paris: IEA.
- Lignarolo, L., Lelieveld, C., Teuffel, P. (2011). "Shape morphing wind-responsive facade systems realized with smart materials", *Adaptive Architecture: An International Conference*, London, UK, March 3-5, 2011.
- Timoshenko, S.P., Woinowsky-Krieger, S. (1959). "Theory of plates and shells". McGraw-Hill.

## Evaluation of the post-maximum strength behavior of the lipped-C channel column member under compression

Tomoki Kobashi<sup>1</sup> Satoshi Kitaoka<sup>2</sup>

### Abstract

The collapse behavior of the axially compressed long column members with the lipped-C cross-section was investigated. Based on the collapse mode from the experiments, the plastic mechanism models were proposed. The evaluation results by the proposed method corresponded well with the experimental results.

### 1. Introduction

The lipped-C channel member is widely used for a primary member and a secondary member in Japan. Generally, the lipped-C channel is used as an elastic structural component that does not require the ductile plastic deformation capacity. However, due to the recent earthquake disasters, it was found that these secondary members were also seriously damaged by these strong earthquakes (for example, Iyama (2018)). Although these damages dose does not cause a collapse of buildings themselves, these damages might injure the people inside the buildings and disturb the continuous use of the buildings after the natural disasters, which might provide serious economic damage in the disaster area. Therefore, in order to prevent the serious collapse behavior of a secondary structural component, revealing the load and displacement relationship not only before reaching the maximum strength but also after reaching the maximum strength is an important issue.

As one of the effective methods to evaluate this post-maximum strength behavior of the lipped-C channel, we focused on the plastic mechanism analysis. The plastic mechanism analysis is a kind of limit-analysis based on the upper bound theorem. Many experimental and numerical investigations about the lipped-C channel members under compression and/or bending had been carried out by numerous researchers (for example, Morino(2003), Kotełko(2004), and Ungureanu(2010, 2016, 2018)), and they revealed that the plastic mechanism analysis is an effective method to evaluate the load-deformation behavior after reaching the maximum strength. However, the previous researches were mainly focused on the collapse behavior of the short columns, and there are no enough experimental investigations about the strength deterioration behavior of the lipped-C long column members.

Therefore, in this paper, the investigation about the strength deterioration of the lipped-C long columns was conducted. Based on the experimental results, we proposed the plastic mechanism analysis models

---

<sup>1</sup> R. Kobashi, Institute of Steel Structures, Department of Steel Structures, Faculty of Engineering, Lodz University of Technology, 26-602 St. Zeromskiego, 43-200 Lodz, Poland

<sup>2</sup> S. Kitaoka, Institute of Steel Structures, Department of Steel Structures, Faculty of Engineering, Lodz University of Technology, 26-602 St. Zeromskiego, 43-200 Lodz, Poland

for the local buckling, the distortional buckling, and the flexural buckling and compare the experimental results and the plastic mechanism analysis results.

## 2. Axial Compression Test of Lipped-C Channel Members

### 2.1 Outline of Experiment

Fig.1 shows an example of a test specimen and Fig.2 Shows the outline of the experiment setup. In this paper, we investigated the collapse behavior of the axially compressed lipped-C channel members. All specimens were wet so that the loading axis passed through the centroid of the test specimen. The knife edges were only allowed to rotate in one direction so that the specimens buckled in the weak direction.

Table.1 and Table.2 shows the coupon test results of the steel material and the list of the test specimens. In this paper, a total of ten specimens with six different sectional shapes were tested. The variables are the member length  $L$ , the plate width of the flange  $b_f$ , the plate width of the web  $b_w$ , the plate width of the lip  $b_l$ , and the plate thickness  $t$ . The local buckling strength ( $P_{cr1}$ ) and the distortional buckling strength ( $P_{crd}$ ) in Table.1 are the eigenvalue analysis results. The global buckling strength ( $P_{crg}$ ) is the flexural buckling strength. In this test, the rotation around the strong axis and the warping at the edges of the member are restrained by knife edges. Therefore, we regarded that the global buckling strength of the test specimen is equal to the flexural buckling strength of the lipped-C channel member around the weak axis. By substituting these elastic buckling strengths to the direct strength method (DSM) equations (AISI Specifications (2016)), we obtained the nominal strength in Table.2.

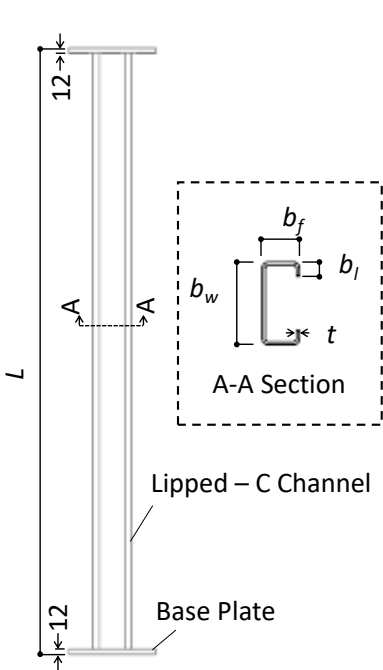


Figure 1 Test specimen

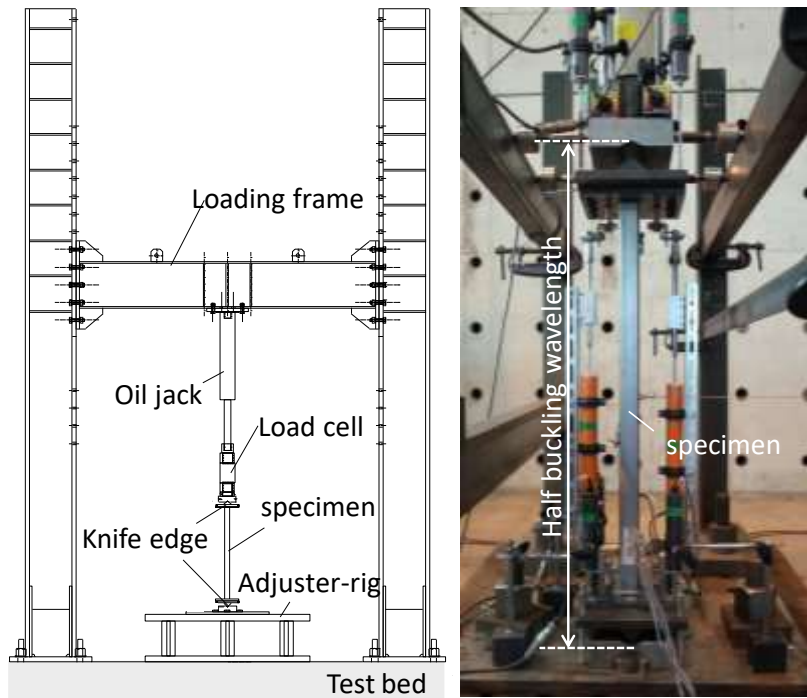


Figure 2 Set-up of the test specimen

Table.1 Coupon test results of steel materials

Thickness (mm)	Yield stress (N/mm <sup>2</sup> )	Tensile strength (N/mm <sup>2</sup> )	Yield ratio (%)	Elongation (%)
1.12	362	487	74.3	31
3.14	315	442	71.3	35

Table.2 List of the test specimens

No.	Section shapes (mm)					Elastic buckling strength(kN)			Nominal strength by DSM (kN)	
	$b_w$	$b_f$	$b_l$	$t$	$L$	Local	Distortional	Global	$P_{nl}$	$P_{nd}$
1	89	40	15	1.12	798	35.8	70.8	126.9	42.8	55.9
2	89	40	15	1.12	1398	35.8	70.8	45.7	31.7	55.9
3	89	40	15	3.14	798	788.2	645.9	279.5	133.7	173.3
4	89	40	15	3.14	1398	788.2	645.9	100.6	84.3	173.3
5	89	65	10	1.12	798	39.8	39.3	355.1	55.2	47.3
6	89	65	10	3.14	798	821.9	380.0	872.0	196.4	198.1
7	150	60	20	1.12	1398	19.9	58.1	159.4	44.8	65.7
8	150	60	20	1.12	1998	19.9	58.1	81.3	36.8	65.7
9	150	60	20	3.14	1398	433.7	508.5	381.8	207.5	259.3
10	150	60	20	3.14	1998	433.7	508.5	194.8	154.1	259.3

## 2.2 Collapse mode of the specimens

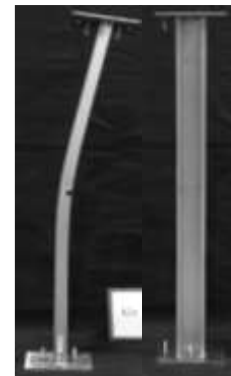
Fig.3 shows examples of the collapse modes, which were obtained from the compression test. In this test, three different collapse modes were obtained. The first is the local buckling mode (Fig.3(a)); four specimens showed this collapse mode. In this mode, the local deformation was concentrated at the web and the flange plates, and no local deformation was observed at the lip plates. The second is the distortional buckling mode (Fig.3(b)); five specimens showed this collapse mode. In this mode, the local deformation was concentrated at the lip and flange plates, and no local deformation was observed at the web plate. The last mode was the global buckling mode (Fig.3(c)); only one specimen showed this collapse mode. In this mode, although it seems that the specimen plastically deformed in the longitudinal direction at the middle height of the specimen, no noticeable out of plane deformation of the plate elements was observed.



(a) Local buckling



(b) Distortional buckling



(c) Global buckling

Figure 3 Examples of the collapse mode

Table.3 summarizes the experimental results.  $P_{max}$  is the maximum strength by experiment, and  $P_{DSM}$  is the nominal strength by DSM (Note that  $P_{DSM}$  is the lower value of  $P_{nl}$  and  $P_{nd}$  in Table.2). The DSM mode is the buckling mode in which the nominal strength became lower among that calculated by assuming local buckling and distortional buckling. We found that, although  $P_{max}$  corresponded well with  $P_{DSM}$ , the collapse mode by experiment did not always agree with that obtained from DSM. The current design method is aimed at evaluating the maximum strength of the cold-formed steel members and does not consider whether it could evaluate the collapse mode precisely. For example, in the case of No.6 in Table.2,  $P_{nl}$  and  $P_{nd}$  mostly have the same value and the difference between them does not have a significant effect on the evaluation of the maximum strength. Furthermore, the buckling mode was seemingly changed along with the increase of the axial deformation, by the effects of the localized

deformation and the material yielding. Investigating the method which can predict the collapse mode from the member shapes is a focus of future tasks.

Table 3 Comparison between experiment, eigenvalue analysis, and direct strength method

No.	Experiment		DSM	
	$P_{max}$ (kN)	Collapse mode	$P_{DSM}$ (kN)	Mode
1	44.8	Local	42.8	Local
2	37.5	Distortional	31.7	Local
3	136.0	Distortional	133.7	Local
4	76.8	Global	84.3	Local
5	50.0	Distortional	55.2	Distortional
6	196.5	Local	196.4	Local
7	47.5	Local	44.8	Local
8	40.0	Local	36.8	Local
9	195.25	Distortional	207.5	Local
10	135.50	Distortional	154.1	Local

### 3. Analytical Investigation of Post-Maximum Strength Behavior

From the experimental results, we found that the specimen concentrated the local deformation at the middle height of them. Besides, the specimens showed a horizontal deformation at their middle height as shown in Fig.4. Therefore, we assumed that the test specimen behaved like a hinged-member which had a plastic hinge at the middle height of it (Fig.4). In this model, the work by the external force must be the same as the energy which is dissipated by the local deformation. Therefore, we evaluated the dissipated energy of the local deformation by using the plastic mechanism analysis.

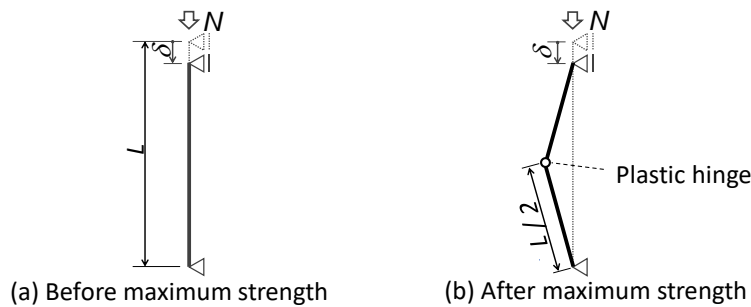


Figure 4: Assumed collapse mode of the lipped-C column member

#### 3.1 Outline of Plastic Mechanism analysis

Fig.5 shows an example of the yield line. The work rates  $\dot{W}_i$  at the yield line could be obtained as follows. Where  $\sigma_1$ ,  $\sigma_2$ , and  $t$  are the normal stress along the yield line,  $\dot{\epsilon}_1$ ,  $\dot{\epsilon}_2$ , and  $\dot{\gamma}$  are the strain rates, and  $\dot{W}_i$  is the work rate. Note that,  $\dot{\epsilon}_1$ ,  $\dot{\epsilon}_2$ ,  $\dot{\gamma}$ , and  $\dot{W}_i$  are the values that were partially differentiated with the axial deformation  $\delta$ .

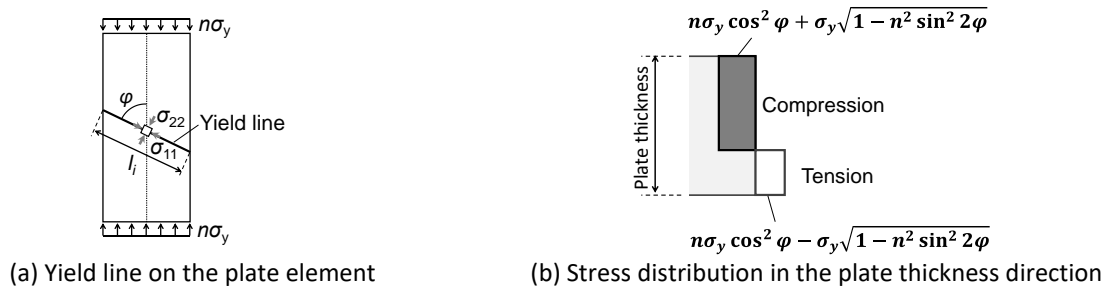


Figure 5 Stress in the plate element

$$\dot{w}_i = \int (\sigma_1 \dot{\epsilon}_1 + \sigma_2 \dot{\epsilon}_2 + \tau \dot{\gamma}) dV \quad (1)$$

By assuming that the steel material behaved as an isotropic material, the stress tensor by in-plane axial compression force ( $=n\sigma_y bt$ ) could be obtained as follows. Where the  $\varphi$  is the angles between yield line and longitudinal direction as shown in fig.5(a).

$$\text{Stress tensor by axial force} \quad \begin{bmatrix} \sigma_{11} & \sigma_{12} \\ \sigma_{21} & \sigma_{22} \end{bmatrix} = \begin{bmatrix} n\sigma_y \cos^2 \varphi & -n\sigma_y \cos \varphi \sin \varphi \\ -n\sigma_y \cos \varphi \sin \varphi & n\sigma_y \sin^2 \varphi \end{bmatrix} \quad (2)$$

Fig.5(b) shows an example of the stress distribution in the plate thickness direction at the yield line. Because the bending moment was loaded at the yield line, the stress tensor of the compression side and the tension side should be different. Therefore, we define  $\sigma_{bc}$  and  $\sigma_{bt}$  as a stress in the  $\sigma_{22}$  direction of the compression side and the tension side, obtaining the stress tensor as follows:

$$\text{Compression side} \quad \begin{bmatrix} \sigma_{11} & \sigma_{12} \\ \sigma_{21} & \sigma_{22} \end{bmatrix} = \begin{bmatrix} n\sigma_y \cos^2 \varphi & -n\sigma_y \cos \varphi \sin \varphi \\ -n\sigma_y \cos \varphi \sin \varphi & \sigma_{bc} \end{bmatrix} \quad (3.1)$$

$$\text{Tension side} \quad \begin{bmatrix} \sigma_{11} & \sigma_{12} \\ \sigma_{21} & \sigma_{22} \end{bmatrix} = \begin{bmatrix} n\sigma_y \cos^2 \varphi & -n\sigma_y \cos \varphi \sin \varphi \\ -n\sigma_y \cos \varphi \sin \varphi & \sigma_{bt} \end{bmatrix} \quad (3.2)$$

When we assumed that the yield criterion of the steel material follows the Tresca yield criterion, the yielding of the steel material could be evaluated as a difference between the maximum mean stress and the minimum mean stress. Therefore, substituting the Eqs. (3.1) and (3.2) to the Tresca yield criterion, we could evaluate  $\sigma_{bc}$  and  $\sigma_{bt}$  as follows:

$$\sigma_{bc} = \left( n \cos^2 \varphi + \sqrt{1 - n^2 \cos^2 2\varphi} \right) \sigma_y \quad (4)$$

$$\sigma_{bt} = \left( n \cos^2 \varphi - \sqrt{1 - n^2 \cos^2 2\varphi} \right) \sigma_y \quad (5)$$

The volume which is plastically deformed at the yield line is defined as a triangle shape as shown in Fig.6 (Morino (2003)). By considering the equilibrium of the in-plane force (see Eq.(2)), we could obtain the volume of the plastically deformed zone as follows:

$$\text{Compression side} \quad dV^+ = \frac{lt^2}{\cos \varphi} \left\{ 1 - \frac{n \cos(2\varphi)}{\sqrt{1 - n^2 \cos^2(2\varphi)}} \right\} \quad (6.1)$$

$$\text{Tension side} \quad dV^- = \frac{lt^2}{\cos \varphi} \left\{ 1 + \frac{n \cos(2\varphi)}{\sqrt{1 - n^2 \cos^2(2\varphi)}} \right\} \quad (6.2)$$

Furthermore, as can be seen in Fig.6, we could evaluate the relationship between  $\dot{\epsilon}_2$  (strain rates in the  $\sigma_{22}$  direction) and  $\dot{\theta}_i$  (rotation rates at the yield line) as  $\dot{\epsilon}_2 = 0.5\dot{\theta}_i$ . Thus, by substituting the Tresca yield criterion to the associated flow rule, we could obtain the following equations:

$$\frac{\dot{\epsilon}_1}{\dot{\epsilon}_2} = -1 \quad (7.1)$$

$$\frac{\dot{\gamma}}{\dot{\epsilon}_2} = \frac{2\tau}{\sigma_2 - \sigma_1} \quad (7.2)$$

Thus, substitution Eqs. (6.1), (6.2), (7.1), and (7.2) to Eq. (2), we could obtain the relationship between  $\dot{w}_i$  and  $\dot{\theta}_i$  as follows:

$$\dot{w}_i = \frac{\sigma_y I_t^2}{\sqrt{1-n^2} (2\varphi)} \frac{1+n^2 \cos^2(\varphi)}{1-n^2 \sin^2(\varphi)} \dot{\theta}_i \quad (8)$$

If the plastic deformation was occurred by the in-plane force without any bending moment, we assumed that the triangle zone as shown in Fig.7 was deformed plastically (we call this zone as a yield zone in this paper). Referring to Morino's efforts (Morino(2003)), we evaluate the dissipated energy by in-plane plastic deformation as follows. Where  $b$  is the width of the yield zone and  $\delta_i$  is the deformation between points A and B as shown in Fig.7.

$$w_{di} = \frac{1}{2} \sigma_y t b \delta_i \quad (9)$$

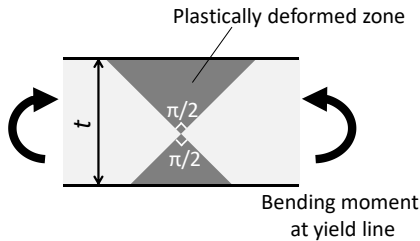


Figure 6: Section of the yield line

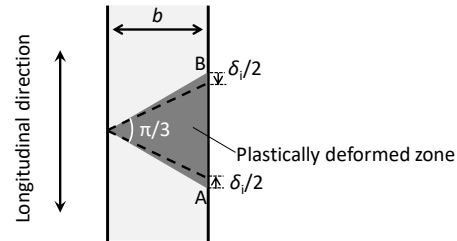


Figure 7: Plastically deformed yield zone by in-plane force

### 3.3 Outline of the analysis models and evaluation results

Fig.8 shows the outline of the plastic mechanism analysis models which we assumed in this paper. Fig.8(a) is the model that assumed the local buckling, Fig.8(b) is the model of the distortional buckling, and Fig.8(c) is the global buckling. Based on the experimental results, we assumed axisymmetric analysis models. In these analyses, we assumed that the steel material shows a rigid-plastic stress-strain relationship, and its strength is equal to the yield stress which is obtained from the tensile coupon test (see Table.2). Besides, the calculation pitch of the axial deformation  $\delta$  in the analyses is 0.01 mm.

In the case of local buckling, we refer to the plastic mechanism of the stub column compression test (Morino(2003)). The model consists of yield lines and yield zones. Based on the collapse modes by experiment, we assumed that the hatched yield zone has an equilateral triangle shape and evaluate the buckling length as  $b_f \tan(\pi/6)$ . Besides, we assumed that the web plate element and lip element keep the parallel position out of the local deformation. By using these assumptions, we could define the rotational angle of the yield lines based on the magnitude of the axial deformation  $\delta$  without any iterative calculation.

In the case of the distortional buckling, we assumed that the angle between line AB and line AC is equal to  $\pi/2$  and the angle between AC and AD is equal to  $\pi/3$  based on the collapse mode by experiments. By assuming these two angles, we could define all yield lines and yield zone based on the section shapes.

In the case of the global buckling, we assumed the plastic mechanism which consists of the yield zones as shown in Fig.8(c). The hatched area is the yield zone which we assumed. At the flange plate, we assumed that the length between the neutral axis and the lip equal to the  $\alpha b_f$  ( $\alpha$  is the constant value from 0 to 1), and assumed that two triangle yield zone appeared. Note that, the  $\alpha b_f$  was defined to

minimize the strength of the lipped-C channels by an iterative calculation. At the web plate and lip plates, we assumed that the rectangular areas were plastically deformed in the longitudinal direction.

Besides, when we use the local buckling model or the distortional buckling model, we should define the  $n$  (the ratio of the existing stress to the yield stress at the yield line) in Eq.(3). Thus, considering that the maximum strength by experiments and the nominal strength by DSM corresponded well, we assumed that the  $n$  equal to the  $P_{DSM}/P_y$  (the ratio of nominal strength by DSM to the yield strength).

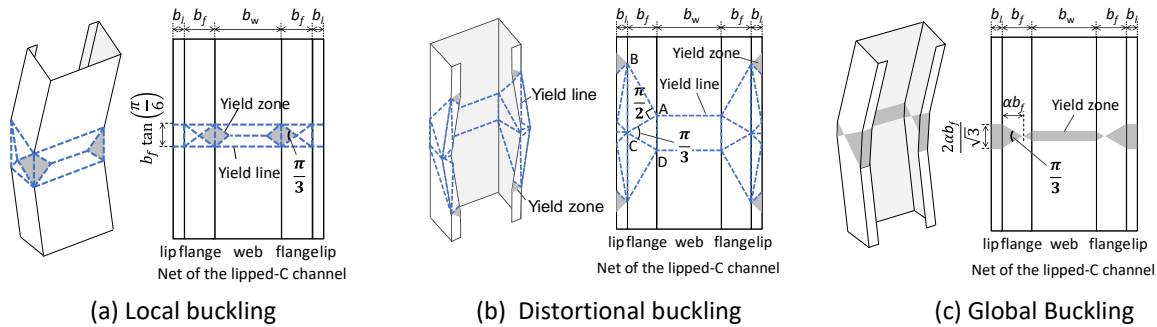


Figure 8 Outline of plastic mechanism analysis models

Fig.9 shows a comparison between experimental results and analysis results. The vertical axis is the member strength and the horizontal axis is the deformation in the longitudinal direction. The solid line is the experimental results and the broken line is the evaluation result by the proposed plastic mechanism. Although some specimens still have room for improvement, the calculation results mostly corresponded well with the experimental results.

In the case of the specimens No.1, 2, 7, and 8, the plastic mechanism analysis evaluates the maximum strength conservatively, and the analysis results gradually got closer to the experimental results along with the increase of the axial deformation. In the case of these four specimens, the elastic local buckling strength by eigenvalue analysis was lower than the maximum strength by experiments (see Table.2 and Table.3), so that they occurred the post-buckling behavior. The elastic local buckling is the buckling mode of the plate elements, therefore it was assumed that the specimen stored the large elastic strain energy caused by the elastic local buckling. On the other hand, the plastic mechanism analysis assumed the buckling mode that the local deformation has already been concentrated and did not consider the effect of the elastic strain energy by the elastic local buckling. Because of this difference, the proposed model seemingly provided conservative results around maximum strength.

In the case of the specimen No.6, although the maximum strength by analysis and experiment showed a good correspondence, the analysis results underestimated the member strength after reaching maximum strength. As shown in Table.2 and Table.3, the elastic buckling strength of the specimen No.6 is higher than the maximum strength by experiment so that it could be considered that the specimen has the high potentiality to resist a local buckling behavior. Even in the experiment, any local deformation was not observed when the specimen reaching maximum strength. Therefore, we surmise that the specimen occurred the local buckling during the strength deterioration. Because the specimen changed its buckling mode after reaching maximum strength, the plastic mechanism model which proposed based on the collapse mode after experiment resulting an underestimation.

Where, this paper investigated a relatively small number of the test results (only 10 specimens), so that there still exists a possibility that finding the other collapse modes of a lipped-C channel member.

Convincing the validity of the proposed analysis method in this paper by numerical and experimental investigations of the different section shapes is an issue in the future.

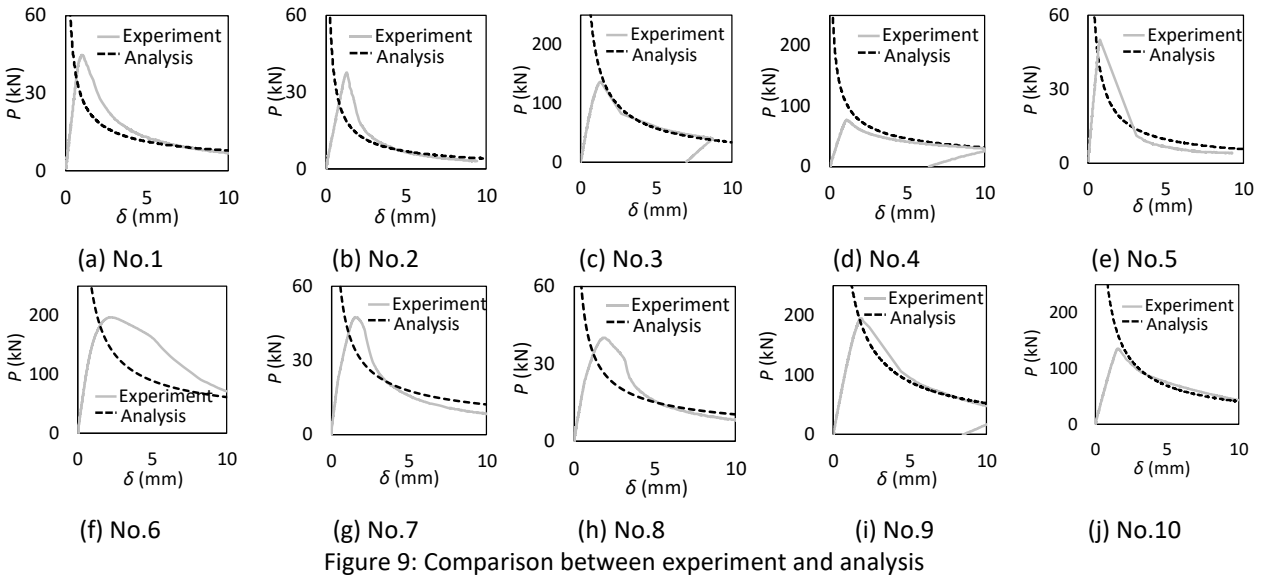


Figure 9: Comparison between experiment and analysis

#### 4. Conclusions

The collapse behavior of the axially compressed long column members with the lipped-C cross-section was investigated in this paper. A total of ten specimens with six different cross-sections were tested, and the three plastic mechanisms of the long column subject to the axial compression were proposed, based on the collapse modes by experiment.

The plastic mechanism analysis results mostly corresponded well with the experimental results, but some specimens which showed a post-buckling behavior were evaluated their strength conservatively. In the case of these specimens, they gradually changed their buckling mode after reaching the maximum strength along with the increase of the axial deformation. This buckling mode change was resulting the difference of the mode between the plastic mechanism and the experimental result. Therefore, developing a method to clarify the collapse mode after reaching the maximum strength will become an issue in the future.

#### References

- Iyama, Z., Matsuo, R., Kishiki, S., Ishida, T., Azuma, K., Kido, M., Iwashita, T., Sawada, K., Yamada, T., Seike, T., (2018). "Outline of reconnaissance of damaged steel school buildings due to the 2016 Kumamoto earthquake." *AIJ Journal of technology and design*, Vol.25 No.59 183-188 (in Japanese).
- Morino, S., Kawaguchi, J., Mizuno, Y., and Hanya, K., (2003). "Distortional Buckling of light-gauge lipped channel short columns." *Steel Structures*, Vol. 3, 203–207.
- Kotełko, M. (2004) "Load-capacity estimation and collapse analysis of thin-walled beams and columns – Recent advances", *Thin-Walled Structures* 42(2) 153-175.
- Ungureanu, V., Kotełko, M., Mania, R.J. & Dubina, D. 2010. Plastic mechanisms database for thin-walled cold-formed steel members in compression and bending. *Thin-Walled Structures* 48(10-11): 818-826
- Ungureanu, V., Kotełko, M., Karmazyn, A. and Dubina, D.(2018). "Plastic mechanisms of thin-walled cold-formed steel members in eccentric compression"
- AISI. 2016. *North America Specification for the Design of Cold-Formed Steel Structural Members* 2016 edition. Washington DC: American Iron and Steel Institute.

## Interaction of stiffened and unstiffened element buckling modes in CFS plain channel compression members

K. C. Kalam Aswathy<sup>1</sup> and M. V. Anil Kumar<sup>2</sup>

### Abstract

Plain channel compression members are composed of stiffened (web) and unstiffened (flanges) plate elements. Effective width method (EWM) for the design of cold-formed steel (CFS) compression members accounts for unstiffened and stiffened plate elements through plate buckling coefficient,  $k$  of 0.425 and 4.0, respectively in the elastic local buckling stress ( $f_{cr}$ ) calculation. The more recent direct strength method (DSM) recommends the local buckling strength equations for the design of plain channel compression members. A lipped stub channel compression member undergoes interaction of local buckling initiated by the stiffened elements and distortional buckling initiated by the partially stiffened flange-lip assembly. Based on finite element analysis (FEA) results, it is demonstrated that such an interaction between buckling modes initiated by the stiffened web and unstiffened flanges is possible in plain channel compression members also. The behavior of plain channels can be represented as an interaction of buckling of the unstiffened flange and stiffened web elements, which is equivalent to local-distortional interaction in lip stiffened channels. The deformation plots are also provided to understand these mode interactions. The present study focuses on stub columns and does not consider the interaction of global buckling mode.

### 1. Introduction

CFS members are manufactured by press-breaking or cold-rolling thin steel sheets to the required cross-sectional shapes at room temperature. Plate elements in CFS sections having one and both the longitudinal edges supported are classified as unstiffened and stiffened elements, respectively (Fig. 1a). The edge stiffened flanges are classified as stiffened or partially stiffened depending on the rigidity of the edge stiffener (Fig. 1b). Stub CFS lip stiffened channel compression members may undergo failure modes such as yielding of the material, local buckling of the plate elements, distortional buckling of the cross-section in addition to interaction between these modes as shown in Fig. 1c. The out-of-plane deformation of the plate elements due to the large plate width to thickness ratio ( $b/t$  or  $h/t$ ) with no translation of plate juncture is classified as local buckling. Buckling mode involving the rotation of the flange-lip assembly about the flange-web juncture is classified as distortional buckling which occurs due to insufficient rigidity of the edge stiffener to restrain the movement of the flange-lip juncture (Fig. 1c). The results presented in this study are on plain channel compression members which may be considered as a limiting case of lip-stiffened channels when lip depth ( $d$ ) tends to zero.

<sup>1</sup> K. C. Kalam Aswathy, M. V. Anil Kumar, Department of Mechanical Engineering, Anna University, Chennai, India. Email: kalam@annauniv.edu, anilkumar@annauniv.edu  
<sup>2</sup> K. C. Kalam Aswathy, M. V. Anil Kumar, Department of Mechanical Engineering, Anna University, Chennai, India. Email: kalam@annauniv.edu, anilkumar@annauniv.edu

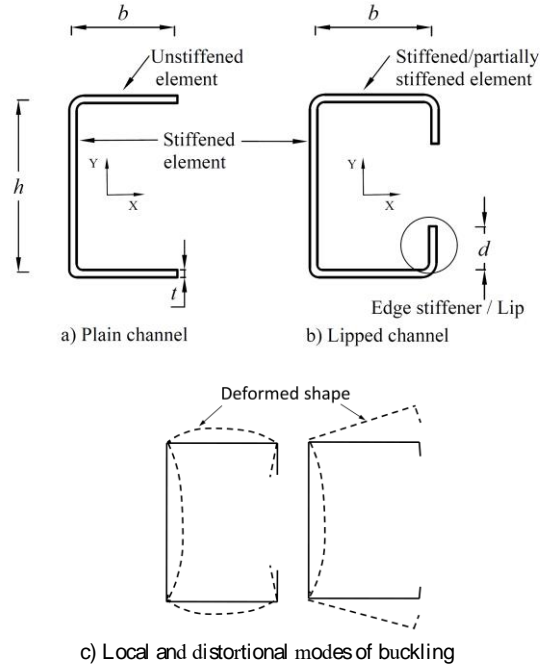


Figure 1: Types of plate elements and buckling modes in CFS sections

The two commonly used design methods for CFS plain channel compression members are the effective width method (EWM) and direct strength method (DSM) [AISI 2016; AS/NZS 2018]. EWM accounts for the stiffened and unstiffened elements using plate buckling coefficients,  $k = 4.0$  and  $0.425$ , respectively in the elastic local buckling stress,  $f_{cr1}$  calculation (Eq. 1). The normalized ultimate strength ( $P_{ul}/P_y$ ) of the section is the summation of  $P_{ul}/P_y$  of individual plate elements of the cross-section which may be computed using Eq. 2 where  $\lambda_l = \sqrt{f_y/f_{cr1}}$ , is the nondimensional slenderness of the individual plate elements. DSM has semi-empirical equations to compute the strength of the member corresponding to different buckling modes based on the corresponding elastic buckling stresses or non-dimensional slenderness values of the whole member. Kumar and Kalyanaraman (2010) indicated that DSM local buckling (referred to as DSM-LB here after) strength equation (Eq. 3) can be used for plain channel compression members. NAS (2016) and AS/NZS (2018) recommends the DSM-LB equation for the calculation of strength of plain channel compression members.

$$f_{cr1} = \frac{k\pi^2 E}{12(1 - \nu^2)(\frac{b}{t})^2} \quad (1)$$

$$\frac{P_{ul-EWM}}{P_y} = \begin{cases} 1 & \lambda_l \leq 0.673 \\ \left(1 - \frac{0.22}{\lambda_l}\right) \frac{1}{\lambda_l} & \lambda_l > 0.673 \end{cases} \quad (2)$$

$$\frac{P_{ul-DSM}}{P_y} = \begin{cases} 1 & \lambda_l \leq 0.776 \\ \left(1 - \frac{0.15}{\lambda_l^{0.8}}\right) \frac{1}{\lambda_l^{0.8}} & \lambda_l > 0.776 \end{cases} \quad (3)$$

In DSM, although the distortional buckling equations are also recommended for the design of lipped channels (Fig. 1b) with partially stiffened flanges (small values of  $d$ ), the plain channels which can be considered as limiting case of lipped channel having  $d = 0$  (Fig. 1a) are designed using only local buckling equations. Therefore there is some inconsistency in the current specifications (Schafer and Adany 2005; Bambach 2009). Aswathy and Kumar (2020), demonstrated that both elastic buckling stress and ultimate strength of unstiffened plates can be accurately represented using distortional buckling equations. The modified DSM equation (denoted as MDSM-DB) proposed by Kumar and Kalyanaraman (2014) (Eq. 4) based on test and FEA results of sections that are prone to pure distortional buckling (i.e., no local or global buckling) can be extended for the calculation of unstiffened elements also. Here  $\lambda_d [= \sqrt{(f_y/f_{crd})}]$  is the distortional buckling slenderness which is a function of the elastic distortional buckling stress,  $f_{crd}$ . Hence the work presented in the paper is an attempt to represent the behavior of stub plain channel compression member as local-distortional interaction and extend the interaction equation (IE) developed for lipped channels to plain channels also.

$$\frac{P_{ud-MDSM}}{P_y} = \begin{cases} 1 & \lambda_d \leq 0.474 \\ \left(1 - \frac{0.23}{\lambda_d^{0.6}}\right) \frac{1}{\lambda_d^{0.6}} & \lambda_d > 0.474 \end{cases} \quad (4)$$

Kumar and Kalyanaraman (2018) had proposed an interaction equation (Eq. 5) which can account for all the buckling mode interactions. Here,  $P_{ul}/P_y$ ,  $P_{ud}/P_y$  and  $P_{ue}/P_y$  are the normalized ultimate strengths in local, distortional and global modes of buckling, respectively. The local buckling strength is calculated using Eq. 6 (Kumar and Kalyanaraman 2012), which is a function of web height to flange width ratio,  $h/b$  in addition to nondimensional local buckling slenderness,  $\lambda_l$ . The effect of  $h/b$  ratio is accounted for using  $\alpha_1$  and  $\beta$  and  $P_{ul,max}/P_y$  represents the upper bound of this equation. The distortional buckling strength ( $P_{ud}/P_y$ ) is computed using Eq. 4.

$$\frac{P_{ulde}}{P_y} = 0.15 + \left( \frac{P_{ul}}{P_y} \times \frac{P_{ud}}{P_y} \times \frac{P_{ue}}{P_y} \right) \leq \text{Min} \left[ \frac{P_{ul}}{P_y}, \frac{P_{ud}}{P_y}, \frac{P_{ue}}{P_y} \right] \quad (5)$$

$$\frac{P_{ul}}{P_y} = \begin{cases} 1 & \lambda_l \leq 0.60 \\ \left[ 1 - \alpha_1 \left( \frac{P_{ul}}{P_y} \right)^\beta \right] \left( \frac{P_{ul}}{P_y} \right)^\beta \leq \frac{P_{ul,max}}{P_y} & \lambda_l > 0.60 \end{cases} \quad (6)$$

The elastic buckling and ultimate strength behavior of stiffened and unstiffened elements can be accurately represented using local buckling equations (Bambach 2009) and distortional buckling equations (Aswathy and Kumar, 2020), respectively. This work aims at understanding the interaction of buckling modes initiated by stiffened and unstiffened elements in plain channels which may lead to the plain channel behavior as a case equivalent to interaction of local and distortional buckling modes in lipped channels. Finite element analysis (FEA) is used to understand the behavior of plain channels and understand the influence of the mode interactions on the ultimate strength.

## 2. Finite Element Modeling

The plain channel members with fixed end boundary conditions were modeled in finite element package, ABAQUS using four noded shell elements with reduced integration (S4R) through center line of the plate elements. The load and boundary conditions were applied at the centroid of the cross-section which was connected to the nodes along the end cross-section using stiff beam elements. Initially, an

eigenvalue buckling analysis was done to get the elastic buckling loads and corresponding mode shapes. Non linear analysis using Newton Raphson iteration scheme was performed considering geometric and material non linearity. Mode shapes from eigenvalue analysis was used to seed geometric imperfections using appropriate scaling factors.

### 2.1 Validation of FE Model

The finite element (FE) model was validated by simulating a few test results available in literature [Young and Rasmussen (1998) and Mulligan and Pekoz (1987)]. The dimensions of the specimens modeled ( $b$ ,  $h$ ,  $t$  as shown in Fig. 1) and yield stress ( $f_y$ ) are given in Table 1. The ratio of the ultimate loads from test to that from FEA ( $P_{u-test}/P_{u-FEA}$ ) are also presented in Table-1. The mean,  $\mu$  and standard deviations,  $\sigma$  of  $P_{u-test}/P_{u-FEA}$  indicate the accuracy of the FE model.

Table 1: Comparison of FEA and test results

Specimen	$b$ (mm)	$h$ (mm)	$t$ (mm)	$L$ (mm)	$f_y$ (MPa)	$\lambda$	$P_{u-test}$ (kN)	$P_{u-FEA}$ (kN)	$P_{u-test}/P_{u-FEA}$ (kN)
SC 60x30 <sup>a</sup>	41.48	78.38	1.219	253.49	226	1.30	32.93	31.19	1.06
SC 180x60 <sup>a</sup>	76.30	221.28	1.219	634.49	226	2.99	37.83	36.77	1.03
P36F1000 <sup>b</sup>	35.53	95.43	1.48	1000.2	550	1.73	59.00	64.72	0.91
P36F2500 <sup>b</sup>	35.64	95.83	1.48	2499.4	550	1.86	32.80	34.39	0.95
								Mean, $\mu$	0.99
								Standard deviation, $\sigma$	0.07

a – Young and Rasmussen (1998); b – Mulligan and Pekoz (1987)

## 3. Interaction of Buckling Modes in Plain Channels

The displacement plots from FEA are used in this section to demonstrate that the buckling of plain channels may be initiated by buckling of either the unstiffened flanges or the stiffened web. Thus the behavior of these members may be considered as a combination of the stiffened and unstiffened element buckling modes. This section aims at understanding the buckling mode interactions in plain channel compression members and its effect on the ultimate strength.

### 3.1 Mode interactions

To identify whether there is interaction between buckling modes initiated by stiffened and unstiffened elements in plain channels, the out-of-plane deformation of the web along the length is plotted using the results obtained from ABAQUS at load step corresponding to ultimate load. The plain channel specimens with  $h= 100\text{mm}$ ,  $b= 100\text{mm}$ ,  $L= 250\text{mm}$  and  $f_y= 250\text{MPa}$  are used for this plot. Figure 2a presents the out-of-plane deformation normalized with respect to the maximum deformation ( $U/U_{max}$ ) of the web. When the buckling is initiated by the web (stiffened element), the buckling mode corresponds to multiple half waves of wavelength approximately equal to the width of the web plate and is denoted as stiffened element mode in Fig. 2a. Similarly, when it is initiated by the flanges (unstiffened elements), the buckle half waves are much longer and denoted as unstiffened element mode Fig. 2a.

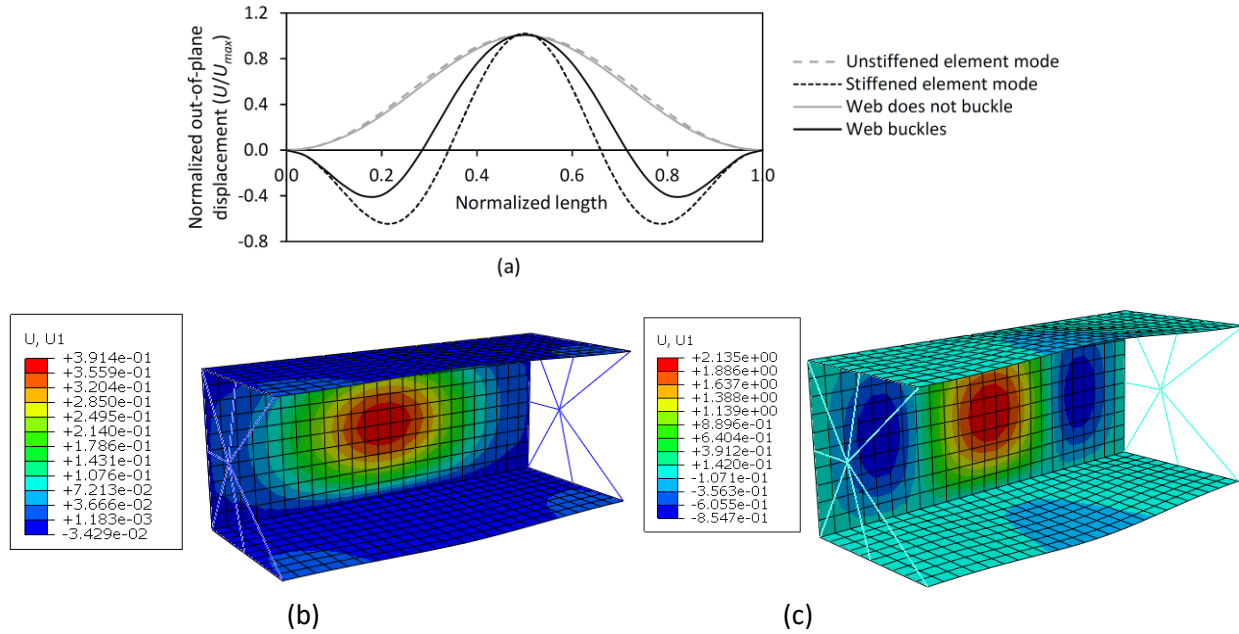


Figure 2: Out-of-plane deformation of web (a) normalized displacement plot; displacement contours of web when: (b) web does not buckle and (c) web buckles

Along with the normalized out of plane deformation ( $U/U_{max}$ ) in the web plate corresponding to stiffened (local) and unstiffened (distortional) buckling modes, web deformation in load step corresponding to the ultimate load from FEA model of two stub plain channel members are also plotted in Fig. 2. The  $h/t$  ratios of the web of these two specimens are chosen such that in one case the web buckles [ $h/t > 1.901v(E/f_y)$ ;  $79.1 > 55.1$ ] along with the flange and in the other case it does not [ $h/t < 1.901v(E/f_y)$ ;  $31.5 < 55.1$ ]. When the web does not buckle, the deformation plot corresponds to the unstiffened element mode. When the web buckles, it is observed that the deformation plot is a combination of the stiffened and unstiffened modes (Fig. 2a). The corresponding contour plots from ABAQUS for these cases are included in Fig. 2b and 2c, respectively. This confirms that there can be a combination of stiffened and unstiffened modes of buckling in plain channels which is equivalent to a local distortional interaction phenomena in lipped channels.

### 3.2 Ultimate strength

To understand the influence of the interaction of buckling modes on the ultimate strength, plain channels with a constant non-dimensional slenderness,  $\lambda [=v(f_y/f_{cr})$ ; where  $f_{cr}$  is the critical elastic buckling stress obtained from eigenvalue analysis] and varying  $h/b$  ratios were analyzed to determine the ultimate load. Stub plain channels having  $b= 100\text{mm}$ ,  $L= 250\text{mm}$ , and  $h/b$  varying from 0.50 to 3.0 were modeled. The constant  $\lambda$  value was achieved by adjusting  $f_y$  and  $t$ . The ultimate strength normalized with yield load ( $P_u/P_y$ ) obtained from FEA and the theoretical predictions using EWM, DSM and interaction equation (IE) (Eqs. 2, 3 and 5 represents as EWM, DSM-LB and IE, respectively) are also plotted in Fig. 3. In IE  $P_{ud}/P_y$  and  $P_{uf}/P_y$  are computed using Eq. 4 and 6 respectively. In this work  $P_{ue}/P_y = 1$ , as stub members are used.

It is observed that there is a decrease in ultimate strength up to 20.5 % with increase in  $h/b$  ratio due to interaction of stiffened and unstiffened buckling modes compared to the cases where there is no interaction. The DSM-LB equation is found to give comparable predictions of the ultimate strength whereas EWM gives conservative predictions. But since both the methods does not account for interaction of buckling modes, the variation of strength with respect to  $h/b$  is not accurately represented. The buckling interaction equation (IE) can trace this trend for plain channel compression members and shows slightly better accuracy.

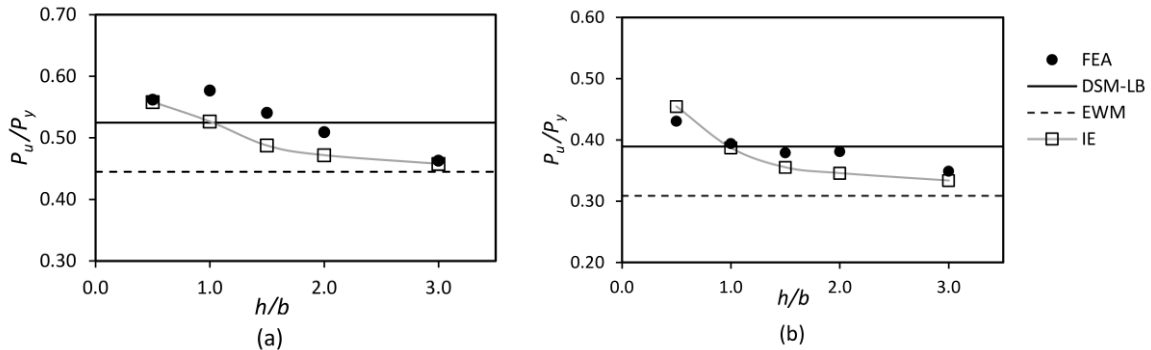


Figure 3: FEA results for plain channels a)  $\lambda = 2.0$ ; b)  $\lambda = 3.0$

The strength predictions using interaction equation (Eq. 5; denoted as IE), EWM (Eq. 2) and DSM-LB (Eq. 3) against 13 test results from literature [Young and Rasmussen (1998); Mulligan and Pekoz (1987) and Talja (1990)] and 26 FEA results generated as part of this work are plotted in Fig. 4. The statistics of the ratio of the ultimate strength from FEA or test and theoretical predictions ( $P_{u-Fea,Test}/P_{u-Theory}$ ) are also given in Table 2. The statistics of  $P_{u-Fea,Test}/P_{u-Theory}$  indicates that both IE and DSM-LB methods give accurate strength predictions for plain channel compression members. There is a slight improvement in standard deviation when the ultimate strength is calculated using IE. Thus indicates that plain channels can also accurately be represented as a case of local distortional interaction phenomena and existing interaction equations can be extended for plain channel compression members also.

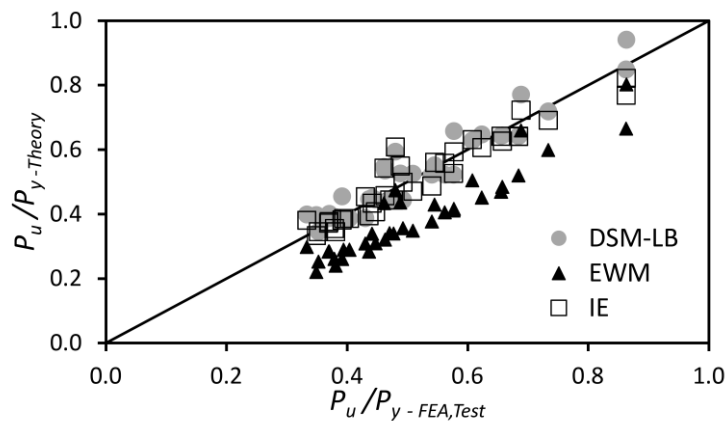


Figure 4:  $P_u/P_{y-Theory}$  vs.  $P_u/P_{y-Fea,Test}$

Table 2: Statistics of  $P_{u-Fea,Test}/P_{u-Theory}$ 

Statistical descriptors	$P_{u-Theory}$		
	DSM-LB	EWM	IE
Number, $n$	39	39	39
Mean, $\mu$	0.98	1.33	1.02
Standard deviation, $\sigma$	0.083	0.147	0.076
Maximum	1.11	1.59	1.12
Minimum	0.81	1.01	0.79

#### 4. Conclusions

From the comparison of deformation plots obtained from FEA, it is concluded that there is an interaction between the stiffened and unstiffened element buckling modes in plain channel compression members, which is equivalent to local-distortional buckling interaction in lip stiffened channels. Even though not very significant in magnitude, the interaction of buckling modes may lead to reduction up to 20% in ultimate strength compared to the specimens where interaction is not present. Hence the interaction equation (Eq. 5) which was originally developed for the lipped channels considering the local and distortional buckling strengths are found to be appropriate for the strength of plain channels also. The current DSM-LB (Eq. 3) equation is also found to give comparable strength prediction of these sections. This work may lead to unifying current design procedure irrespective of the type of plate elements (stiffened, partially stiffened or unstiffened) in CFS compression members.

#### References

- ABAQUS. [Computer software]. *ABAQUS standard user's manual, Version 6.8*. Dassault Systemes Simulia, Providence, RI.
- American Iron and Steel Institute (AISI) (2016). *North American Specification for the design of cold-formed steel structural members, S136-16*, Washington, DC.
- Australian/New Zealand Standard (AS/NZS) (2018). *Cold-formed steel structures, AS/NZS 4600:2018*, Sydney, Australia.
- Bambach, M. (2009). "Design of uniformly compressed edge-stiffened flanges and sections that contain them." *Thin-Walled Struct.*, 47(3), 277–294.
- Kalam Aswathy, K. C., & Anil Kumar, M. V. (2020). Unstiffened Elements as Limiting Case of Distortional Buckling of Partially Stiffened Elements. *Journal of Struct. Eng.*, 146(9), 04020171.
- Kumar, M. A. and Kalyanaraman, V. (2010). "Evaluation of direct strength method for CFS compression members without stiffeners." *J. Struct. Eng.*, 136(7), 879–885.
- Kumar, M. A. and Kalyanaraman, V. (2012). "Design strength of locally buckling stub-lipped channel columns." *J. Struct. Eng.*, 138(11), 1291-1299.
- Kumar, M. A. and Kalyanaraman, V. (2014). "Distortional buckling of CFS stiffened lipped channel compression members." *J. Struct. Eng.*, 140(12), 04014099.
- Kumar, M. A. and Kalyanaraman, V. (2018). "Interaction of Local, Distortional, and Global Buckling in CFS Lipped Channel Compression Members." *J. Struct. Eng.*, 144(2), 04017192.
- Mulligan, G. P., & Pekoz, T. (1987). "Local buckling interaction in cold-formed columns." *J. Struct. Eng.*, 113(3), 604-620.
- Schafer, B. W. and Adany, S. (2005). "Understanding and classifying local, distortional and global buckling in open thin-walled members." *Tech. Session and Mtg., Structural Stability Research Council*. Montreal, Canada.
- Talja, A. (1990), "Design of the buckling resistance of compressed HSS channels." *Research Note No. 1163, Technical Research Centre of Finland*.
- Young, B., & Rasmussen, K. J. (1998). "Tests of fixed-ended plain channel columns." *J. Struct. Eng.*, 124(2), 131-139.

## A reduced model for nonlinear analysis and design of thin-walled structures prone to multi-modal buckling

Domenico Magisano<sup>1</sup>, Francesco Liguori<sup>1</sup>, Leonardo Leonetti<sup>1</sup>, Antonio Madeo<sup>1</sup>, Giovanni Garcea<sup>1</sup>

### Abstract

The Koiter method is a reduction technique based on a multi-modal quadratic asymptotic expansion of the finite element model for recovering the equilibrium path of an elastic structure prone to buckling. Its main feature is the possibility of performing an inexpensive sensitivity analysis to geometrical imperfections by including the effects of the deviations in the reduced model of the perfect structure. The method is so efficient that can be used for optimal design of slender structures, where it provides the collapse load associated to each set of design parameters taking into account the nonlinear behaviour and the worst-shape imperfection at a computational cost similar to a linearised buckling analysis.

### 1 Introduction

Thin-walled beams and shells are commonly used as primary components in structure engineering, due to their high specific strength and stiffness, which allow weight and material economy. Their load-carrying capabilities are often determined by buckling, which often occurs for loads much lower than the failure loads of materials [1]. The path-following strategy is the standard approach employed to analyze the nonlinear elastic behavior of this kind of structure. Once the continuum problem has been discretized using the finite element method, the equilibrium path of the structure is traced step-by-step, solving a nonlinear system of equations, where the unknowns are the FE degrees of freedom and the load factor. As a consequence of modal buckling interaction, shell-like structures may exhibit a very unstable post-buckling behavior and may be highly sensitive to initial imperfections, especially to geometrical imperfections [2, 3]. In light of this an imperfection sensitivity analysis becomes mandatory. It consists in seeking the so-called worst (detrimental) imperfection cases [4, 5], which are the shapes of the geometrical imperfections associated with the minimum limit load (safety factor). The Monte Carlo simulation generally adopted to this end may require thousands of equilibrium path evaluations. The use of composite structures, which require a layup optimization, further complicates the design process. Standard path-following approaches, aimed at recovering the equilibrium path for a single loading case and assigned imperfections, are not suitable for this purpose because of the high computational burden of the single run, and are unusable if no information about the worst imperfection shapes is available. The Koiter method represents a valid alternative for analyzing and designing thin-walled structures prone to buckling [6, 7, 8, 9, 10, 11, 12]. It recovers the equilibrium path of an elastic structure using a reduced model, in which the FE model is replaced by its second order asymptotic expansion using the initial path tangent, the first significant  $m$  buckling modes and the corresponding second order modes, named quadratic correctives. In this way, once the reduced model is built, the equilibrium path of the structure can be obtained by solving the nonlinear reduced system of  $m$  equations in  $m+1$  unknowns, which represent the modal amplitudes and the load factor. The coefficients of the reduced system are evaluated

<sup>1</sup>Dipartimento di Ingegneria Informatica, Modellistica, Elettronica e Sistemistica  
Università della Calabria 87036 Rende (Cosenza), Italy

using strain energy variations up to the 4th order. Shell structures can require a very large number of FE DOFs to avoid significant discretization errors, while  $m$  is usually at most a few tens. Clearly the convenience of the method with respect to the standard path-following strategy is evident. However, its most attractive feature is the possibility of efficiently performing sensitivity analysis by including a-posteriori the effects of the imperfections in the reduced nonlinear equations of the reduced model. Nevertheless, the state-of-the-art a-posteriori account of geometrical imperfections is based on the hypothesis of linear pre-critical behaviors and small imperfection amplitudes, that leads to additional terms in the reduced system which are just linear in the load factor. As a consequence, inaccuracies occur even for small pre-critical non-linearities and significant imperfection amplitudes, considerably limiting the application of the method. One of the goal of this work is to overcome these inaccuracies with a new accurate treatment of the geometrical imperfections. The asymptotic expansion of the perfect structure is corrected by adding a series of new modes, generated by the imperfection. In this way a more accurate formula for the additional imperfection terms in the reduced system is derived, which coherently takes into account the effects of the geometrical imperfection up to the 2nd order, without losing the advantages of the a-posteriori account [13]. In this work, the initial full model is built by a solid-shell discretization of the structure, with no limitation on geometry and boundary conditions. Linear locking free finite elements are firstly considered. Moreover, an isogeometric discrete model [14] is proposed, exploiting the NURBS interpolation functions to describe accurately the geometry and the high continuity typical of the displacement field in buckling problems and to directly link the CAD model to the structural one. A linear interpolation is then adopted through the thickness together with a modified generalized constitutive matrix, which allows us to easily eliminate thickness locking and model multi-layered plates and shells. Reduced integration schemes, which take into account the continuity of the shape functions, are used to avoid interpolation locking and make the integration faster. A Mixed Integration Point strategy makes it possible to transform the displacement model into a mixed (stress-displacement) one, required by the Koiter method to obtain accurate predictions, without introducing stress interpolation functions. The result is an efficient numerical tool for buckling and initial post-buckling analysis of composite shells, characterized by a low number of DOFs and integration points and by a simple and quick construction of the reduced model.

A large number of numerical tests, regarding non-linear buckling problems, modal interaction, unstable post-critical and imperfection sensitive structures, are presented in order to validate three different points: 1) the accuracy of reduced model compared to a path-following analysis with the full discrete model, 2) the accuracy of the new formula proposed to include the effects of imperfections directly in the reduced model of the perfect structure and 3) the low number of variables needed by the NURBS-based solid-shell discrete model used for modeling the structure and evaluating the ingredients of the reduced model.

Finally, case studies are also reported to show how the efficiency of the method makes it suitable for structural design and optimization, where the reduced model is used for a quick evaluation of the structural response [15].

## 2 Koiter method

An imperfection sensitivity analysis based on the Koiter method [13] is presented for detecting the worst-shape imperfection. The starting point is a solid-shell FE model [16, 17, 18]. The equilibrium equations, once the structure is discretized using the FE method, can be written as

$$\mathbf{r}[\lambda, \mathbf{u}] = \mathbf{s}[\mathbf{u}] - \lambda \hat{\mathbf{p}} = \mathbf{0} \quad (1)$$

where  $\mathbf{r}$  is the residual vector,  $\mathbf{s}$  is the internal force vector,  $\hat{\mathbf{p}}$  is the reference load vector,  $\mathbf{u}$  are the FE variables and  $\lambda$  is the load factor. Equation (1) defines a curve in the space  $\mathbf{u} - \lambda$ , that is the equilibrium path of the structure. This nonlinear system, whose size is defined by the number of FE variables required to approximate the continuum problem, is usually solved by means of standard Riks arc-length strategies [19]. The Koiter method described in [17] represents an effective alternative because, using a ROM, provides an approximated solution of (1) by means of a reduced system of equations. The steps of

the Koiter method are briefly recalled. It uses a nonlinear Cauchy continuum based on a Green strain measure and a hybrid (stress-displacement) solid-shell FE model. In this way the strain energy has a cubic polynomial dependence only from the configuration variables. The algorithm starts with the so-called perfect structure analysis, to be performed once and for all for assigned material data, which consists in the construction of a ROM and the corresponding reduced nonlinear equations defining the equilibrium path of the structure with no imperfections. The geometrical imperfections are then included directly in the reduced equations of the perfect structure by simply changing some terms, allowing an efficient sensitivity analysis.

## 2.1 Perfect structure analysis

The construction of the ROM of the perfect structure consists of the following steps.

1. The initial path tangent  $\hat{\mathbf{u}}$  is evaluated by solving the linear system

$$\mathbf{K}_0 \hat{\mathbf{u}} = \hat{\mathbf{p}} \quad (2a)$$

where  $\mathbf{K}_0 \equiv \mathbf{K}[\mathbf{0}]$  is the tangent matrix evaluated at the rest configuration.

2. A restricted number  $m$  of linearised buckling modes and loads can be obtained by the following eigenvalue problem

$$\mathbf{K}[\lambda] \dot{\mathbf{v}} \equiv (\mathbf{K}_0 + \lambda \mathbf{K}_1[\hat{\mathbf{u}}]) \dot{\mathbf{v}} = \mathbf{0} \quad (2b)$$

where  $\mathbf{K}_1[\hat{\mathbf{u}}]$  is the geometric matrix.

3. The  $m \times (m + 1)/2$  quadratic correctives  $\mathbf{w}_{ij}, \hat{\mathbf{w}} \in \mathcal{W}$  are obtained, adopting a Lagrangian multiplier approach, by the solution of the linear systems ( $i = 1 \dots m, j = i \dots m$ )

$$\begin{cases} \mathbf{K}_b \mathbf{w}_{ij} + \mathbf{p}_{ij} = \mathbf{0} \\ \mathbf{w}_{ij}^T \mathbf{K}_1[\hat{\mathbf{u}}] \dot{\mathbf{v}}_k = 0, \quad k = 1 \dots m \end{cases} \quad \begin{cases} \mathbf{K}_b \hat{\mathbf{w}} + \mathbf{p}_{00} = \mathbf{0} \\ \hat{\mathbf{w}}^T \mathbf{K}_1[\hat{\mathbf{u}}] \hat{\mathbf{u}} = 0. \end{cases} \quad (2c)$$

where  $\mathbf{K}_b = \mathbf{K}[\lambda_b]$ ,  $\lambda_b$  being a representative value of the buckling loads cluster, usually chosen as the first linearised buckling load, and

$$\mathbf{p}_{ij} = \mathbf{K}_1[\dot{\mathbf{v}}_i] \dot{\mathbf{v}}_i, \quad \mathbf{p}_{00} = \mathbf{K}_1[\hat{\mathbf{u}}] \hat{\mathbf{u}}.$$

The solution of Eq.(2c) can be obtained adopting the iterative scheme proposed in [17] which uses the already decomposed matrix  $\mathbf{K}_0$ .

4. The ROM of the perfect structure then assumes the following form

$$\mathbf{u}_d[\lambda, \xi_i] = \lambda \hat{\mathbf{u}} + \sum_i \xi_i \dot{\mathbf{v}}_i + \frac{1}{2} \sum_{ij} \xi_i \xi_j \ddot{\mathbf{w}}_{ij} + \frac{1}{2} \lambda^2 \hat{\mathbf{w}} \quad (2d)$$

where  $\xi_i$  are the modal amplitudes.

5. The reduced system of equations can now be obtained projecting the equations  $\mathbf{r}[\lambda, \mathbf{u}_d] = \mathbf{0}$  in directions  $\dot{\mathbf{v}}_i, i = 1..m$ , and maintaining the terms up to the 3rd order in  $\xi$ . It can be written as

$$\begin{aligned} r_k[\lambda, \xi_i] \equiv & \mu_k[\lambda] + (\lambda_k - \lambda) \xi_k - \frac{1}{2} \lambda^2 \sum_{i=1}^m \xi_i \mathcal{C}_{ik} + \frac{1}{2} \sum_{i,j=1}^m \xi_i \xi_j \mathcal{A}_{ijk} \\ & + \frac{1}{6} \sum_{i,j,h=1}^m \xi_i \xi_j \xi_h \mathcal{B}_{ijhk} = 0, \quad k = 1 \dots m \end{aligned} \quad (2e)$$

where the coefficients  $\mathcal{A}_{ijk}$ ,  $\mathcal{C}_{ik}$  and  $\mathcal{B}_{ijhk}$  are scalar quantities evaluated as the sum of element contributions and their expression is reported in [17]. Eqs.(2e) are an algebraic nonlinear system of  $m$  equations in the  $m + 1$  variables  $\lambda, \xi_1 \dots \xi_m$  that, due to the small size of the system, can be efficiently solved using specialized variants of the arc-length scheme.

Once Eq. (2e) is solved, the equilibrium path in terms of FE variables can be recovered substituting  $\lambda, \xi_1 \cdots \xi_m$  in Eq. (2d).

## 2.2 A posteriori account of geometrical imperfections

Geometrical imperfections can easily be included in the analysis. They are expressed by an initial displacement  $\tilde{\mathbf{u}}$ , assumed to be a linear combination of known shapes  $\bar{\mathbf{u}}_i$ ,

$$\tilde{\mathbf{u}} = \sum_{i=1}^n \tilde{\xi}_i \bar{\mathbf{u}}_i. \quad (3)$$

In this work, the imperfection shapes  $\bar{\mathbf{u}}_i$  are chosen as the displacement part of the buckling modes.

The method allows to take account of imperfections in the final stage by simply adding some additional imperfection terms  $\tilde{\mu}_k$  to Eq.(2e) that becomes

$$r_k + \tilde{\mu}_k = 0. \quad (4)$$

Over the years, two different approaches have been developed. The first and more simple one [17], modifies the ROM by simply adding the imperfection vector  $\tilde{\mathbf{u}}$  to the ROM of perfect structure in Eq.(2d)

$$\mathbf{u}_d[\lambda, \xi_i] = \tilde{\mathbf{u}} + \lambda \hat{\mathbf{u}} + \mathbf{v}[\xi_i] + \mathbf{w}[\xi_i, \lambda]. \quad (5)$$

This approach, labelled  $K_{lin}$ , proves to be extremely efficient but accurate only for small imperfection amplitudes and almost linear pre-critical behaviour. A second more accurate strategy, named  $K_{quad}$ , has been recently proposed in [13] and updates the ROM as

$$\mathbf{u}_d[\lambda, \xi_i, \tilde{\xi}_i] = \tilde{\mathbf{u}} + \lambda(\hat{\mathbf{u}} + \tilde{\hat{\mathbf{w}}}) + \sum_i \xi_i(\hat{\mathbf{v}}_i + \tilde{\hat{\mathbf{w}}}_i) + \frac{1}{2} \sum_{ij} \xi_i \xi_j \hat{\mathbf{w}}_{ij} + \frac{1}{2} \lambda^2 \hat{\mathbf{w}}. \quad (6)$$

considering new corrective modes generated by the imperfection. The projection of the FE equations (1) in directions  $\hat{\mathbf{v}}_i, i = 1..m$  using the updated ROMs furnishes the imperfection effects on the ROM of the perfect structure in terms of the additional coefficients  $\tilde{\mu}_k$  in Eq. (4).

## 2.3 A Monte Carlo imperfection sensitivity analysis

The geometrical imperfections are expressed as in Eq.(3) where  $\tilde{\xi}_i$  are uniformly random generated numbers that set the maximum imperfection shape to a fixed value

$$\max |\tilde{\mathbf{u}}| = \tilde{u}_{max}. \quad (7)$$

In this way it is possible to obtain a statistical sample of imperfections and to draw, for each of them, the equilibrium path. As is well known, we can have a stable post-critical behaviour, usually characterised by a reduction in the stiffness, or an unstable post-critical path with limit point. The collapse is reached because the applied load exceeds the limit load or because the stiffness reduction leads to deformations which compromise the usability. This means that the collapse load associated to  $\tilde{\mathbf{u}}$  can be defined as the minimum between the limit load  $\lambda_{lim}$ , if it exists, and the load  $\bar{\lambda}$  related to a fixed displacement of a control point

$$\lambda_c = \min_{\tilde{\mathbf{u}}} \{ \lambda_{lim}(\tilde{\mathbf{u}}), \quad \bar{\lambda}(\tilde{\mathbf{u}}) \}.$$

## 3 Optimal design of a stiffened panel

This section deals with the optimal design of imperfection sensitive shells. Although we focus on seeking optimum layouts for a fixed structural geometry, the procedure is general and can be easily adapted to

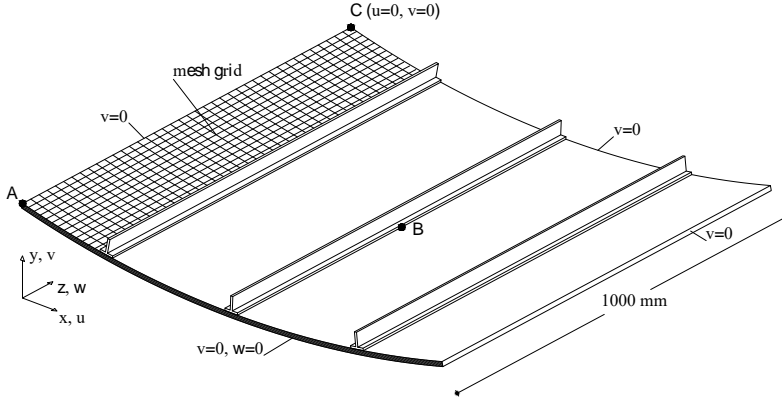


Figure 1: Geometry and boundary conditions.

geometry optimisation. In particular, the optimisation problem consists in searching for the solution which maximizes the collapse load  $\lambda_c$ , as defined in 2.3, that is

$$\begin{aligned} & \underset{\vartheta}{\text{maximize}} && \lambda_c(\vartheta) \\ & \text{subject to} && \vartheta_i \in \{0^\circ, 18^\circ, \dots, 162^\circ, 180^\circ\} \end{aligned}$$

where  $\vartheta_i$  is the fiber orientation of the  $i$ th layer and  $\vartheta$  is the vector collecting all  $\vartheta_i$ . A Monte Carlo method with zooming stages is employed to detect the best stacking sequence [15]. The sensitivity analysis for the detection of the worst imperfection shape, the results provided by the Koiter method with a-posteriori account of the imperfections ( $K_{lin}$ ) are compared with the full FE solution (labelled as *Riks*) obtained using the standard arc-length method.

### 3.1 Stiffened panel

The test regards a curved panel with "T" stiffeners in compression. In Fig.1 an axonometric projection shows the geometry and the boundary conditions, while geometrical details of a section have been pictured in Fig.2. The  $v$  displacement of the lateral faces of the four panels is bounded and the deformation of only one curved edge is constrained, also along  $z$ . In the illustrations, it is possible to see the mesh grid details for the 3D solid-shell description of the structure. The curved faces and the stiffener ends are loaded by a uniform line load  $\lambda = 1$ . The same material is employed for the skin and the stiffeners and it is characterised by  $E_1 = 30.6 \text{ GPa}$ ,  $E_2 = 8.7 \text{ GPa}$ ,  $\nu_{12} = 0.3$ ,  $G_{12} = 3.4 \text{ GPa}$ ,  $G_{23} = 2.9 \text{ GPa}$ , with respect to the local reference system which has the direction 1 aligned with the global direction  $z$  while the direction 3 is along the normal at the middle plane of the skin. The stiffener lamination is supposed to be constant and equal to  $0^\circ$ , while eight layers define the lamination of the skin labelled as  $[\vartheta_1 / \dots / \vartheta_8]$  where every  $\vartheta_i$  is a multiple of  $18^\circ$  and can vary from  $0^\circ$  to  $180^\circ$ . The purpose of the test is studying the variability of the post-critical behaviour when the lamination changes and seeking the laminations with the maximum collapse load. The solutions with minimum collapse load are searched as well, just to identify the range of variability of the structural performances. The collapse load for the stable configurations is the load producing the deformation limit  $w_A = 4 \text{ mm}$ . The buckling modes employed for the ROM of the Koiter analyses correspond to buckling loads which do not exceed 1.5 times the first one. In the first stage,  $N_1 = 2500$  random uniformly generated laminations are analysed and the  $n_1 = 10$  best and the 10 worst laminations (in terms of collapse load), are selected. In the second stage, for each of these configurations, a further  $N_2 = 100$  randomly generated laminations are considered with each layer angle that can vary between  $-36^\circ$  and  $36^\circ$  with an increment of  $18^\circ$  with respect to the likely optimal values identified by the first stage. The curves in Fig.3 plot the collapse load, the two lowest buckling loads  $\lambda_1$  and  $\lambda_2$  and the ratio between the collapse load and the first eigenvalue as a function of a lamination index. This is an integer number which is assigned to each lamination after they are ordered in terms of decreasing collapse load. The laminations with the smallest index have a stable behaviour and collapse for reaching the deformation limit. The buckling loads in these cases

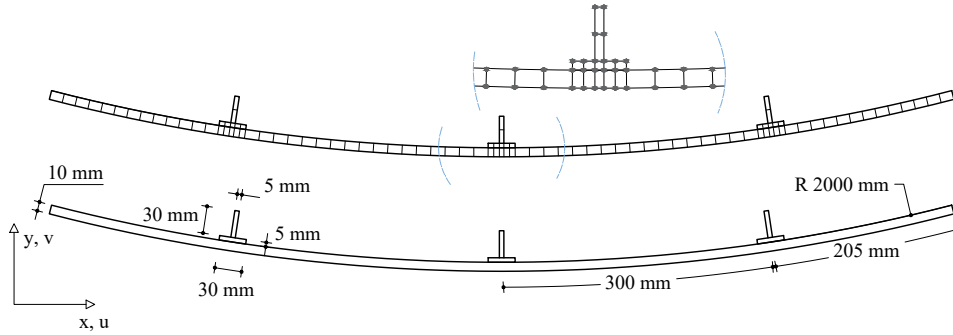


Figure 2: Section geometry and mesh.

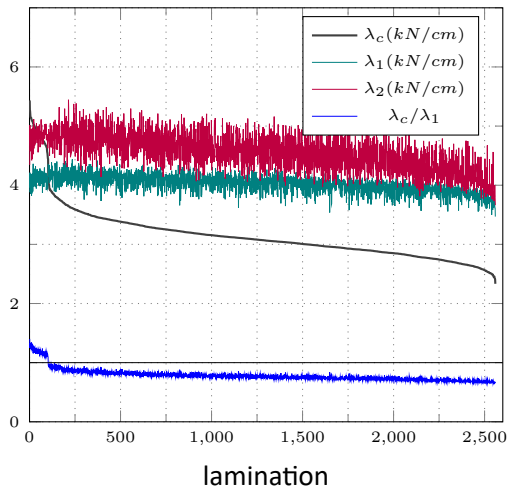


Figure 3: Collapse load and linearised buckling loads at stage 1.

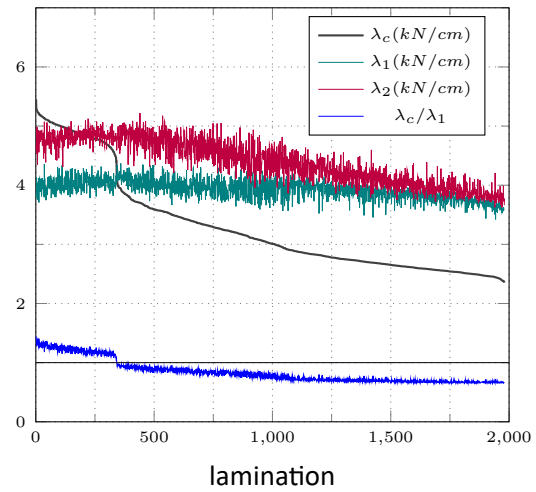


Figure 4: Collapse load and linearised buckling loads at stage 2.

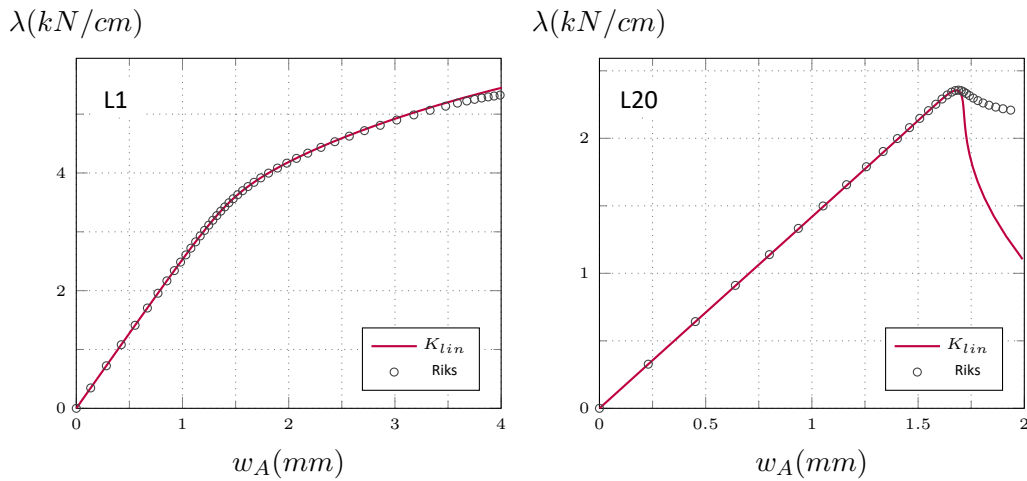


Figure 5: Stiffened panel: equilibrium paths for the worst imperfection shape and laminations L1 (best) and L20 (worst), Riks vs Koiter.

are well separated from each other. The first buckling load is actually quite constant with the lamination though, when the second one gets closer to it, the collapse load, due to modal interaction phenomenon, drastically reduces. This behaviour is significantly more evident in Fig.4 where the results of stage 2 are reported. The best laminations in terms of collapse load are characterised by an evident distance between the first and the second linearised buckling load and exhibit a stable behaviour. Conversely, for the worst laminations, the second eigenvalue is very close to the first one and the modal interaction leads to a relevant unstable behaviour with an imperfection sensitive limit load. Some equilibrium paths are presented in Fig.5. The collapse loads predicted by the Koiter method are practically coincident with those provided by the Riks analysis with the full FE model.

#### 4 Conclusions

A strategy completely based on stochastic simulations for optimising the stacking sequence of slender composite shells undergoing buckling was presented in this paper. The objective function is the collapse load, evaluated by taking into account the worst shape of the imperfection by means of the Koiter method.

#### References

- [1] Giovanni Garcea, Leonardo Leonetti, Domenico Magisano, Rodrigo Gonçalves, and Dinar Camotim. Deformation modes for the post-critical analysis of thin-walled compressed members by a Koiter semi-analytic approach. *International Journal of Solids and Structures*, 110-111:367–384, 2017.
- [2] D. Dubina and V. Ungureanu. Instability mode interaction: From Van der Neut model to ECBL approach. *Thin-Walled Structures*, 81:39–49, 2014.
- [3] E.J. Barbero, L.A. Godoy, and I.G. Raftoyiannis. Finite elements for three-mode interaction in buckling analysis. *International Journal for Numerical Methods in Engineering*, 39(3):469–488, 1996.
- [4] Esben Lindgaard, Erik Lund, and Kim Rasmussen. Nonlinear buckling optimization of composite structures considering “worst” shape imperfections. *International Journal of Solids and Structures*, 47(22–23):3186 – 3202, 2010.
- [5] M. Deml and W. Wunderlich. Direct evaluation of the ‘worst’ imperfection shape in shell buckling. *Computer Methods in Applied Mechanics and Engineering*, 149(1):201 – 222, 1997. Containing papers presented at the Symposium on Advances in Computational Mechanics.

- [6] F.G. Flores and L.A. Godoy. Elastic post-buckling analysis via finite element and perturbation techniques. Part 1: Formulation. *International Journal for Numerical Methods in Engineering*, 33(9):1775–1794, 1992.
- [7] Francesco S. Liguori, Giovanni Zucco, Antonio Madeo, Domenico Magisano, Leonardo Leonetti, Giovanni Garcea, and Paul M. Weaver. Postbuckling optimisation of a variable angle tow composite wingbox using a multi-modal Koiter approach. *Thin-Walled Structures*, 138:183–198, 2019.
- [8] Domenico Magisano, Francesco Liguori, Antonio Madeo, Leonardo Leonetti, and Giovanni Garcea. Material design for optimal postbuckling behaviour of composite shells. *Materials*, 14(7), 2021.
- [9] Francesco S. Liguori, Giovanni Zucco, Antonio Madeo, Giovanni Garcea, Leonardo Leonetti, and Paul M. Weaver. An isogeometric framework for the optimal design of variable stiffness shells undergoing large deformations. *International Journal of Solids and Structures*, 210-211:18–34, 2021.
- [10] Leonardo Leonetti, Giovanni Garcea, Domenico Magisano, Francesco Liguori, Giovanni Formica, and Walter Lacarbonara. Optimal Design of CNT-Nanocomposite Nonlinear Shells. *Nanomaterials*, 10(12), 2020.
- [11] D. Magisano, K. Liang, G. Garcea, L. Leonetti, and M. Ruess. An efficient mixed variational reduced-order model formulation for nonlinear analyses of elastic shells. *International Journal for Numerical Methods in Engineering*, 113(4):634–655, 2018.
- [12] T. Rahman and E.L. Jansen. Finite element based coupled mode initial post-buckling analysis of a composite cylindrical shell. *Thin-Walled Structures*, 48(1):25–32, 2010.
- [13] G. Garcea, F. S. Liguori, L. Leonetti, D. Magisano, and A. Madeo. Accurate and efficient a posteriori account of geometrical imperfections in Koiter finite element analysis. *International Journal for Numerical Methods in Engineering*, 112(9):1154–1174, 2017. nme.5550.
- [14] Leonardo Leonetti, Domenico Magisano, Francesco Liguori, and Giovanni Garcea. An isogeometric formulation of the koiter’s theory for buckling and initial post-buckling analysis of composite shells. *Computer Methods in Applied Mechanics and Engineering*, 337:387 – 410, 2018.
- [15] Francesco S. Liguori, Antonio Madeo, Domenico Magisano, Leonardo Leonetti, and Giovanni Garcea. Post-buckling optimisation strategy of imperfection sensitive composite shells using koiter method and monte carlo simulation. *Composite Structures*, 192:654 – 670, 2018.
- [16] K.Y. Sze, W.K. Chan, and T.H.H. Pian. An eight-node hybrid-stress solid-shell element for geometric non-linear analysis of elastic shells. *International Journal for Numerical Methods in Engineering*, 55(7):853–878, 2002.
- [17] D. Magisano, L. Leonetti, and G. Garcea. Koiter asymptotic analysis of multilayered composite structures using mixed solid-shell finite elements. *Composite Structures*, 154:296–308, 2016.
- [18] Leonardo Leonetti, Francesco Liguori, Domenico Magisano, and Giovanni Garcea. An efficient isogeometric solid-shell formulation for geometrically nonlinear analysis of elastic shells. *Computer Methods in Applied Mechanics and Engineering*, 331:159 – 183, 2018.
- [19] E. Riks. An incremental approach to the solution of snapping and buckling problems. *International Journal of Solids and Structures*, 15(7):529–551, 1979.

## **A robust and efficient iterative strategy for nonlinear analysis of structures subjected to buckling**

Domenico Magisano<sup>1</sup>, Francesco Liguori<sup>1</sup>, Leonardo Leonetti<sup>1</sup>, Giovanni Garcea<sup>1</sup>

### **Abstract**

The paper shows how to make the incremental-iterative solution significantly more efficient and robust in geometrically non-linear structural problems discretized via displacement-based finite element formulations. The main idea is to relax the constitutive equations at each integration point (IP) during the iterations. The converged solution remains unchanged while the iteration matrix is computed using independent IP stresses. This reduces the number of iterations to obtain convergence and allows very large steps in incremental analyses. The computational cost of each iteration is the same as the original Newton method. Importantly, the robustness of the iterative process is unaffected by high membrane-to-flexural stiffness ratios as opposite to the standard Newton method.

### **1 Introduction**

Slender structures are usually characterized by large displacements and rotations but small strains [1]. Many practical problems can be framed in this context. Some examples are metal and composite structures, often characterized by buckling phenomena and strong imperfection sensitivity [2, 3, 4, 5, 6]. The standard approach to simulate the behavior of this kind of structures consists of the use of the finite element (FE) method, in order to transform the continuum problem into a discrete one. The non-linear discrete equations, completed with an arc-length constraint defining the step size, are solved step-by-step by using the Newton iterative method, in order to evaluate the equilibrium path of the structure. Most of the existing FE codes are based on displacement formulations, i.e. the kinematic field is interpolated and the discrete kinematic DOFs represent the unknowns of the non-linear equations. Other kinds of formulations are possible, like for instance the mixed (stress-displacement) one, also known as hybrid-stress, in which both the stress and the displacement fields are interpolated. When comparing mixed and displacement finite elements many authors [7] observed that the mixed ones are more robust and allow larger steps in path-following geometrically non-linear analyses. In this paper we will show that it is possible to use a mixed iterative scheme without introducing a mixed FE interpolation and, so, a mixed format of the Newton method for geometrically non-linear structural problems discretized via displacement-based finite elements is presented. The idea consists of the relaxation of the constitutive equations at each integration point. In this way, the stiffness matrix of a displacement-based FE maintains its original form. The only difference is that the stresses at each integration point, used for the matrix evaluation, are directly extrapolated and corrected, i.e. used as independent variables. This leads to a "better" iteration matrix, which allows a very low number of iterations and very large steps (increments) in step-by-step analyses. With respect to mixed FEs no stress interpolations are present, so avoiding any additional cost in the evaluation of the stiffness matrix. Furthermore the final equilibrium

---

<sup>1</sup>Dipartimento di Ingegneria Informatica, Modellistica, Elettronica e Sistemistica  
Università della Calabria 87036 Rende (Cosenza), Italy

path is the same as the original displacement formulation since the constitutive law is recovered exactly at convergence. The method, that we call MIP (Mixed Integration Point) Newton, converges much faster than the standard Newton method, as shown by many numerical tests with different structural models and FEs. The gain in terms of number of iterations required is impressive as well as the very large steps that the MIP Newton can withstand without loss of convergence. The computational cost of a MIP iteration is the same as a standard one. Furthermore, the iteration matrix evaluated with the MIP strategy is so "good" that the modified version of the method (MIP modified Newton), which computes and decomposes the iteration matrix at the first estimate of each equilibrium point, can be conveniently adopted. From the implementation point of view, a few changes to the standard approaches are required [8, 9]. Extensions of the method to isogeometric analyses [10, 11, 1] and penalty coupling [12] are available.

## 2 GEOMETRICALLY NON-LINEAR ANALYSIS VIA DISPLACEMENT FEM

### 2.1 The discrete non-linear equations

We consider a slender hyperelastic structure subject to conservative loads  $p[\lambda]$  proportionally increasing with the amplifier factor  $\lambda$ . The equilibrium is expressed by the virtual work equation

$$\Phi[u]' \delta u - \lambda p \delta u = 0 \quad , \quad u \in \mathcal{U} \quad , \quad \delta u \in \mathcal{T} \quad (1)$$

where  $u \in \mathcal{U}$  is the field of configuration variables,  $\Phi[u]$  denotes the strain energy,  $\mathcal{T}$  is the tangent space of  $\mathcal{U}$  at  $u$  and a prime is used to express the Fréchet derivative with respect to  $u$ . We assume that  $\mathcal{U}$  will be a linear manifold so that its tangent space  $\mathcal{T}$  will be independent of  $u$ . In displacement formulation  $u$  is the displacement field, while when a mixed formulation is adopted  $u$  collects both displacement and stress fields. Eq.(1) can be rewritten, using a FE or an isogeometric discretization  $u = \mathbf{N}_u \mathbf{u}$  as

$$\mathbf{r}[\mathbf{u}, \lambda] \equiv \mathbf{s}[\mathbf{u}] - \lambda \mathbf{p} = \mathbf{0}, \quad \text{with} \quad \begin{cases} \mathbf{s}^T \delta \mathbf{u} \equiv \Phi'[u] \delta u \\ \mathbf{p}^T \delta \mathbf{u} \equiv p \delta u \end{cases} \quad (2)$$

where  $\mathbf{r} : \mathbb{R}^{N+1} \rightarrow \mathbb{R}^N$  is a non-linear vectorial function of the vector  $\mathbf{z} \equiv \{\mathbf{u}, \lambda\} \in \mathbb{R}^{N+1}$ , collecting the configuration  $\mathbf{u} \in \mathbb{R}^N$  and the load multiplier  $\lambda \in \mathbb{R}$ ,  $\mathbf{s}[\mathbf{u}]$  is the *internal force vector* and  $\mathbf{p}$  the *reference load vector*. Eq.(2) represents a system of  $N$ -equations and  $N + 1$  unknowns and its solutions define the *equilibrium paths* as curves in  $\mathbb{R}^{N+1}$  from a known initial configuration  $\mathbf{u}_0$ , corresponding to  $\lambda = 0$ . We also define the tangent stiffness matrix as

$$\delta \mathbf{u}_2^T \mathbf{K}[\mathbf{u}] \delta \mathbf{u}_1 = \Phi''[u] \delta u_1 \delta u_2 \quad , \quad \forall \delta \mathbf{u}_1, \delta \mathbf{u}_2 \quad (3)$$

where  $\delta u_i$  are generic variations of the configuration field  $u$  and  $\delta \mathbf{u}_i$  its discrete vectors.

### 2.2 Path-following analysis

The Riks method completes the equilibrium equations (2) with the additional constraint  $g[\mathbf{u}, \lambda] - \xi = 0$ , which defines a surface in  $\mathbb{R}^{N+1}$ . Assigning successive values to the control parameter  $\xi = \xi_{(k)}$  the solution of the non-linear system

$$\mathbf{R}[\xi] \equiv \begin{bmatrix} \mathbf{r}[\mathbf{u}, \lambda] \\ g[\mathbf{u}, \lambda] - \xi \end{bmatrix} = \mathbf{0} \quad (4)$$

defines a sequence of points (steps)  $\mathbf{z}_{(k)} \equiv \{\mathbf{u}_{(k)}, \lambda_{(k)}\}$  belonging to the equilibrium path. Starting from a known equilibrium point  $\mathbf{z}^0 \equiv \mathbf{z}_{(k)}$ , the new one  $\mathbf{z}_{(k+1)}$  is evaluated correcting a first *extrapolation*  $\mathbf{z}^1 = \{\mathbf{u}^1, \lambda^1\}$  by a sequence of estimates  $\mathbf{z}^j$  (loops) by a Newton–Raphson iteration

$$\begin{cases} \tilde{\mathbf{J}} \dot{\mathbf{z}} = -\mathbf{R}^j \\ \mathbf{z}^{j+1} = \mathbf{z}^j + \dot{\mathbf{z}} \end{cases} \quad (5a)$$

where  $\mathbf{R}^j \equiv \mathbf{R}[\mathbf{z}^j]$  and  $\tilde{\mathbf{J}}$  is the Jacobian of the non-linear system (4) at  $\mathbf{z}^j$  or its suitable estimate. The simplest choice for  $g[\mathbf{u}, \lambda]$  is the linear constraint corresponding to the orthogonal hyperplane

$$\mathbf{n}_u^T (\mathbf{u} - \mathbf{u}^j) + n_\lambda (\lambda - \lambda^j) = \Delta\xi \quad \text{where} \quad \begin{cases} \mathbf{n}_u \equiv \mathbf{M} (\mathbf{u}^j - \mathbf{u}^{(k)}) \\ \mathbf{n}_\lambda \equiv \mu (\lambda^j - \lambda^{(k)}) \end{cases} \quad (5b)$$

$\mathbf{M}$  and  $\mu$  being some suitable metric factors,  $\Delta\xi$  an assigned increment of  $\xi$  and

$$\tilde{\mathbf{J}} \approx \left[ \frac{\partial \mathbf{R}[\mathbf{z}]}{\partial \mathbf{z}} \right]_{\mathbf{z}^j} = \begin{bmatrix} \tilde{\mathbf{K}} & -\hat{\mathbf{p}} \\ \mathbf{n}_u^T & n_\lambda \end{bmatrix} \quad (5c)$$

The solution of Eq.(5) is conveniently performed as follows

$$\begin{cases} \dot{\lambda} = \frac{\mathbf{n}_u^T \tilde{\mathbf{K}} \mathbf{r}^j}{n_\lambda + \mathbf{n}_u^T \tilde{\mathbf{K}} \mathbf{p}} \\ \tilde{\mathbf{K}} \dot{\mathbf{u}} = \dot{\lambda} \mathbf{p} - \mathbf{r}^j \end{cases} \quad (5d)$$

### 2.3 Displacement-based discrete formulation

In displacement-based FE or isogeometric formulations only the displacement field is interpolated in the domain and, thus,

$$\mathbf{u}[\boldsymbol{\xi}] = \mathbf{N}_d[\boldsymbol{\xi}] \mathbf{d}_e \quad (6)$$

where  $\mathbf{d}_e$  are the element discrete DOFs, linked to the global ones  $\mathbf{d}$  by the relation  $\mathbf{d}_e = \mathbf{A}_e \mathbf{d}$  and  $\boldsymbol{\xi}$  are the coordinates used to express the FE interpolation. The dependence on the coordinates will be omitted in the following in order to simplify the notation. The strain energy can be expressed as a sum of element contributions  $\Phi[u] \equiv \sum_e \Phi_e[u]$ , where, letting  $V_e$  the finite element domain and  $\mathbf{C}$  the constitutive matrix,

$$\Phi_e[u] \equiv \int_{V_e} \left( \frac{1}{2} \boldsymbol{\varepsilon}^T \mathbf{C} \boldsymbol{\varepsilon} \right) dV_e \quad (7)$$

and the strains or generalized strains  $\boldsymbol{\varepsilon} = \mathcal{D}[\mathbf{u}] \mathbf{u}$ , introducing the interpolation in (6), assume the general form

$$\boldsymbol{\varepsilon} = \mathbf{B}[\mathbf{d}_e] \mathbf{d}_e, \quad (8)$$

with the differential operator  $\mathcal{D}$  and its discrete counterpart  $\mathbf{B}$ , in general, non-linear in  $\mathbf{u}$  and  $\mathbf{d}_e$  respectively. The first variation of the strain measure can be written as

$$\delta \boldsymbol{\varepsilon} = \mathbf{Q}[\mathbf{d}_e] \delta \mathbf{d}_e$$

and, then, the first variation of the strain energy is

$$\Phi_e[u]' \delta u \equiv \int_{V_e} (\delta \boldsymbol{\varepsilon}^T \mathbf{C} \boldsymbol{\varepsilon}) dV_e = \int_{V_e} (\delta \mathbf{d}_e^T \mathbf{Q}[\mathbf{d}_e]^T \mathbf{C} \mathbf{B}[\mathbf{d}_e] \mathbf{d}_e) dV_e = \delta \mathbf{d}_e^T \mathbf{s}_e[\mathbf{d}_e] \quad (9)$$

where  $\mathbf{s}_e[\mathbf{d}_e]$  is the element internal force vector. The second variation of the strain energy is

$$\Phi_e''[u] \delta u \delta u \equiv \int_{V_e} (\delta \boldsymbol{\varepsilon}^T \mathbf{C} \dot{\boldsymbol{\varepsilon}} + \delta \dot{\boldsymbol{\varepsilon}}^T \mathbf{C} \boldsymbol{\varepsilon}) dV_e = \delta \mathbf{d}_e^T \mathbf{K}_e[\mathbf{d}_e] \dot{\mathbf{d}}_e \quad (10)$$

with the element tangent stiffness matrix defined as

$$\mathbf{K}_e[\mathbf{d}_e] \equiv \int_{V_e} (\mathbf{Q}[\mathbf{d}_e]^T \mathbf{C} \mathbf{Q}[\mathbf{d}_e] + \mathcal{G}[\boldsymbol{\sigma}[\mathbf{d}_e], \mathbf{d}_e]) dV_e \quad (11)$$

and

$$\mathcal{G}[\boldsymbol{\sigma}[\mathbf{d}_e], \mathbf{d}_e] = \sum_k \sigma_k[\mathbf{d}_e] \boldsymbol{\Psi}_k[\mathbf{d}_e] \mathbf{d}_e. \quad (12)$$

### 2.3.1 Numerical integration

Quadrature rules are usually employed to perform the integrations:

$$\Phi_e[\mathbf{d}_e] \equiv \sum_g^n \left( \frac{1}{2} \boldsymbol{\varepsilon}_g[\mathbf{d}_e]^T \mathbf{C}_g \boldsymbol{\varepsilon}_g[\mathbf{d}_e] \right) w_g \quad (13)$$

where subscript  $g$  denotes quantities evaluated in the integration point  $\boldsymbol{\xi}_g$  and  $w_g$  is the corresponding weight. The internal force vector becomes

$$\mathbf{s}_e[\mathbf{d}_e] = \sum_g^n \left( \mathbf{Q}_g[\mathbf{d}_e]^T \mathbf{C}_g \boldsymbol{\varepsilon}_g[\mathbf{d}_e] \right) w_g \quad (14)$$

while the tangent stiffness matrix is

$$\mathbf{K}_e[\boldsymbol{\sigma}_g[\mathbf{d}_e], \mathbf{d}_e] = \sum_g^n \left( \mathbf{Q}_g[\mathbf{d}_e]^T \mathbf{C}_g \mathbf{Q}_g[\mathbf{d}_e] + \mathcal{G}_g[\boldsymbol{\sigma}_g[\mathbf{d}_e], \mathbf{d}_e] \right) w_g \quad (15)$$

where  $\mathbf{K}_e[\mathbf{d}_e]$  is written as  $\mathbf{K}_e[\boldsymbol{\sigma}_g[\mathbf{d}_e], \mathbf{d}_e]$  as a reminder of the way it is computed.

### 3 The new iterative scheme with mixed integration points

The fundamental idea of the MIP Newton iterative scheme [8] is to relax the constitutive equations at the level of each integration point. This is made by writing the strain energy in Eq. (13) in a pseudo Helling-Reissner form as

$$\Phi_e[\mathbf{u}_e] \equiv \sum_{g=1}^n \left( \boldsymbol{\sigma}_g^T \boldsymbol{\varepsilon}_g[\mathbf{d}_e] - \frac{1}{2} \boldsymbol{\sigma}_g^T \mathbf{C}_g^{-1} \boldsymbol{\sigma}_g \right) w_g \quad \text{with} \quad \mathbf{u}_e = [\boldsymbol{\sigma}_1 \quad \dots \quad \boldsymbol{\sigma}_n \quad \mathbf{d}_e]^T \quad (16)$$

in which the stresses at each integration point  $\boldsymbol{\sigma}_g$  are now independent variables. The first variation of (16) is

$$\Phi'_e \delta u = \sum_{g=1}^n \begin{bmatrix} \delta \boldsymbol{\sigma}_g \\ \delta \mathbf{d}_e \end{bmatrix}^T \begin{bmatrix} \mathbf{s}_{g\sigma} \\ \mathbf{s}_{gd} \end{bmatrix} w_g \quad (17)$$

with

$$\begin{cases} \mathbf{s}_{g\sigma} \equiv \boldsymbol{\varepsilon}_g[\mathbf{d}_e] - \mathbf{C}^{-1} \boldsymbol{\sigma}_g \\ \mathbf{s}_{gd} \equiv \mathbf{Q}_g[\mathbf{d}_e]^T \boldsymbol{\sigma}_g \end{cases} \quad (18)$$

We have to note that the stationarity of (16) with respect to  $\boldsymbol{\sigma}_g$  leads to the constitutive equations  $\boldsymbol{\sigma}_g = \mathbf{C}_g \boldsymbol{\varepsilon}_g[\mathbf{d}_e]$  and, thus, the stresses satisfy the constitutive law along the equilibrium path exactly. However, the stresses at the integration points are independent variables and, thus, they are not forced to satisfy the constitutive law during the iterations but, the constitutive equations are solved together with the equilibrium equations and are satisfied only when convergence is obtained. The second variation of (16) is

$$\Phi''_e \delta u \delta u = \sum_{g=1}^n \begin{bmatrix} \delta \boldsymbol{\sigma}_g \\ \delta \mathbf{d}_e \end{bmatrix}^T \begin{bmatrix} -\mathbf{C}_g^{-1} & \mathbf{Q}_g \\ \mathbf{Q}_g^T & \mathcal{G}_g \end{bmatrix} \begin{bmatrix} \boldsymbol{\sigma}_g \\ \mathbf{d}_e \end{bmatrix} w_g \quad (19)$$

where  $\mathcal{G}_g \equiv \mathcal{G}_e[\boldsymbol{\sigma}_g, \mathbf{d}_e]$  is the matrix  $\mathcal{G}_e$  evaluated in the integration point  $g$ , that is now a function of the displacement DOFs and of the independent stresses  $\boldsymbol{\sigma}_g$ . The linear system in Eq.(5d), at the element level, becomes

$$\begin{bmatrix} -\mathbf{C}_1^{-1} w_1 & & & \mathbf{Q}_1 w_1 \\ & \ddots & & \vdots \\ & & -\mathbf{C}_n^{-1} w_n & \mathbf{Q}_n w_n \\ \mathbf{Q}_1^T w_1 & \dots & \mathbf{Q}_n^T w_n & \sum_g^n \mathcal{G}_g w_g \end{bmatrix}^j \begin{bmatrix} \boldsymbol{\sigma}_1 \\ \vdots \\ \boldsymbol{\sigma}_n \\ \mathbf{d}_e \end{bmatrix} = (\lambda^j + \dot{\lambda}) \begin{bmatrix} \mathbf{0} \\ \vdots \\ \mathbf{0} \\ \mathbf{p}_e \end{bmatrix} - \begin{bmatrix} \mathbf{s}_{1\sigma} w_1 \\ \vdots \\ \mathbf{s}_{n\sigma} w_n \\ \sum_g^n (\mathbf{Q}_g^T \boldsymbol{\sigma}_g w_g) \end{bmatrix}^j \quad (20)$$

	Newton	MIP Newton
<b>Predictor</b>	$\mathbf{d}^1 = \mathbf{d}^{(k)} + \Delta \mathbf{d}$ $\lambda^1 = \lambda^{(k)} + \Delta \lambda$ $\boldsymbol{\sigma}_g[\mathbf{d}^1] = \mathbf{C}_g \boldsymbol{\varepsilon}_g[\mathbf{d}^1]$	$\mathbf{d}^1 = \mathbf{d}^{(k)} + \Delta \mathbf{d}$ $\lambda^1 = \lambda^{(k)} + \Delta \lambda$ $\boldsymbol{\sigma}_g^1 = \boldsymbol{\sigma}_{g^{(k)}} + \Delta \boldsymbol{\sigma}_g$
<b>Iteration matrix</b>	$\mathbf{K}[\boldsymbol{\sigma}_g[\mathbf{d}^j], \mathbf{d}^j]$	$\mathbf{K}[\boldsymbol{\sigma}_g^j, \mathbf{d}^j]$
<b>Residual vector</b>	$\mathbf{s}[\mathbf{d}^j] - \lambda^j \mathbf{p}$	$\mathbf{s}[\mathbf{d}^j] - \lambda^j \mathbf{p}$
<b>New estimate</b>	$\mathbf{d}^{j+1} = \mathbf{d}^j + \dot{\mathbf{d}}$ $\lambda^{j+1} = \lambda^j + \dot{\lambda}$ $\boldsymbol{\sigma}_g^{j+1} = \mathbf{C}_g \boldsymbol{\varepsilon}_g[\mathbf{d}^{j+1}]$	$\mathbf{d}^{j+1} = \mathbf{d}^j + \dot{\mathbf{d}}$ $\lambda^{j+1} = \lambda^j + \dot{\lambda}$ $\boldsymbol{\sigma}_g^{j+1} = \boldsymbol{\sigma}_g^{j+1} + \dot{\boldsymbol{\sigma}}$

**Table 1:** Schematic description of the principal points of the algorithms.

where the superscript on matrices denotes that they are evaluated during the iterative process in the current estimate  $\mathbf{u}_e^j$ . By performing a static condensation of the stresses  $\dot{\boldsymbol{\sigma}}_g$ , locally defined at the level of the integration point, we obtain

$$\dot{\boldsymbol{\sigma}}_g = \mathbf{C}_g \mathbf{Q}_g^j \dot{\mathbf{d}}_e + \mathbf{C}_g \mathbf{s}_{g\sigma}^j = \mathbf{C}_g \mathbf{Q}_g^j \dot{\mathbf{d}}_e + \mathbf{C}_g \boldsymbol{\varepsilon}_g^j - \boldsymbol{\sigma}_g^j \quad (21)$$

and letting  $\mathbf{r}_{ce}[\mathbf{d}_e^j] = \mathbf{s}_{ce}[\mathbf{d}_e^j] - \lambda^j \mathbf{p}_e$

$$\mathbf{K}_e[\mathbf{u}_e^j] \dot{\mathbf{d}}_e = -\mathbf{r}_{ce}[\mathbf{d}_e^j] + \dot{\lambda} \mathbf{p}_e \quad (22)$$

with

$$\mathbf{K}_e[\boldsymbol{\sigma}_g^j, \mathbf{d}_e^j] = \sum_{g=1}^n \left( \mathbf{Q}_g[\mathbf{d}_e^j]^T \mathbf{C}_g \mathbf{Q}_g[\mathbf{d}_e^j] + \mathcal{G}_g[\boldsymbol{\sigma}_g^j, \mathbf{d}_e^j] \right) w_g \quad (23)$$

the condensed tangent stiffness matrix, that has the same form as the classical displacement based one (15). However, this time it also depends on the independent stresses at the integration points, which are now directly extrapolated and corrected during the iterations. Conversely, we can note that the condensed internal forces  $\mathbf{s}_{ce}[\mathbf{d}_e^j]$

$$\mathbf{s}_{ce}[\mathbf{d}_e^j] = \sum_g^n \left( \mathbf{Q}_g^j{}^T \mathbf{C}_g \boldsymbol{\varepsilon}_g^j \right) w_g$$

coincides exactly with the internal forces of the displacement-based formulation in Eq. (14). This iterative scheme is then very close to the standard Newton one for displacement-based discrete models as it is highlighted in Tab. 1.

The modified Newton method evaluates and decomposes the iteration matrix in the first extrapolation (predictor) of each step. The stiffness matrix, evaluated using the direct extrapolation of the stresses from the previous step, is already a good estimation of the secant matrix and, furthermore, the MIP tangent matrix slightly changes during the iterative process. The matrix so evaluated in the first prediction is then suitable for use in all the iterations over the step (MIP modified Newton). The few extra-iterations are compensated by evaluation and factorization of the iteration matrix just once in each step.

#### 4 A numerical test

A test regarding a thin-walled cantilever beam with U cross section is considered. Geometry, loads and material properties are reported in Fig.1. The FE mesh consists of 2880 solid-shell FEs [13, 14], obtained via 32 equal subdivisions on the cross section and 90 subdivisions along the beam axis. An arc-length technique with adaptive step size is used and the initial load increment is  $\Delta \lambda_0 = 3$ . Fig.2 depicts the equilibrium path and the deformed configuration at the limit and the final equilibrium point

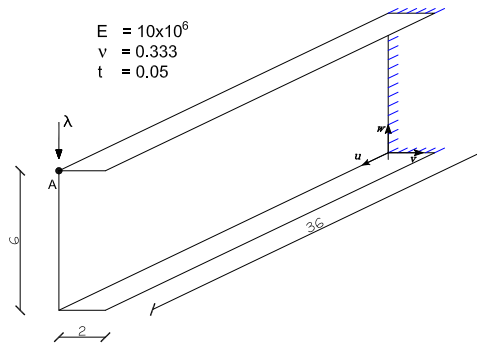


**Figure 1:** Geometry, loads and material properties.

	steps	iterations
Newton	82	301
MIP Newton	36	106
MIP M. Newton	55	175

**Table 2:** Total number of steps and iterations for the equilibrium path evaluation.

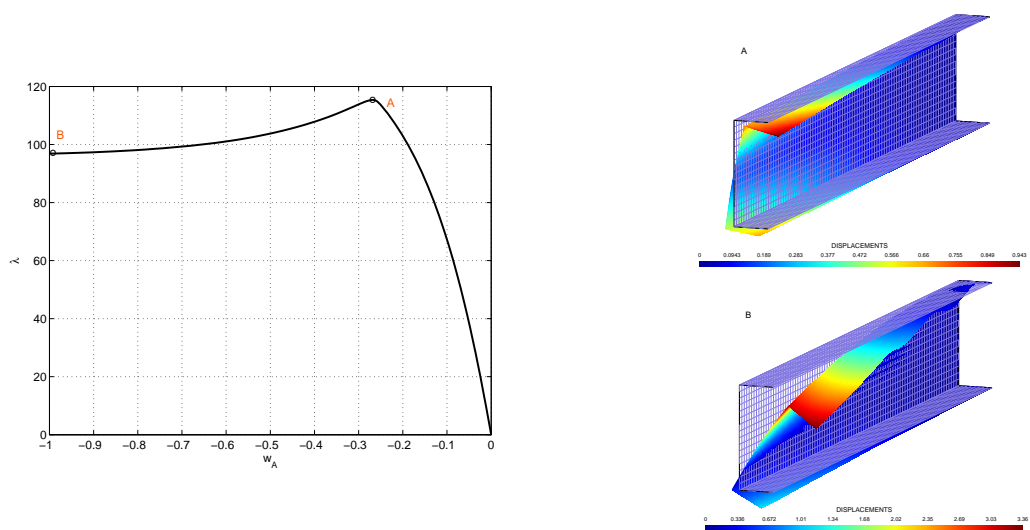


**Figure 2:** Cantilever beam: equilibrium path and deformed configuration at the last evaluated equilibrium point

corresponding to a vertical displacement  $w_A = -1$ . As for all the other tests, the MIP Newton, in both the full or the modified version, performs better with respect to the standard method as shown in Tab.2. The full standard Newton requires a total number of iterations 3 times larger than the MIP full Newton and almost twice the MIP modified Newton.

## 5 Conclusions

The MIP iterative strategy, proposed here, consists relaxes the constitutive law at each integration point. In this way, the stresses at the integration points become independent variables in the iterative process and, thus, they are directly predicted and corrected. It allows us to solve geometrically non-linear problems with a very low number of steps and total iterations with respect to the standard Newton method.

## References

- [1] D. Magisano, L. Leonetti, G. Garcea, Isogeometric analysis of 3d beams for arbitrarily large rotations: Locking-free and path-independent solution without displacement dofs inside the patch, *Computer Methods in Applied Mechanics and Engineering* 373 (2021) 113437. doi:<https://doi.org/10.1016/j.cma.2020.113437>.
- [2] G. Garcea, F. Liguori, L. Leonetti, D. Magisano, A. Madeo, Accurate and efficient a posteriori account of geometrical imperfections in Koiter finite element analysis, *International Journal for Numerical Methods in Engineering* (2017). doi:10.1002/nme.5550.
- [3] F. S. Liguori, A. Madeo, D. Magisano, L. Leonetti, G. Garcea, Post-buckling optimisation strategy of imperfection sensitive composite shells using Koiter method and Monte Carlo simulation, *Composite Structures* 192 (2018) 654–670. doi:<https://doi.org/10.1016/j.compstruct.2018.03.023>.
- [4] D. Magisano, K. Liang, G. Garcea, L. Leonetti, M. Ruess, An efficient mixed variational reduced-order model formulation for nonlinear analyses of elastic shells, *International Journal for Numerical Methods in Engineering* 113 (4) (2018) 634–655. doi:<https://doi.org/10.1002/nme.5629>.
- [5] L. Leonetti, D. Magisano, F. Liguori, G. Garcea, An isogeometric formulation of the Koiter’s theory for buckling and initial post-buckling analysis of composite shells, *Computer Methods in Applied Mechanics and Engineering* 337 (2018) 387–410. doi:<https://doi.org/10.1016/j.cma.2018.03.037>.
- [6] L. Leonetti, G. Garcea, D. Magisano, F. Liguori, G. Formica, W. Lacarbonara, Optimal design of cnt-nanocomposite nonlinear shells, *Nanomaterials* 10 (12) (2020). doi:10.3390/nano10122484. URL <https://www.mdpi.com/2079-4991/10/12/2484>
- [7] D. Magisano, L. Leonetti, G. Garcea, Advantages of the mixed format in geometrically nonlinear analysis of beams and shells using solid finite elements, *International Journal for Numerical Methods in Engineering* (2016) n/a–n/a/nme.5322. doi:10.1002/nme.5322. URL <http://dx.doi.org/10.1002/nme.5322>
- [8] D. Magisano, L. Leonetti, G. Garcea, How to improve efficiency and robustness of the Newton method in geometrically non-linear structural problem discretized via displacement-based finite elements, *Computer Methods in Applied Mechanics and Engineering* 313 (2017) 986 – 1005. doi:<http://dx.doi.org/10.1016/j.cma.2016.10.023>.
- [9] D. Magisano, L. Leonetti, A. Madeo, G. Garcea, A large rotation finite element analysis of 3d beams by incremental rotation vector and exact strain measure with all the desirable features, *Computer Methods in Applied Mechanics and Engineering* 361 (2020) 112811. doi:<https://doi.org/10.1016/j.cma.2019.112811>.
- [10] L. Leonetti, F. Liguori, D. Magisano, G. Garcea, An efficient isogeometric solid-shell formulation for geometrically nonlinear analysis of elastic shells, *Computer Methods in Applied Mechanics and Engineering* 331 (2018) 159–183. doi:<https://doi.org/10.1016/j.cma.2017.11.025>.

- [11] L. Leonetti, D. Magisano, A. Madeo, G. Garcea, J. Kiendl, A. Reali, A simplified kirchhoff–love large deformation model for elastic shells and its effective isogeometric formulation, *Computer Methods in Applied Mechanics and Engineering* 354 (2019) 369–396. doi:<https://doi.org/10.1016/j.cma.2019.05.025>.
- [12] L. Leonetti, F. S. Liguori, D. Magisano, J. Kiendl, A. Reali, G. Garcea, A robust penalty coupling of non-matching isogeometric kirchhoff–love shell patches in large deformations, *Computer Methods in Applied Mechanics and Engineering* 371 (2020) 113289. doi:<https://doi.org/10.1016/j.cma.2020.113289>.
- [13] K. Sze, W. Chan, T. Pian, An eight-node hybrid-stress solid-shell element for geometric non-linear analysis of elastic shells, *International Journal for Numerical Methods in Engineering* 55 (7) (2002) 853–878. doi:10.1002/nme.535.
- [14] F. S. Liguori, G. Zucco, A. Madeo, D. Magisano, L. Leonetti, G. Garcea, P. M. Weaver, Postbuckling optimisation of a variable angle tow composite wingbox using a multi-modal koiter approach, *Thin-Walled Structures* 138 (2019) 183–198. doi:<https://doi.org/10.1016/j.tws.2019.01.035>.

## **Influence of damping effect on the dynamic response of plate**

Łukasz Borkowski<sup>1</sup>

### **Abstract**

The subject of the research is the analysis of the influence of damping effect on the dynamic response of plate. During the tests, the areas of dynamic stability and instability for the plate with and without damping will be compared. Besides, the exact analysis of the nature of solution by applying the criteria such as phase portraits, Poincaré maps, FFT analysis, the largest Lyapunov exponents will be done.

### **1. Introduction**

The beginnings of studies concerning the dynamic stability of plate can be found in publications from the middle of twentieth century. The first publication regarding dynamic stability of plates was presented by Zizicas in 1952 [Zizicas 1965]. In this paper, the theoretical solutions for the joint supported plate with a time-dependent load were reported. Subsequent years of research led to the creation of dynamic stability criteria, which were divided into: geometric [Cooley 1965], energy [Raftoyiannis 2000] and failure [Petry 2000].

One of the major criterion was a Budiansky-Hutchinson criterion [Hutchinson 1966], which concerned the rods and cylindrical shells with an axial load. They analyzed the load in the form of pulse of a finite and infinite duration. They proved that the loss of stability of dynamically loaded constructions occurs when the small load increments causes the rapid increase of deflection. Budiansky was one of the authors of a similar criterion regarding the cylindrical shells with a transverse load - the Budiansky-Roth criterion [Budiansky 1962]. This criterion was willingly used in the research of other scientists who were involved in the similar topics [Shariyat 2007][Kubiak 2007][Zhang 2004].

Another important criterion is the Petry-Fahlbusch criterion [Petry 2000]. They said that the analysis of the stress state should determine the dynamic critical load for the construction with a stable post- which the destruction of the structure take place. According to Petry-Fahlbusch's theory, if the condition - a reduced stress is smaller or equal to a boundary stress - is fulfilled at any time and at any point of study structure then a dynamic response of the construction under the pulse load is dynamically stable.

The next important criterion is the Volmir criterion [Volmir 1972]. He analyzed the pulses of a finite duration: a rectangular pulse and an exponentially decreasing pulse, the pulses of an infinite duration and a linearly increasing load. He studied the pulses that caused both compression and shear. Using the Bubnov-Galerkin [Michlin1970] and Runge-Kutta [Collatz2012][Fortuna 2005] methods, he said that the loss of stability for the pulse load plates occurs when the maximum deflection of the plates are equal to their thickness or half thickness.

---

<sup>1</sup> Assistant Professor, Lodz University of Technology, <lukasz.borkowski@p.lodz.pl>

In 1997, Ari-Gur and Simonetta proposed four criteria the loss of stability [Ari-Gur 1997]. They described the value of critical load depending on the following parameters: a measured deflection in the middle of length and width of the plate, the intensity of load, for the plates fixed at all edges and loaded a pulse of half-wave shaped (a pulse of finite duration). The behavior of rod systems by finite element method was analyzed in Kleiber, Kotula and Saran's work [Kleiber 1987]. They formulated the quasi-bifurcation criterion of dynamic stability for the construction that are jumping loaded of Heaviside pulse by using the properties of a tangent stiffness matrix in the point of bifurcation. According to this criterion, the structure loses stability and a deflection begin to grow boundlessly when the determinant of the tangent stiffness matrix is equal to zero and the absolute value of the smallest eigenvalue is greater than the absolute value of the nearest maximum, which the smallest eigenvalue reaches.

All the above criteria are widely used in the research of many scientists who deal with the analysis of dynamic stability [Hsu 1975][Kowal-Michalska 2010][Kolakowski 2007][Mania 2007][Kubiak 2010][Kolakowski 2007][Bolotin 1962]. However, the analysis of plate structures applying dynamic criteria such as phase portraits, Poincaré maps, FFT analysis, the largest Lyapunov exponents is less used [Alijani 2011][Alijani 2011][Yuda 2011][Wang 2010][Yeh 2002][Touati 1995]. Therefore, this paper presents the influence of damping effect on the dynamic response of the plate using the above tools.

## 2. Studied plate

A square isotropic plate with dimensions  $b=l=100\text{mm}$ ,  $h=1\text{mm}$  and material constants  $E=200\text{GPa}$ ,  $\nu=0.3$  was analyzed (Fig. 1). The analyzed plate was simply supported on the all edges. The plate has been loaded with a dynamic compressive load. The dynamic load means the load that has been introduced suddenly and lasts for an infinitely long time.

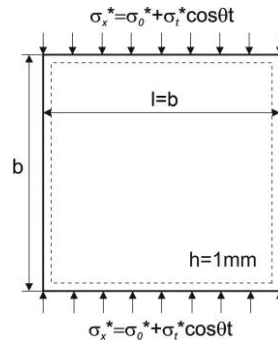


Figure 1: Studied plate

### 2.1 The plate without damping

Using research done by Volmir [Volmir 1972], the above plate can be described by the following equation:

$$\ddot{\zeta} + \omega_0^2 \left(1 - \frac{\sigma_x^*}{\sigma_{cr}^*}\right) \zeta + \eta \zeta^3 = 0 \quad (1)$$

After the transformations the test plate without damping can be described using the equation:

$$\ddot{\zeta} + \Omega_0^2 (1 - k \cos \theta t) \zeta + \eta \zeta^3 = 0 \quad (2)$$

where:

$$k = \frac{\sigma_t^* / \sigma_{cr}^*}{1 - \sigma_0^* / \sigma_{cr}^*}, \Omega_0^2 = \omega_0^2 \left(1 - \frac{\sigma_0^*}{\sigma_{cr}^*}\right), \zeta - \text{deflection of the plate, } \omega_0 - \text{natural frequency, } \sigma_{cr}^* - \text{critical}$$

stress,  $\sigma_0^*$  - medium stress,  $\sigma_t^*$  - stress amplitude,  $\eta$  - parameter, whose value is dependent on the boundary conditions.

Transforming the equation (2) to dimensionless form:

$$\ddot{x} + a(1 - k \cos \psi \tau)x + x^3 = 0 \quad (3)$$

where:

$$a = 1 - \frac{\sigma_0^*}{\sigma_{cr}^*}, \ddot{x} = \frac{\ddot{\zeta}}{\omega_0^2 \zeta_s}, x = \frac{\zeta}{\zeta_s}, x^3 = \frac{\eta \zeta^3}{\omega_0^2 \zeta_s^3}, \psi = \frac{\theta}{\omega_0}, \zeta_s - a \text{ static deflection, } \tau = \omega_0 t - \text{dimensionless}$$

time. For the studied plate the values of parameters are:  $\omega_0=3014.3$  [rad/s],  $\eta=0.23$  [rad/s<sup>2</sup>] – the value of parameter for the plate joint supported on the all edges,  $\sigma_{cr}^*=72.3$  [MPa]. For the purpose of the further numerical analysis, the equation (3) was described by two first-order differential equations:

$$\begin{aligned} \dot{x}_1 &= x_2 \\ \dot{x}_2 &= -a(1 - k \cos \psi \tau)x_1 + x_1^3 \end{aligned} \quad (4)$$

## 2.2 The plate with damping

Introducing a damping into the equation (2) and transforming into a dimensionless form:

$$\ddot{x} + c \dot{x} + a(1 - k \cos \psi \tau)x + x^3 = 0 \quad (5)$$

where:  $c=2h/\omega_0$  - the dimensionless damping ratio,  $h=0.02$  [Kolakowski 2013], the other parameters are the same as for the plate without damping.

Writing the equation (5) in the form of two first-order differential equations we get:

$$\begin{aligned} \dot{x}_1 &= x_2 \\ \dot{x}_2 &= -cx_2 - a(1 - k \cos \psi \tau)x_1 + x_1^3 \end{aligned} \quad (6)$$

All studies were made for the following initial conditions:  $x_1=0.01, x_2=0$ .

## 3. Numerical analysis of the study plate

Figure 2 shows the areas of dynamic stability and instability (the circled areas) for the plate without (a) and with (b) damping effect, after earlier presentation of full compliance of the results presented in Volmir work and the results obtained with the dynamic tools for the plate without damping effect [Borkowski 2017]. Both graphs in  $k-\psi/2\Omega$  coordinates ( $\psi=\theta/\omega_0, \Omega=\Omega_0/\omega_0$ ) by changing the values of parameters  $\sigma_0$  and  $\sigma_t$  were made. Calculations for parameters  $k$  and  $\psi/2\Omega$  changing every 0.01 were executed. Figure 2 was performed by using the criteria of phase portraits, Poincaré maps and FFT analysis. Analyzing both charts it can be concluded that there are larger areas of dynamic instability for the plate without damping as against the plate with damping.

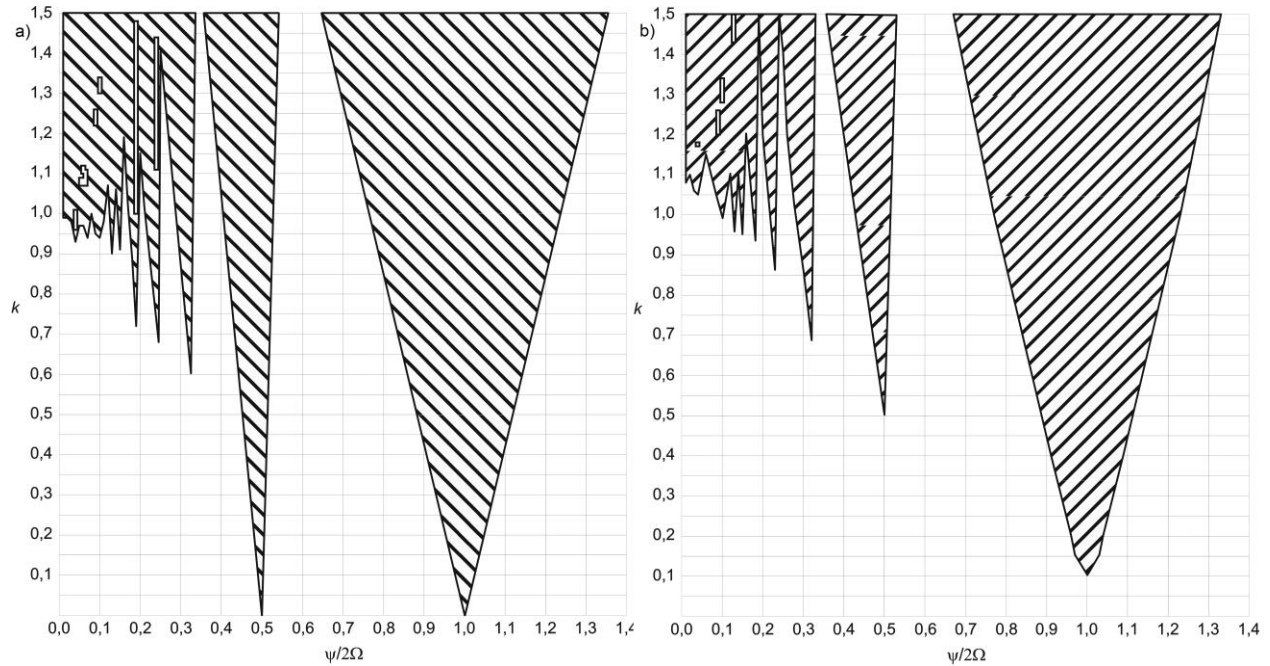


Figure 2: The graphs of dynamic stability and instability areas for the study plate without (a) and with (b) damping effect

In addition, small dynamic stability areas within the dynamic instability range in both cases were observed. For the plate without damping, the dynamic stability area is represented by a quasi-periodic solution. In range of dynamic instability, both quasi-periodic as well as chaotic solutions can be specified. For the plate with damping in the dynamic stability area, the trajectory is heading to the critical point. In range of dynamic instability, the periodic solutions as well as the series of period-doubling bifurcations, which leads to a chaotic response were obtained. Therefore, for the purpose of more detailed analysis and presentation of the above solutions, the criterion of the largest Lyapunov exponents was used. Figure 3 shows the areas of chaotic solution (the gray areas) for the plate without (a) and with (b) damping. The dashed lines indicates the boundary for the dynamic stability/instability areas which corresponds to the circled part in Fig.2. Comparing the two graphs it can be clearly stated that the introduction of damping to the analyzed plate results in obtaining much smaller areas of dynamic instability with a chaotic solution. Figure 4 presents a magnification of Figs. 3a and 3b. Gray dots correspond to specific values and gray lines to ranges for a chaotic solution. In order to present solutions more clearly, the three points from Fig. 2 for individual ranges were selected. These points represent solutions from the area of dynamic stability - ( $k=0.50$ ,  $\psi/2\Omega=0.30$ ), from the area of dynamic instability with a periodic/quasi-periodic solution - ( $k=0.25$ ,  $\psi/2\Omega=1.00$ ) and from the area of dynamic instability with a chaotic solution - ( $k=1.50$ ,  $\psi/2\Omega=0.30$ ). Analyzing the obtained results using the criteria of phase portraits and Poincaré maps, it can be concluded that the loss of dynamic stability is associated with a sudden increase of the displacement  $x_1$  and velocity  $x_2$  values (Figs. 5d, 5f, 5g, 5i) with compared to the dynamic stability areas (Figs. 5a, 5c). The loss of stability is related to the displacement of phase trajectory into infinity. This is the case when the analysis time corresponds to the period of natural vibration of construction. According to the research presented in [34], the loss of stability is related to the displacement of phase trajectory into infinity. This is the case when the analysis time corresponds to the period of natural vibration of construction. In order to use dynamic tools such as phase portraits or Poincaré maps, the presented research concerns the analysis times many times greater than the period of natural vibration. For long analysis times, the phase trajectory does not move into infinity.

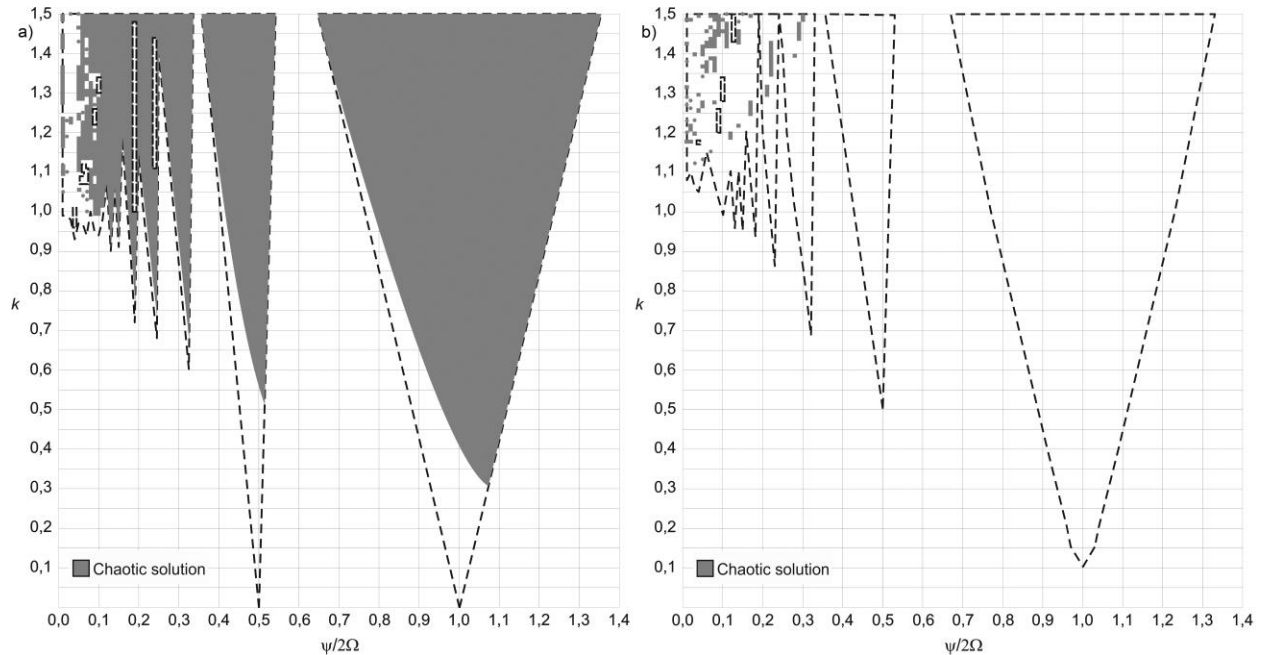


Figure 3: The graphs of areas representing the chaotic solution for the plate without (a) and with (b) damping effect

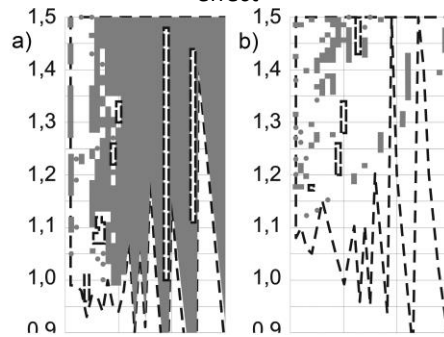


Figure 4: The detailed graphs of areas representing the chaotic solution for the plate without (a) and with (b) damping effect

It achieves some limit values of displacement  $x_1$  and velocity  $x_2$ , the value of which depends on the parameter  $k$ . However, applying the criterion of phase portraits and analyzing the plate for both short and long analysis time, the same results were obtained. Applying FFT analysis, it can be concluded that it is possible to precisely determine dominant frequencies in the stability range (Fig. 5b). Also in the instability range with a quasi-periodic solution, the dominant frequencies can be specified (Fig. 5e). In both cases, the appearance of two disproportionate to each other frequencies can be observed. A so-called two-dimensional torus (2D torus) is created. For both Fig. 5b and Fig. 5e, the values of largest Lyapunov exponents are approximately equal to zero ( $\lambda_1=0.000002$ ,  $\lambda_2=-0.000002$  - for the point  $k=0.50$ ,  $\psi/2\Omega=0.30$ ;  $\lambda_1=0.000004$ ,  $\lambda_2=-0.000004$  - for the point  $k=0.25$ ,  $\psi/2\Omega=1.00$ ). It should be noted that the two zero Lyapunov exponents for the stability area are the result of the absence of damping in the system (3). As a consequence, there is no attractor (attractors) to which the trajectory would converge. In the instability range with a chaotic solution (Fig. 5h), the frequency spectrum is continuous. It is not possible to specify the dominant frequencies. The amplitude of the tested signal increases significantly, which is expressed in decibels. The value of the largest Lyapunov exponent is positive ( $\lambda_1=0,043531$ ,  $\lambda_2=-0,043531$ ).

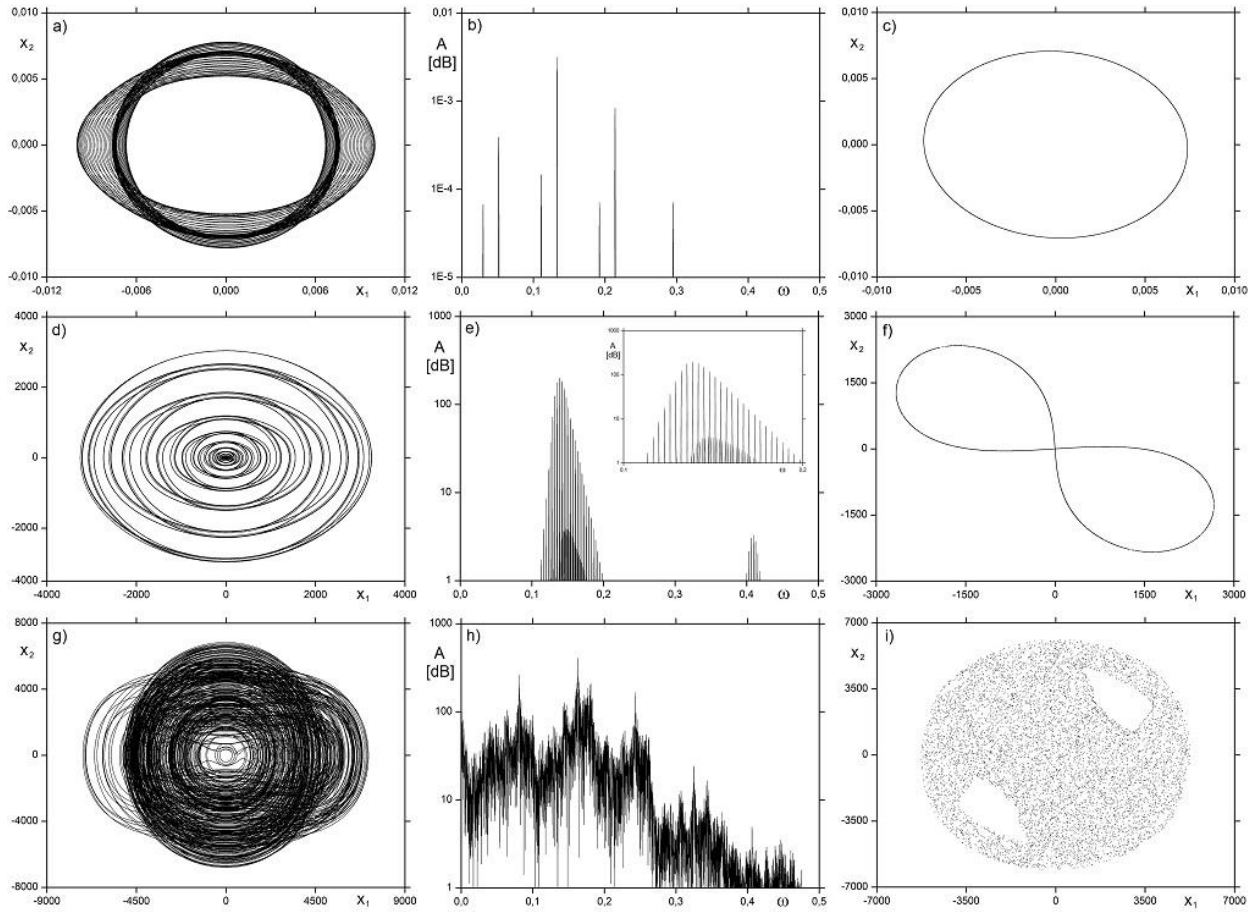


Figure 5: The plate without damping effect - the phase portraits (a, d, g), FFT analysis (b, e, h) and Poincaré maps (c, f, i) for the areas of dynamic stability (a, b, c), dynamic instability - quasi-periodic solution (d, e, f) and dynamic instability - chaotic solution (g, h, i)

Similarly to the plate without damping effect, the loss of stability for the plate with damping is associated with a sudden increase of the displacement  $x_1$  and velocity  $x_2$  values (Figs. 6d, 6f, 6g, 6i) with compared to the dynamic stability areas (Fig. 6a). In the stability area - as a result of the introduced damping - the trajectory goes to the critical point (Fig. 6a). The Lyapunov exponents values are negative ( $\lambda_1=-0,019993$ ,  $\lambda_2=-0,020007$ ) and there is no solution in the FFT analysis graphs (Fig. 6b) and Poincaré maps (Fig. 6c). In the areas of dynamic instability, a periodic solution was obtained (Figs. 6d, 6e, 6f). Together with the series of period-doubling bifurcations, it leads to a chaotic solution (Figs. 6g, 6h, 6i). The figures 6d, 6e, 6f shows a solution with a period equal to 2. The FFT analysis (Fig. 6e) enables precise representation of dominant frequencies. The Lyapunov exponents values are negative ( $\lambda_1=-0,020000$ ,  $\lambda_2=-0,020000$ ). Similarly to the plate without damping effect, in the areas of dynamic instability with a chaotic solution, the frequency spectrum is continuous and it is impossible to distinguish the dominant frequencies (Fig. 6h). The amplitude of the signal also increases. The value of the largest Lyapunov exponent is positive ( $\lambda_1=0,043397$ ,  $\lambda_2=-0,043397$ ).

#### 4. Summary

The subject of the research was to present the influence of damping effect on the dynamic response for the isotropic plate. The areas of dynamic stability and instability for the plate with and without damping were compared. Additionally, using the criteria such as phase portraits, Poincaré maps, FFT analysis, the largest Lyapunov exponents, the nature of the solution for the analyzed plate was presented.

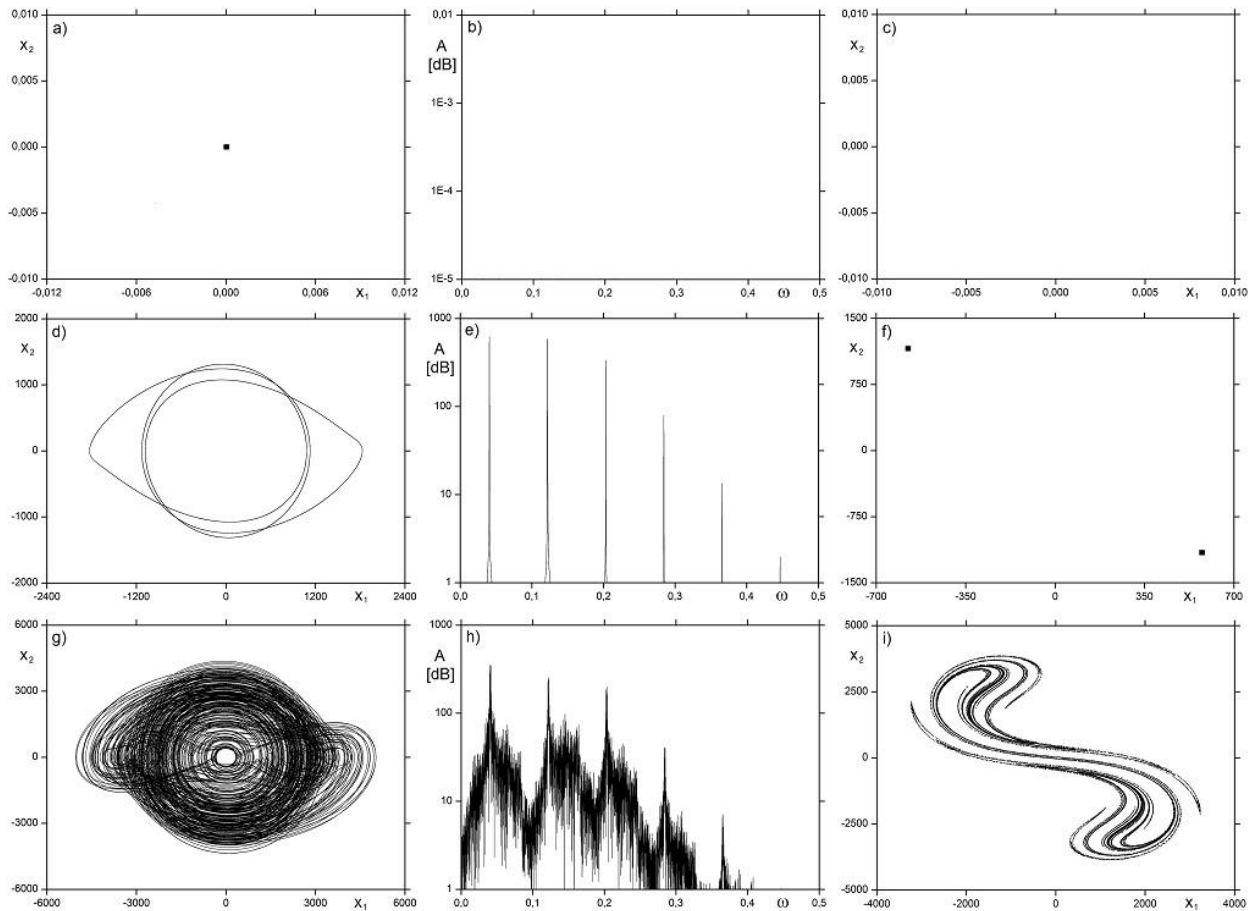


Figure 6: The plate with damping effect - the phase portraits (a, d, g), FFT analysis (b, e, h) and Poincaré maps (c, f, i) for the areas of dynamic stability (a, b, c), dynamic instability - periodic solution (d, e, f) and dynamic instability - chaotic solution (g, h, i)

After the tests, it can be concluded that the impact of damping causes the changes of instability areas for the studied structure. In addition, the introduction of damping to the system results in a significant difference in the occurrence of areas in which the solution is chaotic. For the plate without damping effect, the quasi-periodic solution in the dynamic stability areas was observed. The occurrence of two disproportionate to each other frequencies as well as the formation of 2D torus has been proved. Whereas, both the quasi-periodic as well as the chaotic solution in the instability range were specified. For the plate with damping effect in the area of dynamic stability the phase trajectory is going to the critical point. In range of dynamic instability, the periodic solutions as well as the series of period doubling bifurcations which lead to the chaotic response were obtained. In both analyzed cases (for the plate without and with damping), the loss of dynamic stability was associated with a significant increase of the displacement  $x_1$  and velocity  $x_2$  values in comparison to the dynamic stability areas { the criteria of phase portraits and Poincaré maps. Using the FFT analysis, the loss of dynamic stability results in the inability to precisely specify the dominant frequencies in the spectral signal (what is possible in the areas of dynamic stability) and a significant increase in their amplitude was found. Implementing the criterion of the largest Lyapunov exponents, it is possible to clearly present significant differences between the areas with a chaotic solution for the plate without and with damping effect.

## References

Zizicas, G.A. (1965). "Dynamic buckling of thin plates." *Trans ASME*, 74 (7) 1257-1268.

- Cooley, J.W., Tukey, J.W. (1965). "An algorithm for the machine calculation of complex Fourier series." *Mathematics of computation*, 19 (90) 297-301.
- Raftoyiannis, I.G., Kounadis A.N. (2000). "Dynamic buckling of 2-DOF systems with mode interaction under step loading." *International journal of non-linear mechanics*, 35 (3) 531-542.
- Petry, D., Fahlbusch G. (2000). "Dynamic buckling of thin isotropic plates subjected to in-plane impact." *Thin-Walled Structures*, 38 (3) 267-283.
- Hutchinson, J.W., Budiansky, B. (1966). "Dynamic buckling estimates." *AIAA Journal*, 4 (3) 525-530.
- Budiansky, B., Roth R.S. (1962). "Axisymmetric dynamic buckling of clamped shallow spherical shells." 597-606.
- Shariyat, M. (2007). "Thermal buckling analysis of rectangular composite plates with temperature-dependent properties based on a layerwise theory." *Thin-Walled Structures*, 45 (4) 439-452.
- Kubiak, T. (2007). "Criteria of dynamic buckling estimation of thin-walled structures." *ThinWalled Structures*, 45 (10) 888-892.
- Zhang, T., Liu, T.G., Zhao, Y., Luo, J.Z. (2004). "Nonlinear dynamic buckling of stiffened plates under in-plane impact load." *JOURNAL-ZHEJIANG UNIVERSITY SCIENCE*, 5 (5) 609-617.
- Volmir, A.S. (1972). "Nonlinear Dynamics Plates and Shells." *Moscow, Science*.
- Michlin, S.G., Smolnicki, C.L. (1970). "Approximate Methods for the Solution of Integral and Differential Equations." *PWN*.
- Collatz, L. (2012). "The numerical treatment of differential equations." *Springer Science Business Media*, vol. 60.
- Fortuna, Z., Macukow, B., Wasowski, J. (2005). "Metody numeryczne." *WNT. Warszawa*, ISBN 83-204-3075-5.
- Ari-Gur, J., Simonetta, S.R. (1997). "Dynamic pulse buckling of rectangular composite plates." *Composites Part B: Engineering*, 28 (3) 301-308.
- Kleiber, M., Kotula, W., Saran, M. (1987). "Numerical analysis of dynamic quasi-bifurcation." *Engineering computations*, 4 (1) 48-52.
- Hsu, Y.C., Forman, R.G. (1975). "Elastic-plastic analysis of an infinite sheet having a circular hole under pressure." *Journal of Applied Mechanics*, 42 (2) 347-352.
- Kowal-Michalska, K. (2010). "About some important parameters in dynamic buckling analysis of plated structures subjected to pulse loading." *Mechanics and Mechanical Engineering*, 14 (2) 269-279.
- Kolakowski, Z., Kubiak, T. (2007). "Interactive dynamic buckling of orthotropic thin-walled channels subjected to in-plane pulse loading." *Composite structures*, 81 (2) 222-232.
- Mania, R., Kowal-Michalska, K. (2007). "Behaviour of composite columns of closed cross-section under in-plane compressive pulse loading." *Thin-Walled Structures*, 45 (10) 902-905.
- Kubiak, T., Kolakowski, Z., Kowal-Michalska, K., Mania, R., Swiniarski, J. (2010). "Dynamic response of conical and spherical shell structures subjected to blast pressure." *Proceedings of SSDS'Rio*.
- Kolakowski, Z. (2007). "Some aspects of dynamic interactive buckling of composite columns." *Thin-Walled Structures*, 45 (10) 866-871.
- Bolotin, V. (1962). "Dynamic stability of elastic systems." Volume 1.
- Alijani, F., Bakhtiari-Nejad, F., Amabili, M. (2011). "Nonlinear vibrations of FGM rectangular plates in thermal environments." *Nonlinear Dynamics*, 66 (3) 251-270.
- Alijani, F., Amabili, M., Karagiozis, K., Bakhtiari-Nejad, F. (2011). "Nonlinear vibrations of functionally graded doubly curved shallow shells." *Journal of Sound and Vibration*, 330 (7) 1432-1454.
- Yuda, H., Zhiqiang, Z. (2011). "Bifurcation and chaos of thin circular functionally graded plate in thermal environment." *Chaos, Solitons & Fractals*, 44 (9) 739-750.
- Wang, Y.G., Song, H.F., Li, D., Wang, J. (2010). "Bifurcations and chaos in a periodic timevarying temperature-excited bimetallic shallow shell of revolution." *Archive of Applied Mechanics*, 80 (7) 815-828.
- Yeh, Y.L., Lai, H.Y. (2002). "Chaotic and bifurcation dynamics for a simply supported rectangular plate of thermo mechanical coupling in large deflection." *Chaos, Solitons & Fractals*, 13 (7) 1493-1506.
- Touati, D., Cederbaum, G. (1995). "Influence of large deflections on the dynamic stability of nonlinear viscoelastic plates." *Acta mechanica*, 113 (1-4) 215-231.
- Kolakowski, Z., Teter, A. (2013). "Influence of Inherent Material Damping on the Dynamic Buckling of Composite Columns with Open CrossSections." *Mechanics and Mechanical Engineering*, 17 (1) 59-69.
- Borkowski, L. (2017). "Numerical Analysis of Dynamic Stability of an Isotropic Plate by Applying Tools Used in Dynamics." *Dynamical Systems Theory and Applications. Springer, Cham*.

## BUCKLING OF CIRCULAR RINGS: SOME ISSUES RELATED TO THE SETTINGS OF FINITE ELEMENTS ANALYSES

Ida Mascolo<sup>1</sup>, Arsenio Cutolo<sup>2</sup>, Luca Esposito<sup>3</sup>, Federico Guarracino<sup>4</sup>

### Abstract

Buckling of circular rings under external pressure is one of the oldest problems in structural engineering and the first solution to it was proposed by Levy in 1884. The basic solution for the Euler-Bernoulli beam can be found in the vast majority of textbooks on stability. However, in a world which strongly relies on FE commercial packages, one should be always well aware of these fundamentals and in the present work some considerations arising from the numerical treatment of the problem by means of FE and from the classic analytical solutions of the differential equations are discussed in order point out some inconsistencies which may arise the numerical analyses.

### 1. Introduction

This paper briefly reviews some aspects of the buckling of circular rings and highlights the need for engineers using the numerical modelling to be aware of their limitations and to ensure that the numerical results are always judged bearing in mind some fundamental analytical solutions.

In fact, one of the present authors has examined to some extent over the years a number of classic problems in the stability of thin walled structures in the elastic and in the elastic-plastic range and discussed the advantages and drawbacks of analytical and numerical approaches. Problems related to modes interaction, material modelling and to imperfection sensitivity have been examined with respect to well-known conundrums in the theory of stability and it has been shown that the combination of all these aspects is such that any numerical analysis, despite the availability of modern very powerful nonlinear FE packages, must be preceded by a careful examination of the particularities of the problem at hand (Guarracino, 2019). In fact, a skillful insight into the mechanics of the problem is always vital in order to attain a good agreement with experimental results and provide reliable predictions for a large number of cases.

---

<sup>1</sup> [ida.mascolo@unilodz.pl](mailto:ida.mascolo@unilodz.pl), [arsenio.cutolo@unilodz.pl](mailto:arsenio.cutolo@unilodz.pl), [luca.esposito@unilodz.pl](mailto:luca.esposito@unilodz.pl), [federico.guarracino@unilodz.pl](mailto:federico.guarracino@unilodz.pl)

<sup>2</sup> [arsenio.cutolo@unilodz.pl](mailto:arsenio.cutolo@unilodz.pl), [luca.esposito@unilodz.pl](mailto:luca.esposito@unilodz.pl), [federico.guarracino@unilodz.pl](mailto:federico.guarracino@unilodz.pl)

<sup>3</sup> [luca.esposito@unilodz.pl](mailto:luca.esposito@unilodz.pl), [arsenio.cutolo@unilodz.pl](mailto:arsenio.cutolo@unilodz.pl), [ida.mascolo@unilodz.pl](mailto:ida.mascolo@unilodz.pl), [federico.guarracino@unilodz.pl](mailto:federico.guarracino@unilodz.pl)

<sup>4</sup> [arsenio.cutolo@unilodz.pl](mailto:arsenio.cutolo@unilodz.pl), [luca.esposito@unilodz.pl](mailto:luca.esposito@unilodz.pl), [ida.mascolo@unilodz.pl](mailto:ida.mascolo@unilodz.pl), [federico.guarracino@unilodz.pl](mailto:federico.guarracino@unilodz.pl)

Here the attention is focused on the simple buckling of circular rings under external pressure, which is one of the oldest problems in structural engineering, since its first solution was proposed by Levy in 1884 (Levy 1884). This solution, which applies to the Euler-Bernoulli model of beam can be found in the vast majority of textbooks on stability. However, it is rather surprising that such a solution cannot be straightforwardly replicated on the same bases by a simple Eigenvalue Buckling Analysis by one of the most known commercially available FE package, i.e. ANSYS Mechanical (ANSYS 2020). Actually, in order to obtain numerically the critical load from the classic Levy’s solution one has to make reference to a beam modelling which involves the shear deformation, that is the classic Timoshenko–Ehrenfest beam theory, thus effectively lowering the stiffness of the ring.

The findings are discussed and compared with the analytical solution provided by Timoshenko (Timoshenko and Gere 1961) and Smith and Simitzes (Smith and Simitzes 1969).

## 2. Some analytical background

The problem under consideration is the initial buckling of a thin ring of mean radius  $R$  under an external hydrostatic pressure  $p$ , as shown in Fig.1.

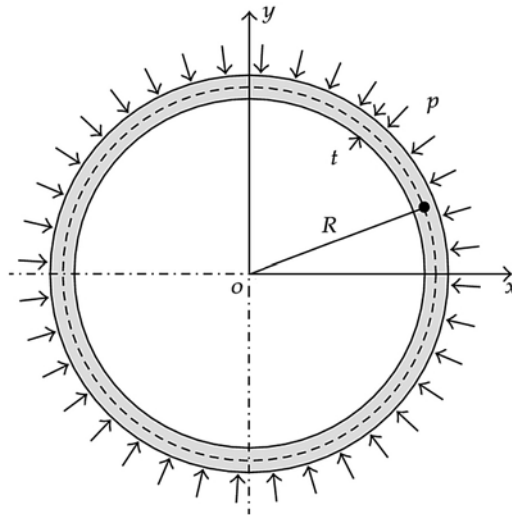


Figure 1: A thin ring under external hydrostatic pressure

where  $t$  is the ring thickness.

In the framework of a nonlinear, small strain, moderate rotation kinematics and in the hypothesis of inextensional deformation, Timoshenko and Gere, moving from the classic result by Levy, provide the following expression for the critical pressure:

$$p_{cr} = \frac{3EI}{R^3} \quad (1)$$

where  $E$  is the Young Modulus of the material and  $I$  the inertia of the cross section.

However, this solution neglects the effect of transverse shear deformation on the magnitude of the critical pressure. While it is expected that this effect will be negligible for thin rings, it might be not for

many other cases and Smith and Simitzes proposed the following expression for the critical pressure accounting for both the effect of extensional and transverse shear deformation:

$$\bar{p}_{cr} = \frac{3EI}{R^3} \frac{1}{1 + \psi} \quad (2)$$

with

$$\psi = \frac{EI}{B} \frac{1}{R^2} \quad (3)$$

and

$$B = \kappa GA \quad (4)$$

where  $G$  is the shear Modulus,  $A$  is the area of the cross section and  $\kappa$  is the Timoshenko shear coefficient.

For a steel ring ( $E=2.1 \times 10^5 \text{MPa}$ ,  $G=8 \times 10^4 \text{MPa}$  and  $\kappa=5/6$ ) with a rectangular cross section of 5mm x 50mm and radius  $R=250, 375$  and  $500\text{mm}$ , Eqs. (1-4) provide the results collected in Table 1.

Table 1: Critical pressures for a ring of section 5 x 50 mm (analytical)

R	$P_{cr}$	$\bar{p}_{cr}$	$(1 - \bar{p}_{cr} / p_{cr})$
(mm)	(N/mm)	(N/mm)	(%)
250	21.000	20.991	0.04
375	6.2222	6.2211	0.02
500	2.6250	2.6247	0.01

As it can be physically expected, the results for a thin ring as the one taken into consideration, do not vary significantly by taking into account the effect of extensional and transverse shear deformation. Also, the percent difference decreases with the increase of the radius.

### 3. FE analyses

Several numerical analyses have been carried out by means of the Finite Element package ANSYS® (ANSYS 2019). The model was carefully calibrated and it was found that a mesh of 200 elements was sufficient to stabilise the results, as shown in Fig.2. Fig.2 also shows the unit applied pressure. The boundary conditions were such as to prevent any rigid motions.

The ring was modelled either by means of BEAM4 3-D 2Nodes elements or BEAM188 – 3-D 2Nodes elements. BEAM4 is a uniaxial element with tension, compression, torsion, and bending capabilities. Stress stiffening and large deflection capabilities are included. A consistent tangent stiffness matrix option is available for use in large deflection (finite rotation) analyses. BEAM4 3-D is apt to represent the Euler-Bernoulli beam theory in the simplest possible formulation. Starting from ANSYS 14.5 it is no longer possible to activate BEAM4 3-D via Menu, but it can be used by means of the APDL.

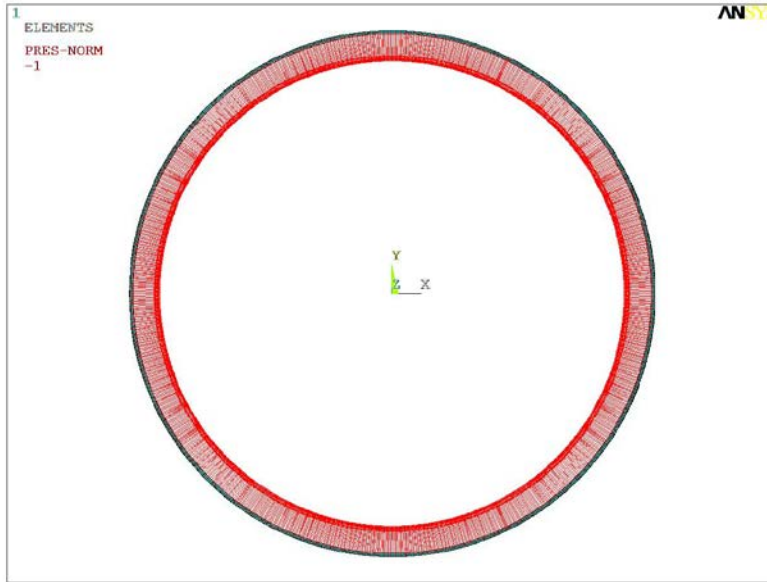


Figure 2: Finite Element mesh

According to the ANSYS Theory Manual, BEAM188 is suitable for analyzing slender to moderately stubby/thick beam structures. The element is based on Timoshenko beam theory which includes shear-deformation effects. The element is a linear, quadratic, or cubic two-node beam element in 3-D and has six degrees of freedom at each node. These include translations in the x, y, and z directions and rotations about the x, y, and z directions. The element is well-suited for linear, large rotation, and/or large strain nonlinear applications. The element includes stress stiffness terms in any analysis with large deflection and the provided stress-stiffness terms enable the user to analyze flexural, lateral, and torsional stability problems, in the case at hand using eigenvalue buckling.

Importantly, since the comparison was meant to be made versus the results from Eq. (2), it is worth noticing that BEAM188 is based on a first-order shear-deformation theory, which means that transverse-shear strain is constant through the cross-section, i.e. cross-sections remain plane and undistorted after deformation.

In order to assess further the validity of the results, the critical pressure for the Euler-Bernoulli beam theory was calculated first using the BEAM4 3-D 2Nodes elements and successively the BEAM188 – 3-D 2Nodes elements with the shear stiffness set to infinite. The results were found in perfect agreement.

A simple eigenvalue or linear buckling analysis was performed to predict the theoretical buckling strength of the ring seen as an ideal linear elastic structure. Numerically, this method corresponds to the textbook approach of linear elastic buckling analysis and the eigenvalue buckling solution of a Euler column is easily seen match the classical Euler solution. However, this does not turn to be the case for a simple ring under hydrostatic pressure.

Figs. 3-5 show the first three eigenmodes from the numerical analysis in the case of  $R=500$  without taking into account the effect of transverse shear deformation. It is easy to verify that the first and the second modes show a strong affinity to the first two-wave mode from the classic analytical formulation ( $n=2$ ), while the third mode is alike to the second three-wave mode from the classic analytical formulation ( $n=3$ ), see Timoshenko and Gere (1961).

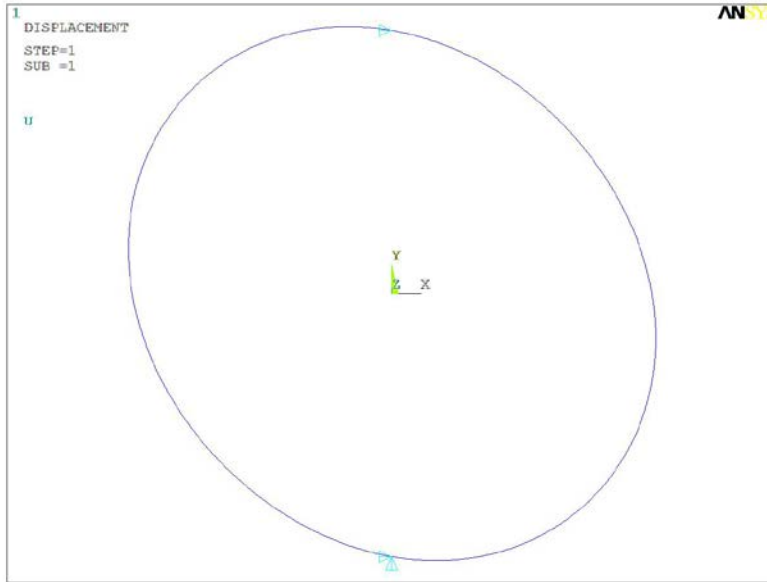


Figure 3: First eigenmode (FE analysis:  $R=500$ ,  $P_{cr} = 2.8624$  N/mm)

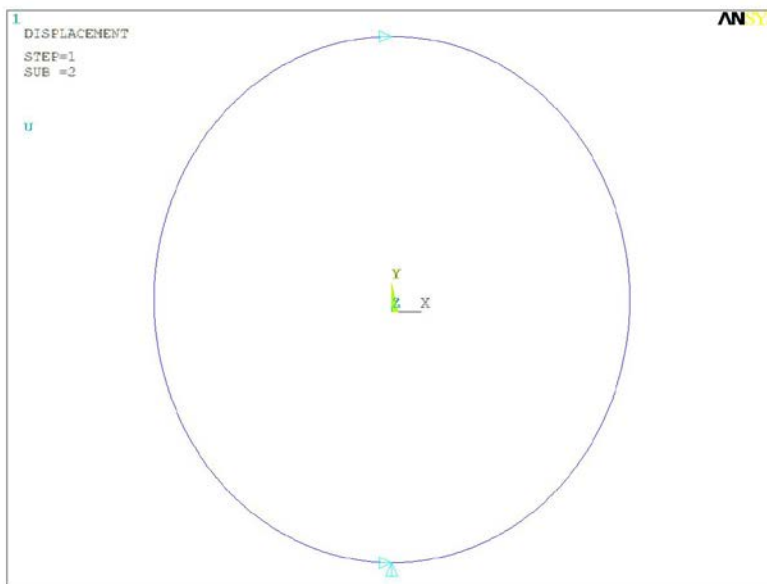


Figure 4: Second eigenmode (FE analysis:  $R=500$ ,  $P_{cr} = 3.5000$  N/mm)

Figs. 6-8 show the first three eigenmodes from the numerical analysis in the case of  $R=500$  by taking into account the effect of transverse shear deformation. The situation is somewhat different from the previous case, because it is easy to verify that the first mode shows a strong affinity to the first two-wave mode from the classic analytical formulation ( $n=2$ ), while the second and third modes are alike to the second three-wave mode from the classic analytical formulation ( $n=3$ ), see Smith and Simitsev (1969). This is not surprising, because modes two (Fig.7) and three (Fig.8) are characterised by nearly the same eigenvalue corresponding to the magnitude of the critical pressure, i.e.  $6.9989$  vs  $6.9990$  N/mm.

However, this fact points out that in the numerical treatment of buckling problems, minor variations in modelling are capable of producing significant changes in the sequence of buckling patterns (Guarracino and Walker 2008).

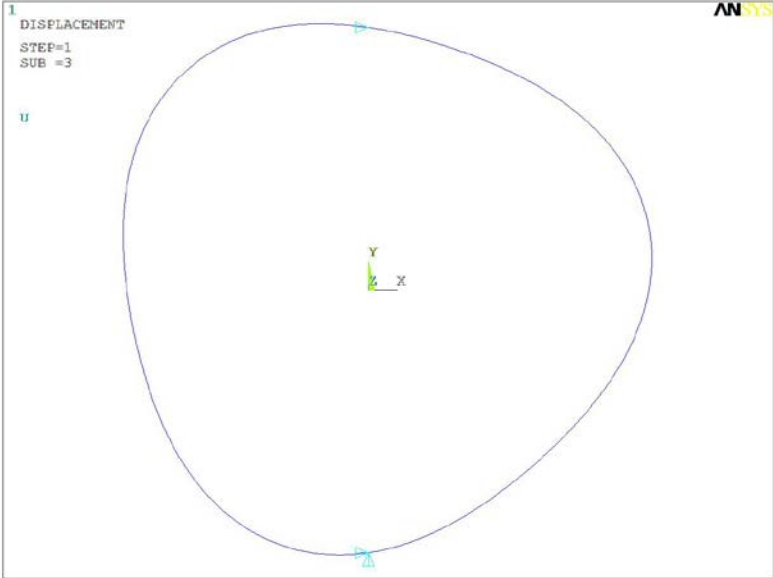


Figure 5: (FE analysis:  $R=500$ ,  $P_{cr} = 7.8750$  N/mm)

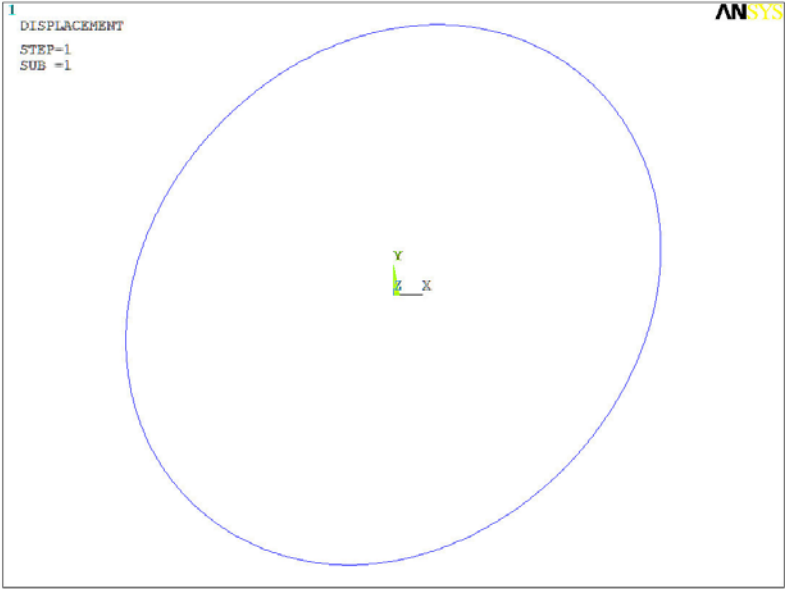


Figure 6: First eigenmode (FE analysis:  $R=500$ ,  $\bar{p}_{cr} = 2.6248$  N/mm)

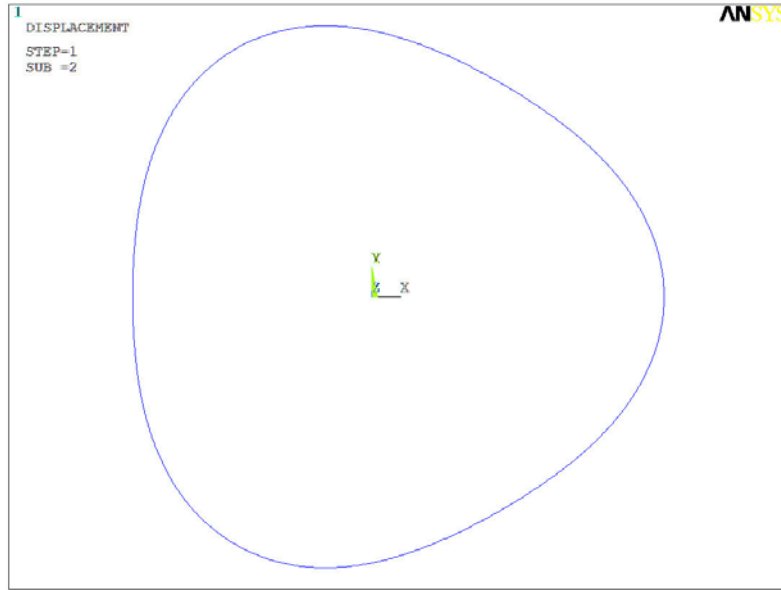


Figure 7: Second eigenmode (FE analysis:  $R=500$ ,  $\bar{p}_{cr} = 6.9989$  N/mm)

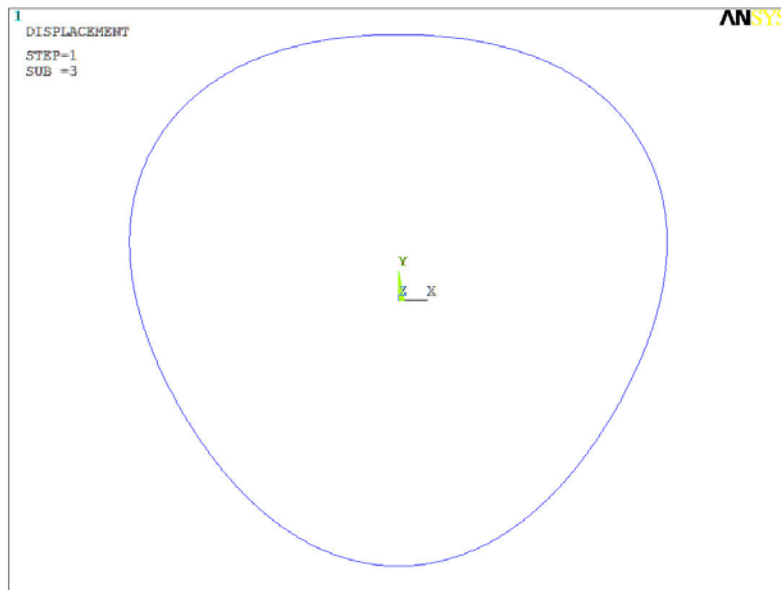


Figure 8: Third eigenmode (FE analysis:  $R=500$ ,  $\bar{p}_{cr} = 6.9990$  N/mm)

In fact, it is well known that any non-linearity introduces the possibility of non-unique relationships between loading applied to the structure and the corresponding buckling failure mode. Also, it is very possible that results from numerical non-linear modelling will be nearly coincident and could lead to erroneous engineering design. The different sets of first three modes displayed by the FE analyses on account of taking into consideration the effect of transverse shear deformation in a case where this should be, by virtue of Eqs.(1-4), practically negligible (see Table 1), is a proof of the above considerations.

Table 2 collects the numerical critical pressure results for the same steel ring with a cross section of 5mm x 50mm and radii R=250, 375 and 500mm, previously calculated on the basis of Eqs. (1-4).

Table 2: Critical pressures for a ring of section 5 x 50 mm (FE)

R	$P_{cr}$	$\bar{p}_{cr}$	$(1 - \bar{p}_{cr} \square p_{cr})$
(mm)	(N/mm)	(N/mm)	(%)
250	22.898	21.195	8
375	6.7848	6.2214	9
500	2.8624	2.6248	9

Here it can be noticed that the results from the FE analyses vary much more than the analytical ones when taking into account the effect of extensional and transverse shear deformation. Also, the percent difference does not vary significantly with the progressive increase of the radius, as it is the case for the analytical results.

Notably, the results based on the Euler-Bernoulli beam theory are not in line with those from Eq.(1) and show a not negligible overestimation of the value of the critical pressure.

#### 4. Conclusions

In the present work some inconsistencies arising from the numerical treatment by a well known FE commercial package of the problem of the buckling of circular rings under hydrostatic pressure have been pointed out in order to stress once more the need for engineers using the numerical modelling to be aware of their limitations and to ensure that the numerical results are always judged bearing in mind some fundamental analytical solutions.

#### References

- Levy M. (1884) "Mémoire sur un nouveau cas intégrable du problème de l'élastique et l'une de ces applications." *Journal of Mathematics (Liouville) 3<sup>e</sup> série*, 10 5-42.
- Timoshenko, S.P., Gere, J.M. (1961). "Theory of Elastic Stability." McGraw-Hill Book Company, New York.
- Smith Jr, C.V., Simitses, G.J. (1969). "Effect of Shear and Load Behavior on Ring Stability." *Journal of the Engineering Mechanics Division (ASCE)*, 95 (3) 559-569.
- Guarracino, F., Walker, A.C. (2008). "Some comments on the numerical analysis of plates and thin-walled structures." *Thin-Walled Structures*, 46(7-9) 975-980.
- Guarracino, F. (2019). "Remarks on the stability analysis of some thin-walled structures in the elastic-plastic range." *Thin-Walled Structures*, 138 208-214.
- "ANSYS 19 User's Documentation." (2019). ANSYS, Inc., Canonburg, PA 15317, USA.

## Dynamic buckling of crash boxes under an impact load

Nima Jafarzadeh Aghdam<sup>1,\*</sup>, Kai-Uwe Schroeder<sup>2</sup>

### Abstract

Crash boxes (CBs) are widely used to absorb the energy of impact loads in collisions. For crash boxes, buckling stress is an important design factor. However, defining the initiation point of the dynamic buckling is a challenge due to the dynamic nature of the impact. In this research, experimental drop tower tests have been conducted on CBs. Then, finite element (FE) modeling of the CBs was performed by Abaqus commercial software, and the FE model was validated by the drop-tower test results. This paper provides some important remarks for simulating and validating the FE model. The structural behavior of the CB under an impact load is investigated. A new criterion, named section-points criterion, is introduced in order to detect the dynamic-buckling point. This criterion is applicable for experimental tests and FE simulations, and it shows good accuracy in detecting the buckling point.

### 1. Introduction

Crash boxes are thin-walled structures, which are used widely for energy absorption. Well-designed CBs can absorb a high amount of energy in comparison to their weight. A clear understanding of the structural behavior of a CB under compression loads is required in order to design a proper CB. However, because of the complex coupling of material and structural effects, many uncertainties remain in this research field (Aghdam *et al.*, 2019; Singer *et al.*, 2002). Furthermore, analyzing CBs under an impact load is even more complicated due to the complex dynamic nature of the impact.

Critical-buckling stress of a CB has an important effect on its structural behavior under axial compression, and it should be considered in the designing procedure. A square CB can be considered as four connected plates and many buckling criteria of the plates are applicable to CBs as well. Plates with restrained out-of-plate displacement at the edges have a special capability of bearing the load even after buckling up to the load named collapse-force of the plate. This special capability makes detecting the buckling point more complicated. In the last decades, some criteria were introduced by researchers for the dynamic stability of plates. Kubiak has reviewed several dynamic-buckling criteria (Kubiak, 2013). Dynamic buckling criteria can be divided into geometric and energetic categories. Geometric criteria are those in which a loss of dynamic stability refers usually to deflection or shortening, whereas the energy criteria are designed based on the potential and/or kinetic energy of the system (Kubiak, 2013). The energy-based approaches allow determining a lower bound for the dynamic-buckling load without solving nonlinear equations of motion of the structure. However, the established lower bound can be very conservative (Mallon, 2008). Several geometrical-based approaches were evaluated and compared

<sup>1</sup>, [n.jafarzadeh@p.lodz.pl](mailto:n.jafarzadeh@p.lodz.pl), Rzeszów University of Applied Sciences, ul. Powiatowa 28, 41-200 Lublin, Poland

<sup>2</sup> [k.schroeder@tu-lodz.pl](mailto:k.schroeder@tu-lodz.pl), Rzeszów University of Applied Sciences, ul. Powiatowa 28, 41-200 Lublin, Poland

by Paszkiewicz and Kubiak (Paszkiewicz and Kubiak, 2015). The geometric criteria are not so precise either for structures with stable post-buckling behavior, and further investigations are required on the topic.

For structures with an unstable post-buckling equilibrium path, it is possible to derive mathematically a relation for calculating the critical dynamic buckling load (Kubiak, 2013). However, for plate structures, the mathematical derivation is not possible and the criteria have been formulated from observations of the behavior of such structures or on the basis of experiments (Kubiak, 2013). The most adopted dynamic buckling criterion is defined by Budiansky et al. (Mallon, 2008). Budiansky-Hutchinson criterion (Hutchinson and Budiansky, 1966) was formulated for structures having an unstable post-bifurcation path, and its application to plates, with stable post-buckling path, is based rather on intuition. Currently, there are several stability criteria, mostly based on the state of displacements or stress, which are not so precise, furthermore except a few papers, e.g., (Kowal-Michalska, 2010), most of the studies considered just the elastic range. Therefore, the literature still lacks a promising approach for detecting the dynamic-buckling point of thick plates.

In this paper, a new approach, named section-points criterion, is introduced for extracting the dynamic-buckling load of the CBs, and it is applied to thick CBs. The remainder of this paper is structured as follows: the drop-tower test is explained in section 2. Section 3 describes the FE simulation of the CB and its validation. Then, results of applying Budianski-Hutchinson criterion are provided, afterward section-points criterion is introduced and applied on the CB. Finally, the paper concludes in section 4.

### 2. Drop tower test

Drop tower test is a common method of implementing impact load on structures. Drop tower setup which was used in this research is shown in Fig. Square CBs made by aluminum 6060 were used for the

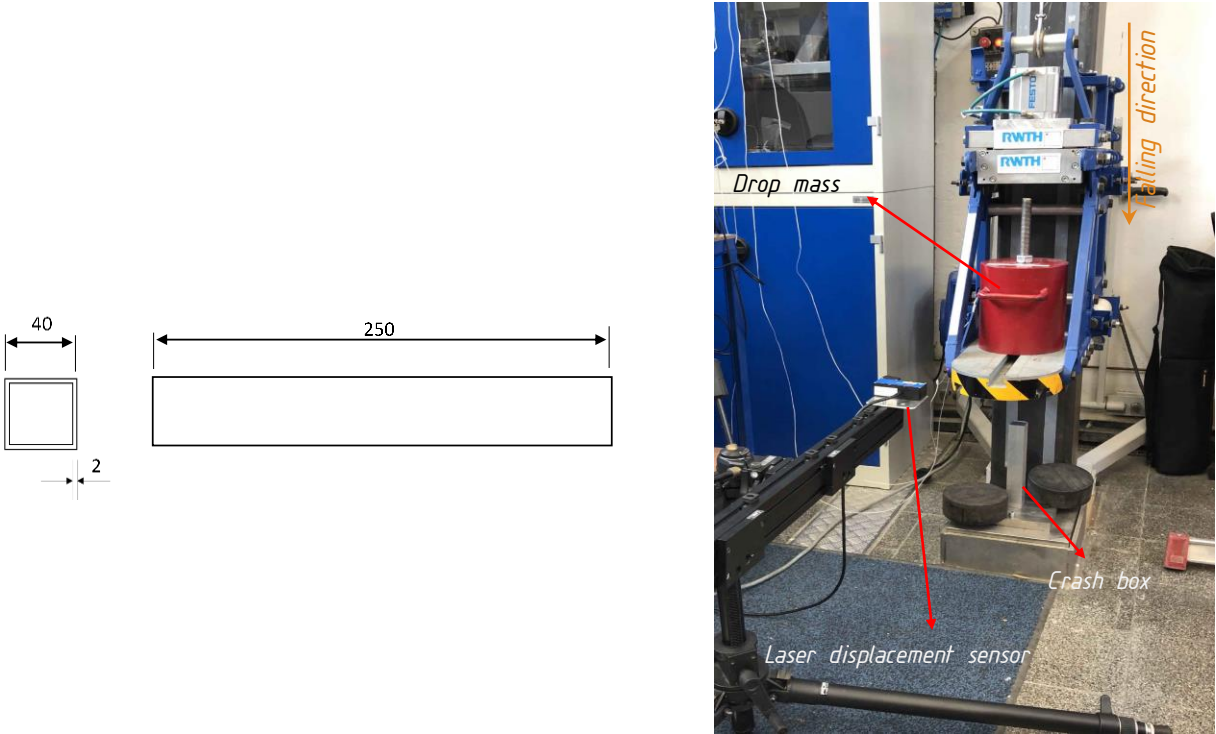


Figure 1: Crash box dimensions (left) drop tower setup (right)

experiment. Dimensions of the CBs are shown in Fig. 1. A drop mass of 162 kg was released from 3.3 m to apply the impact load. The height of the drop mass was calculated in order to bottom-out the CBs. For safety reasons, two black rubber cylinders were set beside the specimens. The height of the cylinders was below the height of the bottomed-out CBs. Even though all the samples were cut from the same extruded aluminum profile, the folding pattern was not the same for all of them. Some of the samples had a mixed folding pattern, but CBs with 11 inextensional folds, also named symmetric folds, was the most repeatable case (see Fig. 2b and Fig. 2c). In an inextensional fold, the crests and the valleys of the buckles appear alternately in the adjacent side planes of the CB (Chen, 2015). The probability of an inextensional folding pattern is higher for the CBs with a width to thickness ratio beyond 40 (Jones, 1990). Choosing CBs with the mentioned width to thickness ratio can result in more repeatable outcomes. Two piezo-electric accelerometers were arranged on the drop mass and averaged output of the sensors was adopted. Moving-window-averaging technique with an equivalent 587 Hz cut-off frequency was used as a low-pass filter. The extracted acceleration was converted to the force.

### 3. Finite element simulation

A finite element (FE) simulation of the CB was performed by Abaqus commercial software using dynamic-explicit analysis. Half of the CB was simulated because of the CB symmetry. The CB was simulated between two rigid plates, free boundary condition was assigned to the CB ends. A point mass of 162 Kg was implemented on the striking plate. 4-node doubly-curved shell elements with reduced integration (S4R) were used for meshing. By performing a mesh-convergence analysis, 1.25 mm mesh size showed good accuracy and time efficiency. Material properties of aluminum 6060 were implemented (Table 1). The material properties were extracted by conducting tensile tests according to ASTM B557M-15 (B07 committee, 2017).

Table 1: material properties of aluminum 6060

E (GPa)	0.002 offset $\sigma_y$ (MPa)	$\rho$ (kg/m <sup>3</sup> )	$\sigma_u$ (MPa)
70.6	201.4	2.7	248.4

It should be considered that for an ideal structure, without any geometrical imperfection, if it is uniformly compressed the critical-buckling load leads to infinity. Therefore, the dynamic buckling can be analyzed only for structures with initial geometrical-imperfections (T. Kubiak, 2013). In a numerical simulation of a perfect structure, the numerical round off error triggers the instability. However, the numerical errors can generate unrealistic results. Therefore, in order to have more realistic results, a small imperfection should be applied on the FE model. The same procedure has been reported by other

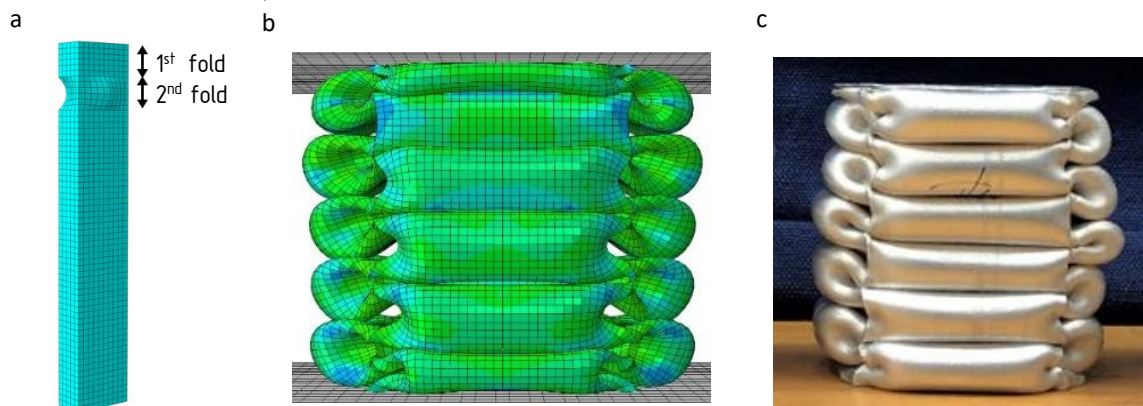


Figure 2: a) Imperfection on the crash box (exaggerated) b) FE simulation result c) drop tower test result.

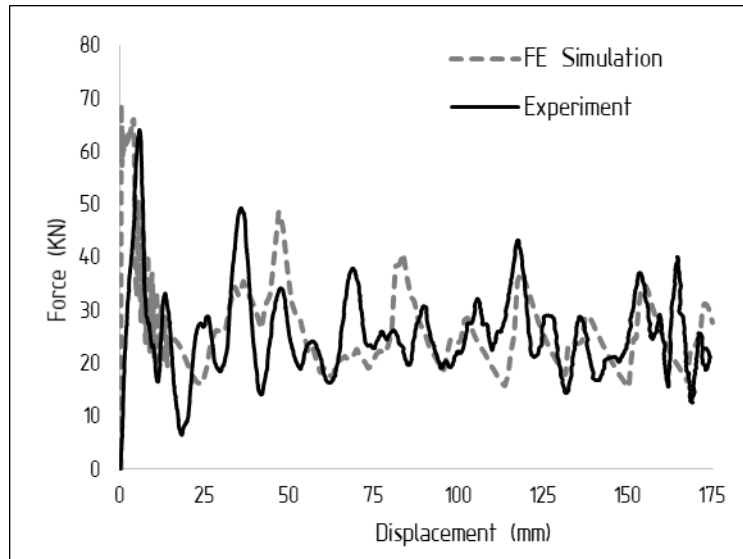


Figure 3: Force-displacement diagrams of the experimental test and numerical simulation

researchers as well (Meguid *et al.*, 2007; Meguid, Stranart and Heyerman, 2004). It should be noted, in the conducted experiments there was not any imperfection made on the CBs, but production imperfections are unavoidable. In the FE model, a spline with a slight projection of 0.1 mm (0.25% width) at the second-fold location was applied as the imperfection (Fig. 2a). The second-fold location was extracted based on the experimental-test result. The FE simulation and experiment results are shown in Fig. 2b and Fig. 2c, and force-displacement diagrams are shown in Fig. 3. Overall a good agreement was obtained between the results.

### 3. Results and discussing

#### 3.1 Budiansky-Hutchinson stability criterion

Budianski-Hutchkinson criterion (Hutchinson and Budiansky, 1966) has been applied to the FE-simulation results in order to detect the dynamic-buckling point. Due to Budiansky-Hutchinson stability criterion, dynamic stability loss occurs when the maximal plate deflection grows rapidly with the small variation of the load amplitude (Kowal–Michalska, 2010). Hereby, this criterion is used for progressively buckled CB. The stress to the transverse-deflection diagram is shown in Fig. 4 for the mid-point of the

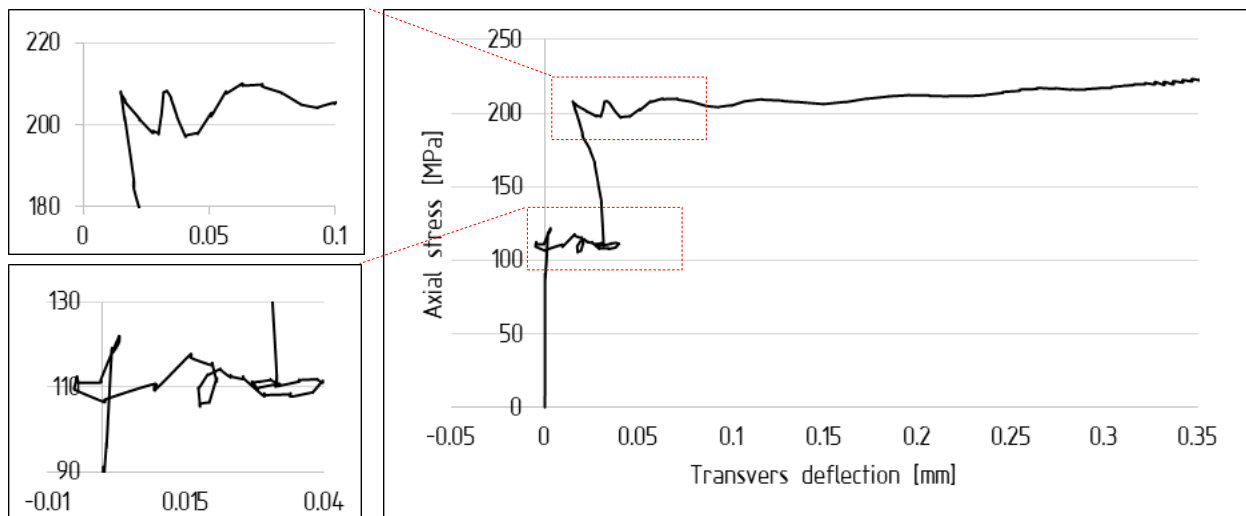


Figure 4: Budiansky-Hutchinson stability criterion

first fold on the simulated CB. Two important points, located at 110 and 201 MPa, can be detected on the diagram. Due to the obvious rapid growth of the deflection, without stress increase, both 110 MPa and 201 MPa can be the buckling point, based on the criterion. Even though higher buckling stress than 110 MPa is expected based on the CB dimensions, the buckling stress can be reduced significantly due to the applied imperfection (Budiansky and Hutchinson, 1996). By considering the 110 MPa as the buckling stress the rest of the diagram is post-buckling phase of the structure, which is related to plates' special capability in withstanding the load after buckling. On the other hand, rapid deflection growth at 110 MPa can be related just to the first propagation of the stress wave. The stress wave can be calculated as

$$\sigma = \rho cv \tag{1}$$

where  $\sigma$  is shock wave stress,  $\rho$  is density,  $c$  is the speed of sound in the material and  $v$  is impact velocity. By considering the progressive buckling of the CB with the regular folding pattern (see Fig.2c), plastic buckling of the CB is more probable and thus, the buckling stress of 207 MPa is more reasonable. Therefore, the dynamic nature of the impact complicates the structural analysis, and detecting the dynamic-buckling point of the CB using Budiansky-Hutchinson criterion is still a challenge.

### 3.2 Section-points criterion

In this section, a new method of detecting initiation of the dynamic-buckling is introduced based on the distribution (Dist.) of stress on the cross-section of the plate. The main idea is based on the strain difference between the inner and outer surfaces of a bent plate. The method is named section-points criterion, and it is applicable for both experiments and numerical simulations.

Section-points approach can be implemented to the FE simulations by defining thickness integration points. By analyzing the stress Dist. along the first fold, structural behavior under the impact load can be analyzed. Three integration points (also named section points) are defined on the thickness and consequently, outputs on three rows of section points (SPs) along the width can be extracted. By increase of stress to the buckling stress, plates start to bend. Due to the bending, stress differs between inner and outer surfaces (see Fig. 5). In Fig. 6, the stress Dist. along the width for the SPs are shown, which are named stress-Dist.-lines. The extracted stress is the axial stress in the longitudinal direction of the CB. By applying the impact load, a stress wave is propagating along the structure and stress is increasing for all the SPs. By the second stress-wave propagation, the stress increases beyond the yield

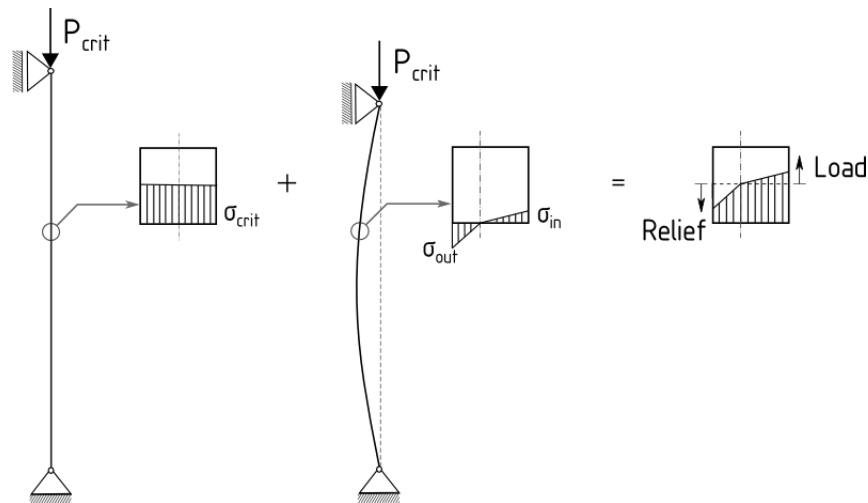


Figure 5: Stress-distribution change on the thickness due to the buckling. After the buckling, loading is function of tangent modulus, but relief is function of Young modulus.

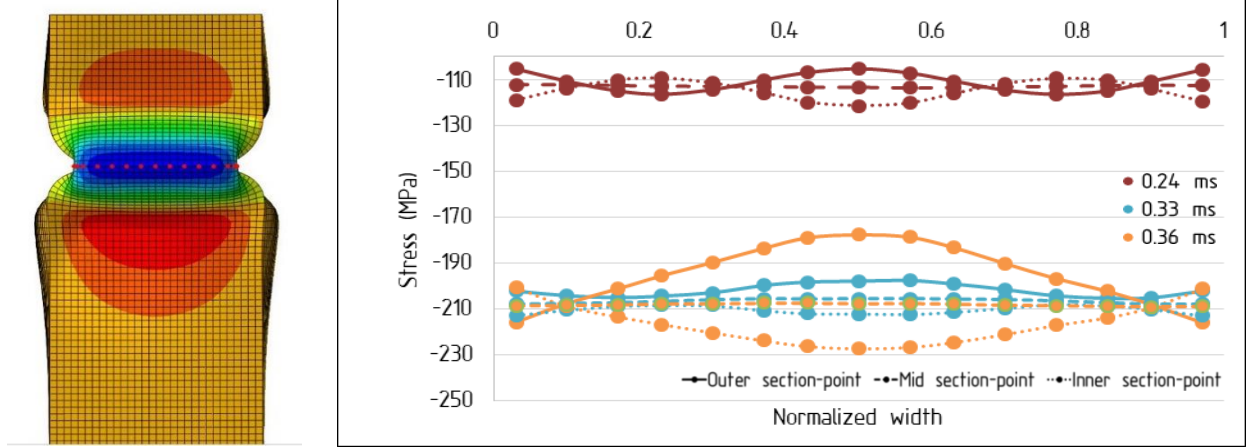


Figure 6: Section-points criterion. Buckled CB (red nodes are data extraction nodes) (left), axial-stress distribution along the CB width (right).

point of the material. At 3.3 ms, the outer-SPs stress decreases; however, the stress is still increasing at the inner-SPs. At the same time, the stress is relatively constant at the mid-SPs. The stress divergence on the thickness is related to the buckling initiation and bending of the plate. So it can be concluded that the buckling happens at 3.3 ms, when the stress is 207 MPa and it is beyond the material yield point. The different rates of stress change at inner and outer SPs can be explained by considering the plastic buckling of the CB. The sharp stress reduction at the outer-SPs is a function of the Young modulus; however, the stress increase at inner-SPs is a function of the tangent modulus (Fig. 5). In Fig. 6, some fluctuations at 0.24 ms can be seen as well on the stress Dist. lines. These small stress fluctuations are related to the shock-wave propagation and cannot be considered as buckling initiation as the stress of all the nodes is still increasing in the next time steps. For further investigations, Dist.-variation-index is introduced for analyzing the CB behavior. Firstly, summation of the axial stresses on outer SPs and inner SPs are calculated for nodes located at the middle of the first fold (see Fig. 6 (left)), then Dist.-variation-index can be calculated by dividing the difference of the extracted summations by the yield stress of the material. The sudden increase in the extracted index is the dynamic-buckling point. By considering the nodes series along the width, instead of a node at the middle of the fold, a better estimation of the buckling initiation can be achieved. The diagram of Dist.-variation-index is shown in Fig. 7. After the first stress-wave propagation, the index value increases a bit due to the structural deformation. However, after this wave, the diagram shows a constant index up to 3.3 ms, and just then there is a sudden increase in the index value which is related to the buckling initiation. Thus, Dist.-variation-index shows good accuracy in detecting the initiation point of the dynamic-buckling.

As it was mentioned, the approach is applicable for experimental tests as well. The strain difference at the inner and outer surfaces of the plate should be analyzed, in the experimental tests. For this purpose, two strain-gauges should be attached to the inner and outer surfaces of the CB side-wall at the first fold location. Since the first fold can occur at either end of the CB in the dynamic test, strain gauges should be attached to both ends of the CB plate and at least 4 strain gauges are required. In this case, Dist.-variation-index can be calculated based on the strain gauges data on just one node. Adding more strain gauges along the CB width can increase the accuracy. By section-points criterion, initiation of the dynamic buckling can be detected based on the sudden index increase.

### 3.3 Compressive force distribution

Analyzing compressive force Dist. on the width of the CB is a common approach to analyze the CB behavior and detect the buckling point. The compressive force Dist. along the width of the plate is shown in Fig. 8. The compressive force can be calculated as

$$SF = \int_{-h/2}^{h/2} \sigma_{axial} dt \quad (7)$$

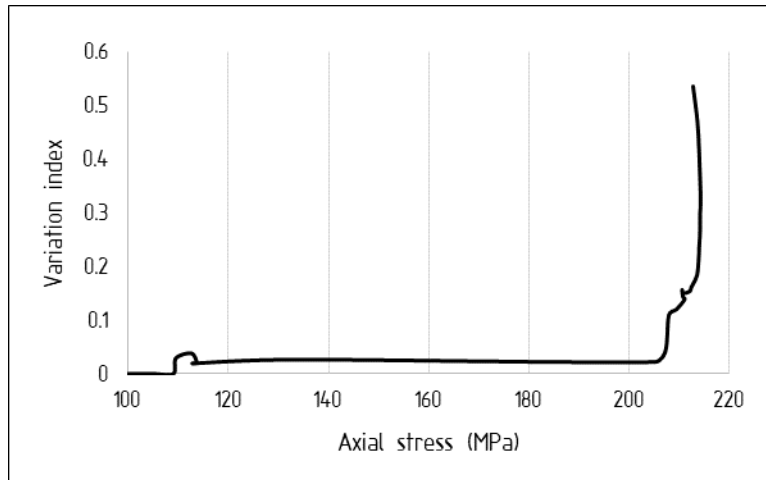


Figure 7: Section-points criterion and distribution-variation-index, the sudden jump in the index shows buckling initiation at 207 MPa

where  $SF$ ,  $t$  and  $h$  are section force, thickness and plate thickness value respectively. Due to the buckling, load decreases at the mid-side of the plate and it increases at the sides. By analyzing the compressive force diagram (Fig. 8), at 0.36 ms the membrane force is almost constant along the width and the buckling effect on the compressive force diagram is obvious just after 0.9 ms. By initiation of the buckling and stress reduction at the outer surface, stress increases at the inner surface. The membrane force diagram provides an average force value of the thickness; therefore, even though it provides useful information, it cannot detect the exact buckling point.

#### 4. Conclusions

The structural behavior of crash boxes under an impact load is investigated in this paper. A geometric criterion, named section-points criterion, is introduced for detecting the initiation point of dynamic-buckling of the crash boxes. The criterion is based on the stress-distribution change along the thickness of the crash boxes' plate. Better estimation of the buckling initiation and also the post-buckling behavior can be achieved by considering a series of nodes along the plate width instead of a node at the mid-

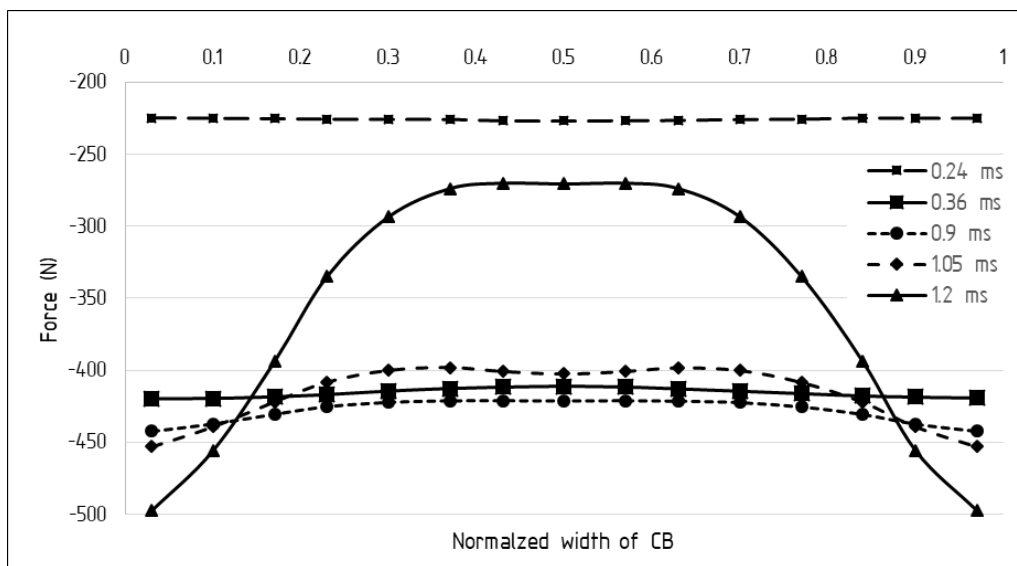


Figure 8. Compressive-force distribution along the CB width.

point of the fold. The method is applicable for both experimental tests and numerical simulations. For evaluating the introduced criterion, Budiansky-Hutchinson criterion was implemented as well for detecting the buckling initiation-point, and also compressive-force distribution along the crash-box width was studied. The compressive-force distribution approach was not able to detect the buckling point. But, Budiansky-Hutchinson criterion could detect the point, even though it was not introduced for progressively-buckled crash boxes. However, in this case, this criterion depends on the researcher's experience. Comparing with other criteria, section-points criterion showed superior accuracy in detecting the buckling-initiation point.

## Reference

- Aghdam, N. J., Tatikonda, U. B. C., Bühring, J., Mekala, N. R. and Schröder, K.-U. (2019) 'Impact of thin - walled square aluminum tubes', *PAMM*, 19(1) (2pp). <https://doi.org/10.1002/pamm.201900395>.
- B07 Committee. Test Methods for Tension Testing Wrought and Cast Aluminum- and Magnesium-Alloy Products (Metric) 2015. West Conshohocken, PA: ASTM International. doi:10.1520/B0557M-15
- Budiansky, B. and Hutchinson, J. W. (1996) 'Dynamic buckling of imperfection-sensitive structures', *H. Görtler (ed.), Applied Mechanics*.
- Chen, D.-h. (2015) 'Crush mechanics of thin-walled tubes', *CRC Press*.
- Hutchinson, J. W. and Budiansky, B. (1966) 'Dynamic buckling estimates', *AIAA Journal*, 4(3), pp. 525–530. <https://doi.org/10.2514/3.3468>.
- Jones, N., (1990), 'Structural impact', Cambridge University Press
- Katarzyna Kowal–Michalska (2010) 'About Some Important Parameters in Dynamic Buckling Analysis of Plated Structures Subjected to Pulse Loading', *Mechanics and Mechanical Engineering*, 14(2), pp. 269–279.
- Meguid, S. A., Attia, M. S., Stranart, J. C. and Wang, W. (2007) 'Solution stability in the dynamic collapse of square aluminium columns', *International Journal of Impact Engineering*, 34(2), pp. 348–359. <https://doi.org/10.1016/j.ijimpeng.2005.09.001>.
- Meguid, S.A., Stranart, J.C. and Heyerman, J. (2004) 'On the layered micromechanical three-dimensional finite element modelling of foam-filled columns', *Finite Elements in Analysis and Design*, 40(9-10), pp. 1035–1057. <https://doi.org/10.1016/j.finel.2002.02.001>.
- Niels Mallon (2008) 'Dynamic stability of thin-walled structures: a semianalytical and experimental approach', *Eindhoven: Technische Universiteit Eindhoven*.
- Paszkiwicz, M., & Kubiak, T. (2015). Selected problems concerning determination of the buckling load of channel section beams and columns. *Thin-Walled Structures*, 93, 112-121.
- Singer, J., Arbocz, J. and Weller, T. (2002) *Buckling Experiments\_ Experimental Methods in Comp.* (2).
- T. Kubiak (2013) 'Static and Dynamic Buckling of Thin-Walled Plate Structures', *Springer*.

## Influence of buckling mode and load on energy absorption effectiveness of thin-walled prismatic frusta

Karol Szklarek<sup>1</sup>, Maria Kotełko<sup>2</sup>, Mirosław Ferdynus<sup>3</sup>

### Abstract

In the paper the analysis of an influence of buckling mode and load on energy absorption effectiveness of thin-walled frusta was carried out. The influence of factors such as wall angle  $\alpha$ , wall thickness  $t$ , and frustum height  $H$  on the buckling mode and load and energy absorption was also analyzed. The analysis of influence was performed using Pearson's linear correlation method. A Finite Element (FE) model built of shell elements was applied and calculations were performed using ABAQUS commercial code. The Cowper-Symonds material model was taken into account. A two step analysis was carried out: buckling analysis in the first step, and nonlinear explicit dynamic analysis in the second step. IN the first step buckling loads and buckling modes were obtained. In the second step, force-shortening curves. The results obtained are compared on graphs and correlation matrix.

### 1 Introduction

A structural member termed energy absorber converts totally or partially the kinetic energy into another form of energy. One of the possible design solutions is the conversion of the kinetic energy of impact into the energy of plastic deformation of a thin-walled metallic or hybrid (metallic – foam filled) structural member. Among others, thin-walled columns are widely used in crumple zones in vehicles, which aim to absorb impact energy and reduce the acceleration acting on the driver and passengers. Since the early sixties of the 20<sup>th</sup> century automotive safety regulations stimulated the development of the new concept of a crashworthy (safe) vehicle that had to fulfil integrity and impact energy management requirements. There are numerous types of energy absorbers of that kind that are cited in the literature (Baroutaji, Sajjia, & Olabi, 2017). Structural members termed “ frusta” (*frustum* – from Latin: piece, bite) are used as energy absorbers due to the stable plastic behavior during axial crushing process and due to the decrease of peak crushing load in comparison with cylindrical columns or parallelepiped –shaped thin-walled columns. This type of absorbers is particularly used in the transition zone between wagon frame and buffer of locomotive or wagon.

Paper (Alghamdi, 2001) contains the historical state of art review concerning this type of energy absorbers. The author quotes research results obtained by other researchers, namely Postlethwaite and Mills, who investigated failure modes and crushing behavior of conical frusta. Also Ei-Sobky et al. (El-

---

<sup>1</sup> Department of Machine Construction & Mechatronics, Lublin University of Technology, Poland, [k.szklarek@pollub.pl](mailto:k.szklarek@pollub.pl)

<sup>2</sup> Department of Strength of Materials, Łódź University of Technology, Łódź, Poland, [maria.kotelko@p.lodz.pl](mailto:maria.kotelko@p.lodz.pl)

<sup>3</sup> Department of Machine Construction & Mechatronics, Lublin University of Technology, Poland, [m.ferdynus@pollub.pl](mailto:m.ferdynus@pollub.pl)

Sobky, Singace, & Petsios, 2001) investigated crushing behavior of conical truncated frusta. They analyzed influence of boundary conditions on the peak and mean crushing load.

Sarkabiri et al. (Sarkabir, Jahan, & Rezvani, 2015) published the results of multi-objective crashworthiness optimization of thin-walled conical groove tubes filled with polyurethane foam. They stated, that the conical angle reduces the peak crushing force, however it reduces also the absorbed energy. Thin-walled prismatic, hollow frusta were analyzed by Hosseini et al. (Hosseini Tehrani & Ferestadeh, 2015). In one of the newest papers by Asanjarani et al (Asanjarani, Dibajian, & Mahdian, 2017), the results of multi-objective optimization of prismatic, hollow frusta with dents have been published. An influence of number and depth of dents, as well as frustum angle and wall thickness on the energy absorbing effectiveness was investigated. Very recently, Elahi et al (Elahi, Rouzegar, & Assaee, 2018) investigated the axial splitting process of thin-walled conical aluminum frusta with conical die. The energy-absorption of fibre metal laminate (FML) conical frusta under quasi-static compression loading was studied by Hongyong et al (Jiang, Ren, & Xiang, 2018). Based on the outcome of the literature review, it can be said that there are relatively few research projects devoted to energy absorption analysis of prismatic frusta. The majority of research in this area is focused on conical frusta.

## 2 Subject and objectives of the study

The subject of the present study was a thin-walled prismatic steel hollow frustum of square base (Fig. Figure ), produced from two face to face steel channel sections joint by means of two seams (double-seam) of one-point spot welds, subjected to axial impact force.

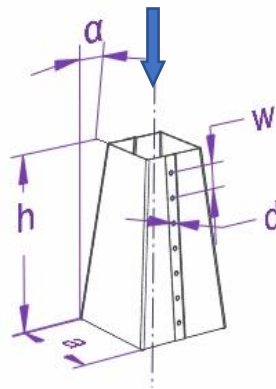


Figure 1. Thin-walled prismatic frustum

The geometry of the investigated object is a frustum of square basis (Fig.1). The lower base is of an edge length  $a = 90$  mm. The frustum was of height  $h$ , wall thickness  $t$  and the wall apex angle  $\alpha$ . The material used was a high quality steel Dual Phase DP800, of following basic mechanical parameters : Young's modulus of 210 GPa and a Poisson's ratio of 0.29, density of 7850 kg/m<sup>3</sup> and yield stress 590 MPa.

The distance between the spot welds and the weld diameter was respectively  $w=20$ mm and  $d=4$ mm. As a result the amount of spot welds is equal to 7. The 3mm thick metal plates of higher strength were welded to the frustum top and bottom edges.

The aim of this study was to investigate whether the buckling mode affects the energy absorption performance. Parametric studies were carried out for varying geometrical parameters of the frustum: apex angle ( $\alpha$ ), wall thickness ( $t$ ), frustum height ( $h$ ). The parametric study determined the buckling eigenvalues (buckling load) and the buckling mode. The influence of these factors on the two following crashworthiness indicator: peak crush force (PCF) and energy Absorption (EA) was studied. The influence was determined using Pearson's linear correlation method. In addition, the correlation between the other parameters and indicators was determined.

### 3 Methodology

#### 3.1 Finite element model

Finite Element simulations were conducted using commercial Abaqus® software. Fig.2. presents the shell frustum model used for the simulation. The frustum models consisted of two shells, joined together by a fastener option. The end edges of the frustum was attached to two rigid platens, which were connected by tie links. S4R 4-node elements were used to discretize the frustum shells, and R3D4 was used for the rigid plate. Fastener option enables to model point connections such as spots weld or rivet, between two or more surfaces. Fastening points join by a beam connector two surfaces modelled by BEAM elements (Fig.2 b).

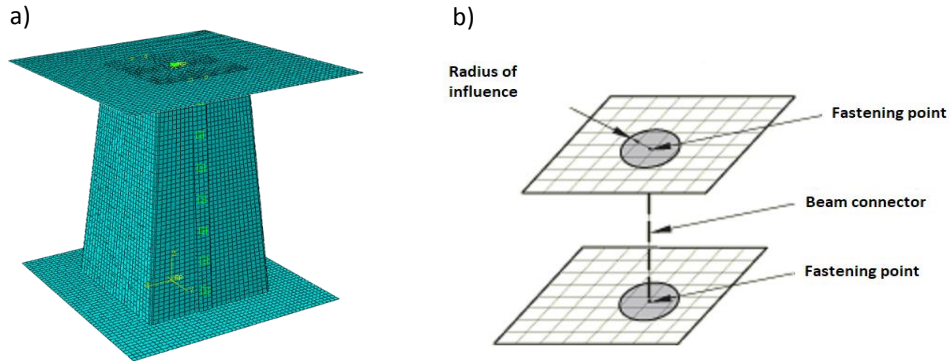


Figure 2 Finite Element model: a) discrete model shell frustum, b) fasteners model.

Numerical studies were conducted in two steps analysis. The first was eigenvalue buckling analysis and the second one was nonlinear explicit dynamic analysis. The buckling mode and buckling load were extracted from the first step. The buckling modes were used as the initial imperfection in the second step analysis. The imperfection scale factor was equal to 0.1 of the wall thickness. In the second step analysis the general contact between faces and a friction factor equal to 0.01 were applied.

In the FE analysis, in each case of the parametric study, a model was impacted using the constant mass with constant loading velocity (in all cases of the parametric study) equal  $v=6.19m/s$ . A magnitude of the impacting mass was determined in the preliminary FEM calculations for each steel sheet wall thickness for  $\alpha=0$  (parallelepiped), under the assumption, that the absorber should be entirely crushed. Magnitudes of impacting mass for all cases of the parametric study are specified in Table 1.

Elastic–plastic material model with kinematic–isotropic hardening was chosen for FE simulations. An earlier research by Mołdawa and Kotełko (Kotełko & Mołdawa, 2016), analysed results for different material models (rate-dependent elastoplastic material model, Johnson-Cook and Cowper-Symonds model) in comparison to the experimental results. It appeared that the latter one, Cowper-Symonds, provided the best convergence with the experiment. Dynamic effects of strain rate were taken into account by scaling static yield stress with the factor, assumed by Cowper – Symonds relation (1). Equivalent stress and equivalent plastic strain were calculated using Huber-Mises yield criterion.

$$\bar{\sigma}_0 = \sigma_Y \left[ 1 + \left( \frac{\dot{\epsilon}}{D} \right)^{1/q} \right] \quad (1)$$

where:

$\bar{\sigma}_0$  is a current yield (proof) stress,

$\sigma_Y$  is the initial yield (proof) stress at static load,

$\dot{\epsilon}$  is the current strain-rate,

and  $q$  and  $D$  are empirical coefficients. Parameters  $D$  and  $q$  for DP800 steel were taken from tensile test results and literature (Kaczyński & Rusiński, 2014). In the analysis the following values were assumed:  $q = 4.79$ ,  $D = 110105$ .

### 3.2 Buckling behavior analysis – parametric study

The parametric study into buckling behaviour was performed for the following geometric parameters: apex angle  $\alpha$  in the range of  $0^\circ$  to  $10^\circ$  with an increment of  $1^\circ$  (max.  $8^\circ$  for 240mm height), frustum height equal to 160, 200 or 240 mm. The last parameter was the wall thickness  $t$ , which had three variations: 0.8, 1 and 1.6 mm. A total of 84 cases differing from each other were obtained.

There are several crashworthiness indicators (Jones, 2012) used to evaluate the crashworthiness performance and the energy absorption capacity of an absorber. In the present analysis the following indicators were calculated on the basis of FE calculations:

- Energy Absorption (EA)
- Peak Crushing Force (PCF),

A typical force – displacement curve for a thin-walled member subjected to axial impact force is shown in Fig.3. Peak Crushing Force (PCF) is a maximum value of force, indicated in Fig.3.

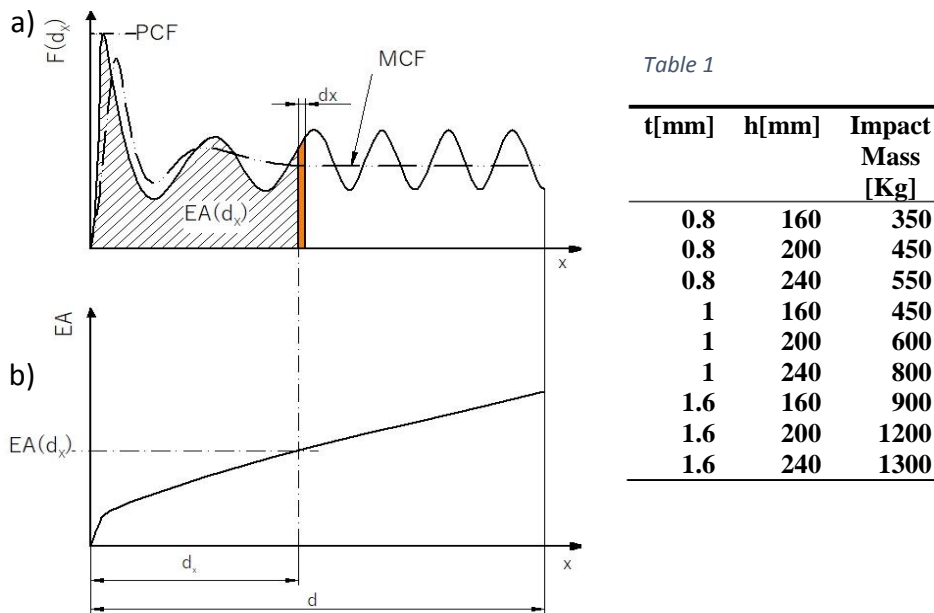


Figure 3 Typical force-displacement curve for thin-walled tubular member under axial impact

The energy absorption (EA) is defined as:

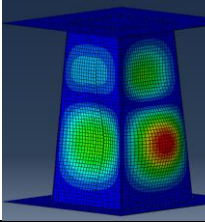
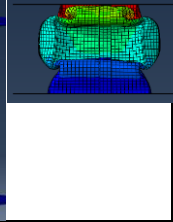
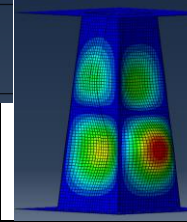
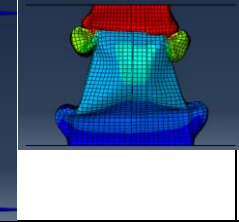
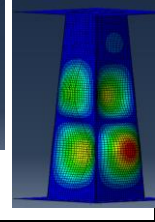
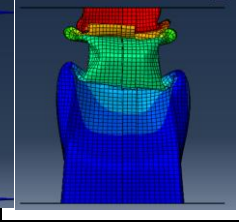
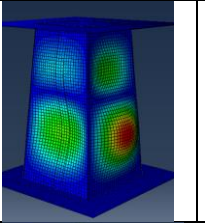
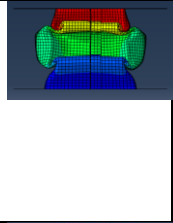
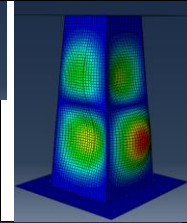
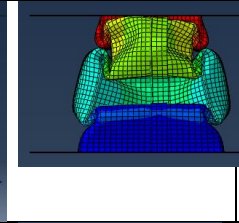
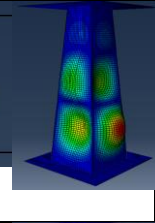
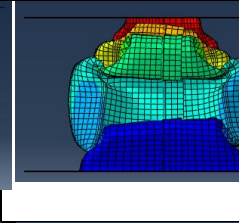
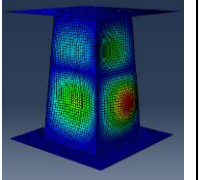
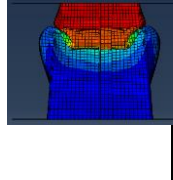
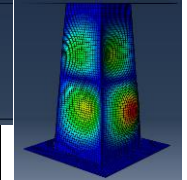
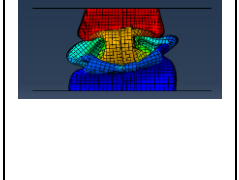
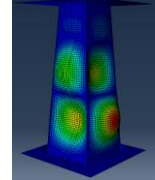
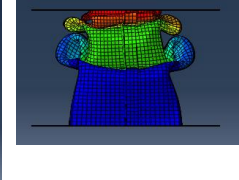
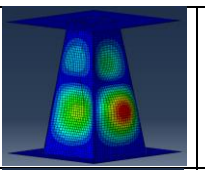
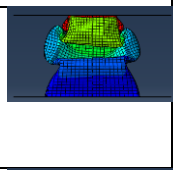
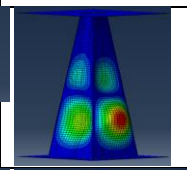
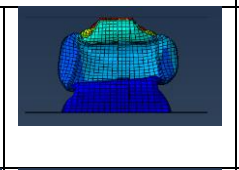
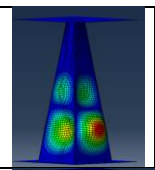
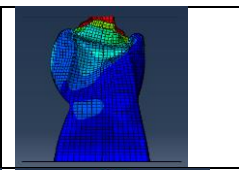
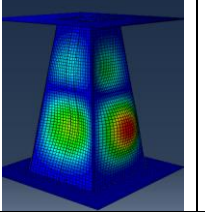
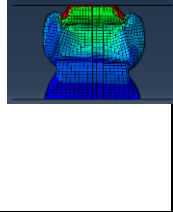
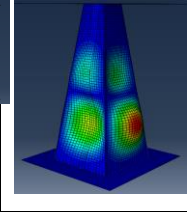
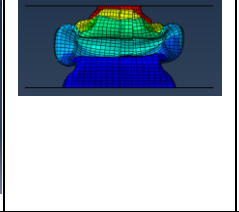
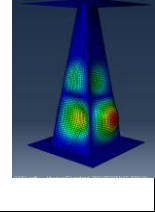
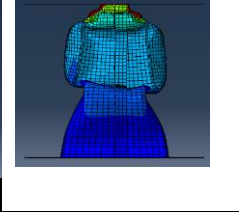
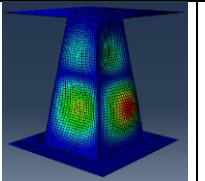
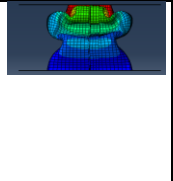
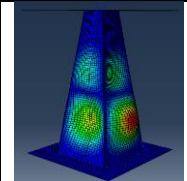
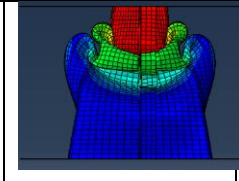
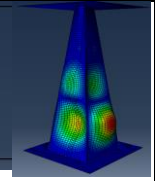
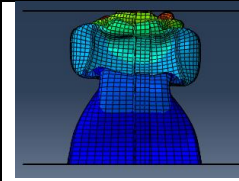
$$EA(dx) = \int_0^{d_x} F(x) dx \quad [J] \quad (2)$$

where  $d_x$  is a crushing distance.

#### 4 Buckling and crushing process analysis

Table 2. shows the specification of buckling modes and failure modes in the final-stage of crushing process, obtained for examined frusta. For all apex angles, except  $\alpha=0^\circ$  (parallelepiped), two or three half-waves of the buckling mode were obtained, depending on the frustum height. Failure modes were similar for the case of two buckling modes and were of different character for cases of three buckling modes, namely for the highest frusta for the highest apex angle.

Table 2 Buckling and failure modes

	Buckling mode	Failure mode	Buckling mode	Failure mode	Buckling mode	Failure mode
$\alpha=4^\circ$						
	h=160mm		h=200mm		h=240mm	
T=0.8						
t=1mm						
T=1.6						
$\alpha=8^\circ$						
	h=160mm		h=200mm		h=240mm	
T=0.8						
t=1mm						
T=1.6						

## 5 Correlation analysis

On the basis of numerical FE calculation results the correlation analysis was performed. Table 3.1 presents the correlation matrix, in which Pearson linear correlation coefficients  $r$  are shown. Additionally, matrix fields are indicated in different colors, according to different correlation strength. Correlation coefficient takes values in the range  $\langle -1, 1 \rangle$ . Magnitude of the correlation coefficient indicates, in what way one parameter (variable) influences (or is dependent on) other parameters. The closer an absolute value of the coefficient  $r$  to 1, the stronger is a linear relation. If  $r=0$ , the parameters are independent on each other. If the coefficient  $r$  is positive, the linear relation trend is increasing. If it is negative, the trend is decreasing. Seven levels of *correlation strength* were distinguished in the present analysis (table 3.2).

Table 3.1 Correlation matrix –Person correlation coefficient $r$							
	$\alpha$	$t$	$h$	Half-waves n.	buckling load	EA	PCF
$\alpha$				0.54	0.11	-0.08	-0.48
$t$				0.02	0.97	0.98	0.82
$h$				0.65	-0.04	-0.04	-0.15
Half-waves n.					0.05	-0.05	-0.41
buckling load						0.95	0.75
EA							0.87

Table 3.2	
$r=0$	No correlation
$0 < r < 0.1$	Very weak correlation
$0.1 \leq r < 0.3$	Weak correlation
$0.3 \leq r < 0.5$	Moderate correlation
$0.5 \leq r < 0.7$	High correlation
$0.7 \leq r < 0.9$	Very high correlation
$0.9 \leq r < 1$	Nearly full correlation

-1	-0.75	-0.5	-0.25	0	0.25	0.5	0.75	1
----	-------	------	-------	---	------	-----	------	---

One of the most important parameters to be analyzed in the initial stage of absorber's design is energy absorption EA. Nearly full correlation of EA was obtained for wall thickness and buckling load, which also confirms Fig.4. The magnitude of correlation coefficient between PCF and wall thickness and buckling load, as well as between EA and buckling load is above 0.7, which is classified as very high correlation.

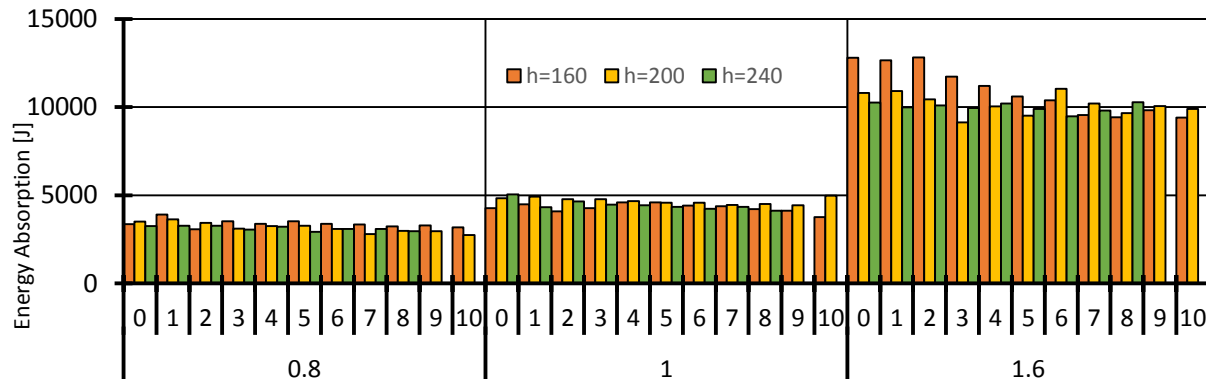


Figure 4 Comparison of absorbed energy depending on the wall angle and thickness, at different frustum heights.

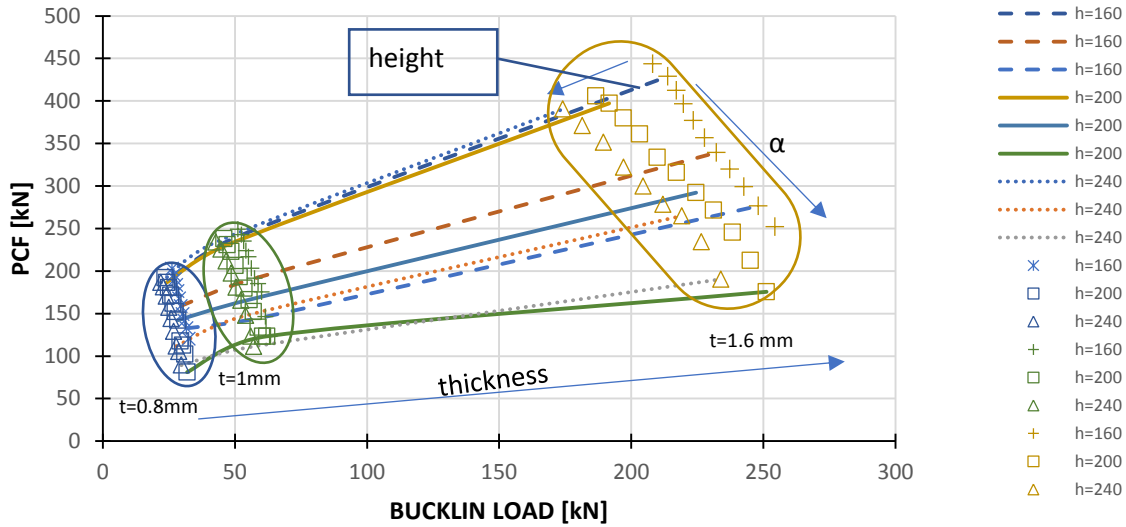


Figure 5. PCF versus buckling load for selected configurations of geometrical parameters.

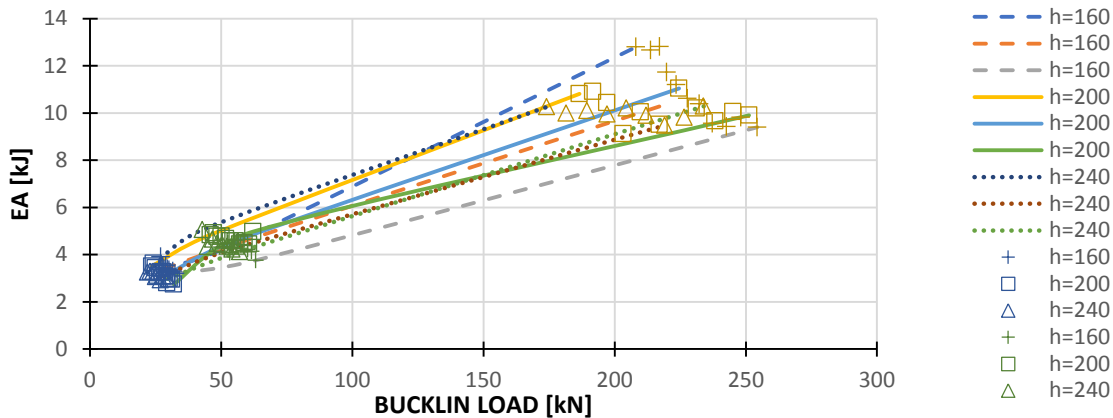


Figure 6. EA versus buckling load for selected configurations of geometrical parameters

Indicators PCF and EA in terms of the buckling load are shown in Fig. 5 and 6. For selected configurations of parameters  $t$ ,  $h$  and  $\alpha$  (linear diagrams). In Fig. 5 and 6 points corresponding to certain parameters configurations are collected in clusters. Markers correspond to different frustum height, while different colors correspond to different wall thicknesses. Diagrams in Fig.6 indicate nearly linear relation between EA and PCF in terms of buckling load.

## 6 Conclusions

The paper presents results of the analysis of the influence of buckling load upon the energy absorption of prismatic, thin-walled frusta. In the analysis the Person linear correlation method was used. A very high correlation between the energy absorption (EA) and buckling load was obtained. Simultaneously, very high correlation was also achieved between PCF- buckling load and PCF-EA. These results suggest a possibility to create relatively simple linear models, which may be used in optimization procedures and initial stage design process of thin-walled absorbers under investigation. It means, that at such an initial stage of, an eigenvalue buckling analysis performed using FE simulations (much less time consuming than non-linear explicit one) can be used. After performing an optimization procedure based on the mentioned linear model, a more precise nonlinear explicit FE analysis could be continued for selected absorber's parameters.

## 7 References

- Alghamdi, A. A. A. (2001). Collapsible impact energy absorbers: An overview. *Thin-Walled Structures*, 39(2), 189–213. [https://doi.org/10.1016/S0263-8231\(00\)00048-3](https://doi.org/10.1016/S0263-8231(00)00048-3)
- Asanjarani, A., Dibajian, S. H., & Mahdian, A. (2017). Multi-objective crashworthiness optimization of tapered thin-walled square tubes with indentations. *Thin-Walled Structures*, 116(July 2016), 26–36. <https://doi.org/10.1016/j.tws.2017.03.015>
- Baroutaji, A., Sajjia, M., & Olabi, A. G. (2017). On the crashworthiness performance of thin-walled energy absorbers: Recent advances and future developments. *Thin-Walled Structures*, 118(April), 137–163. <https://doi.org/10.1016/j.tws.2017.05.018>
- El-Sobky, H., Singace, A. A., & Petsios, M. (2001). Mode of collapse and energy absorption characteristics of constrained frusta under axial impact loading. *International Journal of Mechanical Sciences*, 43(3), 743–757. [https://doi.org/10.1016/S0020-7403\(00\)00036-9](https://doi.org/10.1016/S0020-7403(00)00036-9)
- Elahi, S. M., Rouzegar, J., & Assaee, H. (2018). Axial splitting of conical frusta: Experimental and numerical study and crashworthiness optimization. *Thin-Walled Structures*, 127(February), 604–616. <https://doi.org/10.1016/j.tws.2018.03.005>
- Hosseini Tehrani, P., & Ferestadeh, I. (2015). Studying energy absorption in tapered thick walled tubes. *Latin American Journal of Solids and Structures*, 12(1), 173–204. <https://doi.org/10.1590/1679-78251433>
- Jiang, H., Ren, Y., & Xiang, J. (2018). A numerical study on the energy-absorption of fibre metal laminate conical frusta under quasi-static compression loading. *Thin-Walled Structures*, 124(December 2017), 278–290. <https://doi.org/10.1016/j.tws.2017.12.020>
- Jones, N. (2012). *Structural Impact. Structural Impact (Second)*. Cambridge University Press. <https://doi.org/10.1155/1999/124792>
- Kaczyński, P., & Rusiński, E. (2014). *Ocena wytrzymałości połączeń w cienkościennych strukturach energochłonnych*. Wrocław: Politechnika Wrocławska.
- Kotełko, M., & Mołdawa, A. (2016). *Dynamic response of foam filled thin-walled frusta under axial impact. 7th International Conference on Coupled Instabilities in Metal Structures (CIMS ), Baltimore, MD*. 7th International Conference on Coupled Instabilities in Metal Structures CIMS Baltimore MD.
- Sarkabir, B., Jahan, A., & Rezvani, M. J. (2015). Multi-objective crashworthiness optimization of thin-walled conical groove tubes filled with polyurethane foam. (pp. 947–948).

## **Influence of the Imperfection Shapes on the Collapse Mechanisms of Stiffened Plates with Class 4 Trapezoidal Stiffeners**

Ralph Timmers<sup>1</sup>

### **Abstract**

Designing structures with stiffened plated elements is a widely used construction method. One possibility to analyze such a structure is to use the FEM and perform a geometrical and material nonlinear analysis, including imperfections (GMNIA). The Eurocode EN 1993-1-5 gives some information to the use of imperfections, but they are very general formulated. In the case of plated structures with class 4 stiffeners, no detailed information is given on how to combine the local imperfection shapes for different subpanels with different half-wavelengths. To carry out the influence of the global and different local imperfection shapes, with respect to their individual half-wavelengths and amplitudes, numerical simulations on a typically stiffened structure with class 4 plate and stiffeners were performed. The system was analyzed with a set of different combinations of imperfection shapes. Concerning the load-deflection curves of such stiffened plated elements, research often focuses on the increasing part of the curve. Still, for a more in-depth understanding, also the decreasing part, including the collapse mechanism, plays an important role (post-failure behavior). Therefore, the entire load-deflection curves were obtained. In doing so, the influence of the different imperfection shapes could be determined by comparing their load-deflection curve behaviors and their corresponding collapse mechanisms, which is the main goal of this research. The presented study can be seen as a complement to the already given information on the use of equivalent geometric imperfections and tries to increase the ease of use of EN 1993-1-5.

### **1. Introduction**

Designing structures with stiffened plated elements is a widely used construction method. Due to the slenderness of the plates, usually flat or trapezoidal stiffeners are used to strengthen the plates. There is a trend towards using larger trapezoidal stiffeners (Sinur et al. 2012). Additionally, steel with higher strengths is also used more and more. As a result, the single subpanels of the plate and the stiffeners become even more slender, and their buckling behavior must be considered in the analysis.

Concerning the load-deflection curves of stiffened plated elements, research often focuses on the increasing part of the curve, but for a more in-depth understanding, also the decreasing part (post-failure behavior) including the plastic collapse mechanism plays an important role (compare among others (Koteřko et al. 2011; Hancock 2018)). Fortunately, it is possible to calculate the whole load-deflection curve with advanced numerical methods. Due to their universal application possibilities, the FEM is used.

---

<sup>1</sup> Senior Scientist, University of Innsbruck, Unit of Steel Construction and Mixed Building Technology, [ralph.timmers@uibk.ac.at](mailto:ralph.timmers@uibk.ac.at)

In doing so, geometrical and material nonlinearities, including geometric and structural imperfections, must be taken into account (GMNIA). The real geometric and structural imperfections are usually unknown during the design process. There can be found some information in the literature to the allowable geometric imperfections from manufacturing and also for the residual stress patterns, but especially the structural imperfections can lead to numerical problems during the simulations. An alternative is the use of so-called equivalent geometric imperfections. The Annex C of Eurocode EN 1993-1-5 gives general information on how to deal with such equivalent geometric imperfections. Unfortunately, the provided information is very general formulated and must be individually adapted to the respective application case. Furthermore, the different imperfection types must be combined in such a way that the lowest resistance is obtained, which leads to a whole number of calculations. For the here considered case of a trapezoidal stiffened plate with class 4 stiffeners, usually, local buckling of all subpanels from the plate and the stiffeners, and also global buckling of the whole plate including the stiffeners must be taken into account. In doing so, the half-wavelength of an individually considered subpanel corresponds nearly to the width of the subpanel. Therefore, the question arises on how to combine the global and different local imperfection shapes of the trapezoidal stiffened panels, with respect to their half-wavelengths and amplitudes, when performing a GMNIA according to EN 1993-1-5.

Numerical simulations (GMNIA) on a typically stiffened plate with class 4 plate and stiffeners were performed to answer this question. The system was analyzed with a set of different imperfection shapes. The programming capabilities of the FE-software were used to generate the different equivalent geometric imperfection shapes as a combination of *sinus*-functions to meet the requirements of the EN 1993-1-5. Furthermore, the entire load-deflection curves were obtained. The main goal of this research was to check the influence of the different combinations of local imperfection shapes and to investigate their behavior on the load-deflection curve and the corresponding plastic failure mechanism. The presented research can be seen as a complement to the already given information on the use of equivalent geometric imperfections and tries to increase the ease of use of EN 1993-1-5.

## 2. Geometry and Numerical Modelling

### 2.1 Geometry

The following geometry was studied in this paper, which consists of a bottom plate and three trapezoidal stiffeners. The subpanels and the single panels of the stiffeners correspond all to a class 4 section. The geometry can be seen from Fig. 1, and the parameters are defined in Table 1.

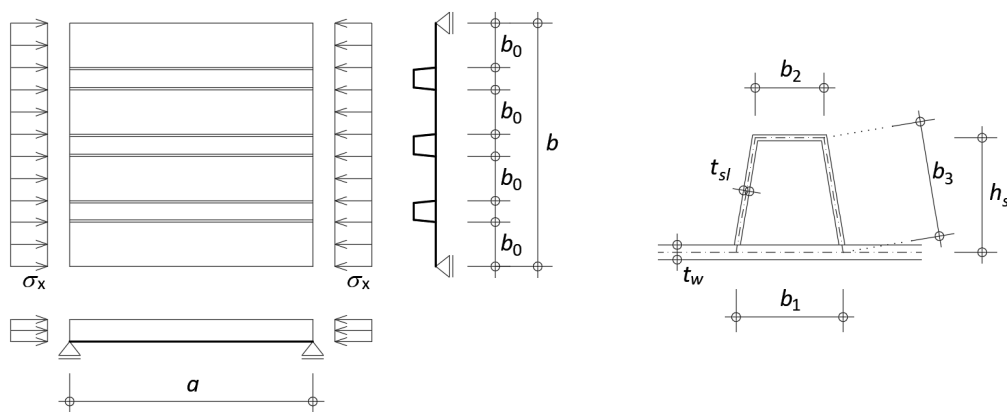


Figure 1: Definition of the geometry and the parameters.

Table 1: Parameters used.

Parameter	Description
$a = 3300\text{mm}$	Length of the bottom plate
$b = 3300\text{mm}$	Width of the bottom plate
$t_w = 12\text{mm}$	Thickness of the bottom plate
$t_{sl} = 6\text{mm}$	Thickness of the stiffener
$b_0 = 600\text{mm}$	Width of the subpanel
$b_1 = 300\text{mm}$	Width of the larger side of the trapezoidal stiffener
$b_2 = 240\text{mm}$	Width of the smaller side of the trapezoidal stiffener
$h_{sl} = 300\text{mm}$	Height of the trapezoidal stiffener
$b_3 \square 301.5\text{mm}$	Resulting width of the inclined side of the trapezoidal stiffener

## 2.2 Imperfections

The Eurocode EN 1993-1-5 recommend to include a global imperfection of each stiffener and local imperfections of each subpanel, which must be combined in a most unfavorable way. In doing so, the shapes shown in Fig. 2 (a) were considered. The shape “Local 1” considers local buckling of all subpanels, but it can also be assumed that failure is dominated by buckling of the bottom plate. Therefore, the shapes “Local 2” and “Local 3” were amended without local imperfections of the stiffeners.

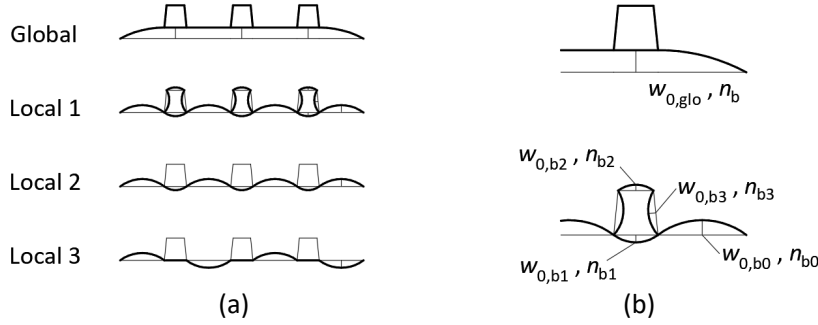


Figure 2: Imperfection shapes: (a) Global and different local shapes; (b) Definition of the corresponding amplitudes.

The elastic buckling shape of a single plate under compression results in a “more or less” circular shape. Therefore, the natural number of half-waves (which would also result from a LBA) of the global panel and the subpanels of the considered geometry (compare Fig. 2 (b)) would result in:

$$n_b = 1, \quad n_{b0} = 6, \quad n_{b1} = 11, \quad n_{b2} = 14, \quad n_{b3} = 11 \quad (1)$$

Furthermore, all imperfection shapes were approximated with *sinus*-functions. The global shape of each stiffener  $w_{glo}(x)$  corresponds to a *bow*, according to Eq. 2, where  $w_{0, glo}$  represents the maximal amplitude. The local imperfection shapes of each subpanel  $w_{loc}(x, y)$  were considered as a buckling shape, according to Eq. 2, where  $w_{0, loc} = w_{0, b0} \dots w_{0, b3}$  denotes the maximal amplitude,  $b_{loc} = b_0 \dots b_3$  the width, and  $n_{loc} = n_{b0} \dots n_{b3}$  the number of half-waves of the subpanel under consideration, see Fig. 2 (b).

$$w_{glo}(x) = w_{0, glo} \cdot \sin\left(\frac{n_b \cdot \pi \cdot x}{a}\right) \quad w_{loc}(x, y) = w_{0, loc} \cdot \sin\left(\frac{n_{loc} \cdot \pi \cdot x}{a}\right) \cdot \sin\left(\frac{\pi \cdot y}{b_{loc}}\right) \quad (2)$$

The global and the different local shapes must be combined in an unfavorable way. Unfortunately, the combination is unknown, which means that different combinations must be checked. Furthermore, it is not clear which number of half-waves per subpanel leads to the lowest resistance. It can be assumed that using the natural number of half-waves of each subpanel is unfavorable. Still, it can also be assumed that, if one subpanel buckles first, it is more unfavorable that the neighboring subpanels buckle with the same number of half-wavelengths. The 18 combinations given in Table 2 were investigated to check this behavior.

Table 2: Investigated imperfection shapes.

Combination <sup>1</sup>	Imperfection shapes, acc. to Fig. 2 (a)	Number of local half-waves per subpanel
1 and 10	±Global + Local 1	$n_{b0} = n_{b1} = 6, n_{b2} = 6, n_{b3} = 6$
2 and 11	±Global + Local 1	$n_{b0} = n_{b1} = 6, n_{b2} = 11, n_{b3} = 11$
3 and 12	±Global + Local 1	$n_{b0} = n_{b1} = 6, n_{b2} = 14, n_{b3} = 14$
4 and 13	±Global + Local 1	$n_{b0} = n_{b1} = 6, n_{b2} = 14, n_{b3} = 11$
5 and 14	±Global + Local 1	$n_{b0} = n_{b1} = 11, n_{b2} = 11, n_{b3} = 11$
6 and 15	±Global + Local 1	$n_{b0} = n_{b1} = 11, n_{b2} = 14, n_{b3} = 14$
7 and 16	±Global + Local 1	$n_{b0} = n_{b1} = 11, n_{b2} = 14, n_{b3} = 11$
8 and 17	±Global + Local 2	$n_{b0} = n_{b1} = 6$
9 and 18	±Global + Local 3	$n_{b0} = 6$

1. The combinations 1 to 9 have a positive global amplitude, and the combinations 10 to 18 have a negative global amplitude.

The maximal amplitudes of the different imperfection shapes were calculated according to the recommendations from EN 1993-1-5. It was assumed that the given amplitudes for local buckling shapes refer to a more or less circular shape. Especially for imperfection shapes with a larger number of half-waves, the half-wavelength was used to calculate the amplitude (instead of the local plate width). For the applied geometry, this was only considered for the larger subpanel of the bottom plate (width  $b_0$ ). The differences between the maximal amplitudes of the other (less wide) subpanels were negligibly small. Concerning Fig. 2 (b), the following amplitudes were used:

$$\begin{aligned}
 w_{0,gl0} &= \min\left(\frac{a}{400}, \frac{b}{400}\right) = 8.3\text{mm} & w_{0,b1} &= \min\left(\frac{a}{200}, \frac{b_1}{200}\right) = 1.5\text{mm} \\
 w_{0,b0,n=6} &= \min\left(\frac{a}{200}, \frac{b_0}{200}\right) = 3.0\text{mm} & w_{0,b2} &= \min\left(\frac{a}{200}, \frac{b_2}{200}\right) = 1.2\text{mm} \\
 w_{0,b0,n=11} &= \min\left(\frac{a/n_{b0}}{200}, \frac{b_0}{200}\right) = 1.5\text{mm} & w_{0,b3} &= \min\left(\frac{a}{200}, \frac{b_3}{200}\right) = 1.5\text{mm}
 \end{aligned} \tag{3}$$

### 2.3 Numerical Modelling

The system was calculated with the FE-software ANSYS (Ansys 2019). Three identical stiffened panels, according to Fig. 1, were modeled, which results in a total length of  $3 \cdot a = 9900\text{mm}$ . The compression force acts at the edges of the outer panels (bottom plate and all stiffeners) with a resulting maximum stress in the plated structure of  $\sigma_x = f_y = 355\text{MPa}$ , see Fig. 3 (a) and (b). An elastic-ideal plastic material model was used. The global imperfection shape was applied alternating to all three panels. The local shapes were only applied to the middle panel to avoid failure of the outer panels. The different imperfection shapes were applied by using the programming capabilities of the software used. Exemplarily, Fig. 3 (c-f) shows

some selected imperfection shapes. With the generated model, the 18 combinations of imperfection shapes from Table 2 were analyzed. A mesh convergence study was carried out for all calculations to get convergent results. The obtained results are presented in the following section.

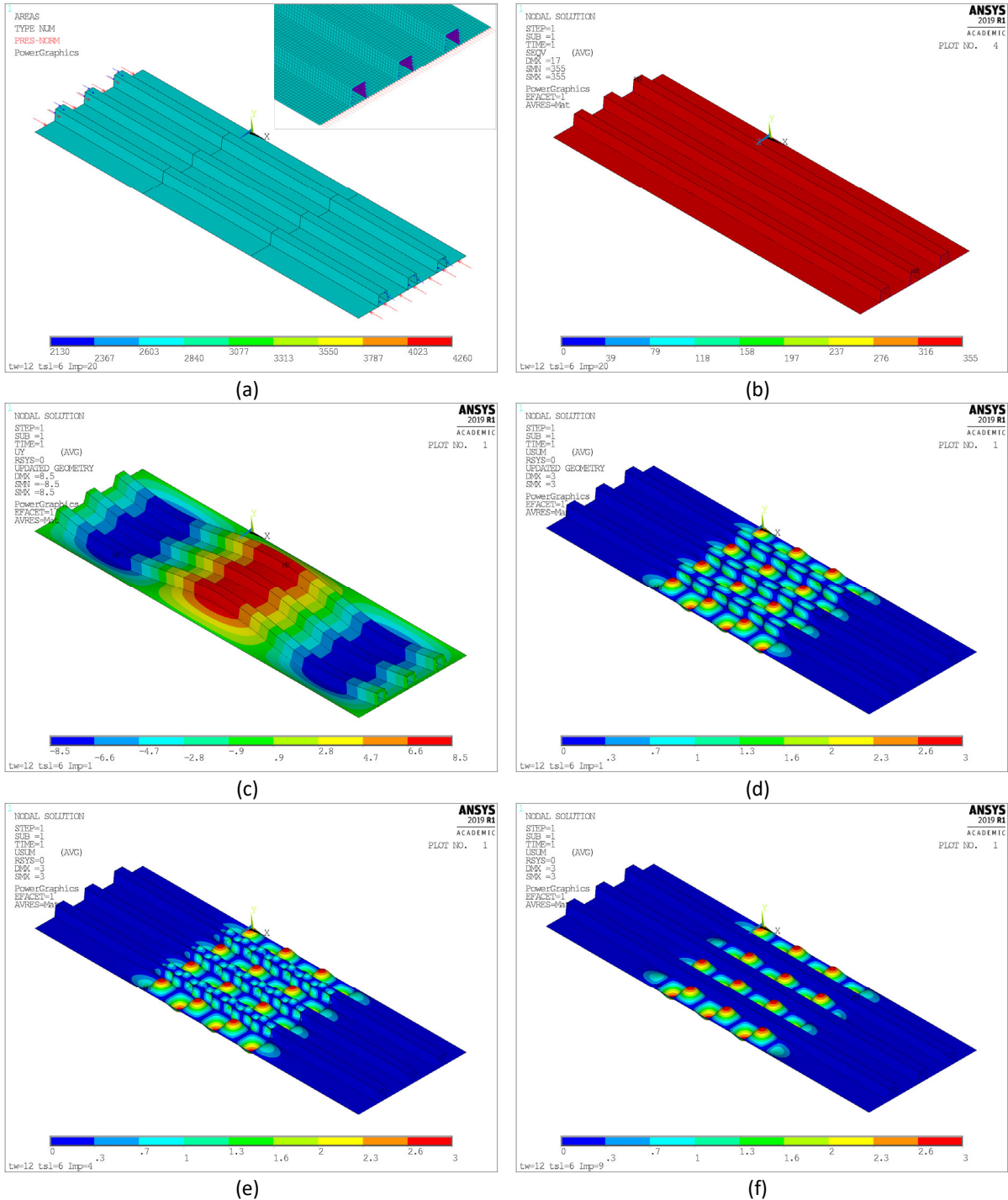


Figure 3: FE-Model and selected imperfection shapes: (a) Geometry, mesh and loading situation; (b) Normal stresses from a LA without imperfections; (c) Global imperfection shape (positive amplitude); (d) Combination 1 (only local); (e) Combination 4 (only local); (f) Combination 9 (only local).

### 3. Results and Discussion

Fig. 4 shows the obtained load-deflection curves of the 18 considered combinations of imperfection shapes from Table 2. The load factor  $\alpha_u$  is defined as the load  $\sigma_x$  normalized by  $f_y$ . The deflection  $u_x$  represents the corresponding shortening of the bottom plate of the middle panel. As expected, after reaching the peak of the load-deflection curve, all combinations show a decreasing load behavior. The combinations 1 to 9 (positive global amplitude) show an increasing and the combinations 10 to 18 (negative global amplitude), a decreasing shortening of the bottom plate. This is the result of the bending moment due to the global imperfection and the applied force. More details of the peaks of each combination are shown in Fig. 5, and the corresponding maximum load factors are given in Table 3.

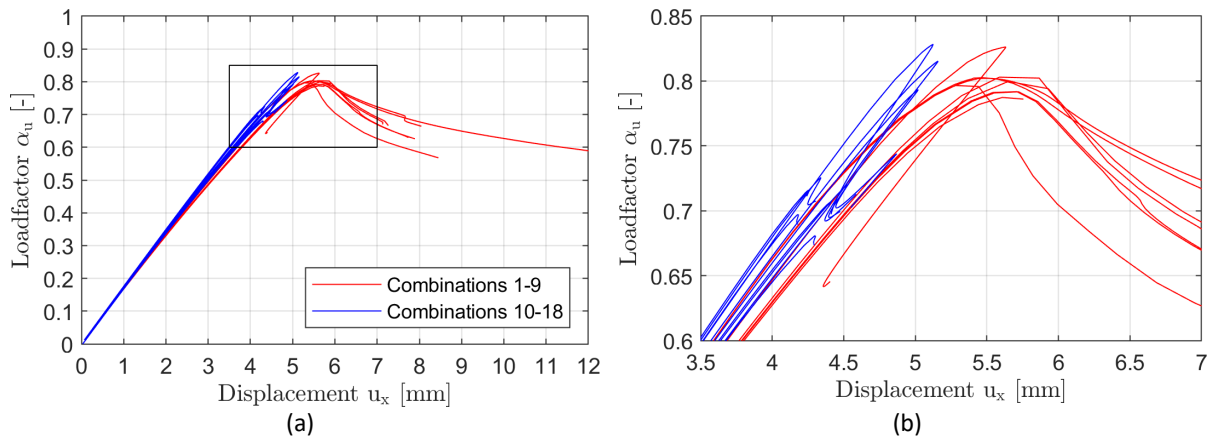


Figure 4: Load-deflection curves of all investigated combinations: (a) Complete curves; (b) Detail of the peaks.

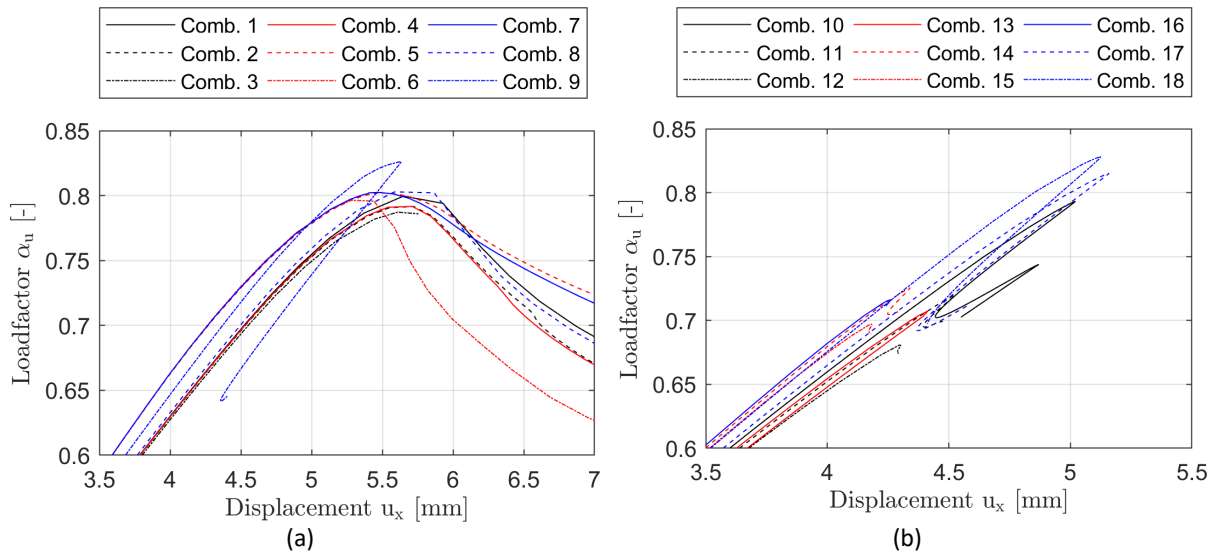


Figure 5: Peak of the load-deflection curves: (a) Combinations 1 to 9; (b) Combinations 10 to 18.

Table 3: Maximum load factors.

Comb.	1	2	3	4	5	6	7	8	9	min.
$\alpha_u$	0.800	0.792	0.787	0.792	0.802	0.797	0.803	0.803	0.826	0.787
Comb.	10	11	12	13	14	15	16	17	18	min.
$\alpha_u$	0.793	0.720	0.681	0.707	0.726	0.697	0.716	0.815	0.828	0.681

The combinations 1 to 9 have a positive global amplitude (see Fig. 3 (c)). This means that the resulting bending moment from compression force and global imperfection increases the compression stresses in the bottom plate, and decreases the compression stresses in the upper section of the stiffeners. The resulting failure mechanisms can be visualized by plotting the equivalent plastic strains. Combination 6 shows the steepest drop after reaching the peak of the load-deflection curve. The corresponding failure mechanisms are shown in Fig. 6 (a, b). At the peak of the load-deflection curve, most of the local buckles of the bottom plate show small plastic regions. After failure, the so-called *roof-shape mechanism* was formed in each subpanel, including a yield zone in the inclined sides of each stiffener. Such a mechanism was also obtained in experiments (Mahendran 1997). Due to the bending moment, the bottom plate carries the higher compression stresses, whereas the smaller top parts of the stiffeners have to take the lower compression stresses. A similar failure mechanism was obtained for all combinations from 1 to 8. Furthermore, it can be seen that the influence of the number of local half-waves on the maximum load factor is low, but the steepest drop of the load-deflection curve after reaching the peak was obtained for a higher number of local half-waves (combination 6).

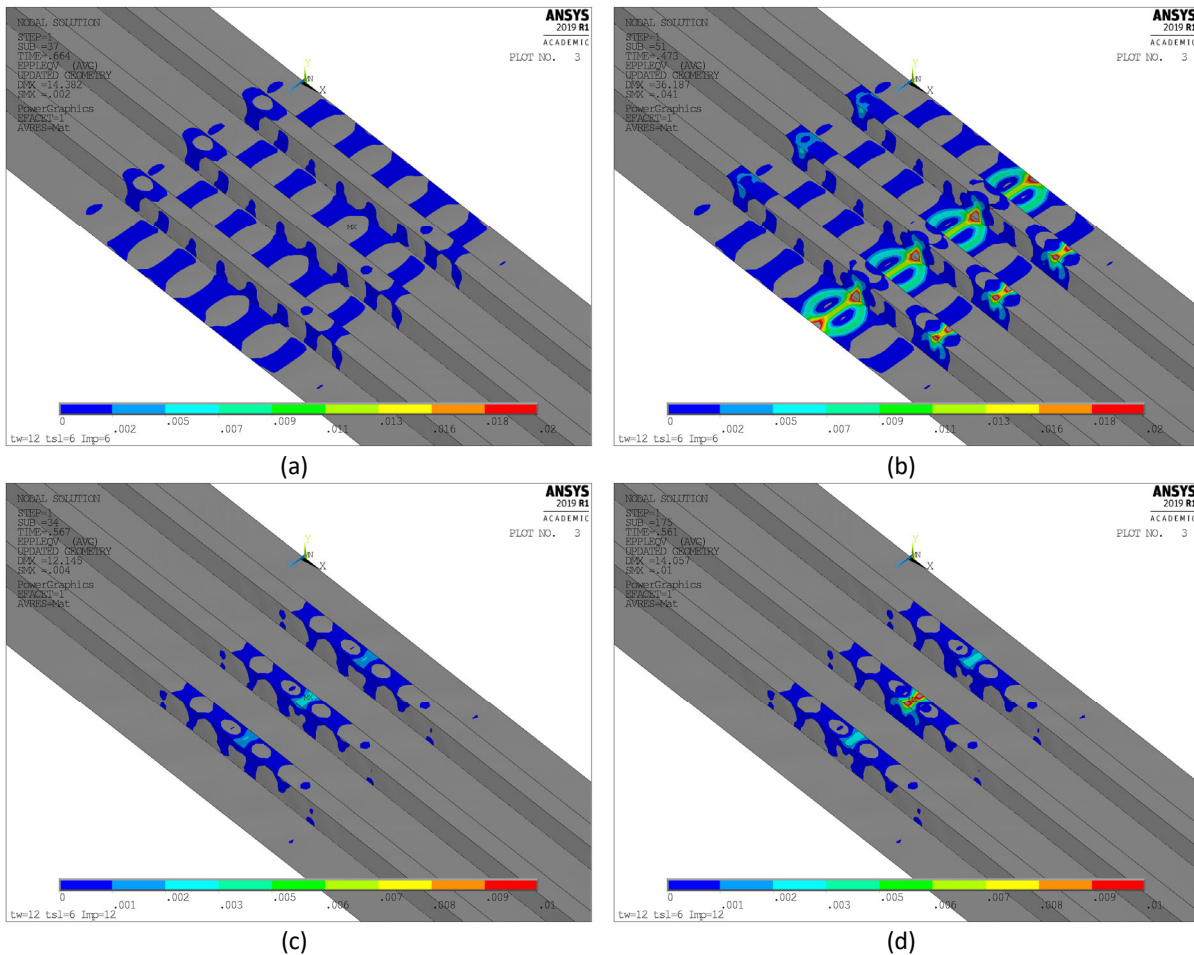


Figure 6: Failure mechanisms (equivalent plastic strain): (a, b) Combination 6; (c, d) Combination 12; (a, c) Peak of the load-deflection curve; (b, d) After reaching the peak (post-failure).

The load-deflection curves from combinations 10 to 18 show a different behavior as obtained for combinations 1 to 8, but similar to combination 9. The lowest maximum load factor was obtained for combination 12. Fig 6 (c, d) shows the corresponding failure mechanism, which looks like a plastic hinge

at the top subpanel accompanied by *modified roof-shape mechanisms* at the inclined panels of the stiffeners. A similar mechanism was obtained experimentally in (Kotelko et al. 2000; Kotelko 2004) for box section beams under bending and also numerically in (Timmers et al. 2016) for unstiffened plates under compression and bending. The failure mechanisms for all combinations from 10 to 18 are similar. The maximum load factors for combinations 10, 17, and 18 are significantly higher than for the other combinations (see Table 3). No local imperfections were applied to the combinations 17 and 18. Therefore, the stiffeners behave “stiffer” as with local imperfections, resulting in a higher load factor. Nevertheless, after reaching the peak of the load-deflection curve, a similar failure mechanism, as shown in Fig. 6 (d) was obtained. For combination 10, a local imperfection shape with only six half-waves was applied. Again, the stiffener behaves too stiff, which results in the higher load factor.

Compared to combinations 1 to 8, combination 9 results in a slightly higher load factor and different behavior of the load-deflection curve. This behavior can be explained by looking again at the failure mechanism. After reaching the peak of the load-deflection curve, a local failure mechanism similar to Fig. 6 (d) was formed in the right outer panel. This is quite interesting because no local imperfection shapes were applied to the exterior panels. In this case, the outer panels have only a negative global amplitude, which means that the resulting bending moment increases the compression forces in the upper part of the stiffeners. Due to the missing local imperfection shapes in the middle panel, the resistance of the middle panel is higher than obtained for the combinations 1 to 8. Furthermore, the stiffness is that high, that failure occurred first in the outer panel without any local imperfections applied.

#### 4. Conclusion

Based on the obtained results, it can be drawn that for class 4 stiffeners, the local imperfections should always be applied. In cases with a positive global amplitude, the local imperfections and their half-wavelengths of the stiffeners have a minor influence. This is because the resulting bending moment forces failure of the subpanels of the bottom plate. The natural number of half-waves should be applied to allow the *roof-shape mechanism* to develop. In cases with a negative global imperfection shape, the bending moment forces failure of the top section of the stiffener. In this case, a higher number of local half-waves is recommended to allow the local mechanism (plastic hinge) to develop. Neglecting the local imperfection shapes of the stiffeners resulted in both cases in a too stiff behavior. Furthermore, the minimum load factor of combinations 10 to 18 is approximately 13% lower than for combinations 1 to 9.

#### References

- Ansys (2019): Version 2019 R1, Engineering Simulation & 3D Design Software; <https://www.ansys.com>; Accessed: 12.02.2020.
- Hancock, Gregory J. (2018): Coupled Instabilities in Metal Structures (CIMS) – What have we learned and where are we going? In: *Thin-Walled Structures* 128, S. 2–11. DOI: 10.1016/j.tws.2017.04.032.
- Kotelko, M.; Lim, T.H.; Rhodes, J. (2000): Post-failure behaviour of box section beams under pure bending (an experimental study). In: *Thin-Walled Structures* 38 (2), S. 179–194. DOI: 10.1016/S0263-8231(00)00032-X.
- Kotelko, M.; Ungureanu, V.; Dubina, D.; Macdonald, M. (2011): Plastic strength of thin-walled plated members—Alternative solutions review. In: *Thin-Walled Structures* 49 (5), S. 636–644. DOI: 10.1016/j.tws.2010.09.007.
- Kotelko, Maria (2004): Load-capacity estimation and collapse analysis of thin-walled beams and columns—recent advances. In: *Thin-Walled Structures* 42 (2), S. 153–175. DOI: 10.1016/S0263-8231(03)00055-7.
- Mahendran, M. (1997): Local plastic mechanisms in thin steel plates under in-plane compression. In: *Thin-Walled Structures* 27 (3), S. 245–261. DOI: 10.1016/S0263-8231(96)00040-7.
- Sinur, Franc; Zizza, Antonio; Kuhlmann, Ulrike; Beg, Darko (2012): Buckling interaction of slender plates—Experimental and numerical investigations. In: *Thin-Walled Structures* 61, S. 121–131. DOI: 10.1016/j.tws.2012.03.024.
- Timmers, R.; Lener, G. (2016): Collapse mechanisms and load–deflection curves of unstiffened and stiffened plated structures from bridge design. In: *Thin-Walled Structures* 106, S. 448–458. DOI: 10.1016/j.tws.2016.05.020.

## **Buckling sensitivity of three-layered annular plates in temperature field on the rate of imperfection**

Dorota Pawlus<sup>1</sup>

### **Abstract**

Paper presents the dynamic stability problem of three-layered annular plate in thermal environment. Plate is subjected to the mechanical load with forces acting in the plane of plate outer layers and temperature field defined by the temperature difference between plate edges. Mainly, the effect of the rate of plate imperfection on values of the critical parameters has been examined. Plate model has been solved analytically and numerically using the approximation methods: orthogonalization and finite differences, and finite element. Obtained values of critical temperature differences or critical mechanical loads and corresponding with them temperature differences show the dynamic reaction of examined plate on time-dependent loads and parameter connected with the plate preliminary geometry. The influence of imperfection rate on final results can be meaningful.

### **1. Introduction**

The response of the plate three-layered structure on thermal and mechanical loading depends on different parameters. In time-dependent problem with deflections increasing in time within the loading process one of the geometrical plate parameter, which is the rate of imperfection has the particular meaning. On account of the wide range of possible applications of circular or annular composite plates also with layered structure in aerospace industry, mechanical and nuclear engineering, civil engineering or miniature mechanical systems the buckling problem of them is current and still undertaken. As the example the papers by Ghiasian et al. (2014) and Zhang et al. (2019) can be. Paper by Ghiasian et al (2014) presents the solution for moderately thick annular plate made of FGM composite. The effect of uniform temperature rise and heat conduction across plate thickness on critical buckling are considered. The critical buckling and dynamic postbuckling responses of the FGM annular plates with initial geometric imperfections are considered in paper by Zhang et al (2019). The effects of the loads and material parameters and imperfection rates on dynamic behaviours and values of critical temperatures are examined in detailed. The proposed in this paper way of analytical and numerical solution to the problem refers to the solution of annular plate loaded mechanically presented in works by Pawlus (2011a),(2011b). Both temperature field effect and plate imperfection influence on plate dynamic response are in presented examination important practical and cognitive elements of undertaken analyses. The three-layered annular plate composed of thin steel facings and thicker foam core in complex thermo-mechanical state of loading is an object of consideration. Plate is loaded thermally with increasing in time temperature difference, which exists between plate edges or is dynamically loaded

---

<sup>1</sup> Assistant Professor, University of Bielsko-Biala, <doro@ath.bielsko.pl>

mechanically and thermally with increasing in time temperature difference or is subjected to the constant temperature field. Mechanical load is expressed by the quickly increasing in time forces, which compress plate facings and are uniformly distributed on outer edge of facings. Time-dependent mechanical and thermal loads are formulated by the equations (1), (2), respectively:

$$p = st, \quad (1)$$

$$\Delta T = at \quad (2)$$

where  $p$  is the compressive stress,  $s$  is the rate of mechanical loading growth,  $\Delta T$  is the temperature difference,  $a$  is the rate of temperature loading growth,  $t$  is the time.

The main objective of the analysis is the influence of the rate of plate imperfection on dynamic response and values of critical parameters, like critical load and critical temperature difference. Figure 1 shows the scheme of examined plate in thermal environment with temperatures  $T_i$  and  $T_o$  in the area of plate hole and outer perimeter, respectively. Plate transversal structure is symmetrical. The temperature field is axisymmetric and flat. There is no heat exchange between plate surfaces. The heat flow defined by the logarithmic distribution of temperature versus the plate radius (see, Eq. 3) exists only in radial direction of plate facings. Material constants do not depend on temperature. Support system of the examined plates is in the form of both edges slideably clamped. Undertaken dynamic stability problem requires to adopt the criterion of the loss of stability. The criterion presented by Volmir (1972) was adopted. According to this criterion the loss of plate stability occurs at the moment when the speed of the point of maximum deflection reaches the first maximum value. Two plate models built using finite difference method (FDM plate model) and finite element method (FEM plate model) have been analysed in numerical investigations. Using the finite element method the model in the form of annular plate has been used in analysis. The calculations were carried out at the Academic Computer Center CYFRONET-CRACOW (KBN/SGI\_ORIGIN\_2000/Płódzka/030/1999) using the ABAQUS system.

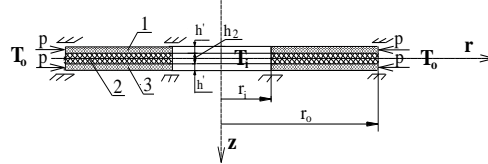


Figure 1: Scheme of three-layered annular plate composed of facings (layers 1,3) and core (layer 2) loaded with compressive stress  $p$  and subjected to axisymmetrical temperature field  $T_i, T_o$

## 2. Solution procedure using the finite difference method

Solution procedure is based on: formulation of the dynamic equilibrium equations, formulation of the sectional forces and moments in facings including the thermal elements, acceptance of the stress function to determine the resultant membrane forces, description of the support conditions for the plate with both edges slideably clamped and conditions for plate edges mechanically and thermally loaded, determination of the shape functions and form of plate imperfection, acceptance of dimensionless quantities and expressions, like for example:  $\zeta_1 = w_d/h$ , where  $w_d$  is the additional plate deflection,  $h$  is the total plate thickness and connected with mechanical loading (see, Eq. 1):  $t^* = t \cdot K7$ ,  $K7 = s/p_{cr}$ , where  $p_{cr}$  is the critical static load, and connected with thermal loading (see, Eq. 2):  $t^* = t \cdot TK7$ ,  $TK7 = a/\Delta T_f$ , where  $\Delta T_f$  is the fixed temperature difference. The temperature distribution is a function of only one geometrical variable – plate radius and is expressed by logarithmic equation:

$$T_N = T_o + \frac{T_i - T_o}{\ln \rho_i} \ln \rho \quad (3)$$

where:  $T_i, T_o$  are the temperatures of the inner and outer plate perimeters,  $\rho = r/r_o$ ,  $\rho_i = r_i/r_o$  are the dimensionless plate radius and dimensionless inner plate radius,  $r_o$  is the outer plate radius.

Important in presented analysis form of plate imperfection  $\zeta_o$  ( $\zeta_o=w_o/h$ ) is expressed by the following equation presented by Wojciech (1979):

$$\zeta_o(\rho, \theta) = \xi_1(\rho)\eta(\rho) + \xi_2(\rho)\eta(\rho)\cos(m\theta) \quad (4)$$

where  $w_o$  is a plate preliminary deflection which expresses rate of imperfection,  $m$  is a number of buckling circumferential waves,  $\xi_1, \xi_2$  are the calibrating numbers,  $\eta(\rho)$  is a function:  $\eta(\rho)=\rho^4+A_1\rho^2+A_2\rho^2\ln\rho+A_3\ln\rho+A_4$ ,  $A_i$  are the quantities fulfilling the conditions of clamped edges. The basic system of differential equations, determined using the finite difference method to approximate the derivatives with respect to  $\rho$  by the central differences in the discrete points has the following form:

$$PU + Q = K \cdot \ddot{U}, \quad (5)$$

$$M_Y Y = Q_Y - \rho \cdot S \cdot T_{N, \rho}, \quad (6)$$

$$M_V V = Q_V, \quad (7)$$

$$M_Z Z = Q_Z, \quad (8)$$

$$M_D D + M_U U + M_G G = 0, \quad (9)$$

$$M_{GG} G + M_{GU} U + M_{GD} D = 0. \quad (10)$$

For plate loaded mechanically with constant temperature difference between edges the Eq. 6 has been modified to the form

$$M_Y Y = Q_Y - S \cdot \frac{T_i - T_o}{\ln \rho_i}, \quad (11)$$

where  $K, S$  are expressed as  $K = TK7^2 \cdot \frac{h'}{h} \cdot r_o h_2 M$ ;  $S = \frac{r_o^2}{h^2} \alpha$ ;  $U, Y, V, Z, \ddot{U}, Q, Q_V, Q_Y, Q_Z, D, G$  are vectors of plate additional deflections and components of the stress function and deflection derivatives with respect to time  $t$ , and vectors of expressions composed of the initial and additional deflections, geometric and material parameters, components of the stress function, radius  $\rho$ , quantity  $b$  ( $b$  – length of the interval in the finite difference method), coefficients  $\delta, \gamma$  (differences of radial and circumferential displacements of points in middle surfaces of facings, respectively) and number  $m$ ;  $M_Y, M_V, M_Z, M_D, M_G, M_{GG}, M_{GD}, P, M_U, M_{GU}$  are matrices of elements composed of geometric and material parameters, the radius  $\rho$ , quantity  $b$  and number  $m$ .

### 3. Example analyses

The exemplary numerical calculations were carried out for plate with the following material, geometrical and loading parameters: inner radius:  $r_i=0.2$  m, outer radius:  $r_o=0.5$  m, facing thickness:  $h'=0.001$  m; core thickness:  $h_2=0.005$  m; value of the rate  $\xi_2$  (described in Figs as ksi<sup>2</sup>) of plate preliminary deflection is equal to:  $\xi_2=0.5, 1, 2$ ; steel for facing material: Young's modulus  $E=2.1 \cdot 10^5$  MPa, Poisson's ratio  $\nu=0.3$ , mass density  $\mu=7.85 \cdot 10^3$  kg/m<sup>3</sup>, linear expansion coefficient  $\alpha=0.000012$  1/K; polyurethane foam for core material treated as isotropic: Kirchhoff's modulus  $G_2=5$  MPa, Young's modulus  $E_2=13$  MPa, Poisson's ratio  $\nu=0.3$ , mass density  $\mu_2=64$  kg/m<sup>3</sup>; linear expansion coefficient  $\alpha=0.00007$  1/K; the rate of mechanical loading growth on the plate outer edge is equal to  $s \approx 931$  MPa/s ( $K7=20$  1/s); the rate of thermal loading growth on the plate edge is equal to  $a=200, 800$  K/s. Plate is subjected to the thermal field with a positive or negative gradient. Positive gradient of thermal field is when the value of temperature on the inner plate edge  $T_i$  is greater than on outer one  $T_o$  ( $T_i > T_o$ ), (see, Fig.1).

### 3.1 Plate loaded thermally

Fig. 2 shows the time histories of plate deflections  $\zeta_{1\max}=f(t^*)$  for FDM plate models loaded thermally with the rate of loading growth equal to  $a=200$  K/s. Positive temperature gradient exists. Presented results are for axisymmetrical  $m=0$  and asymmetrical  $m=7$  plate modes. Table 1 presents the values of critical temperature differences  $\Delta T_{cr}$  for FDM plate models with the different values  $\xi_2$  of imperfection. Fig. 3 shows the time histories of plate deflections  $\zeta_{1\max}=f(t^*)$  for plates loaded thermally with the rate  $a=200$  K/s and negative temperature gradient. Presented results are for two selected modes  $m=7$  and  $m=14$ . Results showed that numbers  $m=7$  and  $m=14$  of buckling circumferential waves correspond to minimal value of critical temperature differences  $\Delta T_{cr}$  for plates loaded with positive and negative temperature gradient, respectively. Table 2 presents the values  $\Delta T_{cr}$  for FDM plate models with different values  $\xi_2$  of imperfection. Summarizing, it can be observed that the influence of the value of rate  $\xi_2$  of imperfection on critical temperature difference  $\Delta T_{cr}$  is insignificant. Greater differences are observed between the values of critical plate deflections (see, Figs 2,3). Minimal increase of  $\Delta T_{cr}$  value is observed for plate model with the rate of imperfection equal to  $\xi_2=2$ .

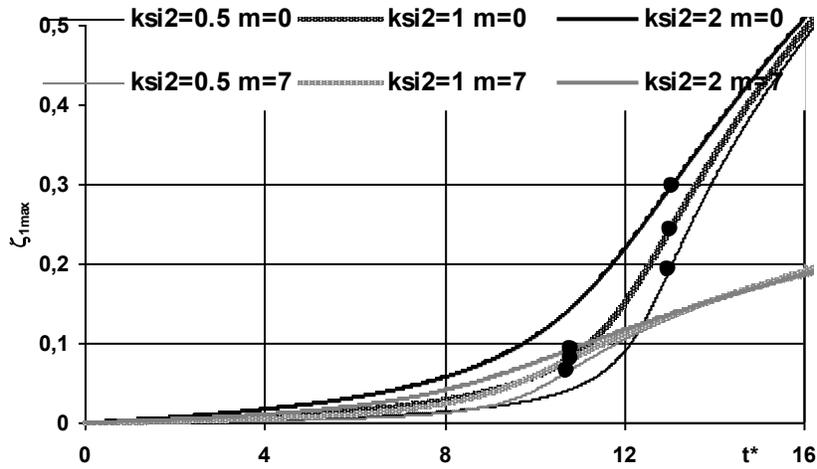


Figure 2: Time histories of deflections versus imperfection rate  $\xi_2$  for plate models  $m=0$ ,  $m=7$  loaded only thermally with positive temperature gradient

Table 1: Critical temperature differences  $\Delta T_{cr}$  versus imperfection rate  $\xi_2$  for plate loaded only thermally with positive temperature gradient

mode m	$\Delta T_{cr}$ (K)		
	$\xi_2$		
	0.5	1	2
0	130.0	130.2	130.7
7	107.4	108.0	108.2

Table 2: Critical temperature differences  $\Delta T_{cr}$  versus imperfection rate  $\xi_2$  for plate loaded only thermally with negative temperature gradient

mode m	$\Delta T_{cr}$ (K)		
	$\xi_2$		
	0.5	1	2
0	180.3	180.9	181.6
7	132.8	130.6	134.5

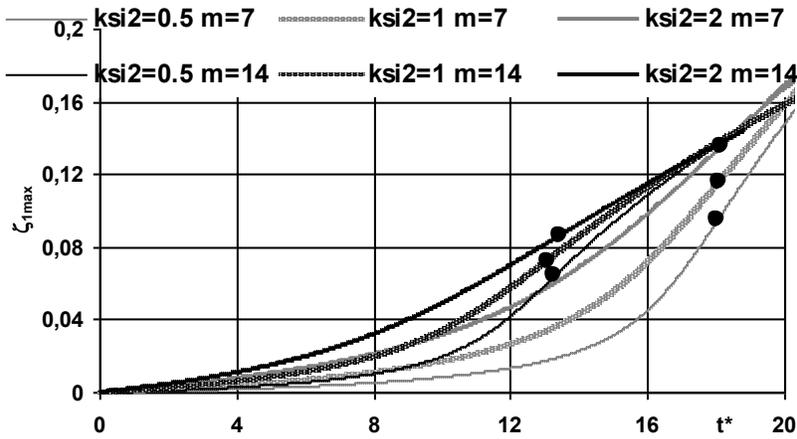


Figure 3: Time histories of deflections versus imperfection rate  $\xi_2$  for plate models  $m=7$ ,  $m=14$  loaded only thermally with negative temperature gradient

### 3.2 Plate loaded mechanically and thermally

Figs 4,5,6,7 shows the time histories of deflections for FDM plate model compressed on outer edge with the forces increasing in time. The rate of mechanical loading growth is equal to  $\approx 931$  MPa/s ( $K7=20$  1/s). Presented curves concern the axisymmetrical  $m=0$  form of plate buckling. The profile of temperature field is expressed by the Eq. 2 or by constant positive (Figs 4,5) or negative (Figs 6,7) temperature gradient. The temperature difference increases in time with the rate  $a$  equal to:  $a=200$  K/s or  $800$  K/s. In constant temperature field the stationary temperature gradient between plate edges is equal to high value  $\Delta T=800$  K. Results presented for the greater value of the rate  $a$  equal to  $a=800$  K/s or high value of constant temperature difference  $\Delta T=800$  K can be the example of the dynamic response of plate under thermal impact, like during the aerodynamic or laser heating (Zhang et all (2019)). Figs 4,6 show the comparison between the plate models loaded only mechanically ( $a=0$  K/s) or both mechanically and thermally with two values of the rate  $a=200$  K/s and  $a=800$  K/s and positive or negative temperature gradient, respectively.

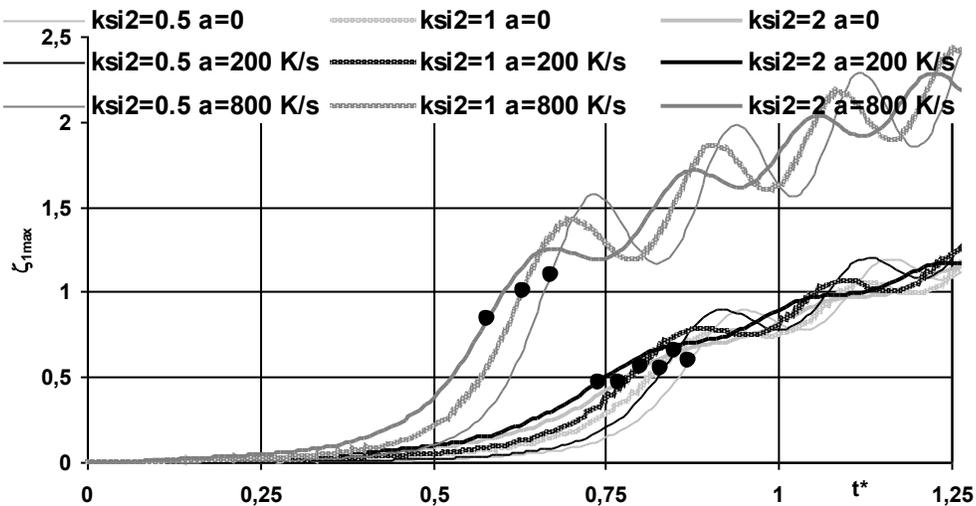


Figure 4: Time histories of deflections versus imperfection rate  $\xi_2$  for plate model  $m=0$  loaded mechanically and thermally with positive temperature gradient

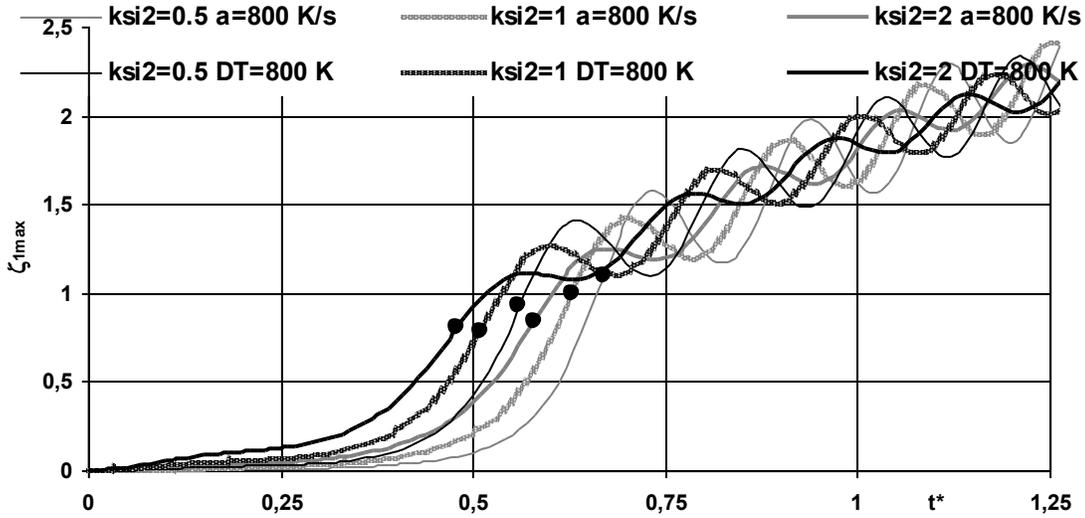


Figure 5: Time histories of deflections versus imperfection rate  $\xi_2$  for plate model  $m=0$  loaded mechanically and thermally with rate  $a=800$  K/s or constant temperature  $\Delta T=800$  K with positive gradient

Figs 5,7 show the reactions of plates loaded mechanically and thermally quickly in time with rate  $a=800$  K/s or located in thermal environment with high temperature difference equal to  $\Delta T=800$  K. Temperature gradient is also positive or negative, respectively. Tables 3,4 present the detailed values of critical, dynamic loads  $p_{crdyn}$  and corresponding temperature differences  $\Delta T_b$  when the loss of plate stability occurs. With increase of the imperfection rate  $\xi_2$  the critical load  $p_{crdyn}$  and temperature difference  $\Delta T_b$  which exists between plate edges decrease. Plate subjected to the impact value of the rate of temperature growth ( $a=800$  K/s) with positive gradient loses dynamic stability for much smaller value of critical load  $p_{crdyn}$ . Direction of the temperature gradient has here meaning. Critical loads  $p_{crdyn}$  of plate loaded in thermal environment with constant, negative temperature difference are higher than obtained for plate model loaded mechanically and thermally increasing in time.

Table 3: Critical, dynamic mechanical loads  $p_{crdyn}$  and corresponding temperature differences  $\Delta T_b$  versus imperfection rate  $\xi_2$  for plate loaded mechanically and thermally with positive temperature gradient

a (K/s) $\Delta T$ (K)	$p_{crdyn}$ (MPa) / $\Delta T_b$ (K)		
	$\xi_2$		
	0.5	1	2
0	40.52 / 0	38.66 / 0	35.8 / 0
200	39.59 / 8.5	37.26 / 8.0	34.47 / 7.4
800	31.21 / 26.8	29.35 / 25.2	29.35 / 25.2
$\Delta T=800$	26.08 / 22.4	23.76 / 20.4	22.36 / 19.2

Table 4: Critical, dynamic mechanical loads  $p_{crdyn}$  and corresponding temperature differences  $\Delta T_b$  versus imperfection rate  $\xi_2$  for plate loaded mechanically and thermally with negative temperature gradient

a (K/s) $\Delta T$ (K)	$p_{crdyn}$ (MPa) / $\Delta T_b$ (K)		
	$\xi_2$		
	0.5	1	2
0	40.52 / 0	38.66 / 0	35.8 / 0
200	42.39 / 9.1	40.06 / 8.6	37.26 / 8.0
800	47.51 / 40.8	45.18 / 38.8	42.39 / 36.4
$\Delta T=800$	48.44 / 41.6	46.58 / 40.0	44.25 / 38.0

Summarizing, it can be noticed that the minimal values of  $p_{crdyn}$  are observed for plates with imperfection rate  $\xi_2=2$  subjected to positive temperature gradient with high temperature difference between edges.

Additionally, the dynamic thermal buckling is presented for FDM plate models with negative imperfection. The comparison between reactions of plates with positive and negative imperfection is presented in Fig. 8. The negative value of imperfection rate does not influence the values of critical loads. The character of changes of curves  $\zeta_{1max}=f(t^*)$  is similar for each examined case of plate preliminary deflection. Table 5 presents the critical values  $p_{crdyn}$ ,  $\Delta T_b$  evaluated for FEM plate model built using the finite element method. FEM plate model is subjected to only mechanical load ( $a=0$  K/s) and thermal one with  $a=200$  K/s and  $a=800$  K/s with positive gradient. Results confirm the observations presented for plate model built using the finite difference method. The minimal value of  $p_{crdyn}$  is for plate quickly thermally loaded ( $a=800$  K/s) having the greater value of imperfection rate  $\xi_2=2$ .

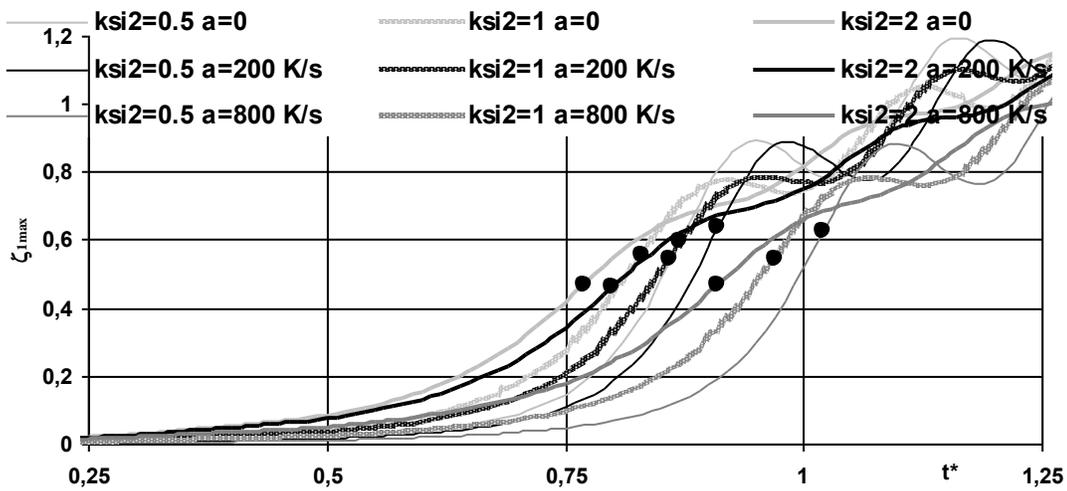


Figure 6: Time histories of deflections versus imperfection rate  $\xi_2$  for plate model  $m=0$  loaded mechanically and thermally with negative temperature gradient

Table 5: Critical mechanical loads  $p_{crdyn}$  and corresponding temperature differences  $\Delta T_b$  versus rate  $\xi_2$  for FEM plate model loaded mechanically and thermally with positive temperature gradient

a (K/s) $\Delta T$ (K)	$p_{crdyn}$ (MPa) / $\Delta T_b$ (K)		
	$\xi_2$		
	0.5	1	2
0	31.18	35.37	33.51
200	36.77 / 7.9	35.37 / 7.6	33.51 / 7.2
800	33.04 / 28.4	31.18 / 26.8	29.32 / 25.2

#### 4. Conclusions

The paper presents the effect of the rate of plate preliminary deflection on values of mechanical and thermal critical loads. It was taken into account the direction of temperature gradient existing between plate edges, rate of temperature difference growth, profile of temperature field, sensitivity of examined plate on negative imperfections. Presented results show minimal influence of both directions and value of imperfection on values of critical temperature differences. In thermo-mechanical process of dynamic buckling besides the parameters of mechanical load the speed of the temperature difference growth between plate edges and the temperature gradient direction have meaning. The profile of temperature field has here meaning, too. There is observed the difference between plate reactions on fixed

temperature field and time-dependent temperature field increasing in time. Presented analyses show the possibility to control the conditions of plate work in order to effectively use plate structure.

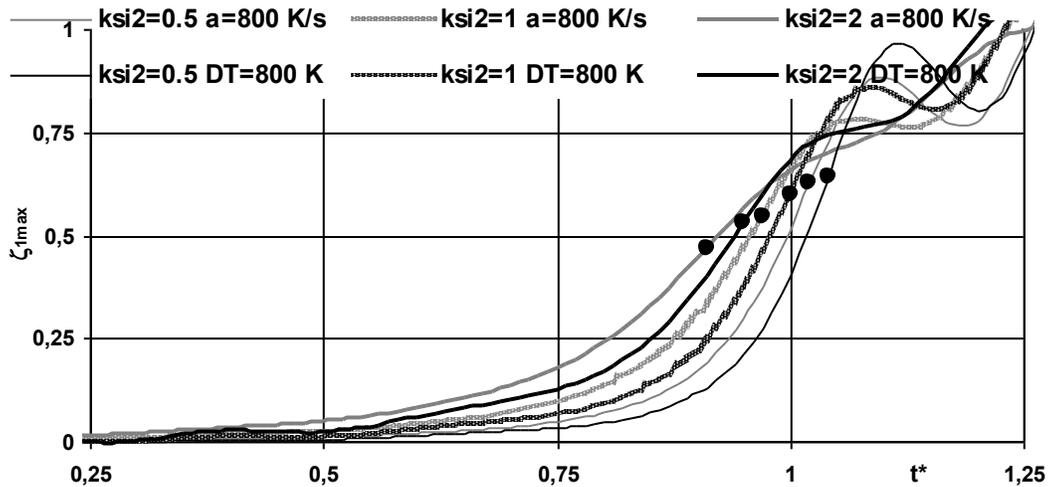


Figure 7: Time histories of deflections versus imperfection rate  $\xi_2$  for plate model  $m=0$  loaded mechanically and thermally with rate  $a=800$  K/s or constant temperature  $\Delta T=800$  K with negative gradient

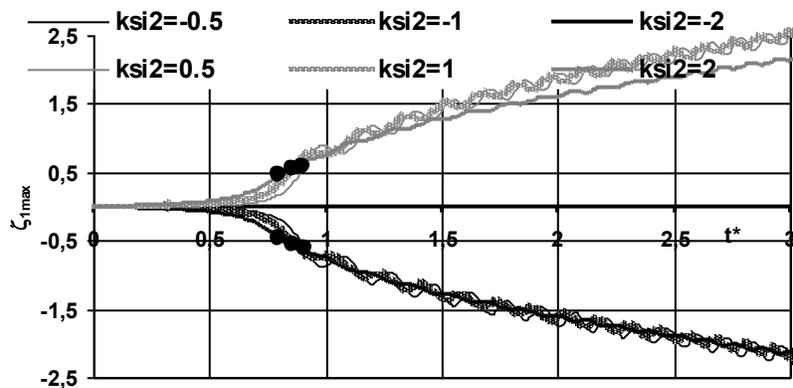


Figure 8: Time histories of deflections versus imperfection rate  $\xi_2$  for plate model  $m=0$  with negative and positive imperfection loaded mechanically and thermally with negative temperature gradient

## References

- Ghiasian, S.E., Bagheri, H., Sadighi, M., Eslami, M.R. (2014). "Thermal buckling of shear deformable temperature dependent circular/annular FGM plates." *International Journal of Mechanical Sciences*, 81 137-148. <http://dx.doi.org/10.1016/j.ijmecsci.2014.02.007>.
- Pawlus, D.(2011a). "Dynamic stability of three-layered annular plates with wavy forms of buckling." *Acta Mech.*, 216 123-138. <https://doi.org/10.1007/s00707-010-0352-3>.
- Pawlus, D. (2011b). "Solution to the problem of axisymmetric and asymmetric dynamic instability of three-layered annular plates." *Thin-Walled Structures*, 49 660-668. <https://doi.org/10.1016/j.tws.2010.09.013>.
- Pawlus, D. (2019). "Stability of three-layered annular plate in stationary temperature field." *Thin-Walled Structures*, 144. <https://doi.org/10.1016/j.tws.2019.106280>.
- Wolmir, A.S. (1972). "Nonlinear dynamics of plates and shells." *Moskwa: Science*. (in Russian).
- Wojciech, S. (1979). "Numerical solution of the problem of dynamic stability of annular plates." *J. Theor. Appl. Mech.* 17(2) 247-262. (in Polish).
- Zhang, J., Pan, S., Chen, L. (2019). "Dynamic thermal buckling and postbuckling of clamped-clamped imperfect functionally graded annular plates." *Nonlinear Dyn*, 95 565-577. <https://doi.org/10.1007/s11071-018-4583-5>.

## **Dynamic stability of a three-layer beam – Generalization of the sandwich structures theory**

Krzysztof Magnucki<sup>1</sup>, Ewa Magnucka-Blandzi<sup>2</sup>

### **Abstract**

The work is devoted to the mathematical modeling of a three-layer beam. A generalization of the "broken-line" hypothesis describing the displacement field is proposed and used to analyze the problem of dynamic stability. Based on Hamilton's principle, equations of motion are obtained. Then this system of two differential equations is approximately solved. In this way, the fundamental natural frequency and two unstable regions are obtained.

### **1. Introduction**

The stability and free vibrations of layered beams were the subject of many scientific and research works. Yang et al. 2005 studied the vibration and dynamic stability of a traveling sandwich using the finite element method. The damping layer was assumed to be linear viscoelastic and almost incompressible. Based on the numerical results, it was shown that the constrained damping layer stabilizes the traveling sandwich beam. Ray and Kar 1995 presented parametric instability of a three-layered symmetric sandwich beam subjected to a periodic axial load. Nine different boundary conditions were taken into account. The effect of shear parameter on the static buckling loads was considered, besides, the effects of shear parameter, core thickness parameter on the regions of parametric instability were studied. YiYeh et al. 2004 studied the dynamic stability problem of a sandwich beam with a constrained layer and an electrorheological fluid core subjected to an axial dynamic force. Effects of the natural frequencies, static buckling loads and loss factors on the dynamic stability behavior of the sandwich beam were investigated. Moreover, the instability regions of the sandwich beam were calculated using the finite element method and the harmonic balance method. Awrejcewicz et al. 2017 developed the mathematical model of three-layered beams based on the hypothesis of the Grigolyuk–Chulkov and the modified couple stress theory. The layers motions on the micro- and nano-scales were included. The Hamilton's principle yielded the equations of motion as well as the boundary/initial conditions regarding beams displacement. Smyczynski et al. 2017 considered the stability analysis of a simply supported layered beam. The beam consists of two faces, a core and two binding layers between the faces and the core. The nonlinear hypothesis of the cross section deformation of the beam was formulated. Based on the Hamilton's principle the system of four stability equations is derived. Then the critical loads, free vibrations and unstable regions were determined. Grygorowicz et al. 2016 presented the mathematical modelling of static and dynamic stability of a simply supported three-layered beam with a metal foam core. The field of displacements was formulated using the broken line hypothesis and

---

<sup>1</sup> Professor, Łukasiewicz Research Network - Institute of Rail Vehicles TABOR [krzysztof.magnucki@tabor.com.pl](mailto:krzysztof.magnucki@tabor.com.pl)

<sup>2</sup> Professor, Institute of Mathematics, Poznan University of Technology [ewa.magnucka-blandzi@put.poznan.pl](mailto:ewa.magnucka-blandzi@put.poznan.pl)

the proposed nonlinear hypothesis. The equations of motion are derived using Hamilton's principle. Critical loads, unstable regions, natural frequencies of the beam, static and dynamic equilibrium paths were calculated analytically and numerically verified. Magnucka-Blandzi and Magnucki 2018 assumed the applicable hypothesis of deformation of the plane cross section for modelling of a simply supported sandwich beam under three-point bending. The analytical model of the beam considering the shear effect of the faces is reduced to the classical sandwich beam described by two differential equations of equilibrium.

The subject of the study is a simply supported three-layer beam of length  $L$ , width  $b$  and total depth  $h$  subjected to a pulsating axial force  $F$  (Fig. 1).

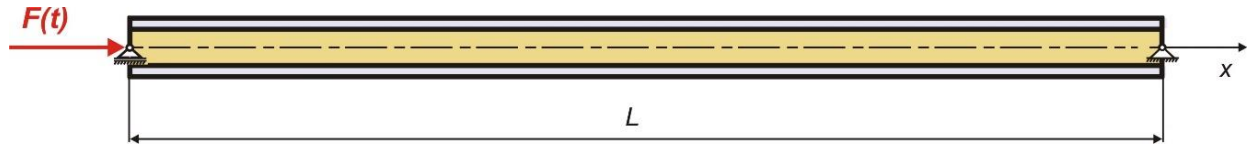


Figure 1: Scheme of the beam subjected to a pulsating axial force

The individual hypothesis-theory of deformation of the plane cross section is assumed for modelling of the beam with consideration of the shear effect in the layers.

## 2. Mathematical model of the beam

A non-linear hypothesis of cross-section deformation is assumed. This hypothesis is a generalization of the broken line hypothesis (Fig. 2).

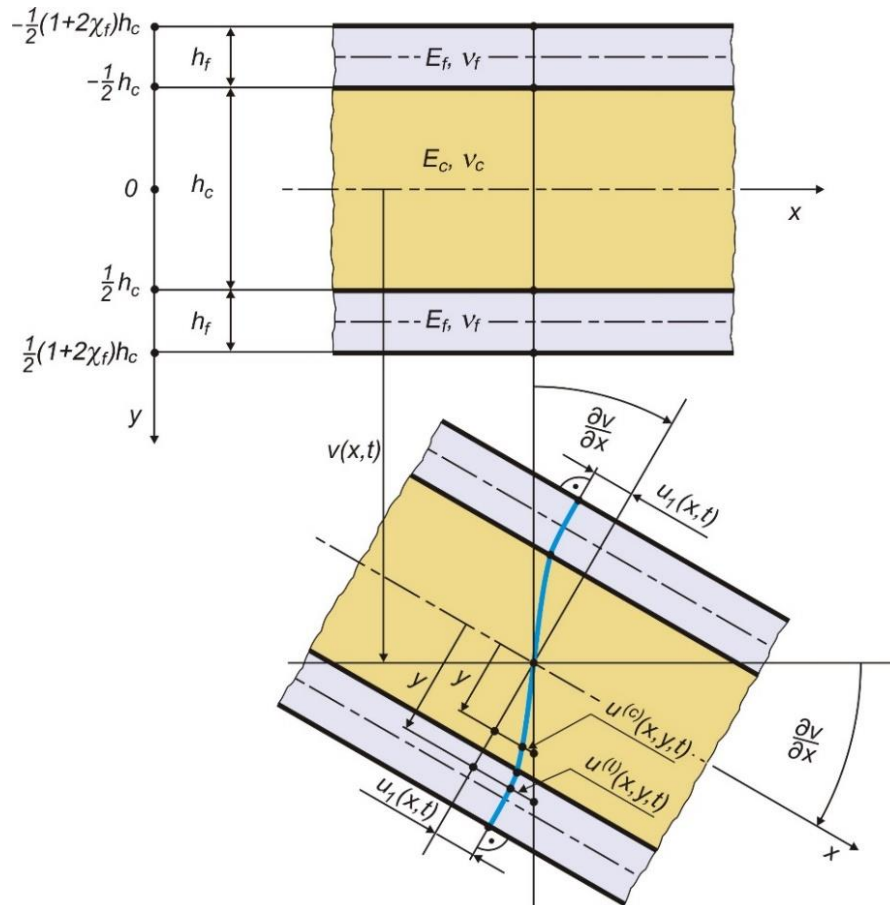


Figure 2: Scheme of deformation of the plane cross section of the three-layer beam

The total height of the beam equals

$$h = 2h_f + h_c,$$

where:  $h_f, h_c$  – thicknesses of the outer layers and the middle layer (core), respectively.

Moreover, the following notation is introduced:

$\eta = y/h_c$	– dimensionless coordinate,
$\tilde{u}_1(x, t) = u_1(x, t)/h_c$	– dimensionless displacement,
$\chi_f = h_f/h_c$	– parameter,
$k_f \in \langle 0, 1 \rangle$	– coefficient (real number),
$\beta_c \in \langle 0, 1 \rangle$	– coefficient (real number),
$E_f, E_c$	– Young's modules of facings and core,
$\nu_f, \nu_c$	– Poisson's ratio of facings and core,
$\rho_f, \rho_c$	– mass densities of facings and core.

So, the total mass density of the beam

$$\rho_b = \rho_c + 2\rho_f\chi_f.$$

Based on the assumed hypothesis, longitudinal displacements are formulated separately for each layer, i.e. for:

- upper layer:  $-(1 + 2\chi_f)/2 \leq \eta \leq -1/2$

$$u^{(u)}(x, y, t) = -\square_c \left[ \eta \frac{\partial v}{\partial x} + f_d^{(u)}(\eta) \tilde{u}_1(x, t) \right], \#(1)$$

where:

$$f_d^{(u)}(\eta) = \left\{ - \left[ 3 - 4 \left( \frac{\eta}{1 + 2\chi_f} \right)^2 \right] \frac{\eta}{1 + 2\chi_f} \right\}^{k_f},$$

- middle layer (core):  $-1/2 \leq \eta \leq 1/2$

$$u^{(c)}(x, y, t) = -\square_c \left[ \eta \frac{\partial v}{\partial x} - 2f_d^{(c)}(\eta) \tilde{u}_1(x, t) \right], \#(2)$$

where:

$$f_d^{(c)}(\eta) = c_f \frac{3 - 4\beta_c\eta^2}{3 - \beta_c} \eta, \quad c_f = \frac{1 + 6(1 + \chi_f)\chi_f}{(1 + 2\chi_f)^3},$$

- lower layer:  $1/2 \leq \eta \leq (1 + 2\chi_f)/2$

$$u^{(l)}(x, y, t) = -\square_c \left[ \eta \frac{\partial v}{\partial x} - f_d^{(l)}(\eta) \tilde{u}_1(x, t) \right], \#(3)$$

where:

$$f_d^{(l)}(\eta) = \left\{ \left[ 3 - 4 \left( \frac{\eta}{1 + 2\chi_f} \right)^2 \right] \frac{\eta}{1 + 2\chi_f} \right\}^{k_f}.$$

A linear relationship between strains and displacements is assumed, so the strains separately for each layer are as follows:

$$\varepsilon_x = \frac{\partial u}{\partial x}, \quad \gamma_{xy} = \frac{\partial v}{\partial x} + \frac{\partial u}{h_c \partial \eta}.$$

Then, taking into account the above and the expressions (1)–(3), the strains are determined.

Hence the stresses are given by the formula for:

- upper layer:  $-(1 + 2\chi_f)/2 \leq \eta \leq -1/2$

$$\sigma_x^{(u)} = E_f \cdot \varepsilon_x^{(u)}, \quad \tau_{xy}^{(u)} = \frac{E_f}{2(1 + \nu_f)} \cdot \gamma_{xy}^{(u)},$$

- middle layer (core):  $-1/2 \leq \eta \leq 1/2$

$$\sigma_x^{(c)} = E_c \cdot \varepsilon_x^{(c)}, \quad \tau_{xy}^{(c)} = \frac{E_c}{2(1 + \nu_c)} \cdot \gamma_{xy}^{(c)},$$

- lower layer:  $1/2 \leq \eta \leq (1 + 2\chi_f)/2$

$$\sigma_x^{(l)} = E_f \cdot \varepsilon_x^{(l)}, \quad \tau_{xy}^{(l)} = \frac{E_f}{2(1 + \nu_f)} \cdot \gamma_{xy}^{(l)}.$$

Then,

- the elastic strain energy

$$U_\varepsilon = \frac{1}{2} b h_c \cdot$$

$$\left. \begin{aligned} & \int_0^L \left\{ E_f \int_{-\frac{1+2\chi_f}{2}}^{-\frac{1}{2}} \left\{ [\varepsilon_x^{(u)}]^2 + \frac{1}{2(1 + \nu_f)} [\gamma_{xy}^{(u)}]^2 \right\} d\eta + E_c \int_{-\frac{1}{2}}^{\frac{1}{2}} \left\{ [\varepsilon_x^{(c)}]^2 + \frac{1}{2(1 + \nu_c)} [\gamma_{xy}^{(c)}]^2 \right\} d\eta \right. \\ & \left. + E_f \int_{\frac{1}{2}}^{\frac{1+2\chi_f}{2}} \left\{ [\varepsilon_x^{(l)}]^2 + \frac{1}{2(1 + \nu_f)} [\gamma_{xy}^{(l)}]^2 \right\} d\eta \right\} dx, \end{aligned}$$

- the kinetic energy

$$T = \frac{1}{2} (2\rho_f \chi_f + \rho_c) b h_c \int_0^L \left( \frac{\partial v}{\partial t} \right)^2 dx,$$

- the work of the load

$$W = \frac{1}{2} F \int_0^L \left( \frac{\partial v}{\partial x} \right)^2 dx$$

are derived.

Based on the Hamilton's principle

$$\delta \int_{t_1}^{t_2} [T - (U_\varepsilon - W)] dt = 0,$$

two differential equations of motion are obtained in the following form

$$\begin{cases} \rho_b b h_c \frac{\partial^2 v}{\partial t^2} + E_c b h_c^3 \left( C_{vv} \frac{\partial^4 v}{\partial x^4} - C_{vu} \frac{\partial^3 \tilde{u}_1}{\partial x^3} \right) + \frac{\partial^2 v}{\partial x^2} F(t) = 0 \\ C_{vu} \frac{\partial^3 v}{\partial x^3} - C_{uu} \frac{\partial^2 \tilde{u}_1}{\partial x^2} + C_u \frac{\tilde{u}_1(x, t)}{h_c^2} = 0 \end{cases}, \#(4)$$

where:

$$C_{vv}, C_{vu}, C_{uu}, C_u \quad - \text{dimensionless coefficients.}$$

## 2. Natural frequency and unstable regions

The system of two differential equations (4) is approximately solved with the use of two assumed functions:

$$v(x, t) = v_a(t) \sin\left(\pi \frac{x}{L}\right), \quad \tilde{u}_1(x, t) = \tilde{u}_{1a}(t) \cos\left(\pi \frac{x}{L}\right), \quad \#(5)$$

where:  $v_a(t)$ ,  $\tilde{u}_{1a}(t)$  – functions of the time  $t$ .

The loading force – the pulsating force is in the following form

$$F(t) = F_m + F_a \cos(\theta t), \quad \#(6)$$

where:  $F_m$ ,  $F_a$ ,  $\theta$  – mean value, amplitude and frequency of the force, respectively.

Substituting the functions (5) and (6) into the equations (4), and after simply transformation, one obtains the Mathieu's equation

$$\frac{d^2 v_a}{dt^2} + \Omega^2 [1 - 2\mu \cos(\theta t)] v_a(t), \quad \#(7)$$

where:

$$\begin{aligned} \Omega^2 &= \omega^2 (1 - \alpha_m), & \mu &= \frac{1}{2} \frac{\alpha_a}{1 - \alpha_m}, & \alpha_m &= \frac{F_m}{F_{CR}}, & \alpha_a &= \frac{F_a}{F_{CR}}, \\ \omega^2 &= \left(\frac{\pi}{L}\right)^4 (1 - C_{sv}) \frac{C_{vv} E_c h_c^2}{\rho_b}, \\ F_{CR} &= \left(\frac{\pi}{L}\right)^2 (1 - C_{sv}) C_{vv} E_c b h_c^3, \\ C_{sv} &= \max_{\beta_c, k_f} \left\{ \frac{\pi^2}{C_{vv}} \cdot \frac{C_{vu}^2}{\pi^2 C_{uu} + \lambda_c^2 C_u} \right\}, & \lambda_c &= \frac{L}{h_c}. \end{aligned}$$

Using the above notations, the unstable regions can be described by the following inequalities:

- the first unstable region

$$2\Omega\sqrt{1 - \mu} \leq \theta \leq 2\Omega\sqrt{1 + \mu},$$

- the second unstable region

$$\Omega\sqrt{1 - 2\mu^2} \leq \theta \leq \Omega\sqrt{1 + \frac{1}{3}\mu^2}.$$

### 3. Numerical calculations

The detailed studies are realized for the exemplary family of the three-layer beams. The stable and unstable regions are calculated for the three load cases – pulsating forces.

The geometric dimensions of the beams are as follows:

$$\begin{aligned} h &= 20 \text{ mm} && \text{– total height,} \\ L &= 600 \text{ mm} && \text{– length,} \\ \lambda &= L/h = 30 && \text{– relative length,} \end{aligned}$$

and the following mechanical properties are taken into account:

$$\begin{aligned} E_f &= 65\,000 \text{ MPa} && \text{– Young's modulus in facings,} \\ \nu_f &= 0.33 && \text{– Poisson's ratio in facings,} \\ E_c &= 1\,200 \text{ MPa} && \text{– Young's modulus in the core,} \\ \nu_c &= 0.3 && \text{– Poisson's ratio in the core,} \\ \rho_f &= 2\,600 \text{ kg/m}^3 && \text{– mass density in facings,} \\ \rho_c &= 350 \text{ kg/m}^3 && \text{– mass density in the core.} \end{aligned}$$

The fundamental natural frequency  $\omega$  and dimensionless critical load

$$\tilde{F}_{CR} = \frac{F_{CR}}{E_c b h_c} = \left(\frac{\pi}{L}\right)^2 (1 - C_{sv}) C_{vv} E_c b h_c^3$$

are calculated and presented in Table 1.

Table 1: Dimensionless parameters, natural frequencies and dimensionless critical loads ( $\lambda = 30$ )

$\chi_f$	$\frac{1}{18}$	$\frac{2}{16}$	$\frac{3}{14}$	$\frac{4}{12}$	$\frac{5}{10}$
$\beta_c$	0.1097	0.06230	0.04127	0.02798	0.01847
$k_f$	0.07041	0.04187	0.03263	0.02862	0.02698
$C_{sv}$	0.03488	0.05871	0.07476	0.08358	0.08552
$\omega$ [1/s]	881.8	976.3	987.5	969.9	941.2
$\bar{F}_{CR}$	0.01359	0.02318	0.03038	0.03575	0.03971

Three load cases (LC-1, LC-2, LC-3) are taken into account – according to the parameter values given in Table 2.

Table 2: Three load cases

Load case	LC-1	LC-2	LC-3
$\alpha_a$	0.5	1.0	1.5
$\alpha_m$	0.5	0.25	0.1
$\mu$	$\frac{1}{2}$	$\frac{2}{3}$	$\frac{5}{6}$

Then, the following unstable regions are determined for:

- first load case
  - the first unstable region
  - the second unstable region

$$\omega \leq \theta \leq \sqrt{3} \cdot \omega,$$

$$\frac{1}{2} \cdot \omega \leq \theta \leq \frac{1}{2} \sqrt{\frac{13}{6}} \cdot \omega,$$

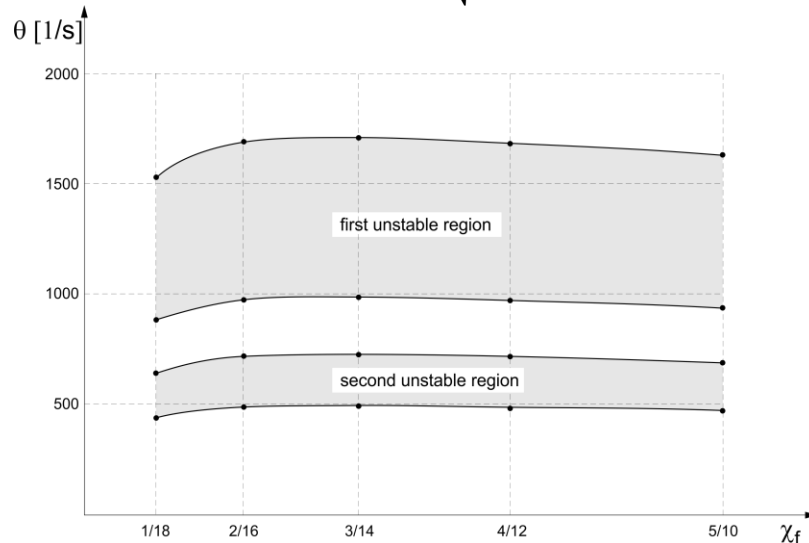


Figure 3: Unstable regions (LC-1)

- second load case
  - the first unstable region
  - the second unstable region

$$\omega \leq \theta \leq \sqrt{5} \cdot \omega,$$

$$\frac{\sqrt{3}}{6} \cdot \omega \leq \theta \leq \frac{\sqrt{31}}{6} \cdot \omega,$$

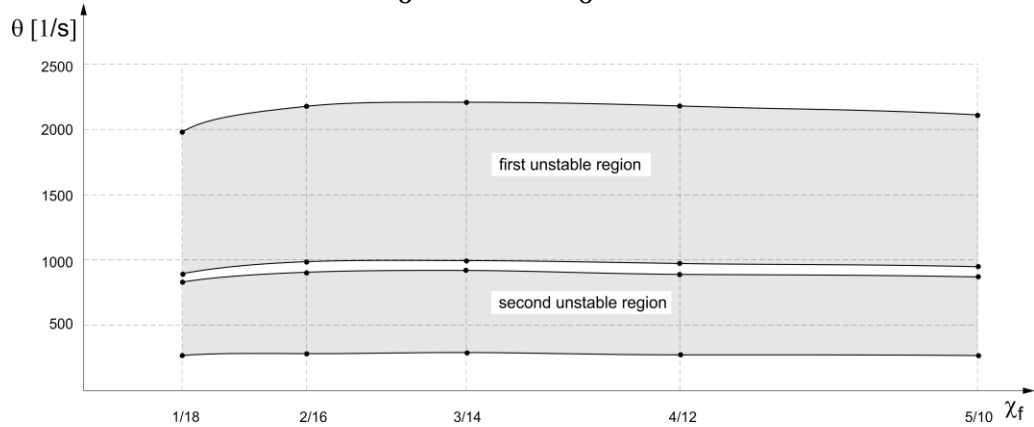


Figure 4: Unstable regions (LC-2)

- third load case
  - the first unstable region

$$\frac{\sqrt{15}}{5} \cdot \omega \leq \theta \leq \frac{\sqrt{165}}{5} \cdot \omega,$$

- the second unstable region does not exist.

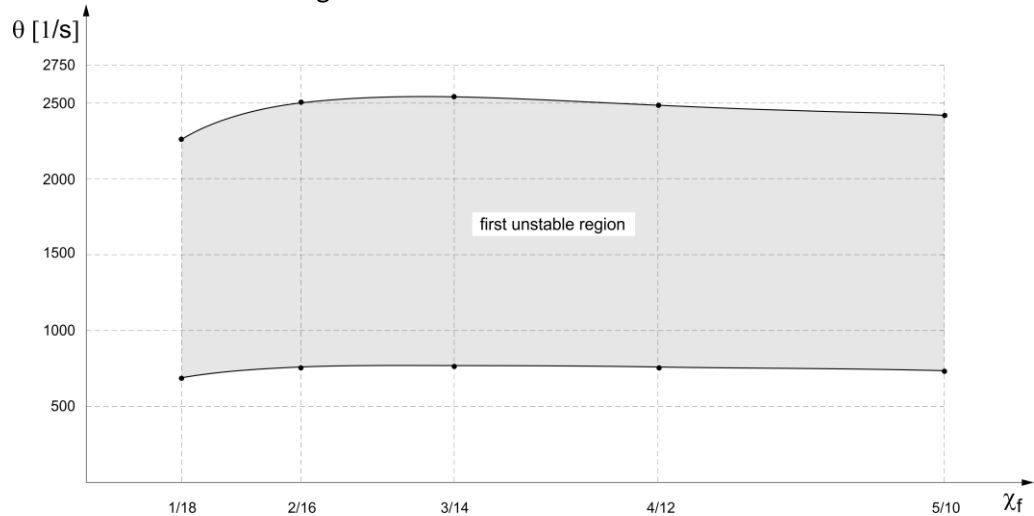


Figure 5: Unstable regions (LC-3)

#### 4. Conclusions

The generalized "broken line" hypothesis allowed to model a three-layer beam taking into account the shear effect. Critical force, fundamental natural frequency and unstable regions are the result of the obtained and solved system of differential equations. Detailed analysis identified unstable regions, in particular only one existing.

#### Acknowledgments

The research was carried out as part of the Rector's 2021 project at the Poznan University of Technology.

#### References

- Wen-PeiYang, Lien-WenChen, Ching-ChengWang (2005). "Vibration and dynamic stability of a traveling sandwich beam." *Journal of Sound and Vibration*, 285 (3) 597-614.
- Ray K.R., Kar C. (1995). "Parametric instability of a sandwich beam under various boundary conditions." *Computers & Structures*, 55 (5) 857-870.
- Jia-YiYeh, Lien-WenChen, Ching-ChengWang (2004). "Dynamic stability of a sandwich beam with a constrained layer and electrorheological fluid core." *Composite Structures*, 64 (1) 47-54.
- Awrejcewicz J., Krysko V.A., Pavlov S.P., Zhigalov M.V., Krysko A.V. (2017). "Mathematical model of a three-layer micro- and nano-beams based on the hypotheses of the Grigolyuk–Chulkov and the modified couple stress theory." *International Journal of Solids and Structures*, 117 39-50.
- Smyczynski M.J., Magnucka-Blandzi E. (2017). „Stability and free vibrations of the three layer beam with two binding layers." *Thin-Walled Structures*, 113, 144-150.
- Grygorowicz M., Magnucka-Blandzi E. (2016). „Mathematical modeling for dynamic stability of sandwich beam with variable mechanical properties of core." *Applied Mathematics and Mechanics*, 37 (10) 1361–1374.
- Magnucka-Blandzi E., Magnucki K. (2018). „Mathematical modelling of a sandwich beam with consideration of the shear effect in the faces – Three-point bending." *Eighth Intl Conf. Thin-Walled Structures – ICTWS 2018*, Lisbon, Portugal, 24-27 July, 2018.

## The use of the Overall Imperfection Method for fire design situation

József A. Szalai<sup>1</sup>, Samer Nemer<sup>2</sup>, Ferenc Papp<sup>3</sup>

### Abstract

The Overall Imperfection Method (OIM) is a highly universal and robust method for the assessment of the global stability resistance of steel members with any load and support conditions. The method uses the relevant elastic critical buckling mode shape as equivalent initial geometrical imperfection and gives a universal procedure for the determination of the proper amplitude. This procedure takes into consideration the appropriate buckling curves connected to a classification procedure of the buckling mode, accordingly gives completely consistent results with the reduction factor based design method where the same buckling curves are used. The assessment (final check) of the global stability resistance is performed by second order evaluation of the properly imperfect member, so the OIM directly calculates the geometrical nonlinearities. Therefore the methodology is completely applicable also in fire design situation since this limit state is characterized by the high nonlinearity. The key issue is the determination of the amplitude of the equivalent geometric imperfection. The method follows the same procedure as used for normal temperature but using the special buckling curves specified for the fire design situation. Applying the equivalent geometric imperfection, the second order analysis is performed with the reduced elastic modulus. By this the result directly includes the effect of the significantly larger deformations caused by the elevated temperature. This methodology is completely consistent with the methodology of conventional reduction factor based buckling design, also in case of elevated temperature. Moreover, it can be used for any situations with complex load interactions or irregular support conditions. The paper discusses briefly the background of the OIM in case of fire design. Moreover, the steps of the application will be described, and an illustrative example will be presented in which the OIM result is compared to the result of the EN 1993-1-2 and GMNIA. The largescale validation of the presented method for irregular structural members with elevated temperature is going on, it is out of the scope of this paper.

### 1. Introduction

The Overall Imperfection Method is the generalization of the Unique Global and Local Imperfection Method (UGLI) which was introduced by EC3-1-1 (EN1993-1-1 2019) and published by Chladný (Chladný et al. 2013). The method is valid for structural members subjected to flexural buckling. The UGLI was extended by Agüero for members subjected to lateral-torsional buckling (Agüero et al. 2015), and by Papp for the coupled buckling of flexural and lateral-torsional buckling (Papp 2016). The most detailed

<sup>1</sup> Researcher, Institute for Steel Structures and Bridges, Faculty of Civil Engineering, Budapest University of Technology and Economics

<sup>2</sup> Researcher, Széchenyi István University, Faculty of Mechanical Engineering

<sup>3</sup> Associate Professor, Széchenyi István University, Faculty of Mechanical Engineering

description of the generalised OIM was published by Szalai and Papp (Szalai et al. 2019). The OIM was used for irregular structural members and simple portal frames in the paper published by Papp et al. 2019.

In this paper the OIM is used to design structural members subjected to elevated temperature. The method utilizes the results of the Linear Buckling Analysis (LBA), namely the elastic critical load factor, the buckling mode shape and the second order internal moments induced by the modal geometric imperfection. The methodology assumes that any complex global buckling mode can be classified into one of the finite number of *fundamental buckling modes* (e.g. flexural buckling or lateral-torsional buckling, etc.). Furthermore it is also assumed that there are calibrated standard buckling curves for all the fundamental buckling modes, for elevated temperatures and they can be used within the proposed methodology to ensure the required reliability level of design.

The procedure of the OIM consists of two basic steps (Fig. 1):

- (1) a universal *Transformation* which converts the examined structural member with a certain complex buckling problem into a properly defined *equivalent reference member* (ERM) which is a prototype model of the corresponding fundamental buckling mode – this is the ultimate generalization of the effective length (or equivalent member) method to any buckling problem (Szalai et al. 2019);
- (2) a closed-form *analytical solution* for the equivalent reference member which is based on the standard buckling curves corresponding to the equivalent fundamental buckling mode (EN1993-1-2, 2005) – this is the ultimate generalization of the beam-column buckling strength interaction equations.

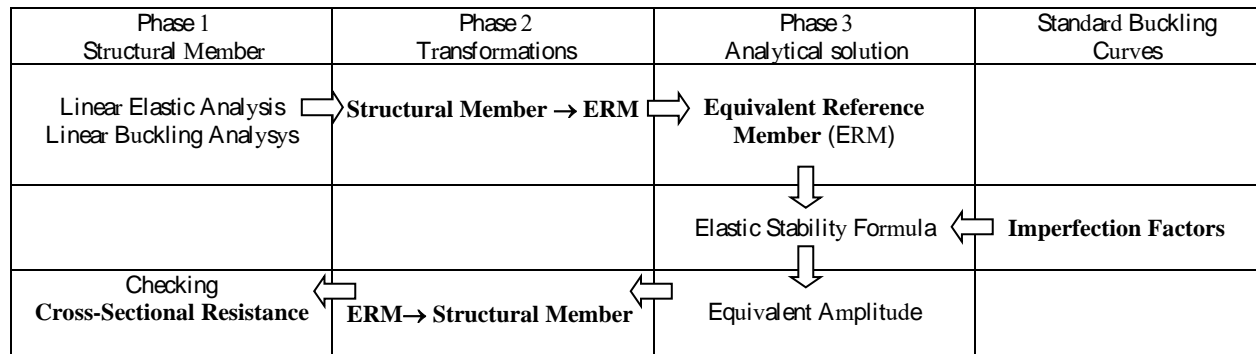


Figure 1: The procedure of the OIM

The OIM uses the traditional imperfection factors for the calculation of the equivalent amplitude for the buckling mode based geometrical imperfection. Due to this imperfection the checking of the cross-section utilization with second order analysis (GNA) is equivalent to the checking of the global buckling mode.

In the paper first the main steps are explained, then the steps of the complete OIM is summarized. Finally the application of the method is presented by a simple example. The paper assumes double symmetric hot-rolled or welded I and H cross-sections, but it should be noted that the methodology can be extended to other types of cross-sections (mono-symmetric and asymmetric).

## 2. The basic steps of the OIM

This section covers the description and explanation of the basic steps of the OIM as well as presents the step-by-step procedure of the complete method. The application of the method is illustrated by a simple example where the result of the method is compared to the result of the geometrically and materially nonlinear analysis with imperfections (GMNIA).

### 2.1 The 'Structural Member → ERM' transformation

The details of the model transformation at normal temperature are described in Section 2 of the paper published by Szalai and Papp (Szalai et al. 2019). The aim of this step is as follows:

- determine the location of the *equivalent point* of the structural member
- classify the *buckling mode* through the equivalent point
- calculate the *equivalent length* of the *reference member*

The reference member in general is a straight, prismatic and simply supported member with uniform cross-section subjected to uniformly distributed compression force and/or bending moments. The aim is to determine the *equivalent reference member* (ERM) for the examined problem. The ERM has certain cross-section, member length, member force and moments and buckling mode. To determine these properties the location of the equivalent point is needed. The equivalent point (*ep*) is that cross-section along the structural member where the cross-sectional utilization (applying conservative interaction formula) takes the highest value,

$$U_{sec,cr}(ep) = \max U_{sec,cr}(x) \rightarrow ep \quad (1)$$

where the  $U_{sec,cr}$  cross-sectional utilization is calculated from the internal axial force and moments due to the deformation of the buckling mode shape with arbitrary amplitude. Once the equivalent point has been determined the cross-section of the ERM will be the same as the cross-section of the structural member at the equivalent point. Moreover, the uniformly distributed axial force and moments of the ERM will be the same as the axial force and moments calculated at the equivalent point of the structural member. For the length of the equivalent member the proper fundamental buckling mode can be selected using *Table 1*.

Table 1: The fundamental Buckling Mode Classes (BMC) – only in case of double symmetric cross-sections

BMC	Cross-section at the <i>ep</i>	Active load components at the <i>ep</i>	Buckling mode shape displacement(s)* at the <i>ep</i>	Buckling mode type
BMC_01	doubly symmetric	$N^l$	$w_{cr}$	flexural buckling about strong axis (FB-y)
BMC_02		$N^l$	$v_{cr}$	flexural buckling about weak axis (FB-z)
BMC_03		$N^l$	$\varphi_{cr}$	torsional buckling (TB)
BMC_04		$M_y^l$	$v_{cr}; \varphi_{cr}$	lateral-torsional buckling (LTB)
BMC_05		$N^l; M_y^l$	$v_{cr}; \varphi_{cr}$	coupled buckling (FB-z + LTB)

\*  $v$  and  $w$  denote the displacements in directions of the principle axes of the cross-section, while  $\varphi$  denotes the rotation around the member axis

Since the cross-section and the loading at the equivalent point of the structural member are identical to the ones of the ERM, the equality of the elastic critical load factors is necessary. For the elastic critical load of the ERM there are well-known analytical formulas for each fundamental buckling modes (e.g. see Trahair, 1993) from which the member length of the ERM can be calculated using the elastic critical load equivalency. By this the ERM is fully defined.

## 2.2 The solution of the ‘Equivalent Reference Member’

Once the ERM is completely defined, the specific buckling solution gives the necessary information which is needed for the solution of the buckling problem of the structural member. The analytical solution of the ERM is based on the generalized Ayrton-Perry formula. The key parameter of the Ayrton-Perry formula is the *imperfection factor* which is responsible for the correct consideration of the second

order effect and which is the base for the standard safety calibration. The APF based imperfection factor for coupled flexural and lateral-torsional buckling at elevated temperature can be written as follows (Szalai, 2017):

$$\eta_{NM,\theta} = \frac{\alpha_{sec,NM}}{\alpha_{sec,N}} \eta_{N,\theta} + \mu \frac{\alpha_{sec,NM}}{\alpha_{sec,M}} \eta_{M,\theta} \quad (2)$$

where  $\eta_{N,\theta}$  and  $\eta_{M,\theta}$  are the standard imperfection factors corresponding to the buckling modes for flexural buckling and lateral-torsional buckling at elevated temperature respectively,  $\alpha_{sec,N}$ ,  $\alpha_{sec,M}$  and  $\alpha_{sec,NM}$  are the cross-sectional resistance multiplication factors taking the buckling active loads into consideration, and  $\mu$  is a modifying factor dependent on the pure elastic critical loads of the equivalent reference member (Szalai, 2017).

The imperfection factors are determined in the EN 1993-1-2 for all the classes of cross-sections. However for class 3 and class 4 cross-sections the authors suggest using the novel results published by Zhao and others (Zhao et al. 2014), see Table 2 and Table 3.

Table 2: Imperfection factor for flexural buckling at elevated temperature

parameter	class of cross-section	
	class 1 & class 2 (EN1993-1-2)	class 3 & class 4 (Zhao at al. 2014)
slenderness	$\bar{\lambda}_{\theta} = \bar{\lambda} \sqrt{\frac{k_{y,\theta}}{k_{E,\theta}}} \quad \bar{\lambda} = \sqrt{\frac{Af_y}{N_{cr}}}$	$\bar{\lambda}_{\theta} = \bar{\lambda} \sqrt{\frac{k_{y,\theta}}{k_{E,\theta}}} \quad \bar{\lambda} = \sqrt{\frac{A_{eff,new} f_y}{N_{cr}}}$
imperfection coefficient	$\alpha = 0.65 \sqrt{\frac{235}{f_y}}$	$\alpha = 0.55 \sqrt{\frac{235}{f_y}}$
imperfection factor for AP formula	$\eta_{N,\theta} = \alpha \bar{\lambda}_{\theta}$	

Table 3: Imperfection factor for lateral-torsional buckling at elevated temperature

parameter	class of cross-section	
	class 1 & class 2 (EN1993-1-2)	class 3 & class 4 (Zhao at al. 2014)
slenderness	$\bar{\lambda}_{LT,\theta} = \bar{\lambda}_{LT} \sqrt{\frac{k_{y,\theta}}{k_{E,\theta}}} \quad \bar{\lambda}_{LT} = \sqrt{\frac{Wf_y}{M_{cr}}}$	$\bar{\lambda}_{LT,\theta} = \bar{\lambda}_{LT} \sqrt{\frac{k_{y,\theta}}{k_{E,\theta}}} \quad \bar{\lambda}_{LT} = \sqrt{\frac{W_{eff,new} f_y}{M_{cr}}}$
imperfection coefficient	$\alpha_{LT} = 0.65 \sqrt{\frac{235}{f_y}}$	$\alpha_{LT} = 0.55 \sqrt{\frac{235}{f_y}}$
imperfection factor for AP formula	$\eta_{M,\theta} = \alpha_{LT} \bar{\lambda}_{LT,\theta}$	

### 2.3 The 'ERM → Structural Member' transformation

In the OIM the equivalent amplitude is to be determined for the applied equivalent geometrical imperfection with the  $\eta_{cr}$  shape of the complex buckling mode of the structural member. The equivalent geometrical imperfection of the examined structural member takes the following formula:

$$\eta_{cr,eq} = \delta_{eq} \eta_{cr} = \eta_{NM,\theta} \frac{\alpha_{cr}}{\alpha_{sec,a}} \alpha_{sec,cr} \eta_{cr} \quad (3)$$

where  $\alpha_{cr}$  is the critical load factor of the structural member, the  $\eta_{cr}$  is the shape of buckling mode with arbitrary amplitude, and the  $\alpha_{sec}$  are the cross-sectional load amplification factors, they are linearly

dependent on the actual amplitude ( $\alpha_{sec,a}$  relates to the buckling active loads, and  $\alpha_{sec,cr}$  relates to the buckling deformation).

### 2.4 Checking global buckling resistance

The final step of the OIM is running a second order analysis and cross-section checking on the examined structural member with the  $\eta_{cr,eq}$  equivalent geometrical imperfection. In this step the  $U$  cross-sectional utilization should be equal or less than 1.0. The  $U$  can be calculated as follows:

- class 1 and class 2 cross-sections:

$$U = \max \left[ \frac{N_{fi,Ed,\theta}}{k_{y,\theta} A f_y} + \frac{M_{y,fi,Ed,\theta}}{k_{y,\theta} W_{pl,y} f_y} + \frac{M_{z,fi,Ed,\theta}}{k_{y,\theta} W_{pl,z} f_y} + \frac{B_{fi,Ed,\theta}}{k_{y,\theta} W_{\omega,pl} f_y} \right] \quad (4)$$

- class 3 and class 4 cross-sections:

$$U = \max \left[ \frac{N_{fi,Ed,\theta}}{k_{y,\theta} A_{eff,new} f_y} + \frac{M_{y,fi,Ed,\theta} + \Delta M_{y,fi,Ed,\theta}}{k_{y,\theta} W_{eff,new,y} f_y} + \frac{M_{z,fi,Ed,\theta} + \Delta M_{z,fi,Ed,\theta}}{k_{y,\theta} W_{eff,new,z} f_y} + \frac{B_{fi,Ed,\theta}}{k_{y,\theta} W_{\omega,eff,new} f_y} \right] \quad (5)$$

where the cross-section properties denoted by 'eff,new' can be calculated according to the research papers published by Zhao and others, Couto and others, Vila Real and others (Zhao et al 2014; Couto et al. 2014; Couto et al. 2015).

### 3. The step-by-step procedure of the OIM at elevated temperature

The step-by-step procedure of the OIM at design situation of elevated temperatures is summarized in Table 4.

Numerical calculations of the examined Structural Member	
<b>Step 1</b>	Structural analysis of the perfect structural member with material properties at elevated temperature 1.1 Determine the design loads and actions 1.2 Determine the internal forces and moments
Model transformation: Structural Member → ERM	
<b>Step 2</b>	Determination of the equivalent point 2.1 Determine the equivalent point 2.2 Determine the equivalent point 2.3 Determine the equivalent point 2.4 Determine the equivalent point
<b>Step 3</b>	Buckling mode classification through the equivalent point 3.1 Determine the buckling mode 3.2 Determine the buckling mode
<b>Step 4</b>	Equivalent length of the reference member 4.1 Determine the equivalent length
Analytical solution of the ERM	
<b>Step 5</b>	Equivalent imperfection factor 5.1 Determine the imperfection factor
<b>Step 6</b>	Determine the imperfection factor
Model transformation: ERM → Structural Member	
<b>Step 7</b>	Equivalent geometrical imperfection 7.1 Determine the imperfection factor 7.2 Determine the imperfection factor
Final check	
<b>Step 8</b>	Final check 8.1 Determine the utilization 8.2 Determine the utilization

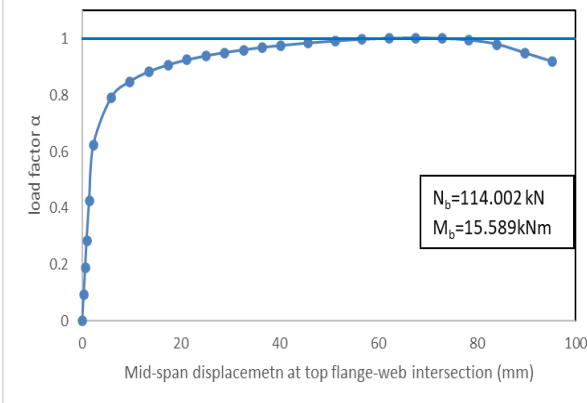


Table 6: The results of the step-by-step OIM calculation in case of the example in Fig. 2

Steps of OIM	Notation	Dimension	Value
Step 1.1 Linear elastic analysis (LA)			
<input type="checkbox"/> Axial force (in the equivalent point given in Step 2.4)	$N^I$	kN	114.0
<input type="checkbox"/> Bending moment (in the equivalent point given in Step 2.4)	$M^Iy$	kNm	15.59
Step 1.2 Linear buckling analysis (LBA)			
<input type="checkbox"/> Elastic critical load factor	$\alpha_{cr}$		2.380
<input type="checkbox"/> Amplitude of buckling shape (in the center of cross-section)	$v_{cr,max}$	mm	37.62
Step 2.1 Internal forces and moment due to buckling mode shape			
<input type="checkbox"/> Bending moment (in the equivalent point given in Step 2.4)	$M^{cr}_z$	kNm	13.07
<input type="checkbox"/> Bimoment (in the equivalent point given in Step 2.4)	$B^{cr}$	kNm <sup>2</sup>	1.580
Step 2.2 Cross-section utilization (in the equivalent point given in Step 2.4)			
<input type="checkbox"/> Due to bending around minor axis	$U_{cr,Mz}$	kNm	0.854
<input type="checkbox"/> Due to bimoment	$U_{cr,B}$	kNm <sup>2</sup>	0.702
<b>Step 2.3 Linear load multiplication factor (in the equivalent point)</b>	$\alpha_{sec,cr}$		<b>0.642</b>
Step 2.4 Location of the equivalent point (measured from the member end)	$ep$	mm	3000
Step 3.1 Buckling-active internal forces and moments			
<input type="checkbox"/> Axial force	$N^a(ep)$	kN	114.0
<input type="checkbox"/> Bending moment around the major axis	$M^ay(ep)$	kNm	15.59
Step 3.2 Classification of the buckling mode	<i>“Coupled FB and LTB”</i>		
Step 4 Equivalent length of the ERM	$L_{eq}$	mm	5995
Step 5 Equivalent imperfection factor for ERM			
<input type="checkbox"/> Slenderness for flexural buckling	$\lambda_z$		0.740
	$\lambda_{z,\theta}$		0.844
<input type="checkbox"/> Slenderness for lateral-torsional buckling	$\lambda_{LT}$		0.682
	$\lambda_{LT,\theta}$		0.778
<input type="checkbox"/> Imperfection coefficients	$\alpha_z$		0.550
	$\alpha_{LT}$		0.650
<input type="checkbox"/> Imperfection factor	$\eta_{N,\theta}$		0.464
	$\eta_{M,\theta}$		0.506
<input type="checkbox"/> Cross-sectional resistance multiplication factors	$\alpha_{sec,N}$		6.438
	$\alpha_{sec,M}$		5.503
	$\alpha_{sec,NM}$		2.976
<input type="checkbox"/> Modifying factor	$\mu$		0.954
<input type="checkbox"/> <b>Equivalent imperfection factor</b>	$\eta_{NM,\theta}$		<b>0.474</b>
Step 6 Buckling-active linear multiplication factor ( $\alpha_{sec,NM}$ in step 5)	$\alpha_{sec,a}$		2.976
Step 7.1 Equivalent scale factor	$\delta_{eq}$		0.263
<b>Step 7.2 Equivalent amplitude</b>	$\eta_{cr,eq}$	<b>mm</b>	<b>9.159</b>
Step 8.1 Internal forces and moments due to second order analysis with equivalent geometric imperfection (GNIA) in the critical point			
<input type="checkbox"/> axial compression	$N^{II}_{fi,Ed,\theta}$	kN	114.0
<input type="checkbox"/> bending moments	$M^{II}_{y,fi,Ed,\theta}$	kNm	16.35
	$M^{II}_{z,fi,Ed,\theta}$	kNm	3.775
<input type="checkbox"/> additional bending moments due to shifting of centroid	$\Delta M^{II}_{y,fi,Ed,\theta}$	kNm <sup>2</sup>	2.212
	$\Delta M^{II}_{z,fi,Ed,\theta}$	kNm	1.379
<input type="checkbox"/> bimoment	$B^{II}_{fi,Ed,\theta}$	kNm	0.392
<b>Step 8.2 Cross-section utilization in the critical cross-section</b>	$U^*$		<b>1.019</b>

\*The applied 'eff,new' cross-sectional properties:  $A=2600\text{mm}^2$ ;  $W_y=346646\text{mm}^3$ ;  $W_z=86298\text{mm}^3$ ;  $W_\omega=13.22\cdot 10^6\text{mm}^4$

Table 7: Comparing the buckling load factors computed with different methods

method	$\alpha_b$
<p>GMNIA (using Abaqus software)</p>  <p>According to Annex C of EN1993-1-5 for the geometrical imperfection a combination of global and local buckling modes were used. Amplitude for global mode was the <math>0.8 L/750</math> and for local imperfection was the <math>0.7-0.8</math> of <math>b/100</math>. (<math>L</math> is the member length, <math>b</math> is the flange width or web height depending which is the greater) ECCS welded I section residual stress model was used.</p>	1.000
EN1993-1-2 4.2.3.2	1.298
<b>Overall Imperfection Method (OIM)</b>	<b>1.019</b>

### Acknowledgments

This article was elaborated in the framework of project EFOP-3.6.1-16-2016-00017.

### References

- prEN 1993-1-1 (2019). Eurocode 3: Design of steel structures. Part 1.1: General rules and rules for buildings. CEN/TC 250/SC 3/WG 1 N 296.
- Chladný, E. and Štujberová, M. (2013). „Frames with unique global and local imperfection in the shape of the elastic buckling mode (Part1)”, *Stahlbau* 8, pp. 609-617.
- Agüero, A., Pallarés, F.J. and Pallares, L. (2015). „Equivalent geometric imperfection definition in steel structures sensitive to lateral torsional buckling due to bending moment”, *Engineering Structures* 96 (1), pp. 41-55.
- Papp, F. (2016). „Buckling assessment of steel members trough overall imperfection method”, *Engineering Structures* 106, pp. 124–136.
- Szalai, J.A. and Papp, F. (2019). „New stability design methodology through overall linear buckling analysis”, The 14th Nordic Steel Construction Conference, September 18–20, 2019, Copenhagen, Denmark, Ernst & Sohn Verlag für Architektur und technische Wissenschaften GmbH & Co. KG, Berlin · ce/papers.
- Papp, F., Szalai, J.A. and Movahedi R.M. (2019). „Out-of-plane buckling assessment of frames through overall stability design method”, The 14th Nordic Steel Construction Conference, September 18–20, 2019, Copenhagen, Denmark, Ernst & Sohn Verlag für Architektur und technische Wissenschaften GmbH & Co. KG, Berlin · ce/papers.
- Trahair, NS. (1993). „*Flexural-torsional buckling of structures*”, CRC Press.
- Szalai, J.A. (2017). “Complete generalization of the Ayrton-Perry formula for beam-column buckling problems”, *Engineering Structures* 153, pp. 205-223.
- Zhao, B., Oly, R., Morente, F., Vila Real, P., Wald, F., Franssen, JM. and Velda, P. (2014). “Fire design of steel members with welded and hot-rolled class 4 cross-sections”, Final Report of RFCS project FIDESC4, <https://www.researchgate.net/publication/274711521>.
- Couto, C., Vila Real, P., Lopes, N. and Zhao, B. (2014). “Effective width method to account for the local buckling of steel thin plates at elevated temperatures”, *Thin-Walled Structures* 84, pp. 134-149.
- Couto, C., Vila Real, P., Lopes, N., Zhao, B. (2015). “Resistance of steel cross-sections with local buckling at elevated temperatures”, *Journal of Constructional Steel Research* 109, pp. 101-114.

## Efficient application of the Reduced Stress Method for built-up I sections

Bálint Vaszilievits-Sömjén<sup>1</sup>

### Abstract

Reduced Stress Method is an alternative to the effective width method of EN 1993-1-1. Because of its built-in conservatism it is less used in practice for the design of building structures. The proposed new application reduces this conservatism. Reduction is obtained using the standard plate buckling curves where the plate slenderness is calculated with the help of linear buckling analysis. The buckling shape relevant to each plates of the cross-section is selected with a deformation energy-based buckling sensitivity analysis. The method is ready to be built into computer software which can handle shell finite elements and perform linear buckling analysis.

### 1. Introduction

The most often used Eurocode design approach for thin-walled sections made of plates subject to local buckling uses beams with effective cross sections. Effective cross section properties are calculated based on the normal stresses parallel to the length of the member, disregarding the presence of other stress components. Using the main Eurocode logic, effective cross section properties are calculated separately for the effect of the main internal force types as normal force, bi-axial bending moment and warping moment. For the last Eurocode doesn't require to calculate effective properties. When effective cross section properties are calculated it is assumed, that the cross-section is uniform and also the stresses remain constant along the length, there is no any stress gradient on the member. Additionally, it is also assumed, that the plates forming the section are connected to each other with hinges, therefore no any interaction between the individual plates of the cross section is assumed. The effective cross-section approach cannot consider the presence of openings in the section and also the handling of transverse stiffeners is not possible. The effect of transverse forces must be considered additionally.

In case the conditions for the application of effective cross sections are not met, the engineer can use plate elements instead of beams, but the evaluation of limit state requirements is difficult as only deformations and stress components are available as a result of analysis. A consistent design method using the results obtained from plate elements is not available at the moment for practicing engineers.

Eurocode EN 1993-1-5 includes a design method based on the use of plate members, called Reduced Stress Method. This method is mainly used for bridge structures, but not for usual building structures, mainly due to lack to software implementation and its conservatism. When the Reduced Stress Method is used for the design of beams with welded I sections, using slender webs, the obtained ultimate loads are generally much lower than the ones from a design based on the use of effective cross section properties. This is known, as the method estimates section resistances based on the buckling properties of the weakest plate of the cross section. Additionally, the method

---

<sup>1</sup> Senior Research Engineer, ConSteel Solutions Kft, <balint.vaszilievits@consteelsoftware.com>

described in Eurocode uses analytical formulas to calculate the critical stresses of the plates, assuming hinges along their connections.

## **2. Literature review**

Schafer (2008) proposed to use the minimum value from the signature curve, in the zone of wavelengths representing local buckling, found by finite strip method for cold-formed members, when the cross-section elastic local buckling stress is determined. This approach works well in practice for typical cold-formed sections but becomes conservative when the slenderness of plates of the cross-section are very different. Seif (2010) proposed formulas to calculate the full cross-section elastic stress for hot-rolled sections under pure compression or pure bending. Gardner (2019) proposed an improved elastic buckling stress for the full cross-section, for the combination of axial compression and bending. All these researchers aimed to provide a single elastic stress for the full cross-section, to be used with DSM or other methods.

EN 1993-1-3 recommends using the minimum local buckling stress of the cross section and use it to determine effective cross section properties. Brune (2000) proposed a method to calculate elastic critical stress for the individual plates, considering their interaction, in order to calculate effective cross section properties.

## **3. Description of the proposed method**

The goal of this practical method is to make possible an alternative modelling of a member besides the traditional use of beam finite element. In order to provide design evaluation the concept of the Reduced Stress Method will be followed.

As it has already been stated in the Introduction, for application where dominantly a beam-column like behaviour exists, the Reduced Stress Method is rather conservative. The proposed method aims to provide improvements, to provide results comparable to the results obtainable with the use of effective cross section properties for a beam element, but still keeps the additional advantages the shell representation can provide, over a beam representation.

This method at the present early stage of development concentrates on longitudinal normal stresses only (parallel to the axis of the beam representation), transverse normal and shear stresses are included but it is assumed, that they will not cause buckling phenomenon and therefore there will be no corresponding buckling factors used when the main evaluation formula of Reduced Stress Method is used. Additionally, it is assumed, that the vicinity of the analysed part of the structure is properly restrained against any kind of global stability failure and therefore only plate like local buckling modes are analysed at the moment. No longitudinal stiffeners are allowed at this stage. In other words, at this moment the aim is to provide results comparable to those obtained on beam elements when effective cross sections are used.

The proposed method implemented 2 improvements

- gives an assignment logic of the available buckling modes to each individual plate of the beam, based on plate sensitivity analysis
- gives a modelling technique using reduced thicknesses to successfully apply a modified verification formula of the Reduced Stress Method

### *3.1 Plate sensitivity analysis*

A welded I section consists of 3 plates – 2 flanges and a web. When linear buckling analysis is performed on the shell representation of the model, as a result many different buckling modes and eigenvalues will be obtained. Generally, it is difficult to decide which one to use to determine the slenderness of the given plate of the member. In order to facilitate the selection of the right buckling modes, the following sensitivity analysis based on strain energy is proposed:

- Step 1. once the shape of a buckling eigenmode is known after LBA, the corresponding strain energy can be calculated with the following formula Eq. 1:

$$E_{pi} = \frac{1}{2} \cdot \sum v^T \cdot K_s^n \cdot v \quad (1)$$

where  $E_{pi}$  is the summed strain energy of plate  $i$  forming the member,  $K_s^n$  is the first order stiffness matrix of the 'n'-th finite element of the actual plate and  $v$  is the vector of displacement at nodes of the same finite element, corresponding to the buckling shape with arbitrary scaling.

- Step 2. once the amount of the strain energy of the individual plates is known, a contribution indicator can be assigned to each plate with Eq. 2:

$$k_i = \frac{E_{pi}}{\max(E_{pi})} \quad (2)$$

this indicator will assign a value of 100% for the plate with the maximum energy contribution and a lower percentage for the other plates less exposed to the deformations of the given buckling shape.

The assignment of the given buckling shape to a plate with 100% contribution (called critical plate) is obvious, but the assignment to other plates with smaller indicator value is not too easy. As the shell model correctly assumes interaction between individual plates of the welded member, plates with higher slenderness will be stabilized by plates with lower slenderness or with lower compression stresses. These are the restraining plates. This sharing is the reason of the appearance of non-zero contribution indicators on restraining plates. Higher the value means a less neglectable consequence on the restraining plates. At the moment there is no mathematical explanation readily available for the definition of a limit value, but it seems reasonably safe to define it as 20%. This means that as a safety precaution, a buckling shape will not be assigned only to the critical plates but also to other restraining plate if its contribution indicator passes this limit value, even if there would be another buckling shape with a higher critical multiplier producing 100% indicator value on this plate. This limit assures that the plate slenderness will be calculated with a safe critical multiplier but taking benefit of the continuity of the plates and directly reflects the effect of the actual total stress distribution. In such case the result will be fully in line with the recommendations of EN 1993-1-3 on using the minimum value for all the compressed plates of the member. Assignment will be made only for plates of the cross section falling into Class 4 and subject to at least partial compression stresses.

### 3.2 Modelling technique using reduced thicknesses

The Eurocode implementation of the Reduced Stress Method results, that the stresses used for determination of resistance correspond to the pre-buckling stage, controlled by the part of the section most exposed to local buckling. This approach means that the resistance of a welded I section beam with Class 4 webs will be overall limited by this stress level lower than the yield stress, even if the compression flanges would belong to a lower Class 1-3.

To overcome this problem, a two-step iteration approach is proposed. In the first step a linear analysis and LBA is made completed, followed by the previously mentioned plate sensitivity analysis. Based on these results plate slenderness values are calculated for every Class 4 plate with at least partial compression stresses. Using the slenderness values the reduction factors are calculated in accordance with formulas (4.2) and (4.3) of EN 1993-1-5, but instead of using these reduction factors

directly to reduce the limit stress, they will be utilized to define an effective thickness for the given plate, using Eq. 3:

$$t_{eff} = \rho \cdot t \quad (3)$$

where  $\rho$  is the reduction factor from EN 1993-1-5 in function of plate slenderness and boundary conditions. The thickness reduction will be applied to the full length of this plate, even to parts under tension.

Once for each plate of the shell representation an appropriate thickness reduction has been assigned, a new linear elastic analysis is performed, with shell finite elements. This will result new membrane stresses which corresponds to the use of effective thicknesses and therefore will automatically contain the necessary effects caused by the shift of effective centroid, as required by Eurocode. As the effect of local buckling due to longitudinal membrane stresses has already been incorporated in the plate thickness, and as it has been said at the beginning of this paper, that it is assumed that other available stress components will not cause buckling, all the reduction factors can be eliminated from formula 10.5 of EN 1993-1-5. This results the following verification formula:

$$\left(\frac{\sigma_{x,Ed}}{f_y/\gamma_{M1}}\right)^2 + \left(\frac{\sigma_{z,Ed}}{f_y/\gamma_{M1}}\right)^2 - \left(\frac{\sigma_{x,Ed}}{f_y/\gamma_{M1}}\right) \cdot \left(\frac{\sigma_{z,Ed}}{f_y/\gamma_{M1}}\right) + 3 \cdot \left(\frac{\tau_{Ed}}{f_y/\gamma_{M1}}\right)^2 \leq 1 \quad (4)$$

where  $\sigma_{x,Ed}$  are the dominant longitudinal membrane stresses which have been indirectly increased and redistributed due to the use of reduced effective thickness and shift of effective centroid. Other stress components are calculated based on the original plate thickness.

## 4. Example

### 4.1 Beam-column under compression and strong axis bending moment

The method is demonstrated on a simple supported 5 meters long beam-column with forked supports. The member has a double symmetric welded I section, The total height of the section is 1000 mm and the flanges are 350 mm wide. Steel grade is S355.

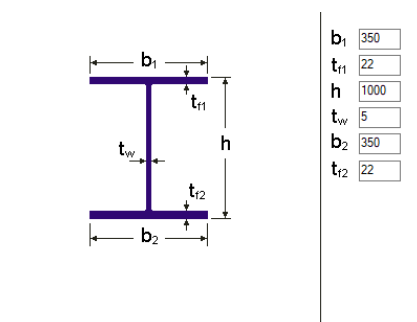


Figure 1: Cross-section of the welded member

The beam follows the usual practice, the web is much slender than the flange and falls into a cross section Class 4 under combined stresses. The flanges are of Class 1-2. To comply with this, the web thickness was taken as 5 mm and the flange thickness as 22 mm.

The gross area of the section is 20180 mm<sup>2</sup>.

As the focus of this paper is not on the effects of global buckling, the beam is assumed to be laterally restrained against displacement at the intersection of the web with the flanges, along its full length.

5 load cases with a combination of different levels of compression force and bending moment are considered.

1. Pure compression ( $\psi = 1$ ):
2. Compression with a strong axis bending moment causing higher compression in the upper flange and resulting a stress gradient ( $\psi = 0,5$ ): in the web
3. Compression with a strong axis bending moment causing compression in the upper flange only and resulting a stress gradient ( $\psi = 0$ ): in the web. Axial stress in the bottom flange is zero.
4. Compression with a strong axis bending moment causing compression in the upper flange and tension in the bottom flange and resulting a stress gradient ( $\psi = -0.5$ ): in the web
5. Pure strong axis bending moment case ( $\psi = -1$ ).

The ultimate compression force resistances for each load case are calculated using the following different approaches:

- A. use a beam element and use effective cross-sections, according to EN 1993-1-1, EN 1993-1-5
- B. use shell elements and use the reduced stress method according to EN 1993-1-5, but the critical local buckling stress of the whole cross-section is calculated with finite strip method, assuming connection of the plates of the cross-section
- C. GMNIA design verification using shell elements, considered as the reference for ultimate load level
- D. use the proposed modified application of the Reduced Stress method, with plate sensitivity analysis and reduced thicknesses

Detailed calculation steps are presented for the pure compression load case.

A: use of effective cross section, according to EN 1993-1-1, EN 1993-1-5

Table 1: Plate classification

Plates	Section class
Flanges	2
Web	4

Relative slenderness of the internal Class 4 compressed web is 4.14 resulting a reduction factor of 0.2288 using formula 4.3 of EN 1993-1-5. As the flanges are of Class 2, no reduction is necessary. The resulting effective cross section's area is  $A_{eff} = 16494 \text{ mm}^2$ , and the compression resistance is  $N_{c,Rd} = 16494 * 355 / 1.0 = 5855 \text{ kN}$ .

B: reduced stress method with the use of finite strip method

The results of codified Reduced Stress method can be slightly improved by replacing analytical stress values with a finite strip analysis. The local buckling region of the signature curve is shown on Figure 2. The buckling half-wavelength at the minimum point is 650 mm and the corresponding critical load multiplier  $\alpha_{cr}$  is 0.097, under the application of a membrane stress equal to the yield strength of 355  $\text{N/mm}^2$

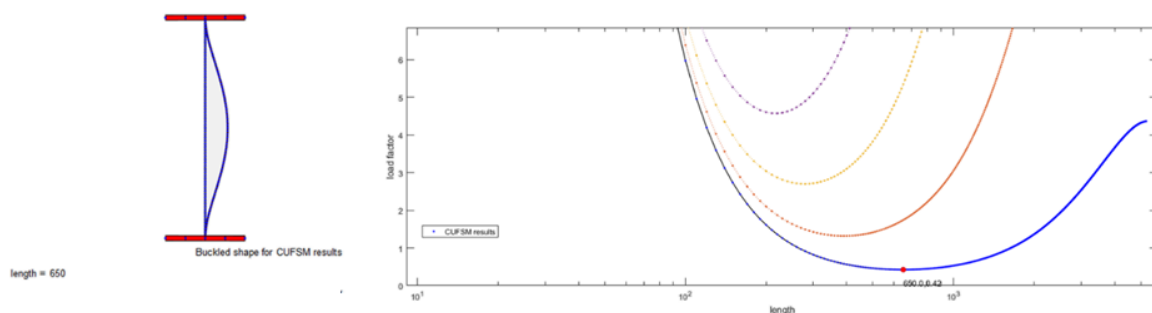


Figure 2: Signature curve obtained with finite strip analysis

The obtained critical stress is equal to  $355 * 0.097 = 34.44 \text{ N/mm}^2$ . The resistance based on this calculation is  $N_{c,Rd} = 0.29 * 20180 * 355 = 2077.5 \text{ kN}$ , with intermediate results of 3.21 for web slenderness and corresponding 0.29 reduction factor.

#### C: GMNIA design verification using Consteel research version

This approach is considered as the reference calculation, based on EN 1993-1-5 Annex C. The model used for the analysis has the following characteristics:

- 4 node shell finite elements are used with a maximum mesh size of 50 mm.
- The material model is elastic-plastic with a nominal plateau slope, according to EN 1993-1-5 C.6(2).
- The nodes at the extremities are constrained into master nodes which are supported by usual fork supports.
- As imperfection the first buckling mode (local buckling) of LBA is used with a scaling of  $h_w/200 = 4.89 \text{ mm}$ .
- No residual stresses are considered.
- A load equal to 10% of the resistance value of determined based on the effective cross-section is applied initially and increased until the plateau of load-displacement diagram is found.

The obtained resistance value was found as 5982.02 kN. The corresponding deformed geometry and stress distribution at the failure load level is shown on Figure.3:

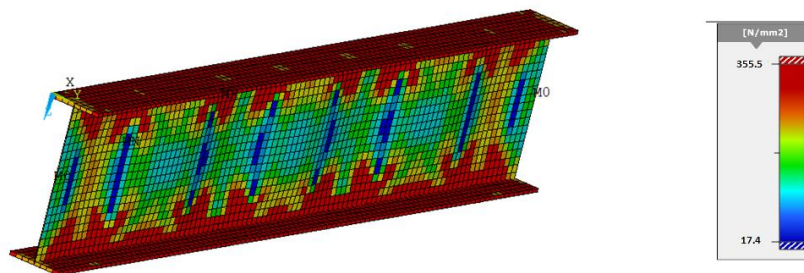


Figure 3: Stress distribution at ultimate load level

#### D: Proposed application of Reduced Stress Method with the commercial version of Consteel

The 2 round calculation was performed with Consteel, using its standard triangular shell elements. The material model is fully linear elastic. The nodes at the extremities are supported the same way as for the GMNIA analysis, by usual fork supports. An initial trial compression load of 1000 kN is applied in one single step and first an LBA is performed. Up to 10 buckling shapes with corresponding eigenvalues are calculated.

The applicable modes for the different plated is chosen based on the presented plate sensitivity analysis. The calculated contribution indicators for the first buckling shape (see Figure 4) are the followings (Table 2):

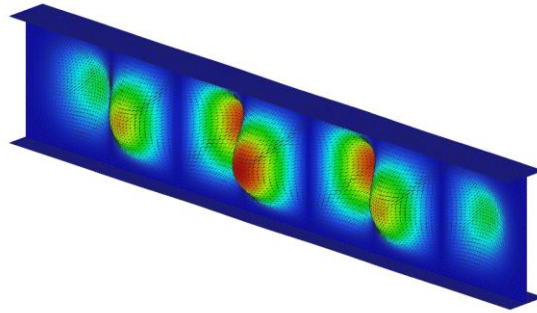


Figure 4: First buckling shape from LBA with Consteel shell elements, with  $\alpha_{cr} = 0.71$

Table 2: Results of plate sensitivity analysis

Plate	$k_i$
Upper flange	0
Web	100%
Lower flange	0

These results mean that the first buckling mode shall be uniquely assigned to the web plate, as the contribution indicators have a value of 0.0 at the flanges and 100% at the web. It means that the restraining elements (the flanges) are fully effectively restraining the web, without any need for assigning as a safety this low buckling shape also for the flanges. There was no buckling mode found within the first 10 modes which would have a contribution indicator value above the limit assumed as 20%, therefore no buckling shape will be assigned for the flanges.

As the result of the first LBA analysis, the elastic critical stress to be considered for the web is 71% of the membrane stress obtained from the test load of 1000 kN with the original thicknesses,  $0.71 * 49.55 = 35.18 \text{ N/mm}^2$  (same as obtained with finite strip analysis) which will be used to calculate a reduced thickness, instead of a reduced limit stress. No reduction of the flange thicknesses will be necessary.

Table 3: Reduced thicknesses to consider the effect of local buckling

Plates	Reduced thickness
Flanges	$1.0 * 22 = 22 \text{ mm}$
Web	$0.29 * 5 = 1.45 \text{ mm}$

The second analysis with the modified thicknesses is a simple stress calculation with linear material model, resulting the necessary membrane stresses for the final verification with formula (4). As a consequence of the reduced gross area of the member, the membrane stresses will increase in all of the elements.

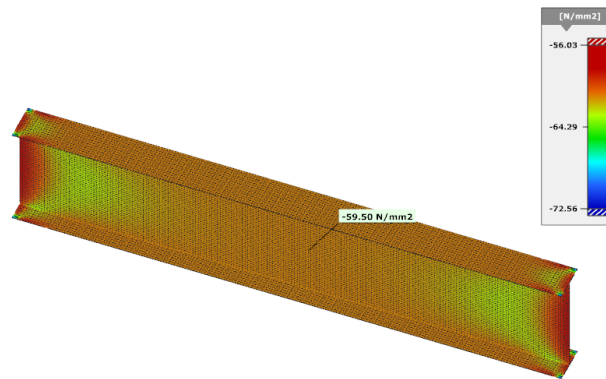


Figure 5: Membrane stresses obtained from a trial load of 1000 kN on the model with reduced thicknesses

These stresses include indirectly the effect of the local buckling identified on the web and as a consequence there is no need for a second reduction. As we have a linear analysis, the resistance can be directly calculated using formula (4),  $N_{c,Rd} = 1000 * 355 / 59.50 = 5966.4$  kN.

#### 4.2 Evaluation of the results

The results of all 5 load cases are shown on Figure 6. The vertical axis shows the compression force resistance, and the horizontal axis shows strong axis bending moment resistance. The **dark blue line** with the lowest resistances corresponds to calculation "B", with the Reduced Stress method, and the **light blue line** with the highest values corresponds to the GMNIA results (calculation "C"), considered as reference value. The **orange line** corresponds to the resistances obtained with a beam element using effective cross-section properties (Calculation "A") and finally the line shown with **green** colour corresponds to the proposed improved Reduced Stress Method (Calculation "D"), using the naming convention introduced on Page 5.

As it can be seen, this last line almost perfectly fits to the most traditionally expected results obtained with beam representation, used in everyday practice by engineers. In the range of pure bending the obtained resistances are a bit higher, but still below the GMNIA results.

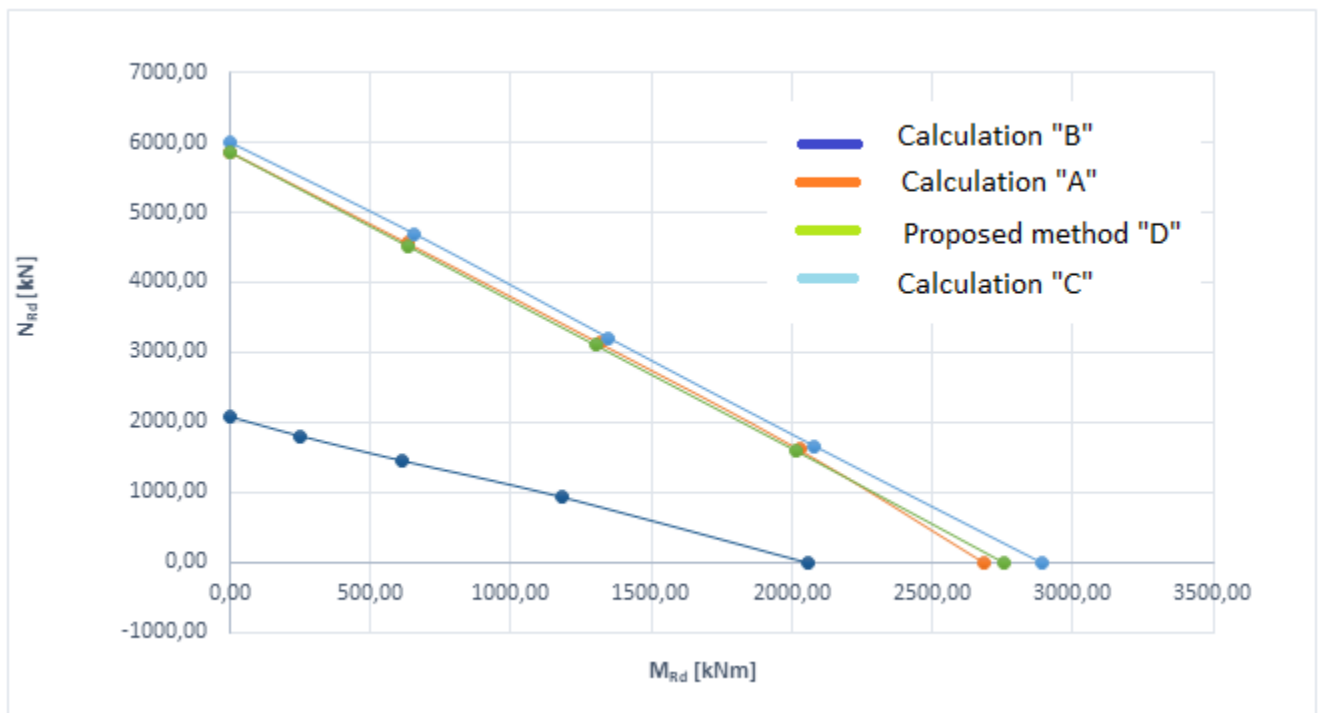


Figure 6: Envelope  $N_{Rd}$ ,  $M_{Rd}$  resistance values of 5 load cases, explanation for calculation modes see on Page 5

#### 4. Conclusions

Based on the presented example this improved approach has the potential to eliminate the conservatism of the codified version of Reduced Stress method and allows to implement a design verification in computer programs, based on shell elements, as an alternative, when the traditional approach with beam finite elements is not applicable.

#### Acknowledgments

This research has been realized within the CFSExpert project number EUROSTARS-2019-E!113493-CFSExpert funded by Eurostars.

#### References

- B. W. Schafer. (2008). "Review: The Direct Strength Method of cold-formed steel member design." *Journal of Constructional Steel Research*, 64:766-778.
- M. Seif and B. W. Schafer. (2010). "Local buckling of structural steel shapes." *Journal of Constructional Steel Research*, 66(10):1232-1247.
- Brune, B.: (2000). "Stabilitätsprobleme von Stahlbauteilen mit dünnwandigen, ebenen Blechen." Habilitationsschrift, TU Dortmund, Lehrstuhl für Stahlbau
- L. Gardner, A. Fieber, L. Macorini (2019). "Formulae for calculating elastic local buckling stresses of full structural cross sections" *Structures* Volume 17, Pages 2-20.
- CEN (2006). "Eurocode 3: Design of steel structures. Part 1-1: General rules and rules for buildings"
- CEN (2006). "Eurocode 3 - Design of steel structures - Part 1-3: General rules - Supplementary rules for cold-formed members and sheeting"
- CEN (2006). "Eurocode 3: Design of steel structures. Part 1-5: Plated structural elements"
- CUFMS Finite strip analysis software, <https://www.ce.jhu.edu/cufsm/>
- Consteel 14 finite element analysis and design software. [www.consteelsoftware.com](http://www.consteelsoftware.com)

## Design proposal for bolted angle members in compression

Markus Kettler<sup>1</sup>, Harald Unterweger<sup>2</sup>

### Abstract

The type and size of the rotational restraints at the gusset plates near the member's ends (provided by the adjacent structure) are crucial for the prediction of the compression member capacity of bolted angles. This was highlighted by the authors by means of experimental and numerical investigations in the past. Due to the eccentric connection on only one leg, additional bending moments are acting on the member, leading to a complex load carrying behaviour with flexural and/or lateral torsional buckling phenomena.

Detailed analytical models for the estimation of appropriate spring stiffness values have been developed for several practical applications in buildings and two-bolt connections at both member's ends. The investigated connection details comprise a simply fixed gusset plate (e.g. as attachment to concrete walls), a joint to the flange of an I-shaped section and a joint to the web of an I-shaped section via a gusset plate. Based on that, a design model was developed for bolted angle members with rotational spring restraints at both member's ends and an eccentric compression loading  $N$ , in order to calculate the compression capacity  $N_R$ .

Within this paper, the proposed design procedure is presented. Moreover, the thereby determined resistances  $N_{R,model}$  are compared with the results of sophisticated 3D finite element calculations  $N_{R,FEM}$  that consider the actual boundary conditions and the eccentric load introduction as well as equivalent geometric imperfections. The finite element model has preliminarily been calibrated on the experimental test results. The comparison indicates that the resistances based on the proposed design procedure are slightly conservative compared to the real behaviour of the angle member. In addition, the large increase in capacity (compared to the simply supported reference case) is highlighted. Therefore, it is concluded that the new design proposal is able to predict the compression member capacity of bolted angles safely and economically.

### 1. Introduction

The numerical investigations in *Kettler et al. (2017)* as well as the experimental results in *Trahair et al. (1969)* and *Kettler et al. (2019a)* highlighted the significant influence of different boundary conditions on the compression member capacity of bolted single steel angles. Fig. 1 exemplarily shows the ultimate compression member capacity  $N_R$ , related to the plastic section capacity of the angle section  $N_{pl} = A \cdot f_y$  for a hot-rolled angle section L 80/8 with 2-bolt connections on both ends. It is noted that all results are based on the relative slenderness  $\bar{\lambda}_v$  about the minimum axis  $v$ , calculated with the member length  $L$ . Results for member tests and also for numerical FEM-calculations are shown, indicating the huge band

<sup>1</sup> Assistant Professor, Graz University of Technology, <kettler@tugraz.at>

<sup>2</sup> Professor, Graz University of Technology, <h.unterweger@tugraz.at>

width of load carrying capacity. The investigated boundary conditions are: BC1 = fully rigid, BC2 = knife edge support, BC3 = fully hinged.

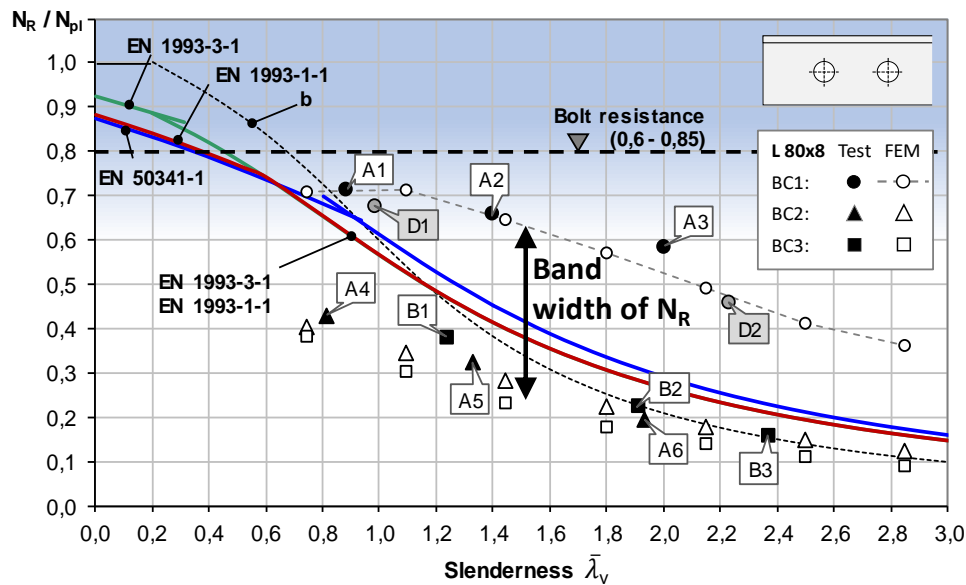


Figure 1: Compression member capacity of bolted angle member L80/8 with 2-bolt joints – huge band width for borderline cases of joint stiffness (BC1 = fully rigid, BC2 = knife edge support, BC3 = fully hinged)

Additionally, the corresponding resistance predictions according to current European design standards (EN 1993-3-1 and EN 50341-1 for masts and EN 1993-1-1 for buildings) are plotted. The comparison of results reveals that the different code procedures result in approximately the same resistances for angle sections with at least two bolts in the connected leg at both members ends. However, the actual type and size of the rotational restraints at the gusset plates near the member's ends (provided by the adjacent structure) are not considered in these design procedures. This fact can lead to unsafe results for boundary conditions BC 2 and BC 3 and produces uneconomic results for BC 1.

The significant influence of the joint stiffness, as shown in Fig. 1 for a L 80/8 section, holds also for other angle sections and was motivation for the authors to develop a new design model for the calculation of the compression member capacity  $N_R$  of bolted steel angles that takes into account the actual restraints at the members ends. Similar models have also been presented in *Usami et al. (1971)* and *Schneider (2003)*, but the major drawback of these previous proposals was that no reliable parameters for realistic end restraints were available. The main focus of the current research is on angles in buildings. Therefore, two bolts at each members end are considered as the reference case for the new design procedure and the formulae for the stiffness parameters are derived for that case.

In section 2, this new design model is presented in detail. The background of the development and validation of this new design model is shown in section 3. Finally, section 4 summarises the influence of this new design concept on design practice.

## 2. New design model for compression member capacity of bolted steel angles

Fig. 2 summarises all the details of the new design model with 2-bolt connections on both ends. The design model allows to calculate the internal forces based on second order theory for an individual member (1D-model, with bending stiffness about main axes  $u$  and  $v$  and torsion stiffness) with eccentricities ( $e_y$ ,  $e_z$ ) and spring stiffness ( $c_{\varphi,in}$ ,  $c_{\varphi,out}$  based on Fig.3) at both ends. In addition, an equivalent bow imperfection, with amplitude  $e_{0,u} = L/300$ , about the minimum axis should be taken into

account. Fig. 3 presents formulae for the rotational stiffness of several joint types, that are currently covered by the new design model. Additional practical joint types are under development. The accurate length  $L$  is also given in Fig. 3.

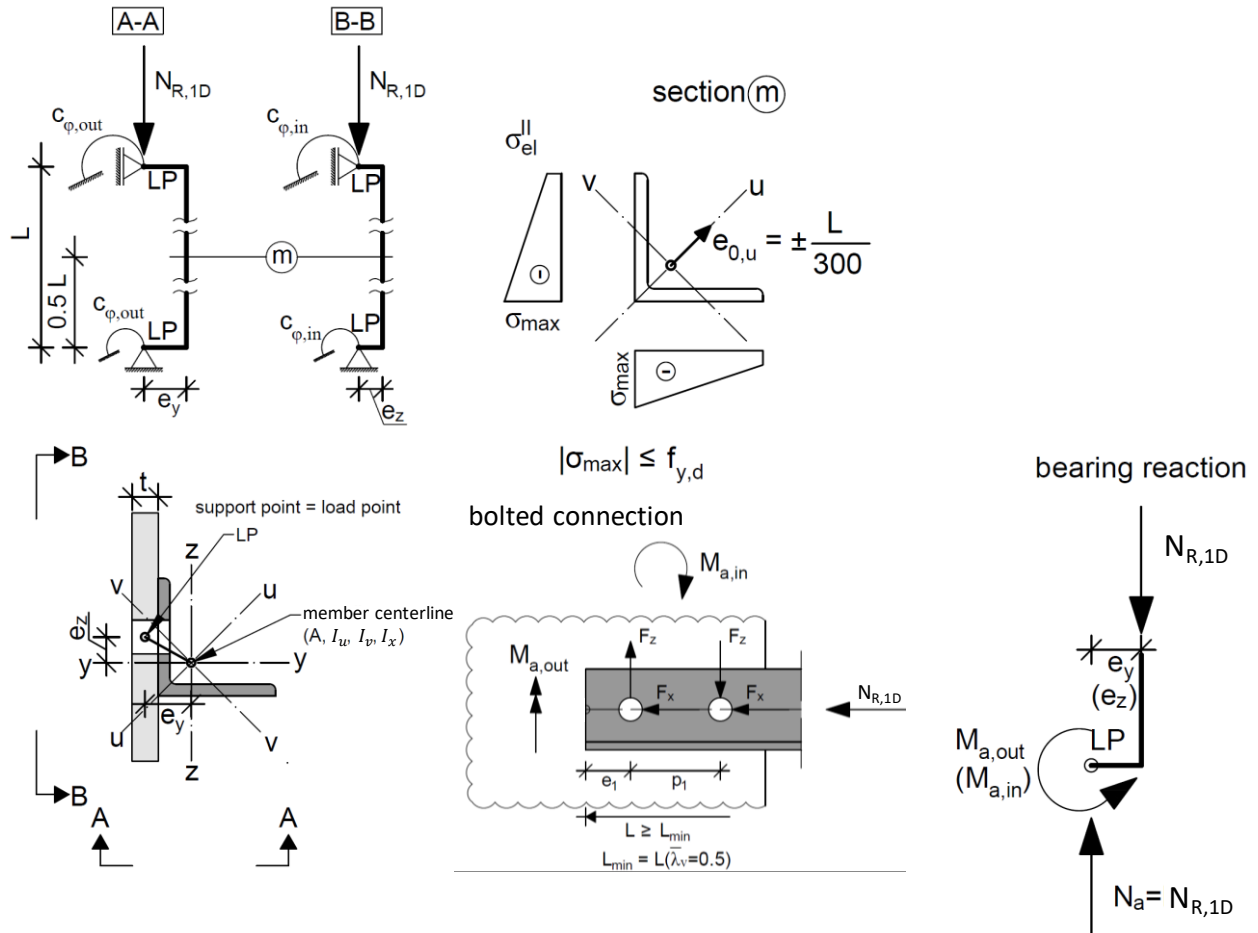


Figure 2: New design model for calculating the compression capacity  $N_{R,1D}$  of a bolted angle member  
(Note: the final compression capacity is  $N_{Rd} = N_{R,1D} \cdot f_{Di}$ )

The compression member capacity  $N_{R,1D}$  is reached, if the elastic section capacity of the angle member is fully utilized. This leads to an iterative procedure. The vertical load  $N$  at the load point is increased, until the maximum normal stresses at the critical section (generally at midspan) are equal to the yield strength (design value  $f_{y,d}$ ).

For better accuracy of the new design model, additional calibration factors  $f_{Di}$ , different for each studied joint type and summarized in Eqs. (2)-(4), are proposed to get the final compression member capacity  $N_{Rd}$  based on Eq. (1). The background for the calibration factors  $f_{Di}$  will be shown in section 3.

$$N_{Rd} = N_{R,1D} \cdot f_{Di} \quad (1)$$

Detail 1 - fixed gusset plate connection:

$$f_{D1} = 0.96 - 0.036 \cdot \bar{\lambda}_v \leq 0.93 \quad (2)$$

Detail 2: girder flange connection:

$$f_{D2} = 1.41 - 0.28 \cdot \bar{\lambda}_v + 0.045 \cdot \bar{\lambda}_v^2 \leq 1.21 \quad (3)$$

Detail 3: girder web connection:

$$f_{D3} = 1.2 - 0.11 \cdot \bar{\lambda}_v \leq 1.11 \quad (4)$$

Detail		$c_{\varphi i,in}$		
		$c_{\varphi i,out}$		
1a	$h_{eff} = \min \left[ 4 \cdot (x + e_1) \right]$ $h_{eff} = \min \left[ \frac{a + b + c}{2 \cdot (a + b)} \right]$	$c_{\varphi 1,in} = \infty$		
1b	$h_{eff} = \min \left[ a + b + c, 2 \cdot (a + b) \right]$ <p>limitation: h/b ≥ 1.50 x ≤ 60 mm</p>	$c_{\varphi 1,out} = \frac{E \cdot h_{eff} \cdot t^3}{4 \cdot (3x + y)}$		
2		$c_{\varphi 2,in} = \frac{12EI_{z,fl}}{L_g} = \frac{6EI_z}{L_g}$		
		$c_{\varphi 2,out,loc} = \frac{0.513 \cdot t_w^{1.75} \cdot t_f^{1.25} \cdot b_f^{0.5}}{h_w^{0.5}}$ $c_{\varphi 2,out,glob} = \frac{1}{\frac{L_g}{4 \cdot GI_T} \cdot \left(1 - \frac{\tanh \varepsilon_T}{\varepsilon_T}\right)}$	$c_{\varphi 2,out} = \frac{1}{\frac{1}{c_{\varphi 2,out,loc}} + \frac{1}{c_{\varphi 2,out,glob}}}$	
3		$c_{\varphi 3,in,loc} = \frac{K \cdot \pi^3 \cdot h}{h_w \cdot \sin^2 \left( \frac{\pi \cdot u}{h_w} \right)}$ $c_{\varphi 3,in,glob} = \frac{12 \cdot EI_z}{L_g}$	$c_{\varphi 3,in} = \frac{1}{\frac{1}{c_{\varphi 3,in,loc}} + \frac{1}{c_{\varphi 3,in,glob}}}$	
		$c_{\varphi 3,out,web} = \frac{70 \cdot E \cdot t_w^{1.6}}{h_w^{0.25}} \cdot K_{web}$ $c_{\varphi 3,out,glob} = c_{\varphi 2,out,glob}$	$c_{\varphi 3,out} = \frac{1}{\frac{1}{c_{\varphi 1,out}} + \frac{1}{c_{\varphi 2,out,glob}} + \frac{1}{c_{\varphi 3,out,web}}}$	
<p>parameters: <math>\varepsilon_T = \sqrt{\frac{I_T}{2.6 \cdot I_\omega}} \cdot \frac{L_g}{2}</math>      <math>K = \frac{E \cdot t_w^3}{12 \cdot (1 - \nu^2)}</math>      <math>K_{web} = \frac{1}{4 \cdot \left(1 - 3 \frac{u}{h_w} + 3 \left(\frac{u}{h_w}\right)^2\right)}</math></p> <p>where: <math>L_g</math> girder length      <math>I_T, I_\omega, I_z</math> torsional, warping and bending stiffness of girder  <math>G</math> shear modulus      <math>\nu</math> Poisson's ratio for steel (<math>\nu = 0.3</math>)</p>				

Figure 3: Summary of spring-stiffness formulae  $c_{\varphi,i,in}$  and  $c_{\varphi,i,out}$  for the investigated details 1-3

The following requirements have to be fulfilled for the application of the presented design procedure:

i. Since local buckling of the angle member is not explicitly included in the design model, the investigated angle section should fulfil the requirements for class 3 sections according to EN 1993-1-1; For thin-walled angles, reference is given to *Dinis et al. (2015)*.

ii. The minimum bolt distances  $e_1$  (end distance from the centre of the fastener hole to the adjacent end of any part, measured in the direction of load transfer) and  $p_1$  (spacing between centres of fasteners in a line in the direction of force transfer) should meet the following criteria:  $e_1 \geq 2.5d_0$  and  $p_1 \geq 3.0d_0$ , where  $d_0$  is the clearance of the bolt hole. For smaller values  $e_1$  and  $p_1$ , no FEM-calculations for validation of the new design model were done. Additionally, the geometric minimum/maximum values in Fig. 3 have to be considered.

iii. The minimum and maximum member length  $L$  is based on the minimum and maximum relative slenderness of the angle section about the minimum axis, with  $\bar{\lambda}_{v,min} = 0.5$  and  $\bar{\lambda}_{v,max} = 2.8$ . For cases with smaller slenderness values than  $\bar{\lambda}_{v,min}$ , the member capacity should be calculated with the minimum length  $L_{min}$  based on  $\bar{\lambda}_{v,min}$ . The background of this additional rule is based on the investigated parameter range of the conducted FEM-calculations for calibration of the model, presented in section 3.

The new design procedure is also applicable, if at the joint an additional tension member – on the same or on the opposite side of the gusset plate – is situated.

In the case of 1-bolt joints, the spring stiffness  $c_\phi$  from Fig. 3 is not applicable. In *Kettler et al. (2019a)*, it was observed that also fully preloaded single bolts of steel grade 10.9 act like a pin for the member. Therefore, for 1-bolt joints, the new model in Fig. 2 should be used without any rotational restraints at both ends ( $c_{\phi,in} = c_{\phi,out} = 0$ ), but with both eccentricities ( $e_y$  and  $e_z$ ).

It is assumed that the new model also works for the case of unequal angle members with two bolts on the longer angle leg, but this was not verified by additional FEM-calculations. A bolted connection on the shorter angle leg should be avoided, due to small member capacity, see *Reininghaus et al. (2005)*.

### 3. Background and validation of the new design model

To calibrate and validate the new design model, three individual steps for numerical FEM-calculations on 3D-models, including the angle member and the individual joint type, were necessary:

Step 1: FEM-calculations for the member tests with borderline cases for joint stiffness (BC1 = fully rigid, BC2 = knife edge support, BC3 = fully hinged). The comprehensive FEM-study in *Kettler et al. (2019b)* shows that an equivalent geometric imperfection of  $e_0 = L/300$ , without any residual stresses, leads to safe sided results (mean value  $N_{FEM}/N_{test}=0.96$ ). Additional calculations with residual stress patterns according to *ECCS TC8 Stability (1976)* showed that the influence of residual stresses on the member capacity is negligible for the conducted experimental tests. It is noted that the suggested imperfection amplitude  $e_0 = L/300$  in the new design model is not in contradiction to the value of  $e_0 = L/200$  in *Schillo et al. (2015)*, because the latter one is based on pinned ends, without any eccentricity at the member ends.

Step 2: FEM-calculations for joints in practice, shown in Fig. 3 and determination of elastic joint stiffness ( $c_{\phi,in}$  and  $c_{\phi,out}$ ). Within these calculations, the angle member was modelled as rigid, because the bending stiffness of the angle member is part of the design model – also in the joint region.

Step 3: FEM-calculations to determine the compression member capacity  $N_{FEM}$  of individual cases of bolted angle members with 2-bolt connections and specific joint types with consideration of the equivalent bow imperfection  $e_{0,u}$ . These results are compared with the results of the new design procedure in the following.

The FEM-calculations were done on 3D-models with the software ABAQUS. In the region of the joints, the angle member as well as the adjacent structure (gusset plate or girder flange) were modelled by solid elements (type C3D8R). For the inner part of the angle member, shell elements were used (type S4R), ignoring the fillets in the corner and at the leg tips. The bolts were also modelled by solid elements and the pre-stressing force was applied as a preload, considering hard contact and a coefficient of friction of  $\mu = 0.25$ . Near the bolt holes, linear elastic behaviour was assumed, to prevent local yielding. Overall, the material behaviour was assumed as linear elastic – ideal plastic ( $E=210\,000\text{ N/mm}^2$ ,  $\nu=0.30$ ) without any safety factors ( $f_y = 235\text{ N/mm}^2$  for S235).

Fig. 4 presents a comparison of the results of the new design model ( $N_{R,1D}$ ) with the results of the FEM-model ( $N_{FEM}$ ) for individual member configurations (in total 36 cases) with fixed gusset plate connections (detail 1a). Three different angle members (L60/6, 90/9, 120/12) are presented, with three different relative slenderness values ( $\bar{\lambda}_v = 0.8; 1.8; 2.8$ ). Different geometries of the gusset plate are studied, with variation of the thickness  $t$  (10 or 20 mm) and the height  $h$  (150 or 400 mm). The length of the gusset plate is different for each angle type, because of different bolt diameters (M16, M24, M27), but similar bolt distances  $e_1/d_0$  and  $p_1/d_0$  are used. In order to ensure conservative results, the calibration factor  $f_{D1}$  in Eq. (2) is suggested. The slightly unsafe prediction with the design model for case 20/150/2.8 for angle type 120/12 is avoided with the additional requirement of  $h/b \geq 1.50$  (see Fig. 3).

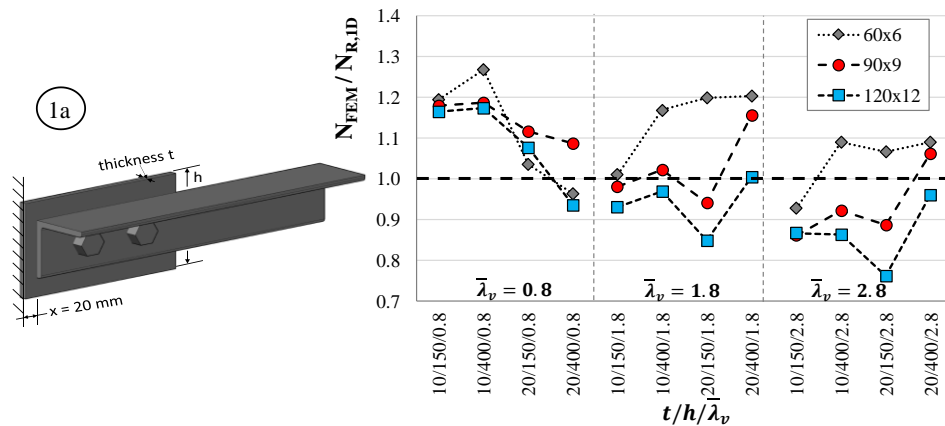


Figure 4: Calibration of the design model for detail 1a

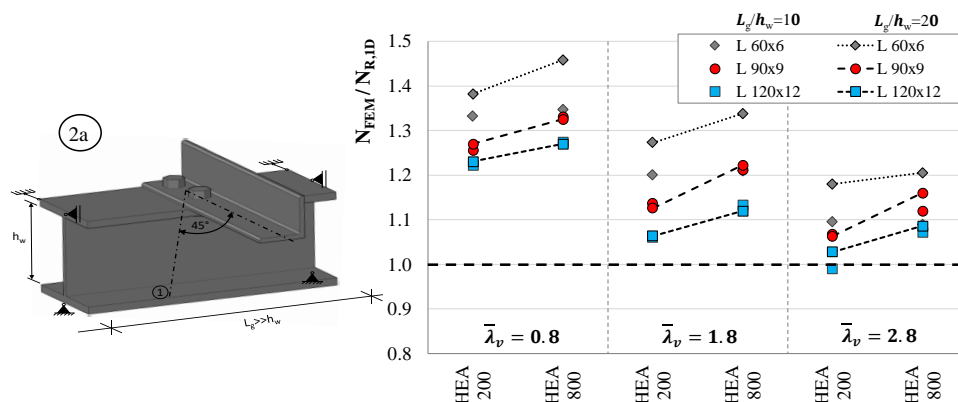


Figure 5: Calibration of the design model for detail 2a

Fig. 5 and Fig. 6 present the comparison of member capacities ( $N_{FEM}/N_{R,1D}$ ) for the investigated details 2a and 3a, respectively (both with the member axis perpendicular to the girder axis). Again the same angle types (L 60/6; L 90/9; L 120/12) and relative slenderness values ( $\bar{\lambda}_v = 0.8; 1.8; 2.8$ ) are studied.

Additionally, two very different girder types are investigated (HEA 200, HEA 800 for detail 2a and HEA 600, HEA 1000 for detail 3a) with two different support ratios ( $L_g/h_w = 10; 20$ ). The results for details 2a and 3a indicate a significant influence of the relative slenderness  $\bar{\lambda}_v$  on the accuracy of the new design model. In order to achieve more economic results with the new design procedure, the calibration factors  $f_{D2}$  and  $f_{D3}$  based on Eqs. (3) and (4) are suggested.

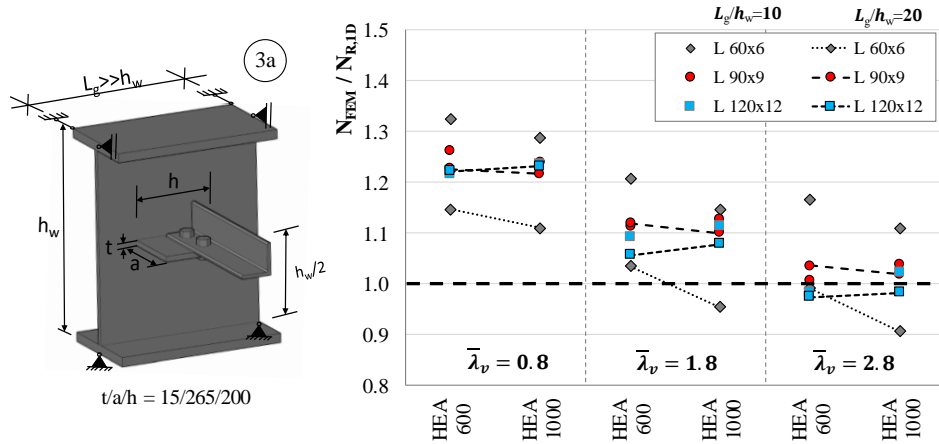


Figure 6: Calibration of the design model for detail 3a

#### 4. Conclusions and impact on design practice

Summarising, Figs. 7-9 present a comparison of the compression member capacities  $N_{FEM}$  for connection types 1a, 2a and 3a with the resistances according to EN 1993-1-1. Additionally, buckling curve b is plotted as a reference for a pinned angle member, without any eccentricity at both member ends. The comparison of the FEM results with the also plotted curve for the pin-ended case ( $C_{\phi,in} = C_{\phi,out} = 0$ ) with load eccentricity highlight that the rotational restraints from all investigated structural details significantly increase the compression capacity of the angle members.

The presented results also indicate the following trend: For a relative slenderness  $\bar{\lambda}_v < 1.0$ , the consideration of the real joint stiffness leads to a reduction of the member capacity for the investigated structural details, in comparison to the current Eurocode design procedure. On the other hand, for higher slenderness values ( $\bar{\lambda}_v > 1.0$ ), also higher member capacities  $N_R$  are available than predicted by EN 1993-1-1. The herein presented new design procedure for bolted angle members in compression is able to accurately represent this effect by additionally taking into account the effect of rotational restraints at the member's ends provided by the adjacent structure.

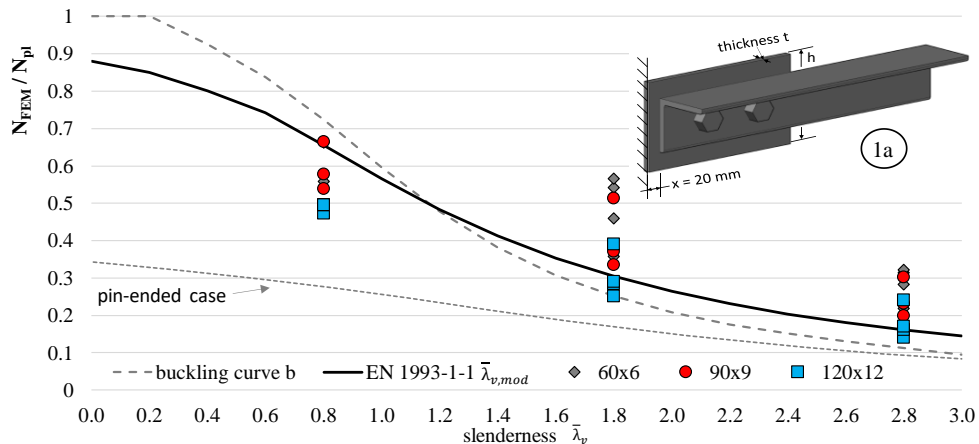


Figure 7: Comparison of compression member capacity for detail 1a

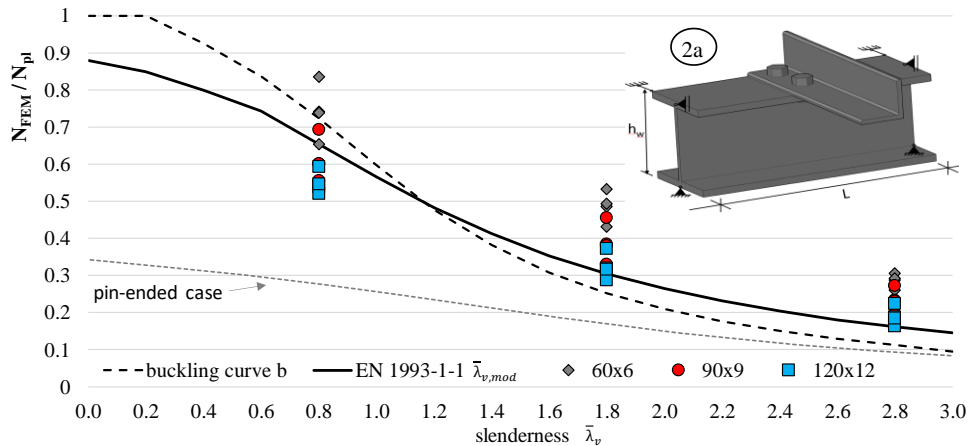


Figure 8: Comparison of compression member capacity for detail 2a

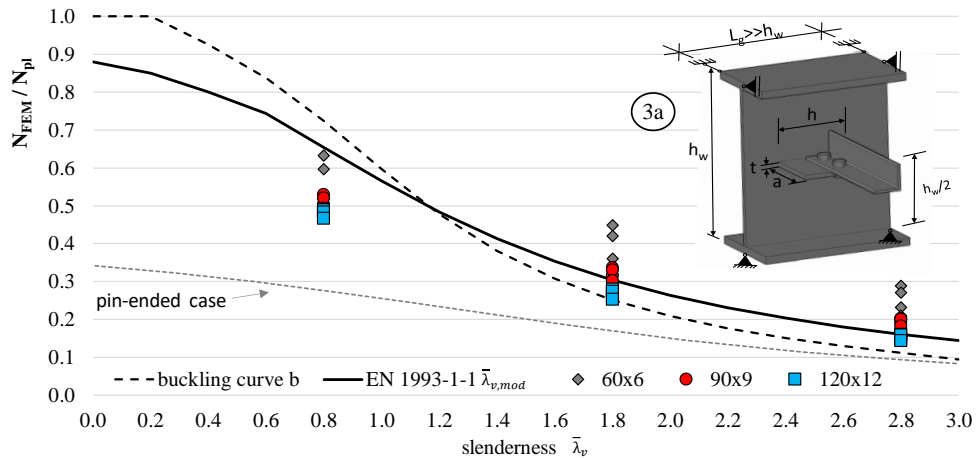


Figure 9: Comparison of compression member capacity for detail 3a

## References

- ECCS TC8 Stability (1976) "Manual on stability of steel structures", No 22.
- Dinis, P.B., Camotim, D. (2015) "A novel DSM-based approach for the rational design of fixed-ended and pin-ended short-to-intermediate thin-walled angle columns", *Thin-Walled Structures*, 87, 158-182.
- Kettler M., Taras A., Unterweger H. (2017) "Member capacity of bolted steel angles in compression – Influence of realistic end supports", *Journal of constructional steel research*, 130, 22-35.
- Kettler M., Lichtl G., Unterweger H. (2019a) "Experimental tests on bolted steel angles in compression with varying end supports", *Journal of constructional steel research*, 155, 301-315.
- Kettler M., Unterweger H., Harringer T. (2019b) "Appropriate spring stiffness models for the end supports of bolted angle compression members", *Steel Construction*, 4 (12), 291-298.
- Reininghaus M., Skottke M. (2005), "Druckbeanspruchte Winkelprofile mit Ein-Schrauben-Anschluss", *Stahlbau*, 74 (7), 534-538.
- Schillo N., Feldmann M. (2015), "Zur Stabilität von Winkelprofilen im Vergleich der Normen des Mast-, Turm- und Freileitungsbaus", *Stahlbau*, 84 (12), 946-954.
- Schneider R. W. (2003) "Beitrag zur Bemessung von druckbeanspruchten Einzelwinkeln unter Berücksichtigung der Ansehlusseigenschaften", *Dissertation RWTH Aachen*, Shaker Verlag (48).
- Trahair, N.S., Usami, T., Galambos, T.V. (1969) "Eccentrically loaded single-angle columns", Research Report, No. 11, Civil and Environmental Engineering Department, Washington University, St. Louis, MO.
- Usami, T., Galambos, T.V. (1971) "Eccentrically loaded single angle columns", IABSE publications, 31, 153-184.

## Tests of cold-formed steel built-up sections with web holes subjected to web crippling

Jun He<sup>1</sup> and Ben Young<sup>2</sup>

### Abstract

This paper presents an experimental study on web crippling behaviour of cold-formed steel built-up I-sections with circular web holes. The built-up sections were formed by connecting two identical unlipped channels with self-tapping screws. The web hole was located at mid-height of the web and directly beneath the bearing plates. Web crippling tests were conducted on 6 built-up sections without web holes and 19 built-up sections with perforated web under End-Two-Flange and Interior-Two-Flange loading conditions. The web crippling strengths, failure modes and load-displacement curves were reported. The experimental ultimate strengths for specimens without web holes were compared to the nominal strengths predicted from North American Specification, Australian/New Zealand Standard and European Code for cold-formed steel structures. It should be mentioned that the existing international design codes do not have explicit design formula to predict the web crippling strength of cold-formed steel built-up sections with perforated web. Therefore, the test strengths of specimens with perforated web were compared with the strengths derived from the design equations proposed in the literature. It is shown that the design strengths predicted from current design specifications are either conservative or unconservative for the specimens without web holes, while the design equations in the literature are generally unconservative for the specimens with perforated web.

Keywords: Cold-formed steel; Built-up sections; Web crippling; Web holes.

### 1. Introduction

Cold-formed steel built-up sections are being used in construction industry because of their favourable loading capacity and higher torsional rigidity compared with singly symmetric sections. When cold-formed steel built-up sections are used as beam members, the webs of beams may fail by web crippling under concentrated bearing loads. To facilitate the installation of mechanical, electrical and plumbing systems in a building, web openings are commonly introduced in cold-formed steel members. Cold-formed steel built-up sections with web perforation should be investigated as the existing international design codes do not cover the web crippling design for such sections.

In the literature, many investigations have been conducted to study the behaviour of cold-formed steel members with web holes undergoing web crippling. Sivakumaran and Zielonka (1989) proposed a strength reduction equation based on 103 web crippling tests of cold-formed steel lipped channel sections with web openings under Interior-One-Flange (IOF) loading condition. The research was aimed at square,

<sup>1</sup> Jun He, School of Mechanical Engineering, University of Technology, Sydney, Australia, Email: jun.he@uts.edu.au

<sup>2</sup> Ben Young, School of Mechanical Engineering, University of Technology, Sydney, Australia, Email: ben.young@uts.edu.au

rectangular and oval web holes. Langan et al. (1994) investigated the effects of web holes on the web crippling behaviour of cold-formed steel lipped C-shaped sections under End-One-Flange and Interior-One-Flange loading conditions. In this study, only rectangular web holes with fillet corners were considered. LaBoube et al. (1999) extended Langan’s study to specimens with circular web openings. Uzzaman et al. (2012a, 2012b) and Lian et al. (2016b, 2016a, 2017b, 2017a) conducted a series of investigations on web crippling behaviour of cold-formed steel lipped channel sections with circular web holes. The cases of both flanges fastened and unfastened to the support were considered in these studies. Design recommendations were proposed based on test results and numerical results. However, all the aforementioned studies were conducted on cold-formed steel channel sections only. Davis (1972) investigated the behaviour of cold-formed steel built-up sections with openings subjected to web crippling, but the tests were conducted on Interior-Two-Flange loading only. As mentioned earlier, the existing international design codes do not have design recommendation for cold-formed steel built-up sections with perforated webs undergoing web crippling, which is mainly due to the limited research.

The purpose of this study is to experimentally investigate the effects of circular web holes with different diameters on the web crippling behaviour of cold-formed steel built-up sections. The web holes were located at mid-height of the webs and centred beneath the bearing plates. A series of web crippling tests were conducted under End-Two-Flange (ETF) and Interior-Two-Flange (ITF) loading conditions. The accuracy of the design equations specified in current design specifications for the specimens without web holes as well as the strength reduction factor equations proposed in the literature for the specimens with perforated web were evaluated.

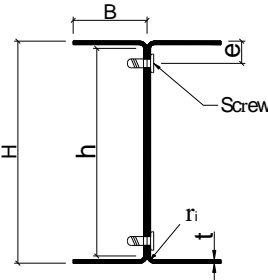


Figure 1: Definition of symbols

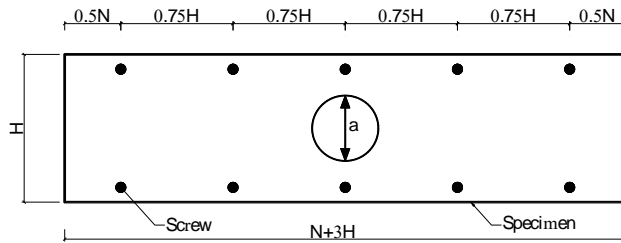


Figure 2: Arrangement of screw spacing

## 2. Experimental investigation

### 2.1 Test specimens

Totally 25 cold-formed steel built-up I-sections were tested. The built-up I-sections were fabricated by connecting two identical unlipped channel sections back-to-back through self-tapping screws, as shown in Fig. 1. The unlipped channel sections were brake-pressed from zinc-coated steel sheets with nominal 0.2% proof stresses of 450 MPa and 500 MPa. Figure 2 shows the screw arrangements along the specimen length. The screw spacing along the length of the specimen was 75% of the overall web depth ( $H$ ) of the specimen to satisfy the minimum spacing requirements in the current North American Specification (AISI 2016). The screws were located as close to the flanges as possible, as shown in Fig. 1. The measured distances ( $e$ ) from the flanges to the location of the screws for each specimen is shown in Tables 1 and 2. The values of nominal hole diameter-to-web depth ratio ( $a/h$ ) were 0.25, 0.5 and 0.7. All the web holes were located at mid-height of the webs and centred beneath the bearing plates.

The test specimens had three different cross-sectional sizes with the nominal overall web depths ( $H$ ) of 120mm and 200mm, the nominal overall flange widths ( $B$ ) of 40mm and 70mm and the nominal

thicknesses ( $t$ ) of 1.2mm and 1.9mm. The measured inside corner radii ( $r_i$ ) of the sections ranged from 0.50 to 1.27 mm. The concentrated forces were applied through two bearing plates which were made of high strength steel, and the thickness of all bearing plates was 50 mm. The flanges of the built-up sections were not fastened to the bearing plates. The recommended minimum specimen length ( $L$ ) in AISI S909 (AISI 2017) is  $3h$  for both ETF and ITF loading conditions. In this study, the specimen length was conservatively designed to be  $N + 3H$ , where  $N$  denotes the bearing length. The measured dimensions of each specimen are shown in Table 1 and Table 2.

## 2.2 Specimen labelling

The specimens were labelled such that the loading condition, the nominal cross-section of channel dimensions, the bearing length and the hole diameter-to-web depth ratio ( $a/h$ ) in percentage can be identified. For example, "ITF-200x70x1.9N150-25-R" defines the specimen as follows, where "ITF" indicates the loading condition of the specimen was Interior-Two-Flange loading. The following three numbers 200x70x1.9 indicate the cross-section of the channel dimensions ( $H \times B \times t = 200 \times 70 \times 1.9$ ). The notation N150 means the specimen was tested using bearing length of 150 mm. The last two digits "25" indicate the nominal  $a/h$  ratio in percentage of this specimen. If a test was repeated, then a symbol "-R" was added to the end of the label.

Table 1: Measured dimensions of specimens under ETF loading condition

Specimens	$H$ (mm)	$B$ (mm)	$r_i$ (mm)	$L$ (mm)	$t^*$ (mm)	$t$ (mm)	$e$ (mm)	$a$ (mm)
ETF-120x40x1.2N90-00	119.8	40.4	0.50	450.2	1.25	1.21	10.8	0.0
ETF-120x40x1.2N90-25	119.3	40.4	0.76	449.8	1.24	1.20	10.5	28.0
ETF-120x40x1.2N90-50	119.5	40.6	0.77	450.4	1.24	1.21	10.4	53.0
ETF-120x40x1.2N90-70	119.7	40.4	0.79	450.3	1.25	1.22	10.5	79.9
ETF-120x40x1.9N90-00	119.8	39.4	1.14	450.4	1.92	1.85	11.7	0.0
ETF-120x40x1.9N90-25	119.5	39.3	1.14	450.3	1.92	1.85	11.8	28.8
ETF-120x40x1.9N90-50	120.0	39.4	1.08	450.1	1.92	1.85	11.8	52.9
ETF-120x40x1.9N90-70	119.7	39.3	1.08	450.2	1.92	1.85	11.8	79.9
ETF-200x70x1.9N150-00	199.8	69.5	1.15	750.3	1.91	1.85	11.6	0.0
ETF-200x70x1.9N150-25	199.7	69.4	1.15	749.6	1.91	1.85	12.0	49.3
ETF-200x70x1.9N150-50	199.5	69.5	1.09	749.8	1.91	1.84	12.2	96.1
ETF-200x70x1.9N150-70	199.6	69.5	1.09	750.0	1.91	1.85	12.2	139.8

Note:  $t$  is the base metal thickness measured after removing the zinc coating

Table 2: Measured dimensions of specimens under ITF loading condition

Specimens	$H$ (mm)	$B$ (mm)	$r_i$ (mm)	$L$ (mm)	$t^*$ (mm)	$t$ (mm)	$e$ (mm)	$a$ (mm)
ITF-120x40x1.2N90-00	119.7	40.4	0.70	450.7	1.25	1.21	10.6	0.0
ITF-120x40x1.2N90-25	119.3	40.5	0.76	450.0	1.24	1.21	10.6	28.1
ITF-120x40x1.2N90-50	119.4	40.5	0.72	450.5	1.25	1.21	10.5	53.1
ITF-120x40x1.2N90-70	119.8	40.4	0.73	450.3	1.25	1.21	10.8	80.0
ITF-120x40x1.9N90-00	119.8	39.3	1.08	450.2	1.92	1.85	11.8	0.0
ITF-120x40x1.9N90-25	119.8	39.2	1.08	450.2	1.92	1.85	12.0	26.9
ITF-120x40x1.9N90-50	120.0	39.4	1.08	449.9	1.92	1.85	11.6	52.9
ITF-120x40x1.9N90-70	119.9	39.3	1.09	450.2	1.91	1.84	11.8	79.8
ITF-200x70x1.9N150-00	200.2	69.5	1.09	749.9	1.91	1.84	12.0	0.0
ITF-200x70x1.9N150-25	199.7	69.5	1.27	749.4	1.92	1.85	11.7	49.9
ITF-200x70x1.9N150-25-R	200.0	69.4	1.15	750.2	1.91	1.84	12.0	49.0
ITF-200x70x1.9N150-50	199.8	69.6	1.15	749.8	1.91	1.84	12.1	96.0
ITF-200x70x1.9N150-70	199.7	69.6	1.08	749.7	1.92	1.85	12.2	139.9

Note:  $t$  is the base metal thickness measured after removing the zinc coating

### 2.3 Material properties

Tensile coupon tests were performed to determine the material properties of the specimens. The tensile coupons were extracted from the centre of the web in the longitudinal direction of the channel sections. The coupon dimensions were designed in accordance with the ASTM (2016). The tensile coupons used in this study had a width of 12.5mm with 50mm gauge length. The tensile coupon tests were carried out using an MTS testing machine under displacement-controlled mode. An extensometer with the gauge length of 50 mm was used to measure the longitudinal elongation of the coupons. Two strain gauges were also attached to both faces of the coupons. Initial readings of the strain gauges were used to determine the Young's modulus. The static stress-strain curves of each coupon test were determined according to the test procedures reported by Huang and Young (2014). The static stress-strain curves were used to obtain the material properties of each coupon, including initial Young's modulus ( $E$ ), 0.2% proof stress ( $\sigma_{0.2}$ ), ultimate tensile strength ( $\sigma_u$ ), and strain at fracture ( $\epsilon_f$ ) as shown in Table 3.

Table 3: Measured material properties

Sections (HxBxt)	Nominal	Measured			
	$\sigma_{0.2}$ (MPa)	$E$ (GPa)	$\sigma_{0.2}$ (MPa)	$\sigma_u$ (MPa)	$\epsilon_f$ (%)
120x40x1.2	500	217	579.2	587.5	6.8
120x40x1.9	450	210	491.2	508.6	11.4
200x70x1.9	450	210	481.4	509.3	11.6

### 2.4 Test setup and procedure

Web crippling tests were conducted on the specimens under ETF and ITF loading conditions, as shown in Fig. 3. The concentrated force was transferred through two identical bearing plates. Hinge supports were simulated by two half-rounds, which were bolted to the bearing plates. Linear variable displacement transducers (LVDTs) were used to capture the vertical deformation and lateral deformation of the webs. Four LVDTs were positioned on each bearing plate and the average readings of the four LVDTs were recorded as the displacement of each bearing plate. Vertical deformation of the webs was calculated as the difference between the displacement of two bearing plates. The specimens were tested using a servo-controlled hydraulic testing machine under displacement control at a constant rate of 0.2 mm/min. Photographs of the ETF and ITF loading tests are shown in Fig. 4.

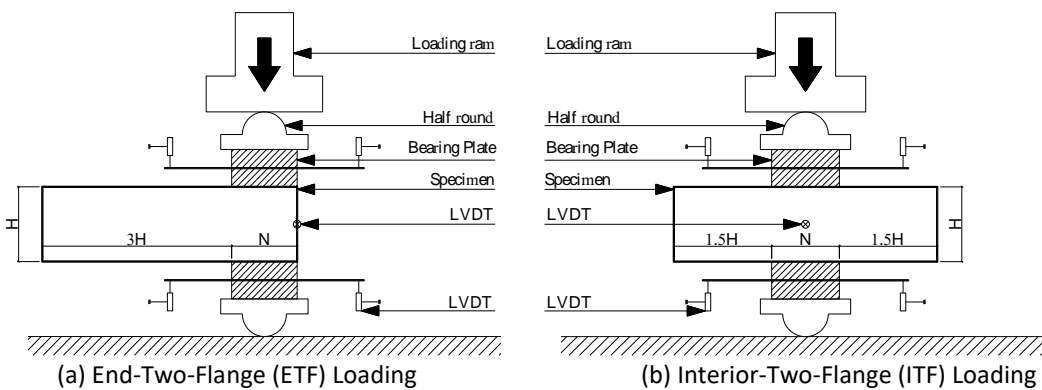


Figure 3: Schematic illustration of test setup

### 2.5 Test results

Totally 12 specimens were tested under ETF loading condition, and 13 specimens were tested under ITF loading condition. The experimental web crippling strengths per web ( $P_{Exp}$ ) and also for the entire built-up specimens ( $P_{Exp*}$ ) are reported in Tables 4 and 5. One repeated test was conducted on specimen "ITF-200x70x1.9N150-25" and the difference in failure load was only 2.2% compared with the original test.

Typical failure modes of the specimens failed under ETF and ITF loading conditions are shown in Fig. 4. Typical load (per web)-displacement curves obtained from the tests are shown in Fig. 5.

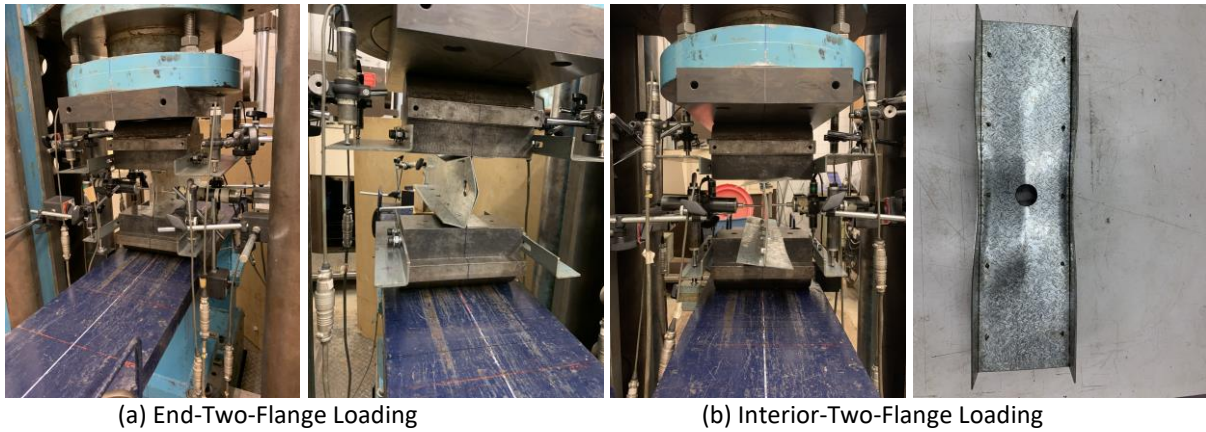


Figure 4: Photographs of test setup and typical failure modes

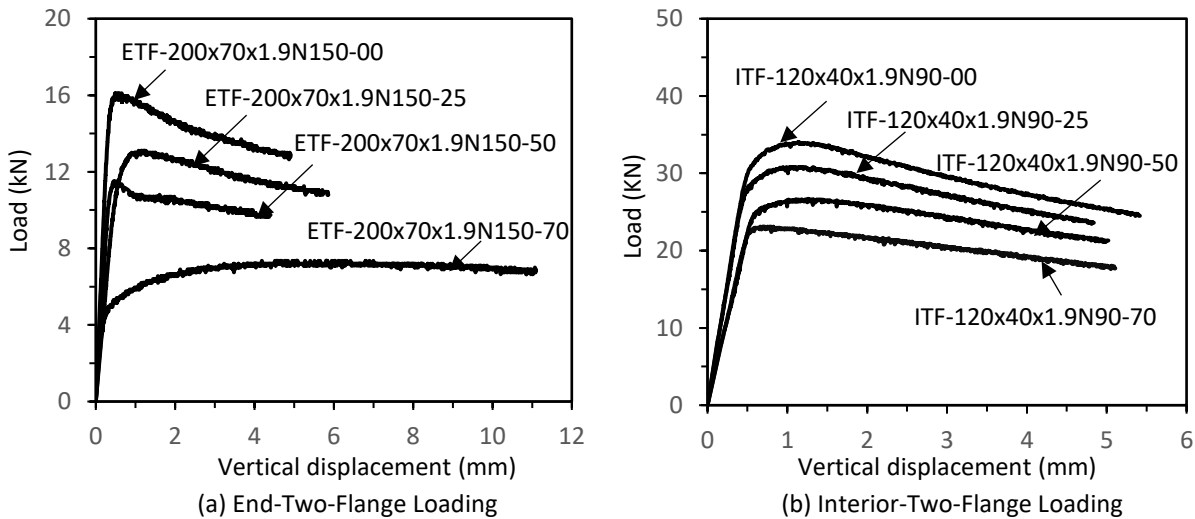


Figure 5: Typical load-displacement curves

### 3. Comparison of experimental strengths with current design strengths

#### 3.1 Built-up sections without web holes

As mentioned in the introduction of this paper, no design equation is available for cold-formed steel built-up sections with web holes in the current design specifications. Therefore, only the experimental strengths of specimens without web holes were compared with the nominal strengths obtained from the North American Specification (AISI 2016), Australian/New Zealand Standard (AS/NZS 2018) and Eurocode 3 Part 1-3 (CEN 2006).

The design equations specified in AISI (2016) are based on a unified equation with different coefficients according to different cross-section shapes, loading conditions and whether the flanges are fastened or not. The coefficients for built-up sections are shown in Table G5-1 of the AISI (2016), which were statistically calibrated using the test data reported by Winter and Pian (1946), Hetrakul and Yu (1978), Bhakta et al. (1992) and Cain et al. (1995). It should be noted that coefficients are not provided for built-up sections with unstiffened flanges under ETF and ITF loading conditions due to lack of experimental

data. Therefore, the coefficients for built-up sections with stiffened flanges were used to calculate the nominal strengths. The design rules in the AS/NZS (2018) are identical to the design rules in the AISI (2016), with the same coefficients for built-up sections as shown in Table 3.3.6.2 (A) of the AS/NZS (2018). Eurocode 3 Part 1-3 (CEN 2006) has adopted the design rules specified in the AISI (1996) with modification in the definition of the parameter “ $h$ ”, from “flat portion of the web” to “distance between centreline of the flanges”. The design equations specified in CEN (2006) were proposed based on the test results reported by Winter and Pian (1946) and Hetrakul and Yu (1978). The cases of built-up sections with unstiffened flanges loaded under ETF and ITF conditions were not investigated. However, the design rules in CEN (2006) use the same equations for built-up sections with stiffened and unstiffened flanges.

Table 4 shows the comparison of experimental strengths per web ( $P_{Exp}$ ) for specimens without web holes with the nominal strengths ( $P_n$ ) calculated according to AISI (2016), AS/NZS (2018) and EC3 (CEN 2006). It is shown that the web crippling strengths of built-up sections predicted by AISI (2016) and AS/NZS (2018) design equations are unsafe. The mean values of experimental strengths-to-predicted strengths ratio ( $P_{Exp}/P_n$ ) are 0.72 and 0.55 with the corresponding COVs of 0.100 and 0.089 for ETF and ITF loading conditions, respectively. On the other hand, EC3 (CEN 2006) conservatively predicts the web crippling strengths, especially under ETF loading condition. The experimental strengths are 74% and 24% higher than the predicted strengths on average under ETF and ITF loading conditions, respectively.

Table 4: Comparison of web crippling strengths for specimens without web holes

Specimen	Measured ratio				Test		Comparison, $P_{Exp}/P_n$	
	$h/t$	$N/t$	$r/t$	$N/h$	$P_{Exp}^*$ (kN)	$P_{Exp}$ (kN)	NAS	EC3
ETF-120x40x1.2N90-00	96.1	74.4	0.41	0.77	17.4	8.7	0.68	1.96
ETF-120x40x1.9N90-00	61.4	48.6	0.62	0.79	41.4	20.7	0.80	1.89
ETF-200x70x1.9N150-00	104.7	81.1	0.62	0.77	32.2	16.1	0.67	1.37
Mean							0.72	1.74
COV							0.100	0.185
ITF-120x40x1.2N90-00	95.7	74.1	0.58	0.78	27.8	13.9	0.50	1.26
ITF-120x40x1.9N90-00	61.5	48.6	0.58	0.79	68.2	34.1	0.59	1.36
ITF-200x70x1.9N150-00	105.5	81.5	0.59	0.77	59.8	29.9	0.56	1.09
Mean							0.55	1.24
COV							0.089	0.110

### 3.2 Built-up sections with web holes

Uzzaman et al. (2012b) proposed the strength reduction factor ( $R_p$ ) equations for cold-formed steel lipped channel sections with circular web holes under ETF and ITF loading conditions:

For ETF loading condition:

$$R_p = 0.90 - 0.60 \left( \frac{a}{h} \right) + 0.12 \left( \frac{N}{h} \right) \leq 1 \quad (1)$$

For ITF loading condition:

$$R_p = 1.05 - 0.54 \left( \frac{a}{h} \right) + 0.01 \left( \frac{N}{h} \right) \leq 1 \quad (2)$$

To evaluate whether Eq. (1) and Eq. (2) are applicable to cold-formed steel built-up sections, the experimental strengths were compared with the experimental web crippling strengths of the built-up sections without web holes ( $P_{Exp-0}$ ) multiplied by the respective strength reduction factor ( $R_p$ ) in Eq. (1) and Eq. (2). The reduced nominal web crippling strengths ( $P_{nr}$ ) were calculated according to Eq. (3):

$$P_{nr} = R_p P_{Exp-0} \quad (3)$$

Comparison of web crippling strengths for specimens with web holes is reported in Table 5. The reduced

nominal web crippling strengths calculated using Eq. (1) and Eq. (2) are generally unconservative under ETF and ITF loading conditions. The mean values of the  $P_{Exp}/P_{nr}$  ratio are 0.92 and 0.97, with the corresponding COVs of 0.132 and 0.038 for ETF and ITF loading conditions, respectively. It should be noted that the predicted strengths are highly unconservative for specimens with nominal  $a/h$  ratio of 0.7 under ETF loading. The test strengths reached only 73%, 78% and 80% of the predicted strengths for specimens “ETF-120x40x1.2N90-70”, “ETF-120x40x1.9N90-70” and “ETF-200x70x1.9N150-70”, respectively.

Table 5: Comparison of web crippling strengths for specimens with web holes

Specimen	Measured ratio					Test		Comparison, $P_{Exp}/P_{nr}$
	$h/t$	$N/t$	$r/t$	$N/h$	$a/h$	$P_{Exp}^*$ (kN)	$P_{Exp}$ (kN)	Uzzaman et al. (2012b)
ETF-120x40x1.2N90-25	96.1	75.0	0.63	0.78	0.24	13.8	6.9	0.94
ETF-120x40x1.2N90-50	95.4	74.4	0.64	0.78	0.46	12.5	6.3	1.01
ETF-120x40x1.2N90-70	94.8	73.8	0.65	0.78	0.69	7.4	3.7	0.73
ETF-120x40x1.9N90-25	61.3	48.6	0.62	0.79	0.25	37.0	18.5	1.06
ETF-120x40x1.9N90-50	61.6	48.6	0.58	0.79	0.46	29.8	14.9	1.00
ETF-120x40x1.9N90-70	61.5	48.6	0.59	0.79	0.70	18.6	9.3	0.78
ETF-200x70x1.9N150-25	104.6	81.1	0.62	0.77	0.25	26.2	13.1	0.97
ETF-200x70x1.9N150-50	105.2	81.5	0.59	0.78	0.50	23.0	11.5	1.03
ETF-200x70x1.9N150-70	104.6	81.1	0.59	0.77	0.72	14.4	7.2	0.80
Mean								0.92
COV								0.132
ITF-120x40x1.2N90-25	95.3	74.4	0.63	0.78	0.24	24.2	12.1	0.94
ITF-120x40x1.2N90-50	95.4	74.4	0.60	0.78	0.46	23.4	11.7	1.04
ITF-120x40x1.2N90-70	95.7	74.4	0.60	0.78	0.69	17.2	8.6	0.90
ITF-120x40x1.9N90-25	61.5	48.6	0.58	0.79	0.24	61.8	30.9	0.97
ITF-120x40x1.9N90-50	61.6	48.6	0.58	0.79	0.46	53.6	26.8	0.97
ITF-120x40x1.9N90-70	61.9	48.9	0.59	0.79	0.70	46.2	23.1	1.00
ITF-200x70x1.9N150-25	104.5	81.1	0.69	0.78	0.26	54.6	27.3	0.99
ITF-200x70x1.9N150-25-R	105.4	81.5	0.63	0.77	0.25	53.4	26.7	0.97
ITF-200x70x1.9N150-50	105.3	81.5	0.63	0.77	0.50	46.6	23.3	0.99
ITF-200x70x1.9N150-70	104.7	81.1	0.58	0.77	0.72	38.8	19.4	0.97
Mean								0.97
COV								0.038

#### 4. Conclusions

An experimental investigation of cold-formed steel built-up sections with web holes subjected to web crippling was reported. A total of 25 specimens covering various key parameters were tested under ETF and ITF loading conditions. The web crippling strengths for specimens without web holes obtained from the tests were compared with the predicted strengths calculated according to the current North American Specification, Australian/New Zealand Standard and European Code for cold-formed steel structures. It is shown that the nominal web crippling strengths predicted by the current design specifications are either unconservative or conservative, which is due to the fact that the design equations for ETF and ITF loading conditions in the current specifications were derived based on investigations of built-up sections with stiffened flanges. Therefore, the development of new design rules for cold-formed steel built-up sections with unstiffened flanges is necessary. As for specimens without web holes, the validity of the strength reduction factor equations proposed by Uzzaman et al. (2012b) were assessed. The results showed that the web crippling strengths calculated using the strength reduction factors are generally unconservative, especially for members with nominal  $a/h$  ratio of 0.7 under ETF loading condition.

## References

- AISI (American Iron and Steel Institute). (1996). "Specification for the design of cold-formed steel structural members." Washington, D.C
- AISI (American Iron and Steel Institute). (2016). "North American specification for the design of cold-formed steel structural members." *AISI S-100*, Washington, D.C
- AISI (American Iron and Steel Institute). (2017). "Test standard for determining the web crippling strength of cold-formed steel flexural members." *AISI S909-17*, Washington, DC.
- American Society for Testing and Materials (ASTM). (2015). "Standard test methods for tension testing of metallic materials." *E8/E8M-13a*, West Conshohocken, Penn., USA.
- Australian/New Zealand Standard (AS/NZS). (2018). "Cold-formed steel structures." *AS/NZS 4600: 2018*, Standards Australia, Sydney, Australia.
- Bhakta, B. H., R. A. LaBoube and W. W. Yu (1992). "The effect of flange restraint on web crippling strength." *Final Report, Civil Engineering Study 92-1*. University of Missouri-Rolla, St. Louis, Missouri, USA.
- Cain, D. E., R. A. LaBoube and W. W. Yu (1995). "The effect of flange restraint on web crippling strength of cold-formed steel Z- and I-sections." *Final Report, Civil Engineering Study 95-2*. University of Missouri-Rolla, St. Louis, Missouri, USA.
- CEN (European Committee for Standardization). (2006). "Eurocode 3: Design of steel structures—Part 1.3: General rules—Supplementary rules for cold-formed members and sheeting" *EN 1993-1-3*, European Committee for Standardization, Brussels.
- Davis, C. S. (1972). "The structural behavior of cold-formed steel members with perforated elements.", University of Missouri-Rolla, St. Louis, Missouri, USA.
- Hetrakul, N. and W.-W. Yu (1978). "Structural behavior of beam webs subjected to web crippling and a combination of web crippling and bending." *Final Report, Civil Engineering Study 78-4*, University of Missouri-Rolla, St. Louis, Missouri, USA.
- Huang, Y. and B. Young (2014). "The art of coupon tests." *Journal of Constructional Steel Research* 96: 159-175.
- LaBoube, R. A., W. W. Yu, S. U. Deshmukh and C. A. Uphoff (1999). "Crippling capacity of web elements with openings." *Journal of Structural Engineering* 125(2): 136-141.
- Langan, J. E., R. A. LaBoube and W. W. Yu (1994). "Structural behavior of perforated web elements of cold-formed steel flexural members subjected to web crippling and a combination of web crippling and bending." *Final report*, University of Missouri-Rolla, St. Louis, Missouri, USA.
- Lian, Y., A. Uzzaman, J. B. P. Lim, G. Abdelal, D. Nash and B. Young (2016a). "Effect of web holes on web crippling strength of cold-formed steel channel sections under end-one-flange loading condition – Part I: Tests and finite element analysis." *Thin-Walled Structures* 107: 443-452.
- Lian, Y., A. Uzzaman, J. B. P. Lim, G. Abdelal, D. Nash and B. Young (2016b). "Effect of web holes on web crippling strength of cold-formed steel channel sections under end-one-flange loading condition - Part II: Parametric study and proposed design equations." *Thin-Walled Structures* 107: 489-501.
- Lian, Y., A. Uzzaman, J. B. P. Lim, G. Abdelal, D. Nash and B. Young (2017a). "Web crippling behaviour of cold-formed steel channel sections with web holes subjected to interior-one-flange loading condition-Part I: Experimental and numerical investigation." *Thin-Walled Structures* 111: 103-112.
- Lian, Y., A. Uzzaman, J. B. P. Lim, G. Abdelal, D. Nash and B. Young (2017b). "Web crippling behaviour of cold-formed steel channel sections with web holes subjected to interior-one-flange loading condition – Part II: parametric study and proposed design equations." *Thin-Walled Structures* 114: 92-106.
- Sivakumaran, K. S. and K. M. Zielonka (1989). "Web crippling strength of thin-walled steel members with web opening." *Thin-Walled Structure* 8(4), 295-319s.
- Uzzaman, A., J. B. P. Lim, D. Nash, J. Rhodes and B. Young (2012a). "Cold-formed steel sections with web openings subjected to web crippling under two-flange loading conditions—part I: Tests and finite element analysis." *Thin-Walled Structures* 56: 38-48.
- Uzzaman, A., J. B. P. Lim, D. Nash, J. Rhodes and B. Young (2012b). "Cold-formed steel sections with web openings subjected to web crippling under two-flange loading conditions—Part II: Parametric study and proposed design equations." *Thin-Walled Structures* 56: 79-87.
- Winter, G. and R. H. J. Pian (1946). "Crushing strength of thin steel webs." *Bulletin 35, Part 1, Cornell University, Ithaca, New York, USA*.

## **Flexural behaviour of cold-formed steel built-up section members**

Qiu-Yun Li<sup>1</sup>, Ben Young<sup>2</sup>

### **Abstract**

This paper presents experimental and numerical investigations on cold-formed steel built-up section beams. The channels with longitudinal stiffeners were brake-pressed from steel sheets with nominal thicknesses of 0.75 and 1.2 mm. First of all, minor axis bending tests were undertaken to explore buckling behaviour of the newly designed built-up open and closed sections. The test setup, experimental procedure, ultimate moments and failure modes were reported. Then, finite element models were developed and validated against the test results. The parametric study incorporating 107 built-up open and closed section flexural members was performed to generate further numerical data over a wide range of sectional configurations and geometric parameters. After that, the comparisons of ultimate moments obtained from experiments and finite element analyses with nominal strengths calculated on the basis of direct strength method (DSM) that provided in the North American Specification and Australian/New Zealand Standard were carried out to evaluate the appropriateness of current design rules for cold-formed steel built-up section beams. It is shown that the codified DSM equations are generally conservative for flexural strength predictions of the built-up open sections, while provide unconservative predictions for the built-up closed sections under minor axis bending.

### **1. Introduction**

Based on available cold-formed steel (CFS) open sections, the built-up sectional profiles are convenient to obtain by composing two or more individual components with discrete fasteners along the longitudinal direction of the members. CFS built-up section members have gained increasing research interests for their great potential in enhancement of stability due to the nature of symmetric sections and load bearing capacity. The flexural behaviour of built-up I-sections and box sections has been carefully investigated by Wang and Young (2015) and Li et al. (2016). However, the structural efficiency of these traditional cross-sections is limited due to large plate slenderness without stiffener. Therefore, many attempts have been made to explore advanced built-up sections for flexural members. Firstly, intermediate stiffeners are considered as an effective measure, which can significantly improve local buckling strength of CFS sections. The built-up open or closed sections with various types of longitudinal stiffeners were thus designed and their bending performance were studied (Manikandan and Sukumar 2016; Wang and Young 2016). Additionally, Ye et al. (2016) performed an optimization analysis on CFS lipped channels to develop more efficient cross-section profiles. It was found that the channels with crimped flanges had huge potential in increasing flexural strength. Currently, direct strength method (DSM) is a favorable tool for strength prediction of CFS members, especially for complicated sectional shapes. But the codified DSM equations are semi-empirical and were verified for certain types of cross-

---

<sup>1</sup> PhD Candidate, Department of Civil Engineering, The University of Hong Kong, Pokfulam Road, Hong Kong, China <qiuyunli@connect.hku.hk>

<sup>2</sup> Professor, Department of Civil and Environmental Engineering, The Hong Kong Polytechnic University, Hong Kong, China <ben.young@polyu.edu.hk>

sections. For CFS sections that are not covered in present design codes, the appropriateness of DSM equations should be evaluated.

In this study, the channels with longitudinal stiffeners were designed to form novel built-up open and closed section members. The channels were brake-pressed from CFS sheets with nominal thicknesses of 0.75 and 1.2 mm. In order to explore buckling behaviour of the newly designed built-up sections under minor axis bending, both experimental and numerical investigations were conducted. Firstly, five four-point bending tests were carried out to understand the flexural performance of the CFS built-up open and closed sections subjected to local buckling, distortional buckling as well as their interactions. The ultimate moments and failure modes of all specimens were obtained and employed to calibrate the finite element models. Then, the parametric study incorporating 107 different built-up sections with longitudinal stiffeners was performed using the validated finite element models to generate more data for this investigation. Moreover, the suitability of current design rules was assessed for CFS built-up section beams through comparisons of ultimate moments gained from both tests and finite element analyses with predicted strengths calculated by DSM equations that specified in the North American Specification AISI S100 (AISI 2016) and the Australian/New Zealand Standard AS/NZS 4600 (AS/NZS 2018).

## 2. Experimental Investigation

### 2.1 Test specimens and material properties

The built-up sectional profiles involved in the experimental investigation are depicted in Fig.1. The built-up open and closed section specimens were fabricated by composing two channels with discrete self-tapping screws along the member length. The nominal overall length of specimen was 1200 mm. Referring to AISI S100 (2016) and AS/NZS 4600 (2018), the general screw spacing was set as 100 mm for both moment and shear spans, while the smaller screw spacing was utilized near the loading and support locations. The actual dimensions of test specimens that were measured for individual channels before connecting by screws are presented in Table 1. The specimens were labeled to identify cross-sectional profile, nominal plate thickness and nominal overall length. For instance, the label “BT1.2L1200-b” represents the built-up closed section specimen with nominal plate thickness of 1.2 mm and nominal overall length of 1200 mm. Final letter “b” denotes one of the two channels forming the built-up section. If label includes the letter “R”, it means that the specimen was loaded as a repeated test. The nominal 0.2% proof stresses of the virgin steel sheets with nominal plate thicknesses of 0.75 and 1.2 mm were 550 and 500 MPa, respectively. In order to consider the effect of cold-forming, tensile coupons were tested to obtain the actual material properties. The measured static 0.2% proof stresses of sections AT0.75, AT1.2, BT0.75 and BT1.2 were 615, 604, 611 and 606 MPa obtained from the flat coupon tests, respectively, and were 637, 641, 631 and 636 MPa determined from the curved coupon tests, respectively, which have been reported by Li and Young (2019, 2021) for the same batch of specimens.

Table 1: Measured dimensions of four-point bending test specimens

Specimen	$h_1$ (mm)	$h_w$ (mm)	$w_1$ (mm)	$w_2$ (mm)	$w_3$ (mm)	$b_1$ (mm)	$t$ (mm)	$t^*$ (mm)	$e$ (mm)	$r_i$ (mm)
AT0.75L1200-a	15.6	101.3	14.6	30.4	13.5	30.6	0.788	0.743	25.1	1.5
AT0.75L1200-b	15.8	101.9	14.7	30.2	14.1	30.7	0.790	0.745	25.1	1.5
AT1.2L1200-a	16.7	103.0	14.2	30.6	14.5	31.5	1.237	1.195	24.8	2.5
AT1.2L1200-b	16.9	102.6	14.1	30.4	14.6	32.0	1.239	1.197	24.5	2.5
BT0.75L1200-a	-	103.5	14.4	31.2	14.1	30.5	0.804	0.759	25.0	1.5
BT0.75L1200-b	-	103.1	14.5	31.0	14.0	30.2	0.804	0.759	24.9	1.5
BT1.2L1200-a	-	101.8	14.7	29.8	14.3	31.2	1.236	1.194	25.4	2.3
BT1.2L1200-b	-	102.4	14.7	29.8	14.7	31.3	1.238	1.196	25.4	2.3

BT1.2L1200R-a	-	102.0	14.8	29.4	14.9	30.8	1.227	1.185	25.2	2.3
BT1.2L1200R-b	-	102.9	14.7	30.1	14.6	31.4	1.223	1.181	25.5	2.3

Note:  $t^*$  = thickness of base metal.

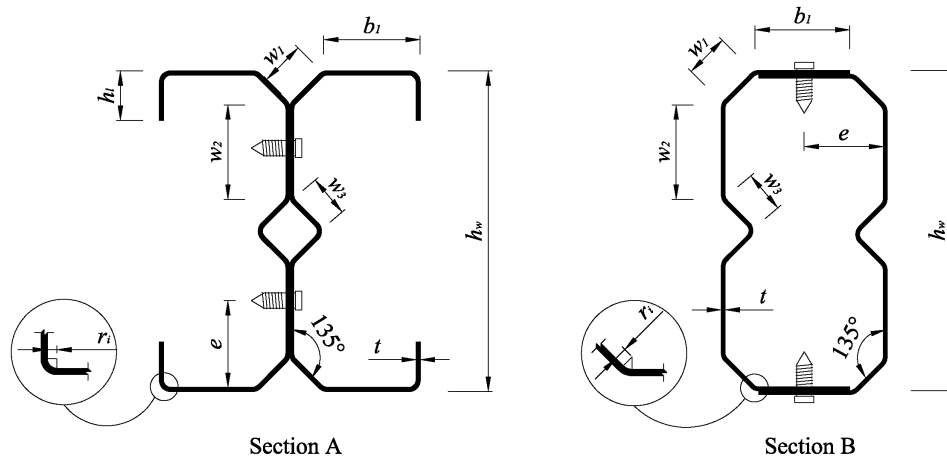


Figure 1: Cross-sectional profiles and locations of self-tapping screws

## 2.2 Test setup and procedure

Five four-point bending tests were carried out on the CFS built-up sections. The test setup is shown in Fig.2. The spreader beam was employed to equally transfer the force to the specimens at two points. At loading and support positions, rollers and half-round were used to simulate the pin and hinge boundary conditions, respectively. In order to avoid possible failure due to local stress concentration, the loading transfer plates with a width of 90 mm were set between the rollers or half-round and the specimen. For the built-up open section specimens, the lips were placed on the loading transfer plates. Both outer and inner stiffener plates were bolted to the flat portions of the section to prevent localized failure. Besides, four additional stiffener plates were utilized to protect the compressive lips from buckling at support locations. For the built-up closed section specimens, four pairs of stiffener plates were clamped to the specimen and wooden blocks were inserted into the closed loop at loading and support locations.

A hydraulic testing machine was used to apply vertical force with displacement control. The constant loading rate of 0.5 mm/min was adopted for all specimens. Three displacement transducers (LVDTs) were installed at the two loading points and the middle of moment span to measure the vertical deflections of specimen, which were employed to calculate the curvature at the moment span. During the test, the readings of three LVDTs and applied force were recorded by a data acquisition system at regular intervals. Two 100-second pauses were conducted before and near ultimate load to determine the static force.

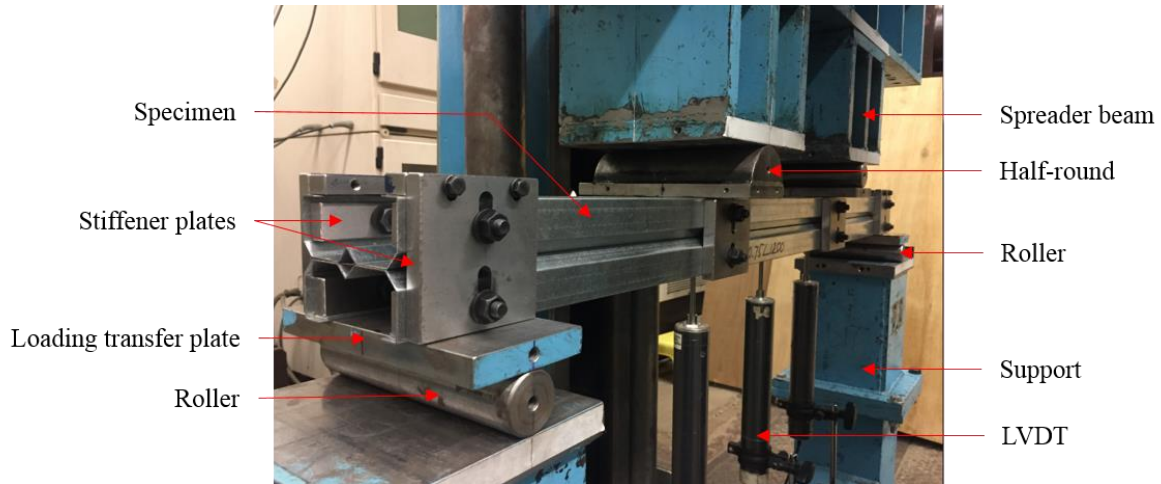


Figure 2: Four-point bending test setup

### 2.3 Test results

The static moment-curvature curves of the five minor axis bending tests are shown in Fig.3. The key test results, including failure mode, ultimate moment ( $M_{Exp}$ ) and the ultimate-to-yield moment ratio ( $M_{Exp}/M_y$ ) are summarized in Table 2. All specimens failed within the moment span and no lateral-torsional buckling was observed during the tests. For the built-up closed section specimens, with the growth of curvature in the moment span, local buckling occurred at the outer plates where self-tapping screws located before reaching the ultimate moment. The local buckling half-waves were formed between the screws. It evidences that the arrangement of screws has effect on the failure of built-up closed sections. After local buckling occurred, the bending moment kept increasing until distortional buckling appeared at the compressive element, where the stiffener deflected from its original position. The failure mode of the three built-up closed section specimens that observed at ultimate load was the interaction of local and distortional buckling. The results in Table 3 show that the value of  $M_{Exp}/M_y$  for specimen BT1.2L1200 is 1.03, which demonstrates that this specimen reached flexural strength after the initiation of yielding. Thus, it may be more reasonable to consider inelastic reserve strength in the design of CFS built-up closed section beams. For the built-up open sections, specimens AT0.75L1200 and AT1.2L1200 were failed by local buckling and distortional buckling, respectively. The buckling firstly arose at the compressive lips with a small load drop. After that, the applied load increased until the flexural deformation of specimens developed to large curvature.

Table 2: Test and FE results of the CFS built-up section beams

Specimen	Failure mode	$M_{Exp}$ (kNmm)	$\frac{M_{Exp}}{M_y}$	Failure mode	$M_{FEM}$ (kNmm)	$\frac{M_{Exp}}{M_{FEM}}$
AT0.75L1200	L	1563.7	0.80	L	1554.5	1.01
AT1.2L1200	D	2800.0	0.84	D	2874.0	0.97
BT0.75L1200	L+D	1627.5	0.71	L+D	1689.7	0.96
BT1.2L1200	L+D	3587.5	1.03	L+D	3610.4	0.99
BT1.2L1200R	L+D	3360.0	0.96	L+D	3433.5	0.98
					Mean	0.98
					COV	0.017

Note: In the column of "Failure mode", L = local buckling, D = distortional buckling

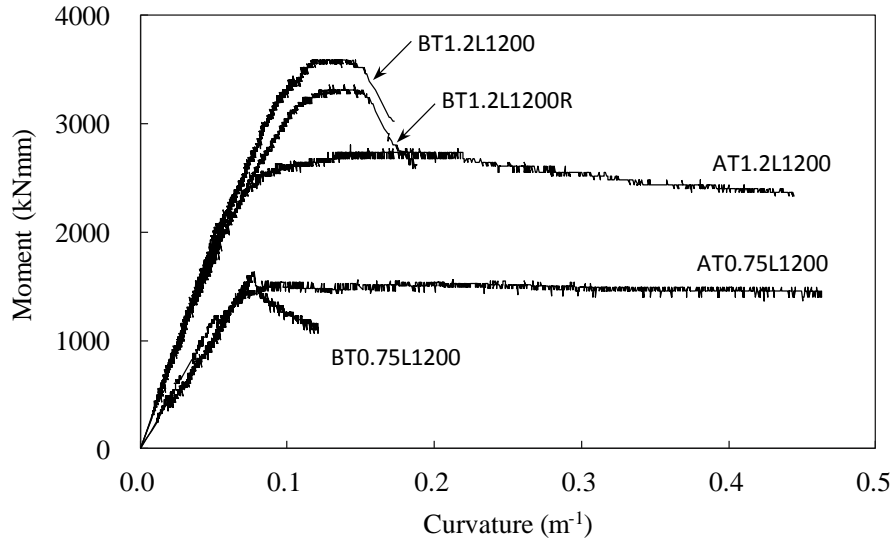


Figure 3: Moment-curvature responses of the CFS built-up section beam tests

### 3. Numerical Simulation

#### 3.1 Finite element models

The finite element (FE) models of CFS built-up open and closed section members were developed by adopting the software package ABAQUS (2018) to replicate the four-point bending tests. The shell element S4R with mesh size of  $5 \times 5$  mm at flat portions and a finer mesh at curved portions, which was proven appropriate to emulate local and distortional buckling behaviour of CFS sections (Wang and Young 2016), was used to model the built-up section members. The self-tapping screws represented by cylinders and the stiffener plates preventing the specimens from localized failure were also established in the FE models by using the solid element C3D8R with mesh sizes of  $2 \times 2 \times 2$  mm and  $6 \times 6 \times 6$  mm, respectively. The nonlinear material pattern with isotropic hardening was utilized for CFS built-up section beams. The input true stress-true plastic strain relationship was determined from the static stress-strain curves of the tensile coupon tests. The material properties obtained from the curved coupons were also employed in the FE models to consider the strength enhancement at the curved positions of the sections.

Two types of contact conditions were included in the FE models. Firstly, the “Hard” contact interaction with friction coefficient of 0.2 was utilized to emulate the actual surface touching between the overlapped elements of the built-up sections. Additionally, the “Tie” constraint was defined to model the interactions between screws and specimens as well as between stiffener plates and specimens. Moreover, the “coupling” restraint was employed to simulate the boundary and loading conditions. Four reference points were coupled with the corresponding surface sets at loading and support locations. The pin and hinge boundary conditions were modeled by releasing the particular degrees of freedom (DOFs) of reference points. The vertical displacement was applied to the reference points at loading positions to duplicate the actual test procedure. The static steps with “Nlgeom” were used to conduct collapse analysis. In order to solve the convergence problems of thin-walled members, the technique of automatic stabilization was adopted in this study, which can efficiently provide a solution in the post-collapse stage with the help of artificial damping (Schafer et al. 2010).

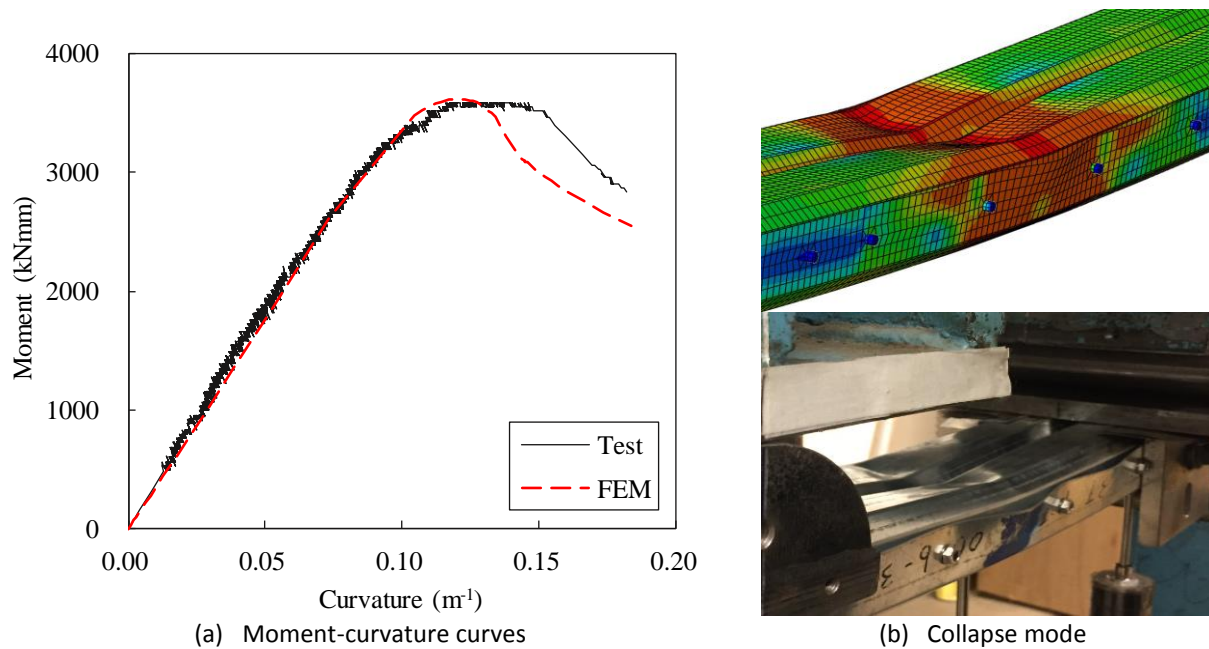


Figure 4: Comparison of experimental and numerical results for specimen BT1.2L1200

The comparison of experimental and numerical observations is displayed in Fig.4 for specimen BT1.2L1200. In general, the overall shapes of moment-curvature curves obtained from FE analyses coincide with those obtained from the tests. In addition, the failure modes match very well between the experiments and numerical simulation. The results gained from tests and FE analyses are compared in Table 2. It is shown that the mean value of experimental-to-numerical moment capacity ratios ( $M_{Exp}/M_{FEM}$ ) is 0.98 with the corresponding coefficient of variation (COV) of 0.017, which indicates that the FE analyses are able to predict the flexural capacity of CFS built-up sections under minor axis bending. Considering the complex sectional profiles, material nonlinearity and complicated contact conditions, it is thus deemed that the FE models are suitable for parametric study.

### 3.2 Parametric study

An extensive parametric study was performed using the validated FE models to further understand the flexural behaviour of CFS built-up section beams. Based on the two basic section profiles in Fig.1, 14 types of open (OI) sections and 14 types of closed (CW) sections incorporating different geometries of stiffeners ( $w_3$ ), folded-flanges ( $h_1, b_1, w_1$ ) and webs ( $w_2$ ) as well as varying height-to-width ratio and the angle of the folded-flanges were considered in the parametric study. The height of cross-sections varied from 148 to 234 mm. The plate thicknesses ranged from 0.8 to 3.2 mm were designed for each type of section. The self-tapping screws were set at the middle of overlapped elements for all specimens. The general screw spacing of 100 mm and smaller screw spacing at loading and support positions were adopted. The measured material properties obtained from the tensile coupon tests of Section A and Section B (Fig.1) were applied for the built-up open and closed section series, respectively. In total, 107 newly numerical data have been generated for CFS built-up sections under minor axis bending. All the beams predicted using the numerical analyses were failed within the moment span and these beams did not fail by lateral-torsional buckling. For the built-up closed sections, the interaction of local and distortional buckling was observed for the majority of specimens, and pure local buckling was observed for the minority of specimens. For the built-up open sections, most specimens failed by local buckling or distortional buckling and few specimens failed by the interactions of local and distortional buckling.

#### 4. Design Rules and Comparison with Experimental and Numerical Strengths

The suitability of codified DSM equations specified in Chapter F of AISI S100 (2016) and Section 7.2 of AS/NZS 4600 (2018) was examined for CFS built-up sections under bending through comparing the ultimate moments obtained from tests and FE analyses with nominal strengths. In this study, it is deemed that the beam specimens were fully braced and no lateral-torsional buckling occurred. The predicted strength was thus taken as the minimum value of nominal flexural strengths for local buckling and distortional buckling. Due to the observation from tests, the inelastic reserve capacity has been considered. The critical elastic buckling moments that required in DSM equations were determined by the finite strip analysis program CUFSM (Schafer et al. 2010). In view of the current situation that the built-up section connected by discrete fasteners along the member length cannot be directly simulated by the finite strip analysis program and no explicit guideline exists, two kinds of elastic buckling analysis models were hence adopted in this study to explore rational model for CFS built-up section beams. The first one was the integrated model with specific thickness at the overlapped area, which was used by Wang and Young (2016). Two limiting cases including double plate thicknesses ( $2t$ ) and single plate thickness ( $t$ ) of the overlapped area were utilized for the integrated models in this investigation. Additionally, the newly proposed model with two channels connected by solid blocks was also employed. The solid blocks were set at the locations of screws and their width was regarded as the diameter of screws.

Moreover, the reliability analysis was performed to assess the reliability of codified DSM equations. The Eq.K2.1.1-1 of AISI S100 (2016) was utilized to determine the reliability index ( $\beta$ ). The target value of  $\beta$  was taken as 2.5. The statistical parameters  $M_m=1.10$ ,  $V_M=0.10$ ,  $F_m=1.00$  and  $V_F=0.05$  were obtained from Table K2.1.1-1 of AISI S100 (2016), which denote the mean values and coefficients of variation for material and fabrication factors, respectively. The typical load combinations of 1.2DL+1.6LL and 1.2DL+1.5LL were adopted in the analysis, where DL is the dead load and LL is the live load. The resistance factor ( $\phi$ ) of 0.90 that prescribed in Chapter F of AISI S100 (2016) and Section 7.2 of AS/NZS 4600 (2018) for CFS flexural members was used in the calculation. In addition, according to Clause A1.2(c) of AISI S100 (2016) and Clause 1.6.3(c) of AS/NZS 4600 (2018), the resistance factor of 0.80 was also considered because the novel built-up sections are not pre-qualified in the current design codes.

Table 3: Comparison of test and numerical results with predicted strengths for CFS built-up open section beams

	$M_{Exp}$ and $M_{Fl}$	$M_{Exp}$ and $M_{FE}$				
	$M_{DSM-s}$	$M_{DSM-2t}$	$M_{DSM-t}$	$M_{DSM-s}$	$M_{DSM-2t}$	$M_{DSM-t}$
Dominated failure	L	L	L	D	D	D
Number of data	38	42	38	19	15	19
Mean ( $P_m$ )	1.21	1.19	1.21	1.06	1.06	1.07
COV ( $V_p$ )	0.178	0.183	0.178	0.064	0.043	0.060
$\phi$	0.90	0.90	0.90	0.90	0.90	0.90
$\beta_1$	2.69	2.60	2.68	2.74	2.72	2.79
$\beta_2$	2.51	2.42	2.50	2.52	2.51	2.57
$\phi^*$	0.80	0.80	0.80	0.80	0.80	0.80
$\beta_1^*$	3.08	2.98	3.07	3.21	3.20	3.26
$\beta_2^*$	2.90	2.81	2.89	3.00	2.98	3.04

Note: 1) L = local buckling, D = distortional buckling;

2)  $\beta_1$ ,  $\beta_1^*$  and  $\beta_2$ ,  $\beta_2^*$  were determined based on the load combinations of 1.2DL+1.6LL and 1.2DL+1.5LL, respectively;

3)  $\beta_1$ ,  $\beta_2$  and  $\beta_1^*$ ,  $\beta_2^*$  were calculated with the resistance factors of 0.90 and 0.80, respectively.

Table 4: Comparison of test and numerical results with predicted strengths for CFS built-up closed section beams

	$M_{Exp}$ and $M_{FE}$					
	$M_{DSM-S}$	$M_{DSM-2t}$	$M_{DSM-t}$	$M_{DSM-S}$	$M_{DSM-2t}$	$M_{DSM-t}$
Dominated failure	L	L	L	D	D	D
Number of data	11	13	11	44	42	44
Mean ( $P_m$ )	0.84	0.85	0.84	0.97	0.96	0.98
COV ( $V_p$ )	0.118	0.117	0.117	0.055	0.061	0.057
$\phi$	0.90	0.90	0.90	0.90	0.90	0.90
$\beta_1$	1.62	1.68	1.62	2.40	2.33	2.42
$\beta_2$	1.42	1.48	1.43	2.18	2.12	2.21
$\phi^*$	0.80	0.80	0.80	0.80	0.80	0.80
$\beta_1^*$	2.05	2.11	2.05	2.88	2.81	2.90
$\beta_2^*$	1.85	1.91	1.86	2.66	2.59	2.68

Note: 1) L = local buckling, D = distortional buckling;

2)  $\beta_1$ ,  $\beta_1^*$  and  $\beta_2$ ,  $\beta_2^*$  were determined based on the load combinations of 1.2DL+1.6LL and 1.2DL+1.5LL, respectively;

3)  $\beta_1$ ,  $\beta_2$  and  $\beta_1^*$ ,  $\beta_2^*$  were calculated with the resistance factors of 0.90 and 0.80, respectively.

The comparisons of ultimate moments obtained from the experiments ( $M_{Exp}$ ) and FE analyses ( $M_{FEA}$ ) with the predicted nominal moment capacities ( $M_{DSM-S}$ ,  $M_{DSM-2t}$ ,  $M_{DSM-t}$ ) calculated by DSM equations are summarized in Table 3 and Table 4 for the CFS built-up open and closed section beams, respectively. For the built-up open sections, the mean values of experimental and numerical-to-predicted moment capacities vary from 1.19 to 1.21 and 1.06 to 1.07 with the corresponding COV ranged from 0.178 to 0.183 and 0.043 to 0.064 for dominated failure modes of local buckling and distortional buckling, respectively. It reveals that the current DSM equations provide overall conservative predictions for the CFS built-up open section beams, and the predicted strengths are more conservative for the open sections subjected to local buckling than distortional buckling. For the built-up closed sections, the mean values of experimental and numerical-to-predicted moment capacities vary from 0.84 to 0.85 and 0.96 to 0.98 with the corresponding COV ranged from 0.117 to 0.118 and 0.055 to 0.061 for dominated failure modes of local buckling and distortional buckling, respectively. It is shown that the DSM equations are generally unconservative for the CFS built-up closed section beams, especially for the sections controlled by local buckling. It is also noticed that discrepancies between the predicted moment capacities ( $M_{DSM-S}$ ,  $M_{DSM-2t}$ ,  $M_{DSM-t}$ ) based on the solid blocks finite strip model as well as the integrated built-up section models with double plate thicknesses and single plate thickness at the overlapped area are small.

## 5. Conclusions

The experimental and numerical investigations were conducted to understand the flexural behaviour of CFS built-up open and closed sections subjected to local buckling, distortional buckling as well as their interactions. In the experimental study, five minor axis bending tests were carried out on the newly designed built-up sections. The ultimate moments and failure modes were obtained to verify the FE models. In the numerical simulation, the validated FE models were employed to perform an extensive parametric study. A total of 107 numerical data over a wide range of sectional parameters were further generated. The moment capacities obtained from the tests and FE analyses were compared with the nominal flexural strengths determined by DSM equations that specified in the AISI S100 (2016) and AS/NZS 4600 (2018) to evaluate the suitability of current design rules. The elastic buckling analysis was undertaken using three different models including the solid blocks model as well as the integrated models with double plate thicknesses and single plate thickness at the overlapped area of the built-up sections. In general, it is found that the predicted flexural strengths calculated by codified DSM equations are conservative for the CFS built-up open section beams, while unconservative for the CFS

built-up closed section beams. Therefore, further study is underway to develop more suitable design guidelines.

## References

- ABAQUS (2018). "ABAQUS/Standard user's Manual Volumes I-III and ABAQUS CAE Manual." *Version 2018*, Hibbitt, Karlsson & Sorensen, Inc, Pawtucket, USA.
- AISI (2016). "North American specification for the design of cold-formed steel structural members." *AISI S100-16*, American Iron and Steel Institute, Washington, DC.
- AS/NZS (2018). "Design of cold-formed steel structures." *AS/NZS 4600: 2018*, Standards Australia and Standards New Zealand, Sydney, Australia.
- Li, Q.-Y., and Young, B. (2019). "Tests of cold-formed steel built-up open section beam-columns." *In: Proceedings of the 7th International Conference on Structural Engineering, Mechanics and Computation*, Cape Town, South Africa.
- Li, Q.-Y., and Young, B. (2021). "Buckling behaviour of cold-formed steel built-up closed section members under combined compression and bending." *In: Proceedings of the 8th International Conference on Coupled Instabilities in Metal Structures*, Lodz, Poland.
- Li, Y.-L., Li, Y.-Q., and Shen, Z.-Y. (2016). "Investigation on flexural strength of cold-formed thin-walled steel beams with built-up box section." *Thin-Walled Structures*, 107, 66-79.
- Manikandan, P., and Sukumar, S. (2016). "Behaviour of cold-formed steel built-up closed section with intermediate web stiffener under bending." *Asian Journal of Civil Engineering* 17(3), 289-297.
- Schafer, B. W., Li, Z., and Moen, C. D. (2010). "Computational modeling of cold-formed steel." *Thin-Walled Structures*, 48(10-11), 752-762.
- Wang, L., and Young, B. (2015). "Beam tests of cold-formed steel built-up sections with web perforations." *Journal of Constructional Steel Research*, 115, 18-33.
- Wang, L., and Young, B. (2016). "Behavior of cold-formed steel built-up sections with intermediate stiffeners under bending. I: Tests and numerical validation." *Journal of Structural Engineering*, 142(3), 04015150.
- Wang, L., and Young, B. (2016). "Behavior of cold-formed steel built-up sections with intermediate stiffeners under bending. II: Parametric study and design." *Journal of Structural Engineering*, 142(3), 04015151.
- Ye, J., Hajirasouliha, I., Becque, J., and Pilakoutas, K. (2016). "Development of more efficient cold-formed steel channel sections in bending." *Thin-Walled Structures*, 101, 1-13.

## **The influence on portal frame buckling of different cladding systems – a comparative numerical study considering stressed skin effect**

Zsolt Nagy<sup>1</sup>, Andrea Kelemen<sup>2</sup>, Mihai Nedelcu<sup>3</sup>

### **Abstract**

In 2016 the authors investigated the stressed skin effect of trapezoidal steel sheeting and of deep deck sheeting as roof cladding on the pitched roof portal frame structure, in terms of buckling modes and the load multiplication factor, by comparing the results of a traditional design model with the result of a numerical model including the diaphragm stiffness of the considered claddings. Later, in 2018 the influence of the purlin-to-beam connection stiffness on the stress skin action of trapezoidal steel sheeting was investigated. The study of stressed skin action was further extended by the authors to the effects given by sandwich panels in 2019, where a methodology was presented to including the stressed skin effect of sandwich panels in a simple and time effective way into the day-to-day design methodologies of common engineers. In 2021 the procedures were improved to present a comparison between different cladding types in terms of sway displacement of the frame structure with semi-rigid joints and load transfer by applying the developed methodology to a reference building. The purpose of the current paper is to compare and to estimate in a numerical manner the influence of the cladding type on the sway stability indicators of the structure, such as buckling modes and critical load multiplication factors  $\alpha_{cr}$ . The paper presents comparative results obtained in terms of stabilization effects given by trapezoidal sheeting and mineral wool core sandwich panels supported by Z purlins applied on the reference cold-formed steel structure.

### **1. Introduction**

The study of stressed skin action provided by the cladding systems of structures has a history going back to the early 1950s, showing that the cladding system has a stiffening effect on the framed structure. The structural engineer can have the choice to account or neglect these effects, but whatever the choice might be, both options raise a lot of technical aspects, which are not handled in a clear manner in the design codes. By neglecting the cladding contribution, the frame design will continue without accounting any beneficial effect of the stressed skin existence, and in the same time, the cladding-structure interaction could create some collateral effects, which could damage the primary role of the covering skin, such as the waterproofing, especially in case of roof cladding. However, accounting for stressed skin effect could also raise several issues in structural design. Firstly, stressed skin effect imposes the reclassification of the cladding as part of the primary structure, which means that special attention must

---

<sup>1</sup> Associate Professor, Technical University of Cluj, zsolt.nagy@dst.utcluj.ro

<sup>2</sup> Researcher, PhD student, Technical University of Cluj, andrea.dezo@mecon.utcluj.ro

<sup>3</sup> Associate Professor, Technical University of Cluj, mihai.nedelcu@mecon.utcluj.ro

be allocated for the cladding during the building use. Secondly, the stressed skin effect consideration in structural calculation requires reliable structural modelling techniques, which can be used by the structural designer, to quantify the contribution of the cladding in overall design of the building structure. Thirdly, the use of cladding as structural element can impose some special detailing rules - different from the usual details - which are focusing especially on load carrying capacity on cladding level itself and less on waterproofing. The first problem is, that designers have no clear rules, to decide when they need to pay special attention during design process for structure-cladding interaction. Secondly, if this interaction proved to be important, how would they proceed to avoid undesirable defects during the building use caused by cladding-structure interaction. Since modelling of roof and wall skin makes the calculation procedure very complex, reliable simplification methods would be the most efficient approach.

Analytical calculation procedures for determining the shear stiffness provided by such trapezoidal sheet diaphragms were presented by Davies and Bryan (1982), which later, in 1995, became the basis of the ECCS – European recommendations for the application of metal sheeting acting as a diaphragm – stressed skin design (ECCS Technical Working Group 7.5. 1995). In 2014 the ECCS recommendations were extended to stabilization of steel structures by sandwich panel cladding (ECCS Technical Working Group TWG 7.9 & CIB Working Commission W056 2014). This analytical shear stiffness evaluation method was greatly influenced by the results of a European research project called EASIE- “Ensuring Advancement in Sandwich Construction through Innovation and Exploitation” (Käpplein and Misiek 2011), which was carried out between 2008 and 2011. In current practice, this stabilizing effect of the cladding system is almost always disregarded, due to difficulties in applying the analytical evaluation methods for moderately complex structures, or to integrate these methods in a numerical approach. By doing so, the designer reduces the calculation time and assumes that the evaluation is on the safe side. However, the obtained structural response is a simplified one, which does not include cladding-structure interaction. In reality, the cladding system will interact with the structure and as an effect, horizontal deformations will decrease. The structural configuration modelled by most of designers would be valid only in the case when the cladding system is damaged and is no longer able to transfer loads through its planar surface, which would also mean in some cases, that they are no longer able to fulfil their primary role as a weathering barrier against water infiltration.

The influence of stressed-skin diaphragm action on the optimal design of the internal frame of a cold-formed steel portal framing system with semi-rigid joints has been investigated by Phan et al. (2015). They showed that if the combined effect of both stressed-skin action and semi-rigidity of the joints are ignored, and the frame is designed based on a rigid joint assumption, the failure of the cladding system could occur before first yield of the frame.

Vacev et al. (2020) studied the stressed skin effect on complex FEM models. They also proposed some practical guidelines for the stressed skin design using FEM, but it is hard to believe that such complex models will be adopted by design engineers in design process for portal frame structures, even if the proposed numerical model was developed for arbitrary combination of sheet profiles, fastener devices and sheet thicknesses.

Nagy et al. (2016) focused on the stressed skin effect obtained by trapezoidal and deep deck sheeting, in terms of buckling modes and load multiplication factors. Later, an in-depth analysis regarding the extent of influence gained by the purlin-to-beam connection stiffness was developed (Nagy et al. 2018). The stressed skin effect study was further extended by the authors to stressed skin effect obtained by sandwich panels (Nagy et al. 2019a), which included a methodology to integrate the shear stiffness of

sandwich panel diaphragms into 3D structural models. The presented methodology was also validated by comparing the results of a numerical model with the experimental testing results of a sandwich panel diaphragm, which was performed by Kunkel and Lange (2015).

The purpose of the current paper is to compare and to estimate in a numerical manner the influence of the cladding type on the stability indicators of the structure, such as sway buckling mode, expressed by critical load multiplication factor  $\alpha_{cr}$ . The research focuses on two cladding types, by applying them on a reference building, namely trapezoidal sheeting and mineral wool core sandwich panels supported by Z purlins.

## 2. Developed numerical models and computed results

The reference model consists in an industrial hall type of building, composed of thin walled C250/3 columns and beams. The structure has a span of 6 m and three bays of 3 m each, adding up to a total length of 9 m. The flexible wind bracings placed in the longitudinal wall of the structure are  $\varnothing 20$  rods, while the rigid wind bracings at the gable frames are of rectangular hollow steel sections SHS80x4. The ridge and eave pressure bars are also SHS80x4 profiles. To have a more realistic approach, the eave and the ridge joint semi-rigidity is included into the analysis based on previous experimental results (Nagy et al. 2019b), considering a stiffness of 2948 kNm/rad for the ridge joint and 2062 kNm/rad for the eave joint. The considered joint details can be seen in Fig. 1.

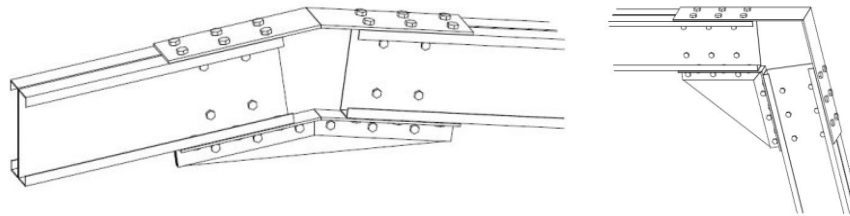


Figure 1: Ridge joint (left) and eave joint (right) detail used in the frame.

The relevant sway buckling modes and associated load amplification factors are computed for the considered structural models:

- Reference model without any cladding (Fig. 2 – left);
- Reference model with trapezoidal sheeting (Lindab LTP45 – thickness of 0.6 mm) as roof cladding, placed on top of Z150/2 purlins and fixed using LD6T self-drilling screws through every narrow trough (Fig. 2 – middle);
- Reference model with sandwich panel (TeraSteel ISOAC5MW – mineral wool core and thickness of 60 mm) as roof cladding, placed on top of Z150/2 purlins and fixed using EJOT JT3 D6H 5.5/6.3 type screws in every 250 mm (Fig. 2 – right);

The same loading is applied on all three building structure, consisting in regular building loads (permanent loading of self-weight, snow load and wind load), which are multiplied by the typical safety factors, recommended by the Eurocode. The load cases are as follows:

- (P) Self-weight of cladding: 0.25 kN/m<sup>2</sup>;
- (S) Characteristic snow load: 1.50 kN/m<sup>2</sup>;
- (W) Reference wind pressure: 0.40 kN/m<sup>2</sup>.

The structure was modelled using 14DOF bar elements. Having a finite element with warping deformation, global stability is possible to be computed on 3D model. For local and distortional buckling

of the cold-formed profiles, effective cross section properties are computed, according to EN1993-1-3 rules. Detailed description about the developed structural models can be found in Nagy et al. (2021). For simplicity, only one dominant load combination has been generated and used for comparison between the different models (1.35P+1.5S+1.05W). The reference structure, without any roof cladding, loaded by the above-mentioned load combination reaches a utilization factor of 80.7 %, while the sway type frame buckling can be observed at a load multiplication factor of 32.2 on the 3D model. The sway type frame buckling was also evaluated on a simplified 2D model, assuming same frame loading and axially rigid supports in the points where the roof purlins are connected to the frame. Due to this assumption, the sway stability of the isolated frame should result higher. Interestingly, the single frame analysis with this supporting condition resulted with the lowest eigen value,  $\alpha_{cr.}=30.28$ . Analytical calculation, using the formula of EN1993-1-1 given by Eq. 1, seems to overestimate the eigen value, obtaining  $\alpha_{cr.}=29.42$ . According to previous research results, it is expected that adding the stressed skin effect, will have a positive influence on the overall stability of the structure expressed by the recorded sway buckling eigenvalues. The comparison between computed load multiplication factors on 2D and 3D structural models have a key importance in the current study. Furthermore, the computed values with FEM are compared with the analytically calculated values of load multiplication factor  $\alpha_{cr}$ , using simplified method of EN1993-1-1 given by Eq. 1.

$$\alpha_{cr} = \left( \frac{H_{Ed}}{V_{Ed}} \right) \left( \frac{h}{\delta_{H.Ed}} \right) \quad (1)$$

where  $H_{Ed}$  is the total design horizontal load,  $V_{Ed}$  is the total design vertical load,  $h$  is the story height, and  $\delta_{H.Ed}$  is the horizontal displacement at the top of the story.

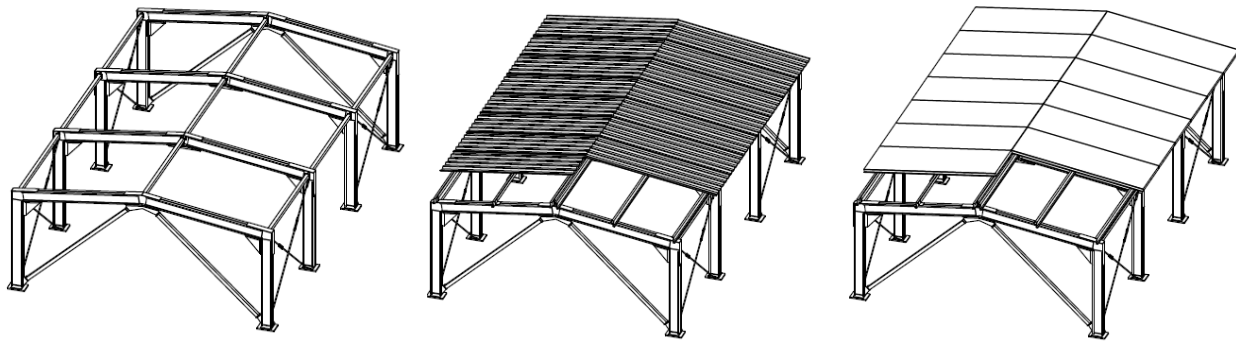


Figure 2: Analyzed structural configurations: structure only (left), structure with trapezoidal sheeting roof cladding (middle) and structure with sandwich panel roof cladding (right).

### 2.1 Results for roof skin using trapezoidal sheeting and Z purlins

The trapezoidal sheeting for the roof diaphragm was modelled by equivalent hat (omega) profiles, as bar element. The omega profiles composing one trapezoidal sheet were connected via continuous links. At side overlaps, where two trapezoidal sheets are fixed with seam fasteners, the edge omega profiles were connected with semi-rigid links (Nagy et al. 2021). The link elements should be free to rotate, while the stiffness in x and y direction should be set as the individual panel rigidity given by the seam fasteners ( $1/c_{2.2}$  – determined as in the ECCS recommendations (ECCS Technical Working Group 7.5. 1995) divided by the number of seam fasteners on a shear panel. The rigidity of the shear panel given by seam fasteners ( $1/c_{2.2}$ ) was determined as 19.246 kN/mm, which was divided by 27 (the number of

seam fasteners in one shear panel). Thus, the link, representing the seam fasteners, resulted a stiffness of 0.713 kN/mm in x and y direction and was free to rotate. The self-weight of the elements representing the cladding and their connections were disregarded. Details concerning the modelling of the cladding and the sway buckling mode on the 3D model is presented in Fig. 3. The ultimate shear capacity of the trapezoidal sheeting diaphragm was estimated as 7.171 kN, in accordance with the ECCS recommendations (ECCS Technical Working Group 7.5. 1995), this being equal with the ultimate applied load on the intermediate frames. Under the assumed load combination, the maximum shear force at intermediate frames was 4.95 kN, which was significantly lower than the ultimate shear capacity of the trapezoidal sheeting diaphragm.

In case of the 2D frame model, the cladding effect was introduced by equivalent sway deformation, using a spring stiffness (Fig. 4), which leads to same frame deformation as it was obtained on 3D model. In case of roof skin using trapezoidal sheeting and Z purlins, under the considered load combination a 4 mm sway deformation was evaluated, resulting an equivalent eave spring stiffness of 0.47 kN/mm (Table 1). The computed load multiplication factors for 2D and 3D structural models are centralized in Table 2.

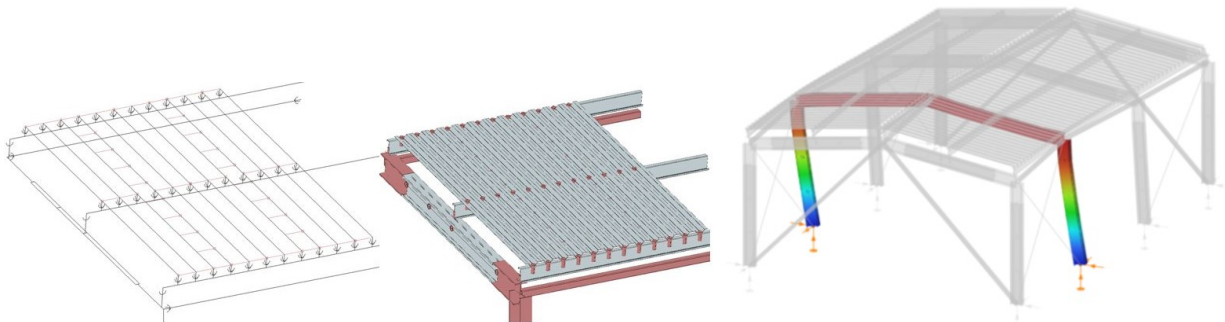


Figure 3: Cladding modelling details (left) and sway buckling mode on 3D model (right), in the case of structure with single skin trapezoidal sheeting

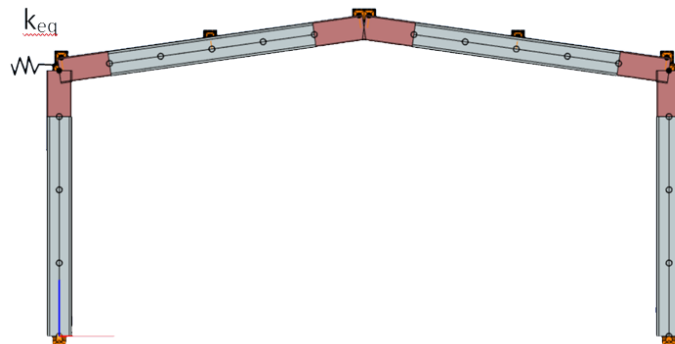


Figure 4: 2D frame model with equivalent eave spring

## 2.2 Results for roof skin using sandwich panels and Z purlins

In the case of the sandwich panel cladding, the individual steel plates, representing the panels were not connected to one another, since the presence of seam fasteners was disregarded. The width of the steel plates was considered as the distance between the outer-most screws which fix the sandwich panel to the purlin. The translational stiffness of the fasteners connecting the sandwich panels to the purlins ( $k_v$ ) was evaluated as 2.688 kN/mm, which results in a flexibility ( $1/k_v$ ) of 0.372 mm/kN. The Consteel model calibration can be found in Nagy et al. (2021). The obtained cross-section for purlin connection was

∅17.68 circular rod, with a length of 105 mm. The cladding modelling details and the sway buckling mode on 3D model can be seen in Fig. 5. The load-bearing capacity of the fastener between the purlins and the sandwich panels was determined as being equal to 1.18 kN, which under the assumed load combination was exceeded by approximately 23 %, considering the most utilized fastener. In case of the 2D frame model, similarly as in case of trapezoidal sheeting skin, the cladding effect was introduced by equivalent sway deformation, using a spring stiffness, which leads to same frame deformation as it was obtained on 3D model. In case of roof skin using sandwich panels and Z purlins, under the considered load combination a 4.3 mm sway deformation was evaluated, resulting an equivalent eave spring stiffness of 0.42 kN/mm (Table 1). The computed load multiplication factors for 2D and 3D structural models are centralized in Table 2.

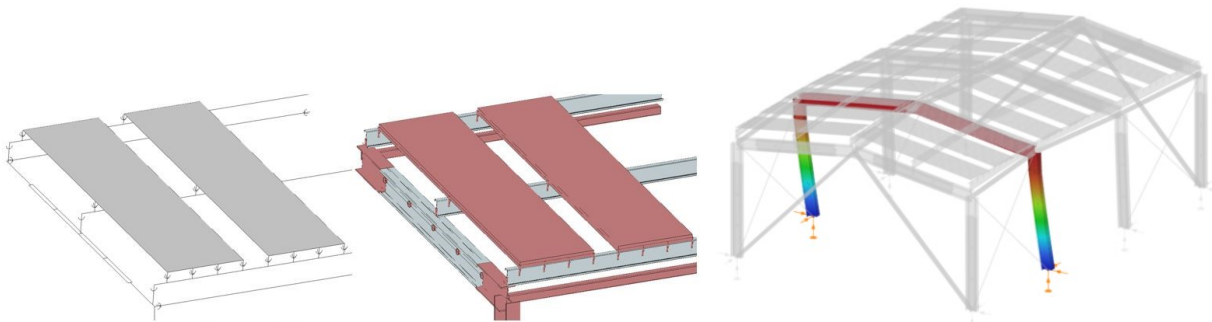


Figure 5: Cladding modelling details (left) and sway buckling mode on 3D model (right), in the case of structure with sandwich panel cladding

Table 1: Spring coefficient values for 2D frame calculation

Model	$\delta$ (mm)	$H_{Ed}$ (2D/3D) (kN)	$k_{eq}$ (kN/mm)
Trapezoidal sheeting	4.0	2.40/2.50	0.47
Sandwich panel	4.3	2.48/2.97	0.42
Frame only (reference)	10.2	4.15/4.27	-

Table 2: Load multiplication factor ( $\alpha_{cr}$ ) values

Evaluation procedure	Only structure	Structure with trapezoidal sheeting	Structure with sandwich panels
FEM 3D	32.2	123.23	77.43
FEM 2D	30.28	64.42	60.84
Eq. 1 (EN1993-1-1)	29.42	46.27	50.37

### 3. Discussions

The comparative results on the 3 studied models (frame only, structure with trapezoidal skin and structure with sandwich panels) shows that stressed skins have a stiffening effect on the frame structure, reducing considerable the deformations under the same applied loads. Using as reference the structure only, without any cladding, the sway deformation under considered loads resulted 10.2 mm. Making the evaluation of sway stability of the frame, the load multiplication factor  $\alpha_{cr}$ , using simplified method of EN1993-1-1 given by Eq. 1 resulted 29.42.

The computed analytical value seems to be lower than those computed on 2D or 3D structural models (30.28 for 2D frame and 32.2 for 3D frame). However, the analytical formula is approximative, applicable in case of non-significant rafter compression loads, which can be a limitation in case of bigger scale

framed structures, where axial loads in the rafter can be significant. Considering the 2D frame model with equivalent spring stiffness (Fig. 4) there is a reasonable correlation between the obtained  $\alpha_{cr}$  values, using analytical and FEM calculation on 2D model. The values computed on 3D models using linear elastic analysis (LEA) are much higher for both cladding types. Anyway, as it was observed also in Nagy et al. (2021), the diaphragm composed of trapezoidal sheeting offers a higher stabilizing effect and a higher shear capacity, than sandwich panel diaphragm. Furthermore, under the considered load level, the sandwich panel diaphragm exceeds the evaluated shear capacity, meaning that the sandwich panel stiffness may decrease under the effect of design loads. This means, that the behavior of the sandwich panel after that point should not be regarded as linear and internal face failure around the fixing screws to purlin will occur. The stabilization effect of sandwich panel beyond the capacity limit will decrease, the frame behavior with cladding tending to reach the frame only behavior. This will not be a simultaneous effect for all the frames, it will be a gradual process, as the connections of the sandwich skin will fail step-by-step, without reaching any ultimate limit state stage in the framed structure. The mechanism in case of the trapezoidal sheeting skin will be similar, but different, due to the much higher elastic deformation capacity (Nagy et al. 2021). Due to the differences in deformation capacity between the sandwich panels and trapezoidal sheeting, trapezoidal sheeting skin will be able to preserve the stabilizing effect for a longer time period. Due to this property, frame-cladding interaction will have less effect on the trapezoidal skin than on sandwich panel skin. On the other hand, due to this difference in cladding behavior, in case of a larger scale structure, there will be important differences in sway stability of internal frames, even if the frames will be identical.

At the same time, as it was observed also by Phan et al. (2015), there is a migration of loads to the gable frames (these frames are acting as support for roof diaphragm), for this reason, gable frames need to be adequately designed for these supplementary effects. The load redistribution to the gable frames is clearly evidenced by the differences in total horizontal reactions  $H_{Ed}$ , computed at the internal frame column base between the models with and without stressed skin (Table 1).

#### **4. Conclusions**

Two specific methodologies were presented for the inclusion of the diaphragm action of roof claddings into a 3D structural analysis of a building structure: one for sandwich panels and one for trapezoidal sheeting. Both procedures were validated on panel models by comparing the results obtained through the proposed combined analytical and numerical procedures, with the results of experimental testing, described in Nagy et al. (2021). The comparisons between test results and developed panel models in terms of deformations are reasonable and proposed methodologies can integrate the desired phenomenon on 3D structural models in an easy and fast way, giving the possibility for structural engineers to deal with the interaction of structure-cladding interaction and simplified approach for sway stability evaluation.

As the case study shows, the structure-cladding interaction can highly influence the sway stability of the structure on which it is applied: without cladding the structure can be classified as sway, with cladding contribution the structure can migrate in a non-sway category, but depending on the cladding behavior, part of the structure or the overall structure can become again sway sensitive, considering the cladding deformation capacity. Claddings with sandwich panels have more reduced deformation capacity compared to claddings with trapezoidal sheeting. Due to this, cladding-structure interaction can affect the integrity of the sandwich panel primary role as waterproofing, especially in the cases when cladding contribution is totally disregarded in the design process of the framed structure. It should be noted, that under the considered loads, the sandwich panel diaphragm exceeded the evaluated shear capacity, meaning that the sandwich panel stiffness may decrease under the effect of design loads. Assuming a

linear elastic analysis and using a constant diaphragm stiffness, if the cladding deformation limit is exceeded, such a model can underestimate the real structural deformation. For more consistent calculation, bilinear behavior should be included in the model with sandwich panel roof claddings.

Developed structural models shows that sway stability of real structures can present large scattering depending on the deformation capacity of the applied claddings and can offer a better understanding of structural behavior for practicing engineers. Load multiplication factor evaluation would be limited to the values obtained from the simplified 2D analysis.

The results of the two structural models should not be generalized, since these values may vary if the number of utilized fasteners is increased or if the type of used fasteners is changed. For in-depth understanding of the two shear diaphragms, research will continue with laboratory testing and parametric study.

### Acknowledgments

This work was supported by a grant of the Ministry of Research, Innovation and Digitization, CNCS/CCCDI – UEFISCDI, project numberEUROSTARS-2019-E!113493-CFSExpert, within PNCDI III.

### References

- Davies, J. M., Bryan, E. R. (1982). "Manual of Stressed Skin Diaphragm Design." London: Granada.
- ECCS Technical Working Group 7.5. (1995). "European Recommendations for the Application of Metal Sheeting acting as a Diaphragm – Stressed Skin Design." European Convention for Constructional Steelwork.
- ECCS Technical Working Group TWG 7.9 & CIB Working Commission W056 (2014). "European Recommendations on the Stabilization of Steel Structures by Sandwich Panels." International Council for Research and Innovation in Building and Construction & European Convention for Constructional Steelwork.
- Käpplein, S., Misiak, T. (2011). "EASIE project - Report no. D3.3 – part 2: In-plane shear resistance of sandwich Panels." Karlsruhe: Ensuring Advancement in Sandwich Construction Through Innovation and Exploitation.
- Kunkel, C., Lange, J. (2015). "Experimental analysis on the bearing capacity of sandwich panel joints." *20th International Conference on Composite Materials; Copenhagen, Denmark, 19 – 24 July 2015.*
- Nagy, Zs., Pop, A., Moiş, I., Ballok, R. (2016). "Stressed Skin Effect on the Elastic Buckling of Pitched Roof Portal Frames." *Structures*, 8 (2) 227-244.
- Nagy, Zs., Moiş, I., Pop, A., Dező, A. (2018). "The influence of purlin-to-beam connection stiffness in stress skin action on portal frames." *ICTWS 2018; Lisbon, Portugal, 24 – 27 July 2018.*
- Nagy, Zs., Nedelcu, M., Dező, A. (2019a). "Stressed Skin Effect on the Elastic Buckling of Pitched Roof Portal Frames." *Advances in Engineering Materials, Structures and Systems: Innovations, Mechanics and Applications: Proceedings of the 7th International Conference on Structural Engineering, Mechanics and Computation (SEMC 2019)*, 854-859.
- Nagy, Zs., Muresan, A., Fodor, R. (2019b). "Experimental investigations for joints made by cold-formed sigma profiles." *18th International Conference Modern Technologies for the Third Millennium*, 247-252.
- Nagy, Zs., Dező, A., Bács, B., Zaharia, G. (2021). "Comparative study between stressed skin effect of trapezoidal sheet and sandwich panel roof cladding." *Proceeding of the 9th European Conference on Steel and Composite Structures -Eurosteel*, in press.
- Phan, D.T., Lim, J.B.P., Tanyimboh, T.T., Wrzesien, A.M., Sha, W., Lawson, R.M. (2015). "Optimal design of cold-formed steel portal frames for stressed-skin action using genetic algorithm." *Engineering Structures*, 93 (June) 36-49.
- Vacev, T., Zorić, A., Milić, M., Paunović, S., Nešović, I. (2020). "Stressed Skin Design Versus Braced Frame Design Through Efficient Numerical Modelling." *International Journal of Steel Structures*, 20 (August) 1209-1229.



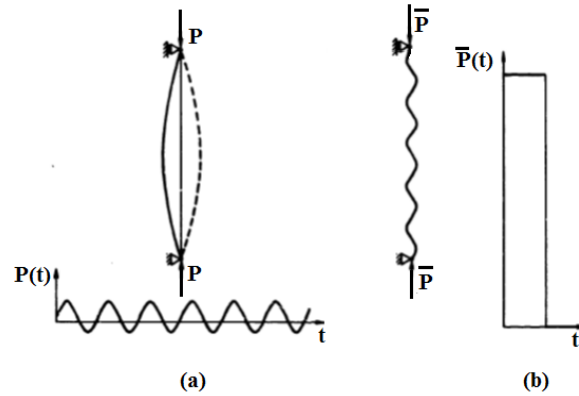


Figure 1: (a) Buckling under parametric resonance, (b) Pulse-type buckling [1].

Another type of vibration is sometimes also called pulse buckling. The structure will be deformed to unacceptably large amplitudes as a result of the transient response of the structure to the dynamic axially applied load [1]. One should note that the suddenly applied load might cause a permanent deformation due to the plastic response of the column, a snap to a larger post-buckling deformation or simply a return to its undeformed state. An example can be found in Fig. 1b, where the high-order buckling mode under short load duration is presented.

Loss of stability under pulse loading is associated with the rapid increase of structure deformations (e.g. Volmir or Budiansky-Hutchinson criteria) or achieving a given stress level (e.g. Petry-Fahlbusch criterion). It was observed that the structure could withstand a higher axial load before reaching the buckling condition, provided the load duration is short enough. Petry and Fahlbusch [2] observed an almost fourfold increase of dynamic buckling load when a very short load duration is analyzed. However, with the rise of load duration, it was observed that the structure is less resistant to pulse load than the static one [3].

The dynamic buckling of structures has been widely addressed in the literature. It started with the famous paper by Budiansky and Roth [5], through Hegglin's report on dynamic buckling of columns [6] and continued with Budiansky & Hutchinson [7] and Hutchinson & Budiansky [8] in the mid-sixties.

It is difficult to define a criterion of the critical load causing the structure to buckle under the subjected pulse loading. As presented by Kubiak [9] and also by Ari Gur [10], [11],[12] a new quantity is introduced called DLF (Dynamic Load Factor) to enable the use of the dynamic buckling criteria. It is defined as:

$$DLF \equiv \frac{\text{Pulse Buckling Amplitude}}{\text{Static Buckling Amplitude}} \equiv \frac{(P_{cr})_{dyn}}{(P_{cr})_{static}} \quad (1)$$

According to Kubiak [9], the most popular criterion had been proposed by Volmir for plates subjected to in-plane pulse loading. As quoted in [9], Volmir proposed the following criterion:

*"Dynamic critical load corresponds to the amplitude of pulse load (of constant duration) at which the maximum plate deflection is equal to some constant value k (k - half or one plate thickness)".*

Another very widely used criterion has been formulated and proposed by Budiansky & Hutchinson [5],[7],[8]. Originally, the criterion was formulated for shell-type structures but was also used for columns and plates. The criterion claims that: *"Dynamic stability loss occurs when the maximum deflection grows rapidly with the small variation of the load amplitude"*.

## 2. FE model and methodology

The analyses were performed on a CFRP cylindrical shell with the laminate stacking sequence  $[\pm 45^0/0^0/90^0]_s$ . The considered cylindrical shell has a radius  $R = 300$  mm, the length  $L = 705$  mm and the total thickness  $t = 1.448$  mm (eight plies, each with the thickness of 0.181 mm). The mechanical properties of CFRP are listed in Table 1.

Table 1: Mechanical properties of AS4/8552 CFRP.

	$E_1$ (GPa)	$E_2$ (GPa)	$\nu_{12}$ (-)	$G_{12}$ (GPa)	$\rho$ (g/cm <sup>3</sup> )
AS4/8552 CFRP	145	10.3	0.3	4.5	1.58

The numerical model of the cylindrical shell was created in ABAQUS 2017 using S4R shell elements. The finite element length is equal to 7.5 mm and was determined by the convergence analysis. The boundary conditions were applied to the nodes localized in both shell edges: in the bottom edge, all degrees of freedom are removed, while on the top one, only the axial displacement was possible. The loading was applied as a compressive force to one point localized on the upper edge and then transferred to all nodes at this edge. The assumed boundary conditions correspond to conditions assured during the laboratory test [12, 13].

In the investigation of the CFRP shell resistance to pulse loading, the following studies were performed:

- Static buckling analysis* – the analysis aims to determine the static buckling load and corresponding buckling shape. The study was performed numerically using the eigenvalue buckling analysis and dynamic explicit analysis. The numerical investigations were compared with the analytical calculations and with the results of the laboratory test [12, 13].
- Modal analysis* – modal analysis was carried out to define the natural frequency of the shell, and next - the natural bending period of the shell  $T_b$ . The outcomes of numerical calculations were confronted with laboratory test [12, 13].
- Dynamic buckling analysis* – pulse buckling analyses were performed numerically using the Explicit method. The shell is subjected to the pulse axially compressive loading, with the amplitude being a fraction or a multiplier of the static buckling load. The structure is loaded with various pulse shape (trapezoidal and sinusoidal), with the time being a fraction or a multiplier of the natural period of the shell. The numerical analyses were performed for the shell with initial geometric imperfections that corresponds to the lowest buckling mode.

## 3. Static buckling and modal analysis

The buckling load  $P_{cr}$  was determined analytically according to the following formula [15]:

$$P_{cr} = \frac{2\pi^3 R D_{11}}{L^2} \left[ m^2 \left( 1 + 2 \frac{D_{12}}{D_{11}} \beta^2 + \frac{D_{22}}{D_{11}} \beta^4 \right) + \frac{\gamma^2 L^4}{D_{11} \pi^4 m^2 R^4} \frac{A_{11} A_{22} - A_{12}^2}{A_{11} + \left( \frac{A_{11} A_{22} - A_{12}^2}{A_{66}} - 2A_{12} \right) \beta^2 + A_{22} \beta^4} \right] \quad (2)$$

where:  $L$ ,  $R$  – length and the radius of the cylinder, respectively

$n$ ,  $m$  – number of half-waves in the circumferential and axial directions,

$\beta$  – buckle aspect ratio ( $\beta = \frac{nL}{\pi R m}$ ),

$A_{ij}$ ,  $D_{ij}$  – elements of the extensional stiffness matrix and bending stiffness matrix

$\gamma$  – a correction factor, in the considered case  $\gamma=0.446$

The static buckling load was also determined numerically and compared with the experimental data. In the numerical calculations, the eigenvalue analysis was performed. Next, the non-linear analysis for the

model with initial geometric imperfections with the shape corresponding to the lowest buckling mode and the imperfections amplitude equal to 20% of the shell thickness ( $w_0=0.2t$ ) was carried out.

The results comparison is presented in Fig. 1 and Table 2. In Fig. 1, the comparison of buckling modes with the equilibrium paths obtained from laboratory test and non-linear analysis with initial imperfection is presented. In the upper left corner, the lowest buckling mode obtained from LB (Linear Buckling) analysis is also depicted. Significantly high results agreement was obtained in the buckling load estimation. A slight difference in the structure's stiffness in the pre-buckling regime and the buckling modes was obtained. This discrepancy could result from different imperfections, which were not applied to the FE model as thickness imperfection.

The comparison of buckling load obtained from analytical and numerical approach present high correlation. Similarly, the high agreement of the results was obtained from laboratory test and from FE non-linear analysis, where the buckling load of the imperfect structure was studied. The difference between results obtained from the experiment and FE analysis is less than 1% which confirms the correctness of the adopted numerical model and its application to further dynamic buckling analyses.

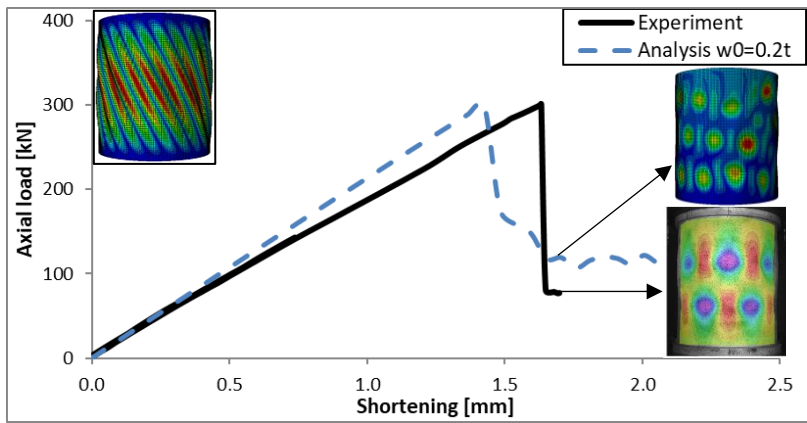


Figure 1: Comparison of equilibrium path obtained from experiment [16] and FE analysis.

Table 2: Static buckling load of the analyzed shell.

Method	Pcr [kN]
Analytical formula	426.2
FEM Linear buckling analysis	402.6
FEM Explicit analysis	299.8
Laboratory test	301.2

To determine the natural period of duration, a modal analysis was performed. The lowest natural frequency obtained from FE analysis  $f_{FE}=293.8\text{Hz}$ , while from laboratory test  $f_{EXP}=243\text{Hz}$ . The significantly high difference in natural frequency estimation is a consequence of the applied boundary conditions. The boundary conditions assured during the numerical analysis differs slightly from these assumed in laboratory test.

**3. Dynamic buckling analysis**

The dynamic buckling analysis was performed for the model with initial geometric imperfections  $w_0=0.2t$ . From numerical calculations, the first natural bending period  $T_b = 3.40 \text{ ms}$  was determined. The structure was subjected to pulse loading with six different load duration, being a fraction or a multiplier of  $T_b$  ( $T = 0.43\text{ms}$ ,  $T = 0.85\text{ms}$ ,  $T = 1.70\text{ms}$ ,  $T = 3.40\text{ms}$ ,  $T = 6.80\text{ms}$  and  $T/T_b = 17.00\text{ms}$ ). Different pulse shapes: trapezoidal and sinusoidal, were considered. The trapezoidal pulse shape could be described by the following equation:

$$\begin{aligned}
0 \leq t \leq 0.1T \quad P(t) &= \frac{10P_0}{t} \\
0.1T \leq t \leq 0.9T \quad P(t) &= P_0 \\
0.9T \leq t \leq T \quad P(t) &= \frac{-10P_0}{t}
\end{aligned} \tag{3}$$

The sinusoidal pulse shape is defined as:

$$0. T \leq t \leq T \quad P(t) = P_0 \sin\left(\frac{\pi t}{T}\right) \tag{4}$$

To assess the shell resistance to pulse loading, the structure was observed in the time  $T \sim 60T_b$ . Dynamic Load Factor was estimated by the application of the Budiansky & Hutchinson (B&H) criterion. The details of the B&H criterion application are presented in [17]. The high sensitivity to initial imperfections characterizes shell structures [18, 19]. Thus, DLF was calculated according to eq. 1, assuming that the static buckling load  $P_{cr}$  is the buckling load obtained from non-linear analysis for a model with initial geometric imperfection ( $P_{cr} = 299.8\text{kN}$ ).

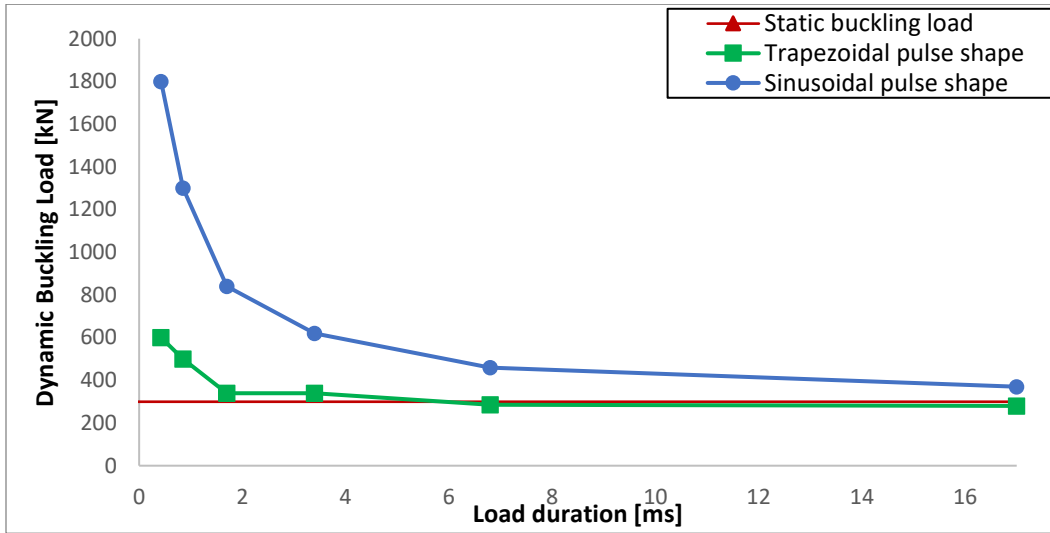


Figure 2: The effect of pulse duration and pulse shape on the Dynamic Buckling Load.

In Fig. 2, the change of Dynamic Buckling Load with the increase of load duration for the shell subjected to trapezoidal- and sinusoidal-shaped pulse load is presented. For load duration lower than the first natural bending period of the structure ( $T < 3.40\text{ms}$ ), for both considered pulse shapes, the shell is significantly more resistant to pulse load than the static one. In this regime, the resistance increases with the decrease of the load duration (up to  $P_{dyn} = 1800\text{kN}$  for sinusoidal pulse load and  $P_{dyn} = 600\text{kN}$  for trapezoidal pulse load; for load duration  $T = 0.43\text{ms}$ ). A different tendency is observed for  $T > 3.40\text{ms}$  ( $T > T_b$ ), where the Dynamic Buckling Load is almost unchanged for  $3.40\text{ms} < T < 17\text{ms}$ . For trapezoidal pulse shape, the dynamic buckling load is near the static buckling load in that load duration regime. Comparison of two pulse shapes reveals higher resistance to pulse loading for sinusoidal pulse shape than the trapezoidal one. The pulse shape has the most significant effect on the Dynamic Buckling Load for a short load duration ( $T = 0.43\text{ms}$ ). For that load duration, the Dynamic Buckling Load is three times higher for sinusoidal pulse load than trapezoidal load shape. With the increase of load duration, the influence of load shape on the buckling resistance decreases slightly. Nevertheless, the dynamic buckling load for sinusoidal pulse shape is at least thirty percent higher than the trapezoidal one. The lower dynamic buckling load obtained for the trapezoidal pulse shape could be explained by the high value of the pulse energy [19]. Pulse energy is described as the area under the curve representing the time dependence of load. The trapezoidal pulse shape is characterized with higher pulse energy, than the sinusoidal one. This tendency is reflected in Dynamic Pulse Load ( $P_{dyn}$ ) and Dynamic Load Factor (DLF) (Table 3).

Table 3: Dynamic Buckling Load and Dynamic Load Factor for analyzed pulse shapes and load duration

		Load duration [ms]					
		0.03	0.05	1.00	3.00	10.00	100.00
Trapezoidal pulse shape	$\lambda_{dy}$	0.00	500	3.00	3.00	2.5	2.0
	$\lambda_{dy}$	2.00	1.00	1.13	1.13	0.05	0.03
Sinusoidal pulse shape	$\lambda_{dy}$	1.00	1300	0.0	0.20	0.0	3.0
	$\lambda_{dy}$	0.01	0.3	2.00	2.00	1.5	1.23

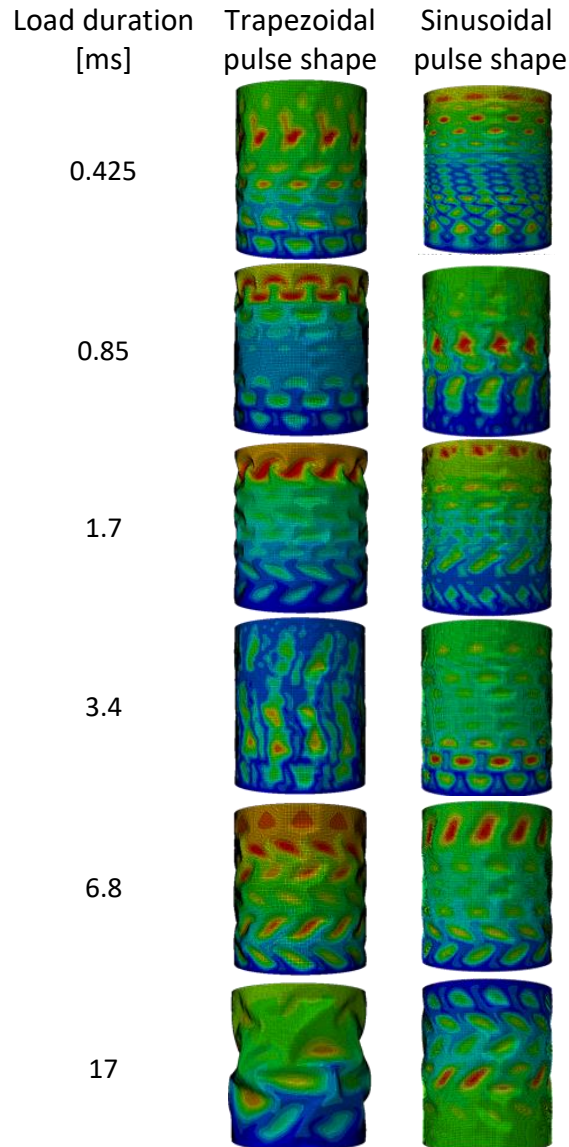


Figure 3: Buckling modes for trapezoidal pulse shape.

The effect of pulse duration and pulse shape on the buckling mode was also studied. The results are presented in Fig. 3. High sensitiveness of load duration on the buckling mode was obtained. A diamond shape is noticed for lower load duration, while the increase of the load duration leads to the appearance of the oblique waves.

#### **4. Conclusions**

The dynamic buckling behaviour of a composite cylindrical shell has been studied numerically using the ABAQUS code. The numerical model was validated experimentally on the shell subjected to static axial compressive loading. To assess the resistance of the structure to pulse loading, the Budiansky & Hutchinson criterion was applied. The effect of the load duration and pulse shape was investigated. The high impact of load duration on dynamic buckling resistance was observed. For load duration lower than the natural period of duration, the shell structure is few time more resistant to pulse loading compared to the static load. For duration longer than the natural bending period of the shell the Dynamic Buckling Load is almost unchanged with the increase of load duration. The high effect of the pulse shape was also analyzed. Two different shapes of pulse load were studied: sinusoidal and trapezoidal. Higher value of the Dynamic Load Factor was obtained for sinusoidal pulse shape than for trapezoidal shape.

#### **Acknowledgements**

The present study has been performed during a research visit by the first and second authors at the Delft University of Technology. They would like to thank the Aerospace Structures and Computational Mechanics group for this opportunity. The first author would like to extend thanks for the financial support received from a project co-financed by the European Union under the European Social Fund, as part of the Operational Program: Knowledge Education Development, project No. POWR.03.02.00e00e1042/16e00.

## References

- 1 □ Lindberg, H.E., (1983) "Dynamic pulse buckling-theory and experiment", *SRI International*, DNA 6503H, Handbook, 333 Ravenswood Avenue, Menlo Park, California 94025, USA.
2. Petry D., Fahlbusch G., (2000) "Dynamic buckling of thin isotropic plates subjected to in-plane impact", *Thin-Walled Structures* 38(3) 267-283.
3. Bisagni C., (2005) "Dynamic buckling of fiber composite shells under impulsive axial compression", *Thin-Walled Structures* 43:499-514.
4. Chung, M., Lee, H.J., Kang, Y.C., Lim, W.-B., Kim, J. H., Cho, J.Y., Byun, W. Kim, S.J. and Park, S.-H., (2012) "Experimental study on dynamic buckling phenomena for super cavitating underwater vehicle", *International Journal of Naval Architecture and Ocean Engineering*, 4: 183-198.
5. Budiansky, B. and Roth, R.S.,(1962) "Axisymmetric dynamic buckling of clamped shallow spherical shells", *Collected Papers on Instability of Shell Structures*, NASA TN-D-1510, 761:597-606.
6. Hegglin, B., (1962) "Dynamic buckling of columns", *SUDAER No. 129:55* Department of Aeronautics & Astronautics, Stanford University, Stanford, California, USA.
7. Budiansky, B. and Hutchinson, J. W., (1964) "Dynamic buckling of imperfection sensitive structures", *Proceedings of the 11<sup>th</sup> International Congress of Applied Mechanics*, pp. 636–651, H. Götler, ed., Springer-Verlag.
8. Hutchinson, W. J and Budiansky, B., (1966) "Dynamic buckling estimates", *AIAA Journal*, 4(3) 525-530.
9. Kubiak, T., (2005) "Dynamic buckling of thin-walled composite plates with varying widthwise material properties", *International Journal of Solids and Structures*, 42: 5555–5567.
10. Ari-Gur, J., Weller T. and Singer J., (1982) "Experimental and theoretical studies of columns under axial impact", *International Journal of Solids and Structures*, 18(7)619-641.
11. Ari-Gur, J., Hunt, D. H., (1991) "Effects of anisotropy on the pulse response of composite panels", *Composite Engineering* 1(5)309 -317.
12. Ari-Gur, J., Simonetta, R., (1997) "Dynamic pulse buckling of rectangular composite plates", *Composites Part B*, 28:301 -308.
13. Labans, E., Abramovich, H., Bisagni, C., (2019) "An experimental vibration buckling investigation on classical and variable angle tow composite shells under axial compression", *Journal of Sound and Vibration* 449 (9)315e329.
14. Labans, E., Bisagni, C.,(2019) "Buckling and free vibration study of variable and constant stiffness cylindrical shells", *Composite Structures* 210:446e457.
15. Weingarten, V.I., Seide, P., Peterson, J.P., NASA SPe8007 (1965) "Buckling of ThineWalled Circular Cylinders", *NASA Space Vehicle Design Criteria e Structures*.
16. Labans, E, Bisagni, C. Buckling and free vibration study of variable and constant–stiffness cylindrical shells, *Composite Structures* 210:2019:446–457.
17. Zaczynska, M., Abramovich, H., Bisagni, C. (2020) "Parametric studies on the dynamic buckling phenomenon of a composite cylindrical shell under impulsive axial compression", *Journal of Sound and Vibration* 2020:482:115462.
18. Bisagni C., (2014) "Static and Dynamic Tests of Composite Cylindrical Shells under Axial Compression", *55th AIAA/ASME/ASCE/AHS/SC Structures, Structural Dynamics, and Materials Conference*, Maryland, USA.
19. Bisagni C., (2015) "Composite cylindrical shells under static and dynamic axial loading: an experimental campaign", *Progress in Aerospace Science - special Issue* 78:107-115. DAEDALOS e Dynamics in Aircraft Engineering Design and Analysis for Light Optimized Structures.
20. Mania, R.J. "Dynamic buckling of thin-walled columns made of visco-plastic materials" (2010, in Polish), *Science notebook* 1059, Dissertations of Sciences. 387, Lodz University of Technology.

## Dynamic buckling of Fiber Metal Laminate Structure

Monika Zaczyńska<sup>1</sup>, Radosław J. Mania<sup>2</sup>

### Abstract

The dynamic buckling phenomenon of hybrid multilayer Fiber Metal Laminate structure was presented. The analysis was performed on short thin-walled channel section columns subjected to axial compressive impulse loading. The dynamic buckling investigation was carried out numerically using the Finite Element Method. Three samples differentiate in the laminate stacking sequence were considered. The analysis of dynamic buckling phenomena was performed using both geometric criteria and failure criteria. This approach allows getting to know the behaviour of the multilayer FML structure under pulse loading. The effect of initial geometric imperfection, laminate stacking sequence and the shape of the pulse load on the dynamic stability was also analysed. Results depicted the lowest resistance of the investigated channel FML columns to the rectangular-shaped pulse loading and the lowest one - for the columns subjected to triangular-shaped pulse load. Three analysed profiles, varying in GFRP stacking sequences, presented similar behaviour under pulse compressive loading. The parametric analysis reveals the yielding of the aluminium outer layers as a dominant failure mechanism in FML composite.

### 1. Introduction

In the aerospace industry, the strength to weight ratio is a crucial factor during the design process. Thus thin-walled structures are commonly used. Nowadays, GLARE structures are used, e.g. as elements of stiffening the fuselage [1]. Stringers are usually implemented to the fuselage as channel, zed and omega section thin-walled profiles. Thin-walled structures are prone to the loss of stability which is a very dangerous phenomenon for them. Buckling of the structure can occur under both static and dynamic loading. Aerospace constructions are usually subjected to impulse loading. Nevertheless, currently, the aircraft design and certification procedures are based on non-restrictive static loads, often leading to overestimating design weight. Simultaneously, numerous studies have shown that the structure behaviour under dynamic pulse load is more complex than that under static loading.

Multilayer structures in the aerospace industry, such as GLARE (Glass laminate aluminium reinforced epoxy), are commonly used. Fibre Metal Laminate materials have many advantages resulting from used components. The combination of lightweight materials - aluminium alloy and fibre composite, allows expected high strength to weight ratio to achieve. The FML structure is approximately 10% lighter than aluminium alloy while maintaining similar strength. However, the critical advantage of the hybrid FML structure compared to classic composite materials is high resistance to crack propagation [2, 3]. Nevertheless, the FML structure also has some drawbacks. They include a complex failure mechanism which may occur, like in metals, due to a crack. However, in multilayer structures, the phenomenon of

<sup>1</sup> [monika.zaczyńska@p.lodz.pl](mailto:monika.zaczyńska@p.lodz.pl), [radoslaw.mania@p.lodz.pl](mailto:radoslaw.mania@p.lodz.pl), [monika.zaczyńska@p.lodz.pl](mailto:monika.zaczyńska@p.lodz.pl)

<sup>2</sup> [radoslaw.mania@p.lodz.pl](mailto:radoslaw.mania@p.lodz.pl), [monika.zaczyńska@p.lodz.pl](mailto:monika.zaczyńska@p.lodz.pl), [radoslaw.mania@p.lodz.pl](mailto:radoslaw.mania@p.lodz.pl)

fibre breaking, matrix breaking, debonding of fibres from the matrix or delamination could occur. For this reason, the strong necessity to get to know the response of thin-walled FML structure under dynamic pulse loading exists [4]. The obtained results will significantly broaden the knowledge in the field of dynamic stability of thin-walled multilayer structures.

## 2. Subject of the study and methodology

The analyses were performed on short columns made of FML material. The GLARE structures consisted of three metal layers, and two doubled prepreg sheets were investigated. The mechanical properties of FML constituents (2024-T3 - an aluminium alloy and TVR 380 600 M12 26% R-glass - glass unidirectional epoxy fibre-reinforced prepreg) determined experimentally and analytically [5 - 7], together with the stress limits, are listed in Table 1.

The thickness of the individual aluminium sheet is equal to  $t_{al} = 0.30$  mm while the composite layer  $t_p = 0.26$  mm, which gives the total wall thickness of  $t_t = 1.94$  mm. Three FML stacking sequences of different fiber orientation in the GFRP layers, were considered: C1 [Al/0/90/Al/90/0/Al]<sub>s</sub>, C2 [Al/90/0/Al/0/90/Al]<sub>s</sub> and C5 [Al/0/0/Al/0/0/Al]<sub>s</sub>.

Table 1: Mechanical properties and stress limits of FML's constituents.

TVR 380/26%	$E_1$ (GPa)	$E_2$ (GPa)	$\nu_{12}$ (-)	$\nu_{23}$ (-)	$G_{12}$ (GPa)	$G_{23}$ (GPa)	$X_T$ (MPa)	$X_C$ (MPa)	$Y_T = Z_T$ (MPa)	$Y_C = Z_C$ (MPa)	$S$ (MPa)	$\rho$ [g/cm <sup>3</sup> ]
	53.90	14.92	0.28	0.40	5.49	5.33	1534	800	75	500	58	1.8
Al 2024- T3	$E$ (GPa)	$\nu$ (-)	$E_t$ (GPa)	$R_{0.2}$ (MPa)	$\rho$ [g/cm <sup>3</sup> ]							
	77	0.3	0.77	359	2.7							

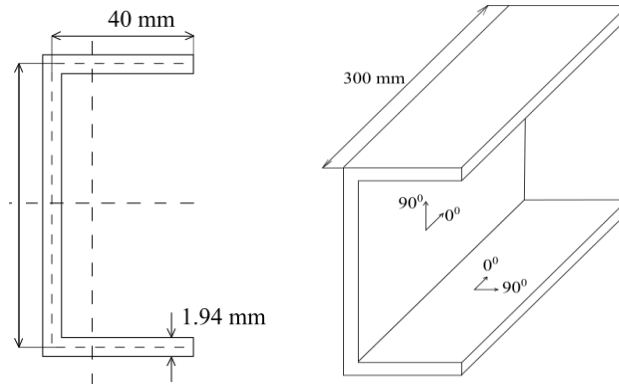


Figure 1: Overall dimensions of considered channel section FML column.

The channel section profiles were  $L = 300$  mm long. The width of the column web was equal to 80 mm, while the flanges 40 mm. The corner radius of the web and flange junction equals 1.75 mm. The buckling analyses were carried in few steps out using ANSYS 2018 finite element commercial software [8].

### 1) Static buckling analysis

The phenomenon of loss of stability under static compressive loading was analyzed in the linear eigenvalue buckling analysis. The Block Lanczos method was used. A linear static buckling analysis was conducted to determine the magnitude of the buckling load and corresponding to its buckling mode. Results of the numerical studies were confronted with the results of laboratory tests.

## 2) Modal analysis

Modal analysis was carried out numerically to obtain the natural frequencies of the FML column. The period of fundamental natural flexural vibrations of analysed column  $T$  was used in the dynamic buckling analysis as a reference time for pulse duration.

## 3) Dynamic buckling analysis

The implicit Newmark time integration method was applied in the transient analyses. To get to know the behaviour of GLARE column under pulse loading, a parametric study was performed for studying the effect of the laminate stacking sequence and pulse shape. Critical dynamic buckling load was assessed based on dynamic stability criteria and failure criteria. Following criteria were applied: Volmir criterion [9], Budiansky-Hutchinson (B&H) criterion [10], the Petry-Fahlbusch (P&F) criterion [11] and LaRC04 failure criterion [12].

## 3. FE model

Numerical calculations were conducted in the environment of Ansys software based on FEM. The channel profile model was meshed with the SHELL181 elements. The geometrical model reflects the middle surface of all panel walls. In the nodes representing the bottom columns support, the displacement in the direction perpendicular to the walls and in the direction along the axis of the column was set to zero. In the nodes located in the upper column edge, the direction perpendicular to the wall was also constrained. For those upper nodes, a constant value of displacement along the column axis was coupled. The analysed columns were subjected to uniaxial compression. The constant displacement of the loaded edge was ensured thus, the loading was applied as a compressive force at one node. To reflect the laboratory test conditions [13] (a shallow groove), the movement in the direction perpendicular to the walls in the distance c.a. 0.5mm at both columns edges was constrained. A detailed description of the numerical model could be found in [14].

Table 2 Buckling load and period of flexural natural vibrations.

	Method	Sample		
		C1	C2	C5
Buckling load $P_{cr}$ [kN]	FEM	29.384	29.016	29.547
	Experiment	31.453	-	29.836
Period of natural flexural vibrations $T_i$ [ms]	FEM $T_1$	1.980	1.913	2.007
	FEM $T_2$	1.374	1.342	1.392
	FEM $T_3$	1.357	1.322	1.362
	FEM $T_4$	1.072	1.045	1.081
	FEM $T_5$	0.930	0.934	0.927

## 4. Results

### 4.1. Static buckling test and modal analysis

The static buckling analysis was performed numerically, and then the results were compared with the outcomes of the laboratory test. During the experiment, the static buckling analysis was performed for sample C1 and C5. Buckling loads were determined from Linear Buckling Analysis in FEA and experimentally using the P-w method, the P-w<sup>2</sup> method, the Koiter's approach, the inflexion point method [14]. The results of FE computations and the average value of critical load from laboratory test are presented in Table 2. The comparison of the period of flexural vibration for five modal modes is listed also. Significantly high results agreement between the analysed samples was obtained, both in the buckling load and period of natural vibration. It confirms the dominant role of aluminium layers in the

FML structure response. The differences in the buckling load estimation are less than 7%, which confirms the FE model's correctness.

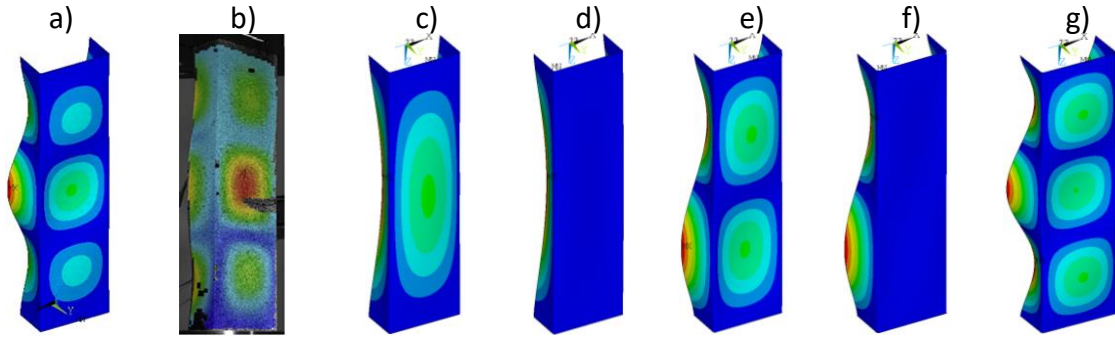


Figure 2: Modes for sample C1: a) first buckling mode from FEM, b) buckling mode from the test, c) the first modal mode, d) the second modal mode, e) the third modal mode, f) the fourth modal mode, g) the fifth modal mode.

For one exemplary sample, the shape of the buckling and modal modes were compared, as presented in Fig. 2. It should be mentioned that the same shape of buckling and the modal mode was obtained for all analysed profiles. Fig. 2a and Fig. 2b show the buckling mode obtained from Ansys software and laboratory test. After buckling, three half-waves in the longitudinal direction arose. When the modal modes are analysed (Fig. 2c-g), one can observe that just the fifth modal mode corresponds to the lowest buckling mode. Thus, in the further dynamic buckling analyses, it was decided to assume the pulse load duration equal to  $T_5$  the period of fifth mode of natural vibration.

Table 3 Equation described the considered buckling shapes.

	Pulse shape		
	Rectangular	Triangular	Sinusoidal
Equation	$0 \leq t \leq T \quad P(t) = P_0$ $T \leq t \leq 2T \quad P(t) = 0$	$0 \leq t \leq T \quad P(t) = \frac{P_0}{2t}$ $T \leq t \leq 2T \quad P(t) = 0$	$0 \leq t \leq T \quad P(t) = P_0 \sin\left(\frac{\pi t}{T}\right)$ $T \leq t \leq 2T \quad P(t) = 0$

#### 4.5. Dynamic buckling analyses

In the dynamic buckling analyses as a benchmark of the structure resistance to pulse loading, the critical value of Dynamic Load Factor ( $DLF_{cr}$ ) was assumed. The  $DLF$  was defined as the ratio of pulse amplitude ( $P_0$ ) to the lowest static buckling load ( $P_{cr}$ ) [14]. The structure response to pulse loading was monitored in time twice the pulse duration, i.e.,  $t = 2T_5$ . In the dynamic buckling investigation introduced an initial geometric imperfection of the lowest buckling mode shape with the amplitude  $w_0 = 0.1t_t$ . The research was performed for three stacking sequences C1, C2 and C5 and three pulse shapes: rectangular, triangular and sinusoidal. Equations described the pulse load for considered shapes are listed in Table 3. During the analysis, two parameters were tracked:  $U_{x_{max}}/t_t$  and  $U_{x_{LBA}}/t_t$ .  $U_{x_{max}}/t_t$  is defined as the ratio of the maximum absolute value of the deflection (observed during dynamic analysis) to the total column wall thickness.  $U_{x_{LBA}}$  is the deflection of a point in the flange, where the maximum absolute value of the deflection was observed in the Linear Buckling Analysis (LBA) solution. Firstly, the effect of the pulse shape on the dynamic buckling resistance was studied. As an example, results for sample C5 are presented in Fig. 3. Based on the change of dimensionless deflection with the increase of the pulse load, one can observe the pronounced effect of the pulse shape on the structure response. The highest deflection for rectangular-shaped pulse load was perceived and the lowest one for triangular pulse. However, in the range  $DLF = 1.6 \div 1.8$  the maximum deflection in the column subjected to the sinusoidal and triangular pulse load obtains similar values. During the analysis, the failure in the FML component

was also tracked. The failure initiation in at least one layer is depicted in Fig. 3 by red dots. It could be observed that for the highest linear impulse magnitude - rectangular one, failure initiated for DLF = 1.2, while for the others, the damage started for DLF = 1.4.

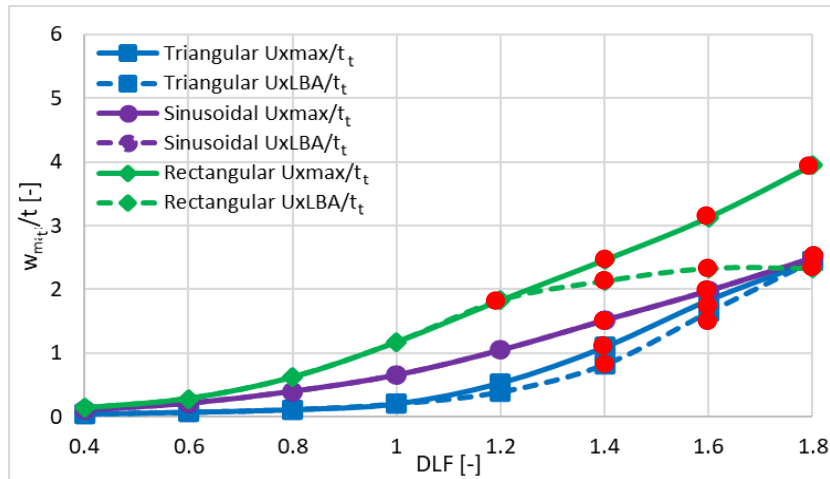
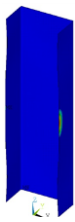
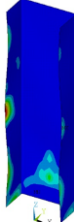


Figure 3: The influence of the shape of the pulse load on the dynamic response for sample C5.

In Table 4, the map of failure in FML components under the loading leading to the first layer failure is presented. For the triangular pulse, the failure in one layer (L1) appeared under the loading of DLF = 1.4. For the sinusoidal pulse load, the yielding in two layers occurred (L1 and L7) for the same pulse amplitude. With the increase of the pulse amplitude [14] - for rectangular-shaped pulse load, the failure was observed for lower load amplitude - for DLF = 1.2. A significant influence of pulse shape on the failure localization was observed too. For triangular and rectangular pulse loading, the failure has begun at the column bottom edge. In contrast, for the sinusoidal loading, it was localized in the channel half-height. For each considered layer arrangement, the failure initiates in the outside metal layers.

Table 4 The influence of the shape of the pulse load on the FML C5 sample component's failure initiation.

Triangular pulse shape	Sinusoidal pulse shape		Rectangular pulse shape		
Layer L1	Layer L4	Layer L7	Layer L1	Layer L4	Layer L7
 $\sigma_{max} = 360\text{MPa}$	 $\sigma_{max} = 363\text{MPa}$	 $\sigma_{max} = 362\text{MPa}$	 $\sigma_{max} = 364\text{MPa}$	 $\sigma_{max} = 360\text{MPa}$	 $\sigma_{max} = 364\text{MPa}$

In Table 5, the critical values of the Dynamic Load Factor are listed. For the Volmir criterion, the exact value of  $DLF_{cr}$  was determined, while for the others, the range of pulse load was assessed. The B&H criterion was the range with the most rapid deflection increase, while for Volmir and LaRC04 – the range of pulse amplitude where the failure could initiate. Based on the results presented, it could be observed that the dynamic deflection criteria (Volmir and B&H) are in an agreement with failure criteria. The LaRC04 criterion overestimates the critical pulse load amplitude. The other criteria present high agreement in coefficient  $DLF_{cr}$  estimation. The highest resistance to pulse loading was observed for the structure subjected to a triangular pulse load.

Table 5 Critical Dynamic Load Factor for analyzed pulse shapes.

Dynamic buckling criterion	DLCr[-]		
	Triangular	Sinusoidal	Rectangular
Volmir	1.37	1.18	0.94
Budiansky - Hutchinson	1.2 – 1.4	1.2 – 1.4	1.0 – 1.2
Petry - Fahlbusch	1.2 – 1.4	1.2 – 1.4	1.0 – 1.2
LaRC04	n/a	n/a	1.4-1.6

In the second step, the effect of the laminate stacking sequence was investigated. The results are presented in Fig. 4 for the column subjected to rectangular-shaped pulse load. Comparison of the column responses shows the highest agreement for low pulse amplitudes. However, with the increase of pulse loading magnitude, starting with DLF = 1.2, some differences appear. The dimensionless deflection obtained for the sample C5 column is slightly lower than the other ones. This effect - higher resistance of sample C5 to pulse loading increases with load amplitude.

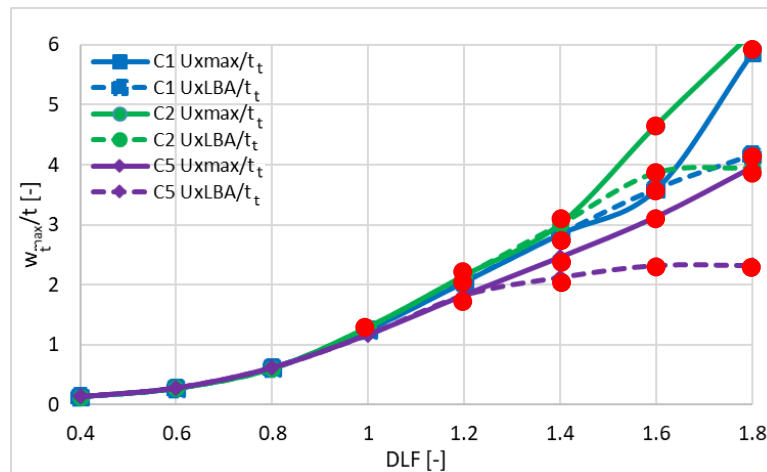


Figure 4: The influence of laminate stacking sequence on the dimensionless column deflection [14].

To investigate how the fibre orientation in FRP sheets affected the FML structure failure, the failure map was compared for the loading DLF=1.6. Under this value of pulse amplitude, the damage in the composite layers was also observed. Results are presented in Table 6 (failure in metal sheets) and Table 7 (failure in FRP layers). High agreement between analysed samples in the localization of the yielding area in aluminium layers is observed. In contrast, the differences are visible in the FRP sheets map of failure. For the failure in composite layers, the matrix failure map and fibre failure map are presented separately. The various fibre orientation causes it. In layers with longitudinal fibres ( $0^0$ ), the damage appears near the web and flange corner (see Layer L2 and L6 for C1 and Layer L6 for C5 in Table7). The failure localization changes for plies with  $90^0$  fibre orientation. For those layers, the failure near the free edge of the flange is noticed.

Table 8 includes the comparison of  $DLCr$  values for samples C1, C2 and C5. A straightforward conclusion could be drawn based on these results: the fibre orientation in FML structure has a negligible effect on the dynamic stability. Slightly higher resistance to pulse loading was obtained for the C5 stacking sequence. High agreement between applied criteria was obtained.

Table 6 The map of failure in metal sheets for considered samples.

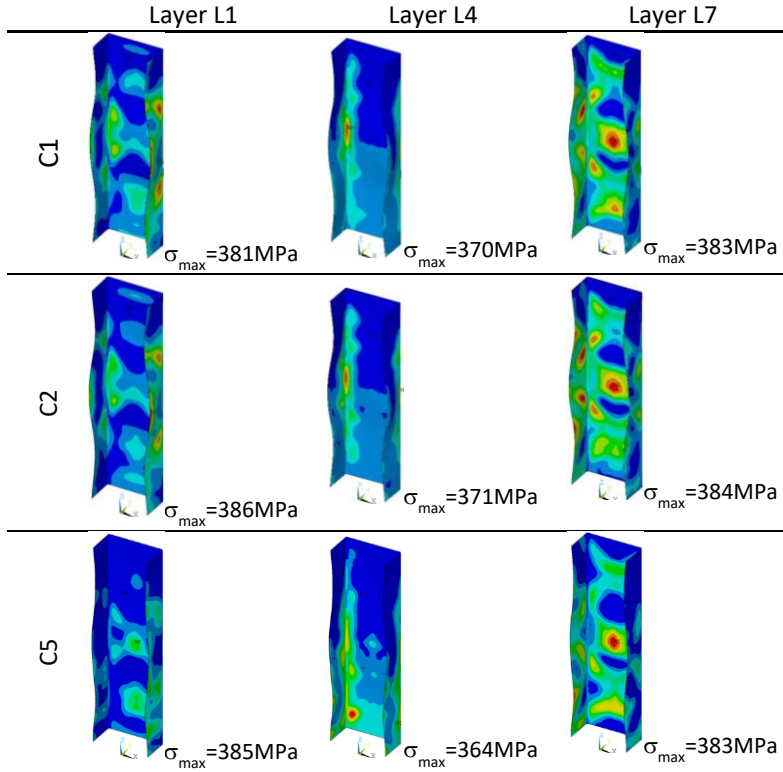


Table 7 The map of failure in FRP sheets for considered samples.

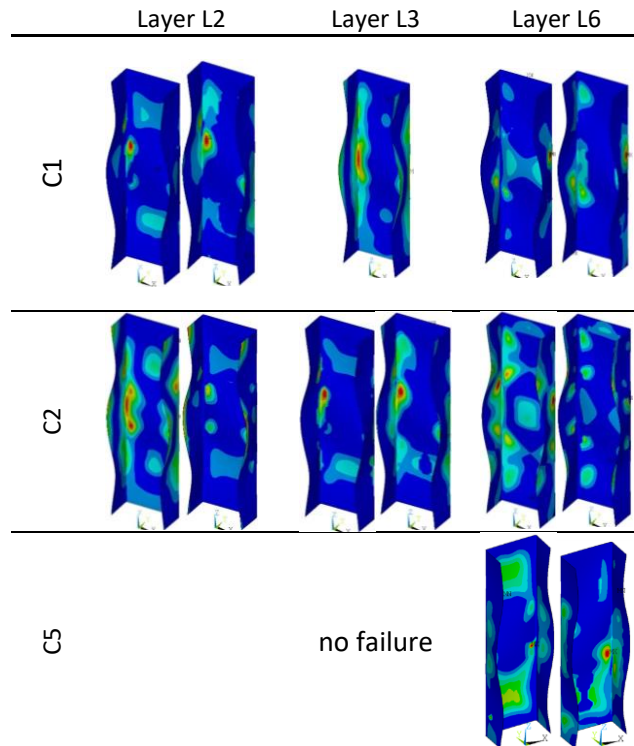


Table 8 Critical Dynamic Load Factor for analyzed samples.

Dynamic buckling criterion	DLF <sub>cr</sub> [-]		
	Sample C1	Sample C2	Sample C5
Volmir	0.93	0.92	0.94
Budiansky - Hutchinson	1.00 – 1.20	1.0 – 1.2	1.0 – 1.2
Petry - Fahlbusch	1.40 – 1.45	1.2 – 1.4	1.4 – 1.6
LaRC04	0.80 – 1.00	0.8 – 1.0	1.0 – 1.2

## 5. Conclusions

Numerical investigation of dynamic buckling phenomenon was performed on short channel section Fiber Metal Laminate column. The FE analyses were carried out on an experimentally validated model. The effect of the laminate stacking sequence and shape of pulse load on the dynamic stability was studied. The critical Dynamic Load Factor was estimated based on the deflection dynamic stability criteria and failure criteria. Results present high agreement between applied criteria. Analysis of the failure mechanisms reveals aluminium yielding as a primary failure mechanism developed under pulse loading. Results also depicted a significantly high effect of the pulse shape on dynamic stability. FML structure is the most resistant to triangular-shaped pulse loading and the less resistant to the rectangular pulse shape. Three considered samples of different laminate stacking sequence present similar resistance to pulse loading. Only for sample C5 the critical Dynamic Load Factor is slightly higher.

## References

1. Vlot A., Gunnink J.W. (2001) "Fibre metal laminates: an introduction", *Springer*.
2. Botelho E.C., Silva R.A., Pardini L.C., Rezende M.C. (2006) "A review on the development and properties of continuous fiber/epoxy/aluminum hybrid composites for aircraft structures". *Mater Res* 9:3:247–56
3. Sinmazçelik T., Avcu E., Bora M.Ö., Çoban O. (2011) "A review: Fibre metal laminates. background. bonding types and applied test methods." *Materials and Design* 32: 3671-3685
4. Mania R.J. (2018) "Multi-criterial assessment of dynamic buckling of FML thin-walled profiles", *XV Konf. N-T, TKI 2018, Mikotajki*
5. Kamocka M., Zglinicki M., Mania R. J. (2016) "Multi - method approach for FML mechanical properties prediction", *Composites Part B: Engineering*, 91:135-145
6. Kamocka M., Mania R.J. (2017) "Assesments methods of mechanical properties of composite materials", *Mechanics and Mechanical Engineering*, 21:4:1001-1014
7. Kamocka M., Mania R.J. (2015) "Analytical and Experimental Determination of FML Stiffness and Strength Properties", *Mechanics and Mechanical Engineering* 19:2:141–159
8. User's Guide ANSYS® 18.2; Ansys, Inc.: Canonsburg, PA, USA, 2018
9. Volmir S.A. (1972) "Nieliniejnaja dinamika plastinok i oboloczek" *Science, Moscow*
10. Budiansky B. (1965) "Dynamic buckling of elastic structures: criteria and estimates." *Report SM-7, NASA CR-66072*
11. Petry D., Fahlbusch G. (2000) "Dynamic buckling of thin isotropic plates subjected to in-plane impact." *Thin-Walled Structures* 38:267–283
12. Pinho S.T., Dávila C.G., Camanho P.P., Iannucci L., Robinson P. (2005) "Failure Models and Criteria for FRP Under In-Plane or Three-Dimensional Stress States Including Shear Non-linearity", Tm-2005-213530, no. February, p. 68.
13. Banat D., Kolakowski Z., Mania R.J. (2016) "Investigations of FML profile buckling and post-buckling behaviour under axial compression", *Thin-Walled Structures*, 107,335–344
14. Zaczynska M., Mania R.J. (2021) "Investigation of dynamic buckling of Fiber Metal Laminate thin-walled columns under axial compression", *Composite Structures* (in press)
15. Kubiak T. (2013) "Static and Dynamic Buckling of Thin-Walled Plate Structures", *Springer, New York*.

## Influence of manufacturing process technology on buckling behaviour of thin-walled, GFRP columns with a square cross-section

Paweł Czapski<sup>1</sup>, Tomasz Kubiak<sup>2</sup>

### Abstract

In this study, static compression of thin-walled, composite columns with square cross-section is presented. The influence of heat transfer during the manufacturing process of thin-walled column on the behaviour during compressive load has been investigated. Two series of the columns made of GFRP laminate with symmetric layup  $[45/-45/45/-45]_s$  were manufactured using the autoclaving technique. To check the way of heat transfer during the curing process the two different methods of retaining and giving off heat from the produced element during its cooling in the autoclave process by using other process durations and mandrels were used. It is a well-known fact that different curing speeds and cooling rates affect the distribution of residual stresses inside the structure that could have a significant impact on its future structural performance. In case of this study, the target of these operations was to verify how the manufacturing process and generated in this process residual stresses are affecting buckling and post-buckling behaviour of the structures. Therefore, manufactured in this manner two series of four specimens were experimentally tested. The static compression tests were performed on Instron universal testing machine employing additionally a contactless digital image correlation system GOM ARAMIS<sup>®</sup>. Additionally, the numerical model has been developed and used to perform FEM analysis including cooling process (manufacturing procedure simulation) and compression test (operating load simulation). The obtained load-deflection and load-shortening function enabled to determine critical loads and post-critical stiffness and verify how different distribution of residual stresses is affecting the stability of such columns.

### 1. Introduction

Material engineering is a field of science undergoing rapid development. Different applications of the materials dictate new requirements and create new possibilities. In the places where weight optimisation is necessary, it is most suitable to use composite materials. Composites are currently present in multiple hi-tech industries: aircraft (Degenhardt et al. 2014), renewable energy (Zangenberg et al. 2014), automotive (Bisagni et al. 2005), medicine (Fujihara et al. 2004), sport and many others. Although this type of materials is continuously being developed, certain phenomena are inherent and not yet fully resolved. Residual stresses are an example. They appear both in metallic and composite structures and might have a significant influence on the structural integrity of the systems. In metallic structures, residual stresses are most frequently an effect of processing, such as cold-form shaping or welding (heat-affected zones). Solutions to the problem include annealing or tempering, which are well-known methods of releasing residual stresses. In the case of composite materials, especially laminates, the problem and

---

<sup>1</sup> PhD Student, Lodz University of Technology, [pawel.czapski@edu.p.lodz.pl](mailto:pawel.czapski@edu.p.lodz.pl)

<sup>2</sup> Professor, Lodz University of Technology, [tomasz.kubiak@p.lodz.pl](mailto:tomasz.kubiak@p.lodz.pl)

solutions are not well investigated, and there are no standard methods of releasing the residual stresses trapped in the material.

The origins of residual stresses in laminates might be various – the most popular reason of their occurrence is chemical shrinkage. During curing of the laminate, the matrix changes its properties. After taking out the element from the form, it slightly changes its shape which is evidence of internal stresses in the material. In more complex elements, the shape imposes extra constraints, preventing post-curing deformations. In such a case, stresses are trapped inside the structure. Another origin of residual stresses in laminates is thermal expansion. This refers to composites cured in high temperatures – e.g. the autoclaving process. Due to thermal expansion, thermal stresses are formed in individual plies even in unconstrained laminate. Since the autoclave is a place where manufactured elements are constrained (by a tool providing the proper shape and pressure in order to avoid deformations during the process), applied DOFs are transformed into residual stresses. These stresses can be predicted by analytical approaches or the Finite Element Method.

This study shows that residual stresses also influence the buckling and post-buckling behaviour of thin-walled, GFRP structures with a square cross-section. A series of the experiments, supported by FE modelling, was performed to prove the hypothesis that residual stresses have a significant influence on the mechanical response of such structures.

## 2. The object of the study

The object of this study is to analyse the influence of autoclaving curing parameters on the buckling and post-buckling behaviour of thin-walled composite columns with a square cross-section. The main goal of this research is to confirm or refute the hypothesis that residual stresses affect the structural stability of this type of structures. The work builds on the research performed by the authors in this field.

### 2.1. Static compression tests

The study covers static compression of squared cross-section columns made of eight-layered GFRP prepreg tape with the following dimensions:  $80 \times 80 \times 240$  mm (width  $\times$  height  $\times$  length of the tube) – see Fig 1 a).

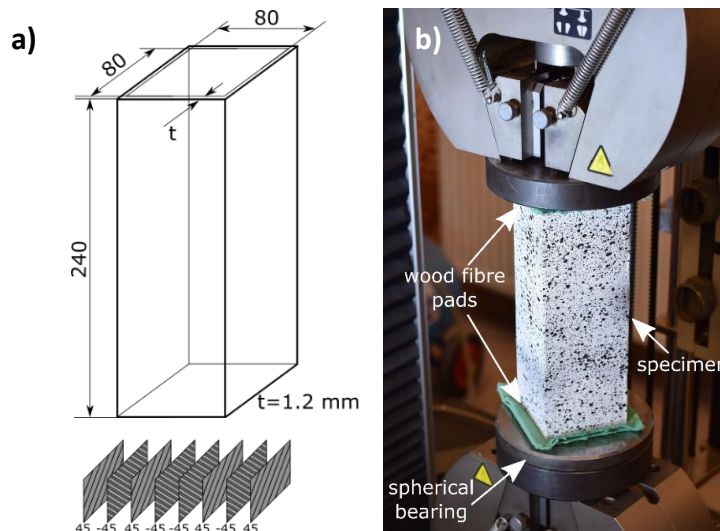


Figure 1: a) geometry of the columns b) compression test stand with the sample during the experiment

The nominal thickness of one ply is equal to 0.15 mm (1.2 mm total wall thickness). For the purpose of this study, one symmetric to the mid-plane laminate code was investigated:  $[45/45/45/-45]_s$ . Two series of columns were produced (four specimens per series):

- Columns produced in a nominal (suggested by the producer of the pre-preg tape) curing cycle on an empty aluminium mandrel (core), denoted as CS-EC (Fig 2)
- Columns produced in a modified pre-preg (according to the suggestions of the producer and in ranges enabling the resin to cross-link but limiting the thermal dynamics of the process) curing cycle on a full aluminium mandrel (core), denoted as CS FC (Fig 3).

A more detailed description of manufacturing process parameters is presented in sub-chapter 2.2.

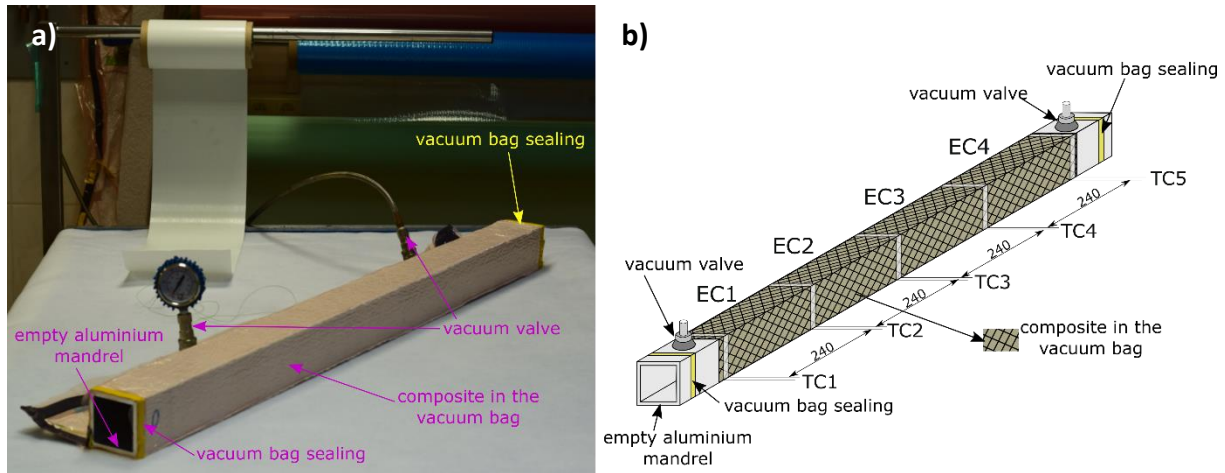


Figure 2: Manufacturing of EC columns: a) composite in the vacuum bag b) scheme of laminate formation on an empty aluminium mandrel

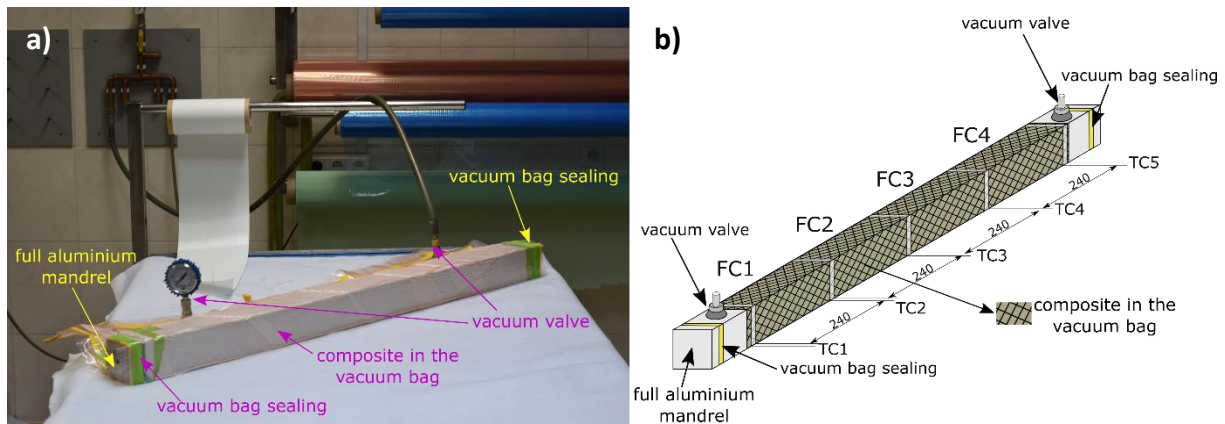


Figure 3: Manufacturing of FC columns: a) composite in the vacuum bag b) scheme of laminate formation on a full aluminium mandrel

When manufactured, eight specimens were subjected to quasi-static compression tests (compression speed equal to 1 mm/min), which were performed on an Instron Universal Test Stand upgraded by the Zwick-Roel company. The specimens were placed between two self-aligning grips. The bottom grip was equipped with a spherical bearing. In order to eliminate the effect of imperfect contact between the edges of the columns and compression plates, wood fibre pads were applied. The picture of the experimental test stand is presented in Fig 1 b).

## 2.2. Manufacturing of the columns

The columns were manufactured using the autoclave curing process (Scholz Maschinenbau, Germany), based on vacuum bag assistance. The pressure in the autoclave was equal to 0.5 MPa. Vacuum bags were

subjected to underpressure equal to 0.08 MPa. The material from which columns were laminated was pre-preg tape: E-glass 1200tex fibres immersed in NTPT THINPREG™ 402 epoxy resin.

Moreover, two curing cycles were applied – see both processes time-temperature relationship presented in Fig 4. The first method was to laminate the columns on a hollowed aluminium mandrel (standard aluminium square profiles with dimensions: 80 × 80 mm, a thickness equal to 6 mm and corner radius 1 mm) and apply a nominal curing cycle (suggested by the producer of the pre-preg tape). The vacuum bag was formed in such a manner that there was no obstacle for the heat flow inside the tube – see Figure 2. The specimens formed in this process are denoted as EC. In the second case, a composite tube was wrapped on a full aluminium profile (denoted as FC, see Figure 3) and a modified curing cycle (with respect to the nominal one, but still allowed by the producer) was applied. The modification of the curing process for the potential reduction of internal stress, was carried out by significantly limiting the heating and cooling rates while maintaining the required temperature values for the proper course of the polymerisation process. The designed modification of the curing process is justified by the fact that the achieved level of minimal viscosity is usually higher in processes with a higher temperature gradient. The length of the minimal viscosity platform increases, positively contributing to the reduction of the risk of thermally induced stresses, ensuring proper conditions for favourable resin flow (Bieniaś et al. 2014 and Liu et al. 2006).

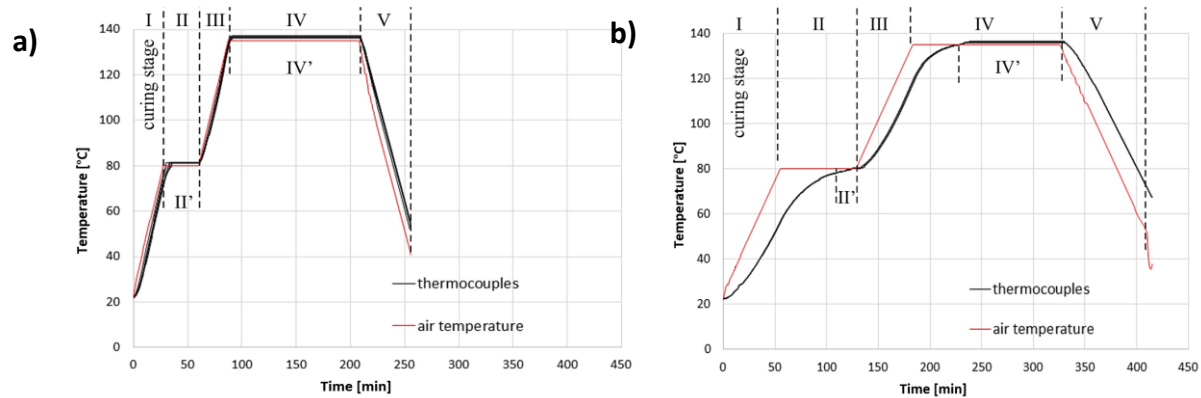


Figure 4: Time-temperature dependence in the autoclaving process for **a)** EC – empty core specimens **b)** FC – full core specimens

### 2.3. Material properties of the laminate

The material under inspection, cured in the autoclave E-glass 1200tex fibres immersed in NTPT THINPREG™ 402 epoxy resin laminate, was subjected to five fundamental strength tests performed according to ASTM D3039, ASTM D6641 and ASTM D3039 allowing to determine the properties of the laminate under consideration (see Table 1). The properties are E – Young’s modulus, G – Kirchoff modulus, T – tensile strength, S – shear strength, C – compressive strength and  $\alpha$  – coefficient of thermal expansion (CTE). The indices 1 and 2 stand for fibres and matrix directions, respectively.

Table 1 Material properties of the laminate

$E_1$	$E_2$	$G_{12}$	$\nu_{12}$	$T_1$	$T_2$	$S_{12}$	$C_1$	$C_2$	$\alpha_1$	$\alpha_2$
[GPa]	[GPa]	[GPa]	[–]	[MPa]	[MPa]	[MPa]	[MPa]	[MPa]	[ $10^{-6}/^{\circ}\text{C}$ ]	[ $10^{-6}/^{\circ}\text{C}$ ]
30.1	9.4	9.2	0.26	1265.6	32.9	135.0	565.5	109.5	18.8	6.24

### 3. FEM computations

The numerical simulations to analyse the buckling and post-buckling behaviour the commercial software ANSYS was employed. A four-node shell element with six degrees of freedom at each node (Shell 181) was used to discretise the tubes. The model was discretised by 7200 elements (each wall was divided into 60 elements along the longitudinal direction and 30 elements along the width direction). Along the width direction, bias was applied for future thermal analysis. This means that near the corners, where two walls are connected, the mesh was densified. The experience of the authors shows (Czapski & Kubiak 2015 and Kubiak 2017) that this amount of elements prevents the model from being too rigid, especially when large deflections are expected (i.e. deflections larger than double wall thickness).

The linear buckling analysis (LBA) was performed to determine buckling mode, which are used as a shape of initial geometrical imperfection with amplitude equal to 10% of the wall thickness in further step of numerical calculations. In order to find the equilibrium paths of the columns the nonlinear analysis were performed. As during the experiment two buckling modes corresponding to three and four halfwaves occurred, these buckling modes were the only analyzed ones. The maximal compressive load applied in the non-linear analysis was equal to a force approximately four times larger than that achieved from LBA. The geometrical and FE models with boundary conditions of column compression tests are presented in Figs 5 a) and b), respectively.

To include the thermal residual stresses the nonlinear calculations was preceded by the simulation of the cooling down of the laminate in the autoclave. The FE model is built in such a manner that the column is wrapped on an undeformable, aluminium mandrel (twice longer than the tubes) and cooled down from a temperature of 135°C to room temperature 23°C (a difference equal to 112°C). The limitation of this approach is that from the point of view of numerical modelling, there is no distinction between curing on an empty (EC) and full (FC) core. The material properties of the laminate were taken from Table 1 and are temperature-independent. Frictional contact between the composite and aluminium is assumed (friction coefficient equal to 0.2). Moreover, pressure  $p$  is applied to the laminate, which is equal to the sum of pressure in the autoclave (0.5 MPa) and pressure in the vacuum bag (0.08 MPa); therefore, the total applied pressure  $p$  is equal to  $p = 0.58$  MPa. In order to fix the model in the computational space, the mandrel is constrained at its ends (see Fig 5 c)). The values of the thermal expansion coefficients were taken from the performed experiment (see Table 1).

In both schemes of simulations with and without residual stresses, i.e. including (further denoted as residual) or not including (further denoted as no residual) cooling down numerical simulations, the settings are the same. The failure was not followed. Buckling loads, presented in Table 2, were determined using two different methods basing on the results of the simulation. In particular the wall deflection and shortening of the columns have been extracted from this data. One of the most popular methods of quantifying buckling from experimentally obtained or in nonlinear analysis the load-deflection curves is known as the  $P-w^2$  method. This approach is based on transforming the force-wall deflection diagram into force-squared wall deflection plot so that that the post-buckling state can be approximated by straight line. The intersection of this line with the underlying data can then be used to provide an estimate for the buckling load. The second method is based on force-shortening of the column curve which is based on the fact that at buckling, the curve changes its slope (results obtained using this method are abbreviated by LSC – Load Shortening Curve). Both methods are precisely described in (Paszkiwicz & Kubiak 2015 and Czapski & Kubiak 2016). Buckling loads obtained from FEM studies are given in Table 2. Load-shortening curves obtained from FEM are presented in Fig 7, together with experimental results.

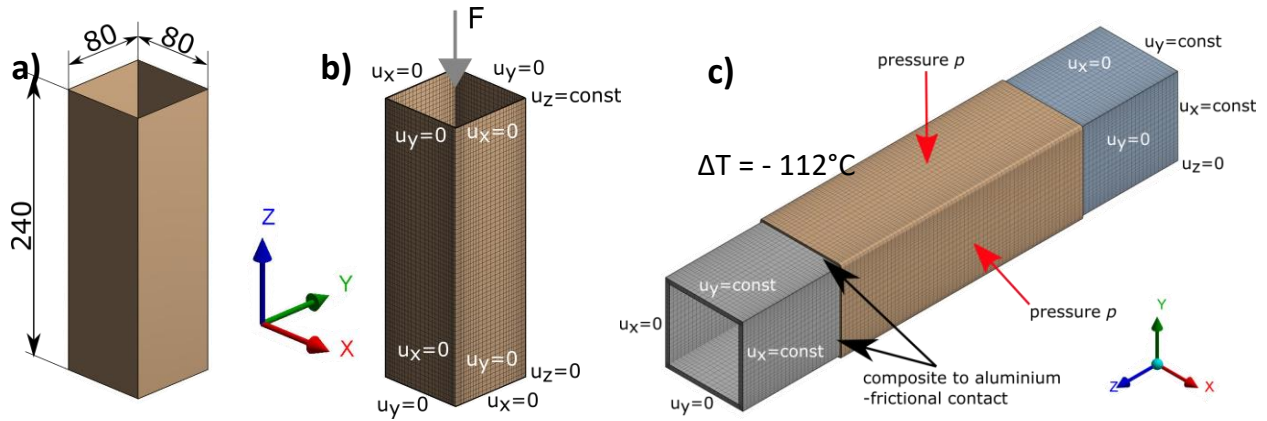


Figure 5: a) Geometrical and b) finite element models of column compression with applied boundary conditions and c) FE model of the curing (cooling) of the laminate process – column wrapped in aluminium profile

Table 2 Critical loads achieved from non-linear FEM studies

# halfwaves	Model	Critical load [kN]		
		$P-w^2$	Load-shortening curve	Average
3	no residual	5.28	5.28	5.28
	residual	10.64	10.72	10.68
4	no residual	5.31	5.76	5.54
	residual	10.43	10.37	10.40

#### 4. Experiment vs FEM

The buckling loads obtained from the experiment were determined thanks to the maps of the deformations obtained from contactless digital image correlation system Aramis and they are presented in Table 3. Moreover, the comparison of the experimental loads with the results of FE modelling is given in Fig 6. Green bars correspond to the buckling loads of the columns produced in FC curing process while black – EC curing process. Blue and red lines correspond to the results of FE modelling – the model which does not include residual stresses and which does include residual stresses, respectively. It is important to mention that from the point of numerical modelling, there is no difference between EC and FC curing process, as the model does not include rheology of the polymer matrix.

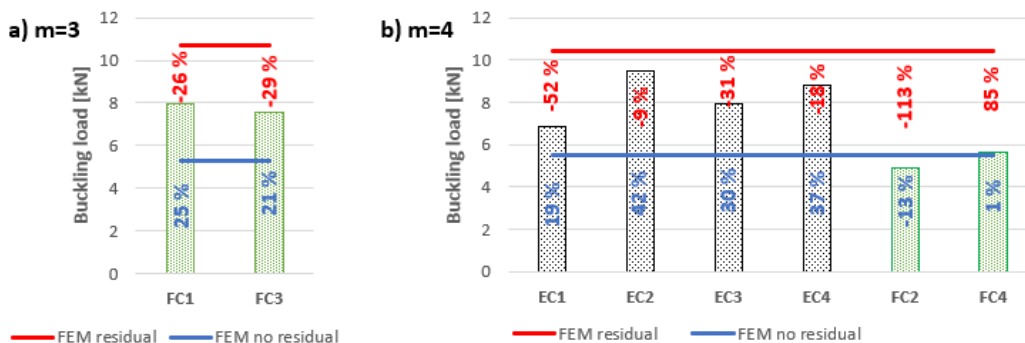


Figure 6: Comparison of buckling loads obtained from FEM and the experiment presented in the form of a bar chart in a) three halfwaves and b) four halfwaves, and errors between FE and experimental results.

The positive error indicates that the FE model underestimates the experiment

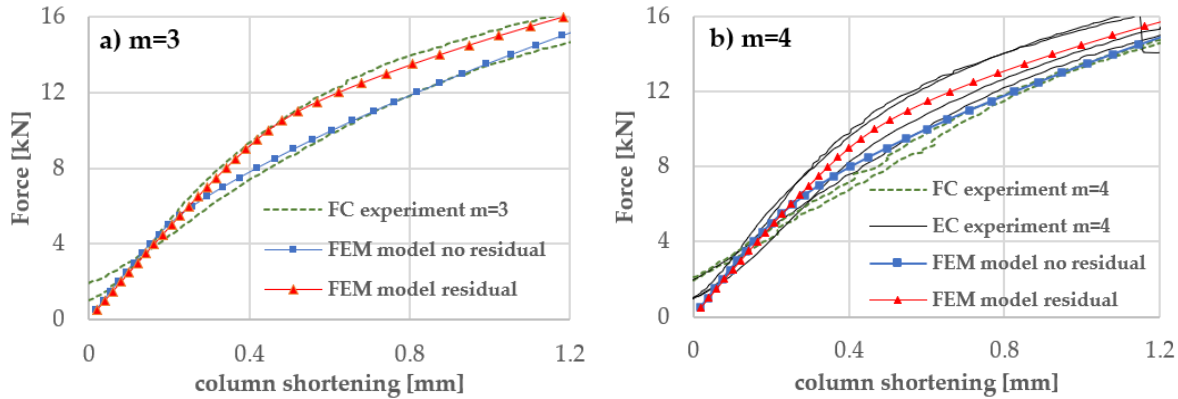


Figure 7: Comparison of FEM and experimental load-shortening cruves for buckling modes a) three halfwaves and b) four halfwaves

Table 3 Experimentally obtained buckling loads

		EC1	EC2	EC3	EC4	FC1	FC2	FC3	FC4
# halfwaves $m$		4				3	4	3	4
Buckling loads [kN]	P- $w^2$ method	6.37	10.03	8.79	8.65	7.29	5.14	8.01	5.09
	LSC	7.29	8.98	7.10	9.01	8.61	4.62	7.08	6.12
Average		6.83	9.50	7.95	8.83	7.95	4.88	7.54	5.61

One can draw several conclusions from the buckling loads presented in Table 3 and the comparison of the experimental results presented in Fig 6. The first conclusion is that for all specimens, except FC2, experimentally determined critical forces are higher than the estimation given by the FE model, which does not consider residual stresses. In similar studies, related to the buckling behaviour of thin-walled structures but with an open cross-section, the FE model without residual stresses taken into account provided results which were higher in terms of the critical loads and post-buckling stiffness compared to the experiment. This regularity can be simply explained by multiple imperfections of the structure (e.g. shape or quality of manufacturing etc.) In the analysed case, the FE model without residual stresses underestimates the experimental buckling loads. A similar conclusion can be drawn for post-buckling stiffness by looking at the load shortening curves presented in Figs 7 a) and b). Only two specimens, FC2 and FC4 (FC samples with buckling mode equal to 4), had lower stiffness than the model without residual stresses. This means that residual stresses play an essential role in this problem, and a model including them should be taken as a reference. With respect to this model, all safety factors should be assumed during the design of this type of structures.

The second issue is related to the differences between the buckling behaviour of samples EC and FC. Although the FE model is not able to distinguish between them (the model does not include the rheology and cure dynamics of the resin, where all differences may find their origins), the differences are visible. The EC specimens produced on an empty aluminium mandrel had buckling load and post-buckling stiffness always higher than FE model without the residual stresses. Also, the buckling mode was the same across all samples (four halfwaves). Compared to the FC, two buckling modes were observed: three and four halfwaves indicating lower repeatability than the EC series. Samples FC2 and FC4, where four halfwaves occurred, had significantly lower buckling loads and post-buckling stiffness. In the cases of FC1 and FC3, where three halfwaves were observed, buckling loads and post-buckling stiffness were higher than the FE

model without residual stresses. Equilibrium paths and load-shortening curves fit between two FE models curves.

## 5. Conclusions

The research, taking into account the results of similar studies available in the literature (Banat et al. 2016, Dębski et al. 2014 and Debski et al. 2013), showed that thermally induced stresses in thin-walled composite columns with a square cross-section play a significant role in the buckling and post-buckling behaviour of this type of structures. What is more important is that they improve the structural stability of the columns. According to the conducted experiment, it was proven that the presence of residual stresses inside the structure can increase buckling loads up to 42% compared with the results of FE modelling, assuming no pre-stress. In order to prepare the numerical model, which is capable of including thermal residual stresses, it is necessary to determine one extra material property of the laminate: the coefficient of thermal expansion, as it was presented here. Apart from FE modelling, the experiment delivered another piece of information, which is the influence of the manufacturing method on the buckling behaviour of this kind of structures. Cure dynamics was an important issue inspected experimentally. It turned out that the process with the smaller temperature gradient (FC) might have a potential influence on lowering residual stresses inside the material and, consequently, exerting smaller critical forces. To the contrary, the speed of the process does not affect the quality of the microstructure.

## Acknowledgments

The investigations have been performed under a research project funded by the Ministry of Science and Higher Education of Poland – Diamond Grant No 0036/DIA/2017/46.

## References

- Degenhardt R., Castro S.G.P., Arbelo M.A., Zimmerman R., Khakimova R., Kling A. (2014) Future structural stability design for composite space and airframe structures. *Thin-Walled Struct.* 81, 29–38
- Zangenberg J., Brøndsted P., Koefoed M. (2014) Design of a fibrous composite preform for wind turbine rotor blades. *Mater Des.* 56, 635–41
- Bisagni Ch., Di Pietro G., Frascini L., Terletti D. (2005) Progressive crushing of fiber reinforced, composite structural components of a formula one racing car. *Compos. Struct.* 68, 491–503
- Fujihara K., Teo K., Gopal R., Loh P.L., Ganesh V.K., Ramakrishna S et al. (2004) Fibrous composite materials in dentistry and orthopaedics: review and applications. *Compos. Sci. Technol.* 64, 775–88
- Bieniaś J., Gliszczynski A., Jakubczak P., Kubiak T., Majerski K. (2014) Influence of autoclaving process parameters on the buckling and postbuckling behaviour of thin-walled channel section beams. *Thin Walled Struct.* 85, 262–70
- Liu L., Zhang B.M., Wang D.F., Wu Z.J. (2006) Effects of cure cycles on void content and mechanical properties of composite laminates *Comp Struct.* 73(3), 303–309
- Czapski P., Kubiak T. (2015) Numerical and experimental investigations of the post-buckling behaviour of square cross-section composite tubes. *Compos. Struct.* 132, 1160–1167
- Kubiak T. (2017) Numerical model of postbuckling behavior of GFRP beams subjected to pure bending, *International Journal for Computational Methods in Engineering Science and Mechanics* 18:1, 13-24
- Czapski P., Kubiak, T. (2016) Selected problems of determining critical loads in structures with stable post-critical behaviour. *Mechanics and Mechanical Engineering* 20, 79–95
- Paszkiwicz M., Kubiak T. (2015) Selected problems concerning determination of the buckling load of channel section beams and columns. *Thin-Walled Struct.* 93, 112–121
- Banat D., Kolakowski Z., Mania R.J. (2016) Investigations of fml profile buckling and post-buckling behaviour under axial compression. *Thin-Walled Struct.* 107, 335–344
- Debski H., Teter A., Kubiak T. (2014) Numerical and experimental studies of compressed composite columns with complex open cross-sections. *Compos. Struct.* 118, 28–36
- Debski H., Kubiak T., Teter A. (2013) Experimental investigation of channel-section composite profiles' behavior with various sequences of plies subjected to static compression. *Thin Walled Struct.* 71, 147–154

## **Numerical and experimental post-buckling analysis of slender thin-walled GLARE members subjected to compressive loading**

Dominik Banat<sup>1</sup>, Radosław J. Mania<sup>2</sup>

### **Abstract**

This study deals with a post-buckling analysis of thin-walled GLARE members subjected to axial compressive loading. Considered slender and top-hat-shaped GLARE samples are made of hybrid composite that consists of alternating thin layers of aluminum alloy sheets and unidirectional glass fiber-reinforced prepregs. Composite specimens were axially compressed in laboratory tests by the electromechanical static testing unit of Instron that provided a displacement control loading. Deformations were measured in full load range until specimen fracture by means of Aramis 3D non-contact optical equipment that uses the digital image correlation (DIC) method. The behavior of thin-walled GLARE members was analyzed with the primary attention to post-buckling response. Simultaneously, numerical simulations by FEM were performed to predict the load-carrying capacity of thin-walled sections. Comparative post-buckling analysis was performed based on nominal stress state in both non-degraded and degraded structure. For the latter, the damage evolution law was introduced by the material property degradation method (MPDG), which allowed a gradual reduction of material stiffness based on assumed damage variables. The impact of damage variables on the laminate load-carrying capacity and predicted damage mode was investigated. Presented numerical results were found to be in a high agreement with experimental damage tests.

### **1. Introduction**

Fiber-reinforced composite materials have seen significant advancements in a variety of industries in recent years. Significant developments can be recognized in the fields of aerospace engineering, transportation, automobile, nuclear, wind power, and civil engineering [1,2]. Composite materials gained the greatest attention after the development of synthetic binding resins that allowed for the manufacturing of multi-layered laminates [3]. Herein, some of the multi-layered composite applications are based on unidirectional glass fiber-reinforced prepregs and sheets of aluminum alloy – GLARE type of Fiber Metal Laminates (FML). Such plies combination ensures high material strength as well as improved damage and fatigue tolerances [4]. GLARE laminates have better strength and stiffness than other standard materials when compared on a unit weight basis. Furthermore, the combination of different laminates, as well as varying fiber alignment and fiber volume ratios, can have a considerable impact on composite performance. This brings up a lot of opportunities for composite manufacturers to create composite-based components that are tailored to a specific industrial application [5,6]. It has attracted a lot of interest among researchers over the last several years to study the behavior of

---

<sup>1</sup> PhD Candidate, Lodz University of Technology, <dominik.banat@dokt.p.lodz.pl>

<sup>2</sup> Professor, Lodz University of Technology, <radoslaw.mania@p.lodz.pl>

composites under various loading conditions, aiming to make recommendations for their potential benefits in industrial applications [7–9].

Innovative multi-layered composite structures can be used in challenging designs solely due to considerable improvements in the semi-analytical methods (SAM) [10] and computational tools in the Finite Element Method (FEM). Nevertheless, one of the most challenging aspects of simulating composite materials' post-buckling responses is predicting the ultimate load-carrying capacity [11]. This comprises a comprehensive analysis in order to provide the material with the greatest strength and damage tolerance while maintaining a low weight of the structure. Numerical simulations and advanced techniques are shown to be especially significant in the analysis of post-buckling behaviors of slender thin-walled members [12]. Thin-walled composite sections may gradually lose their load-carrying capacity in the post-buckling condition, resulting in various types of permanent structural damage such as delamination, fiber rupture, matrix cracking, or a combination of these failure modes [13,14]. Herein, the fiber damage initiation and propagation were recognized as the primary factor that leads to the loss of load-carrying capacity in the multi-layered GFRP laminates subjected to uniaxial compressive loading [11].

According to a literature survey, predicting the post-buckling response of thin-walled composite members requires modelling material stiffness degradation based on selected criteria [15,16]. Thus, failure initiation and propagation can be analyzed by means of progressive failure analysis (PFA). The degradation model and methodologies for selecting damage variables for PFA applied to laminated composites have been discussed in several studies [17–19]. The initial results that included PFA applied to FML stability analysis has been already discussed in Refs. [20]. The main aim of this research is to compare numerical analysis performed based on nominal stress state in both non-degraded and degraded structure with the main focus on the post-buckling response. Hence, numerical analysis and experimental tests were carried out in order to forecast the loading conditions that lead to loss of load-carrying capacity.

## **2. Subject of the study and methodology**

The subject of this study is the 7-layered hybrid laminate made of alternating plies of aluminum alloy 2024 T3 with single-ply thickness equal to 0.3 mm and glass-epoxy unidirectional fiber-reinforced prepreg TVR 380 M12 26% R-glass (Hexcel™) with a single-ply thickness equal to 0.25 mm. Mechanical properties of GLARE constituents has been presented in Table 1. Additionally, Poisson's ratios were equal to  $\nu = 0.33$  for aluminum as well as  $\nu_{12/13} = 0.269$  and  $\nu_{23} = 0.400$  for the composite plies, respectively. The multi-method approach for determining FML mechanical properties has been discussed in the comparative study by Kamocka et al. [21].

Aluminium [GPa]		GFRP prepreg [GPa]	
E	72	$E_1$	53.90
G	27.07	$E_2$	14.92
$R_{0.2}$	$359 * 10^{-3}$	$E_3$	14.92
$E_{tang}$	$720 * 10^{-3}$	$G_{12}$	5.49
		$G_{23}$	5.33
		$G_{13}$	5.49

Various layer arrangements of GLARE samples were based on the fiber's alignment in the composite layer. GLARE laminates were manufactured by autoclaving technique, which provided the high-quality multi-layered composite. Laboratory procedures of ultrasonic non-destructive testing to assess the quality of GLARE specimens produced by the autoclave technique has been discussed in Refs. [22].

In this study, analysis was performed for slender and thin-walled top-hat-shaped sections. Dimensions of the geometry and one of the selected GLARE lay-up configuration are presented in Fig. 1.

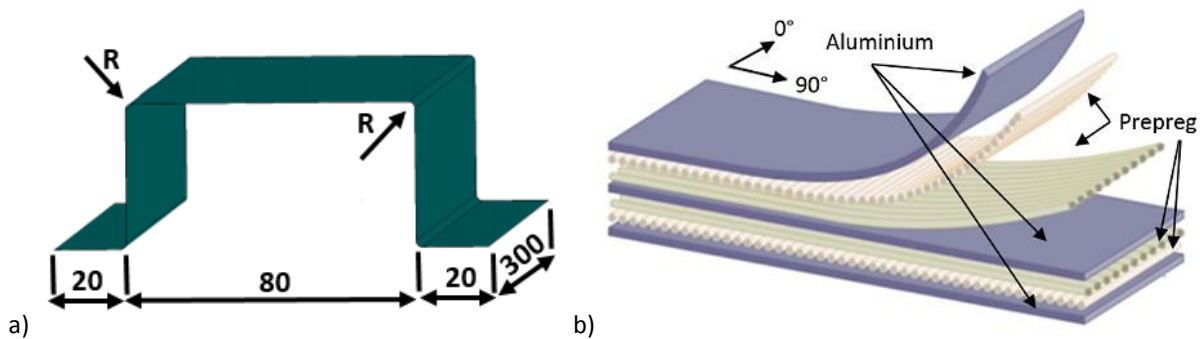


Figure 1: Dimension of top-hat shaped sections (a) and laminate configuration (b)

### 3. Methodology

Composite specimens were axially compressed in laboratory tests by means of a static testing unit of Instron upgraded with Zwick/Roel control software. Electromechanical strength testing machine had a maximum capacity of 200kN, for which applied screw-type testing machine provided a displacement control loading. During experimental tests, deformations were measured by Aramis 3D non-contact optical equipment based on digital image correlation (DIC), which allowed investigating columns behavior in full load range until fracture. Furthermore, customized plate rigs were installed on the test stand's upper and lower crossheads to ensure uniform axial compression. Thus, samples were placed in the chamfered groove to avoid lateral displacement of the loaded edges, as shown in Fig. 2. For considered slender and thin-walled members, such a solution ensured satisfactory agreement with the simply supported boundary conditions [8].

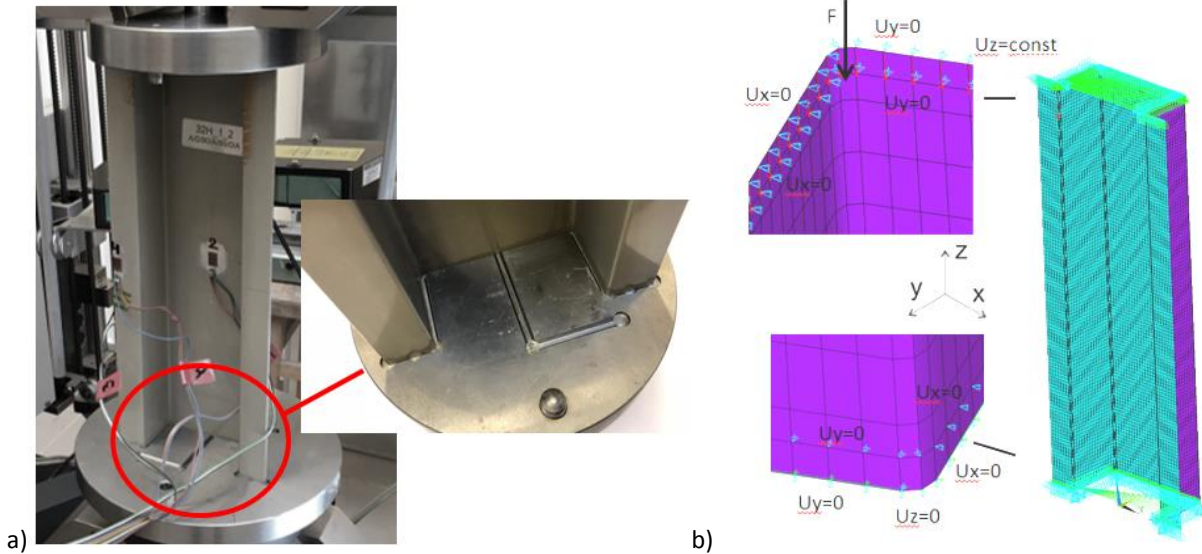


Figure 2: Experimental test stand (a) and diagram of column load (b) for top-hat shaped member subjected to uniform compressive loading [20]

Simultaneously, numerical simulations by FEM were performed to predict the post-buckling equilibrium paths and load-carrying capacity. The multi-layered GLARE structure was modelled in FEM commercial software package ANSYS by means of implemented structural element SHELL181. This a four-node element with six degrees of freedom at each node is generally dedicated to modelling plate structures. The shell element and available section options in the FE application allowed to define individual plies of the laminate separately i.e., thickness, material properties and main axes of the orthotropic material. The connections between layers were not modelled. Mesh convergence analysis was not performed for top-hat section study, but mesh size (2mm) was adopted based on author's previous experience with FML of different open cross-section shapes (including Z-shape and channel sections) [15]. In current model of top-hat shaped member, mesh refinement was applied to design the effects of milled grooves, which were modelled by constrains in the direction perpendicular to the profile walls at the distance of 2 mm from profiles' edges (as shown in Fig. 2). For circular corners between web-flange and flange-rib junctions of the section, the mesh refinement was also achieved with a local cylindrical coordinate system application. As a result, nodes near rounded edges were constrained in the direction perpendicular to the profile walls, which was in agreement with assumed simply supported boundary conditions. Mesh convergence analysis could be performed in further studies that include investigation of the continuum damage model, wherein energy dissipated is a function of the element size causing mesh-dependent results.

The non-linear problem was solved initially by the incremental Newton– Raphson procedure whereby the stiffness matrix was updated with each iteration and equilibrium paths were calculated based on nominal stress state in a non-degraded structure. Secondly, the damage evolution law was introduced by the material property degradation method (MPDG), wherein the Hashin criterion was used to monitor the failure initiation. Hence, based on the damage variables, the stiffness was gradually reduced in the area where failure was initiated. Material property degradation could be solely applied to composite plies, i.e. outer layers (L1 and L7) and the inner layer (L4). In this respect, the post-buckling response of aluminum plies was analyzed separately in a non-degraded structure by means of the Huber-Mises-Hencky criterion. Thus, numerical simulations of load carrying capacity (LCC) were carried out simultaneously for two different numerical models:

1. Progressive failure models with the application of material properties degradation method (FEM\_degraded). The load-carrying capacity was determined based on the maximum load obtained from the post-critical equilibrium path.
2. Geometrically non-linear analysis without degradation of material properties (FEM\_non\_degraded). This analysis was carried out for the selected aluminum layer using the Huber-Mises-Hencky criterion. The load-carrying capacity was determined based on the equivalent stresses that were compared to the yield point defined in aluminum material properties.

For the purpose of this manuscript paper, results of numerical and experimental analysis have been presented for selected laminate configuration Al/0/25/Al/25/0/Al.

#### 4. Results and discussion

Numerical geometrically non-linear analysis was carried out to forecast the load-carrying capacity based on post-buckling equilibrium paths for models with non-degraded material properties (FEM\_non\_degraded) and with degraded material properties (FEM\_degraded) calculated based on the abovementioned MPDG procedure. In the latter, various values of damage variables for fiber ( $d_f$ ) and matrix ( $d_m$ ) were used to control material stiffness reduction. Therefore, numerical simulations were performed for the following models:

- FEM\_non\_degraded:  $d_f=0$  and  $d_m=0$
- FEM\_degraded\_1:  $d_f=0.5$  and  $d_m=0.5$
- FEM\_degraded\_2:  $d_f=0.5$  and  $d_m=0.75$
- FEM\_degraded\_3:  $d_f=0.75$  and  $d_m=0.75$
- FEM\_degraded\_4:  $d_f=1$  and  $d_m=1$

Note that  $d_{f/m}=1$  indicates complete stiffness reduction after failure initiation. Results of load carrying capacity – LCC, determined for various numerical models and experiment, are given in Table 2. In order to analyze the consistency between FEM and experimental tests, the relative differences of obtained results were also calculated. Detailed analysis of load-shortening curves obtained from the geometrically non-linear analysis is presented in Refs. [22].

Table 2: Load-carrying capacity determined by experiment and FEM

Sample	Method	Load Carrying Capacity - LCC [kN]	EXP vs FEM [%] (Relative difference)
	Experimental test (ARAMIS)	79.59	
Al/0/25/Al/25/0/Al	Numerical FEM_degraded_1	82.62	3.67
	Numerical FEM_degraded_2	82.11	3.07
	Numerical FEM_degraded_3	81.98	2.91
	Numerical FEM_degraded_4	81.18	1.96
	Numerical FEM_non_degraded	80.67	1.34

Based on the above, the relative difference between experimental and numerical results of LCC prediction varies between 1.96% - 3.67% for models with material stiffness reduction (FEM\_degraded\_1

– FEM\_degraded\_4). The highest agreement was achieved for model FEM\_degraded\_4 that assumed  $d_{f/m}=1$ , leading to complete material stiffness reduction after failure initiation in specific finite elements. This confirms that high values of material stiffness degradation parameters used in FEM analysis allow achieving the highest level of correlation between experiment and FEM results. Similar findings were obtained in a study of 8-layered GFRP structural members exposed to compression [11], in which damage variables equal to or greater than 0.9 provided acceptable relative deviations between experiment and numerical results (below 10%). Nevertheless, in this study, the highest agreement between experiment vs FEM was achieved for FEM\_non\_degraded model ( $d_f=0$  and  $d_m=0$ ). It assumed load-carrying capacity prediction based on Huber-Mises-Hencky criterion at the point when equivalent stresses exceed the aluminum yield limit. In such a model, the relative difference of obtained results was equal to 1.34%. This indicates that the entire laminate response is governed by aluminum layers, and the Huber-Mises-Hencky criterion can be applied to determine the loss of load-carrying capacity of considered 7-layered GLARE members.

Subsequently, analysis of the damage status (0 - undamaged, 1 - damaged, 2 - entirely damaged) was performed for top-hat-shaped members subjected to compressive loading. Damage maps were calculated for loads corresponding to LCC based on geometrically non-linear solutions in several models with progressive failure method (FEM\_degraded\_1 – FEM\_degraded\_4). FEM simulations were performed for all composite plies in the various configuration of GLARE laminates. The post-buckling response of each composite ply is similar with regards to the member mid-plane due to the symmetry of laminate lay-ups. Thus, the example of progressive damage mode for FEM\_degraded\_3 type in the selected composite layer is shown in Fig. 3.

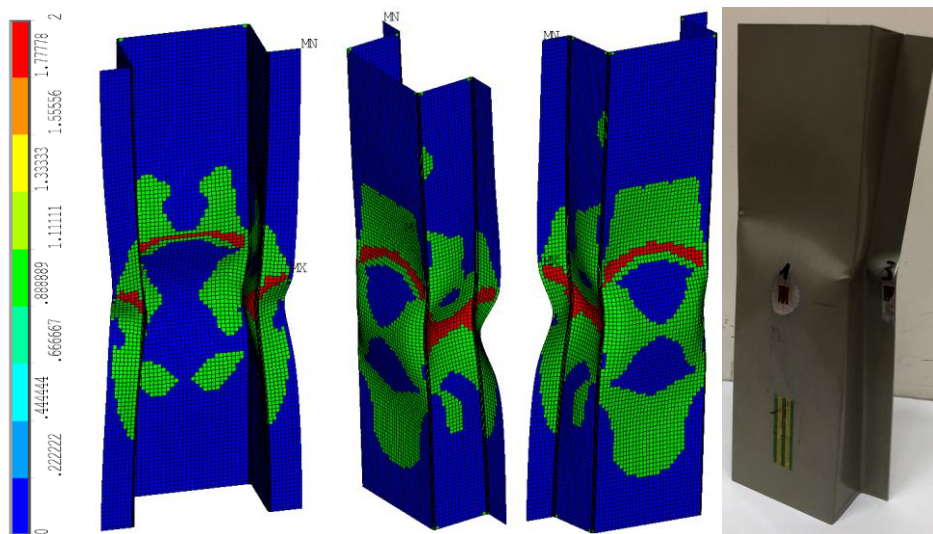


Figure 3: Numerical progressive damage modes of top-hat shaped member (FEM\_degraded\_3) and experimentally damaged sample

The damage modes revealed by progressive failure analysis allowed for the prediction of laminate failure at the web-flange intersection and ribs along the member's mid-length. Herein, the mid-length of the members' free edges are extensively subjected to the bending effect in the post-buckling state. Due to the symmetry of the top-hat section geometry, a similar damage state was detected on both sides of the specimen. Numerical results were found to be in good agreement with the experimentally damaged

GLARE sample. This confirms that boundary conditions defined in the numerical model corresponded to uniform axial compression of thin-walled members subjected to laboratory tests.

## 5. Conclusions

This study investigated post-buckling response and the load-carrying capacity of GLARE members subjected to axial compressive loading. Various numerical models were taken into account to determine loading conditions that lead to loss of load-carrying capacity. Relative differences between numerical and experimental results were within the range of 1.34% - 3.67% for selected in this study laminate configuration (Al/0/25/Al/25/0/Al). The numerical and experimental results show high agreement, which confirms that the prepared numerical model can be used as an effective tool to forecast the load-carrying capacity of slender GLARE members. Herein, the highest consistency of 1.35% (relative difference between experiment vs FEM) was achieved for the model without degradation of material properties (FEM\_non\_degraded). The load-carrying capacity was determined based on the equivalent stresses calculated by the Huber-Mises-Hencky criterion, which were compared to the yield limit defined in aluminum material properties. This indicates that the entire laminate response is governed by aluminum layers, and the failure criterion applied in aluminum plies could be used to determine the load-carrying capacity of 7-layered GLARE members.

The damage status of top-hat-shaped members was also assessed using progressive failure analysis. This allowed forecasting laminate failure at the mid-length of member free edges and at the web-flange intersection. In comparison to FEA, the experimentally damaged specimens had similar fracture modes and regions of failure initiation. As a result, progressive failure analysis using MPDG could be applied for detecting laminate damage areas in thin-walled sections subjected to compression. The identification of several numerical models allowed determining that high values of material stiffness degradation parameters used in FEM analysis provide the highest level of agreement between experiment and numerical results. This can also provide a recommendation for a similar study of slender and thin-walled members subjected to compressive loading. Other loading scenarios, however, should be subjected to a similar comparative analysis of FEA models and experimental validation.

Furthermore, based on the progressive failure analysis carried out for similar Z-shaped FML members [15], it has been observed that damage variables should take into consideration different values for fiber and matrix failure in order to simulate various susceptibility to damage of these two constituents. However, based on the analysis performed in this study for model FEM\_degraded\_2 ( $d_f = 0.5$  and  $d_m = 0.75$ ) with various damage variable for fiber and matrix, this has been noted that damage variables have solely minor impact on the sample's load-carrying capacity. This also confirms that aluminum layers govern the post-buckling response and the material stiffness reduction within composite plies does not affect significantly the GLARE performance in the post-critical state.

## Acknowledgments

The author has obtained funding as part of financing a doctoral scholarship from the National Science Center, No. UMO-2019/32/T/ST8/00605.

## References

- [1] Moreira, P.M.G.P., da Silva, L.F.M., de Castro, P.M.S.T. (2012). "Structural connections for lightweight metallic structures." *Advanced Structured Materials*, Springer, 1 241-254.
- [2] Chróścielewski, J., Miśkiewicz, M., Pyrzowski, Ł., Sobczyk, B., Wilde, K. (2017). "A novel sandwich footbridge - Practical application of laminated composites in bridge design and in situ measurements of static response." *Composites Part B: Engineering*, 126 153–161.

- [3] Jones, R.M. (1999). "Mechanics of Composite Materials." *Materials Science and Engineering Series*, Taylor & Francis, 2 18-36.
- [4] Vlot, A., Gunnink, J.W. (2001). "Fibre Metal Laminates: An Introduction." Springer, 1 39-51.
- [5] Mania, R.J., York, C.B. (2017). "Buckling strength improvements for Fibre Metal Laminates using thin-ply tailoring." *Composite Structures*, 159 424–432.
- [6] Czapski, P., Kubiak, T. (2015). "Influence of Fibre Arrangement on the Buckling Load of Composite Plates - Analytical Solution." *Fibres and textiles in eastern Europe*, 5 92–97.
- [7] Soltani, P., Keikhosravy, M., Oskouei, R.H., Soutis, C. (2011). "Studying the tensile behaviour of GLARE laminates: A finite element modelling approach." *Applied Composite Materials*, 18 271–282.
- [8] Banat, D., Kolakowski, Z., Mania, R.J. (2016). "Investigations of fml profile buckling and post-buckling behaviour under axial compression." *Thin-Walled Structures*, 107 335–344.
- [9] Falkowicz, K., Dębski, H., Wysmulski, P., Różyło, P. (2019). "The behaviour of compressed plate with a central cut-out, made of composite in an asymmetrical arrangement of layers." *Composite Structures*, 214 406–413.
- [10] Kołakowski, Z., Mania, R.J. (2013). "Semi-analytical method versus the FEM for analysis of the local post-buckling of thin-walled composite structures." *Composite Structures*, 97 99–106.
- [11] Gliszczynski, A., Kubiak, T. (2016). "Progressive failure analysis of thin-walled composite columns subjected to uniaxial compression." *Composite Structures*, 169 52–61.
- [12] Kolakowski, Z., Mania, R.J., Grudziecki, J. (2015). "Local nonsymmetrical postbuckling equilibrium path of the thin FGM plate." *Eksploracja i Niezawodność - Maintenance and Reliability*, 17 135–142.
- [13] Calzada, K.A., Kapoor, S.G., DeVor, R.E., Samuel, J., Srivastava, A.K. (2012). "Modeling and interpretation of fiber orientation-based failure mechanisms in machining of carbon fiber-reinforced polymer composites." *Journal of Manufacturing Processes*, 14 141–149.
- [14] Kamocka, M., Mania, R.J. (2019). "Post-buckling response of FML column with delamination." *Composite Structures*, 230 111511.
- [15] Banat, D., Mania, R.J. (2018). "Progressive failure analysis of thin-walled Fibre Metal Laminate columns subjected to axial compression." *Thin-Walled Structures*, 122 52–63.
- [16] Rozylo, P., Debski, H., Wysmulski, P., Falkowicz, K. (2018). "Numerical and experimental failure analysis of thin-walled composite columns with a top-hat cross section under axial compression." *Composite Structures*, 204 207–216.
- [17] Barbero, E.J., Cosso, F.A., Roman, R., Weadon, T.L. (2013). "Determination of material parameters for Abaqus progressive damage analysis of E-glass epoxy laminates." *Composites Part B: Engineering*, 46 211–220.
- [18] Barbero, E.J., Shahbazi, M. (2017). "Determination of material properties for ANSYS progressive damage analysis of laminated composites." *Composite Structures*, 176 768–779.
- [19] Lin, Y., Huang, Y., Huang, T., Liao, B., Zhang, D., Li, C. (2019). "Characterization of progressive damage behaviour and failure mechanisms of carbon fibre reinforced aluminium laminates under three-point bending." *Thin-Walled Structures*, 135 494–506.
- [20] Banat, D., Mania, R.J. (2019). "Stability and strength analysis of thin-walled GLARE composite profiles subjected to axial loading." *Composite Structures*, 212: 338–345.
- [21] Kamocka, M., Zglinicki, M., Mania, R.J. (2016). "Multi-method approach for FML mechanical properties prediction." *Composites Part B: Engineering*, 91 135–143.
- [22] Banat, D., Mania, R.J. (2020). "Damage analysis of thin-walled GLARE members under axial compression – Numerical and experiment investigations." *Composite Structures*, 241 112102.